PROCEEDINGS



Battlespace Atmospheric and Cloud Impacts on Military Operations

(BACIMO)

Conference
1-3 December 1998

19990427 074

Held at the
Air Force Research Laboratory
Hanscom Air Force Base, MA

AFRL-VS-HA-TR-98-0103
Environmental Research Papers, No. 1217

PROCEEDINGS OF THE BATTLESPACE ATMOSPHERIC AND CLOUD IMPACTS ON MILITARY OPERATIONS (BACIMO) CONFERENCE, 1-3 DECEMBER 1998

Editor:
Paul Tattelman

6 November 1998

APPROVED FOR PUBLIC RELEASE; DISTRIBUTION UNLIMITED.



AIR FORCE RESEARCH LABORATORY
Space Vehicles Directorate
29 Randolph Road
AIR FORCE MATERIEL COMMAND
HANSCOM AIR FORCE BASE, MA 01731-3010

DTIC QUALITY INSPECTED 2

"This technical report has been reviewed and is approved for publication."

PAUL TATTELMAN
Program Manager

DONALD A. CHISHOLM
Branch Chief
Tactical Environmental Support Branch

This report has been reviewed by the ESC Public Affairs Office (PA) and is releasable to the National Technical Information Service (NTIS).

Qualified requestors may obtain additional copies from the Defense Technical Information Center. All others should apply to the National Technical Information Service.

If your address has changed, or if you wish to be removed from the mailing list, or if the addressee is no longer employed by your organization, please notify AFRL/VSOS-IMA, 29 Randolph Road, Hanscom AFB, MA 01731-3010. This will assist us in maintaining a current mailing list.

Do not return copies of this report unless contractual obligations or notices on a specific document requires that it be returned.

REPORT DOCUMENTATION PAGE

Form Approved
OMB No. 0704-0188

Public reporting burden for this collection of information is estimated to average 1 hour per response, including the time for reviewing instructions, searching existing data sources, gathering and maintaining the data needed, and completing and reviewing the collection of information. Send comments regarding this burden estimate or any other aspect of this collection of information, including suggestions for reducing this burden, to Washington Headquarters Services, Directorate for Information Operations and Reports, 1215 Jefferson Davis Highway, Suite 1204, Arlington, VA 22202-4302, and to the Office of Management and Budget, Paperwork Reduction Project (0704-0188), Washington, DC 20503.

1. AGENCY USE ONLY *(Leave blank)*	2. REPORT DATE	3. REPORT TYPE AND DATES COVERED
	6 November 1998	Scientific, Interim

4. TITLE AND SUBTITLE
Proceedings of the Battlespace Atmospheric and Cloud Impacts on Military Operations (BACIMO) Conference, 1-3 December 1998

5. FUNDING NUMBERS
PE: 63707F
PR: 2688
TA: GU
WU: 02

6. AUTHOR(S)
Editor: Paul Tattelman

7. PERFORMING ORGANIZATION NAME(S) AND ADDRESS(ES)
Air Force Research Laboratory
Battlespace Environment Division
29 Randolph Road
Hanscom AFB, MA 01731-3010

8. PERFORMING ORGANIZATION REPORT NUMBER
AFRL-VS-HA-TR-98-0103
ERP, No. 1217

9. SPONSORING/MONITORING AGENCY NAME(S) AND ADDRESS(ES)
U.S. Air Force Assistant for Battlespace Environment
Office of Defense for Research and Engineering
The Pentagon, Washington, DC

10. SPONSORING/MONITORING AGENCY REPORT NUMBER

11. SUPPLEMENTARY NOTES
Co-sponsored by the Air Force Research Laboratory, the Army Research Laboratory, and the Space and Naval Warfare Systems Center

12a. DISTRIBUTION AVAILABILITY STATEMENT
Approved for Public Release; distribution unlimited

12b. DISTRIBUTION CODE

13. ABSTRACT *(Maximum 200 words)*

These Proceedings contain the papers presented at the first Battlespace Atmospheric and Cloud Impacts on Military Operations (BACIMO) conference held at Hanscom Air Force Base, Massachusetts, December 1-3, 1998. The Air Force Research Laboratory Battlespace Environment Division at Hanscom hosted the 1998 conference.

BACIMO conferences are convened annually at the request of the Assistant for Battlespace Environments Office of Defense Research and Engineering and are co-sponsored by the Air Force Research Laboratory, the Army Research Laboratory, and the Space and Naval Warfare Systems Center (SPAWAR). BACIMO brings together the two previously separately-held Battlespace Atmospheric (BAC) and Cloud Impacts on DoD Operations and Systems (CIDOS) conferences. The conference objective is to enhance cooperation and coordination among U.S. military services, the civilian community, and allied nations in developing technology to specify and predict atmospheric and cloud impacts on military operations.

This three-day conference had over 65 presentations including video and computer demonstrations organized according to the following 9 sessions: Program Overviews; Cloud and Cloud Effects Models; Radio Propagation; Measurements of Clouds and Cloud Parameters; Modeling and Simulation (M&S) of Atmospheric and Cloud Effects; Measurements and Modeling of EO Parameters; Decision Aids; Battlespace Sensing Techniques and Applications; and Meteorological Modeling and Data Assimiliation.

14. SUBJECT TERMS
Clouds, Radio Propagation, Cloud Parameters, Atmospheric Modeling and Simulation, Cloud Modeling and Simulation, EO Parameter Measurement, EO Parameter Modeling, Decision Aids, Battlespace Sensing, Meteorological Modeling, Meteorological Data Assimilation

15. NUMBER OF PAGES

16. PRICE CODE

17. SECURITY CLASSIFICATION OF REPORT	18. SECURITY CLASSIFICATION OF THIS PAGE	19. SECURITY CLASSIFICATION OF ABSTRACT	20. LIMITATION OF ABSTRACT
UNCLASSIFIED	UNCLASSIFIED	UNCLASSIFIED	UL

Standard Form 298 (Rev. 2-89) (EG)
Prescribed by ANSI Std. 239.18
Designed using Perform Pro, WHS/DIOR, Oct 94

This page intentionally left blank.

BACIMO 98 EXECUTIVE COMMITTEE

Col Alan R. Shaffer
U.S. Air Force Assistant for Battlespace Environment
Office of Defense Research and Engineering

CONFERENCE CHAIR

Mr. Paul Tattelman
Air Force Research Laboratory
Space Vehicles Directorate
Battlespace Environment Division
Tactical Environmental Support Branch
Hanscom Air Force Base MA

TECHNICAL COMMITTEE

Mr Paul Tattelman

Dr. Juergen H. Richter
SPAWAR Systems Center
Propagation Division
San Diego CA

Dr. Alan Wetmore
Army Research Laboratory
Information Science & Technology Directorate
Battlefield Environment Division
Atmospheric Acoustics and E-O Propagation Branch
Adelphi MD

CONFERENCE COORDINATORS

Ms Jeanne McPhetres
Air Force Research Laboratory
Space Vehicles Directorate
Battlespace Environment Division
Tactical Environmental Support Branch
Hanscom Air Force Base MA

Mr René V. Cormier
Dynamics Research Corporation

This page intentionally left blank.

TABLE OF CONTENTS[1]

PAGE

Executive Committee.....iii

Preface.....xiii

Program Overviews

Eis, Kenneth E. and Thomas H. Vonder Haar
DoD's Center for Geosciences and Atmospheric Research.....3

Evans, James E.
Application of the FAA's Integrated Terminal Weather System Technology to Theatre Weather Information Support.....10

Hodur, Richard M.
Numerical Weather Prediction for the U. S. Navy.....18

Szymber, Richard J. and Doug McDonald
Joint Meteorological and Oceanographic (METOC) 2010 Vision and Architecture.....26

Tattelman, Paul
Progress Update on the AFRL Weather Impact Decision Aids Program.....31

Cloud and Cloud Effects Models

Ayer, Steven M. and Joel B. Mozer
A Distributed, Parallel Method for Texture Image Calculation in Cloud Visualization.....41

[1] **The Sessions are listed in the order of the Conference Agenda. Within Sessions, papers are listed alphabetically by first author and include both platform and poster presentations. The paper presenter is in bold type.**

PAGE

Gordon, Sara C., Guy P. Seeley, Joel B. Mozer, Alan Wetmore, Patti Gillespie, Samuel Crow and David Ligon
Objective Comparisons of Real and Synthetic Cloud Imagery.....46

Jackson, Artie, Doug Hahn and Allan Bussey
Statistical Contrail Forecasting: Using Satellite Data and Numerical Weather Prediction Model Output.....52

Mozer, Joel B. and Steven M. Ayer
Objective Techniques for Fusion and Analysis of Mesoscale NWP and Satellite-Derived Cloud Data.....57

Turkington, Ryan B. and Maureen E. Cianciolo
Cirrus Model Testing in the CSSM.....65

Radio Propagation

Boehm, Albert and Welman Gebhart
Simulated Rain Fields for Radar Propagation in FASTPROP.....75

Fast, Stephen A., Jason Nathaniel Bode and George S. Young
A Three Dimension Matching Method for Tropospheric Features.....81

Kang, Steve, Janet Stapleton and Russell Wiss
Direct Measurement of RF/EO Propagation Factors in Coastal Region.....89

Measurements of Clouds and Cloud Parameters

Caudill, Thomas R. and Donald C. **Norquist**
Three-Dimensional Cloud Depictions Based on Field Experiment Measurements.....101

Eloranta, E. W., R. E. Kuehn and R. E. Holz
High Spectral Resolution Lidar Measurements of the Backscatter Phase Function in Cirrus Clouds.....105

PAGE

Hornstein, John, Eric Shettle, Mark Daehler and Richard Bevilacqua
POAM Measurements of Stratospheric and Upper Tropospheric Clouds, Aerosols, and Ozone.....109

Huffman III, Arlie C., Thomas H. **Vonder Haar** and Graeme L. Stephens
Physical Characterization of Clouds and Precipitation using 94 GHz and 13.8 GHz Radar.....117

Kropfli, R.A., B.E. Martner, S.Y. Matrosov, R.F. Reinking, A.S. Frisch and T. Uttal
Radar and Radiometer Measurements of the Physical Parameters of Clouds and Precipitation at the NOAA Environmental Technology Laboratory.....125

Post, Madison J., Kenneth P. Moran, Brooks E. Martner and Kevin B. Widener
Unattended 35-GHz Cloud-Profiling Radar.....133

Walter, Steven J., Graeme L. Stephens and Deborah G. Vane
The CloudSat Mission.....139

Weiss-Wrana, Karin
Optical Properties of Cloud Layers Derived from Measured Particle Size Distributions.....146

Wylie, Donald P. and W. Paul Menzel
High Cloud Statistics Measured by HIRS.....155

Modeling and Simulation (M&S) of Atmospheric and Cloud Effects

Bonito, Nelson A., Harris L. Gilliam and Captain Mark M. Edwards
Enhancing Wargame Realism Through Atmospheric Effects.....165

Dailey, Peter S., Todd A. Hutchinson and Steve O. **Ouzts**
Algorithms for Real-Time Tailoring of Environmental Data for Modeling & Simulation (M&S).....174

Dailey, Peter S., Todd A. **Hutchinson,** Robert A. Reynolds, Dana Sherer, Eric A. Kelley and James R. Staudinger
Using a Numerical Weather Prediction (NWP) Model to Create Synthetic Environments for Military Training and Analysis and Cloud Animations.....182

PAGE

Dimmeler, A. and D. Clement
Modelling of the Performance of Laser Range Finders under the Influence of Obscurants.....188

Gillespie, Patti, Alan Wetmore, David Ligon and Michael Seablom
HLA Compliant Total Atmospheric Simulations in Real Tactical Scenarios.....196

McWilliams, Gary
Results of the Representational Resources Integration Experiments.....207

Noble, John M.
Scanning Fast Field Program (SCAFFIP).....213

Shanks, Joseph G., Bruce V. Shetler, Steven J. Heising and William A.M. Blumberg
Assessment of Spectral-Spatial Information Content using CLDSIM / GENESSIS / MOSART and Optimal Filters.....221

Smalley, David J. and Joel B. Mozer
AFRLDIAG: Tailored Meteorological Products for M&S.....230

Wetmore, Alan E., Patti Gillespie, David Ligon, Mike Seablom and Robert Reynolds
An Object-Oriented Paradigm for the WAVES/TAOS Interface.....235

Measurements and Modeling of EO Parameters

Andrews, William S., Johnathan R. Costa and Gilles Roy
Modelling Concentration Distributions Within Transient Aerosol Plumes.....243

Burke, Hsiao-hua K., Michael K. Griffin, Dan C. Peduzzi, Kristine E. Farrar, Carolyn A. Upham, Steve Adler-Golden and Mike W. Matthew
Retrieval of Atmospheric Water Vapor from Hyperspectral Imaging Sensors.....251

Frederickson, Paul, Kenneth Davidson, Carl Zeisse and Ike Bendall
Estimating Near-Surface Scintillation (C_n^2) for Overwater Littoral Paths.....259

Hiett, Timothy
A Mobile Laboratory for Measurement of Nighttime Light Spectra.....267

PAGE

Knapp, Kenneth, Kenneth **Eis** and Thomas H. Vonder Haar
Multi-Sensor Aerosol Detection: Combining Aerosol Information from the GOES-8 and 9 Imagers and NOAA/AVHRR.....274

Snow, J.W., H. K. Burke, M.K. Griffin and C.A. Upham
Hyper- and Multispectral Aerosol Detection and Compensation.....282

Wash, Carlyle H., Mary S. Jordan, Philip A. Durkee, Pepijn Veefkind, Gerrit de Leeuw, Michael H. Smith and Martin K. Hill
Satellite Estimates of Optical Depth during EOPACE.....290

Weiss-Wrana, Karin
Measurement of Solar Ultraviolet Radiation at Different Geographic Locations.....299

Decision Aids

Bensinger, Richard B., Melanie J. Gouveia, Glenn J. Higgins, Jeffrey S. **Morrison**, Ryan B. Turkington and Craig V. Gilbert
Target Acquisition Weather Software (TAWS).....303

Bensinger, Richard B., Ronald F. Fournier, Glenn J. Higgins, Melanie J. Gouveia, Jeffrey S. Morrison and Ronald F. Wachtmann
Weather Automated Mission Planning System (WAMPS) Demonstration Prototype....311

Fournier, Ronald F. and Richard B. Bensinger
Real-Time Cloud Depiction Integration into the Army's Battlefield Maneuver Control System.....318

Gouveia, Melanie J., Glenn J. Higgins, Jeffrey S. Morrison, Richard B. Bensinger, Craig V. Gilbert and Ryan B. Turkington
Night Vision Goggles Operations Weather Software (NOWS).....328

Neith, LCDR Mike and Sam Brand
Meteorological Decision Aid Development and Validation for Naval Aviation.....336

Seeley, Guy and Steve Luker
Infrared Target Scene Simulation Software.....340

PAGE

Shirkey, Richard C. and Donald W. Hoock
Weather Impacts for Aggregated Simulations.....346

Stark, Espen
Statistical Description of Detection Range for an Infrared Missile Sensor.....352

Meteorological Modeling & Data Assimilation

Doggett, Capt. Mathew K., Michael Squires, Raymond Kiess, Glenn E. Van Knowe, John W. Zack and Donald Norquist
An Evaluation of the Quality of Local Climate Statistics Generated from the Output of a 3-D Mesoscale Atmospheric Model for DoD Applications in Data Sparse Regions.....363

Haack, Tracy, Stephen D. Burk, Clive E. Dorman and David P. Rogers
Mesoscale Modeling of Marine Refractive Conditions during the Coast96 Field Experiment.....371

Ruggiero, Frank H., George D. Modica and Alan E. Lipton
Assimilation of Surface Observations and Cloud Image Data to Analyze Convective Potential.....379

Wash, Carlyle H., Mary S. Jordan and John Cook
Evaluation of COAMPS Mesoscale Modeling in the Persian Gulf Region.....387

Wyngaard, John C., Martin Otte, Kenneth E. Gilbert, Xiao Di and Nelson Seaman
The Refractivity Structure of the Lower Atmosphere: Connecting Turbulence and Meteorology.....396

Zou, Xiaolei, Qingnong Xiao, Alan E. Lipton and George D. **Modica**
4DVAR Mesoscale Data Assimilation of GOES-8 and DMSP Moisture Soundings.....401

PAGE

Battlespace Sensing Techniques and Applications

Aïdonidis, Michel, Marcel Zéphoris and Franck Lavie
SSBC: An Accurate Atmospheric Sounding System.....411

Cogan, J., E. Measure, E. Vidal, E. Creegan and G. Vaucher
The MMS-Profiler: Present and Future.....418

Duncomb Jr., Capt Robert, Robert J. Farrell Jr. and Paul F. Gilgallon
Passive Radar Observation of the Battlespace Environment: Weather Echoes from Exploitation of an ASR-9.....426

Ince, Turker, Andrew L. Pazmany, Steve J. Frasier and Robert E. McIntosh
A High-Resolution FMCW S-Band Radar for Boundary Layer Profiling and Cloud Applications.....432

Jones, Andrew S., Stephen **Barlow** and Thomas H. Vonder Haar
Advanced Remote Sensing Concepts in Soil Moisture Analysis.....440

Kidder, Stanley Q., Andrew S. **Jones**, James F. W. Purdom and Thomas J. Greenwald
First Local Area Products from the NOAA-15 Advanced Microwave Sounding Unit (AMSU).....447

Kidder, Stanley Q., Kenneth E. **Eis** and Thomas H. Vonder Haar
New GOES Imager System Products Suitable for Use on Field-Deployable Systems.....452

Philbrick, C. Russell and Daniel B. Lysak, Jr.
Optical Remote Sensing of Atmospheric Properties.....460

Sekelsky, Stephen M., Robert E. McIntosh, Warner L. Ecklund and Kenneth S. Gage
Multiple-Frequency Radar Observations of the Atmospheric Boundary Layer.....469

Walter, Steven J. and Philip I. Moynihan
Battlespace Forecasting of Aviation Icing Hazards.....476

This page intentionally left blank.

PREFACE

The BACIMO 98 Conference Preprinted Proceedings contains the papers that will be presented at the first Battlespace Atmospheric and Cloud Impacts on Military Operations (BACIMO) conference to be held at Hanscom Air Force Base Massachusetts, December 1-3, 1998. The Air Force Research Laboratory at Hanscom is hosting the 1998 conference.

BACIMO conferences are convened annually at the request of the Assistant for Battlespace Environments Office of Defense Research and Engineering and are co-sponsored by the Air Force Research Laboratory, the Army Research Laboratory, and the Space and Naval Warfare Systems Center (SPAWAR). BACIMO brings together the two previously separately-held Battlespace Atmospheric (BAC) and Cloud Impacts on DoD Operations and Systems (CIDOS) conferences. The conference objective is to enhance cooperation and coordination among US military services, the civilian community, and allied nations in developing technology to specify and predict atmospheric and cloud impacts on military operations.

This three-day conference will consist of platform presentations and poster presentations that include video and computer demonstrations. BACIMO 98 is organized according to the following 9 sessions:

Program Overviews
Cloud and Cloud Effects Models
Radio Propagation
Measurements of Clouds and Cloud Parameters
Modeling and Simulation (M&S) of Atmospheric and Cloud Effects
Measurements and Modeling of EO Parameters
Decision Aids
Meteorological Modeling and Data Assimilation
Battlespace Sensing Techniques and Applications

The BACIMO 98 Technical Committee gratefully acknowledges direction from the BACIMO sponsor, Col Alan R. Shaffer, the U.S. Air Force Assistant for Battlespace Environment, Office of Defense Research and Engineering, and the support of the Air Force Research Laboratory in hosting this year's BACIMO Conference. The excellent cooperation and contributions of the session chairs and the presenters is also acknowledged.

Paul Tattelman
Conference Chair

This page intentionally left blank.

Program Overviews

DOD's Center for Geosciences and Atmospheric Research

Kenneth E. Eis* and Thomas H. Vonder Haar
Center for Geosciences/Atmospheric Research
Colorado State University
Fort Collins, CO 80523-1375
(970) 491-8397, fax 8241, eis@cira.colostate.edu
Sponsor: Army Research Laboratory

Objective: This paper will describe a 4-year DOD-sponsored research initiative beginning in September 1998. The Center for Geosciences/Atmospheric Research (CG/AR) is the third phase of DOD-funded research, which began in 1986. The reason for this presentation is to inform the DOD weather community of the existence of CG/AR and to allow you to provide feedback and make research topic suggestions within the research themes of the cooperative agreement. This is an opportunity for DOD managers to have research conducted for zero cost to their programs. Your feedback should be directed to Dr. Douglas Brown, Army Research Laboratory.

Background: CSU has conducted Army and DoD-wide relevant research in the area of meteorology and hydrology since 1986 under the Center for Geosciences (CG) as a multi-disciplinary effort. This research, totaling over $15M, has had a successful history of results as documented in the final reports for the first two phases of the CG (Vonder Haar et al., 1992 and 1998). DOD moneys through the Army Research Office funded the first two CG phases. Both basic and applied research was completed. As a result of this funding, many research topics have matured and have already been, or are ready for, technical transition to operational users. Many of the completed research projects and substantial results of work in progress may be found on our web site **http://www.cira.colostate.edu/GeoSci/overview.htm**

Research themes: CSU has proposed six broad-based research themes to a tri-service committee, which have been approved. These themes are as follows

Hydrometeorology

Hydrometeorology is a significant operational consideration for the DOD. Rain, mud, and river flooding are all issues that have impacted operations in the last few years. The Sava River flooding delayed deployment of NATO ground forces into Yugoslavia and rain and mud impacted the end run maneuver during the 100 hours of Desert Storm's ground war. Wet ground also effects target detection since with both IR and visible wavelength backgrounds are "darkened".

This theme will include research and field data collection that focuses on atmospheric water vapor variations, rainfall analysis and prediction, and the coupled hydrology and land surface modeling needed to describe flash flooding, trafficability, and surface moisture parameterizations that effect the earth-atmosphere boundary. Specific research includes support to Waterways Experiment Station (WES) objectives to model larger watersheds than attempted in Phase II, possibly using DOD supercomputer resources. This work would include coupled meteorological/hydrological modeling research focused on medium to large watersheds.

CG/AR will also study error propagation analysis including space-time variation of quantitative precipitation index methods coupled to the hydrologic modeling. This analysis would include sub-grid scale effects associated with surface inhomogeneities and sub-pixel sampling. The activity is expected to create soil moisture analysis products for designated DOD regions of interest to provide prototype products and validate and calibrate the indices with respect to soil types and actual trafficability values. This research would include collaboration with selected DOD facilities (e.g. WSMR) and possibly with CSU's Center for Ecological Management of Military Lands (CEMML). Quantitative Precipitation Indices, and forecast-related research will be conducted that focuses on combined satellite/radar analysis for operational analysis and on modeling for the forecasting component. Improved initialization schemes such as using high-resolution soil moisture indices will be investigated. The theme will also address the hydrological model development. One of the more fundamental activities of this theme area is to improve the physical parameterizations within the hydrology models.

Improved water vapor detection and remote sensing (using GPS/Met and microwave sensor data as examples) will be explored to support the hydrometeorological research. In the data fusion area we also expect to develop advanced techniques for merging ground sensor data with radar and satellite data to better define the rainfall patterns currently poorly observed. Lastly, we plan to integrate the effort by exploring realistic feedback processes between hydrological, surface moisture, and mesoscale meteorological models such as fog formation, and thunderstorm initiation in preferred areas.

Cloud Structure, Dynamics and Climatology

The results of this research theme will benefit the peacetime, peacekeeping, and wartime mission of all branches of the DoD. A better understanding, and subsequent ability to analyze and forecast complex layered clouds, will have a significant impact on weapon system selection and deployment, site selection (basing), reconnaissance, as well as the obvious impact on synoptic forecasting. In addition, the multi-year global database and products derived from that database will provide a significant improvement in the availability of input to simulations involving optical or thermal detection.

Any cloud analysis done on the new layered cloud product proposed in this theme improves the resolution of today's layered cloud databases by over two orders of magnitude. Neither the USAF Real-time Nephanalysis (RTNEPH), nor the International Satellite Cloud Climatology Project (ISCCP) cloud analysis models (nor both combined) use all of the input data that is being processed to build the Geoscience Center layered cloud product.

This theme will focus on satellite/aircraft analysis of clouds to improve our ability to determine cloud types, thickness, bases, the measurement of cloud phase, and the dynamics of their distribution in space and time. Special emphasis will continue on complex, non-precipitating layered clouds. These clouds have demonstrated serious impacts on recent DoD operations. We will also explore the microphysics of clouds as it relates to icing, precipitation, and multi-spectral radiative transmission.

High-resolution cloud data set analysis, based on advanced cloud typing methods will be used as a basis to develop conditional probabilities for cloud structures, precipitation and severe weather. These site specific analyses can be developed as prototype forecaster aids and training

devices for both military and civilian locations. A continuation of Phase II's highly successful work on cloud typing will be conducted using clustering, fractal, and neural network tools. This work will move into the validation phase with collaborative field activities shared with other research theme areas. Vertical cloud distribution determination, using new sensors, such as aircraft and satellite-based cloud radar, Unmanned Air Vehicles, combined with conventional satellite imagery and surface observations will be explored. Data fusion techniques will be employed to improve our analysis of cloud bases and layers.

N-Dimensional Data Assimilation & Data Fusion

Improved short-range, battlespace forecasting will help the DoD in peacetime, and in peacekeeping, and wartime operations. We can note especially improved forecasts of surface and near-surface weather (e.g. visibility); upper level winds for artillery and NBC concerns; and winds and cloud layers for strike mission planning.

The Navy has already recognized some of these opportunities and is sponsoring university/industry radar (radiances) tests in small-scale models for coastal applications. NRL-Monterey also plans a special effort in 3D/ 4D VAR Development and testing during 1998 and beyond.

This research topic directly addresses the need within DOD to exploit high-resolution remotely sensed data in numerical weather prediction (NWP). Models of the atmospheric boundary layer (ABL) need high-resolution near-real time updates of observations within the region of interest that (likely) only satellite observations can provide. The work proposed develops a more complete data assimilation methodology that explicitly produces error analysis fields of the derived retrieval parameters. This should allow for the reliable inclusion of the retrieved products into battlefield visualization products and into DOD tactical decision aids. In addition, the observation-based error analysis procedure described in this proposal is a necessary step toward the goal of allowing models to produce internally generated model error estimates, since the observation uncertainties are a key source of model output error. The practical result of being able to assimilate heterogeneous fields should significantly affect various weather phenomena, particularly boundary layer processes that are driven by (currently) relatively poorly-known heterogeneous surface forcing.

This research theme focuses on the application of advanced numerical data assimilation techniques, and multisensor/multispectral remote sensing data fusion techniques. Two, three, and four-dimensional assimilation techniques will be explored including adjoint techniques that were discussed in the Phase I and II research activities. Other assimilation techniques will be explored that related to diagnostic model modes such as "coupled" data/model systems to produce a soil moisture index.

These assimilation techniques show great promise in terms of determining parameters (eg. Surface pressure) over remote and data-denied areas that are not directly accessible from the satellite or other remote sensing radiance values. They will provide much improved data fusion capabilities for future battlefield awareness and forecasts. Part of this research will be the fusion of IR, microwave, and visible radiances from satellites and subsequent inclusion of unmanned air vehicle and surface data into a fully assimilated adjoint initialization. Products that would result from this research include soil moisture, surface temperatures, high resolution wind fields, water

vapor profiles, cloud liquid water path, and ice water path. Parallel activities to improve the computational efficiency of adjoint methods will also be explored. After the new methods are developed and tested, research will be conducted to explore sub-grid phenomena, both within the model and resulting from sensor resolution.

Adjoint modeling will also be used to interpret Lidar measurements taken during CASES-99, a field experiment that CG/AR will be supporting in collaboration with NOAA's Environmental Technical Laboratory in Oct 1999. This activity will support detailed investigations of the very stable boundary layer, an area of major significance to the chemical/biological dispersion arena.

Chemistry, Aerosols, and Visibility

Horizontal visibility, and slant path visibility for aircraft to surface target engagement are critical to all three services. Detection and lock-on range for EO weapons sensors are dependent upon aerosol scattering. Aerosol scattering also effects remote sensing of land surfaces. Only with a full knowledge of the scattering and absorption by the atmosphere can land/ocean use remote sensing correctly determine the radiation properties of the earth's surface.

This theme will continue the research in Phase II to measure visibility via space-based sensors. It will explore the measurement of aerosol optical depth using two simultaneous visible channels and the phase function (BDRF) changes of an aerosol's reflectance as measured by two different satellites. It will also determine how aerosol chemistry and relative humidity effect the accuracy of the aerosol optical depth retrievals. Lastly, it will explore methods of determining boundary layer near-horizontal visibilities from the satellite detected total atmospheric optical depth analysis. The determination of visibility from optical depth requires an understanding of the distribution of aerosol scatters in the vertical. We will address methods to consider the homogeneous spreading of aerosols within the boundary layer leads to reduce error in the visibility measurements derived remotely.

Remote Sensing and Modeling of Battlespace Parameters

This theme will address several new remote sensing technologies including radar, acoustic, Lidar, and GPS-MET to better observe the earth's atmosphere over Battlespace dimensions. The research will be coordinated with the data fusion and assimilation theme and will be required in many instances to fully exploit the remotely sensed data. Some of the research areas include:

- New information on the nocturnal boundary layer from highly sensitive geostationary infrared sensors, including detection of low level winds and surface cooling rates

- Combining OLS and SSM/I sensor data to obtain improved estimates of cloud liquid water over both land and oceans. This would lead to the production of CLW climatologies for forecasting and EM propagation studies.

- Exploring the remote sensing limitations of bi-static radar configurations using non-optimized radar frequencies. This research would use existing receiver units developed and

likely to be available at the Rome Air Development Center and the CHILL radar to explore meteorological features which can be detected with various configurations and geometries of receiver, transmitter, and target (nocturnal boundary layer studies are one example);

- Satellite-based cloud radar studies. The DoD in interested in this technology that uses active satellite systems to remotely determine cloud bases. This research would conduct tradeoff studies, sensitivity analysis (for instance the off nadir performance of a cloud radar) and other investigations to determine the utility of such a space-based system.

- GPS tomography. Currently differential GPS systems are being used to measure total integrated water vapor content. That process discards most of the atmospheric information the ground system receives from the 4-5 GPS satellites always above the horizon. This task will explore using all the available GPS transmissions and closely spaced GPS receivers to solve for the vertical and horizontal structure of the atmosphere.

- Combining remote sensing with *in-situ* UAV data sampling. Specific research could be done on the nocturnal boundary layer problem. Collaboration with NPS's UAV activities could allow tracking and analysis of processes associated with the upper regions of the NBL.

- Development of error propagation analysis techniques for use with advanced numerical data assimilation methods and multi-sensor satellite data sets will be one of the key activities associated with this theme. One aspect of this research will be to provide a generic error propagation technique based on studies of adjoint model experiments. This research would allow sensor errors to be introduced and resulting forecast error statistics to be determined. It is an advanced form of the older Observational System Simulation Experiment methods. Forecasting model sensitivity to input errors and internal errors can be explored explicitly. In coordination with new remote sensing of the nocturnal boundary layer, we are considering certain small-scale modeling experiments coupled with new observational data sets.

For a sampling of research already completed see the following papers in this proceedings:
1. Physical Characterization of Clouds and Precipitation Using 94 GHz and 13.8 GHz Radiometer - by Huffman
2. Advanced Remote Sensing Concepts on Soil Wetness Analysis – by Jones
3. Multi-sensor Aerosol Detection: Combining Aerosol Information from the GOES-8 and NOAA/AVHRR – by Knapp

Besides these themes that address new research initiatives the CG/AR will have a substantial effort in transferring technology generated in both the current and past research phases. This will be done via long-term visits by DOD scientist to CSU and CSU researchers visiting DOD laboratories and operational centers, as well as collaboration via internet and video teleconferencing. Some of the potential technologies that can be transferred and those that have already been transferred are as follows:

- Hydrometeorology – The CASC2D hydrology model is running at the Army Corp of Engineers Waterways Experiment Station (WES) Future versions with improved overhand and subsurface flow parameterizations will follow. The future goal is also to improve the size

of the watershed being analyzed to a mega-pixel or greater then 10,000 km2. With improved computer resources we can expect to cover an entire theater of operations.

- Cloud Drift Winds – This multi-satellite method of determining cloud heights and winds is currently running in a research mode. Technology Transfer is expected to both the Navy in support of improved NOGAPS initialization and to support the Army's battlefield profiler analysis via IMETS.
- Implement the temporal nudging neural network-based cloud classification method. This new technology is also the subject of a patent application. The cloud classifier has been so successful that future use of the tool may also provide improvements in profiler, physical phase of clouds, and cloud base analysis.
- Creation of a second year of the CHANCES cloud climatology. This 5-km resolution, hourly, global cloud database has already been produced for 1994. The 1997 year will be produced to give researchers and military planners an anomalous (El Nino) year. The database will be made available to the Master Environmental Library and the AFCCC as requested.
- Climatologies or mixed phase clouds, and aerosol total optical depth over land can be created for use in electro-optical propagation studies.
- Implementation of the Beysian analysis scheme for retrievals of water vapor and temperature from satellite soundings. This method is already a candidate method for the NPOESS.
- Remote sensing of soil moisture values and surface temperature. These methods have been demonstrated to work and to improve forecast initialization accuracy. Trafficability, fog forecasting, and thunderstorm forecasting will all benefit from this new approach. Prior to transfer a formal validation process will need to be conducted.
- New adjoint modeling approaches, used not only to improve forecasting, but also improve analysis of raw instrument data, battlefield data fusion methods, and chemical dispersion accuracy will be transferred.
- The deployment of a new lost cost satellite earth station. These systems are currently collecting all GOES, AVHRR, and Meteosat data. They have been developed with current state-of-the-art PC and programmable gate array technology which allows a satellite ingest system to be housed in a single PC cabinet.

References

Vonder Haar, T.H., and Participating Scientists, 1998: DoD Center for Geosciences - Phase II, Final Report under DoD grant DAAH04-94-G-0420 to the U.S. Army Research Office; see (http://www.cira.colostate.edu) and also the list of publications (Appendix D).

Vonder Haar, T.H., K.E. Eis, and J. Harper, 1997: Proposal for the Department of Defense Center for Geosciences Phase II at Colorado State University. White paper, 38 pp.

Vonder Haar, T.H., with Principal Investigators and Co-Investigators, 1992: Final Report on Geoscience Center Research under ARO grant DAAL03-86-K-0175 to the Army Research Office, Geosciences, 195 pp.

Acknowledgement

The completed work under Phase II of the Center for Geosciences was under DOD Grant DAAH04-94-G-0420

The Phase III work discussed for the future will be under a DOD funded Army Research Laboratory Cooperative Agreement

APPLICATION OF THE FAA'S INTEGRATED TERMINAL WEATHER SYSTEM TECHNOLOGY TO THEATRE WEATHER INFORMATION SUPPORT[1, 2]

James E. Evans
Group Leader, Weather Sensing Group
MIT Lincoln Laboratory
244 Wood Street
Lexington, MA 02420-1985
Telephone: 781-981-7433; fax: 781-981-0632
JIME@LL.MIT.EDU

I. Introduction

Historically Department of Defense battle space weather support has relied heavily on satellite data and numerical modeling as the principal inputs to trained meteorologist forecasters who would then provide the weather products for operational decision-makers. This paradigm made eminent sense when applied to long-range, wide area operations against an adversary such as the USSR. However, a number of recent DoD deployments have involved operations on a much more local scale wherein very detailed real time environmental information in many locations is required simultaneously by a variety of operational commands. Major improvements in acquisition of surface data and product distribution have been accomplished by the IMETS system and its Navy counterparts. However, the product generation paradigm has continued to be meteorologist intensive.

We propose a complementary paradigm that has been very successful in operational use for the FAA and the air carriers that also focus on using weather sensing radars, fully automatic short-term "nowcast" product generation algorithms, direct product distribution to operational decision-makers without any intervening meteorologist input, and collaborative decision-making between the various operational users to achieve coordinated operations. This paradigm facilitates highly adaptive, opportunistic decision-making in real time at many locations simultaneously without the high personnel costs that would be required to achieve the same weather product generation capability manually.

In this paper, we describe key features of the FAA's Integrated Terminal Weather System (ITWS) that have been used to provide operational service at four major terminal areas (Dallas, Memphis, Orlando, New York) since 1994. We then discuss how this technology can be applied to DoD theatre applications to fill in some important gaps between DoD users' needs and the current DoD capability.

[1] This work was sponsored by the DDRE. The views expressed are those of the author and do not necessarily reflect official policy or position of the U.S. government.
[2] Opinions, interpretations, conclusions, and recommendations are those of the author and are not necessarily endorsed by the U.S. Air Force.

II. Integrated Terminal Weather System (ITWS) Features

Operational Needs

a. Products required

The ITWS addresses both the safety and efficiency needs of civilian aviation operations in adverse weather at the busiest terminal areas in the world. The initial safety focus is on providing detection and short-term (20 minute) "nowcasts" of low altitude wind shear and convective weather (including hail and tornadic storms). It is anticipated that the safety product mix will be extended to include icing products. The ITWS improves operations efficiency (e.g. reduces delays) by supporting proactive traffic routing during adverse weather through predictions of the future locations of convective weather and wind shifts at airports and by providing 3D winds information inside and outside the terminal area to support traffic merging and sequencing. Predictions of ceiling and visibility and convective storm growth and decay are very important, as well, and are being developed as preplanned product improvements for the ITWS.

b. Concept for operational use

The operational concept for ITWS product usage is that various Air Traffic, pilot, and airline users will be able to directly use the products for decision making without any further meteorological analysis or interpretation.
ITWS color graphical displays[3] are typically used intermittently for short periods to make decisions. Thus, the display must facilitate quick decision-making as well as having "alert" features that indicate when the user may need to look at the display. Since the ITWS users are very busy with little or no formal meteorological training, the products themselves must have a high degree of integrity (e.g., reliable depiction of significant weather with minimal false depictions). This operational concept is necessary in the FAA domain due to the many decisions that must be made by a multitude of spatially distributed users together with the limited budget for human meteorological support.

To illustrate the spatial extent of a contemporary ITWS, the key FAA NY ITWS users include four principal airport towers (Newark, Kennedy, LaGuardia, Teterboro), the NY terminal radar room and NY en route center (both on Long Island), the Boston en route center (Nashua, NH), the Washington en route center (near Leesburg, VA), and the FAA Command Center (near Reston, VA). Major airline systems operations centers as far away as Houston, Dallas, Pittsburgh, and Chicago, together with airline operations centers at the NY airports, also have real time access to the products. This shared operational awareness is essential if there is to be coordinated real time decisions on flight operations at a variety of time and spatial scales as various weather phenomena move near and through the New York terminal area.

[3] The ITWS display is a color multi-window display. An example can be viewed on the Lincoln aviation weather WWW site:
http://www.LL.MIT.edu/AviationWeather/

A few words are in order about the relationship of the ITWS product usage to the weather decision support provided by NWS meteorologists. FAA towers and terminal radar rooms have historically relied on radar depiction of weather with no local meteorological support, so ITWS is consistent with a longstanding operational concept. In the en route centers, there are NWS meteorologists to support Air Traffic. At these centers, the meteorologists and Air Traffic users have moved to a new paradigm whereby ITWS provides "nowcasts" with the meteorologists focusing on longer-term forecasts that cannot be automated. Since the meteorologists have an ITWS display, they can provide warnings to operational users in the relatively rare cases where automation is not handling well (e.g., dry cold fronts not sensed by the radars).

c. Coverage, resolution, and update rates

The geographical region covered by the Integrated Terminal Weather System at major terminal areas includes the terminal area and the "transitional" en route airspace that surrounds major terminal areas. Figure 2 shows a contemporary ITWS system at New York City that commenced operations in the New York (NY) terminal area in August 1998. The NY ITWS provides storm location and movement information with 1 km spatial resolution every 30 seconds over a region of 120,000 km^2. This geographical extent is comparable to possible DoD theater areas such as Bosnia, Korea, and the area near Kuwait. This extended coverage is needed because the "gates" through which aircraft transition from the en route airspace to the terminal area (and vice versa) can be major bottlenecks during convective weather. The very high spatial resolution is required because users need to be able to identify small gaps in convective weather that can be exploited for aircraft movements while the high time resolution is needed to handle rapid storm growth and decay.

Providing the Desired ITWS Capability

The ITWS achieves the desired capability by fully automatic data fusion algorithms operating on data from a wide variety of sensors. The New York ITWS integrates information from seven different FAA and NWS weather sensing radars as well as using NWS rapid update cycle (RUC) numerical model results, surface sensor data, and in situ measurements of temperature and winds from aircraft. The data fusion algorithms use the multiplicity of sensors to extend the capability of individual sensors and edit bad data (1-4). To illustrate, a key sensor in achieving the very high update rates on convective weather is the FAA fan beam ASR9 that updates reflectivity maps every 30 seconds. However, the ASR9 does not provide 3D storm information and is currently susceptible to anomalous propagation induced ground clutter (AP). These problems are remedied by using data from pencil beam radars to provide 3D information (e.g., echo tops, hail) and edit the ASR9 data. Forecasts are made by combining thermodynamic information (from surface sensors, aircraft in flight, and numerical weather models) with the radar data. Winds from a wide variety of sensors and numerical weather models are combined using statistical estimation algorithms to provide high-resolution 3D wind grids.

The production [4] ITWS products are generated by a Sun 4000 multiprocessor system that fits into a 19" rack. The production system displays are Sun Ultra 5 workstations. External users

[4] The production ITWS is in Full Scale Development by the Raytheon Corporation under a contract from the FAA. Initial deliveries of the production ITWS are planned for 2001.

(e.g., airline dispatch) access and display products from a WWW site. Communications to most sensors and users are via standard (e.g., 19 kbs) ground lines with the exception of the TDWR (that uses T1 lines to transfer "raw" TDWR data so that expanded TDWR product generation can be accomplished by the ITWS).

Work is currently underway to use satellite data in conjunction with the initial ITWS sensor data mix for both ceiling/visibility and convective storm predictions.

III. Achieving an ITWS Like Capability in DoD Applications

Operational Needs

The ability of the U.S. military to use "smart" military weapons, perform battle space surveillance, and conduct air, land, and sea operations is significantly impacted by precipitation, visibility, and clouds. There are a number of military operational decisions that would be greatly facilitated by frequently updated (e.g., every 5 minutes), high spatial resolution "nowcasts" (i.e., 0-60 minute prediction periods) that can be produced reliably with the ITWS weather detection/prediction technology. Localized unit operations (e.g., Army or Marine battalion, artillery fire, Air Force guidance for aircraft in flight or that could reach the area of interest in 60 minutes, Navy carrier operations, strike operations with "smart" weapons, air drop, and UAV operations) are analogous in many ways to the operations conducted in civil aviation that involve very localized information for many different locations at any moment in time.

Operational Usage Concept

We envision these "nowcasts" being provided with spatial resolution on the order of 0.5-2 km, with update rates of 1-5 minutes. Achieving this high degree of space/time resolution simultaneously at hundreds of locations over spatial domains of 300 X 400 km can only be accomplished by fully automatic product generation algorithms with products being provided in a form that operational users can use directly to make operational decisions. This will require widespread graphical product distribution to individual operational decision-makers with displays that are analogous to COTS laptops. Users with no room for a graphical product display could receive rapidly updated text messages over pager-like units (analogous to the ACARS text messages provided to commercial aircraft by the ITWS). These text messages would update every 1-5 minutes.

The products produced by such a system would complement the support provided by military meteorologists. Updating a 0-60 minute forecast for many different locations every 5 minutes is not a job that humans can do well for prolonged periods. Additionally, since most of the near-term products would have a significant weather radar component, this concept is not very different from the use of weather radar data in many CONUS military operations that have access to NEXRAD data. Such a military version of the ITWS would provide the integrated assessment of the current weather situation as an input to the mesoscale models and meteorologists that will provide weather predictions with longer forecast times.

Achieving the Requisite Weather Surveillance Capability

The IMETS system (with the near-term planned enhancements) provides an excellent infrastructure for implementing the FAA ITWS technology. If the U.S. military currently had the sensor densities that the combination of the FAA and the NWS have in the CONUS in densely populated regions such as the Northeast corridor, it would clearly be straightforward to operationally deploy much of the ITWS capability. The challenge to an individual service is that the current military operational area sensor densities (especially of weather sensing radar) are much less than that in the civilian sector.

However, there are some solutions to this problem. First, many of the recent foreign deployments have involved deployment of weather sensing radars for special applications and/or occurred in regions in which there were preexisting civilian weather radars on the "blue" side. Both the USAF and Marines will have tactical deployment weather radars that could be utilized. Development of interfaces and software to acquire and integrate these is relatively straightforward (e.g., the ITWS algorithms handle automatically the situation where sensors go up and down, and may even be in different locations at different times). We should note that the operators of such radars could benefit greatly from the integrated product since physically small tactical radars typically operate at C- or X-band and hence may suffer significantly from rain attenuation. The FAA experience has been that mosaics are much less susceptible to rain attenuation due to the diversity in line-of-sight paths.

Additionally the military has a large number of pulse Doppler microwave target detection radars that can economically be augmented to provide a weather detection capability analogous to that provided by the FAA ASR9, the FAA/USAF ASR11 and the FAA/USAF ARSR4. Figure 2 shows the canonical approach used by the FAA for accomplishing this. Basically, one must obtain data from an appropriate polarization channel if circular polarization is used in the target channel to reject rain returns. Weather parameter estimation is accomplished using well-understood techniques that can be implemented on relatively low cost COTS processors. In most applications where precipitation data alone is required, the normal pulse compression processing used for the target channel will suffice.

We should note that this type of weather channel add-on is being accomplished by Lockheed Martin for the AEGIS SPY-1 radar [1]. Table 1 shows some other examples of candidates for a weather channel. One of the major challenges for air strike weather surveillance is radar line-of-sight limitations for ground/ship-based radars. The AWACS radar would be an ideal complement to the ground-based radars to provide precipitation information at long ranges.

The other need (especially for highly localized forecasting of ceiling and visibility) is a wide network of surface weather stations in critical locations near the front. We are investigating some interesting technologies in this area that will be the topic of a later paper.

	Frequency	Type of Beam	Scanning	MTI
AEGIS	S	Pencil	Electronic	yes
SPS-48	S	9 stacked beams	mech az	yes
SPS-49	L	Fan beam	mech az	yes
AWACS	S	6 stacked beams	mech az	yes
FPS-117	L	Fan beam	mech az	yes
TPS-59	L	Pencil	mech az	
PATRIOT	C	Pencil	Electronic	yes
AN/TPQ-37	S	Pencil	45 deg az/10 deg el	yes
AN/TPQ-36	X	Pencil	45 deg az/10 deg el	yes
HADR	S	Pencil	mech	yes
AN/TPS-32	S	Pencil		yes

Table 1: DoD Surveillance Radars That Could Have a Weather Channel

Next Steps

From a technology development viewpoint, achieving an ITWS-like DoD capability would require:

(a) developing interfaces between IMETS and the tactical radars under procurement (including the modified SPY-1)

(b) modification of existing military target detection radars to provide a "weather channel" and interfacing that channel to the IMETS

(c) integration using adapted ITWS algorithms

Accomplishing these tasks is relatively straightforward technically. We see the most critical issues as gaining acceptance of the operational concept and the utility to the operational

military decision-maker. The utility (and priority) of such a system is unclear to a decision-maker who has never been provided with this type of information previously. Additionally, there is the question of whether the service weather information providers can accept an operational concept where some weather products go directly to operational users with no intervening meteorologist review.

In this connection, we should note that some of the highest benefits provided by the ITWS to civil aviation operations have occurred from better decision-making by users that the FAA air traffic requirements service had not planned to provide access to the information when the program started. It was only via prototype operations in which experimental products were provided to a wide variety of users that these important operational needs were recognized.

To that end, we recommend a near term requirements/operational benefits experiment be carried out in a convective weather impacted training or potential operational area in which civilian radars are used as surrogates for candidate modified military radars and in which candidate operational users are provided products via IMETS or by using low cost COTS product distribution and display approaches (e.g., cellular phones and laptop PCs). The objective here is to assess the operational utility and acceptability of automatically generated high resolution "nowcasts" for direct operational use without any intervening interpretation by trained meteorologists. Such a demonstration must include simultaneous product distribution to the local military weather support facility to determine the operational suitability of the proposed new paradigm for weather decision support.

Reference:
H. S. Owen, H. Urkowitz, N. J. Bucci, J. V. Melody, R. McLean, "Tactical Weather Radar Experiment For a Shipbome Radar," Proceedings of Battle space Atmospherics Conference; Naval Command, Control and Ocean Surveillance Center, RDT&E Division; San Diego, CA; December 3-5, 1996 [ADA 323038].

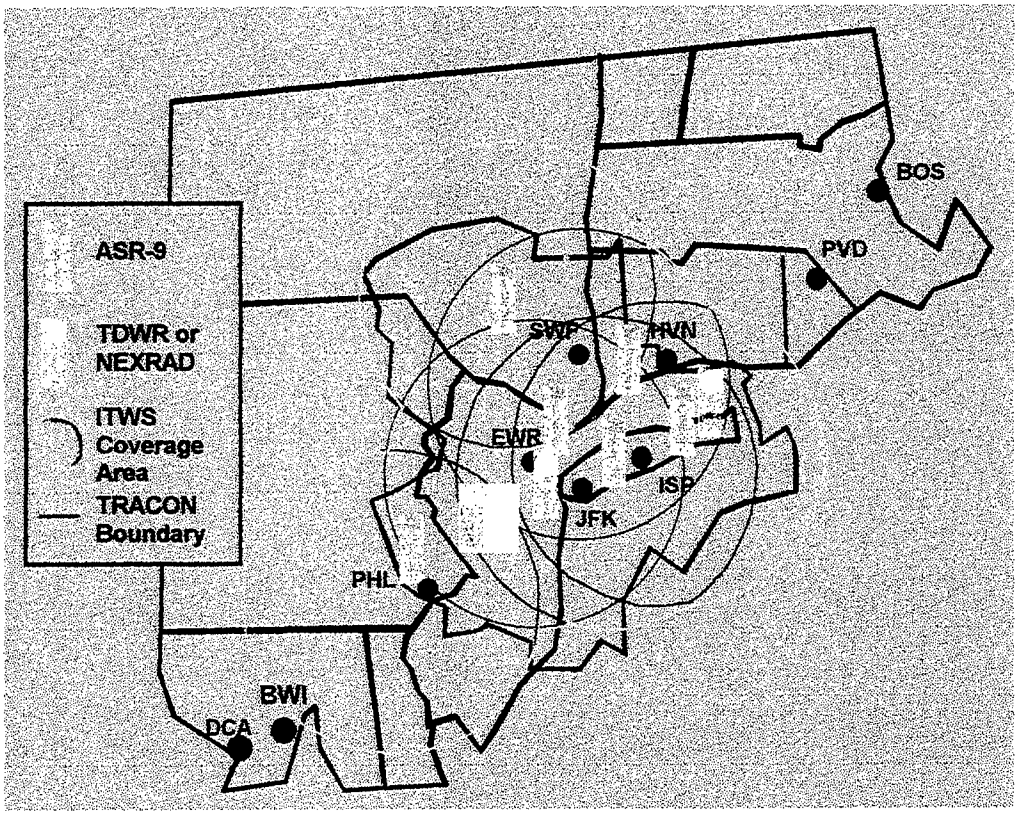


Figure 1: New York ITWS

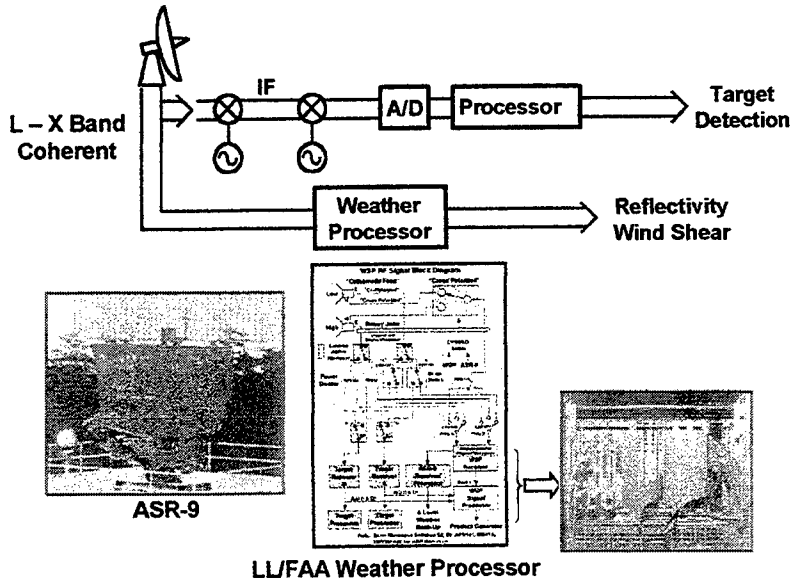


Figure 2: Weather Data Extraction From MTI Radar

NUMERICAL WEATHER PREDICTION FOR THE U. S. NAVY

Richard M. Hodur
Marine Meteorology Division
Naval Research Laboratory
Monterey, CA 93943-5502

1. INTRODUCTION

The Marine Meteorology Division of the Naval Research Laboratory (NRL MMD) is actively involved in the field of Numerical Weather Prediction (NWP) to provide continuous weather support to the U. S. Navy for both wartime and peacetime missions. This support extends from the surface of the earth to altitudes exceeding 10 km, and for time scales ranging from a few hours up to 7 days. The NWP products provide valuable information on tactical parameters such as wind speed and direction, temperature, precipitation, and clouds. Analyses and forecasts of these parameters are crucial for the success of many military missions.

The wide range of time and space scales of significant meteorological events necessitates the use of a dual-modeling system approach. Although computer technology continues to expand rapidly, it has yet to reach the point where only one modeling system can be used in a timely manner to capture the details of the current dual-modeling system approach. For scales of motion greater than about 1000 km, NRL MMD has developed the Navy Operational Global Atmospheric Prediction System (NOGAPS; Hogan and Rosmond 1991). For the short-term (24-48 h) prediction of smaller-scale phenomena, NRL MMD has developed the Coupled Ocean/Atmosphere Mesoscale Prediction System (COAMPS; Hodur 1997). NOGAPS has been proven to be useful for the prediction of large-scale trends, and phenomena such as synoptic-scale cyclones, and tropical cyclones; while COAMPS has been found to be particularly useful in the prediction of mesoscale phenomena associated with coastal regions and areas of significant topographic features. These systems are linked (nested) together in such a way that the larger-scale fields forecast by NOGAPS are used to supply the lateral boundary conditions to COAMPS. This dual-modeling system approach is useful in the prediction of multi-scale events, in that one forecast from NOGAPS can supply the boundary conditions for a fixed number of higher resolution COAMPS areas. The following sections of this paper describe the NOGAPS and COAMPS prediction systems, present applications of both, and provide an overview of the future advances planned for these systems.

2. PREDICTIVE SYSTEMS

NOGAPS and COAMPS are sophisticated data assimilation schemes, with the data assimilation scheme in each system based on four principal components. The first component is the quality control of observations, in which observational data is screened for errors, redundancy, consistency with the previous forecast, etc. (Baker 1992). The second component is the analysis, in which the irregularly-spaced, quality controlled data are interpolated to the model's regularly-spaced grid. The interpolation method used by both NOGAPS and COAMPS is based on the multivariate optimum interpolation method (MVOI; Lorenc 1986). In the third component, model initialization, the analyzed fields are adjusted to conform to one of more dynamic and/or

physical constraints. Finally, the fourth component is the numerical model, which integrates the initialized fields forward in time to a specified future time, using some approximate formulation of the primitive equations. The forecast fields can then be used as the background field at the next analysis time. This process is important to maintain spatial and temporal consistency, and to allow for the history of previous observations to be maintained in future analyses. In so doing, the model is allowed to generate useful information in data-void regions, based on the interpolation of the observations from adjacent areas and in relying on the dynamics and physics of the model to project this data forward in space and time. The performance of each of the four components of the data assimilation system is critical to the overall performance of the entire system.

NOGAPS is comprised of the four components for data assimilation described above. In addition to applying quality control procedures and utilizing the standard observations in the MVOI analysis, synthetic observations are generated for all tropical cyclones with maximum winds in excess of 35 m/s. These synthetic observations describe the general wind structure of the cyclone, such as the radius of 35 and 50 knot winds, but do not attempt to describe the mesoscale structure associated with the inner eyewall. These synthetic observations are treated as valid radiosonde reports to ensure that significant tropical cyclones are included in the analyses and subsequent forecasts. The NOGAPS analysis increments are initialized using a nonlinear normal mode initialization. The NOGAPS forecast model is based on the hydrostatic approximation to the primitive equations. The equations are written in spectral form, to avoid the convergence of points at the poles associated with regularly-spaced grid point models. NOGAPS uses state of the art physical parameterizations for boundary layer processes, precipitation, and radiation. The radiation scheme includes short- and long-wave parameterizations, and each interacts with the model forecast cloud field.

COAMPS represents an atmosphere-ocean coupled system. For the purposes of this paper, only the atmospheric portion of COAMPS will be discussed. The COAMPS grid can be set to any size, within the constraints of the computer system being used, and can be located anywhere over the world. The atmospheric portion of COAMPS is also comprised of the four components of a data assimilation system as described above. With minor exceptions, the quality control and analysis components of COAMPS are the same as those used for NOGAPS. Two options are available for initialization: a hydrostatic balance of the analyzed height and temperature increments (Barker 1980), or a digital filter. The atmospheric forecast model in COAMPS uses the nonhydrostatic form of the primitive equations as described in Klemp and Wilhelmson (1978). The nonhydrostatic form of the equations is necessary for modeling systems using a horizontal resolution less than approximately 10 km. For these resolutions, the vertical acceleration may become important, such as in convective systems or flow around steep topography. The COAMPS equations are solved on a staggered C-grid, which can contain any number of nested grids. The grid spacing is reduced by a factor of 3 between each nest. In this manner, the COAMPS grid can telescope down to resolutions of less than 10 km for areas in which high resolution is a necessity. COAMPS contains an advanced moist physics parameterization (Rutledge and Hobbs 1983), which is used in lieu of convective parameterization below 10 km grid spacing. This parameterization contains explicit equations for water vapor, cloud droplets, raindrops, ice crystals, and snowflakes. In addition, COAMPS uses state of the art parameterizations for boundary layer processes and radiation.

The development of NOGAPS and COAMPS is a central component to the work performed at NRL MMD. Both systems are used in NRL MMD basic and applied research programs and both systems have been transitioned to the Fleet Numerical Meteorology and Oceanography Center (FNMOC) for operational use. Active research programs include predictability studies focussed on the development of a targeted observation strategy using singular vectors; the study of topographic and fetch-limited flows; atmosphere-ocean coupling for both the global and mesoscale systems; studies of physical processes and subsequent modification and/or development of parameterizations; aerosol retrieval, assimilation, analysis, and prediction; and the study of advanced data assimilation techniques.

3. APPLICATIONS

NOGAPS has been operational at FNMOC since 1982, at which time it had a resolution of 4° x 5°, with 6 vertical levels. Currently, NOGAPS uses a T159 spectral grid (approximately 80 km resolution) with 24 levels, and uses a 6 hour incremental data assimilation cycle. The increase in model resolution has been attained through a combination of advances in computer technology, implementation of more efficient algorithms, and improved programming practices. The NOGAPS forecast model is run to 7 days at 0000 and 1200 UTC daily using the T159 resolution, and the forecast continues to 10 days at a reduced resolution of T79 (approximately 150 km).

Since 1982, incremental upgrades have been made to NOGAPS, resulting in a steady growth in its forecast accuracy. One of the more uniformly accepted forms of validation used for global models is the 500 mb height anomaly correlation. The annual anomaly correlations for NOGAPS from 1988 through 1997 are shown in Fig. 1. In general, the scores show an increase in skill during this ten year period, with the skill at any given forecast time in 1997 comparable to the skill in 1988 for a forecast time 24 hours earlier. In other words, NOGAPS forecasts have increased in skill by 1 day over the past 10 years. This has also been noted in other measures of skill, such as the root-mean-square error of winds, heights, and temperatures (not shown).

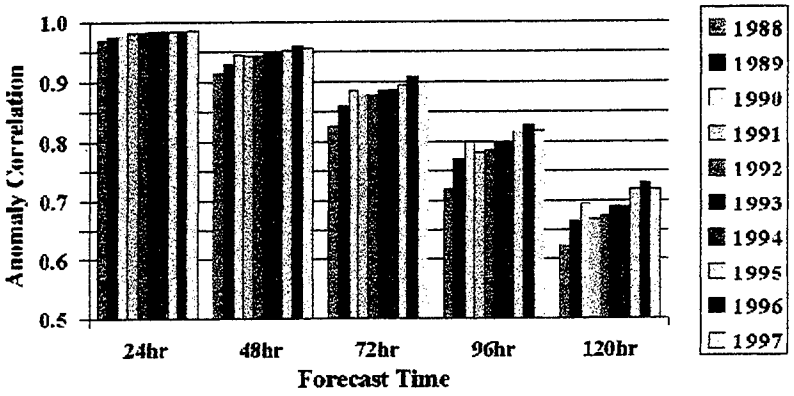


Fig. 1. *Global 500 mb height anomaly correlation for NOGAPS 24, 48, 72, 96, and 120 hour forecasts for each year from 1988 through 1997. An anomaly correlation of 1.0 is considered a perfect forecast, and an anomaly correlation of below 0.6 is considered to have no skill.*

Another measure of NOGAPS skill is its performance in the prediction of the tracks of tropical cyclones. NOGAPS has been found to be quite accurate for this particular forecast problem even

though it uses a relatively coarse resolution compared to other models that are used exclusively for tropical cyclone track prediction. Although NOGAPS cannot resolve the inner eyewall dynamics of a tropical cyclone, it can represent the large-scale flow that plays a major role in the steering of these cyclones. In addition, since NOGAPS is a global model, it does not suffer from the requirement of lateral boundary conditions of regional/mesoscale models. This means that there are no restrictions on the interaction of the tropical cyclone with any surrounding features and there are none of the problems that are typically associated with an over-specification of boundary conditions in regional models.

An example of a NOGAPS forecast for Hurricane Bonnie, which affected the east coast of the U.S. in August 1998, is shown in Fig. 2. This figure shows the NOGAPS 10 m wind analysis at 1200 UTC 25 Aug 1998 and the NOGAPS 48 h forecast 10 m wind field generated from this analysis, valid at 1200 UTC 27 Aug 1998. During this time, Hurricane Bonnie moved generally toward the northwest, making landfall in North Carolina. The official warning position from the National Hurricane Center at 1200 UTC 27 Aug 1999 was 35.0N, 77.1W. NOGAPS 48 h forecast appears to be approximately 50 n. mi. to the southwest of this position based on the streamlines in Fig. 2.

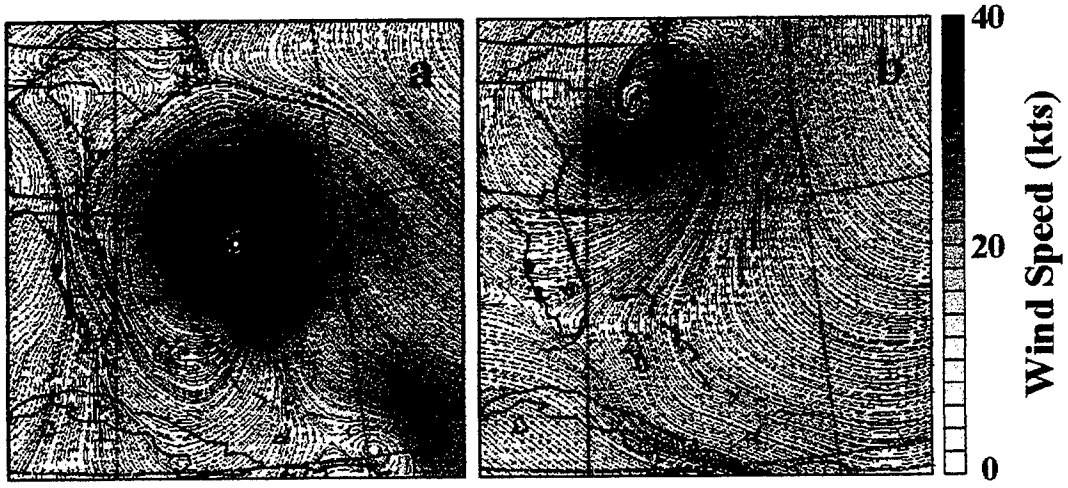


Fig. 2. *NOGAPS (a) analyzed and (b) 48 h forecast 10 m winds (streamlines and gray-shaded isotachs) for Hurricane Bonnie. Analysis field is valid at 1200 UTC 25 August 1998 and the forecast field is valid at 1200 UTC 27 August 1998.*

COAMPS has been operational at FNMOC since June 1998, and is currently run operationally over three areas. These areas cover the Mediterranean Sea, Southwest Asia, and the east coast of Asia (Fig 3). The Mediterranean and Southwest Asia areas utilize triply-nested grids with resolutions of 81, 27, and 9 km, while the east coast of Asia area utilizes a doubly-nested grid configuration using resolutions of 81 and 27 km. All COAMPS areas use 30 vertical levels. The length of the COAMPS forecast varies based on the area and the nest. The longest forecasts (72 h) are for the Mediterranean 81 and 27 km grids, while the shortest forecasts (all 9 km grids) extend only to 24 h.

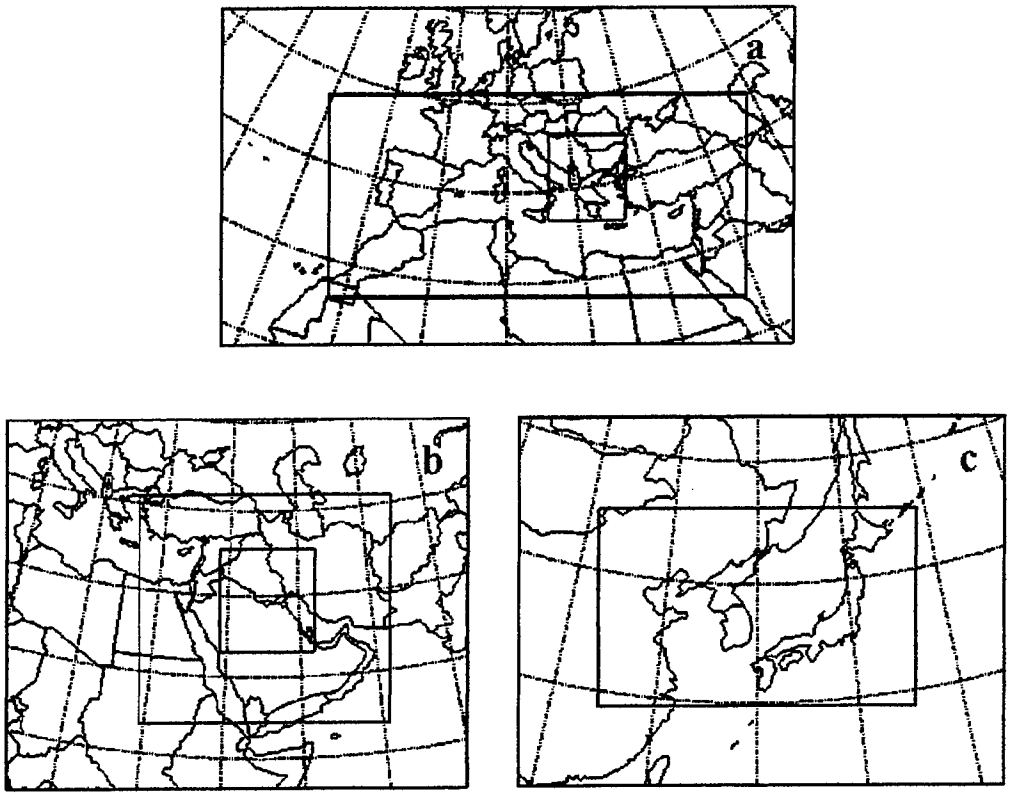


Fig. 3. *COAMPS areas run operationally at FNMOC: (a) 81/27/9 km triply-nested grid for Mediterranean, (b) 81-27/9 km triply-nested grid for Southwest Asia, and (c) 81/27 km doubly-nested grid for the east coast of Asia.*

The use of high-resolution grids and a detailed description of the earth's topography has been shown to be effective in the prediction of topographically forced mesoscale events. One such example is shown in Fig. 4, which represents a 36 hour COAMPS forecast of the 10 m wind field valid at 0000 UTC 13 October 1998 over the western Mediterranean. This forecast was made by the FNMOC operational Mediterranean area (27 km nest) illustrated above. In this forecast, a strong (40 knot) Mistral is present extending from the southern coast of France to the north coast of Africa. This wind is typically formed through the channeling of northerly winds between the Alps to the east and the Pyrennes to the west. Another smaller local wind maximum, often referred to as the Mestral, extends into the Mediterranean from the Ebro River valley off the northeast coast of Spain. With 27 km resolution, COAMPS is able to resolve many of the local wind patterns that develop in the Mediterranean and other parts of the world. Furthermore, COAMPS shows skill in the temporal and spatial variations of these features.

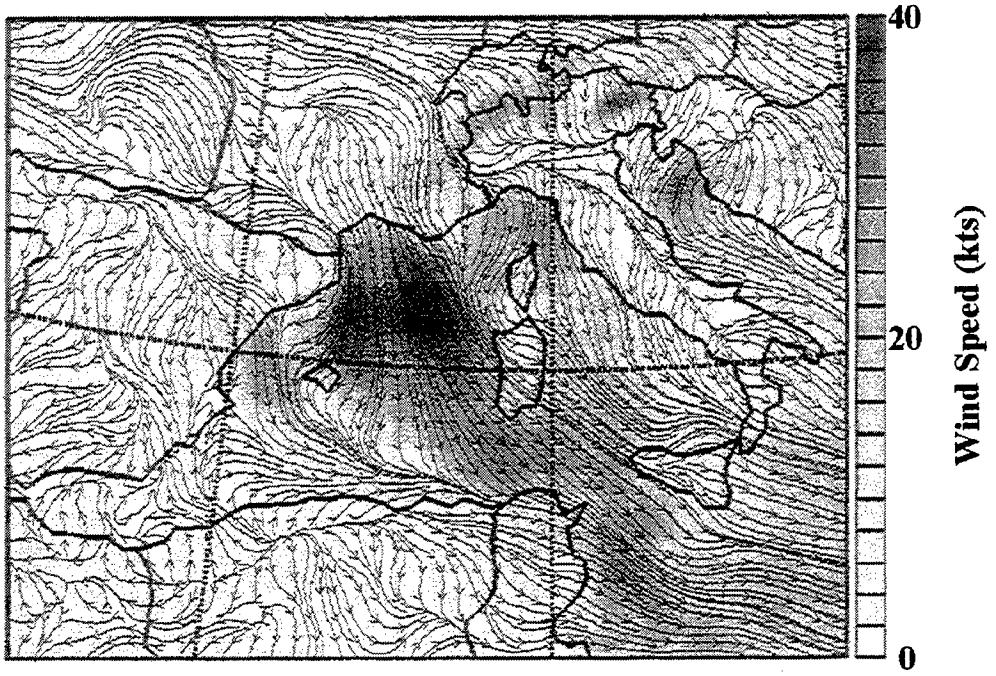


Fig. 4. *COAMPS 36 h forecast of 10 m winds (streamlines and gray-shaded isotachs) valid at 0000 UTC 13 October 1998. Area in display represents only a portion of the full 27-km grid shown in Fig. 2.*

The recent development of powerful workstations and high-speed communications has made it possible to utilize COAMPS at remote sites that require the use of mesoscale model output. In addition, these sites may have additional local observations that may provide important additional information for the analysis and/or prediction of the weather in the local region. To support this use, NRL MMD has developed the Tactical Atmospheric Modeling System/Real-Time (TAMS/RT). TAMS/RT combines the COAMPS data assimilation system, a powerful graphical-user-interface (GUI), tactical application programs, and additional analysis tools into a workstation-based system for an analysis/nowcast/short-term (0-36 h) forecast system for remote site users. The version of the COAMPS forecast model is identical for both the FNMOC and the TAMS/RT applications. TAMS/RT is currently undergoing demonstration projects at Navy facilities in San Diego and Bahrain. It is planned for TAMS/RT to be installed at all U. S. Navy regional centers within the next 1-2 years.

4. CONCLUSIONS AND FUTURE PLANS

NRL MMD continues to develop and extend the use of the global and mesoscale modeling systems NOGAPS and COAMPS. Both systems represent complete data assimilation systems to best define the initial conditions for their respective models using all available current data blended with their own background fields, which contain information from previous observations. NOGAPS is used to provide relatively coarse resolution (approximately 80 km) forecasts for the entire globe out to 7-10 days. Statistics demonstrate that this system is among the best global data assimilation systems in the world for 0-10 day predictions of transient weather systems, and is particularly useful for the prediction of the track of tropical cyclones.

COAMPS is used as a globally relocatable data assimilation system for the prediction of mesoscale events that require higher resolution than can currently be attained by NOGAPS. The COAMPS analyses/forecasts can be made either at FNMOC or at a remote site. In the latter case, the TAMS/RT system is used, utilizing powerful workstations. NOGAPS and COAMPS are used in a synergistic manner to yield the most timely and accurate forecasts possible for any given area of the world. The systems are intrinsically tied through the use of NOGAPS fields on the lateral boundaries of all COAMPS areas.

Significant improvements are planned for NOGAPS and COAMPS. First, a 3-dimensional variational analysis (3D VAR) is being developed. The 3D VAR will enable a more optimal fit of the data and the background field. This analysis tool will replace the current MVOI analysis in both NOGAPS and COAMPS. Both NOGAPS and COAMPS are being recoded for use on distributed memory computers. Several modifications are being developed and tested specifically for NOGAPS. These include the inclusion of semi-Lagrangian advection, to allow for more accurate prediction of moisture and a larger time step; the development of differentiable physical parameterizations, which will allow for an improved coupling of the model with the analysis; and coupling the NOGAPS model with an ice and ocean model. Other modifications are now being developed and tested for COAMPS. These include the addition of an improved surface parameters database; an improved soil model, testing the effects of coupling to a 3-dimensional ocean model; and the inclusion of aerosol analysis, initialization, and prediction components. These improvements will be included in both the FNMOC and TAMS/RT applications of COAMPS.

ACKNOWLEDGEMENTS

The author wishes to acknowledge the sponsors, the Office of Naval Research, through programs PE-0601153N, PE-0602435N and PE-0602704, and the Space and Naval Warfare Systems Command, through program PE-0603207N, for their support of the projects described in this paper. The author also thanks the many individuals at NRL MMD who have worked to help make these programs a success.

REFERENCES

Baker, N. L., 1992: Quality control for the Navy operational database. *Wea. Forecasting*, **7**, 250-261.

Barker, E. H., 1980: Solving for temperature using unnaturally latticed hydrostatic equations. *Mon. Wea. Rev.*, **108**, 1260-1268.

Hodur, R. M., 1997: The Naval Research Laboratory's Coupled Ocean/Atmosphere Mesoscale Prediction System (COAMPS). *Mon. Wea. Rev.*, **125**, 1414-1430.

Hogan, T. F., and T. E. Rosmond, 1991: The description of the Navy operational global atmospheric prediction system's spectral forecast model. *Mon. Wea. Rev.*, **119**, 1786-1815.

Klemp, J., and R. Wilhelmson, 1978: The simulation of three-dimensional convective storm dynamics. *J. Atmos. Sci.*, **35**, 1070-1096.

Lorenc, A. C., 1986: Analysis methods for numerical weather prediction. *Quart. J. Royal Meteor. Soc.*, **112**, 1177-1194.

Rutledge, S. A., and P. V. Hobbs, 1983: The mesoscale and microscale structure of organization of clouds and precipitation in midlatitude cyclones. VIII: A model for the "seeder-feeder" process in warm-frontal rainbands. *J. Atmos. Sci.*, **40**, 1185-1206.

JOINT METEOROLOGICAL AND OCEANOGRAPHIC (METOC) 2010 VISION AND ARCHITECTURE

Richard J. Szymber *
US Army Research Laboratory
Fort Huachuca, AZ
DSN: 879-0723 E-mail: rszymber@arl.mil

Doug McDonald
Defense Information Systems Agency
Falls Church, VA
DSN: 761-2404 E-mail: mcdonald@ncr.disa.mil

INTRODUCTION

The phrase Meteorological and Oceanographic (METOC) pertains to the endeavor concentrating on natural atmospheric and oceanic phenomena that affect military operations. The intent of METOC operations is to provide Joint forces timely, accurate, and relevant METOC information necessary for warfighters to anticipate and exploit the physical environment to gain a decisive advantage over adversaries. The ability to shape the battlespace for maximum result requires the METOC community to provide the information needed to assess the contribution of the physical environment to the differential performance between friendly and threat forces. This difference or "delta" in performance is the relative tactical advantage friendly forces have over the enemy. This information is essential for commanders to understand the differential impacts of the physical environment on systems, personnel, operations and tactics, so they can anticipate and exploit the environment to their benefit. The US Army and Air Force refer to this concept as "Owning the Weather."

METOC information is crucial to realizing Joint Vision 2010 (JV 2010). The enhanced operational concepts described in JV 2010 are: dominant maneuver, precision engagement/strike, full-dimensional protection, focused logistics, and information superiority/dominance. To support these operational concepts, the objective of METOC operations is to produce a collaborative, virtual, common operational/intelligence and logistical picture of the battlespace integrated with METOC information and automatically integrated into weapons/sensor systems and Command, Control, Communications, Computers and Intelligence (C4I) systems. This integration requires robust communications for the timely distribution of relevant METOC information.

METOC STEPS TO 2010

Some positive characteristics of METOC today are: a) Skilled METOC personnel capable of handling complicated technical equipment and applications; b) Increasing availability of commercial technology and METOC data from multiple sources (e.g., air traffic control radar

systems) to METOC operators; c) Improving Meteorological Satellite (METSAT) capability (although Joint forces are dependent on foreign METSATs for OCONUS geostationary satellite data); and d) Physical environmental impacts on friendly systems/operations are well understood (however, our knowledge of the corresponding impacts on threat systems, operations and tactics is more limited).

Current shortfalls in the four main METOC functional areas are: a) *Data Acquisition*: inadequate METOC observation network with insufficient data over remote/denied areas and on the space environment; and interoperability limitations in data dissemination; b) *Characterization*: low resolution numerical METOC models; c) *Application*: limited interoperability with and applications for C4I systems; and physical environment not represented in Modeling and Simulation (M&S) systems; and d) *Doctrine/Training*: moderate capacity to focus Service capabilities for Joint operations.

The objective for 2010 is efficient, timely, and focused METOC for the warfigther. Objective characteristics of METOC in 2010 for the four functional areas are: a) *Data Acquisition*: enhanced METOC observing/sensing systems with complete, continuous collection coverage (space, air, ground, ocean); collection of data from non-traditional METOC sources (e.g., weapons/sensor systems); and interoperable architecture to handle data communications and changing requirements; b) *Characterization*: reliable, high resolution METOC prediction models; improved battlespace visualization techniques and products; and improved and interoperable tactical METOC systems; c) *Application*: automated determination of environmental effects on friendly and threat systems/operations and tactical advantage assessment; an integrated suite of qualitative (rules-based) and quantitative (physics-based) METOC Tactical Decision Aids (TDAs); high fidelity representation of environment/effects in M&S systems; interoperability and integration with operator C4I systems; and Joint METOC applications on the Global Command and Control System (GCCS); and d) *Doctrine/Training*: focus on exploiting the "differential advantage" the environment can provide friendly forces; and multilevel security and automated coalition support.

The roadmap (1999-2010) for evolving METOC to 2010 consists of an axis for each major functional area: a) The *data acquisition* timeline tracks the following observing/sensing systems: National Polar-orbiting Operational Environmental Satellite System (NPOESS) and other US/foreign METSATs; Joint Unmanned Aerial Vehicle (UAV) – dropsonde and meteorological sensor; tactical doppler weather radar; tactical atmospheric profiler; tactical automatic/remote surface meteorological sensor/system; and Observing System - 21st Century (OS21); b) The *characterization* timeline traces the following tactical forecasting/processing systems: Integrated Meteorological System (IMETS); New Tactical Forecast System (N-TFS) and Forecast System - 21st Century (FS21); Tactical Environmental Support System Next Century (TESS-NC); and/or (to be determined) Commercial Off- the-Shelf (COTS) system; c) The *application* timeline marks the following TDAs: Integrated Weather Effects Decision Aid (IWEDA); Target Acquisition Weather Software (TAWS); and Composite Querry Analysis Display (COMQUAD). M&S systems of concern are the Joint Warfighting System (JWARS) and Joint Simulation System (JSIMS) with high-resolution scene simulation. Also of concern are a set of Joint METOC applications (e.g., overlay of METOC information on the common operational picture (COP)) for GCCS and the Joint Mission Planning System (JMPS); d) The

doctrine/training timeline lays out the following Joint doctrine and architecture developments: Joint Pub 3-59 and Joint Pub 2-03; Joint METOC Architecture; and Joint METOC Data Standardization and Logical/Conceptual Data Model (to provide standardization of data elements and data exchange format for improved data sharing and interoperability among METOC information systems). Joint exercise and experimentation training areas of concern are: Joint METOC Training Handbook; Multiservice Tactics, Techniques, and Procedures for Night and Adverse Weather Combat Operations; Joint Warfighting Experiments and Advanced Warfighting Experiments; and Advanced Concept Technology Demonstrations and Advanced Technology Demonstrations.

JOINT METOC ARCHITECTURE

The primary purposes of the Joint METOC Architecture (JMA) are to facilitate the interoperability of tactical METOC systems and to improve the quality and conduct of Joint METOC operations. The architecture is designed to support the intent of METOC operations and to set the foundation to support JV 2010 joint warfighting concepts and operational capabilities. The official objective of the JMA is: "... set forth an interoperable system design capable of providing Joint METOC operations with rapid, error-free exchange of METOC information into, out of, and within a Joint Force Area of Operations (AO)." The associated "desired end state" is: "METOC units – from all Services and at all echelons of command – operating in a Joint, deployed environment receive all necessary input data in a timely fashion. And, to the extent necessary, all Service METOC and Command and Control (C2) elements are able to seamlessly exchange raw data and finished products with minimal effort as a routine part of their every day way of doing business."

Three architectural views are used to define the JMA: an operational architecture, technical architecture, and systems architecture. The Joint METOC *operational architecture* describes the functions, operational elements, and information flows needed for successful Joint METOC operations that provide the Commander, Joint Task Force (CJTF) and the Services' operational-level command elements with accurate, timely, relevant and tailored METOC information. The Joint METOC *technical architecture* identifies standards and existing/emerging technologies necessary for developing an interoperable systems architecture. The Joint METOC *systems architecture* prescribes a hardware/software configuration that corrects the interoperability deficiencies recognized in the operational architecture assuming the state of emerging technologies. It focuses more on automated communications and information systems located in the AO than those used at the METOC Forecast Centers (MFCs).

The current operational architecture poses several challenges related to conducting Joint METOC operations. Difficulty exists in sharing METOC observations among tactical units and in the timely transmission of observational data to the MFCs, in part due to the old AUTODIN message traffic system (AUTODIN is being replaced by the timelier Defense Message System (DMS)). METOC products generated by the MFCs cannot be easily disseminated to lower echelon tactical units because of insufficient connectivity and/or bandwidth. Problems exist in sharing METOC products among Service tactical METOC and C2 systems due to

communications constraints and incompatible data transfer formats, mapping standards and database application program interfaces.

The technical architecture assesses emerging enabling technologies associated with interoperable METOC systems and communications. Global, broadband satellite broadcast services will be available to support Joint METOC operations by 2003, with two-way satellite systems (e.g., MILSTAR II) to provide additional capability (assuming resolution of bandwidth allocation issues). Lower echelons of command will have increasing access to tactical Transmission Control Protocol/Internet Protocol (TCP/IP) networks, and common Information Dissemination Management (IDM) segments will become part of the Defense Information Infrastructure Common Operating Environment (DII COE). National Imagery Transfer Format (NITF) formats (for geo-referenced imagery) and World Meteorological Organization (WMO) METOC data exchange formats will remain the standard for at least the next decade. METOC data standardization efforts will emphasize the meta-data of METOC products (for search engines), and the Joint Mapping Tool Kit (JMTK) will eventually satisfy the requirements of all the Services.

The suggested systems architecture recommends two new approaches for disseminating METOC data to support Joint METOC operations: the use a Joint METOC Database (JMDB) and the Global Broadcast Service (GBS). The JMDB would be the central repository for all METOC data/products (e.g., observations, forecasts, warnings, gridded data, METSAT imagery, TDAs, and overlays) required in the AO by the Services and approved by the Joint Force METOC Officer (JMO). It would manage all METOC information requests and distribution of requested information in the AO from user profiles and ad hoc requests. It would also operate with GBS IDM system components and manage the routine push of collected data in the AO. The JMDB concept permits the database to be "mirrored" at alternate locations and provides easy access to data/products through web-based technologies. The JMO and Senior METOC Office (SMO) can establish flexible access rights for updating and accessing the database compliant with Joint doctrine. The GBS will be capable of disseminating large-volume data sets and local observations to all METOC units in the AO. But since it cannot meet all requirements in the AO, two-way satellite communications will provide additional support to Joint METOC operations.

Some issues exist regarding GBS that must be resolved. The GBS Joint Operational Requirements Document (JORD) states that it is not a critical C2 system. GBS receive terminals are connected to IP networks, requiring access to tactical IP router networks. Also, wide fielding of receive terminals to lower echelons may be limited due to the relatively high cost per receiver. Furthermore, even though GBS furnishes large bandwidth, METOC must compete with other functional areas for priority in bandwidth allocation, which is controlled by the Commander in Chief (CINC) in the AO. Despite all this, the use of GBS in supporting Joint METOC operations is consistent with current fielding plans by the Services and bandwidth allocation plans at the CINCs.

Today's METOC interoperability problems result from a lack of a complete Joint systems solution for sharing METOC information among the Services. However, the following three initiatives should greatly improve Joint interoperability and METOC operations: a) Use of a

JMDB to easily manage and administer access to all Joint METOC information (including collection and dissemination of local observations); b) Utilization of GBS and tactical IP networks to distribute regularly scheduled, large-volume METOC data; and c) Migration of Service-unique and Joint METOC applications/products to standard WMO-based exchange formats and NITF-based imagery formats. Joint METOC forces engaged in future combined/allied operations with systems that exploit standard IPs and web technologies will promote interoperability.

CONCLUSION

The METOC capabilities of the Services must be focused to support Joint operations in a Joint/Coalition environment. Present-day METOC has several attributes that give it a good start for beginning the next century. Joint METOC architecture and doctrine has been created and the road to standardization and compliance is under way within the Department of Defense. Although current METOC is dynamic and capabilities are constantly improving, certain investments must be made and challenges met in order to fully achieve the METOC 2010 vision. METOC is a critical aspect in attaining JV 2010 dominant battlespace awareness.

PROGRESS UPDATE ON THE AFRL WEATHER IMPACT DECISION AIDS PROGRAM

Paul Tattelman
Air Force Research Laboratory
Hanscom AFB, MA 01731
DSN: 478-5956
tattelman@plh.af.mil

The Air Force Research Laboratory is a DoD leader in the creation of tailored weather products that translate conventional weather information into impacts on system performance. The Weather Impact Decision Aids (WIDA) program produces physics-based software to predict the influence of weather and other environmental parameters on the operational performance of Electro-Optical (EO) sensors (infrared, laser, visible) used in air-to-ground munitions, navigation systems, and Night Vision Goggles (NVGs). .

Products under development include an IR scene visualization capability for aircrew situational awareness, an environmental support tool for NVG operations, a joint-service upgrade to the currently operational EO Tactical Decision Aid (EOTDA), and a methodology for automating weather impacts in mission planning for Air Tasking Order (ATO) generation and reprogramming. An interim environmental support capability for 3-5 micron sensors was recently completed in the form of a modification to EOTDA V3.1.

Unique measurement facilities have been established to evaluate EO target and background signature models in the infrared (3-5 and 8-12 micron) and near-infrared (.7-.9 micron). EO data and imagery along with supporting meteorological and geophysical data are collected for systematic model validation. For IR sensors, experimental data for a three-year period were collected at a fixed site at Hanscom AFB, Massachusetts. A mobile platform equipped to conduct both IR and NVG experiments has been used to collect data at several sites on Otis ANGB, Cape Cod, Massachusetts. In addition, actual IR cockpit video collected at Fallon NAS, Nevada and Eglin AFB, Florida are being used to evaluate IR scene-visualizations and ensure realism.

The WIDA program has made some significant headway over the past year, both technologically and in scope. This presentation will provide an overview on the program, report on progress made over the past year, and provide an update on anticipated WIDA product deliveries over the next several years.

1. Introduction

The Weather Impact Decision Aids (WIDA) program at the Air Force Research Laboratory is developing new products that provide performance predictions for EO Systems. Current focus is on IR and night vision systems. The goal is to translate conventional weather

data into information needed to anticipate and exploit the impact of the battlespace environment on systems used by both friendly and enemy forces. WIDA products provide the warfighter with predictions and visualizations of the influence of weather and other environmental parameters on Electro-Optical (EO) Sensors (infrared, laser, visible) used in air-to-ground munitions, navigation systems, and night vision goggles (NVGs). These products allow mission planners to factor weather into key decisions such as mission time, target approach heading, tactics, and weapons selection. They provide combat aircrews with detection/lock-on range predictions and/or target scene predictions, facilitating target location and positive identification.

A survey of EO requirements was conducted for the WIDA program in CY95. This study acknowledged the importance of understanding and exploiting weather effects on EO systems. The survey of planners and pilots pointed out numerous requirements including the need for simultaneous guidance for multiple targets, guidance for weapon selection, target-area visualization, and more wavelengths than the current EOTDA.

The current WIDA program is divided is the following four projects:

a. Infrared Target-scene Simulation Software (IRTSS) - Develops and upgrades models for predicting and visualizing weather impacts on air-to-ground IR targeting and navigation.

b. Night Vision Goggle (NVG) Operations Weather Software (NOWS) - Develops and integrates models for determining the influence of weather and illumination on the performance of NVGs.

c. Target Acquisition Weather Software (TAWS) - Utilizes the models developed in IRTSS, NOWS, and other research programs to predict the impact of weather and environmental effects on IR, TV, NVG and Laser weapon and navigation system performance (e.g. lock-on range).

d. Weather Automated Mission Planning Software (WAMPS) - Integrates the models developed and incorporated in the above three projects into a product that will automate the generation of EO weather impacts in force-level automated mission planning systems.

The above components and recent progress are discussed in more detail in the following sections.

2. IR Target-scene Simulation Software (IRTSS)

IRTSS provides an IR visualization of the target scene (currently 8-12 μm, but 3-5 μm will be added). The visualization capability includes terrain shadowing, realistic vegetation graphics and animated fly-throughs that allow for 3-dimensional positioning of the sensor to view the scene from any angle. IRTSS was developed for incorporation into the AF Mission Support System (AFMSS) that will support aircrew mission planning and execution. Plans also include the transition of a web-based capability to the AF Weather Agency (AFWA) that would

be available to AF weather support personnel in the field. IRTSS development includes the following components:

a. Thermal Contrast Model - Physics models are used to calculate the IR radiance of elements of the targets and surrounding terrain. The currently operational Electro-Optical Tactical Decision Aid (EOTDA) uses a Thermal Contrast Model (TCM2) for targets and backgrounds. IRTSS is upgrading TCM2 for targets, and evaluating radiance models developed by the Smart Weapons Operability Enhancement (SWOE) Program for backgrounds. The upgrade to TCM2 is based on TCM2 assessment measurements made using a FLIR 2000 IR sensor to observe simple test targets along with a comprehensive suite of meteorological observation equipment including a TPQ-11 cloud profiling radar. Data are being used to identify weather sensitivities causing differences between observed and predicted radiance. Current modeling is for 8-12 μm; a 3-5 μm model will be added in the future.

b. Atmospheric Transmission Model - Atmospheric transmission is calculated using MODTRAN, but calculation time is minimized using a spatial interpolation scheme developed for IRTSS.

c. Sensor Performance Model - Sensor performance modeling characterizes the ability of specific IR sensors to distinguish targets and backgrounds. IRTSS will include an improved sensor performance model to overcome limitations in the models currently used in the EOTDA.

In addition, automated data management techniques to drive the above models are being developed for IRTSS. Geographic data sets are generated using ARC/INFO, a commercial Geographic Information System (GIS). Geographic data sets are generated from a variety of sources, including National Imagery and Mapping Agency (NIMA, formerly DMA), USGS, commercial satellites, and national imagery, and can support large areas (e.g. 40 km x 40 km at 10m resolution). The GIS is being programmed to fully automate this process. IRTSS models are also driven using real-time weather derived from the AF Weather Information Network (AFWIN).

Progress over the past year includes the following:

a. Addition of an IR (and visible) cloud rendering capability that includes first order cloud radiative effects,
b. A reduced fidelity mode that does not use detailed geographic backgrounds, which runs considerably faster, allowing for immediate global coverage. The generated imagery includes a target on a specified monochrome background, with atmospheric transmission and sensor effects,
c. A capability for rendering camouflage netting over targets,
d. An upgrade to utilize the OpenGL 1.1 graphics library,
e. Transition of IRTSS Version 2.0 to the AFMSS Program Office,
f. Integration of software for custom target building, and
g. Side-by-side comparison between IRTSS synthetic imagery and IR cockpit video

3. Night Vision Goggle (NVG) Operations Weather Software (NOWS)

The NOWS effort began with a deficiency in AFSOC weather support to covert nighttime helicopter air refueling using NVGs. After meeting with pilots of the 9th Special Operations Squadron and AFSOC weather personnel in March 91, Phillips Lab (PL) Geophysics Directorate, an AFRL predecessor, initiated an R&D effort to predict weather impacts on the performance of NVGs. A contractual effort began in FY92. The prototype NOWS was delivered in FY94 and demonstrated to AFSOC and ACC. This led to a greatly expanded list of requirements for NOWS to support differing scenarios, targets, backgrounds and hazards for NVG operations. The NOWS Graphical User Interface (GUI) and products were developed in close coordination with AFSOC and ACC. NOWS Version 1.0 was delivered in FY95 for evaluation by AFSOC weather (16th OSS). NOWS Version 4.0 was completed in Nov 97 and almost 100 copies were distributed to AFSOC and ACC units for feedback.

NOWS has distinct advantages over other NVG support products including:

a. Physics-based models incorporating relevant weather for target detection range,
b. Upward and downward lines-of-sight,
c. Atmospheric attenuation and path radiance effects,
d. NVG sensor modeling,
e. Terrain elevation and features, and
f. An urban illumination model.

NOWS incorporates worldwide map backgrounds for displaying, choosing, and tracking missions. It provides alerts to NVG operations hazards such as loss of horizon and towers, and provides NVG ranges as a function of user-selected probabilities. It also depicts optimum azimuth to approach a target or background. Weather-data input is automated with manual override capability.

NOWS progress over the past year in preparation for the completion of Version 5.0 in Feb 99 includes the following:

a. A new operating environment that provides Windows 95/97 look and feel,
b. Maps based on National Imagery and Mapping Agency (NIMA) Vector Smart Map (Vmap) instead of the outdated Digital Chart of the World,
c. Customized NVG sensor option allowing user-defined sensors,
d. AFWIN data access, and
e. Additional targets.

Currently planned NOWS milestones call for completion of Version 5.0 in Feb 99, and Version 6.0 in Feb 00. Subsequently, NOWS will be incorporated into TAWS.

4. Target Acquisition Weather Software (TAWS)

TAWS is planned as a replacement for the EOTDA. EOTDA Version 3.1 was delivered in 1994, and is currently being used operationally by the AF and Navy. This product was developed during a period of relatively primitive PC and workstation capabilities, limiting its utility. Furthermore, the EOTDA had only limited validation, is tedious to run, and often requires subjective manipulation by forecasters to adjust for discrepancies or bias in the core physics models.

IRTSS and NOWS models will provide the IR and NVG portions of TAWS, which will also include an upgraded TV model and a laser model. TAWS is being developed as a joint AF/Navy/Army program with the AF Research Laboratory as the lead agency. TAWS will provide more accurate acquisition and lock-on ranges, support MWIR in addition to LWIR, provide improved guidance on tactics, far superior visualizations, probability outputs, the ability to support multiple tasking, automated weather input, and guidance on weather sensitivities.

TAWS is being developed over a four-year period that began in Aug 97 and will include five major software releases. Development will incorporate customer/user feedback (e.g. pilots, mission planners).

Progress over the past year includes the following:

a. Agreement with Naval Research Laboratory (NRL) and Space and Naval Warfare Systems Center (SPAWAR) for incorporating Navy requirements,
b. Preliminary agreement with the Army to incorporate their requirements,
c. Development of a Graphical User Interface (GUI) and other related software efforts for the TAWS beta release.

Currently planned TAWS milestones call for completion of the beta-test version for user evaluation and feedback in Feb 99, completion of Version 1.0 as the anticipated replacement for the EOTDA in Aug 99, followed by several upgrades leading to completion of Version 4.0 in Aug 01.

5. Weather Automated Mission Planning Software (WAMPS)

Currently, weather impacts on systems and operations are not included in force-level automated mission planning systems. In order to support the appropriate selection of weapon and navigation sensors for hundreds, or even thousands of sorties, it is imperative that mission planners have decision aids that automatically assess weather impacts for specific sensors against selected targets and backgrounds.

Whereas TAWS is primarily a tool to support mission execution, WAMPS is envisioned as a force-level (24-72 hrs) stoplight weather impact mission planning capability. By providing

red/yellow/green (unfavorable/marginal/favorable) guidance for each weapon/target combination, planners can better select weapons or alternatives or modify times-over-target. WAMPS will integrate new technologies developed in the PL WIDA program with other decision aids available in the EOTDA and elsewhere. The goal here is to demonstrate how weather decision aids can greatly enhance mission planning by exploiting both offensive and defensive weather sensitivities.

Progress over the past year includes the following:

a. Development of a WAMPS first-prototype demo of WIDA interaction within force-level planning using a scripted sequence in the development of the Air Tasking Order, and,
b. Discussions with AF Electronic Systems Center regarding collaboration in the tailoring of WAMPS for mission planning systems under development.

Current plans call for a prototype demo in Dec 98, followed by 3 upgrades between then and Aug 01.

6. WIDA Model Validation

An integral part of the PL WIDA program is product validation. Two separate facilities are used to make comprehensive meteorological and sensor measurements. A fixed site at the Geophysics Directorate at Hanscom AFB, MA., (about 15 miles north of Boston) is used to collect all meteorological and EO data required by the IRTSS thermal models. In addition to comprehensive meteorological and EO-related measurements, imagery is collected using a FLIR 2000 (8-12 μm), a FLIR PRISM (3-5 μm), and a TV camera (visible) observing two simple test targets. Currently, only the 8-12 μm data are being used for thermal-model validation and improvement.

A mobile platform has also been instrumented for IRTSS and NOWS validation measurements. Data collection using the mobile (trailer) facility will be primarily at the Camp Edwards range at Otis ANGB, Cape Cod, MA. For NOWS, the mobile facility includes measurements utilizing three laboratory-grade radiometers, NVGs, and tailored bar targets. The fixed and mobile facilities are referred to as WIDA Lab, and data collected ensure that WIDA products will be thoroughly evaluated during their development. In addition, IRTSS is being evaluated by the 46th Test Wing and 46th Weather Squadron at Eglin AFB, FL. Pilots are briefed using IRTSS, and cockpit video and meteorological validation data are returned for analysis and product upgrade. Madsen (1998) provides a more detailed presentation of validation efforts.

Progress over the past year includes the following:

a. The mobile platform was deployed for 10 weeks at Otis ANGB making illumination measurements in all 4 seasons and numerous moon stages,
b. The NOWS contractor analysis of the data to validate the illumination and target models, and

c. Collection and analysis of cockpit video against the IRTSS synthetic imagery.

7. Additional Activities

Another major activity over the past year was the development of an MWIR upgrade to the EOTDA V3.1, which was delivered to AF Weather Agency in June 98. This was in response to an urgent requirement from USAFE to provide weather decision aid support to the new AGM-130. In January 98, AFRL proposed an approach to incorporate an interim capability into the EOTDA to provide the needed support until it was available in TAWS. Operational AF Weather led by the AF Director of Weather reached agreement for this approach upon review of the AFRL proposal and other options.

8. Closing Remarks and Summary

The Department of Defense has spent considerable sums of money trying to engineer "all-weather" systems that are not impacted by the environment. A recent study by the GAO found that "all-weather" effectiveness was overstated by DoD, that precision guided munitions functioned effectively only in optimum conditions, and that IR, EO, and laser systems were seriously degraded by weather. Considerable improvement could be obtained by tailoring weapon choice, time of attack, and tactics to the weather. The use of validated environmental decision aids in mission execution and the automated mission planning process would bring current "smart systems" closer to the desired "all-weather" capability than trying to engineer-out the weather, and at a small fraction of the cost.

The WIDA program is developing products that translate conventional weather data into information that the warfighter needs to exploit the battlespace environment. This article presented an overview and progress report on the current program, with near-term plans for product deliveries. Future efforts will incorporate joint DoD requirements and model upgrades into decision aids that will enhance all levels mission planning and execution.

References

1. Madsen, D. (1998) Weather Impact Decision Aids – IR and NVG Model Validation, AFRL-VS-HA-TR-98-0022, Reprinted from Proceedings of the Battlespace Atmospherics Conference, 2-4 December 1997, March 1998 [ADA 339641].

This page intentionally left blank.

Cloud and Cloud Effects Models

A Distributed, Parallel Method for Texture Image Calculation in Cloud Visualization

Steven M. Ayer
Radex Corporation
Bedford, Massachusetts 01730

Joel B. Mozer
USAF Research Laboratory, VSBE
Hanscom Air Force Base, Massachusetts 01731-3010

Abstract

Recent software methods and graphics hardware developments afford the possibility for fast, realistic cloud rendering. Through the use of advanced texture-mapping techniques on high-end SGI workstations, clouds images are currently rendered at near real-time speeds with sufficient fine detail for high resolution fly-through simulations. [1] These methods, however, depend upon the ray-tracing of the cloud optical field prior to the actual simulation run, a complex set of calculations, the demands of which are in direct proportion to the realism of the scene; more detail requires more resolution. The generation of realistic cloud scenes is typically one component of a complex simulation. The computational resources available for the task are often limited. Therefore, an efficient, scalable approach to the realistic rendering of clouds is needed.

We present a method for distributing the computationally-expensive ray-tracing of clouds to a number of processors as a parallel task. This method allows for the operation to complete in a compressed time frame, while the machine performing the actual scene visualization is busy with other pre-processing tasks, so that the cloud texture image is ready when rendering begins. This method improves total time-to-scene performance by a scalable, significant factor.

1 Introduction

During development of a cloud rendering method for the AFRL Weather Impact Decision Aids (WIDA) program's Infrared Target Scene Simulation Software (IRTSS), it became evident that the slow step was not the cloud rendering itself, but the ray-tracing required beforehand to create a texture image necessary for texture mapping hardware on certain Silicon Graphics workstations used to achieve high frame rates.

IRTSS is a high-resolution target and geographic features rendering package that is capable of generating realistic atmospheric and weapons sensor effects on a target scene. It renders scenes quickly after a short spin-up period while data are loaded into memory and thermal and atmospheric transmission models are run. One of the goals of adding cloud rendering to IRTSS was that no additional spin-up time would be added to the existing IRTSS processes. This led to the decision that the texture image processing would have to be done on a remote processor.

Fortunately, given an environment of fast computers linked by fast networks, this computational work can be farmed out to a remote machine or set of machines capable of performing tasks in tandem with the graphics workstation running the IRTSS, and of performing parallel computation on a decomposed input domain, then delivering the results to the IRTSS just in time for the rendering step. This distributed, parallel computing model removes the burden of doing ray-tracing on a graphics workstation, eliminating the data generation time penalty from the IRTSS cloud rendering option.

We describe our simple method for ray-tracing on a remote set of processors in parallel with near-linear scalability. This modular approach allows for easy replacement of the major aspects of the processing architecture, from the ray-tracing software to the hardware upon which the remote processes run.

2 The Texture Image Calculation

The texture image is produced by ray-tracing 3D cloud liquid water content (LWC) and extinction coefficient fields produced by running the Cloud Scene Simulation Model (CSSM) and Fastmap, respectively.

The CSSM produces a 3D gridded field of cloud liquid water content. Fastmap is a CSSM post-processor that uses lookup tables of optical and radiative properties to map CSSM liquid water content fields to particle-size distribution information and graphical quantities such as extinction optical depth. [2]

The texture image consists of two components, a brightness and opacity for each cell. Opacity is obtained by scaling LWC into the range 0.0-1.0, then mapping this value onto an 8-bit transparency value.

We calculate brightness from the extinction coefficient grid. A path is ray-traced from each gridcell toward the sun's position. Grid-wise extinction coefficients are integrated along this path. The extinction coefficient value for each grid cell is treated as nominal for the center of the grid cell, and tri-linear interpolation is used to get the "true" extinction for each sample's fractional offset from a grid cell center. Only the direct solar beam is

ray-traced; diffuse or scattered sources are ignored in this version of the software.

Application of Beer's law, which states that $I = I_0 e^{-d}$, where I_0 is the intensity of the incident beam and d is the integrated extinction value for that ray trace to the sun, mapped onto an 8-bit grey-scale, gives the final brightness for each cell.

The resulting texture image is then loaded into an OpenGL 3D texture map for rendering by IRTSS on an SGI workstation with hardware texture-mapping capability.

3 Decomposition of the Data

Spatial domain decomposition was used to parallelize the texture image construction algorithm. This data subsetting describes the division of work among processors and is a critical step because an inappropriate method can cause processor load imbalances or excess process-to-process communication that reduce the scalability of the problem. Because of texture memory restrictions on SGI texture-mapping hardware, a tiling scheme was already in place before this project began that would accommodate large cloud fields. This tiling technique subsets the data grid with vertical slices. The procedure then chooses tile size to match the amount of texture memory on the graphics workstation running IRTSS. All tiles are identical in size.

Decomposing the data for parallelization was made simple by tiling; the number of tiles is divided by the number of processors available, and each processor receives only its own data tiles. This method satisfies memory conservation goals by eliminating duplication of core memory images across the domain, a necessary consideration for large datasets.

4 Distribution of the Calculation

In order to execute the texture image calculations on a remote machine, the ray-tracing portion of the cloud rendering software was extracted from the IRTSS to create a stand-alone executable. Required data input for this executable consists of a CSSM LWC file and a Fastmap extinction grid file, so the ray-tracing can be done on any machine where these files are accessible via an nfs mounted filesystem.

IRTSS spawns the ray-tracing process by remote UNIX shell during its initial set-up routine. Remote processing of the cloud field is user switchable in IRTSS if the computing resources aren't available. Upon completion, the software writes one file of texture image values per tile, which IRTSS then reads from the same nfs mount point before it renders the cloud field.

5 Parallelization

To ensure portability and simplify implementation of the parallelization, we chose Message Passing Interface (MPI), a standard library of communications software for parallel computation. MPI provides a C-language application programmer's interface (API) through which data can be moved among various processors at run-time. In our implementation of the parallel ray-tracing, one master process reads the data from disk, then sends each waiting process its portion of the data via message passing. Once data is distributed, each processor performs ray-tracing one tile at a time, writing the resulting texture image to disk.

6 Performance

Scalability was measured on two parallel platforms, an SGI Origin 200 with two 185 MHz R10000 processors, and a rack of 4 120 MHz Pentium PCs running Linux connected by a 100 mbs fast Ethernet. The ray-tracing software was run on three data samples on each platform with a varying number of grid cells.

CPU	Pentium			R10000	
Gridcells	1	2	3	1	2
4M	2093.08	1090.97	595.97	518.11	275.95
2M	1093.00	981.57	516.77	532.55	277.84
1M	542.57	290.01	159.35	131.57	69.10

Run-times in seconds for two different platforms with a varying number of processors.

7 Future Directions

At present ray-tracing stops at a tile boundary. If that boundary is vertical and the ray elevation is low, then a great deal of information is lost in that trace. A scheme has been drawn up to pass messages that convey data from the portion of a ray's trace that enters another tile.

We also plan to add multi-scattering effects to the ray-tracing algorithm. The replacement of cloud field ray-tracing with a radiative transfer model is under consideration.

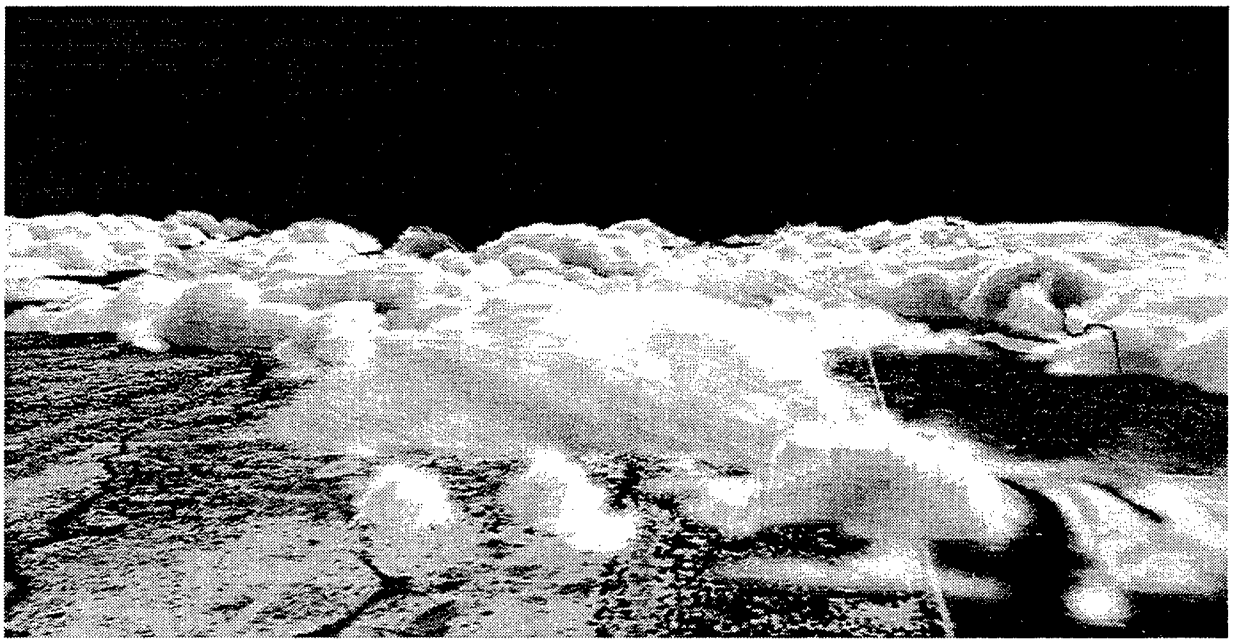


Figure 1: Stratocumulus clouds over a $6.4km$ x $6.4km$ region at $25m$ resolution.

8 Conclusions

Distributed, parallel processing allows the inclusion of cloud effects into scene visualizations without a spin-up time penalty before rendering. By using remote computers to process cloud data, large domain size and high resolution are possible with practical time-to-scene constraints.

References

[1] Ayer, S.M., Mozer, J.B., "Visualization Of Cloud Effects In Battle-scene Modeling And Simulation," *CIDOS 97*, September 1997, PL-TR-97-2112, ADA330020.

[2] Cianciolo, M.E., M.E. Raffensberger, E.O. Schmidt, J.R. Stearns, 1996: Atmospheric scene simulation modeling and visualization. PL-TR-96-2079, ADA312179, USAF Phillips Laboratory, Hanscom AFB, MA.

OBJECTIVE COMPARISONS OF REAL AND SYNTHETIC CLOUD IMAGERY

*Sara C. Gordon, Guy P. Seeley
Radex Corp - Bedford, MA

Joel B. Mozer
Air Force Research Laboratory - Hanscom AFB, MA

Alan Wetmore, Patti Gillespie, Samuel Crow, David Ligon
Army Research Laboratory - Adelphi, MD

Phone:781-275-6767
Fax:781-275-3303
Email:gordon@sastrugi.plh.af.mil
mozer@hurricane.plh.af.mil

Abstract

The Air Force Cloud Scene Simulation Model (CSSM) generates high-fidelity cloud liquid water content fields in 4D that can be visualized to produce realistic 2D synthetic images of clouds. We provide a quantitative comparison between imagery based on CSSM output and actual imagery of clouds taken from ground based sensors. A field experiment was held 27 April to 1 May, 1998 at Hanscom AFB to provide data for this comparison. A test site with full meteorological instrumentation, balloon radiosonde launches, and TPQ-11 cloud profiling radar provided input data for the CSSM. A visible band spectraradiometer was used for radiometrically accurate imagery collection of the clouds over the experiment site.

The spectraradiometer imagery was classified, by hand, according to cirriform, cumuliform and stratiform cloud types. Synthetic cloud scenes, which were heuristically consistent with the observed clouds meteorological conditions, were produced using the CSSM for each of the three cloud types. A set of candidate image-based metrics were computed both the real and synthetic imagery. A Multiple Discriminant Analysis (MDA) was performed on both sets of data to determine which of the candidate metrics were most effective for objectively discriminating among the three cloud types. In this paper we present the spectraradiometer imagery, the metrics used in the analysis, and the results of the MDA.

OBJECTIVE

Synthetic natural environments are an increasingly important component of high-fidelity models and simulations of DoD sytems and operations. Atmospheric clouds are a crucial component in many simulations where missions occur in or through the atmosphere, such as with an airborne or spaceborne weapon or surveillance sensor. Despite their importance, clouds are often neglected in such simulations because of the extreme complexity and general lack of understanding of the physical phenomena involved.

Accurate modeling of clouds and cloud-related effects involves the understanding of a broad range of physical processes and their interactions. Over broad geographic areas, the problem of representing clouds is intimately coupled to the large-scale dynamics of the atmosphere. At the opposite end of the spatial spectrum where the fine-scale features of the cloud are important, a

detailed knowledge of the microphysical composition of the cloud is needed. This is a complex situation involving knowledge of aerosols, cloud chemistry and ice physics. Closely related to this are the optical properties of clouds, the radiative interactions between clouds and various natural and artificial illumination sources across the spectrum from radio frequencies to longwave infrared.

The Cloud Scene Simulation Model (CSSM) was developed to produce realistic spatially and temporally varying cloud fields at high resolution for the simulation of cloud effects on DoD operations and systems. The CSSM is based on empirical fractal techniques coupled with cloud macrophysical models that utilize information regarding the ambient meteorological conditions. The free parameters of the CSSM core algorithms have been chosen based on extensive investigation of the statistics of cloud liquid and ice water content in real clouds (Cianciolo, et al, 1996, Turkington, et. al, 1998). To validate this selection in terms of the two-dimensional imagery, which is often produced by the CSSM, a separate analysis is required.

In the present work, we construct a technique to quantitatively compare cloud imagery using a set of image-based metrics. To test the validity of using these metrics to represent inherent features of the cloud images, they were used to objectively discriminate between three cloud types (cirriform, cumuliform, and stratiform). This was achieved through the use of Multiple Discriminant Analysis (MDA).

We constructed a technique to quantitatively compare cloud imagery using a set of image-based metrics. To test the validity of using these metrics to represent inherent features of the cloud images, they were used to objectively discriminate between three cloud types (cirriform, cumuliform, and stratiform). This was achieved through the use of Multiple Discriminant Analysis (MDA).

RESEARCH ACCOMPLISHED

Images were collected using a Real-Time Imaging SpectroRadiometer (RTISR) built by Surface Optics Corporation of San Diego, California. The RTISR collects a cube of radiometrically and spectrally calibrated images at an update rate dependent on the ambient light level up to a maximum of 15 Hz. The RTISR uses a zoom lens and a retractable tele-extender lens to provide fields-of-view of 29x22 degrees down to 1.9x1.4 degrees. The collected light then passes through a circular variable filter spanning the range of 390nm to 950nm over which 20 or 30 images may be collected per image cube. The bandpass for each image increases linearly over the range and is 2.5% of the center wavelength giving a FWHM bandpass of 9.9nm at 396nm, 17.5nm at 700nm, and 23.7nm at 950nm. The filtered light is then coupled to a micro-channel plate image intensifier using a fiber-optic taper. The image intensifier amplifies the light and then couples to a CCD focal plane array via a fiber-optic bundle. The focal plane array is 256 elements wide by 192 elements high. The images are digitized using a 12-bit A/D converter, calibrated, stored in memory, and then dumped to a computer via an IEEE-488 interface. (Gillespie et al. 1995a)

Data were acquired were from 27 April through 01 May 1998. The image cubes consisted of sets of 20 images collected at 16nm intervals over a wavelength range of 396nm to 700nm. The update rate depended on the ambient light conditions but was typically 1Hz. This relatively slow update rate was not significant for the data collected. Horizontal views of the sky, clouds, and the horizon were collected with a field-of-view of 29x22 degrees. Images of the ground targets were

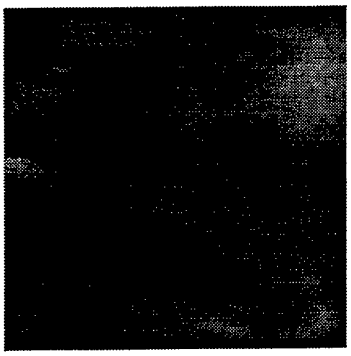
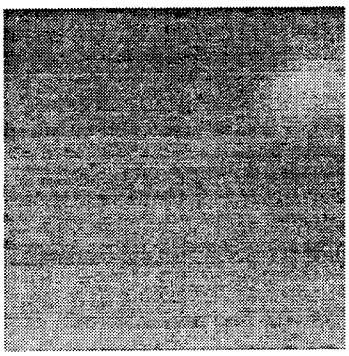
a.  b. 

Figure 1: a) 684 nm cumulus cloud image b) 396 nm cumulus cloud image

collected with a field-of-view of 14.5x11 degrees.

Since the images were rectangular and extended below the horizon, a 128x128 pixel region was cropped out of each image. This resulted in two sets of 73 images, one in the near ultraviolet wavelength range (396 nm) and one at the red end of the visible range (684 nm). The images were human classified and there was 1 cirrostratus cloud image, 11 cumulus cloud images, 34 stratus images and 27 clear sky images. Example images are presented in Figure 1. Figure 1a is a 684 nm cumulus cloud image and Figure 1b is the corresponding 396 nm cumulus cloud image.

Synthetic cloud images were produced using the AFRL Infrared Target Scene Simulation Software (IRTSS). IRTSS is capable of producing high resolution visible and infrared images of cloud scenes. Synthetic fields of cloud liquid water content were generated using the Cloud Scene Simulation Model (CSSM)(Cianciolo, et al. 1996). These 3D grids of liquid water content were transformed into grids of extinction coefficient data using the Fastmap (Cianciolo, et al. 1996) optical properties tool. Fastmap uses look up tables that map cloud type and liquid water content to optical and graphical quantities. Once the transformation of the data to extinction coefficient has taken place, rays are traced from each grid cell to the sun. The aggregate optical depth is computed and the direct solar beam is attenuated according using Beer's Law. The resulting field is then volume rendered using OpenGL texture mapping facilities. There is no treatment of diffuse sky radiation. 512 x 512 pixel images in the visible band were generated with a view vector looking vertically up into the generated cloud deck. The images had a resolution of approximately 9.75 meters/pixel. An example IRTSS image is shown in Figure 2. This figure shows a 512x512 synthetic stratus cloud image.

Several possible image metrics were selected from Parker (1997), Laws (1980) and Wilks (1995). A number of metrics were based on features of the grey level co-occurrence matrix (GLCM) (described below). Another class of metrics investigated were the textural energy metrics defined by Laws (1980). These metrics involve 5x5 convolution masks to detect the presence of edges, levels, or ripples in the image. An example metric is E5L5. A couple of metrics were based on Fast Fourier Transform (FFT) power spectra.

The GLCM is a NxN matrix where N is the number of grey levels present (in our case, 256):

$$\text{GLCM}(i,j) = \text{The probability of a pixel valued } i \text{ being horizontally adjacent to a pixel valued } j$$

In a previous study of implementing image metrics in atmospheric simulation-visualization models (Gillespie et al. 1995b, Rollins, 1995), the analysis using the GLCM and power spectra

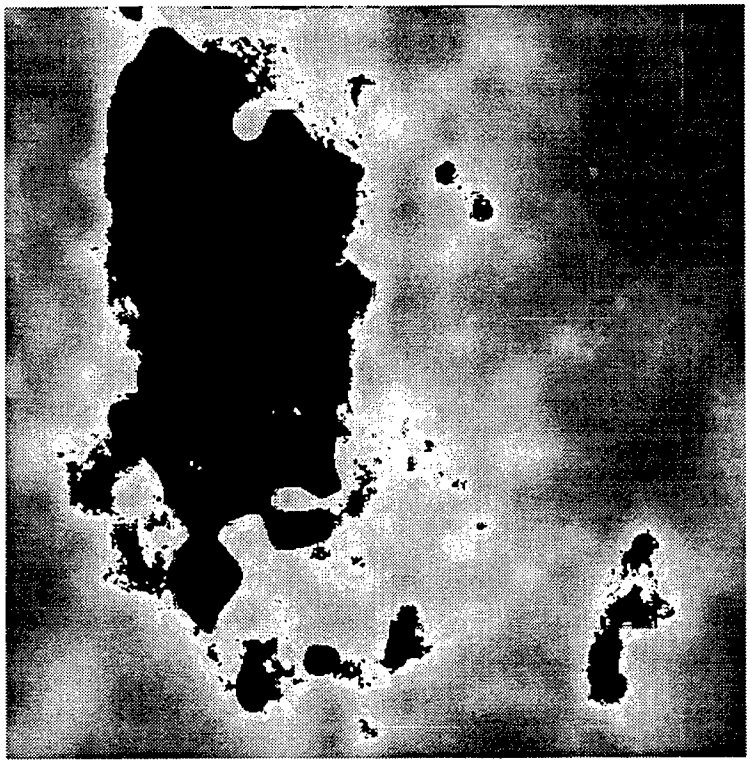


Figure 2: IRTSS stratus cloud image

resulted in indications that the radiative transfer model over-estimated the contrast and the turbulence model used in that case under-estimated the turbulence (Gillespie et al. 1995b). In this study, a multiple discriminant analysis (MDA) method was implemented to determine what metrics can be used to distinguish between cloud types. We employed an MDA method using the DSCRM function from the IMSL libraries by Visual Numerics, Houston TX.

The real cloud images first are human identified. Then the MDA method can be used to classify the images in one of two fashions: one, the MDA method classifies the images in one input image set; two, one image set can be used as a basis to classify a second image set.

The following metric combination could identify 88% of the 684 nm images and 82% of the 386 nm images. If these two sets are combined into one set containing 146 images, this metric combination could identify 76% of the images. If this set is used as a basis to classify the IRTSS images, 62% of the synthetic images were correctly identified.

1. Fast Fourier Transform
2. Summation of angles of edge pixels
3. skewness (of GLCM)
4. E5L5

1. The Fast Fourier Transform (FFT) metric is recorded as the summation of the low frequency FFT values. This summation is defined as the sum of the dot products in the center 32x32 window of a 256x256 image.

2. The summation of the angle of edge pixels metric measures uses two 3x3 convolution masks to measure the magnitude of the horizontal and vertical edge component for each pixel in the input image. The angle in radians for a given pixel location is obtained by computing $atan(\frac{vertical\ component}{horizontal\ component})$. The sum of the angles over all pixel locations is the metric value.
3. The skewness metric measures the skewness of the GLCM image created from the input image. Skewness is defined by:

$$Skewness = \frac{1}{n}\sum_{i=1}^{n}(x_i - \bar{x})^3$$

where n is the number of pixels in the GLCM image
4. The energy metric E5L5 is defined by multiplying the edge detecting E5 vector {-1, -2, 0, 2, 1} by the level detecting L5 {1,4,6,4,1} vector to obtain a 5x5 matrix. This 5x5 matrix can be used to convolve the input image. Edges are detected by the existence of the one zero crossing in the E5 vector and levels are detected by the lack of zero crossings in the L5 vector. The E5L5 metric measures the total horizontal edge content in the input image.

CONCLUSIONS AND RECOMMENDATIONS

Metric values can be used to discern cloud type with reasonable levels of accuracy. Two of the four metrics employed played to the edge features in the input images. One metric measured low frequency content. The remaining metric was independent of spatial image features and assessed grey level features in the cloud images. Hence, the four metrics essentially quantified different characteristics of the cloud images. These metrics not only can be implemented to distinguish between real cloud images, the metrics can also be used to discern synthetic cloud image types with the real cloud images defining the cloud types in this case study. A more detailed study using textural analysis to identify and classify cloud types is underway here at our laboratory.

REFERENCES

1. Cianciolo, M. E., Raffensberger, M. E., Schimdt, E. O., and Stearns, J. R., (1996), *Atmospheric Scene Simulation Modeling and Visualization*, PL-TR-96-2079, TASC, Reading, MA. ADA 312 179

2. Evans, F., (1997), SHDOM - Spherical Harmonic Discrete Ordinate Method for 3D Atmospheric Radiative Transfer, *http://nit.colorado.edu/~evans/shdom.html*.

3. Gillespie, P., S. Crow, and D. Tofsted, (1995a), *Atmospheric Experiments with an Imaging Spectral Radiometer*, Proceedings of the 1995 Battlefield Atmospherics Conference, U.S. Army Research Laboratory, Battlefield Environment Directorate, White Sands Missile Range, NM.

4. Gillespie, P., J. M. Rollins, and D. Tofsted, (1995b), *Evaluation of WAVES Using Image Statistics*, Proceedings of the 1995 Battlefield Atmospherics Conference, U.S. Army Research Laboratory, Battlefield Environment Directorate, White Sands Missile Range, NM.

5. Laws, K. I., (1980), *Textured Image Segmentation*, Ph.D. Thesis, U. Southern California, Los Angeles, CA.

6. Mozer, Joel, Guy Seeley, Alan Wetmore, Patti Gillespie, David Ligon, and Samuel Crow, (1997), *Radiometric Validation of CSSM*, Proceedings of the 1997 CIDOS (Cloud Impacts on DoD Operations and Systems), Naval War College, Newport, RI. ADA 330 020

7. Parker, J. R., (1997), *Algorithms For Image Processing and Computer Vision*, John Wiley & Sons, Inc.

8. Rollins, Michael, (1995), *Evaluation of the Weather and Atmospheric Effects for Simulation (WAVES) Using Image Statistics*, STC-TR-6259.

9. Turkington, R. B., M. E. Cianciolo, and M. E. Raffensberger, (1998), *Development of an Atmospheric Scene Simulation Model*, final technical report, TASC Technical Report TR-08607-1.

10. Wetmore, Alan, Patti Gillespie, David Ligon, Samuel Crow, Michael Seablom, Guy Seeley, and Joel Mozer, (1997), *Experimental Evaluation of the Integrated WAVES-CSSM Model*, Proceedings of the 1997 Battlefield Atmospherics Conference, San Diego, CA.

11. Wilks, D. S., (1995), *Statistical Methods in the Atmospheric Sciences*, Academic Press, Inc.

12. Zardecki, Andrew, (1993), *Three-Dimensional Extension of Boundary Layer Illumination Radiation Balance Model for Imaging Applications*, Final Report for Contract No. DAAL03-91-C-0034, TCN Number: 92-480, Delivery Order No. 0541.

STATISTICAL CONTRAIL FORECASTING:
Using Satellite Data and Numerical Weather Prediction Model Output

Artie Jackson*
Doug Hahn
Allan Bussey
Air Force Research Laboratory
Hanscom AFB, Bedford MA
Phone: 781-377-2958 Fax: 781-377-8892 email: jackson@plh.af.mil

ABSTRACT

Current operational Air Force contrail forecast procedures still rely on the Appleman technique, developed in the 1950's, with minor modifications. The Appleman technique depends on accurate measurements or forecasts of ambient flight level temperature, relative humidity and pressure as well as the amount of heat and water vapor in the exhaust plume of an aircraft to determine if the aircraft will produce a contrail. Current atmospheric measurement and numerical weather prediction technologies do not provide a sufficiently accurate description of ambient flight level conditions for the Appleman technique, thus operational contrail forecasts based on the Appleman technique are relatively poor. A Statistical Contrail Forecast Model has been developed which makes use of logistic regression techniques to relate contrail-YES/contrail-NO observations with coincident-in-time/space radiosonde measurements. The Statistical Contrail Forecast Model developed using radiosonde measurements provides a significant improvement in contrail forecasts when compared to current operational Air Force contrail forecasts. A new project is underway to develop Statistical Contrail Forecast algorithms using satellite sounding and satellite imagery data, and Numerical Weather Prediction model output as predictors. A contrail forecast algorithm developed using satellite data and Numerical Weather Prediction model output is desirable because it can be applied in data void areas where routine radiosonde measurements are not available. Since this project is in the early stages, an overview of project plans will be discussed in this paper. Preliminary results will be presented at the conference.

1. INTRODUCTION

In 1995, a program was initiated to study the formation of contrails by jet aircraft. The objective of the program is to measure the spatial distribution of atmospheric variables, particularly water vapor, with ground, air and space-based sensors with the ultimate goal to develop techniques to improve the capability to forecast the occurrence of contrails generated by jet aircraft. The program has resulted in two accomplishments thus far. First, a Field Program was conducted in eastern Massachusetts during a two week period in September 1995, in which coincident in time/space radiosonde measurements and aircraft contrail-YES/contrail-NO observations were collected. Second, a Statistical Contrail Forecast Model was developed which relates contrail-YES/contrail-NO observations with coincident in time/space radiosonde

measurements. The Field Program and results of the Statistical Contrail Forecast Model developed using radiosonde measurements are discussed in detail in Jackson, et al (1997).

Current Air Force operational contrail forecast procedures still rely on the Appleman technique (Appleman, 1953) developed in the 1950's, with minor modifications (Schrader, 1996). Over the years several modifications have been suggested to account for the variations of water and heat production in the plumes of major types of modern jet aircraft (Peters, 1993 and Schrader, 1996). A contrail forecast scheme developed for AFWA (Bjornson, 1992) used discriminant analysis techniques to relate temperature, altitude and vertical motion to contrail formation showed some improvement over the Appleman technique, but overall results were inconclusive.

The Appleman technique depends on accurate measurements or NWP forecasts of ambient flight-level temperature, relative humidity and pressure as well as the amount of heat and water vapor in the exhaust plume of an aircraft to determine if the aircraft will produce a contrail. NWP model forecast data and climatological relative humidity data used as input to these techniques often do not represent the true state of the atmosphere, thus resulting in poor contrail forecasts. Our strategy has been to take advantage of regression techniques to account for the biases of inaccurate atmospheric measurements, NWP model forecast data and aircraft engine-related factors.

Table 1 compares results of the Statistical Contrail Forecast Model (SM) developed using radiosonde data from the September, 1995 Field Program and the AFWA contrail forecast algorithm (AFWA) using the updated contrail factors suggested by Schrader (1996). The SM is a statistical algorithm which uses logistic regression techniques to relate contrail-YES/contrail-NO observations with coincident-in-time/space radiosonde measurements (Jackson, 1997). The SM significantly outperforms the AFWA model for all statistics except FAR. The Percent Correct (PC) for the AFWA model is .57, while the PC for the SM is .85. The Probability of Detection (POD) for the AFWA model is .33, while the POD for the SM is .91. The False Alarm Rate (FAR) for the AFWA model is .01, while the FAR for the SM is .13. The Discriminant V Score (VDS) is .32 for the AFWA model, while the VDS for the SM is .66. In all aspects except FAR, the SM performance is superior to the AFWA model. The smaller FAR for the AFWA model is somewhat deceiving because the AFWA/Appleman model characteristically underpredicts contrail occurrences (Speltz 1995, Peters 1993). Note in Table 1, that the AFWA model only predicted 116 of 355 contrail occurrences while the SM predicted 322 of 355 occurrences. The strong tendency of the AFWA/Appleman model to underpredict the occurrence of contrails results in a small FAR. The results obtained in this study for the AFWA/Appleman techniques are consistent with those reported by Speltz (1995) and Peters (1993).

The Statistical Contrail Forecast Model developed using radiosonde data is a valid contrail forecasting tool when radiosonde data is available. It is also a valuable proof-of-concept for the development of Statistical Contrail Forecast techniques using satellite sounding and satellite imagery data, and NWP model forecast data in areas void of conventional radiosonde data. The ability of the regression techniques to account for biases in atmospheric measurements including radiosonde data, satellite data and NWP model forecast data, and aircraft engine-related factors provides a potential advantage over the operational Appleman technique which requires accurate measurements or predictions to produce accurate contrail forecasts. The successful results obtained using regression techniques in the development of the Statistical Contrail Forecast

Model based on radiosonde data suggests that using satellite data and NWP model forecasts as input to regression-based contrail forecast techniques may also be successful.

TABLE 1: COMPARISON OF LOGISTIC REGRESSION STATISTICAL CONTRAIL FORECAST MODEL (SM) AND AFWA CONTRAIL FORECAST MODEL (AFWA)

Correct: Total of correct forecasts
Yes/FYes: Observed Yes, Forecast Yes
Yes/FNo: Observed Yes, Forecast No
No/FYes: Observed No, Forecast Yes
No/FNo: Observed No, Forecast No

POD: Probability of Detection
FAR: False Alarm Rate
CSIY: Critical Success Index/Yes
CSIN: Critical Success Index/No
PC : Percent Correct
VDS: Discriminant V Score

Model	# Correct	Yes/FYes	Yes/FNo	No/FYes	No/FNo	POD	FAR	CSIY	CSIN	PC	VDS
SM	474	322	33	50	152	0.91	0.13	0.80	0.65	0.85	0.66
AFWA	317	116	239	1	201	0.33	0.01	0.33	0.46	0.57	0.32
Contrail Yes Obs	355										
Contrail No Obs	202										

2. STATISTICAL CONTRAIL FORECASTING: USING SATELLITE DATA AND NWP MODEL OUTPUT

The long-term goal of this project is to develop new contrail forecast techniques using satellite data and NWP model forecast data to improve operational contrail forecast capabilities in areas void of conventional radiosonde data. Travis (1994, 1997) used satellite imagery data to detect contrails and as input to regression techniques to predict the occurrence of large scale outbreaks of contrails in a study of the effects of long-lived contrails on climate. Current AFWA contrail forecast techniques use a blend of NWP model forecast data and climatological data as input (Shull, 1998). Our intent is to develop and test statistical algorithms derived from the two data sources, satellite data and NWP model forecast data, using each data source exclusively, and the two data sources in combination.

Satellite sounding and satellite imagery data have the potential to be valuable predictors for contrail forecasting. Satellite soundings and imagery data are available over most of the globe at regular intervals, as frequently as every half hour. Satellite soundings provide valuable information on the horizontal and vertical distribution of temperature and water vapor in the atmosphere. Satellite imagery data provide valuable information on the horizontal distribution of water vapor, cloud amount and cloud type. Travis (1994) found the GOES 6.7 um water vapor radiance data to be the most significant predictor in a logistic regression model developed to predict the occurrence of persistent contrails. Detwiler and Pratt (1984) found that contrails often form under certain synoptic situations, such as ahead of cyclonic storms, which are often preceded by particular cloud types, such as cirrus. Thus, the presence of particular cloud types may be a useful predictor for contrail prediction.

Table 2 lists the satellite sounding and imagery predictors which will be included in the data set used to develop and test statistical algorithms. GOES data will be used for the sounding and

imagery products. Other geostationary or orbitting satellites with sounding and imagery capabilities could be used in an operational setting.

TABLE 2: SATELLITE SOUNDING AND IMAGERY PREDICTORS

Retrieved Temperature Sounding
Retrieved Moisture Sounding
6.7 micron Water Vapor Radiance
Outgoing Longwave Radiance
Presence/Absence of Cirrus Cloud
Presence/Absence of Sub-Visual Cirrus Cloud
Distance to Nearest Cirrus Cloud
Distance to Nearest Sub-Visual Cirrus Cloud
Height of Cirrus
Height of Sub-Visual Cirrus
Cirrus Cloud Amount
Sub-Visual Cirrus Cloud Amount
Presence of Other (Non-Cirrus) Cloud
Height of Other (Non-Cirrus) Cloud
Other (Non-Cirrus) Cloud Amount

NWP model output variables are currently used as predictors in regression techniques to forecast many meteorological parameters such as cloud amount, cloud height and precipitation probability. The ability of regression techniques to account for model biases provides a distinct advantage over operational contrail forecast algorithms which require accurate model forecasts to produce accurate contrail forecasts. A data set consisting of MM5 (Fifth-Generation Penn State/NCAR Mesoscale Model; Grell, 1995) initial analyses and forecasts will be used to build the predictor data set for development of the statistical contrail forecast algorithm. Predictors will include temperature, humidity, wind speed, wind direction, vertical velocity and other derived parameters.

3. SUMMARY

The logistic regression contrail forecast model using radiosonde data to predict contrail formation provides results which are superior to operational AFWA contrail prediction techniques. A new data set is being created to develop and test new statistical algorithms to forecast contrails using satellite sounding and satellite imagery data, and NWP model forecast data. A contrail forecast algorithm using satellite data and NWP model output is desirable because it can be applied in data void areas where routine radiosonde measurements are not available.

4. ACKNOWLEDGMENTS

We thank Mr Scott Lambert from the FAA Air Route Traffic Control Center in Nashua, New Hampshire for providing their facilities, allowing us to document aircraft type, altitude and speed in real time. The aircraft data obtained was invaluable to this study.

5. REFERENCES:

Appleman, H.S., 1953: "The Formation of Exhaust Condensation Trails by Jet Aircraft", Bulletin of the American Meteorological Society, Vol 34, pp 14-20.

Bjornson, B.M., 1992: "SAC Contrail Formation Study", USAFETAC/PR-92/003, USAF Environmental Technical Applications Center, Scott AFB, IL. [ADA 254410].

Detwiler, A., and Pratt, R., 1984: "Clear-Air Seeding: Opportunities and Strategies", Journal of Weather Modification, Vol 16, pp 46-60.

Grell, G., Dudhia, J., and Stauffer, D., 1995: "A Description of the Fifth-Generation Penn State/NCAR Mesoscale Model", NCAR/TN-398+STR, National Center for Atmospheric Research, Boulder, CO, 122pp.

Jackson, A., Newton, B., Hahn, D., and Bussey, A., 1997: "Statistical Contrail Forecasting", Preprints, Cloud Impacts on DOD Operations and Systems 1997 Conference, PL-TR-97-2112. [ADA 330020].

Peters, J.L., 1993: "New Techniques for Contrail Forecasting", AWS/TR-93/001, HQ Air Weather Service, Scott AFB, IL. [ADA 269686].

Schrader, M.L., 1996: "Calculations of Aircraft Contrail Formation Critical Temperatures", Submitted to Journal of Applied Meteorology.

Shull, J.D., 1998: "A Validation Study of the Air Force Weather Agency (AFWA) JETRAX Contrail Forecast Algorithm", Master's Thesis, Air Force Institute of Technology. [ADA 340994].

Speltz, D.J.,1995: "Validation of the Appleman Contrail Forecasting Scheme Using Engine-Specific Aircraft Data", Preprints, Cloud Impacts on DOD Operations and Systems Conference 95, PL-TR-95-2129. [ADA 300914].

Travis, D.J, 1994: "Jet Aircraft Condensation Trails: Their Radiative Impacts and Association With Atmospheric Conditions", PhD Dissertation, Indiana University.

Travis, D.J., Carleton, A.M., and Changnon, S.A., 1997: "An Empirical Model to Predict Widespread Occurrences of Contrails", Journal of Applied Meteorology, Vol 36, pp 1211-1220.

OBJECTIVE TECHNIQUES FOR FUSION AND ANALYSIS OF MESOSCALE NWP AND SATELLITE-DERIVED CLOUD DATA

Joel B. Mozer
Air Force Research Laboratory
Hanscom AFB, MA 01731
Mozer@plh.af.mil

Steven M. Ayer
Radex Corp.
Bedford, MA 01730

OBJECTIVE

Accurate information regarding the location, altitude, and coverage of clouds over a theater-scale geographic region is crucial to a variety of DoD missions. Meteorological satellite imagery is a principal resource for the determination of current, or at least recent, cloud conditions over a given region where such data is available. Satellites, however, do not provide forecasts of these cloud data. Current operational mesoscale numerical weather prediction models are capable of producing prognostic fields of cloud water content allowing for the prediction of clouds at a future point in time. These forecasts, however, are highly dependent on the cloud field initial conditions available to the model. Due to a lack of observational data, these initial fields are often nonexistent (i.e. the model spins-up its own clouds) or are based on the previous forecast, or on the output of another, larger-scale, model. In either case, the initial cloud conditions are typically not representative of the real state of the atmosphere.

An obvious solution to the cloud initialization problem is to utilize the quantitative information that can be derived from the satellite data to produce initial fields for the numerical model integration. This is a formidable task for two principal reasons: 1) Satellite radiance data must somehow be converted into 3D fields of cloud liquid and ice water content in order to be usable by the model, and 2) satellites are capable only of producing data relevant to the tops of clouds. The cloud bases, or thickness of clouds is typically not available from satellite imagery. In the case of multiple, optically thick layers of clouds, lower clouds are missed completely by a satellite image analysis.

We have developed methods to remedy these situations by providing a methodology to utilize objectively analyzed satellite cloud imagery along with mesoscale model analysis fields to produce a consistent depiction of clouds information over a forecast region. In this paper, we describe these methods and demonstrate their use for a case study using GOES satellite data and COAMPS model forecasts.

RESEARCH ACCOMPLISHED

The objective satellite analysis algorithms used are based on the Survey of Environmental Requirements for Cloud Analysis and Archive (SERCAA) processes which form the foundation of the Cloud Depiction and Forecast System 2 (CDFS-2), which will become the operational analysis tool at the Air Force Weather Agency (AFWA). For this work, the SERCAA algorithms relevant to geostationary satellites were extracted and ported to a Unix workstation. SERCAA provides cloud analyses of multispectral satellite imagery, providing detail for on up to four layers of clouds (Gustafson, et. al, 1994). The principal analysis fields produced for this work were cloud altitude, type, and coverage. These fields were produced at the resolution of the satellite imagery, meaning that a value for each of these quantities on all four levels was available for every pixel in the image.

The SERCAA algorithms were developed to operate independently of Numerical Weather Prediction (NWP) data. Consequently, cloud radiance temperatures are converted to altitudes through the use of standard atmospheric profiles, or other relevant climatological data. To gain consistency between the NWP data and the SERCAA analyses, the forecast temperature fields replaced these profiles.

The substitution of smooth, monotonic profiles characteristic of climatological profiles with the more realistic data available from the mesoscale model presents a considerable difficulty. Given the radiance temperature of a cloud-top pixel, an altitude cannot simply be chosen from the NWP data because the temperature profile is often nonmonotonic. Other information, such as lapse rate and humidity profiles must be used to select the most appropriate altitude for the cloud. For this reason, a set of simple rules, evaluated with fuzzy-logic were developed to facilitate this selection.

For the limited set of imagery considered we chose temperature, relative humidity, and static stability as the three indicators of cloud. Vertical profiles of these quantities were used as input for the fuzzy-logic evaluation procedure. Table 1 gives the specific criteria and their relative weights. Every point on a COAMPS profile corresponding to a satellite-derived radiative cloud temperature is given a score based on these criteria. The cloud is placed at the altitude of the point on the profile corresponding to the highest score. The algorithm is flexible and allows for any number of criteria to be used. In the absence of observations to serve as ground-truth, these three criteria were deemed sufficient for the case study presented here.

	Criteria	Weight	Goal
C_1	$\lvert T_{radiative} - T_{air} \rvert$	1.0	minimize
C_2	Relative Humidity	1.0	maximize
C_3	Static Stability	0.5	minimize

Table 1 – Criteria used in the initial fuzzy logic selection of cloud altitude given a radiative temperature ($T_{radiative}$) from the satellite image.

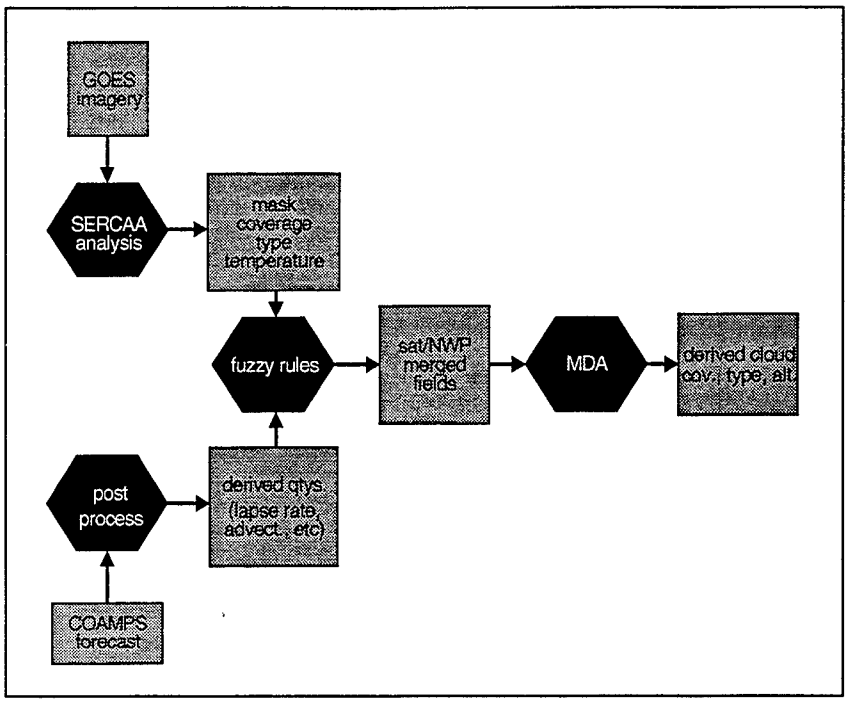


Figure 1 – Block diagram showing the satellite/NWP data fusion and objective analysis procedure.

Once the cloud-top altitudes are chosen, thicknesses are estimated based on the cloud type identified by the SERCAA algorithms. Since the ultimate goal is to provide input to the NWP model, the 3D cloud mask field is resampled to match the model horizontal and vertical resolution. Typically the satellite analysis is at a higher resolution than the model grid.

Figure 1 shows a block diagram describing the overall processing of satellite and NWP data. There are two useful termination points in this diagram. After the fuzzy rules are applied, the data from the two sources exist in on a common grid and are useful for further interpretation or as initial conditions for another forecast. For many applications one would choose to stop the process at this point. However, this data is suitable for further analysis to determine the correlation between the NWP-derived data and the satellite-derived data. In the present study Multiple Discriminant Analysis is applied to this fused data and provides the potential to derive improved cloud estimates where no satellite image is available (such as for a forecast). This process is described later in this paper.

A simple case study is presented here to demonstrate processing techniques. Figure 2 shows the GOES-9 visible satellite image for 27 October 1998 at 1800Z. A deck of cirrus clouds is apparent over the middle of this domain with thin streaks of transmissive cirrus to the east. A lower, denser deck of stratus clouds appears along the southwest edge of the domain.

Figure 3 shows the distribution of clouds over the southern California domain as determined from the satellite and COAMPS analysis. The map on the left shows the within-pixel cloud coverage averaged over a vertical column from the surface to 200 mb as determined by SERCAA analysis for the GOES-9 image shown in Figure 2. A strong correlation to the clouds in the satellite image is apparent. The map on the right consists of the column-integrated cloud water content (liquid and ice) from the COAMPS analysis. The pattern is quite different in this case, with little evidence of the cirrus clouds. All of the cloud water produced by COAMPS is below the 500 mb level. A patch of cloud water off of the coast is indicated and is consistent with the low-level clouds from the satellite image; however COAMPS places these clouds north and east of the actual clouds.



Figure 2 – Visible satellite imagery from GOES-9 over souther California on 27 October 1997 at 18Z. The region shown is identical to the nested (9km) COAMPS used in this study. A cirrus deck is visible over th emiddle of the region with an indication of a low stratus deck to the south.

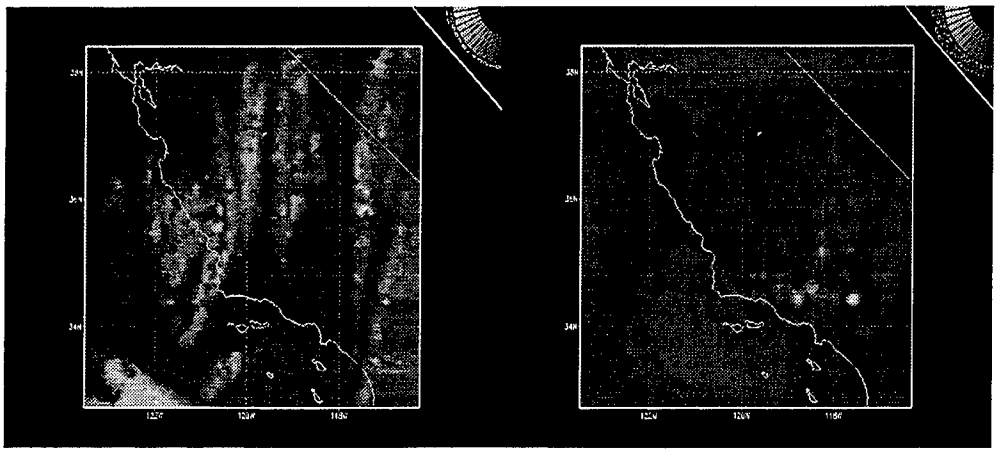


Figure 3 – Left: cloud coverage field derived from the GOES-9 satellite image. Right: column-integrated cloud water content from COAMPS.

The vertical distribution of cloud water is different for the two sources of data as well. Figure 4 shows domain-wide vertical profiles through the merge data set. The average cloud coverage over the domain (solid line) indicates that the majority of the clouds identified by the satellite algorithm are at high levels in the atmosphere with a peak at 300 mb. This corresponds to the cirrus clouds identified earlier. A second maximum near 700 mb corresponds to the stratus clouds. The COAMPS integrated water content profile, on the other hand, is strongly biased towards the surface, with relatively small amounts of cloud water near 700 mb and none above 500 mb.

Although general statements cannot be made based on this single case study, this distribution of high satellite clouds versus low model clouds is typical of the data sets analysed to date. This is particularly true for cases where cirrus clouds are indicated in the satellite imagery. This phenomena is attributed to two factors: 1) COAMPS may be underpredicting cirrus clouds (through the prognostic cloud ice water content field) and 2) Low clouds are missed by satellite imagery when an upper-level deck is present. In either case, the data from the two sources are complementary so that the data fusion process gives a better depiction of the environment.

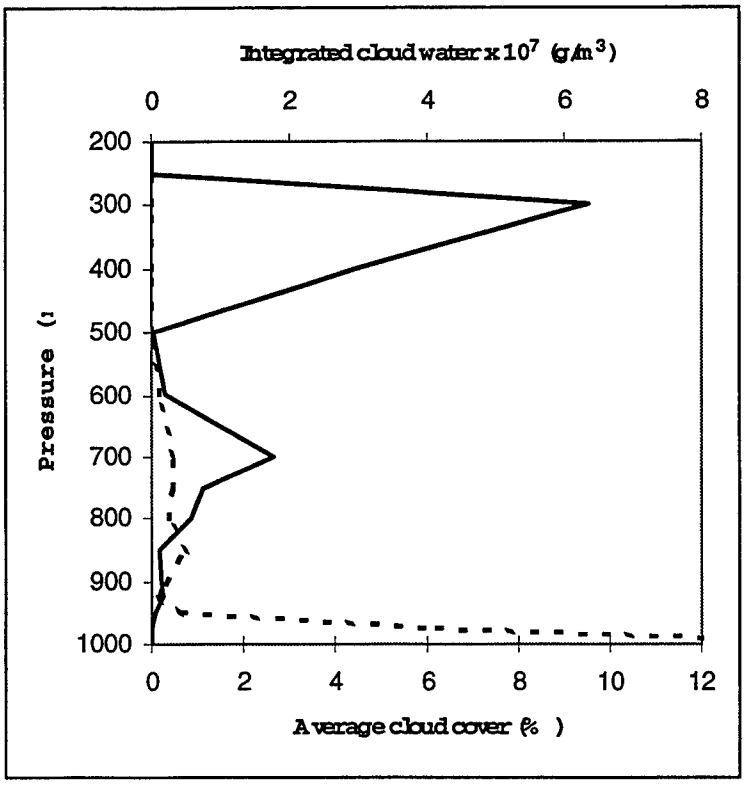


Figure 4 – Domain-wide integrated profile of cloud water content produced by COAMPS (dashed line) and layer-mean cloud coverage derived from the satellite image (solid line). The COAMPS profile indicates predominantly low clouds (e.g. marine stratus) whereas the satellite analysis indicates predominantly high cirrus clouds. Both sources reveal the presence of mid-level clouds.

Applied to an historical data set for which the forecast output (including nonzero cloud fields) of a mesoscale model is available, a further analysis can be

applied to the merged satellite and model data. Specifically it is useful to determine the correlation between all of the model forecast fields and the 3D cloud mask constructed in the process described above. These diagnostic relationships, if robust, would be valuable for producing cloud masks in the absence of satellite imagery.

To investigate the feasibility of constructing a 3D cloud mask based only on the forecast fields, a Multiple Discriminant Analysis (MDA) was performed. The MDA technique (Wilks, 1995) is useful for determining linear combinations of predictor variables, called discriminant functions, which discriminate among a set of discrete categories, or predictands. In the present work the predictor variables are the grid point values of the model prognostic fields and appropriate derived quantities. Table 2 lists the quantities used as predictor variables in the case study. Only two predictand categories are considered—the presence, or absence of clouds at a grid point. Specifically, the truth data used to determine the discriminant functions is the cloud mask determined in the merging procedure above.

Quantity	Units
cloud water content	g/m3
horiz. wind speed	m/s
geopotential height	m
T	deg. C
W	m/s
lapse rate	deg. C / m
dew point T	deg. C
relative humidity	percent
vorticity	1/s
vorticity advection	1/s2
T advection	T/s
RH advection	1/s
RH convergence	1/s
height gradient	m/km
Tsfc	deg. C
P msl	mb
terrain altitude	m

Table 1 – List of predictor variables used used to classify a region as cloud-filled or cloud-free by the Multiple Discriminant Analysis

For the present case study, the MDA was applied to every (3D) grid-point in the COAMPS domain using the entire column of 15-levels as a source of predictor variables. This treatment has the advantage that it takes into account vertical structure of the predictor variables in determining cloud height. More importantly, however, it compensates for errors in estimating the height of the cloud during the fusion process since data from above and below the cloud are used to form the discriminant functions.

Figure 5 shows the MDA results for a COAMPS/GOES-9 merged data set from 18 August 1997 at 21Z for the same domain as in Figure 3. Three images for each of the fourteen pressure levels between 1000 mb and 250 mb are presented. The leftmost

image for each level corresponds to the cloud mask as determined by the SERCAA analysis. A black pixel corresponds to a cloud-free region and a grey pixel corresponds to a cloud-filled region. The middle and rightmost images show the clouds as determined by the discriminant function which was trained using the SERCAA data. The middle column of images gives the probability of cloud occurrence based on the discriminant function; the lighter shades of grey correspond to a high probability of clouds existing in the region. The rightmost image is constructed by thresholding these probabilities. Regions that have a greater than 50 percent probability of being cloud-filled according to the MDA are shaded grey, otherwise they are black.

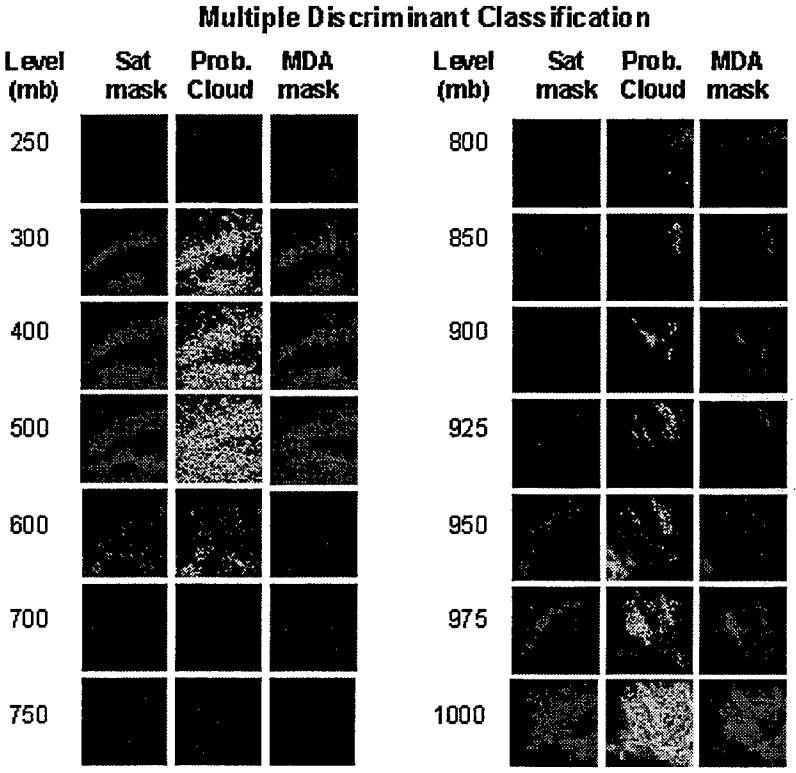


Figure 5 - MDA results for 18 August 97 COAMPS/GOES-9 fused data set. Each image covers the domain shown in Figures 2 and 3. The leftmost column corresponds to the cloud mask determined from the GOES-9 imagery, the middle column is the probability of cloud occurrence as determined by the MDA discriminant functions. The rightmost column corresponds to the cloud mask determined from the MDA.

These images are encouraging because they demonstrate that there is information in the NWP fields which correlates to the cloud masks determined by the satellite analysis. Because the MDA masks generally, have the same distribution of clouds as the actual analysis we conclude, for this case, that the discriminant functions are useful for diagnosing clouds. Further work must be performed to determine the degree to which these determinant functions may be applied data other than the training set.

FUTURE DIRECTIONS

The principal value of MDA, in this study, is that once the discriminant functions are determined for a training data set, they can be applied to other data. That is, we are able to develop the relationships between the NWP fields and the satellite-derived clouds for cases where imagery is available and use these relationships to diagnose clouds where imagery is not available. To this end, we applied MDA to a single time period of a 12-hourly COAMPS forecast, then used the discriminant functions to diagnose the clouds at all other times. The results of this study (not shown) demonstrated that there may be reasonable utility in using this approach to augment cloud fields in NWP forecasts. A detailed study of this application of MDA is left for future research.

REFERENCES

Gustafson, G. B., R.G. Isaacs, R.P. d'Entremont, J.M. Sparrow, T.M. Hamill, C. Grassotti, D.W. Johnson, C.P. Sarkisian, D.C. Peduzzi, B.T. Pearson, V.D. Jakabhazy, J.S. Belfiore, A.S. Lisa, *Support of environmental requirements for cloud analysis and archive (SERCAA): Algorithm Descriptions*, PL-TR-94-2114. ADA 283240.

Wilks, D.S. (1995), *Statistical Methods in the Atmospheric Sciences*, Academic Press, Inc.

CIRRUS MODEL TESTING IN THE CSSM

Ryan B. Turkington* and Maureen E. Cianciolo
LITTON/TASC
Reading, MA 01867-3297
Phone: (781) 942-2000
Fax: (781) 942-2571
E-Mail: rbturkington@tasc.com
Government Sponsor: AFRL/VSBE

1. INTRODUCTION

The Cloud Scene Simulation Model (CSSM) includes models for stratiform, cirriform, and cumulus cloud types. It generates high-resolution cloud scenes for use in a wide variety of simulation applications including mission rehearsal, sensor test and evaluation, and scene visualization.

The CSSM builds four-dimensional (space and time) cloud scenes consistent with user-supplied coarse-resolution cloud and meteorological input fields. The primary output variable of the model is water content (g/m^3) at every gridpoint in a user-defined simulation domain. Typical scenes, with output resolutions of 10-100 meters, take only seconds to build on a standard workstation.

The CSSM is a parametric model that relies on stochastic field generation algorithms (the Rescale and Add fractal algorithm [Saupe 1989]) to build external cloud structures and their internal water density perturbation fields. For stratiform and cirriform cloud types, the resulting perturbation fields are converted to absolute water content using computed field statistics and a mean Liquid Water Content (LWC) profile given by the Feddes model [Feddes,1974].

Recent development efforts have focused on improving the cirriform model, including: tuning existing cirrus model parameters and verifying the "tuned" model using statistical hypothesis tests. An overview of each of these tasks is presented in this paper.

2. CONCEPTUAL CIRRUS MODEL DESIGN

The CSSM baseline cirrus model was developed under a previous effort [Cianciolo, 1991]. It was implemented then as a complement to the stratiform model and uses many of the same algorithms. Parameters within the model were originally selected based on a limited qualitative comparison with satellite cloud imagery and photographs. The baseline model creates visibly realistic simple cloud structures, such as thin cirrus layers with realistic horizontal bands, but the model parameters have never been quantitatively estimated from in-situ water content data.

This effort focused on improving the cirriform model in the CSSM by estimating the model parameters from observed water content data. Although no one model can capture the nearly infinite variety in cirriform cloud types and structure, we simplified the possibilities into two primary cloud categories: non-precipitating and precipitating types. *Non-precipitating* cloud types (cirrus, cirrostratus, cirrocumulus in our model) include those types in which the horizontal scale dominates the vertical scale and ice

precipitation is relatively limited. Conversely, the *precipitating* cloud type (cirrus uncinus in our model) is that in which the vertical scale dominates and vertical motion is non-negligible.

We built our cirriform model development plan based on these two cloud categories. The plan consists of two parts: first, to improve the existing cirriform cloud model within the CSSM and second, to implement a new precipitating cirrus cloud model. At this time, we have completed only the first of those two parts. It is the subject of the remainder of this paper.

3. DESCRIPTION OF AIRCRAFT DATA

The primary task to improve the existing non-precipitating cirrus models is to tune internal model parameters by comparing model output fields with in-situ cirrus observations. Data used for this parameter tuning process came from the Subsonic aircraft: Contrail and Cloud Effects Special Study (SUCCESS) project based at Salina, Kansas, during April and May of 1996. We selected the SUCCESS experiment for its excellent spatial resolution, availability, and range of experimental locations. The primary purpose of the SUCCESS mission was to analyze the microphysical structure of aircraft contrails and compare it to the microphysical structure of cirriform clouds [SUCCESS Mission Homepage, 1997]. Water content values were measured by three separate instruments; the CVI, PVM-100A, and the PMS 2D-C. These instruments were mounted on the exterior of a DC-8 aircraft. For this effort, we utilized CVI data, since it covered the greatest range of particle sizes of all the instruments in addition to having a high sampling rate (1 Hz) [Twohy, 1996].

Our analysis of the SUCCESS data led to the extraction of 29 path segments from the aircraft data, sampled across five days (several of these paths were generated by breaking longer paths into consecutive smaller path segments). Descriptions of the selection criteria can be found in Turkington, [1998]. Of these five sampling days, three were in geographically unique locations: Oklahoma/Kansas, Wisconsin, and Coastal Oregon. Of the 29 paths selected, 25 traversed through cirrus clouds and four through cirrostratus. Cirrocumulus clouds were not present in any of the 29 aircraft paths and were not sampled during the SUCCESS experiment. Therefore, we are unable at this time to estimate parameters for the cirrocumulus model. We will test the cirrocumulus model in future efforts.

4. PARAMETER ESTIMATION PROCESS

The CSSM is very sensitive to the model parameters that control the water content output. We used an iterative approach to estimate model parameters which produce simulated water content paths with characteristics similar to the observations described above. This process consisted of the following several steps:

- *Initialize CSSM* — We initialized the model with meteorological, cloud, and terrain information which was coincident with the cloud data.
- *Run the baseline model* — We ran ten unique runs of the baseline model for four different aircraft path observations (two cirrus, two cirrostratus).
- *Extract data paths from CSSM output fields* — Simulated water content paths were extracted from each simulation in each ensemble, matching the aircraft conditions.

- *Compare aircraft and simulated paths* — The simulated water content paths were compared to the aircraft paths qualitatively (by comparing fractal dimensions, water content means, standard deviations, and autocorrelation functions).
- *Derive new CSSM parameters* — A new set of model parameters was derived, based on statistical comparisons between the aircraft and model data, keeping in mind how each parameter controls the character of the output field.
- *Repeat process* — This process was repeated until the simulated paths' characteristics agreed (within statistical limitations) with the observed paths' characteristics.
- *Run remaining cases* — After we developed an acceptable set of parameters, we ran the CSSM ten times each for each of the 25 remaining aircraft paths for final tuning and hypothesis testing.

5. TUNED MODEL RESULTS

Initial comparison of the baseline model to the SUCCESS aircraft data indicated that changes were necessary to some model parameters. The baseline model fields were qualitatively too "bumpy." Through analysis and extrapolation of basic statistics and fractal dimensions from the SUCCESS data, we estimated new parameters for cirrus and cirrostratus clouds.

Of those tunable model parameters referenced in Turkington, [1998], five were changed for cirrus and cirrostratus clouds. Tables 1 and 2 outlines the baseline and tuned model values.

Table 1. Baseline Cirriform Model Values

	Cirrus	Cirrostratus
Hurst Parameter (internal)	0.3	0.3
Hurst Parameter (external)	0.3	0.3
standard deviation ratio	50%	50%
k_{max}	4	4
lattice resolution	2, 10	2, 15

Table 2. Tuned Cirriform Model Values

	Cirrus	Cirrostratus
Hurst Parameter (internal)	0.5	0.4
Hurst Parameter (external)	0.6	0.5
standard deviation ratio	120%	50%
k_{max}	2	2
lattice resolution	6, 18	10, 15

The net effect of modifying these five variables was a smoother water content field (further explanation of each model parameter and its effects can be found in Turkington, [1998]. The modification of these model parameters yielded model water content data which was in better agreement with the SUCCESS water content data. However, these new parameters were estimated based on a very limited set of only four water content paths. For verification of the improved model, the model was run for the remaining 25 aircraft paths. Analysis of the new parameters was achieved through statistical comparisons and hypothesis testing, as described in the following subsections.

6. STATISTICAL COMPARISON OF AIRCRAFT AND MODEL PARAMETERS

Having tuned the model parameters to better replicate the statistical characteristics observed in just four of the aircraft paths, we then ran the tuned CSSM for the remaining 25 aircraft paths

and analyzed the output water content fields to determine if the aircraft-based measurements and CSSM simulations of water content are consistent with a single distribution. We used several analysis techniques for our determination. A brief look at the results from two of those techniques is reported in this paper:

- Qualitative visual inspection of Ice Water Content (IWC) data paths.
- Statistical hypothesis testing.

The analysis process consisted of generating ten CSSM runs for each of the aircraft paths. The ten CSSM runs were identical in all aspects except for the initial random number seed, thus providing a range of paths sampled from one underlying water content distribution. We computed the following variables for all ten CSSM paths and the associated aircraft path: mean IWC, standard deviation of IWC, measured Hurst parameter, and time at which the autocorrelation function reaches zero.

6.1. VISUAL INSPECTION

The first step in the analysis process was to simply look at the IWC data series and determine whether the model paths agreed qualitatively with their aircraft counterparts. As expected, our initial visual comparisons between baseline model data and aircraft data showed significant discrepancies between model and observed data. The baseline CSSM cirrostratus and cirrus models produced ice water content paths in which the IWC spatial correlations were too short, and the variances were too high. Continued analysis led us to modify the k_{max} parameter, lattice resolution, the standard deviation ratio, and the external Hurst parameter (used to control the external cloud shapes). The final combination of parameters and the associated initial values were presented in Tables 1 and 2.

Figure 1 shows a side-by-side view of observed and simulated IWC paths for only two of the initial test cases. It is easy to see that for the cases shown, the new model parameters produce a more realistic IWC distribution. The overall amount of variability and the intervals between IWC peaks agree favorably with the tuned model.

6.2. STATISTICAL HYPOTHESIS TESTING

Another method which can be used to determine if the CSSM generated cirriform data is realistic is to perform statistical hypothesis testing. Here, we determine a null hypothesis and attempt to disprove it. For this effort, the null hypothesis is that the aircraft-based measurements and the CSSM data are drawn from the same distribution function. One method which we used to test our null hypothesis is called the Tshebycheff inequality test [Laha, 1979].

Unlike many other hypothesis tests, the Tshebycheff inequality test assumes a more general form for the underlying distributional form of the test data; it does not assume normal distributions. Thus, it does not assume that the underlying cirrus ice water content data is normally distributed. It is defined in a probability statement as follows:

$$P(| x-E(x) | \geq \lambda\sigma) \leq 1/\lambda^2$$

where

- x is an individual IWC value sampled from the aircraft data.

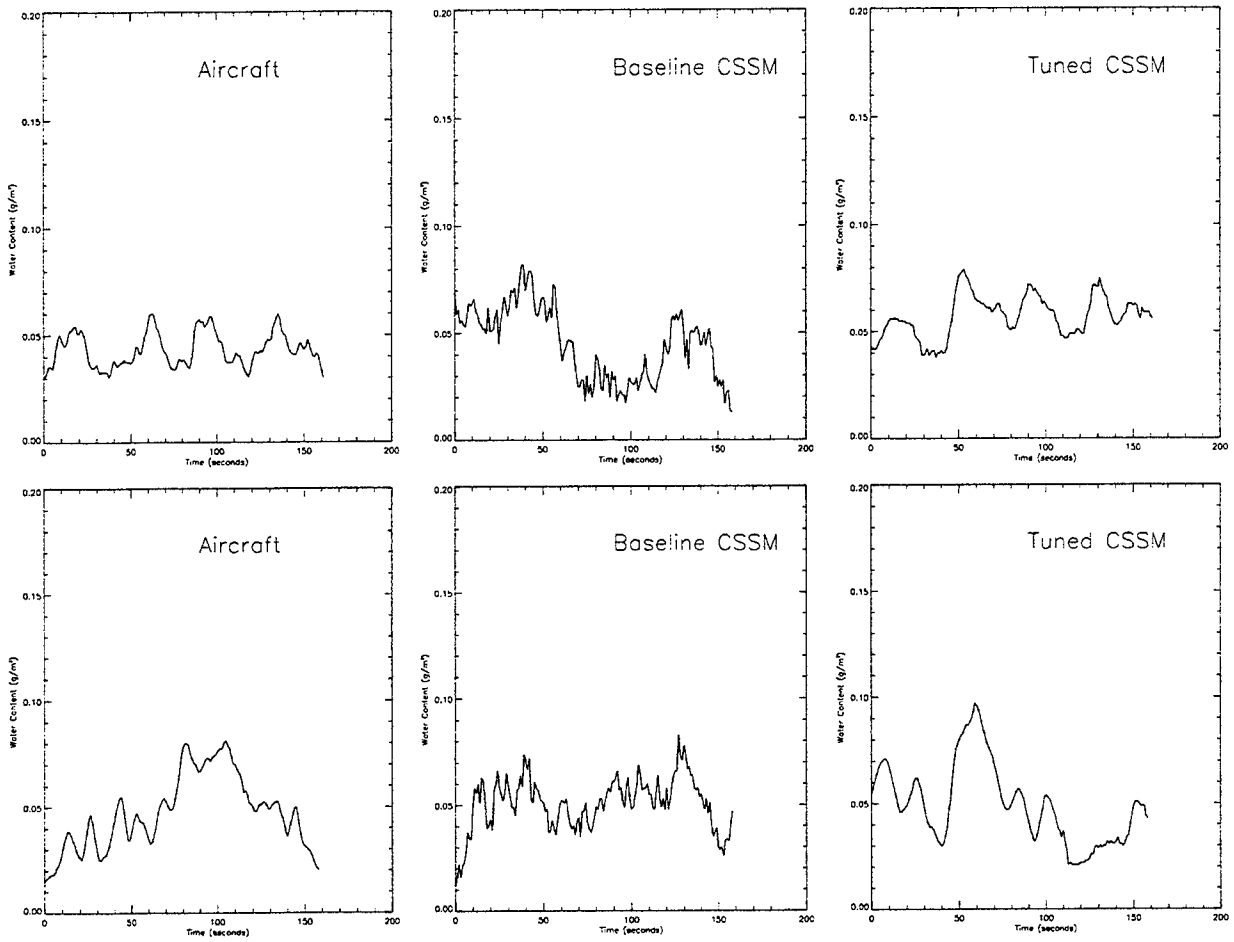


Fig. 1. Cirrostratus Path 2-2 (top row) and Cirrus Path 12-1 (bottom row) — IWC sampled along horizontal paths showing the qualitative agreement between observed and simulated clouds (left — aircraft observations; middle — baseline CSSM; right — tuned CSSM).

- $E(x)$ is the expected value of x (i.e., the mean IWC value predicted by the theoretical CSSM distribution).
- λ is a constant (e.g., 2,3,4,5).
- σ is the standard deviation of the theoretical distribution.

The Tshebycheff inequality states that the probability that a given value in a data set exceeds some constant, λ, times σ is less than $1/\lambda^2$. For example, we should not expect to find more than 6.25% (i.e., $1/4^2$) of aircraft IWC values data values that are more than 4σ from the mean predicted by the CSSM.

One quick way to determine what percentage of data samples exceed various sigma levels (i.e., 2σ, 3σ, 4σ, 5σ) is to plot histograms of the quantity "$|x-E(x)| / \sigma$." Then we can simply count how many of those exceed 2, 3, 4, 5, etc. We then compare that actual percentage with the maximum percentage predicted by the Tshebycheff inequality.

To build up the histogram of Tshebycheff values, we chose to use the theoretical mean IWC predicted by the Feddes model within the CSSM for the expected value, $E(x)$. This mean is our best estimate for $E(x)$. The means predicted by the Feddes curve at temperatures present during the SUCCESS experiment are 0.06 and 0.04 g/m^3 for cirrostratus and cirrus types, respectively. We evaluated each aircraft data point (x_i) against an equivalent set of data points sampled from each of the corresponding ten CSSM runs. The reference standard deviation for each x_i was estimated from the ten CSSM data points. The result is a histogram of Tshebycheff quantities for each of the 29 cases.

One sample case is illustrated in Figure 2. The other cases are available in Turkington, [1998]. The leftmost plot shows ten CSSM IWC data paths and the corresponding aircraft data path making up the case. The IWC paths are overlaid on a single axis which allows a good view of the cloud data. One can quickly understand the amount of variability within a single CSSM path as well as across the group of paths. Recall that each of the 10 CSSM runs is generated by using a unique random number seed when initializing the CSSM. The overall shapes and characteristics of the IWC paths are clearly seen. The middle plot of each row contains a histogram of the dimensionless Tshebycheff quantities (i.e., $|x-E(x)| / \sigma$). The information printed on the right-hand-side of the row contains the actual and predicted percentages of data points exceeding a list of sigma levels (2-5). Those percentages are derived directly from the histogram data. The final column shows whether or not the two distributions pass the Tshebycheff inequality test (yes or no).

The results from our analysis indicated that with only two exceptions, the aircraft and CSSM data distributions pass the Tshebycheff test at all sigma levels used. That is, the actual number of aircraft data points which fall outside an envelope defined by the mean IWC $\pm 2\sigma$, 3σ, 4σ, etc. is less than the Tshebycheff inequality value $1/2^2$, $1/3^2$, $1/4^2$, etc. Therefore, our results from this statistical hypothesis test indicate that the aircraft and model datasets are consistent with a single distribution.

Note however that the Tshebycheff inequality test only evaluates the overall difference in values from the mean. It does not evaluate whether or not the data paths have the correct variances, correlation lengths, "bumpiness," etc. To fully understand whether or not the CSSM output paths simulate the type of data seen in the observed data sets, we need to rely on a range of analysis tools such as those presented in this report.

7. CONCLUSIONS

The CSSM includes models for stratiform, cirriform, and cumulus cloud types. Our design includes changes to the existing CSSM models for cirrus and cirrocumulus clouds. Aircraft-based observations of ice water content are used to estimate model parameters that control the statistical characteristics of the resulting water content fields. Statistical hypothesis testing revealed that CSSM output matches the CSSM output generally well. More work will follow on model implementation and verification in future efforts.

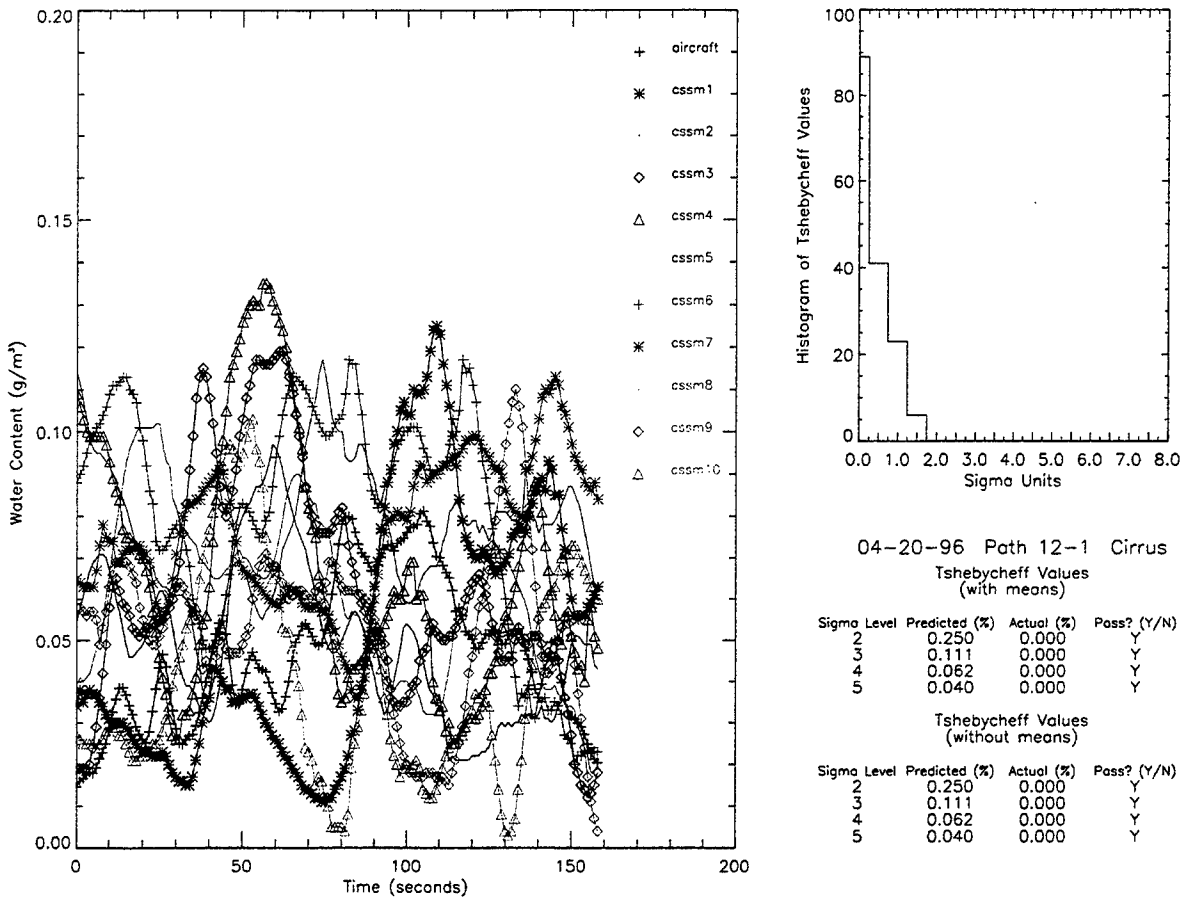


Fig. 2. Data and results from the sample Tshebycheff analysis. IWC data paths for aircraft and ten CSSM runs are presented on the left. Histogram of Tshebycheff inequality values are presented in the middle. Tshebycheff summary statistics are printed on the right.

8. REFERENCES

1. Cianciolo, M. E., Hersh, J. S., and M. P. Ramos-Johnson, 1991: Cloud Scene Simulation Modeling —Interim Technical Report, PL-TR-91-2295 [NTIS AD-A256 689].

2. Feddes, R. G., 1974: A synoptic-scale model for simulating condensed atmospheric moisture, USAFETAC-TN-74-4 [NTIS AD-A002 118].

3. Laha, R.G., and V.K. Rohatgi, 1979: *Probability Theory*, Wylie, New York, p. 33.

4. Saupe, D., 1989: Point Evaluation of Multi-Variable Random Fractals, Visualisierung in Mathematik and Naturwissenschaft, H. Jurgens and D. Saupe, Eds., Springer-Verlag, Heidelberg.

5. SUCCESS Misson Homepage, 1997, electronic version, http://cloud1.arc.nasa.gov.

6. Turkington, R. B., Cianciolo, M. E., and M. E. Raffensberger, 1998: Development of an Atmospheric Scene Simulation Model – Final Technical Report, AFRL-VS-HA-TR-98-0051 [NTIS Number not yet available].

7. Twohy, C. H., 1996: NCAR Airborne Instrumentation Information, electronic version, http://www.atd.ucar.edu/dir_off/airborne/cvi.html.

Radio Propagation

SIMULATED RAIN FIELDS FOR RADAR PROPAGATION IN FASTPROP

Albert Boehm* and Welman Gebhart

Nichols Research Corporation

2501 Ermine Dr., Huntsville, Al 35810

Tel: 256 859-8051, Email: Boehm@ziplink.net and gebhartw@nichols.com

Space and Missile Defense Command

1. OVERVIEW

This paper first presents a brief description of the overall FASTPROP computer program. The Crane Attenuation model is described. The rest of the paper emphasizes the theory, development, and implementation of the rainfields in the current FASTPROP module.

2. FASTPROP IN GENERAL

FASTPROP simulates atmospheric impacts on electro-optical propagation. So far visible, infrared, and radar frequencies propagation has been implemented. In particular cloud and rain fields have been implemented as well as refraction.

The current FASTPROP version:

- Is limited to a window 250 by 250 km in areal extent.
- Has data sets for 12 sites. (It takes several days to create a data set for a new site.)
- Has weather specified by:
    1. Random choice consistent with the site, season, and time of day.
    2. The X percent worst cloud cover, rain, ceiling, or surface visibility.

  or 3. A specific weather observation.
- is ultra-fast and intended for multiple moving targets and sensors.
- Is written in ANSI C.
- Is modular but has only been plugged into EADSIM. (Extended Air Defense Simulation)
- Includes (for radar) basic solar, lunar, and surface reflection effects.
- Has a GUI but without online HELP.

3. THE REVISED 2 COMPONENT CRANE RAIN MODEL

Robert Crane developed and documented (Crane, 1996) a consistent climatological model for radar propagation through rain which is designated here as R2CM (Revised Two Component

Model) The two components are heavy rain in cells and lighter widespread rain. A meteorologist would identify these as cumulo-nimbus and strato-nimbus rain.

3.1 Point Rain Rate

Crane has found a different rain rate distribution for each of the two types of rain. Specifically, for widespread rain, called debris rain by Crane, the rain rate distribution is lognormal while the heavy rain in cells, called volume cells by Crane, is exponentially distributed. The total rain rate distribution is given by the union of the two probabilities assuming independence,

$$P(r \geq R) = Pc\ E[Rc] + Pd\ L[Rd,Sd] - (Pc\ E[Rc])\ (Pd\ L[Rd,Sd]) \quad (1)$$

where $P(r \geq R)$ is the total probability of rain rate, r, exceeding a given threshold, R (mm/hr), Pc and Pd are the probabilities of having rain from cells or widespread respectively. E[Rc] is the exponential distribution with parameter Rc,

$$E[Rc] = \exp(-R/Rc) \quad (2)$$

and L is the lognormal distribution with parameters Rd and Sd,

$$L[Rd, Sd] = N[\ln(R/Rd)/Sd] \quad (3)$$

where N[T] is the upper integral (from the threshold, T, to infinity) of the normal distribution.

In R2CM, the globe is divided into 12 regions. Each region has the five parameters, Pc, Rc, Pd, Rd, Sd, fitted to observed rain rates. For example, the region extending from West TX up through SD and eastward to ME has the following values:

Pc = 0.031, Rc = 23.2, Pd = 8.19/100, Rd = 0.463, Sd = 1.34.

Values for all the regions are given in Table 3.2 of Crane (1996). Warning! Pd is given as a percent not a probability. Maps delineating the regions are given in Figures 3.2, 3.3, 3.4, 3.7 and 3.8 of Crane (1996). Crane has also developed a computer program that specifies a region and its parameters given a latitude and longitude. A Modified (from C++ to C and a bug fixed) version of this program is included in the current FASTPROP.

Crane (1996, p137) points out that "The way to the future is to provide a means to determine the parameters . . . from available local climatological data...". Accordingly, we programmed the Tattelman et al. (1995) model that gives monthly rain distribution for a site that has climatological data. Also we programmed the capability to add diurnal variation by varying the probability of rain. These programs have been tested but not yet implemented in FASTPROP.

3.2 Point Radar Attenuation

The assumption is that at a point, actually a small (say, one cubic meter) volume, the rain rate and rain drop distribution is homogeneous. Mie theory can be used to calculate attenuation by a droplet of a given size and shape. Using a droplet distribution, (Crane uses the Laws and Parson's (1943) distribution), shape, and Mie theory, the point attenuation can be calculated for a given wavelength. Crane approximates this attenuation with,

$$\gamma(R) = \kappa R^{\alpha} \qquad (4)$$

where γ is the extinction cross section per unit volume,

R is the rain rate (mm/hr)

κ and α are non-dimensional parameters which are a function of wavelength and polarization and are plotted in figures 4.3 and 4.4 of Crane(1996). For example for 10Ghz circular polarization, $\kappa = 0.0105$ and $\alpha = 1.18$ approximately.

3.3 Path Integrated Rain Rate and Attenuation

Rain is not homogeneous along a path. A path may cross multiple heavy rain cells or none at all. Within each cell, the rain rate varies.

Furthermore, if a good estimate of average rain rate along a path can be obtained, it will not give the average attenuation since the relation between rain rate and attenuation is non-linear as shown by equation 4.

The most important assumption/approximation used by Crane to estimate attenuation along a path is that variation along a path is specified by the correlation function fitted to data as shown in figure 1 which is based on Crane's (1996) figure 2.39.

The attenuation along a path is broken into two parts,

$$P(a \geq A) = Pc(a \geq A) + Pd(a \geq A) \qquad (5)$$

where Pc is due to convective cells and Pd is due to stratiform rain.

The convective cell probability takes into account both the probability of encounter of a cell and the variation within a cell. For ground to space paths, the length of the path through possible rain is longer for convective cells since, on the average, they have higher tops than stratiform rain. Both Pc and Pd are ultimately calculated by numerical integration. See Crane's equation. 4.70 and preceding for Pc, and Crane's equation. 4.79 and preceding for Pd. The required numerical integrations are implemented in C in FASTPROP.

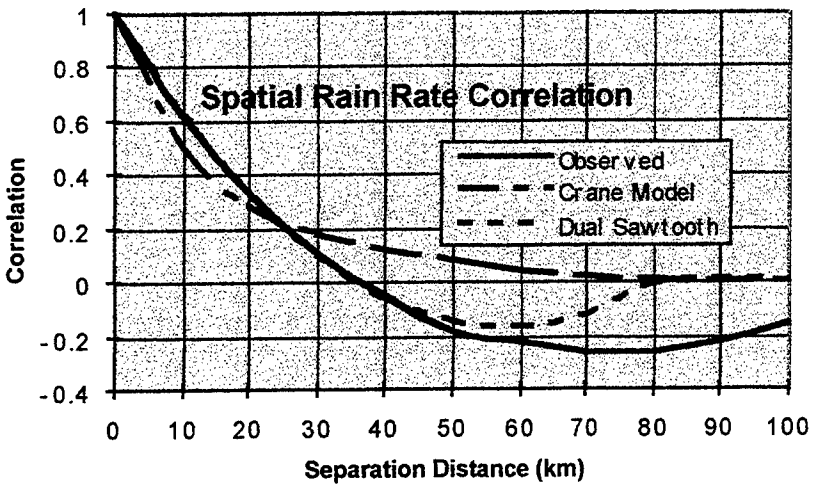


Figure 1 Values for observed and Crane Model are from Crane (1996) figure 2.39. The dual sawtooth is nearly identical to the observed correlation from 1 to -0.1.

4. Realizations drawn from R2CM

Crane's R2CM is a climatological model; it gives the probability, over time, of a given attenuation being exceeded. It deals with an average distribution. On a specific day, cells and attenuation will vary considerable from the average. At a given time, attenuations can vary greatly between paths along different azimuths. However, it is the goal of the FASTPROP rain simulation model to: 1. Be consistent with the various sub-models on which R2CM is based, and 2. Converge to the R2CM probabilities when the simulation is averaged over many Monte Carlo runs.

Much of R2CM such as the chosen relationship between rain rate and attenuation is directly implemented. The hard part is to specify a realization that matches the observed correlation in figure 1. A second difficult part is given a mathematical description of a particular realization, how does one embody the information into simple geometric figures so that quires for a given azimuth and elevation can be calculated very rapidly.

4.1 Generating a Field with a specified correlation

The sawtooth generator (Gringorten and Boehm, 1987) uses a superimposition of randomly oriented sawtooth waves (in this case two dimensional) to produce a random field with a specified correlation. A two dimensional sawtooth generated field has the correlation structure (Boehm, 1997) of:

$$\text{for } \sigma \le 1, \quad \rho(\sigma) = 1 - \frac{12}{\pi}\sigma + 3\sigma^2 \qquad \text{and } \sigma = \frac{s}{\lambda} \tag{6}$$

$$\text{for } 1 < \sigma \le 2, \quad \rho(\sigma) = 1 - \frac{12}{\pi}\sigma + 3\sigma^2 - \arcsin(1/\sigma) - \sqrt{\sigma^2 - 1} + 12 \qquad (7)$$

where ρ is correlation between point separated by standardized distance σ which is actual distance s standardized by the sawtooth wavelength λ. These formulas and formulas for higher values of σ are derived in Boehm (1997).

For the rain rate correlation, a good fit was found by using two wavelengths,

$$\rho = (\rho_1 + \rho_2)/2 \qquad (8)$$

with corresponding $\lambda_1 = 79.3$km and $\lambda_2 = 118.4$km. The fit is nearly identical from correlations 1 to -0.1 as seen in Figure 1, and is always closer to the observed curve than the Crane model is. Further for longer separation distances the low absolute values of the correlation have relatively little effect on the simulation, and as Crane points out the observed values have some uncertainty for large separation distances since fewer data are used.

4.2 Approximating a Rain Field with Geometric Objects

If a simulation is to be useful it must approximate the pertinent effects of reality, but in addition the simulation must be fast enough so that it can be used with multiple scenarios, viewing angles, and replications. In order to achieve the necessary speed, FASTPROP employs geometric objects of various complexity. For the rain fields, there are two types of objects: cylinders for the convective cell rain and oval shaped volumes with flat tops for the steady rain. It is recognized that rain fields consist of intricate detail; yet these simple shapes are sufficient to represent them for the application at hand.

The objects are specified using the following algorithm.

First, a dual sawtooth field is generated on fine grid. This field is a Gausian field - that is, each value comes from a normal distribution with mean zero and variance one. The correlation between points varies with distance between points as shown in Figure 1.

Next, the maximum value is found. A cell is placed at that location. The next highest value that is not within a cell is found and a cell placed there. This placement of cells continues until the desired (either specified or drawn randomly from climatology) coverage is obtained.

Oval shaped steady rain areas are located around each cell although there may be more than one cell in a oval area if they are close to each other. Their size is determined from the desired coverage.

Rain rate intensities for the cells and steady rain areas are chosen from the R2CM distribution. Attenuation along a path is calculated using the R2CM algorithm.

For random coverage, the coverage is chosen from the CUB (Boehm, 1992) model using the point probability of rain and the mean correlation from the dual sawtooth correlation. given in equation 8.

The resulting set of object represents the main attributes of a rain field. Furthermore, it is very fast to calculate attenuation for different azimuths and elevation angles.

5. Limitations and Validation

The current version of the FASTPROP rain model is an approximation to Crane's R2CM model. Numerous checks were made of each component algorithm to insure that error introduced by each approximation is reasonable for the intended goal. of specifying radar attenuation. Use of this model for a different purpose, say water accumulation in a watershed region would require additional testing and probable modification.

The R2CM model is currently a state-of-the-art model. However, Robert Crane (personal communication) is continuing to refine the model. For example, work is underway to produce a better model for the tops of convective cells. His work in validating the model using independent radar observations has found a complicating factor - water on the radoms!

Independent validation of the FASTPROP radar attenuation model is being accomplished by Ernest Moyers of AEgis Research Corporation.

6. Acknowledgment

This Research is sponsored by National Missile Defense Ground Based Radar Project Office under contract SETAC Task Order 53 with Susan Campbell as point of contact.

7. Bibliography

Boehm, A., 1992: CUB A general Purpose Coverage Algorithm, Prepritns of the Fifth International Meeting On Statistical Climatology, Toronto, Canada, American Meteorological Society, Boston, MA.

Boehm, A., 1997: The Correlation Structure of Randomly Oriented 1,2,...N Dimensional Waves, PL-TR-97-2061, 26pp. [ADA 329463].

Crane, Robert K., 1996: Electromagnetic Wave Propagation Through Rain, John Wiley & Sons, New York, 273pp.

Gringorten, I., and Boehm, A., 1987: The 3 D-BSW Model Applied to Climatology of Small Areas and Lines, AFGL-TR-87-0251, ADA 199114, 91pp

Tattelman, P., Larson, K. P,. Mazzella Jr., A. J., 1995: A Climatology Model for 1-min Precipitation Rates, J. Applied Meteorology, V34, No 5, 1020-1027.

A THREE DIMENSION MATCHING METHOD FOR TROPOSPHERIC FEATURES

Dr. Stephen A. Fast*
Applied Research Laboratory, The Pennsylvania State University
P.O. Box 30
State College, Pa 16801-0030
Phone: (814) 863-6241
Fax: (814) 863-6239
E-mail: sfast@psu.edu

Jason Nathaniel Bode
Applied Research Laboratory, The Pennsylvania State University
P.O. Box 30
State College, Pa 16801-0030
Phone: (814) 863-0738
Fax: (814) 863-6239
E-mail: jbode@psu.edu

Dr. George S. Young
Department of Meteorology, The Pennsylvania State University
503 Walker Building, University Park, PA 16802
Phone: (814) 863-4228
Fax: (814) 865-3663
E-mail: young@ems.psu.edu

ABSTRACT

In order for high fidelity radio wave propagation models to make accurate predictions, a correct model of the refractivity is required. To this end several methods have been developed to match refractivity profile structures between multiple range dependent profiles. There is broad agreement that using refractivity to match features dismisses relevant information that should be used. The method presented here takes a different approach. When the parabolic equation methods are used to calculate propagation loss, the refractivity is only required at each range step. Hence any method which can correctly predict refractivity at the range step is appropriate. Previous methods match features for a given vertical cut of the atmosphere, thus introducing sampling errors and ignoring off planar effects. Here we match features in three dimensions using the potential temperature, a conserved quantity derived from temperature and pressure. The variables used to compute refractivity are then interpolated in this matched coordinate system using splines. This results in a correct mapping of features over a region which resolves sampling issues thus replacing refractivity with a smooth function in three dimensions. Therefore as a parabolic equation steps in range the refractivity is derived from the matched gridded data. This paradigm eliminates the burden of refractivity interpolation/extrapolation from the propagation prediction software. Examples of matched atmospheres are presented along with propagation predictions based upon the matched atmosphere.

OBJECTIVE

Produce continuous two-dimensional modified refractivity fields given discrete vertical profiles of temperature, pressure, and humidity (specifically, the mixing ratio) at particular locations.

INTRODUCTION

Long distance propagation calculations via the high fidelity PE models [Ryan, 1991][Space and Naval Warfare Systems Center, 1998] require accurate M-fields in the vertical planes of propagation [Kuttler and Dockery, 1991]. Because the models require accurate M-fields with x and z resolutions much higher than that of soundings, numeric weather prediction (NWP) models, or other possible input data, physically based interpolation is required [Saucier, 1955].

Because virtual potential temperature (θ_v) is a physically based parameter, computing M after interpolating pressure (P), temperature (T), and humidity (q) along θ_v surfaces offers the accuracy required by the propagation models. This is the case because θ_v is conserved in many atmospheric processes, making most atmospheric motion occur along rather than across θ_v surfaces [Holton, 1972]. Thus, many parameters are also mixed along rather than across the θ_v surfaces [Petterssen, 1956]. This means that these parameters vary little along θ_v surfaces, and, hence, the dependence of the resulting M field on interpolation accuracy is minimal. Furthermore, the θ_v surfaces tend to be more numerous (densely packed) in fronts and inversions [Saucier, 1955], hence giving high resolution where ducts are most likely to occur. Therefore, the areas of greatest change and, consequently, greater interest will have more θ_v surfaces giving greater accuracy.

In contrast, non-physically based schemes, such as horizontal interpolation, smooth out the drastic changes in the thermodynamic variables generally observed in those zones where ducts are most likely to be found: often the sloping zones with high θ_v gradients which are indicative of fronts and inversions. The smoothing of the thermodynamic variables occurs because the θ_v surfaces (surfaces of least change) slope so that horizontal interpolation averages low and high gradient layers. The consequences of such averaging out of high gradients between data columns are severe, as it can easily cause ducts existing at two data columns to vanish in between them. This form of analysis error would cause the propagation characteristics between data columns to be erroneously construed to be much different than those in the data columns.

The present models either use horizontal interpolation or try to match M features in adjacent profiles. Both of these approaches interpolate linearly across M. However, assuming linearity of the M field assumes nonlinearity of P, T, and q fields, because M is a nonlinear function of these variables, which in practice, vary more or less linearly along the θ_v surfaces as discussed above. Although the differences of the assumed values of P, T, and q from their interpolated values may appear trivial, it is known that small error in these values can cause significant changes in N-units [Bean and Dutton, 1968] and, hence, M-units. Thus, obtaining accurate M values at x and z resolutions much higher than that of soundings and NWP models are best done not by interpolating M in the horizontal or even M feature matching, but rather by interpo-

lating P, T, and q on θ_v surfaces and only then computing M. This procedure is described in detail below.

PROCEDURES

The vertical profiles input into this analysis routine should be data columns of P, T, and q. The two most common sources of such data are soundings and NWP models. Although soundings typically have enough z resolution to resolve fronts, they are restricted not only by the sporadic spacing (in x axis) and the z decimation inherent in standard data transmission, but also by the varied availability (availability is highly dependent on whether those taking the measurements desire to share them). On the other hand the NWP models can offer world-wide coverage [Rosmond, 1992][Bayler and Lewit, 1992] with at least 30 vertical levels [Hodur, 1997] and with an x resolution as small as 5 kilometers [Hodur, 1997]. Moreover, the NWP models offer higher resolution near the ground, rather than at higher elevations [Bayler, 1992][Hodur, 1997], giving the ability to resolve the fronts important to radio wave propagation.

The general method of producing the M-field from the data columns is quite simple. First, the θ_v value for each data point of the data columns is computed. This is done by first calculating the potential temperature, θ, using the equation $\theta = T \cdot \left(\frac{1000}{P}\right)^{\frac{R}{C_p}}$ where T is temperature in Kelvin, P is pressure in millibars, $R = 287$ J/K*kg is the dry air gas constant, and $C_p = 1004$ J/K*kg is the specific heat at constant pressure [Bohren and Albrecht, 1998]. It is then straightforward to calculate θ_v: $\theta_v = \theta \cdot \left(1 + 0.3732 \cdot \frac{e}{p}\right)$ where e is the vapor pressure in millibars derived from p and q [Bohren and Albrecht, 1998]. Then, the θ_v surfaces are found by matching points of equal θ_v value. At this point, M is calculated by first linearly interpolating P, T, and q along these surfaces and then evaluating M using the equation

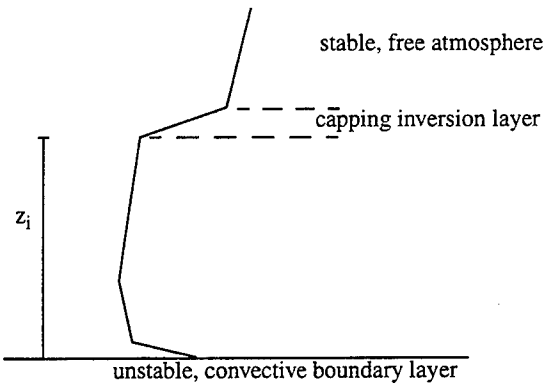
$$M = \frac{77.6}{T} \cdot \left(P + 4810 \cdot \frac{e}{T}\right) + \frac{h(P,T,e)}{a} \cdot 10^6$$

where a is the radius of the earth in meters, P, T, and e are as in the θ_v equation, and h is the height above sea level calculated by the hypsometric equation [Wallace and Hobbs, 1977].

There are several complications in this process, though. One being that the θ_v surfaces will occasionally intersect the ground. This problem occurs when the θ_v value for a given θ_v surface is found in one profile but not in an adjacent profile. It is resolved by estimating an intermediate range (x position) where the θ_v surface intersects the ground and then finding the range of this surface point by linearly interpolating between the surface values of θ_v. At this point T, p, and q are also determined by interpolation along the ground surface. Then, all thermodynamic variables along the ground intersecting θ_v surface are linearly interpolated with respect to range between the ground intersecting point and the nearest point where the θ_v surface intersected a profile.

Not only do θ_v surfaces intersect the ground, but they commonly intersect the upper boundary of the profiled volume. This boundary condition is dealt with analogously to the problem of ground intersection with the upper boundary surface treated as the ground.

Although θ_v typically increases with height, there are cases when there is a decreasing segment near the surface. These cases are statically unstable and have the general form depicted in [Stull, 1988]. The strong inversion layer (i.e. $\frac{\partial \theta_v}{\partial z} \gg 0$) above the resulting convective boundary layer is called the capping inversion layer and the height of its lower bound is labelled z_i (note that z_i frequently varies with range). Above z_i the free atmosphere is stable so θ_v matching, as described above, may be applied. Below z_i lies a turbulent and unstable convective boundary layer that makes the θ_v matching approach both ambiguous and physically inappropriate.



Therefore, below z_i the matching of points is done differently. Because z_i is a feature that always exists in unstable atmospheres, it is possible to match the points at z_i in each adjacent profile (feature matching). Then, intersections of θ_v surfaces above z_i with the z_i surface are dealt with in the same manner as the earlier described intersection of the θ_v surfaces with the Earth's surface, except that the z_i surface is used instead of the Earth's surface. Then, below the z_i surface, points of equal fractional height of z_i ($z^* \equiv \frac{z}{z_i}$ is constant where z is height) are matched [Deardorff, 1970][Brost and Wyngaard, 1984] and the thermodynamic variables are interpolated between them with respect to range. Note that this approach prevents the interpolating surfaces in the convective boundary layer from intersecting either the ground or the z_i surface.

Because of the prevalence of surface and surface based ducts it is best to interpolate across more layers near the Earth's surface than near the z_i surface. Most surface and surface-based ducts below z_i, which is typically greater than or equal to 1 km [Stull, 1988](ref overland), occur no more than several hundred meters above the surface and typically, as in the case of evaporation ducts, no more than several tens of meters above the surface. This shallowness implies more points are needed to match near the surface and less points near z_i.

Of course, use of this approach makes it necessary to find z_i. An accurate approximation of z_i is the height of the last point in the vertical profile with θ_v value less than the surface θ_v value [Stull, 1983] (Stull BLX 83). This simple algorithm makes finding z_i remarkably easy.

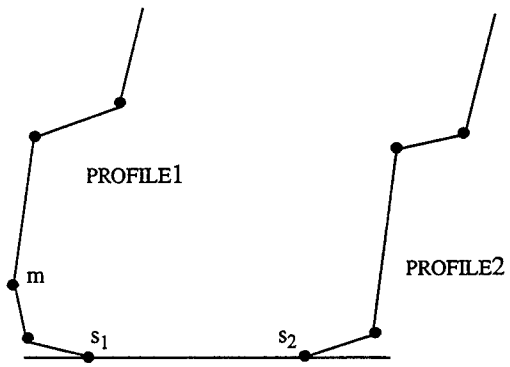


Figure 1

In the case that an unstable profile is adjacent to a stable profile, points of equal θ_v are matched with certain restrictions. To visualize these difficulties consider Figure 1 where s_1 and s_2 are the surface points of unstable profile *profile*1 and stable profile *profile*2 respectively, and m is the point of *profile*1 with minimum θ_v. Because θ_v does not decrease with height in *profile*2 the unstable part of *profile*1 must vanish before *profile*2 in the region between the two profiles. Therefore, every point of *profile*1 below m is matched to a point at an intermediate range on the surface.

The method for finding these points at intermediate ranges depends on how the $\theta_v(m)$ relates to the $\theta_v(s_2)$. If $\theta_v(m)$ is greater than the $\theta_v(s_2)$ then the intermediate point to where m is to be matched is found using the same method as the earlier described scheme used to intersect θ_v surfaces into the ground in the standard (stable) case. Then, if there is a point of *profile*2 which is still unmatched (it has a θ_v less than the $\theta_v(m)$), it is matched to a point on the ground found using the interpolation just described.

If, on the other hand, the $\theta_v(m)$ is less than $\theta_v(s_2)$, the problem of determining the intermediate points becomes slightly more difficult. Because the unstable layer is being pushed into the ground by the stable layer somewhere between the two profiles, the θ_v surface including m must go to the ground at an intermediate range. This range is found using a form of linear interpolation:

$$r_{new} = r_1 + \frac{\theta_v(s_1) - \theta_v(m)}{\theta_v(s_1) + \theta_v(s_2) - 2 \cdot \theta_v(m)} \cdot (r_2 - r_1)$$

Finding the values of other parameters at this point is more complicated. The pressure is linearly interpolated between the values of s_1 and s_2 as a function of range. Because the instability of the atmosphere is usually due primarily to temperature variations, humidity is interpolated analogously to pressure, and the temperature is recovered from the equation for θ_v (which depends on temperature, pressure, and humidity). For clarity, let n be the point which has just been created.

Then the points of *profile*1 below m are matched to the corresponding points of equal θ_v between s_1 and n. These corresponding points are found by linearly interpolating all parameters between s_1 and n with respect to θ_v. Those points of *profile*1 above m are then matched to either a ground point or a point of *profile*2 depending on their θ_v values.

RESULTS

Overall the algorithm functioned well in our test cases; ranging from the simple examples to extremely complicated ones. Of these examples, only a relatively small representative set can be given here due to space restrictions. Each of the three examples given below were chosen with a

particular purpose: the first is a simple case with which feature matching is not reliable, the second is a case where neither feature matching nor horizontal interpolation is reliable, and the last is merely a difficult case which the algorithm described here handles with relative ease. The latter is derived from five profiles from the Persian Gulf assumed to be equidistant. The two former examples are each derived from only two profiles and come from Dhahran and the Persian Gulf in that order. In all of the examples, only the bottom kilometer of the atmosphere is being shown, as this is where most ducts lie.

This is a case of a refractively standard atmosphere adjacent to a simple duct. In Figure 2 the simple duct is a surface duct at a height of 41 meters. In this analysis the surface duct is slowly melded into the standard atmosphere as is desired. Remember that only the two profiles on the extremities are the originals, all intermediate profiles were produced by the matching algorithm described in this paper.

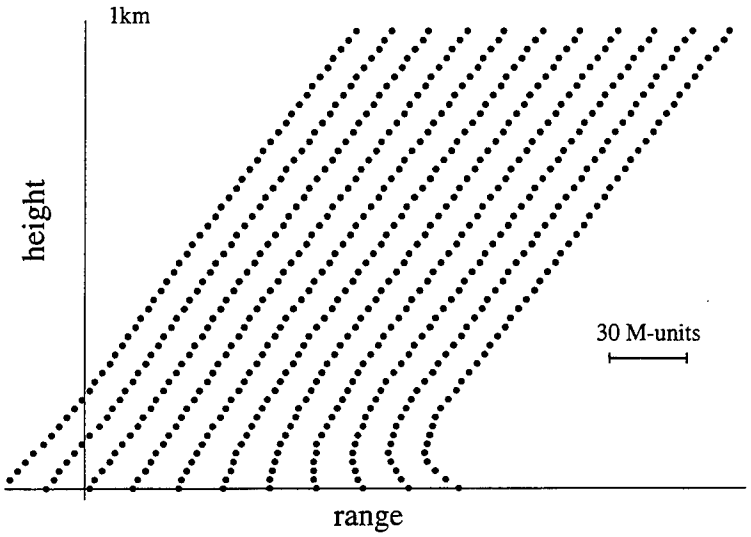


Figure 2

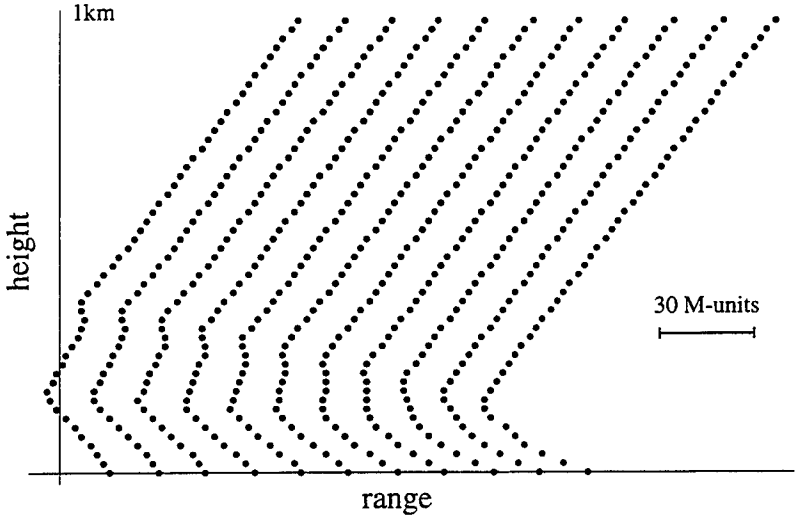


Figure 3

Again, in Figure 3 only the first and last profiles are the original observations. This is a case of a profile with two ducts adjacent to a single duct profile. Note that the surface duct of the first profile is not being matched directly to the surface duct of the last profile; it is, in fact, being matched to a level slightly below both the duct height of the second observed profile and its starting level in the first observed profile. Moreover, the elevated duct of the first profile descends to the peak of the duct of the last profile. Thus, the two ducts of the first profile merge to produce a fairly strong surface duct in the final profile.

The final example, shown in Figure 4, is interesting in that a double duct converges to a single duct and then eventually rises and evolves back to a double duct. This example exemplifies the ability of the algorithm described in this paper, for both ducts can be followed in the features of all the profiles.

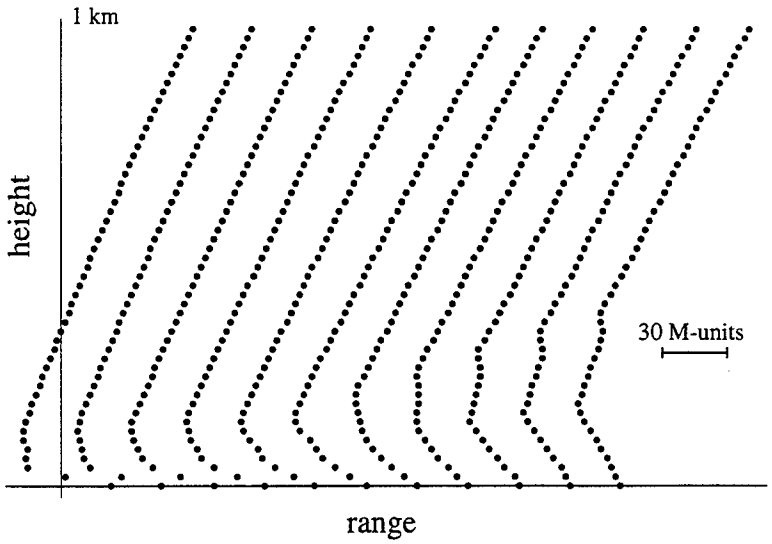


Figure 4

CONCLUSIONS

The thermodynamic foundation of the algorithm described here has proven to be stable, as the algorithm performs well, even in cases where current algorithms are unreliable.

This robustness allows us to generalize to three dimensions without fear of inducing large error. When the input is a 2-D gridded array of profiles (invariant x and y axis spacing), the 3-D generalization is especially easy, as it is analogous to bilinear interpolation: (1) the 2-D interpolation method described above (2-D algorithm) is applied along the arrays of profiles in the x dimension and (2) the 2-D algorithm is reapplied in the y dimension.

On the other hand, the generalization to a 3-D algorithm on an irregular network of profiles is slightly more complicated: (1) triangulate the grid with Delaunay triangulation, (2) find in which triangle the point lies (simple algorithm), (3) find which sides of the triangle are directly above and below the point with respect to the y-axis (if the point lies on a side which is parallel to the y axis, then skip to step 5), (4) use the 2-D algorithm to produce the profiles on these sides which are directly above and below the point with respect to the y-axis, and (5) use the 2-D algorithm again applied to the profiles directly above and below the point with respect to y-axis (possibly the vertices of the triangle) to produce the profile at the point in question.

BIBLIOGRAPHY

1. B. Bayler, H. Lewit; The Navy Operational Global and Regional Atmospheric Prediction Systems at the Fleet Numerical Oceanography Center; Vol 7, 1992; *Monthly Weather Review*; pgs 273-279.

2. B. R. Bean, E. J. Dutton; *Radio Meteorology*; Dover Publications, New York; 1968, 435 pgs.

3. C. F. Bohren, B. A. Albrecht; *Atmospheric Thermodynamics*; Oxford University Press, New York; 1998, 402 pgs.

4. R. A. Brost, J. C. Wyngaard;Top down and bottom up diffusion of a scalar in the convective boundary layer; Vol 41, 1984; *Journal of Atmospheric Science*; pgs 102-112.

5. T. D. Crum, R. B. Stull; Surface layer air versus height in the entrainment zone; Vol 44, 1987; *Journal of Atmospheric Science*; pgs 2743-2753.

6. J. W. Deardorff; Convective velocity and temperature scales for the unstable planetary boundary layer and for Rayleigh convection; Vol 27, 1970; *Journal of Atmospheric Science*; pgs 1211-1213.

7. G. D. Dockery, J. R. Kuttler; Theoretical description of the parabolic approximation / Fourier split-step method of representing electromagnetic propagation in the troposphere; Vol 26, Number 2, 1991; *Radio Science*; pgs 381-393.

8. Holton; *An Introduction to Dynamic Meteorology*; Academic Press, New York; 1972, 319 pgs.

9. S. Petterssen; *Weather Analysis and Forecasting*; McGraw-Hill, New York; 1956.

10. F. J. Ryan; User's Guide for the Variable Terrain Radio Parabolic Equation Computer Model; Technical Report 1456; Ocean and Atmospheric Sciences Division, Naval Systems Center, San Diego; 1991, 51 pgs.

11. T. E. Rosmond; The Design and Testing of the Namy Operational Global Atmospheric Prediction System; Vol 7, 1992; *Monthly Weather Review*; pgs 262-272.

12. W. J. Saucier; *Principles of Meteorological Analysis*; University of Chicago Press, Chicago; 1955.

13. R. B. Stull; *An Introduction to Boundary Layer Meteorology*; Kluwer Academic Publishers, Hingham; 1988, 666 pgs.

14. J. M. Wallace, P. V. Hobbs; *Atmospheric Science, an Introductory Survey*; Academic Press, New York; 1977, 467 pgs.

15. Author not applicable; Software Requirements Specification for the Advanced Propagation Model CSCI (version 1.0); Space and Naval Warfare Systems Center San Diego, San Diego; 1998.

DIRECT MEASUREMENT OF RF/EO PROPAGATION FACTORS IN COASTAL REGION

Steve Kang*, Janet Stapleton, and Russell Wiss
Naval Surface Warfare Center Dahlgren Division (NSWCDD)
Code T44
17320 Dahlgren Road
Dahlgren, VA 22448
V/F (540) 653-4751/4046, kangss@nswc.navy.mil

1. INTRODUCTION

RF propagation at low altitude is strongly affected by the structure of the refractive index of the lower atmosphere. RF propagation in this region, especially down at 10 meters above the sea surface, has long been known to vary with altitude, range, time and frequency. Over 15 dB of variation in one-way propagation loss was observed for target height differences of 3 feet, or time periods of less than 20 seconds. Longer-term variations from ducting to subrefractive environments that resulted in a 40 dB change in one-way loss were also observed (Ref. 1). Under subrefractive conditions, the radar horizon may be significantly reduced. Under enhanced propagation conditions (ducting), deep nulls have been both predicted and observed. A number of threats have been designed to take advantage of these low altitude phenomena. Environmental effects dominate the detection and tracking of low flying cruise missiles by shipboard radars. Characterization of these effects is critical to the design of next generation sensor systems.

The Naval Surface Warfare Center Dahlgren Division (NSWCDD) was tasked by Office of Naval Research (ONR35, TASK 5WSDSFC02) to develop the means to allow ships to remotely sense low altitude propagation and clutter, using shipboard fire control sensors and local meteorological measurements. The information will be used to improve sensor and combat system performance through adaptation to existing conditions. Adaptation will include selection of frequency for fire control radars; selection of zones of minimal multipath and clutter degradation; determination of optimal range and bearing dependent threshold setting; and better weighing of Radar and Electro-Optical (EO) track sensor use and data.

The Interactive Adaptation of Fire Control Sensors to the Environment Field Test was conducted off the eastern Virginian shore, Wallops Island during March 4 through April 3, 1998. The goal of the test was to demonstrate that exploitation of environmental and tactical sensor data would improve sensor resource management and fire control in stressing environments by increasing detection and firm track ranges. The test would validate operational propagation and meteorological systems and performance prediction models to accurately characterize the environment. This test was a collaborative effort of both government and university organizations to characterize EM/EO propagation effects in the low altitude region of 10 meters and less above the sea surface. The participants to this joint effort included: NSWCDD, Naval Postgraduate School (NPS), The Space and Naval Warfare Systems Center San Diego (SSC-SD), Naval Research Laboratory Monterey, and Johns Hopkins University Applied Physics Laboratory (JHUAPL).

The purpose of this paper is to briefly describe the field test and the type of data collected. Detailed analysis and discussion of all the data collected and their effects are beyond the scope of this paper. Only some of the direct RF and IR measured propagation data will be presented. A detailed analysis of any particular data collected or type of measurement is left for other papers to follow.

2. OBJECTIVES AND APPROACH

The main objective for this field test was to measure the RF and IR propagation versus range using RF and IR signal sources and receivers to satisfy the mandated need for propagation ground truth measurements. The measured data will then be compared to the modeled propagation using TEMPER (Routine Tropospheric Electromagnetic Parabolic Equation) developed by JHUAPL for propagation factor by utilizing all applicable evaporative duct height models, and the mesoscale atmospheric data assimilation system, COAMPS (Coupled Ocean/Atmosphere Mesoscale Prediction System, Ref. 2) results for refractivity. To obtain the necessary refractivity profiles to input into the propagation model, meteorological measurements such as temperature, relative humidity, and atmospheric pressures were made using the met sensors mounted on the towers, buoys, boats, and a helicopter. Although previous work was focused on radar bandwidth usage versus environment type, other goals include environmental sensing modes for EM/EO sensors, and optimization of thresholds and waveforms.

3. MEASUREMENT SYSTEMS AND DATA COLLECTED

3.1 Direct RF/IR Propagation Measurements

NSWCDD has developed two systems to directly measure RF propagation for targets at one to ten meters in altitude (Ref. 3 and 4). The Single Frequency System (SFS) consisted of a transmitter receiver pair, which can operate at either X band or Ku band. It is designed to probe propagation profiles versus range. A single receiver is mounted on a tower to simulate various test radar heights. A single transmitter emitting 0.5 watts of continuous wave RF signal was placed on moving shuttle on a tower that was mounted on the stern of the boat, *Sealion*. The transmitter was moved up and down the tower by a computer-controlled motor, covering target heights from one to ten meters. The receivers measured the received signal levels and calculated the one way propagation loss using the calibrated transmitter output power levels. During this field test, SFS operated in Ku band.

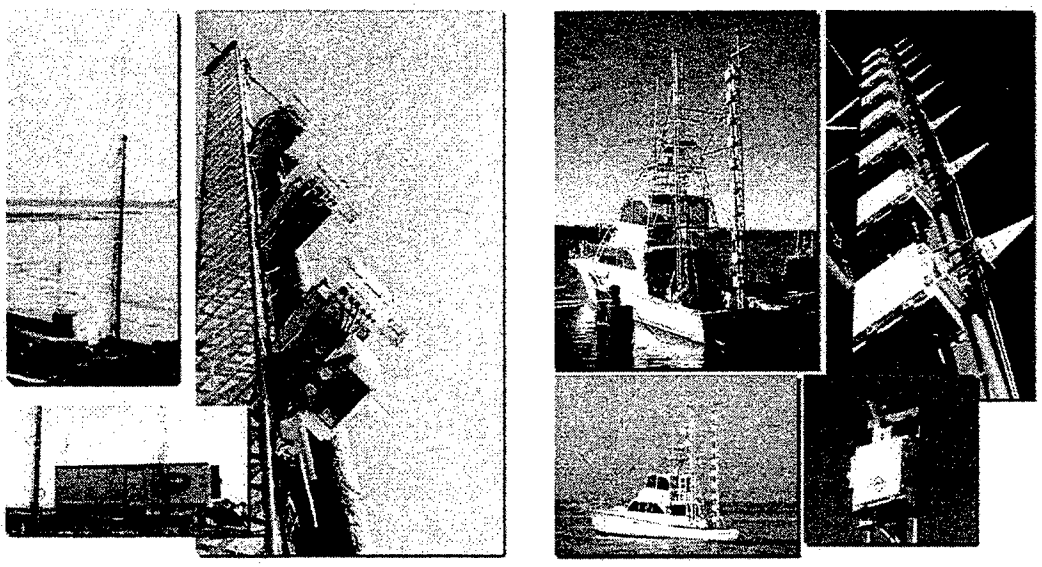
The Microwave Propagation Measurement System (MPMS) is a wideband propagation measurement system covering the 2 to 18 GHz frequency band in sixteen discrete frequency steps. Each frequency is switched at 2 Hz rate. The system consisted of ten transmitters, with 3 feet of spacing between each transmitter, mounted on a 30-foot tower on *Sealion* and four receivers mounted on a 100-foot tower on shore. This configuration gives 40 simultaneous propagation paths. The one-way pathloss is measured with four receivers each placed at four radar heights of interest. The output signals from the transmitters are separated by predetermined audio-frequency offsets

from a common carrier frequency. Each receiver channel performs Fast Fourier Transforms (FFT) on incoming sampled data allowing discrimination between the individual transmitters and transmitter heights using the position of each received signal in the output frequency spectrum. The four receivers were placed at 15, 47, 60, and 77 feet above the mean sea level during this field test. The MPMS allows propagation effects measurement versus range over a wide frequency band at a high temporal rate.

F1	F2	F3	F4	F5	F6	F7	F8
2.365	3.700	4.635	5.900	7.145	7.530	8.475	9.295
F9	F10	F11	F12	F13	F14	F15	F16
10.400	12.300	13.390	13.570	14.490	15.000	15.900	17.350

Table 1. List of 16 MPMS Test Frequencies in GHz.

In order to measure the infrared horizon detection range, a 20 W/str heater was mounted on a roving shuttle where the SFS transmitter was also placed. A Radiance I camera, manufactured by Amber Engineering, with 3-5 μm spectral band was placed at 60 feet above the mean sea level. The sensor has noise equivalent irradiance of 6.3×10^{-14} W/cm^2 and 33 μrad detector angular resolution. The analog video from the camera was digitized and processed by Datacube 6U VME board.



(a) (b)

Figure 1. Microwave Propagation Measurement System (MPMS) and Single Frequency System (SFS) (a) Receivers on shore and (b) Transmitters on *Sealion.*

3.2 Meteorological Data

Meteorological parameters such as temperature, wind speed, relative humidity and pressure, were needed to calculate refractive profiles used as input to the microwave

propagation models for comparison with the directly measured RF propagation factor. These data were collected using an array of ten meteorological sensors mounted on a 100-ft tower, collocated with the microwave propagation receivers, on shore. Nine sensors were mounted at fixed heights and one was mounted on a moving shuttle that traveled between fixed sensors acting as an offset and calibration measurement. Near-surface airflow properties and refractivity profiles from immediately above the sea surface to levels above the atmospheric boundary layer were obtained from three buoys, two vessels, and a helicopter. Three buoys, one NSWCDD owned and two provided by Naval Postgraduate School, and JHUAPL owned vessel, *Chessie*, provided meteorological data from fixed locations. The NSWCDD project boat *Sealion* and the JHUAPL owned helicopter equipped with meteorological sensors flying in a sawtooth pattern provided meteorological data along the propagation paths. NASA weather and the tide information using GPS were also recorded.

3.3 Coherent AN/SPY-1A Sea Clutter Data

Coherent AN/SPY-1A sea clutter data was collected to validate the current AEGIS sea clutter models. Both temporal and spatial clutter models will be examined in the light of this database. Sea clutter detections will be correlated with sea clutter amplitude data in an effort to develop a comprehensive sea spike model that is consistent with the sea clutter amplitude distribution. Also, using sea clutter magnitude as a function of range to deduce propagation conditions will be examined. The types of sea clutter data include: Doppler Waveform Data at a single azimuth, Wide Coverage sea clutter data, Frequency Correlation Data at a single Azimuth, sphere and Continuous Static Target (CST) calibration, and Radar Control Computer to Signal Processor Interface Tap data.

3.4 SPANDAR

NASA's Space Range Radar (SPANDAR) was used to obtain sea clutter maps for development and testing of Refractivity-From-Clutter (RFC). RFC is an ongoing effort by the Space and Naval Warfare Systems Center, San Diego (SSC-SD) and Duke University to estimate evaporation duct heights using radar clutter from the sea surface.

4. MEASUREMENTS

4.1 Ducting

One common existing refractivity feature over the ocean is the evaporation duct, which occurs due to the rapid decrease in humidity just above the ocean surface. It is an atmospheric condition in which rays are trapped and propagated longer distances parallel to the earth's surface. Examples of ducting conditions are shown in Figure 3 and Figure 4.

The measured MPMS propagation data from March 13 are shown in upper subplot in Figure 3. The model output using the measured duct height of 15 feet is shown in the lower subplot. Although four receivers measure propagation factors for sixteen frequencies in 2 to 18 GHz range, only data from one receiver for four selected frequencies are shown in the plot. The SFS data from the same run is plotted and shown in Figure 4. Both figures illustrate the data in a coverage diagram format with propagation factor relative to freespace shown using a gray scale. The horizontal axis

shows the range as determined by GPS, and the vertical axis represents the height of the target. Short black stripes of data at approximately 5 nautical miles away in Figure 3 and black stripes in Figure 4 signify invalid data points due to the boat's movement. The gray vertical stripe in Figure 3 represents a period of missing data.

The MPMS data shown in Figure 3 show the effect increased trapping at higher frequencies. For target heights of higher than ten feet, one-way propagation factors are better than or equal to –5dB (relative to the freespace) out to 10 nautical miles in cases of two lower frequencies. But for the SFS and the two higher frequencies of MPMS, 13.95 GHz, 10.4 GHz and 15 GHz, the propagation factor of better than or equal to –5dB from the free space is extended out to 15 nautical miles.

The multipath null structure for 15 GHz seen as darker lines on two subplots in Figure 3 starts at nearly the same height of about 20 feet at 5 nautical miles then rises to 33 feet at about 7 nautical miles. The measured and the TEMPER predicted output are in very good agreement for both MPMS and SFS data.

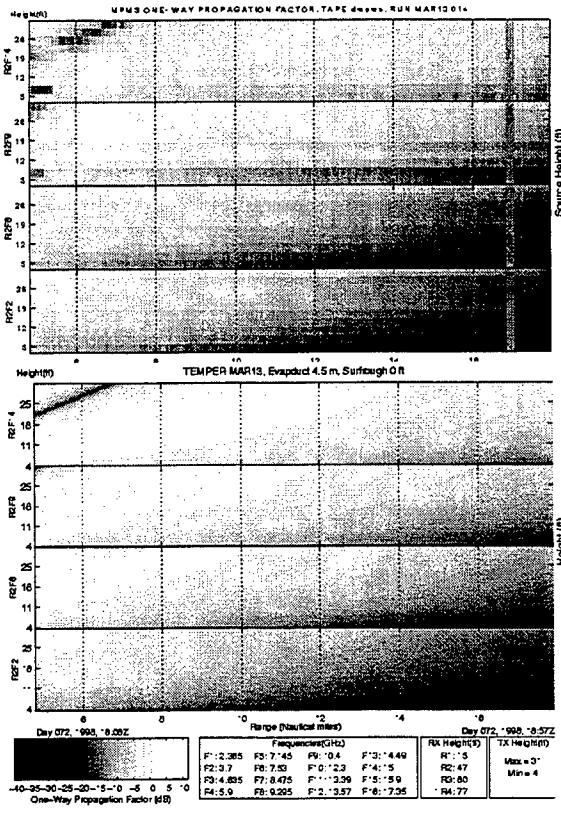


Figure 3. MPMS Propagation Data Under Ducting Condition, Measured vs. Model Output.
Receiver height: 47 ft,
Freq.(GHz): 15(top), 10.4, 7.53, 3.7.

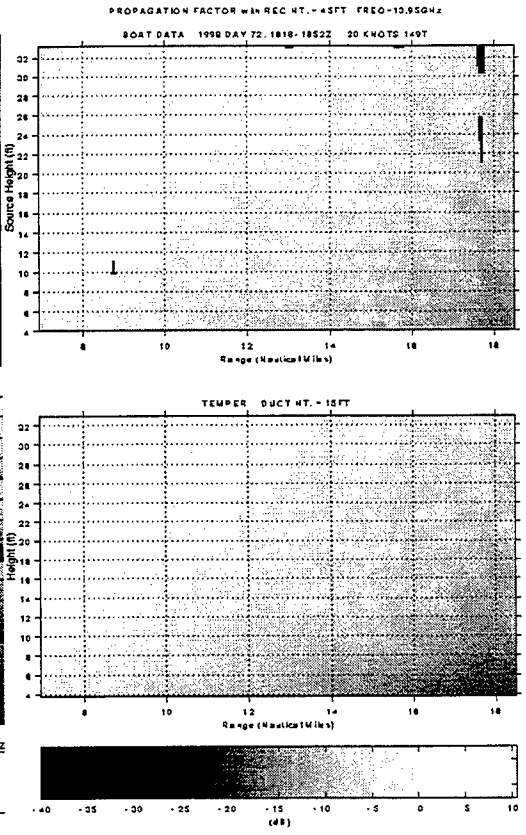


Figure 4. SFS Propagation Data Under Ducting Condition, Measured vs. Model Output.
Receiver 45 ft, Freq. 13.95 GHz,
Range: 5 to 18.5 nmi.

4.2 Subrefraction

When the atmospheric index of refraction increases, rather than decreases, with increasing height, the rays curve upward and the radar range is reduced compared to

normal conditions. This is called subrefraction. Subrefraction results when warm moist air flows over a cool ocean or cool dry air. Subrefractive layers are often deep enough to impact most frequencies of interest.

On March 31, the data collected indicated a subrefractive environment. This condition lasted for two days. One example of subrefractive case is shown in Figure 5. The solid gray vertical stripe in this plot denotes a period when no data was available. During this period, at boat ranges from 8.3 nautical miles to 8.9 nautical miles, attenuation-setting changes in the receivers were performed. It is evident from the plot that after 10 nautical miles, the propagation factor drops off very rapidly, causing the signals to be in the noise. The MPMS multi-frequency plot shows that all of the frequencies in 2 to 18 GHz range suffer from poor propagation. Under subrefractive conditions, wider bandwidth usage does not offer significant advantage over narrow band radars.

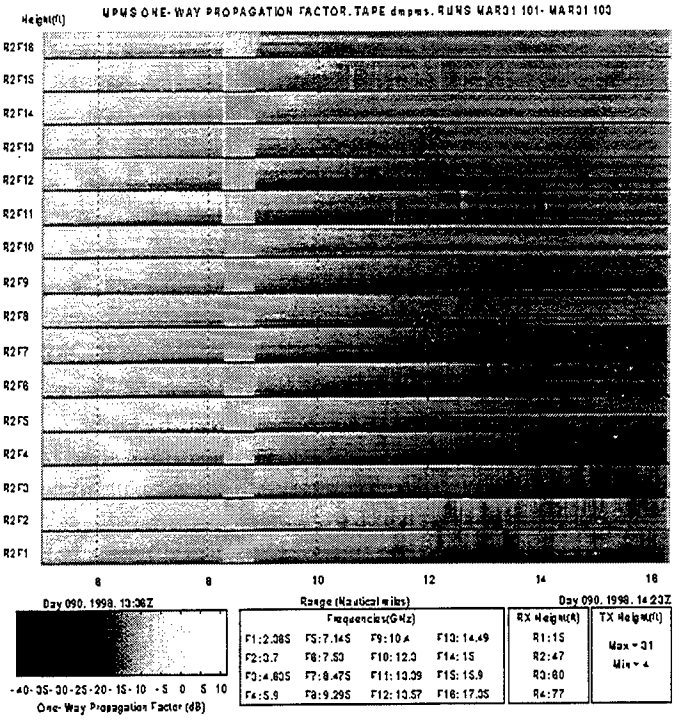


Figure 5. Measured MPMS Propagation Data in Subrefractive Condition for All 16 frequencies. Receiver Height: 47 ft.

4.3 Multi-modal Propagation (Surface-Based Duct)

Surface-based ducts are typically caused by the advection of warm dry air from land over the moist marine boundary layer, resulting in an elevated temperature inversion and the trapping of moisture below the inversion. Surface-based duct conditions can drastically increase the strength of land clutter returns from as far away as several hundred miles.

After two days of subrefraction, the conditions changed dramatically on April 2. A very strong surfaced based duct developed, causing the signal to be trapped in the duct and creating multi-modal interference patterns. The data collected on April 2 are shown in Figure 6 and Figure 7. The data shows a very strong enhancement of propagation and multiple skip zone effects. Although the measured and the modeled output using the refractive profiles collected by the helicopter do not match exactly, they agree very well.

The presences of double nulls especially in 15 GHz plot and SFS plot are quite evident, and the shapes of the nulls agree. The black vertical stripe at 23 miles in Figure 7 represents missing data due to a problem with the roving shuttle. For four frequencies shown in the MPMS data plot as well as the SFS data, there is significant enhancement of signals. Overall propagation factors are up to 10 dB better than freespace, even just above the water surface. In such cases, the surface clutter will be greatly increased which would lead to an increased false alarm threshold level for some type of radars and lead to reduced radar sensitivity.

The range coverage during this day was far greater than the other "normal" days. From a typical coverage of 20 nautical miles, the range coverage is increased to approximately 35 miles. Even at 35 nautical miles, strong signal levels were detected.

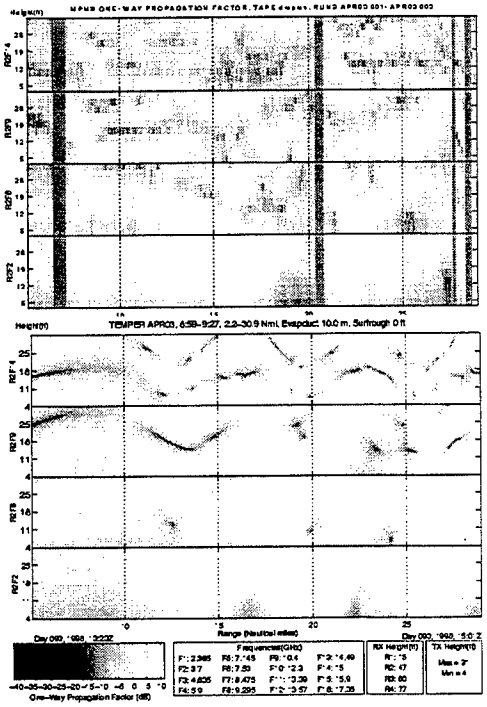


Figure 6. MPMS Propagation Data Under Surface-Based Ducting Condition, Measured vs. Model Output

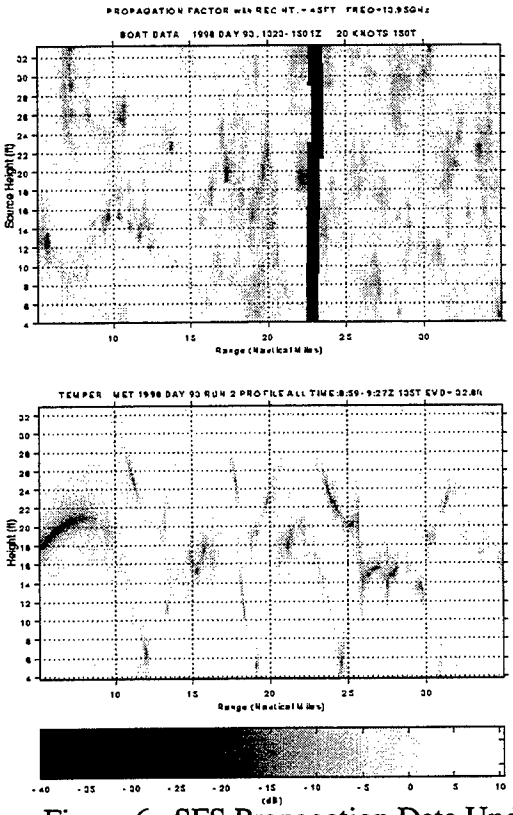


Figure 6. SFS Propagation Data Under Surface-Based Ducting Condition, Measured vs. Model Output.

The surface clutter measurements using SPANDAR support this phenomenon where surface clutter returns were measured from as far away as 250 km, compared to 25 km during an evaporating ducting condition.

4.4 Infrared Propagation

The air-sea temperature difference (ASTD) is the gauge most often used to indicate the atmospheric condition for infrared propagation. Under unstable condition, indicated by a negative ASTD, the range to the horizon is reduced. Under this subrefractive condition, a mirage often forms. Stable conditions occur when the air is warmer than the water, positive ASTD. Stable (super-refractive) conditions produce an increased range to the horizon. Zero ASTD corresponds to a neutral atmosphere. The occurrence of ASTD measurements from 13 test days is shown in Figure 8, and the maximum intervisibility range (MIVR) as a function of ASTD for the target height of 33 feet is shown in Figure 9.

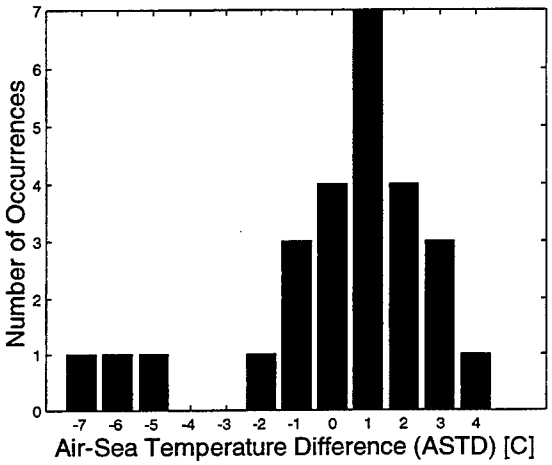


Figure 8. Occurrence of ASTD Measurements for IR Propagation

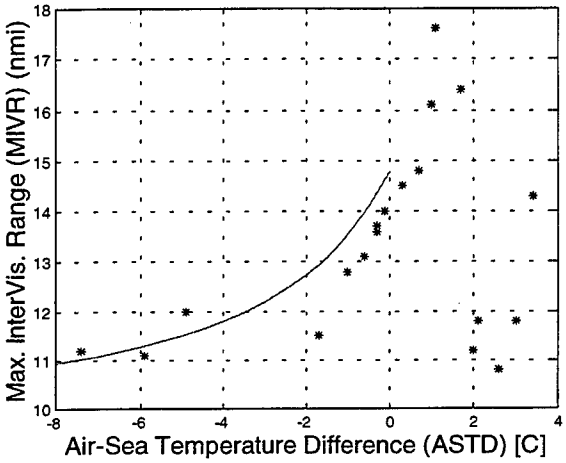


Figure 9. Measured and Modeled [Ref 5] Maximum Intervisibility Range vs. ASTD

4.5 Data Summary

Direct propagation measurements were made on fifteen days during this test period. There were total of thirty-eight boat runs made. The typical ranges that covered were from six to twenty nautical miles. Eight of the thirty-eight runs were categorized as 'short runs' covering less than twelve nautical miles from the receivers. During the test period a wide range of propagation conditions from strong ducting to subrefraction occurred. During the fifteen testing days, two days of standard atmospheric (or 4/3 earth) conditions, two days of subrefractive conditions, two days of strong surface based ducting conditions, and nine days of evaporative ducting conditions were observed.

5. CONCLUSION

A detailed analysis of all the data collected is still being conducted. NSWCDD continues comparison of the measured propagation data to predicted data by TEMPER and other propagation models. The results from this Interactive Adaptation of Fire Control Sensors to Environment Field Test will be used to validate the propagation and duct height models, and meteorological data collection techniques such as SEAWASP (Shipboard Environmental Assessment/WeApon System Performance) in MORIAH

(Operational Environmental Sensing System). The results will also provide clutter and ground truth data to support the AN/SPY1 clutter modeling effort, and evaluate high-resolution weather now/fore casting. Through improved sensor resource management by exploitation of environmental and tactical sensor data, increased performance against the sea skimming threat can increase the battlespace. The Interactive Adaptation of Fire Control Sensors to Environment task has strong impact on future Navy systems by reducing the costs associated with achieving increased radar performance over more typical enhancements.

6. References

[1] S. Kang and J. Stapleton, "Microwave Propagation Measurements in the Low Altitude Region Using Single Frequency and Wideband Systems," Battlespace Atmospherics Conference Proceedings, December 1996, pp. 165-174. [ADA 323038].

[2] Richard M Hodur, "The Naval Research Laboratory's Coupled Ocean/Atmosphere Mesoscale Prediction System (COAMPS)," Monthly Weather Review, Volume 125, July 1997, pp. 1414-1430.

[3] J. Stapleton and S. Kang, "Wideband Low Elevation Microwave Propagation Measurements," NSWC/Dahlgren Division Report, NSWCDD/TR-95-18, February 1995.

[4] J. Stapleton and S. Kang, "Ku-Band Propagation Measurements In the Low Altitude Region," NSWC/Dahlgren Division Report, NSWCDD/TR-95-66, October 1995.

[5] A. J. Beaulieu, "Atmospheric Refraction Model and the Effects of Surface Waves," DREV Report 4661/92, May 1992.

This page intentionally left blank.

Measurements of Clouds and Cloud Parameters

THREE-DIMENSIONAL CLOUD DEPICTIONS BASED ON FIELD EXPERIMENT MEASUREMENTS

Thomas R. Caudill and Donald C. Norquist*
Air Force Research Laboratory/VSBE
C/O AFWA/DNX
106 Peacekeeper Drive
Offutt AFB, NE 68113-4039
Phone: (402) 232-8282
Fax: (402) 294-2892
E-mail: norquisd@afwa.af.mil

INTRODUCTION

The Air Force Scientific Advisory Board (SAB) has determined that cloud depiction and prediction ranks as one of the highest need environmental support issues facing the Air Force. Knowledge of the present and future three-dimensional cloud structure over a mesoscale area, at horizontal grid spacings as fine as 1 km and cloud base altitude specification within 10 percent, is required for efficient and effective Air Force mission operations. The SAB cites the present lack of cloud structure measurements among the problems limiting the Air Force's ability to provide accurate cloud depictions and predictions to Air Force customers.

Currently, the Air Force's RTNEPH cloud analysis model (Hamill et al., 1992) is used to provide global depictions of cloud structure, based on polar orbiting satellite imagery data and, where available, surface observations. The RTNEPH cloud analysis has a 48 km grid spacing, and involves many assumptions which limit its credibility. A new cloud analysis model, the Cloud Depiction and Forecast System - II (CDFS-II), relies on polar-orbiting and geostationary satellite imagery and improved cloud top placement algorithms. However, the CDFS-II cloud specification model is designed to use satellite imagery as its only observational data source to specify the cloud distribution. This "top-down-only" perspective can't explicitly account for underlying clouds obscured from view by higher clouds, nor can it provide a measurement of cloud base altitude. Thus, there is a need to develop accurate, three-dimensional depictions of cloud structure using a complement of observing systems, supplemented by gridded specifications of non-cloud weather variables.

The current research project makes a first step towards a comprehensive cloud analysis capability by attempting to construct three-dimensional cloud depictions based entirely on cloud observations and measurements. Several recent cloud measurement field experiments have been conducted, and it is of interest to determine how fully their measurements can be used to construct a quantitative depiction of the cloud state. Such an exercise serves a number of useful purposes. First, what we learn from placing complementary measurements in the depiction may be useful in developing a functional cloud analysis capability. Second, an accurate depiction based on field experiment measurements can be used as "ground-truth" against which to validate analyses or forecasts of the cloud state based only on routinely available observations. Third, a simultaneous depiction of the commonly observed cloud variables (fractional cloud cover, cloud type, cloud base and top altitudes, all of which shall hereafter be referred to as "cloud observables") and the cloud water content (liquid and ice) may provide the information needed to

develop relationships between the two. Such relationships could prove useful in transforming analyses of the cloud observables into cloud water content to initialize a numerical weather prediction model. Fourth, quantitative cloud depictions could be used to improve the cloud-effects physics in radiation parameterization schemes in weather and climate prediction models.

METHOD

We used a subset of the cloud measurement data set collected in Phase 3 of the Space-Based Infrared System (SBIRS) field experiment (Caudill et al., 1997) to construct the cloud depictions. Table 1 gives a list of the SBIRS sensor-data types used in this study.

Cirrus clouds were the primary focus of SBIRS, and mission days were selected for observations of tropical cirrus largely unobscured by lower clouds. SBIRS Phase 3 was conducted at Everglades City, FL during the period 4-23 September 1996. The data set was chosen because of the wide variety of sensor measurements available, and the fact that AFRL-Hanscom was designated as the data archival center.

The first step in transforming the individual sensor's measurements into a sequence of three-dimensional cloud depictions was to process the raw data. We created a processed data file of measurement records for each mission day for each sensor from the raw data. Each record included the time, latitude, longitude, and altitude and relevant data value(s). For example, particle probes on board the HARP aircraft (Morrison et al., 1997) supplied ice particle counts in a range of particle size bins, from which the ice water content was computed and placed as the relevant data value in the processed data files. For the aircraft and many of the ground-based remote sensors, observations were taken nominally at one-second intervals. The typical observing mission lasted 3-4 hours.

Once the processed data files for each sensor were generated for each mission, we consolidated the observations into a sequence of three-dimensional grids. The consolidation algorithm was designed to first ingest all of the available sensor-data types. After surveying the time, latitude, longitude, and altitude extents of all of the sensor-data types, the algorithm determines the time and space boundaries for the depiction sequence that can accommodate all of the data. Histograms of the magnitude of the displacement between sequential measurements are computed for both the horizontal and vertical, and grid cell sizes are determined in such a way that little or no averaging is necessary. Then the consolidation algorithm assigns each sensor-data observation taken within a pre-set time interval to the appropriate grid box to construct the depiction for that time interval. The time interval is chosen as a compromise between filling the largest number of grid cells but minimizing the "steady-state" assumption for the clouds. We may be able to use observed or analyzed winds to "advect" a measurement to another location at a subsequent time where no measurement is available, but this step is not yet included in the consolidation routine. When the depiction is sufficiently filled, we can optionally apply a smoothing to the depiction for spatial continuity. As a final step in the consolidation process, we compute the cloud fractional coverage over desired groupings of the grid boxes.

Once the time sequence of the three-dimensional depictions is generated for a given mission day sampling period, we display the products graphically in an animated fashion. This gives us an idea of the visual realism of the depictions, which we may be able to validate subjectively against footage or satellite imagery. We hope to be able to show several of the depictions at the conference.

Table 1. SBIRS sensor-data types used in three-dimensional cloud depiction

Component	Source	Data Type	Product
High Altitude Recon. Aircraft	Learjet	radar, lidar, particle probes	cloud top, ice shape/size
High Spectral Resolution Lidar	lidar	line-of-sight backscatter	cloud opt. depth, top, depth
Volume Imaging Lidar	scanning lidar	3-D high-resolution images	navigated 3-D cloud fields
Cloud Profiling Radar System	scanning radar	3-D radar images	navigated 3-D cloud fields
SERCAA* cloud analysis	polar, geo. sat. imagers	multispectral cloud imagery	large-scene cloud top map
Carbon dioxide slicing	polar, geo. sat. imagers	multispectral radiance	vertical cloud properties

*SERCAA: Support of Environmental Requirements for Cloud Analysis and Archive (Gustafson et al., 1996)

Future Work

After the simultaneous depictions of cloud water content and cloud observables are generated, we can begin the work of developing relationships between the two. We plan to begin by developing empirical relationships for cloud water content as a function of the cloud observables. The latter are what would be commonly provided by a cloud analysis procedure based on routinely available cloud observations. The relationships can be used to convert gridded analyses of cloud observables into gridded cloud water concentration values. We must first look at what other investigators have done to pose such relationships. Their work may give us guidance in the process. Almost certainly, the empirical relationships will involve some statistical processing of the depicted cloud data. We will likely develop the relationships using dependent data from some of the mission days. We would then apply the relationships to independent cloud observables from the other mission days, and validate the resulting cloud water concentrations against the three-dimensional depictions of the same on the mission days from which the independent data was taken.

If this work is successful as applied to the cirrus data in the SBIRS field experiment data sets, we may be able to apply the methods to other collections of cloud measurements. These may involve more than a single cloud type present within the depiction grid at the same time. We consider this as the next step towards the ultimate design of a cloud analysis utility that generates depictions of cloud observables based on routinely available cloud measurements.

References

Caudill, T.R., W. A. M. Blumberg, A. Griffin, and J. Wise, 1997: Cloud database collected in support of the Space-Based Infrared System phenomenology exploitation program. Preprints, *Cloud Impacts on DoD Operations and Systems 1997 Conference*, 23-25 September 1997, Newport, RI, 140-143, PL-TR-97-2112. [ADA 330020].

Gustafson, G., R.P. d'Entremont, and R.G. Isaacs, 1996: *Support of Environmental Requirements for Cloud Analysis and Archive (SERCAA): Final Report,* PL-TR-96-2224, Hanscom AFB, MA, 71pp.

Hamill, T.M., R.P. d'Entremont, and J.T. Bunting, 1992: A description of the Air Force real-time nephanalysis model. *Wea. Forecasting,* 7, 288-306.

Morrison, B.J., R. Hobbs, D. Rusk, J. Jung, and R.L. Rose, 1997: *The High Altitude Reconnaissance Platform (HARP) SBIRS Final Report.* AEROMET/TUL 9704211, Aeromet, Inc., P.O. Box 701767, Tulsa, OK 74170-1767.

High Spectral Resolution Lidar Measurements of the Backscatter Phase Function in Cirrus Clouds.

E. W. Eloranta*, R. E. Kuehn and R. E. Holz
University of Wisconsin
1225 W. Dayton St., Madison, WI 53706
Phone 608-262-7237, Fax 608-262-5974
eloranta@lidar.ssec.wisc.edu

1 Introduction

Satellite derived climatologies of cirrus clouds find that approximately 40% of the earth is covered with visible cirrus clouds (Wylie et al. ,1994). The sensors used to derive these statistics do not detect clouds with optical depth below ~ 0.1 (Wylie et al., 1995). As a result, when sub-visual cirrus are included the cirrus coverage is likely to be larger than 40%.

Most cirrus clouds have optical depths of less than one and appear tenuous to the visual observer. However, even optically thin cirrus can seriously degrade military system performance. Space borne surveillance systems monitoring missile launches may detect false targets due to the specular reflection of sun light from oriented crystals. Aircraft mounted IR sensors looking horizontally though cirrus layers may encounter large optical depths which obscure targets. Both the tracking system and the laser weapon of an airborne laser missile defense systems may encounter large cirrus optical depths during the launch phase of the target missile.

Cirrus clouds have a major impact on the radiation balance of the earth. Thus, information on their optical properties and spatial distribution are required to model climate change.

The University of Wisconsin lidars are employed in studies to improve our knowledge of cirrus cloud optical properties and spatial distributions. One measurement strategy uses our Volume Imaging Lidar (VIL) to generate three-dimensional images of cirrus clouds. Under favorable conditions, these images depict cloud structure over dimensions greater than 100 km while providing resolutions as small as 15m. The images are then converted into 3-d fields of backscatter cross section using simultaneous measurements with our High Spectral Resolution Lidar (HSRL). The VIL provides rapid scanning and high spatial resolution while the HSRL provides absolutely calibrated profiles of optical depth, backscatter cross section and depolarization. The VIL data are corrected for attenuation using values of the backscatter phase function derived from the HSRL. The phase function is also used

to convert VIL measured backscatter cross sections into the total scattering cross sections. Total scattering cross section values are required to compute radiative transfer in clouds.

This paper examines backscatter phase function measurements provided by the HSRL.

2 Backscatter phase function measurements

A large data set acquired with the HSRL in 1994 and 1995 has been analyzed to determine the backscatter phase function in cirrus clouds. The HSRL provides direct measurements of the optical depth and the backscatter cross section as a function of altitude. The backscatter phase function, $\frac{\mathcal{P}(180,r)}{4\pi}$, is computed from:

$$\frac{\mathcal{P}(180,z)}{4\pi} = \frac{\beta'(z)}{\beta_s(z)} \tag{1}$$

where: $\beta_s(z) = \frac{d\tau}{dz}$, τ = optical depth, $\beta'(z)$ = the backscatter cross section and z= altitude.

The backscatter phase function values computed from this equation are sensitive to noise in the HSRL measured profile of τ. To minimize noise the HSRL data was averaged over 3 minute time intervals and 165 m altitude layers. Data points were selected to include only points with a statistical error of less than 5%. Only points with a measured depolarization of greater than 20% were selected to insure that the cloud consisted of ice crystals. In addition only uniform sections of the cloud were selected for analysis to prevent errors due to averaging between cloudy and clear parcels. Uniform cloud parcels were selected by limiting the analysis to those points where the backscatter of the point did not vary by more than 15% from adjacent points. Figure 1 shows the distribution of backscatter phase function values computed in this manner. It shows a prominent peak at $\mathcal{P}(180)/4\pi \approx .04$. It is interesting to note that this is the value which would be expected for a particle whose phase function consisted of a diffraction peak containing 1/2 of the scattered energy with the rest of the energy scattered isotropically. This particle would have a backscatter phase function, $\mathcal{P}(180)/4\pi = 1/8\pi = .0398$. It is significant that values of the backscatter phase function computed by ray tracing for various geometrically perfect crystal types would suggest a much wider distribution of values. However, ice crystals collected from clouds seldom consist of single crystal type and few natural crystals exhibit the perfect symmetries of the model crystals.

Despite the stringent selection process used to select data points for inclusion in figure 1, we were concerned about errors in the derivative, $\frac{d\tau}{dz}$. To increase our confidence, we hand picked 34 cirrus clouds from the data set. These were selected for uniformity such that we could form long time averages without introducing errors due to averaging over inhomogeneities. To minimize noise in the derivative we have calculated the bulk value of the backscatter phase function averaged through the cloud. Here the backscatter phase function is computed from the integral of the backscatter cross section through the cloud and the optical depth of the cloud. By measuring the optical depth between the cloud base and a point well above the cloud top, we also minimize multiple scattering errors. At this point most multiple small angle forward scattering from the cloud will have escaped from the 160μrad receiver field of view.

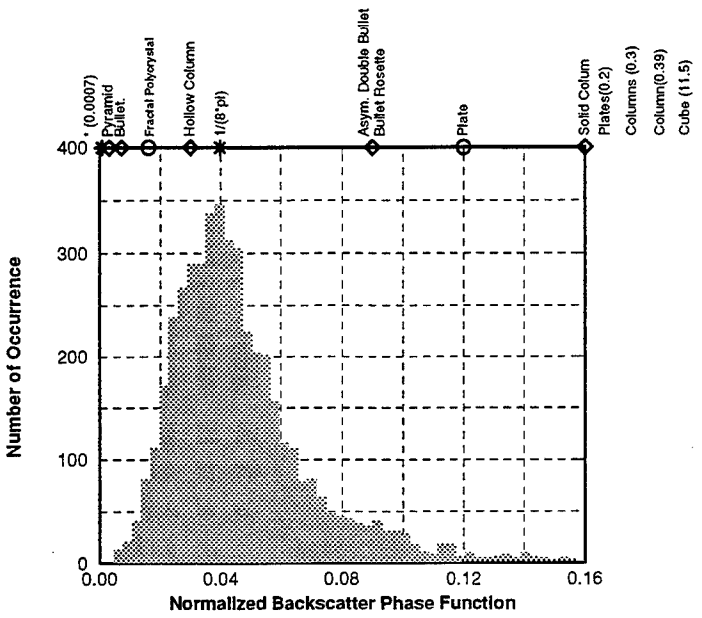


Figure 1. Number of occurrences of a given value of the backscatter phase function. Values of the backscatter phase function generated by means of ray tracing computations are shown above the figure. Values for the cube and values marked with diamonds are from Macke, 1993. The value for the column(0.39) and those marked with circles are from Macke et al., 1998. Values for columns(0.3) and plates(0.3) on the right are from Cai and Loiu, 1982.

Figure 2 shows the distribution of backscatter phase functions and a plot of the backscatter phase function versus depolarization for the select cases. Notice that the distribution in figure 2 is more strongly peaked than that of figure 1. However, careful examination of the data point at 0.09 shows that it is valid and must represent the variability predicted by ray tracing simulations. This variability makes it dangerous to assume a single value of the backscatter phase function for all cirrus clouds.

The right panel of figure 2 shows that the depolarization increases with increasing backscatter cross section. This can be explained by differences between external and internal reflections from the ice crystals. External reflections from facets which return energy to the receiver must occur from facets which are oriented normal to the lidar beam. These reflections are completely polarized and the facets are not very efficient reflectors because the Fresnel reflectivity of ice is low. Front surface reflections from randomly oriented convex ice particles would generate a $\frac{\mathcal{P}(180)}{4\pi} = 0.007$. Internal corners of the crystals are efficient retro-reflectors. In this case the light rays must enter and leave the crystal through a tilted surface which induces depolarizations. Consequently, because the fraction of the scattering from internal corners and external facets will be a function of crystal morphology, we can expect that the depolarization and the backscatter phase function will be correlated.

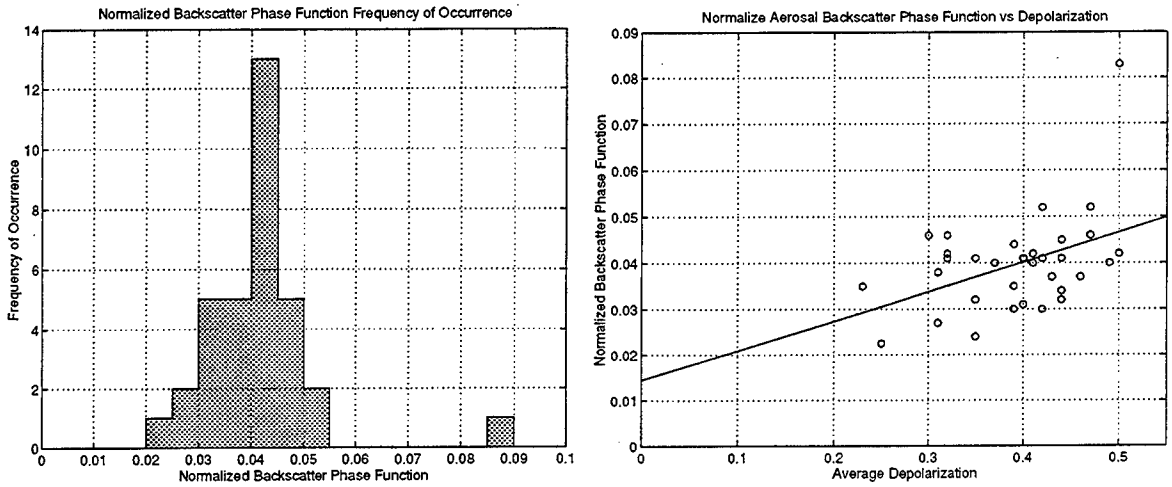


Figure 2. A histogram of cloud layer average backscatter phase functions (left panel) and the dependence of cloud layer average backscatter phase function on cloud layer average depolarization (right panel).

3 References

- Cai Q. and Kuo-Nan Liou, 1982: Polarized light scattering by hexagonal ice crystals: theory, *Applied Optics*, **21**, 3569-3580.
- Macke, A, 1993: Scattering of light by polyhedral ice crystals, *Applied Optics*, **332**, 2780-2788.
- Macke, A, P. N. Francis, G. M. McFarquhar and S. Kinne, 1998: The role of particle shapes and size distributions in the single scattering properties of cirrus clouds, *J. of Atmospheric Sciences*, **55**, 2874-2883.
- Wylie, D. P., W. P. Menzel, H. M. Woolf and K. I. Strabala, 1994: Four Years of Global Cirrus Cloud Statistics Using HIRS, *J. of Climate*, **7**, 1972-1986.
- Wylie, D. P., P. Piironen, W. Wolf and E. W. Eloranta, 1996: Understanding Cirrus cloud Climatologies with Calibrated Lidar Optical Depths, *J. of Atmospheric Sciences*, **52**, 4328-4343.

4 Acknowledgments

The 1994 HSRL data was collected by Paivi Pirronen. Funding for this research was provided by National Science Foundation Grant ATM-9321330 and Air Force contract F19628-96-C-0097.

POAM Measurements of Stratospheric and Upper Tropospheric Clouds, Aerosols, and Ozone

John Hornstein*, Eric Shettle, Mark Daehler, and Richard Bevilacqua
Naval Research Laboratory
Naval Research Laboratory, Code 7220
4555 Overlook Avenue, SW
Washington, DC 20375-5351
202-767-0766 (fax: 0005), email: hornstei@poamb.nrl.navy.mil

The Polar Ozone and Aerosol Monitor (POAM) instruments on SPOT-3 and SPOT-4 measure vertical profiles of ozone, aerosols and subvisual clouds in the stratosphere and upper troposphere. Measurements are made each day around two seasonally varying circles of latitude, one circle at high latitudes in each hemisphere, with about 14 samples per day around each circle. POAM is therefore able to monitor both the long term variations and the short term variability of the listed atmospheric components. POAM also provided the first measurements of optical extinction by Polar Mesospheric Clouds (noctilucent clouds). Calculations show that the atmospheric components measured by POAM can strongly affect the performance of optical systems in the UV, visible, and IR, and POAM measurements show that the distributions of these components vary strongly in space and time.

INTRODUCTION

The distributions of the absorbing and scattering ingredients of the atmosphere must be known both for calculating the emission and transmission of optical signals and for forecasting the weather. Monitoring of these distributions is moderately adequate for the troposphere, but is much less adequate for the stratosphere and mesosphere. Even for the upper troposphere, high, optically thin clouds are poorly monitored because they are invisible to nadir-viewing instruments.

This paper provides examples of the spatial and temporal variability of some of the important radiatively active trace ingredients of the middle atmosphere. The data are from the Naval Research Laboratory's Polar Ozone and Aerosol Monitoring (POAM) instruments. The examples show that the variability can be large, and exploratory calculations show that the large variability can strongly affect the performance of optical systems. On this basis, suggestions are made for using POAM data in various applications as a supplement to the climatological distributions, and for monitoring the actual distributions on an operational basis.

POAM

The POAM instruments (POAM II and POAM III) are spaceborne instruments that measure the vertical distributions of ozone, aerosols, optically thin clouds, water vapor, NO2, and the bulk atmospheric density and temperature in the upper troposphere, the stratosphere, and

the mesosphere. POAM works by measuring the changing attenuation of sunlight as the instrument watches the Sun rise and set behind the Earth's atmosphere. Measurements are made in 9 narrow spectral channels spaced across the near-UV, visible, and near-IR portions of the spectrum, from 353 to 1059 nm.

The limb-viewing geometry provides good vertical resolution: about 1 km. The horizontal resolution perpendicular to the line of sight is about 30 km, and the horizontal resolution along the line of sight is about 200 km.

The limb-viewing also geometry makes POAM sensitive to aerosol layers and optically thin clouds because it looks through their wide dimensions. Consequently POAM can detect clouds and aerosol layers that are invisible to nadir viewing sensors or to observers on the ground. These subvisual layers can substantially affect the performance of off-nadir optical systems, as shown below.

POAM measures transmitted light from a source which remains constant during a sunrise or sunset, not emission by the atmosphere itself. The data is therefore self-calibrating, in the sense that most instrumental drifts cancel from the transmittance ratio. This enables good comparisons between sunrises and sunsets at different places and times, and good comparisons between different POAM instruments.

POAM II is on the SPOT-3 remote sensing satellite, owned and operated by the Centre National d'Etudes Spatiales (CNES, the French Space Agency), and POAM III is on SPOT-4. The SPOT satellites are in polar Sun-synchronous orbits, so there is one sunrise and one sunset per orbit, for a total of 14 sunrises and 14 sunsets per day. During each day the sunrises occur around a circle of latitude in the northern polar region and the sunsets occur around a circle of latitude in the southern hemisphere. The two circles of latitude vary slowly from day to day, with a seasonal dependence that repeats from year to year.

SPOT-3 was launched on September 26, 1993, and POAM II obtained data from October 8, 1993 until the spacecraft failed on November 13, 1996. The references list some POAM II publications relevant to the subject of this conference. POAM III is carried by SPOT-4, which was launched on March 24, 1998. POAM III operation began on April 21, 1998, and will continue for the foreseeable future.

POAM OBSERVATIONS OF SPATIAL AND TEMPORAL VARIABILITY

Although POAM II was launched more than two years after the June 1991 eruption of Mount Pinatubo, the volcanic enhancement of the stratospheric aerosol layer remained strong for about five years. POAM II was able to observe the gradual return of the aerosol burden toward its unenhanced level. POAM II measurements of extinction coefficients followed the gradual cleansing, but the cleansing also manifested itself by gradual changes in POAM's ability to measure at low tangent altitudes. The high sensitivity of the limb viewing geometry to optically thin layers cuts both ways: when the aerosol layer is dense and/or there are too many vertically thick and optically thick clouds high in the troposphere, POAM's Sun-tracker loses its ability to

track the Sun's center of brightness, and the data terminate at an anomalously high altitude. POAM II's ability to measure deeper in the atmosphere improved significantly from year to year. This directly confirms the effect of aerosol variability on optical system performance that is discussed later in this paper.

POAM measures three kinds of optically thin clouds (Fig. 1): cirrus clouds, polar stratospheric clouds (PSCs), and polar mesospheric clouds (PMCs, also known as noctilucent clouds, NLCs). PMCs are extremely thin optically, but are highly structured and can produce significant clutter (see below). POAM was the first instrument to detect PMCs in extinction. PSCs and cirrus are also frequently sub-visual, as was the case for the clouds shown here. Both the PSC and cirrus shown here have vertical optical depths of about 0.01, so they would not have been detected by a nadir-viewing satellite or by observers on the surface, and would therefore not be included in the Air Force Real-Time Nephanalysis (RTNEPH). Nonetheless they can significantly affect airborne or limb-viewing optical systems, as shown below.

POAM II has accumulated a large database of measurements of PSCs. For most types of PSCs POAM is able to measure profiles of the extinction coefficients at several wavelengths, but POAM measurements of ice PSCs are indirect and partial: these clouds are so dense optically that they cause the data to terminate at an anomalously high altitude, as discussed above. Climatologies have been developed from the POAM II PSC observations in the northern and southern hemispheres (see the references). POAM III has already observed many PSCs.

Because POAM observes closer to the pole in the southern hemisphere than in the north, almost all the POAM observations of PMCs are in that hemisphere. Statistics of PMC altitudes, slant optical depths, and extinction coefficients have been extracted from the POAM II data: see the references.

Ozone, a significant absorber of UV and IR radiation, is also quite variable. An example of the spatial variability of the ozone on a given day is shown in Figure 2. At some altitudes the concentration of ozone varies by more than an order of magnitude: for example, compare the concentration between longitudes between 50 and 160°E to that between 200 and 30°E.

EFFECTS ON OPTICAL SYSTEM PERFORMANCE

Atmospheric properties measured by POAM can significantly affect the performance of optical systems. This section presents the results of calculations of these effects for several typical scenarios: (1) an air-to-air scenario, showing the effect of sub-visual cirrus; (2) a space-to-air scenario, showing the effect of a sub-visual polar stratospheric cloud; and (3) a space-to-air scenario, showing the effect of stratospheric aerosols.

(1) Air-to-air scenario, with sub-visual cirrus

Figure 3 shows the reduction in detection and recognition ranges due to cirrus obscuration and clutter in an air-to-air scenario.

The MWIR sensor used in the calculation is notional, but would be readily achievable with present technology. In the calculation it is at an altitude of 12 km. The target has a projected cross sectional area of 0.6 m^2, and travels at Mach 2 at an altitude of 12 km. Its temperature is 359 K, due to aerodynamic heating. The cirrus cloud was similar to the that shown in Figure 1. The cloud's vertical optical depth was only 0.01, so it would not be visible to a nadir-viewing space based instrument or from the ground, and would not be included in RTNEPH products.

As Figure 3 shows, sub-visual cirrus has a significant effect on performance. Detection range is reduced from 610 km (no cloud) to 150 km. Recognition range is reduced from 460 to 90 km.

(2) Space-to-air scenario, with polar stratospheric clouds

The reduction in detection and tracking ranges due to PSC obscuration and clutter has been calculated for a space-to-air scenario. The calculation is for a notional sensor similar to the SPIRIT III band A sensor on MSX, but adapted to allow it to observe at lower tangent altitudes. The sensor is at an altitude of 900 km, corresponding to the orbit of MSX. The target has a projected cross sectional area of 0.3 m^2, and travels at Mach 2 at an altitude of 15 km. Its temperature is 435 K, due to aerodynamic heating, since it is no longer in boost phase. The polar stratospheric cloud, which was based on one seen by POAM, was at an altitude of 20 km and was 2 km thick. The cloud's vertical optical depth was only 0.005 (about half the optical depth of the PSC shown in Figure 1), so again it would not be visible to a nadir-viewing space based sensor or from the ground.

The calculation was restricted to ranges where the target would be viewed against the limb rather than against the large background signal from the Earth's surface. For a sensor at the altitude of MSX this corresponds to sensor-to-target ranges between 3189 to 3953 km, and to sensor-to-target Earth-centered angles between 26 and 32.9°.

The PSC significantly affected detection of the target. Detection was possible against the limb over a 3.65° range of Earth-centered angles when the PSC was absent, this was reduced to 0.094° when the PSC was present. Comparing this to the range (6.9° = 32.9° - 26°) of Earth-centered angles over which the target is viewed against the limb, detection would be possible during 53% of the limb-viewing configuration in the absence of the PSC, but only during 1.4% when the PSC is present. The reduction in performance was partly due to obscuration by the cloud, but clutter from the cloud edges played the major role.

Some high orographic clouds, the nacreous clouds, are very similar to PSCs; and can occur in many parts of the world, not just at high latitudes. High orographic clouds could produce comparable or worse reduction in performance than the free PSC considered here, because they can be denser than cirrus or PSCs, and can have sharp clutter-producing edges.

(3) Space-to-air scenario, with stratospheric aerosols

The reduction in detection and tracking ranges due to stratospheric aerosols has been calculated for two types of sensors in a space-to-air scenario. The two sensors are (i) the same notional variant of the SPIRIT III sensor used in the previous example, and (ii) a sensor much like SPIRIT III, but using the MW infrared window band (3 to 5 microns). As in the previous calculation, the target is at 15 km altitude, has a cross sectional area of 0.3 m^2, and is at a temperature of 435 K. The scenario's geometry was the same as in the previous example.

The aerosol attenuated the radiation from the target and increased the target-independent path radiance received at the sensor, but was assumed not to have the sudden spatial variations typical of clouds, and hence was not a source of clutter. (When aerosol spatial variations are sharp, performance will be worse than calculated here.) The calculations were performed for daytime conditions, so the path radiance includes scattered sunlight as well as thermal emission. To show the full range of possible daytime effects the calculation was performed both for background stratospheric aerosol loading and for the extreme volcanic aerosol model from MODTRAN. This is representative of some of the conditions observed following the eruption of Mt. Pinatubo in 1991, (and the eruptions of Krakatoa and Katmai in 1883 and 1912 respectively).

For the sensor resembling band A of SPIRIT III, when the stratospheric aerosol was at background strength both detection and tracking were possible over much of the part of the orbit where the target is viewed against the limb, but when the aerosol was strongly volcanically enhanced detection was not possible at all in the relatively favorable limb-viewing geometry. The MW infrared sensor gave much better detection and tracking against background aerosol, but fared much worse against the strongly enhanced aerosol, because path radiance due to scattered sunlight is much stronger in the MWIR. For the MWIR sensor the range of Earth-centered angles for detection was 6.4° in the presence of background aerosol, and 0° in the presence of strongly enhanced aerosol, corresponding respectively to 93% and 0% of the limb-viewing opportunity.

While volcanic eruptions as large as Mt. Pinatubo only occur about once per century, volcanic eruptions which result in significant increases in the stratospheric aerosol loading occur on the average once or twice a decade.

CONCLUSIONS AND RECOMMENDATIONS

The distributions of radiatively active trace ingredients of the middle atmosphere exhibit large variations in space and time, and these variations can strongly affect the performance of systems operating in the UV, visible, and IR portions of the spectrum. The effects are most significant for limb viewing systems, and more generally, for all systems that obtain wide area coverage by allowing for operation at large off-nadir angles.

Even fine grained climatologies include only smoothed versions of the types of variability discussed here, and some include no variations with longitude at all. Therefore it would be

prudent, when designing systems for surveillance and warning, reconnaisance, tactical remote sensing, target-homing, and free-space laser communication systems, to use realistic examples of atmospheric variability along with the climatologies presently used. The same is true for simulations used for training, and for war gaming.

POAM measurements of the distribution of a radiatively active gas, such as ozone or water vapor, can be used to predict the effects of the gas at any wavelength. For aerosols and clouds, whose size distributions are incompletely sampled by the POAM wavelength set, the POAM data still provide partial information on the effects of these atmospheric ingredients at other wavelengths. Thus data from the POAM database can be used as a source of realistic atmospheric variations.

POAM data can also be used to refine the existing climatologies, and can contribute to the eventual development of covariance matrix climatologies, which would capture some of the space and time correlations exhibited by atmospheric fluctuations, and would also be of great value in calculating atmospheric parameters from remote sensing data.

An database of calculated effects on the performance of particular optical systems, together with either climatologies or current observations of the distributions of important trace species, could lead to increasingly adaptive tactical decision aids.

The distribution of ozone, aerosols, and high clouds is also important for weather forecasting.

For this reason, and also because the distributions of the radiatively important trace ingredients of the middle atmosphere are important for long range weather forecasting, the distributions should be monitored operationally, with good vertical resolution, and on a grid fine enough to capture their important geographic and time variations.

Acknowledgements

Fabrication of the POAM II and initial algorithm development was sponsored by BMDO. Fabrication of POAM II was sponsored by ONR. Spacecraft integration and initial data downlinks for both instruments were sponsored by the DoD Space Test Program.

REFERENCE

Bevilacqua, R.M., C.P. Aellig, D.J. Debrestian, M.D. Fromm, K.W. Hoppel, J.D. Lumpe, E.P. Shettle, J.S. Hornstein, and C.E. Randall, "POAM II Observations in the Antarctic Ozone Hole in 1994, 1995, and 1996", *J. Geophys. Res.*, 102, 23643-23657, 1997, and references cited therein.

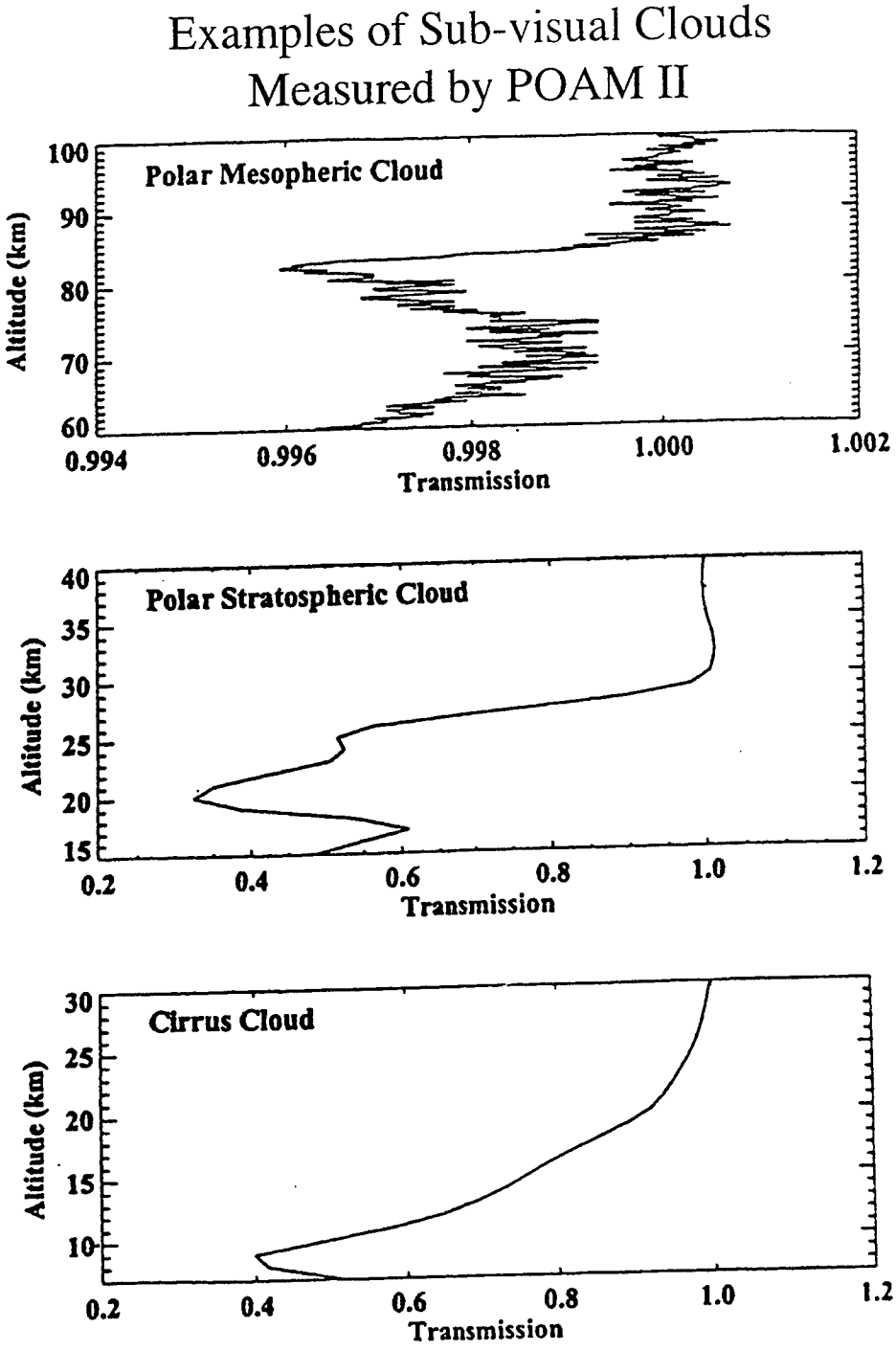


Figure 1. Examples of the three types of sub-visual clouds observed by POAM.

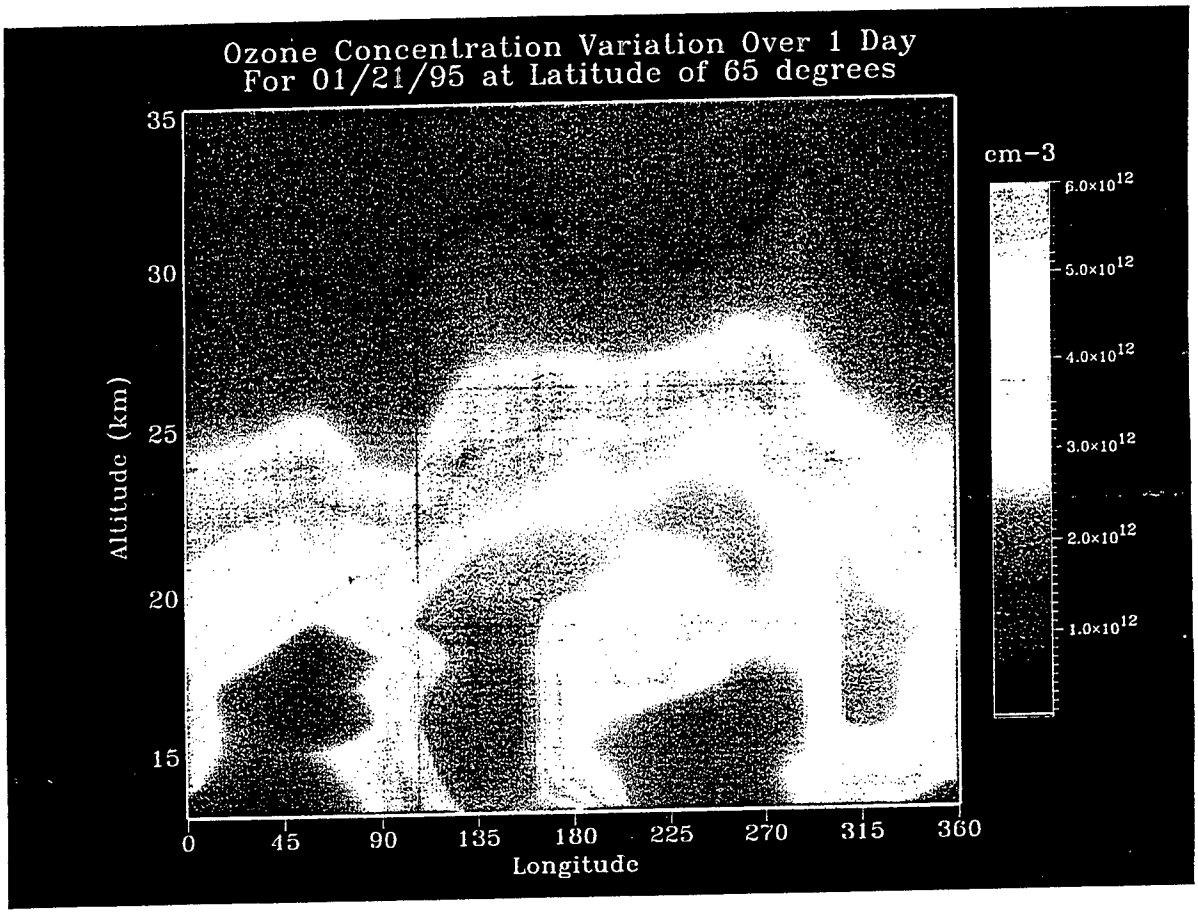


Figure 2. An illustration of the variability of ozone with location and altitude.

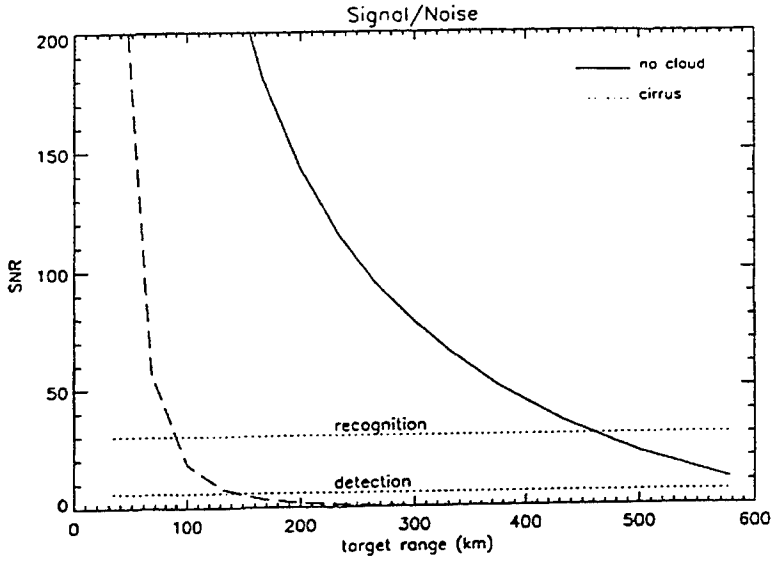


Figure 3. Effect of a subvisual cirrus on detection and tracking by a notional MWIR sensor, in an air-to-air scenario.

PHYSICAL CHARACTERIZATION OF CLOUDS AND PRECIPITATION USING 94 GHz AND 13.8 GHz RADAR BACIMO 98

Arlie C. Huffman III, Thomas H. Vonder Haar* , and Graeme L. Stephens

Cooperative Institute for Research in the Atmosphere
Colorado State University
Fort Collins, CO 80523-1375
Phone: (970) 491-7484
Fax: (970) 491-8241
E-mail: arlie @ atmos.colostate.edu

ABSTRACT

Two military environmental shortfalls are cloud vertical profiles (bases and thickness) and precipitation rates. Satellite based 94 GHz (0.32 cm wavelength) and 13.8 GHz (2.17 cm wavelength) radars can be used to profile cloud systems, as well as to characterize precipitation events. The Tropical Rainfall Measurement Mission (TRMM) is currently using a 13.8 GHz radar with great success. Experiments with a 94 GHz radar such as were performed during the Cloud Layer Experiment (CLEX) in 1996 have shown that this frequency is especially useful to parameterize thin clouds like cirrus and marine stratocumulus. Radar reflectivity is calculated as a function of cloud liquid and ice water content and effective radius of the cloud particles. In order to make a meaningful comparison between the calculated and measured reflectivities, some a priori knowledge of the cloud type is required, which limits the possible range of cloud physical parameters.

Rainfall measurements present a challenge to the 94 GHz system because of the large amount of attenuation. However, model results show that, given typical drop size distributions, over 75% of tropical stratiform rainfall events can be directly measured. Heavier rain such as from convection attenuates most of the 94 GHz signal within a few kilometers, but at 13.8 GHz, the attenuation losses are minimal. By comparing the reflectivity and attenuation of these two wavelengths in a variety of rainfall regimes, the characteristic parameters of precipitation events can be derived. This paper will present analysis of these radar data. Analysis of this type can be used by military planners in conjunction with TRMM and future data to better estimate global cloud precipitation distributions.

This work is sponsored by DoD, the U.S. Army Research office, under the Center for Geosciences Phase II grant DAAH04-94-G-0420.

1. OBJECTIVE

A satellite-based 94 GHz (W band) radar system has been proposed for cloud imaging and may become operational early in the next century. One of the major questions remaining, however, is the utility of this wavelength for detecting precipitation. Electromagnetic energy at this frequency is highly attenuated by liquid hydrometeors at the sizes encountered during rain events, especially in convective systems, where the average raindrop diameter approaches the

radar wavelength (3.2 mm). Presently, the NASA/TRMM (Tropical Rainfall Measuring Mission) Precipitation Radar operates at a frequency of 13.8 GHz and is providing high-quality images of precipitating clouds. The lower frequency (longer wavelength) of this system attenuates less in rain events. In this study the attenuation and reflectivities at 94 and 13.8 GHz are calculated using simple one-dimensional models appropriate to tropical precipitation systems.

2. RESEARCH ACCOMPLISHED

a. Use of MCTEX data

During the Maritime Continent Thunderstorm Experiment (MCTEX) in late 1995, a dual-polarized C band radar and a dual-wavelength, dual-polarized W and Ka band (35 GHz) radar were operating in the tropics north of Darwin, Australia. Keenan et al. (1994) provides an overview of the MCTEX project and dataset. The main purpose of this experiment was to study the large convective cells that erupted each afternoon, producing very heavy rainfall and frequent lightning. One of the best cases during MCTEX occurred on 28 November.

We study two separate times for this case. The first occurs during convective rainfall, with rain rates ranging from 25 to 100 mm hr^{-1}. Just over two hours later, as the convection dissipated, the rain regime was stratiform in character. Rain rates at this time varied between 1 and 10 mm hr^{-1}. Since these two rainfall types are associated with different drop size distributions (Tokay and Short, 1996), the effect of the drop size distributions on attenuation at these two frequencies can be investigated.

b. Definition of microphysics

Profiles of hydrometeor types and distributions were constructed using the C band radar derived microphysics. We used the relation Z vs. Z_{dr} to estimate number density according to plots from Illingworth et al. (1987). The University of Massachusetts W and Ka band radar data along with data from the Bureau of Meteorology Research Centre's CPOL radar, the bulk microphysical modeling results from Petersen (1996), in-situ Videosonde data as described in Takahashi (1990), in-situ airborne measurements from CEPEX (McFarquhar and Heymsfield 1997), and historical data of Heymsfield and Platt (1984) all serve as a guide for the model input parameters. One column was constructed for stratiform rain (Figure 1) and one for convective rain (Figure 2). The stratiform case contains raindrops, frozen raindrops, ice crystals (plates), and aggregates (snow). The strong updrafts in the convective case allow for liquid and frozen drops at higher altitudes, as well as graupel particles and a distinct melting layer. Temperature and humidity soundings taken close to the time of convection provide additional guidance about the melting layer when constructing the hydrometeor columns.

c. Model development

We model the attenuation as seen by space based 13.8 and 94 GHz radars in tropical rainfall for our two hydrometeor columns. The scattering coefficients of each type and size of hydrometeor is calculated using transition Matrix theory (T-Matrix) of Barber and Yeh (1975), e.g. Bringi et al. (1991). Dielectric properties of ice and water are taken from Ray (1972), and the shape parameter for water defined in Chuang and Beard (1990) is used. The attenuation and reflectivity are then calculated using the Mueller-matrix method of Vivekanandan et al. (1991).

d. Modeled precipitation regimes

Table 1 shows the modeled attenuation over the atmospheric column for five of the seven rain rates, at both frequencies. At high levels where only ice crystals and aggregates are present, the attenuation is always about 0.5 dB km^{-1} for the 94 GHz signal. The addition of frozen drops from 8 km to 4 km raises the attenuation significantly, as does the melting layer near the 5 km level. Note that between 4 and 7 km, all modeled hydrometeor types are represented (see Figure 2). The stratiform rain rates have a maximum attenuation of about 0.5 dB km^{-1} for 94 GHz, at a rate of 10 mm hr^{-1} within the 4 to 7 km range. A rain rate of 1 mm hr^{-1} only attenuates at a rate equal to that of the ice crystals and aggregates in the cloud.

Table 1. Attenuation (dB/km) vs. height for five of the modeled rain rates

Height AGL (km)	Frequency (GHz)	1.0 mm hr^{-1} (dB/km)	5.0 mm hr^{-1} (dB/km)	10.0 mm hr^{-1} (dB/km)	25 mm hr^{-1} (dB/km)	100 mm hr^{-1} (dB/km)
0.0	13.8	1.3×10^{-4}	1.7×10^{-3}	5.2×10^{-3}	1.6×10^{-2}	1.2×10^{-1}
	94	1.2×10^{-1}	1.2	3.0	6.9	25.1
5.0	13.8	5.2×10^{-3}	5.6×10^{-3}	6.5×10^{-3}	4.1×10^{-2}	1.7×10^{-1}
	94	3.6	4.0	4.6	21.6	42.9
10.0	13.8	5.5×10^{-4}	5.5×10^{-4}	5.5×10^{-4}	1.1×10^{-2}	1.1×10^{-2}
	94	5.5×10^{-1}	5.6×10^{-1}	5.6×10^{-1}	7.8	7.8
15.0	13.8				5.1×10^{-3}	5.1×10^{-3}
	94				3.0	3.0

e. Rain rate calculations

Assuming a dynamic range for a space-based radar of 70 dB and a minimum detectable signal of -30 dB at the orbit height of 500 km, the effective range for our reflectivity measurements would be from 40 to -30 dB. Using the calculated one way attenuation over our model vertical profiles, a simple integration of the attenuation was used to calculate the attenuated reflectivity. The results of the precipitation modeling are shown in Figures 3 and 4 for 13.8 and 94 GHz signals respectively. The level at which the propagating radar signal is attenuated to below -30 dB is shown in Table 2 for three different convective rain rates, and Table 3 for four stratiform rain rates. As the figure and tables show, the 13.8 GHz radar signal is never fully attenuated at any of the modeled rain rates. In fact, the effects of attenuation on this frequency are minimal, even at the highest rain rates. However, the 94 GHz radar signal becomes fully attenuated right above ground level at the 5mm hr^{-1} rain rate. The attenuation is so great in the convective cases at this frequency that the signal is fully attenuated while still in the cloud.

Table 2. Height above ground level of signal attenuation to below -30 dB in convective rain

RR (mm hr^{-1})	13.8 GHz	94 GHz
25	0.00 (km)	7.42 (km)
50	0.00	7.89
100	0.00	8.03

Table 3. Height (above ground level) of signal attenuation to below -30 dB in stratiform rain

RR (mm hr^{-1})	13.8 GHz	94 GHz
1.0	0.00 (km)	0.00 (km)
2.5	0.00	0.00
5.0	0.00	0.42
10.0	0.00	2.44

At any frequency, if there are gates below the freezing level that are not completely attenuated some assessment of rain rate can be made. This can be accomplished by removing the attenuation due to ice hydrometeors, then using a reflectivity/rain rate relation on data from those gates that are not attenuated to below –30 dBZ. This particular calculation was not attempted in this study, however.

f. Histograms of attenuation data

When histograms of the Keenan et al. (1998) data are plotted, it becomes apparent that the vast majority of rainfall events in these MCTEX cases produce very small values of attenuation, even at 94 GHz. Figure 5 shows a PDF of rain rate versus attenuation for all three frequencies. As is apparent, the 13.8 GHz radar signal has essentially a maximum two-way attenuation of 10 dB for the heaviest rainfall, with no significant attenuation due to atmospheric water vapor or oxygen. Choosing a 40 dB two-way attenuation, the 94 GHz system will measure approximately 80 percent of the precipitation events. As a result of this high success rate, the space-based 94 GHz radar will be able to make meaningful measurements of most of the rainfall events it images.

The simplification of the ice distributions in this study introduces errors into the calculated attenuations and reflectivities. These errors are small in comparison to the attenuation and reflectivity due to the raindrops for all but the smallest rain rates. The inclusion of a melting layer (radar bright band) makes a significant impact. At the melting layer, the melting ice hydrometeors are producing similar reflectivities to the liquid hydrometeors, resulting in an apparent increase in the concentration of liquid particles. In contrast, warm rain processes dominate in the tropics outside of the strongest convective cores and evaporation is less of an issue. An issue that also should be addressed is the use of scattering theory for axisymmetric particles in the T-matrix code. This theory is complete for our purpose, but simplification to the symmetric view as seen by a nadir viewing space based radar would give similar results.

3. CONCLUSIONS AND RECOMMENDATIONS

This study has shown that effective rain rate measurements from satellite based 13.8 and 94 GHz radars can be made under a variety of conditions with certain stipulations. The sensitivity of the rain rate reflectivity relationship is such that only rain rates below 50 mm hr^{-1} can be assessed. Attenuation below this rain rate is not significant for the 13.8 GHz frequency, but is a significant factor for 94 GHz measurements. Using our model parameters, the 94 GHz frequency signal will fully penetrate 5 mm hr^{-1} rainfall, and come to within 2 km of the ground in a 10 mm hr^{-1} rainrate. When these limits are compared to actual rain rate data from MCTEX, it is found that the 94 GHz system will be able to detect nearly 80 percent of the precipitation events. Finally, even if the signal near the ground is fully attenuated, an estimate of rain rate can be made if there are gates that are not completely attenuated below the freezing level.

References

Barber, P. and C. Yeh, 1975: Scattering of electromagnetic waves by arbitrarily shaped dielectric bodies. *Applied Opt.*, **14**, 2864-2872.

Bringi, V.N., V. Chandrasekar, P. Meischner, J. Hubbert and Y. Golestani, 1991: Polarimetric radar signatures of precipitation at S- and C-bands. *IEEE Proceedings-F*, **38**,109-119.

Chuang, C. and K.V. Beard, 1990: A numerical model for the equilibrium shape of electrified raindrops. *J. Atmos. Sci.*,**47**, 1374-1389.

Heymsfield, and C.M.R. Platt, 1984: A parameterization of the particle size spectrum of ice clouds in terms of ambient temperature and the ice water content. *J. Atmos. Sci.*, **41**, 846-855.

Illingworth, A.J., Goddard, J.W. and S.M. Cherry, 1987: Polarization radar studies of precipitation development in convective storms. *Q. J. R. Meteorol. Soc.*, **113**, 469-489.

Keenan, T., G. Holland, S. Rutledge, J. Simpson, J. McBride, J. Wilson, M. Moncrieff, R. Carbone, W. Frank, b. Sanderson and J. Hallet, 1994: Science plan - Maritime Continent Thunderstorm Experiment, *BMRC Research Report*, **44**, 61pp.

McFarquhar, G.M. and A.J. Heymsfield, 1997: Parameterization of tropical cirrus ice crystal size distributions and implications for radiative transfer: Results from CEPEX. *J. Atmos. Sci.*, **54**, 2187-2200.

Petersen, W.A., 1997: *Multi-Scale Process Studies in the Tropics: Results from Lightning Observations*. Ph.D. Dissertation, Dept. Atmospheric Science, Colorado State University, Fort Collins, Colorado.

Ray, P.S., 1972: Broadband complex refractive indices of ice and water. *Appl. Opt.*, **11**, 1836-1844.

Takahashi, T., 1990: Near Absence of Lightning in Torrential Rainfall Producing Micronesian Thunderstorms. *Geophysical Research Letters*, **17**, 2381-2384.

Tokay, A. and D. A. Short, 1996: Evidence from tropical raindrop spectra of the origin of rain from stratiform versus convective clouds. *J. Appl. Meteor.*, **35**, 355-371.

Vivekanandan, J., W. M. Adams and V.N. Bringi, 1991: Rigorous approach to polarimetric Radar Modeling of hydrometeor Orientation Distributions. *J. Appl. Meteor.*, **30**, 1053-1063.

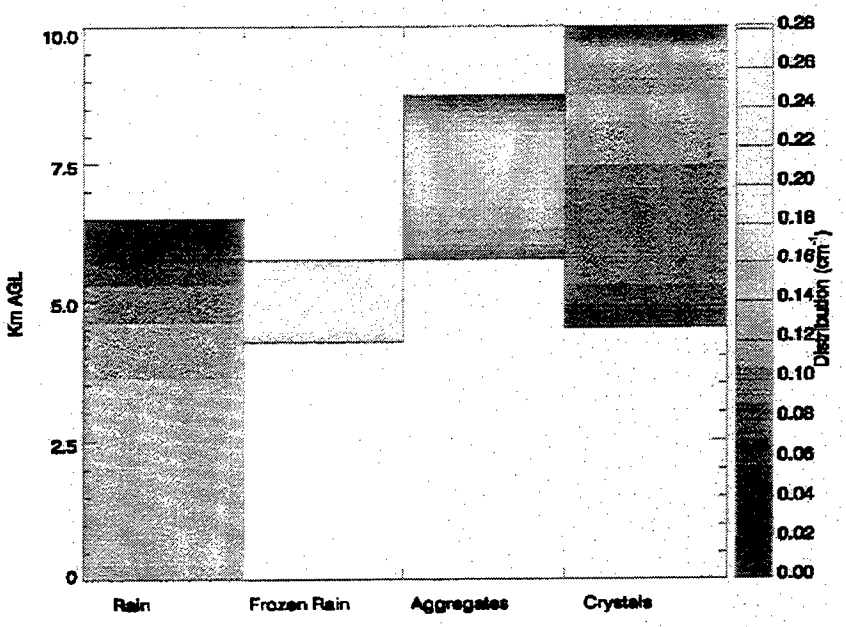


Figure 1. Column representation of the modeled hydrometeors for the stratiform regime.

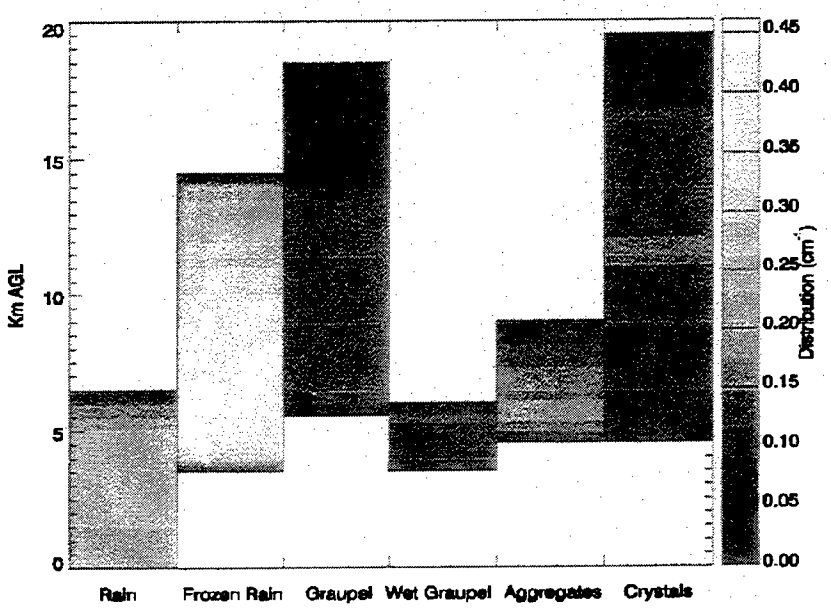


Figure 2. As in Figure 1, but for the convective regime.

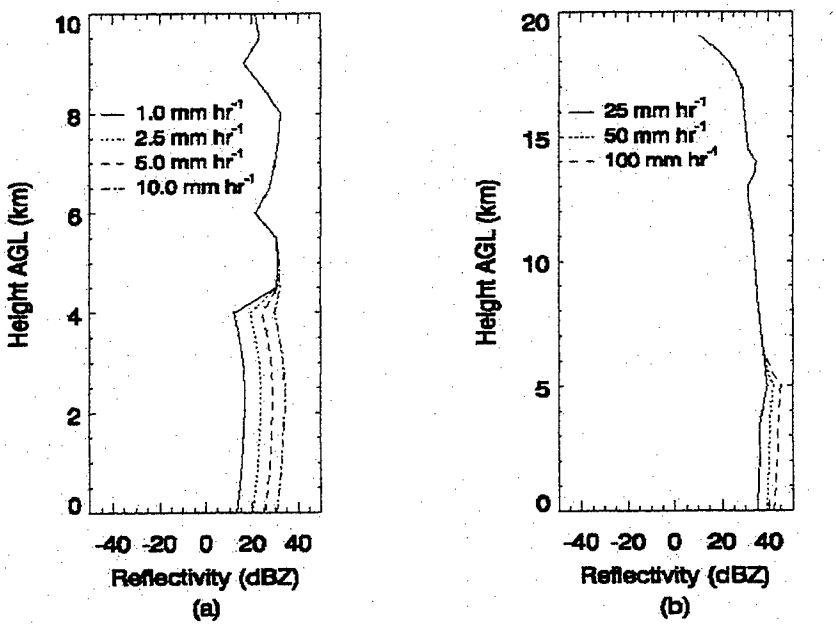


Figure 3. Model results at 13.8 GHz for the seven rain rates showing changes in reflectivity with height. (a) Shows stratiform rain, (b) shows convective rain.

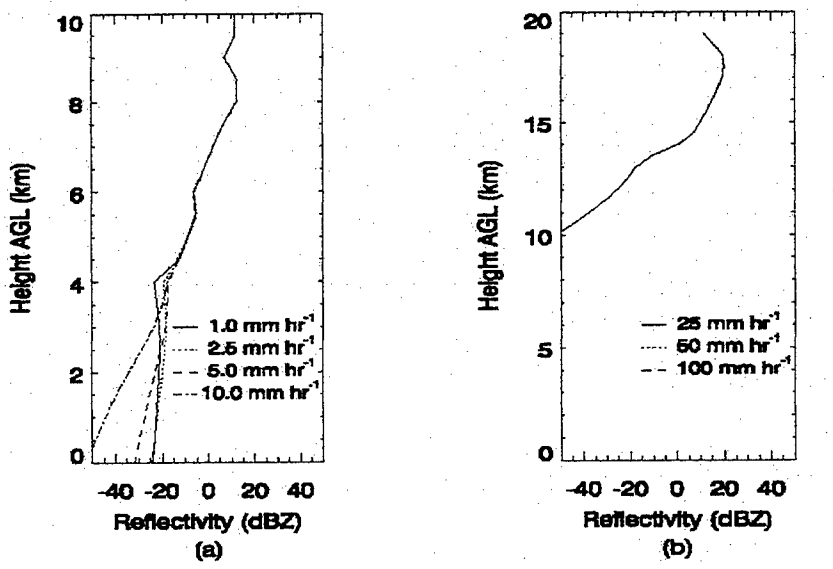


Figure 4. As in Figure 3, but for 94 GHz.

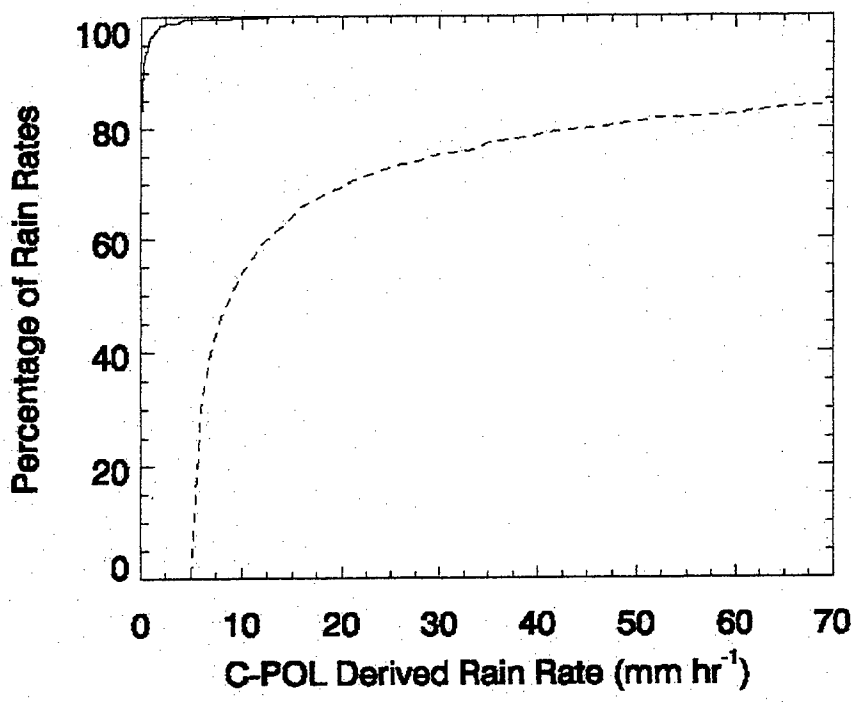


Figure 5. PDF of rain rates vs. attenuation from rain only. The 13.8 curve is solid, and the 94 GHz is a long dash.

RADAR AND RADIOMETER MEASUREMENTS OF THE PHYSICAL PARAMETERS OF CLOUDS AND PRECIPITATION AT THE NOAA ENVIRONMENTAL TECHNOLOGY LABORATORY

R.A. Kropfli[1]*, B.E. Martner[1], S.Y. Matrosov[2], R.F. Reinking[1], A.S. Frisch[3], and T. Uttal[1]

1. NOAA Environmental Technology Laboratory, R/E/ET6, 325 Broadway, Boulder, CO 80303
2. Cooperative Institute for Research in Environmental Sciences at the University of Colorado and NOAA/ETL
3. Cooperative Institute for Research in the Atmosphere at Colorado State University and NOAA/ETL

* Phone: 303-497-6235, FAX: 303-497-6181, e-mail: rkropfli@etl.noaa.gov

1. Introduction

Recent advances in millimeter-wave radar technology, coincident with new requirements to observe clouds, have stimulated interest in mm-wave radar. Weather modification activities, general cloud physics investigations, research on icing hazards, and studies of cloud-radiation interactions affecting climate have all created a need for better ways to observe clouds than those available to most researchers in the past. The sensitivity to small hydrometeors, excellent spatial resolution, minimal susceptibility to ground clutter, and easy transportability of mm-wave radars make them ideal tools for these research areas. They can operate from mobile ground-based, airborne, and space-based platforms as well as from ships (Kropfli and Kelly, 1996). In atmospheric science, mm-wave radars have become known as "cloud" radars. A recent extension of this technology to unattended cloud monitoring is described by Moran et al. (1998), and in this conference by Post et al. (1998). When used in combination with infrared and microwave radiometers, cloud radars can provide extensive information about the microphysical structure of clouds overhead which goes far beyond mere monitoring of cloud heights. These techniques are briefly reviewed in this article.

Attenuation by liquid water prevents mm-wave radars from being used in moderate to heavy rainfall. They are most effectively used for observations of non-precipitating clouds or clouds with snowfall or light rain, and over shorter pathlengths than is possible with longer wavelength microwave radars. Although ice particles generally cause low attenuation at these wavelengths, non-Rayleigh scattering can cause signal reduction. However, if two wavelengths are used, i.e., one microwave (e.g. X-band) and one millimeter-wave (e.g. Ka-band), the signal reduction due to non-Rayleigh scattering at the shorter wavelength may be useful in quantitative snowfall estimation (Matrosov, 1992), ice crystal sizing in cirrus clouds (Matrosov, 1993), and in measuring cloud liquid water content (Martner et al., 1993).

The mm-wave radar's relative immunity to ground clutter allows for close-range observations, well within the minimum ranges possible at longer wavelengths. Thus, very low reflectivities, e.g., - 50 dBZ at 1 km range, can be measured with mm-wave radars. At the same range, mm-wave radars generally have finer spatial resolution (by an order of magnitude) than microwave radars with longer transmitted pulses and broader beam widths. These characteristics make them especially useful in observing low-level marine and continental stratus clouds, fog, cirrus clouds, orographic wave and

cap clouds, and early stages of convective clouds. They can also be useful in high-resolution studies of the cloudless convective boundary layer using naturally occurring particulate tracers of air motion as has been shown for microwave radars (Kropfli, 1986).

2. Active and Passive Remote Sensing Instrumentation

ETL's NOAA/K 35-GHz (Ka-band, 8.7-mm wavelength) cloud-sensing radar is a scanning Doppler system developed primarily for observations of non-precipitating and weakly precipitating clouds. By virtue of its short wavelength, it has excellent sensitivity to very small hydrometeors and is remarkably insensitive to ground clutter (Kropfli and Kelly, 1996). The radar has been used extensively for research of the radiative effects of clouds for climate change programs and for observations of winter storms. Rotating quarter-wave and half-wave plates allow transmission of a continuous sequence of polarizations from circular to elliptical to linear. The radar's ability to vary the polarization of the transmitted signal, along with its dual receivers and scanning capabilities provide a powerful combination for determining cloud hydrometeor shapes and types. The radar transmits 85-kW of peak power in a 0.5-degree conical beam width using a 1.2-m parabolic antenna with an offset Cassegrain feed. Radial velocity, reflectivity, and depolarization ratio are routinely measured with 37.5-m resolution using PPI and RHI or fixed beam scans. Sensitivity is about -30 dBZ at 10-km range. A new processor, soon to be installed will extend the radar's capabilities even further. The radar's antenna and mount are shown in Figure 1.

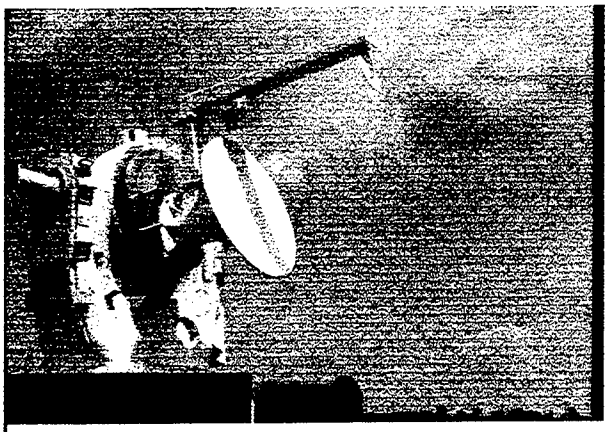


Figure 1. The NOAA/K 35-GHz Scanning Cloud

NOAA/ETL also operates several passive remote sensors for cloud studies. These provide path-integrated measurements. ETL's steerable microwave radiometer contains three independent radiometer channels: 20.6-GHz which is sensitive primarily to water vapor; 31.65-GHz which is sensitive primarily to cloud liquid water at any temperature; and 90.0-GHz which is sensitive to both vapor and liquid. However, the 90-GHz channel is approximately six times more sensitive to liquid water than is the 31.65 GHz channel; thus, the third frequency increases the sensitivity of the instrument to small amounts of cloud liquid. These radiometers are coupled into an antenna system that is slowly steerable in both azimuth and elevation. Therefore, the system may be used to study both spatial and temporal variability of liquid water in clouds and atmospheric water vapor. The antenna beamwidth is 2.5-degrees. Other versions of this instrument at ETL point vertically only. A commercially-available narrowband infrared radiometer operating at 10.6 microns also frequently accompanies the ETL radars and microwave radiometers in cloud observation experiments. It is useful for measuring cloud optical depth and, in the case of optically thick clouds, cloud base temperature.

3. Cloud Structure and Statistics with MM-Wave Radar

The excellent sensitivity and resolution of mm-wave radars allows clouds to be observed with remarkable detail. This includes very weak non-precipitating clouds and multiple cloud layer situations, which are difficult to observe with other methods. Knowledge of cloud layer heights and thicknesses (cloud macrostructure) is vitally important for atmospheric radiation studies and aviation operations. To obtain cloud climatology statistics, a mm-wave radar is usually operated with the antenna pointing vertically for long periods at a site. In this mode, detailed time-height cross sections of intricate cloud structure are readily obtained. Algorithms can be developed to give automated, objective determinations of the cloud layer echo heights and thicknesses for computing their long-term statistics (Uttal et al. 1993). One of the results of such preliminary studies is that, when clouds are present, it is more likely than not that there exists more than one cloud layer.

4. Ice Cloud Parameter Determination from Combined Radar/Radiometer Measurements

Microphysical cloud parameters such as particle characteristic size, concentration and cloud ice mass content are important to climate studies. Unfortunately, radar measurables alone cannot be unambiguously and accurately related to any of these cloud parameters. However, for ice clouds, such as cirrus, Matrosov et al. (1992, 1994) have shown that the combination of vertically-directed radar and radiometer data can be used to retrieve vertical profiles of all of the cloud parameters of interest. In this technique, IR radiometer measurements are used to estimate cloud optical thickness, which when properly combined with the radar's measurements of reflectivity and time-averaged vertical Doppler velocity, allow height-resolved estimates of the characteristic ice particle sizes and concentrations to be obtained with 37.5-m height resolution and 30-s temporal resolution. From these derived quantities, the cloud's ice mass content and ice mass flux can be calculated. Limited comparisons of the ice mass content, median volume diameter and total ice particle concentration parameters retrieved by the radar/radiometer technique with in-situ sampling by research aircraft lend considerable confidence to the usefulness of this remote sensing method (Matrosov et al. 1998). Unlike passive satellite techniques, high-resolution vertical profiles are obtained.

5. Identification of Hydrometeor Types and Shapes Using Radar Polarization

A method to identify different types of hydrometeors and to estimate their mean aspect ratios (shapes) based on radar polarization measurements has been developed (Matrosov et al., 1996). Knowledge of hydrometeor types and shapes is important for many meteorological applications including cloud-climate interactions, aircraft icing, water resources, and studies of winter storms. This approach was demonstrated with ETL's NOAA/K radar for identifying different ice hydrometers (Reinking et al. 1997), but it can also be used to distinguish between regions of ice crystals and water drops in clouds. This capability has particular relevance to the detection of icing hazards to aircraft and to cloud seeding operations.

The approach uses the radar's measurements of depolarization ratio (DR), which is defined as the logarithmic difference of radar echoes in the main and orthogonal receiving channels: This ratio depends primarily on the mean aspect ratio of hydrometeors in the polarization plane, the incident (transmitted) polarization state, and the particle orientations in this plane (for non-circular polarization). Elliptical polarization states which are nearly circular enhance the signal in the orthogonal channel, making depolarization measurements possible for very weak echoes.

Depolarization measurements taken at different elevation angles can be used to assess the mean hydrometeor aspect ratio (shape) in the radar polarization plane at any height. For horizontally homogeneous cloud layers, the predominant ice particle types (columnar, planar, aggregate) can be identified from elevation angle dependencies of DR. For planar crystals (e.g., dendrites, plates) there is a monotonic decrease of DR as the radar elevation increases. Columnar-type particles (e.g., columns, bullets, needles) exhibit either an opposite trend or no trend, depending on the transmitted polarization used. Aggregates show very low depolarization and a very weak elevation angle dependence. Cloud and drizzle drops show the lowest DRs and no elevation angle dependence.

6. Radar/Radiometer Studies of Liquid Water Stratus Clouds and Drizzle

Marine stratocumulus clouds are also a very important component of the climate system. Retrievals of cloud parameters for non-precipitating marine stratus clouds and drizzle were developed by Frisch et al. (1995a). Millimeter-wave radar is most suitable for this purpose because of the sensitivity, immunity from ground clutter, and fine spatial resolution. Vertical profiles of cloud droplet liquid water content, effective radius, and concentration can be retrieved from this technique using radar reflectivity and microwave radiometer for clouds which contain only small droplets. In essence, the microwave radiometer provides the path-integrated total amount of liquid and the radar reflectivity provides its vertical distribution. Based on the radar's reflectivity and vertical velocity data, the hydrometeors can be classified as cloud droplets, or as larger drizzle drops. In the case of drizzle, the radar measurements alone are sufficient for the microphysical retrievals.

7. Turbulence

The formation and evolution of the cloud-capped boundary layer is critically dependent on turbulent entrainment processes at cloud top. These processes can be characterized by vertical profiles of in-cloud turbulent vertical velocity variance and skewness. One of the objectives of ASTEX, conducted during June 1992 in the eastern Atlantic, was to obtain this information with Doppler radar and lidar. Frisch et al.,1995b described the use of the NOAA/K radar with the antenna pointed vertically to measure the vertical velocity turbulent structure of the boundary layer clouds. Turbulence calculations were restricted to low-reflectivity portions of clouds where particle fallspeeds make negligible contributions to the measured vertical Doppler velocities. The traditional velocity-azimuth-display (VAD) technique which uses fixed-elevation, conical scanning can also be employed in the clear convective boundary layer and in widespread clouds to observe vertical profiles of turbulent momentum flux and turbulent kinetic energy (Kropfli, 1986; Frisch et al., 1989).

8. Mapping Cloud Liquid Water Content with Differential Attenuation

Although mm-wave radars can provide useful data in heavy snowfall, the very high attenuation coefficient of liquid water at these frequencies prevents their use in moderate or heavier rainfall. For at least one application, however, this "limitation" can be used to advantage. A proposed dual-wavelength differential attenuation radar technique for measuring and mapping the liquid water

content in clouds, uses K_a-band in concert with a longer wavelength, such as X-band (Westwater and Kropfli, 1989; Gossett and Suavegeot,1992). The moderately-attenuated K_a-band reflectivity signals returned from clouds are reduced in comparison to the slightly-attenuated X-band signals by small but measurable amounts which depend on the liquid water content present. For Rayleigh scattering conditions, the range derivative of the X-K_a reflectivity difference along the beam is directly proportional to the liquid water content between the derivative end points. The technique does not require the radars to be calibrated. Initial field tests in Colorado reported by Martner et al. (1993a, 1993b) showed some promising results, but also uncovered several practical difficulties, including the need for closely matched beam sample volumes and frequent violation of the method's Rayleigh assumption where large snowflakes coexist with the cloud droplets. The technique, which could be used from the ground or onboard airplanes, has potential applications for avoiding aircraft icing or for identifying cloud seeding target locations in clouds.

9. Summary

Numerous techniques involving millimeter-wave radar and radiometers provide ground-based remote sensing means for observing both the macrophysical and microphysical features of ice and liquid water clouds and some kinds of precipitation. NOAA/ETL has been at the forefront of this research. The techniques in use at ETL are listed in Table 1, which also shows the required measurements, degree of difficulty, limitations, estimates of achievable accuracy, and representative open-literature references for each method.

10. Acknowledgments

Radar and radiometer-based cloud research and technique development work at NOAA/ETL has been supported by several agencies including the NOAA Office of Global Programs, NASA's FIRE, CERES and TRMM programs, the U.S. Department of Energy's Atmospheric Radiation Measurement program, NSF's Surface Heat Budget of the Arctic Ocean experiment, and the Federal Aviation Administration's Aviation Weather Research Program.

Table 1. Radar/Radiometer Techniques at NOAA/ETL for Measuring Physical Properties of Clouds and Precipitation

PROPERTIES	METHOD	MEASUREMENTS	DIFFICULTY	ACCURACY	LIMITATIONS	REFERENCES
Total water vapor along path	Passive	Microwave radiometer	low	very good (±10%)	not usable with rain along beam	Hogg et al. (1983), Martner et al. (1993)
Total cloud liquid along path	Passive	Microwave radiometer	low	very good (±10%)	not usable with rain along beam	Hogg et al. (1983), Martner et al. (1993c)
Cloud layer heights and thickness	Reflectivity profiling	Ka-band radar	low	about ±50m	base obscured by virga; attenuation by rainfall	Uttal et al.(1995)
Horizontal homogeneity	RHI scanning of reflectivity	Scanning cloud radar	low	qualitative from scan images	attenuated by rainfall	
Ice mass content	Radar retrieval	Radar reflectivity	low	poor (±100%)	function of cloud type; attenuation by rainfall	Brown et al.(1995), Sassen and Liao(1966)
Ice mass content	Radar/ radiometer	Ka-band reflectivity, IR radiometer, (+MW radiometer)	moderate	good (±50%)	no liquid water can be present	Matrosov(1997), Matrosov(1998)
Ice mass content	Radar/ radiometer	Ka-band radar reflectivity, IR radiometer, (+MW radiometer)	moderate	good (±50%)	no liquid water	
Ice particle size and concentration	Radar/ radiometer	Ka-band radar reflectivity, IR radiometer, (+MW radiometer)	moderate	size: ±30% concentration: ±100%	no liquid water	Matrosov (1997), Matrosov et al. (1998)
Ice particle shape/type (plates, columns, etc.)	Radar depolarization	Ka-band radar	moderate	confident signatures several particle types	sample must be dominated by one type	Matrosov(1996), Reinking et al. (1997)
Cloud water content-profiles	Radar/ radiometer	Ka-band radar + microwave radiometer	moderate	good (estimate ±50%)	marine stratus only	Frisch et al., (1995a)
Cloud water content-mapping	Dual-λ reflectivity	Ka-band and X-band radar	moderate	good (±50%)	no large ice crystals, matched beams	Martner et al. (1993)
Cloud droplet size	Radar/ radiometer	Ka-band radar + microwave radiometer	moderate	good (estimate ±50%)	marine stratus only	Frisch et al., (1995a)
Cloud droplet concentration	Radar/ radiometer	Ka-band radar + microwave radiometer	moderate	fair (estimate ±100%)	marine stratus only	Frisch et al., (1995a)
Drizzle liquid water content	Radar retrieval	Ka-band radar first 3 Doppler moments	moderate	untested	marine stratus only	Frisch et al., (1995a)
Turbulence	VAD scanning	X-band or Ka-band Doppler radar	moderate	untested (u'w',v'w',	requires particulates for air	Kropfli (1986),

				w'w', etc. available)	motion tracers	Frisch et al. (1992)
Turbulence	Vertical Doppler	X-band or Ka-band Doppler radar	moderate	very good (w'^2) good (w'^3)	requires particulates for air motion tracers	Frisch et al.,(1995b), Martner et al (1995)
Snowfall Rates	Radar reflectivity	X-band or Ka-band radar	low	poor (±200%)	large uncertainties in empirical Z/S relationship	Matrosov (1992)
Snowfall Rates	Dual λ reflectivities	X-band and K_a-band radar	moderate	good (±70%)	requires information about snow density	Matrosov (1999)
Melting layer	Reflectivity or polarization	X-band or Ka-band radar	low	very good (±50m for height)		Martner (1991)
Rainfall rate	Radar reflectivity	X-band radar	low	fair (±100%)	degraded by many common problems	Battan (1973)
Rainfall rate	Differential prop. phase	X-band radar	moderate	good (±30%)	not good in heavy rainfall, best at low elevation	Matrosov et al. (1999)
Rainfall liquid water content	Reflectivity	X-band radar	low	fair (±100%)	uncertainties in rainfall/reflectivity	
Rainfall liquid water content	Differential prop. phase	X-band radar	moderate	good (±30%)	won't work in heavy rainfall (>20mm/hr)	
Rainfall sizes and shapes	ZDR + Kdp	X-band radar	moderate	good (±30%)	won't work in heavy rainfall (>20mm/hr)	Matrosov et al. (1998)

11. References

Battan, L.J., 1973, *Radar Observation of the Atmosphere*, Univ. Chicago Press, 324 pp.
Brown et al., 1995, *J. Applied Meteorology*, **34**, 2346-2366.
Browning and Wexler, 1968, *J. Applied Meteorology*, **7**, 105-113.
Frisch et al. 1989, *Boundary Layer Meteorology.*, **49**, *331-337.*
Frisch et al., 1990: *AMS Preprints, 9th Symposium on Turbulence and Diffusion*, Denmark, 82-85.
Frisch et al., 1992, *Monthly Weather Review*, **120**, 3-16.
Frisch et al., 1995a, *J. Atmospheric Science*, **52**, 2788-2799.
Frisch et al., 1995b: *J. Atmospheric Science*, **52**, 2800-2808.
Gossett and Sauvageot, 1992, *J. Atmos. and Ocean. Tech.*, **9**, 538-547.
Hill, G.E., 1992, *J. Applied Meteorology*, **31**, 397-401.
Hogg et al., 1983, *J. Climate and Applied Meteorology*, **22**, 789-806.
Kropfli, R.A., 1986, *J. Atmospheric and Oceanic Technology*, **3**, 305-314.
Kropfli and Kelly, 1996, *Meteor. and Atmos. Physics*, **59**, 105-121.
Martner, B.E., 1991, AMS *Preprints, 25th Conference on Radar Meteorology*, 813-816.
Martner, B.E., 1993a, *NOAA Tech. Memo., ERL WPL-235, Boulder, CO,* 47 pp.
Martner, B.E., 1993b, *AMS Preprints, 26th Intl. Conf. on Radar Meteor.*, Norman, OK, 596-598.
Martner et al., 1993c, *Bulletin of the American Meteorological Society*, **74**, 599-613.
Martner et al., 1995, AMS *Preprints, 27th Conference on Radar Meteorology,* Vail, CO, 485-487.
Matrosov, S.Y., 1992, *IEEE Transactions on Geoscience and Remote Sensing*, **30**, 454-461.
Matrosov, S.Y., 1997, *J. Applied Meteorology*, **36**, 633-648.
Matrosov, S.Y, 1999, *J. Applied Meteorology*, **38**, (in press).
Matrosov et al., 1992, *J. Geophysical Research,* **97**, 1567-1574.
Matrosov et al., 1994, *J. Appl. Meteor.*, **33**, 617-626.
Matrosov et al, 1996, *J. Atmospheric and Oceanic Technology*, **13**, 85-96.
Matrosov et al., 1998, *J. Atmospheric and Oceanic Technology*, **15**, 184-196.
Matrosov et al., 1999, *J. Applied Meteorology*, **38** (in press).
Moran et al., 1998, *Bulletin of the American Meteorological Soc.*, **79**, 443-455.
Post et al., 1998, *Proc. of BACIMO-98, Hanscom AFB, MA,* (in this volume).
Reinking et al., 1997, *J. Applied Meteorology*, **36**, 322-339.
Sassen and Liao, 1996, *J. Applied Meteorology*, **35**, 932-938.
Snider et al., 1980, *Radio Science*, **15**, 682-693.
Uttal et al., 1993: *NOAA Tech. Memo., ERL WPL-233, Boulder, CO,* 28 pp.
Uttal et al., 1995, *Journal of Atmospheric Science*, **52**, 4276-4284.
Westwater and Kropfli, 1989, *NOAA Tech. Memo., ERL WPL-215*, Boulder, CO, 28 pp.

Unattended 35-GHz Cloud-Profiling Radar

Madison J. Post*, Kenneth P. Moran, Brooks E. Martner
NOAA Environmental Technology Laboratory
325 Broadway, Boulder, CO 80303
*Ph./Fax 303-497-6048/6574, mpost@etl.noaa.gov

and

Kevin B. Widener
DOE Pacific Northwest National Laboratory
P.O. Box 999, Richland, WA 99352
Ph./Fax 509-375-2487/4545, kb_widener@ccmail.pnl.gov

INTRODUCTION

At the Battlespace Atmospherics Conference in 1996 we reported on the design and initial deployment of a new unattended 35-GHz cloud-profiling Doppler radar [Post and Moran, 1996]. Since then five millimeter-wave cloud radars (MMCRs) have been built. Three have been used extensively in continental (north central Oklahoma) and polar climate regimes (north Alaska and on the polar icecap). Two more are being prepared for delivery to tropical Pacific islands (Nauru Island in November 1998, and Manus Island, Papua New Guinea in spring 1999). One of the MMCRs in the Arctic was operated on a ship frozen into the north polar icecap, for the year-long Surface Heat and Energy Budget of the Arctic (SHEBA) campaign, beginning September, 1997. NOAA will deploy that radar in its next mission aboard the research vessel *Ronald H. Brown* for a series of cruises spanning several months in the Indian and Pacific Oceans in 1999.

MMCRs are currently being used primarily for long-term climate research in diverse climatic regions world-wide as part of DOE's Atmospheric Radiation Measurement (ARM) program [Moran et al., 1998]. A companion paper in this conference [Kropfli et al., 1998] discusses new scientific applications of millimeter-wave radars, including retrievals of cloud microphysical properties (size distributions, ice and water loading, etc.). The MMCRs should also be of interest to DoD because of its small size, unattended and remote mode of operation, and its potential to aid air operation controllers and tactical planners. A functionally similar military radar, the AN/TPQ-11, was decommissioned in the early 1970s because of low reliability. It was significantly more expensive and less sensitive than this newer radar.

We report here on the performance of these "cloud" radars during their first two years of operation, give examples of data and derived products, and discuss impending improvements and commercialization.

PERFORMANCE

The K_a-band Doppler radars are designed to stare vertically and sequence through up to four customized modes of operation, to best measure the wide range of cloud and precipitation scenarios possible at a particular location. The modes typically require 10 s each to execute, so that the pattern repeats itself every 40 s or so. Table 1 lists radar parameters for the modes currently in use by the radar at Barrow, Alaska, together with calculated sensitivity. The radars achieve high sensitivity by using pulse compression, a large antenna (2-3 m diameter), and high average power (up to 25 w), despite low peak power (100 w peak for the Traveling Wave Tube Amplifier - TWTA). Nearly all visible clouds overhead are detected by the radars, even high, tenuous cirrus clouds. At this frequency cloud attenuation is by cloud liquid water is minimal, so multiple cloud layers are readily detected, unlike lidars. The radars are linearly polarized but do not currently detect cross-polarized returns.

Table 1
MMCR Operating Mode Parameters at Barrow, AK

Parameter	Mode 1	Mode 2	Mode 3	Mode 4
Range Res. (m)	45	90	90	45
Height Range (km)	0.1 - 9.8	0.1 - 14.3	0.1 - 14.2	0.1 - 10.0
Unambiguous Vel. Range (± m/s)	3.2	3.1	3.2	11.9
No. FFT Points	64	64	64	128
No. Spectral Avg.	50	23	70	20
No. Coherent Avg.	10	6	7	2
No. Coded Bits	8	32	0	0
Min. Sensitivity (dBZ) @ 5 km	-44	-52	-40	-32
Processor Efficiency	24%	11%	34%	5%

It is possible to record full Doppler spectra, but since the data rate is so high the radar is usually programmed to calculate and record only the first three spectral moments, which correspond with reflectivity, vertical velocity, and spread in vertical velocity.

Figure 1 shows 24-hr time-height cross-sections produced from these data. Such images are produced locally and remotely in near real-time (visit **http://www4.etl.noaa.gov/cloudrad.html** for up-to-date images from Oklahoma and Alaska). In Fig. 1 the melting layer bright-band is

readily seen at 2.5-km altitude in all three moments. Cloud layers and interspersed clear regions are readily discerned. Aircraft operations at airfield and in the battlespace could be greatly aided by simple cloud radar images such as these. For example, pilots can be confidently vectored to cloud-free altitudes to improve their flying visibility, or into the middle of cloud layers to provide protection against optically-guided munitions. Icing conditions can be avoided by choosing altitudes with no cloud echoes or below the melting layer bright band.

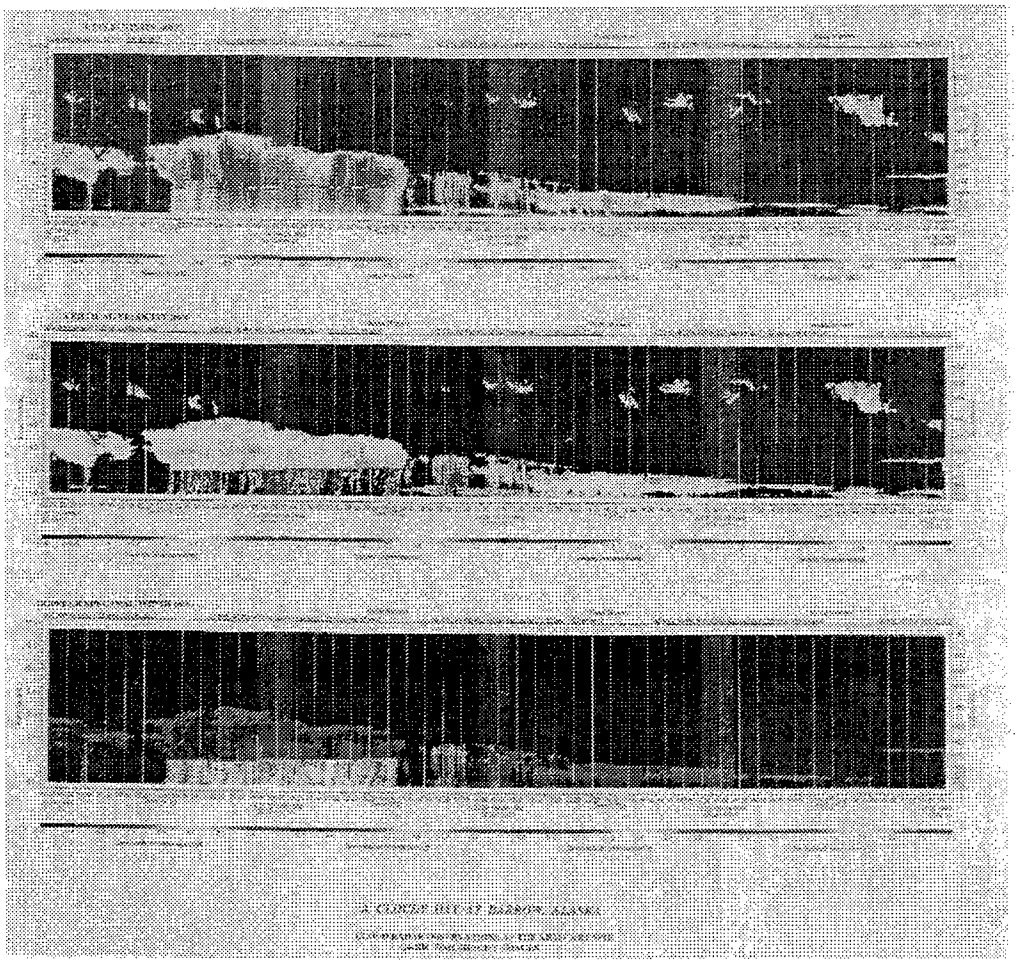


Fig. 1. Example of twenty-four hour time-height cross-sections of reflectivity (top), vertical velocity (middle), and velocity spectral width for the MMCR at Barrow, AK.

Table 2 lists the reliability statistics of the two DOE radars that have the longest hands-off operational history, and that are run 24 hours per day, 365 days per year. The Southern Great Plains (SGP) MMCR near Lamont, Oklahoma, has been operating since November, 1996, while the North Slope of Alaska (NSA) MMCR has been operating since March, 1998. Many of the operational "bugs" were installation-specific and have been fixed. We have therefore seen reliability increase significantly at both sites since initial installation. Power problems at SGP will probably persist, however; the UPS system cannot keep the radar up during extended power

outages, often caused by lightning. Still, the radar gracefully shuts down before loss of UPS power and automatically reboots when power is restored, negating the need for human intervention. Numerous over/under temperature shut-downs at NSA immediately after installation were caused by improper circulation of air in the radar building. Ductwork was improved and the radar has subsequently experienced nearly flawless operation.

Table 2
MMCR Reliability Statistics
(through 1 September 1998)

Parameter	Southern Great Plains	North Slope of Alaska
Total Hours in Operation	16,500	3,900
Total Hours Down Time	420	370
Overall Reliability	97.4 %	90.5%

PLANNED IMPROVEMENTS

While the radars have received wide acclaim from the climate community for their many new insights to regional and seasonal cloud features, two minor problems need attention. The binary-phase pulse coding used to increase sensitivity produces artifacts in the lower altitude data, and in regions of high reflectivity or velocity gradients. To reduce the artifacts requires higher processor efficiency, so that the number of phase bits used in a mode can be reduced without losing sensitivity. The processor efficiencies for the various modes in Table 1 can be increased to nearly 100% by using multiple processors in the radar's data acquisition and processing computer. DOE has funded NOAA's Environmental Technology Laboratory (ETL), the designer of the MMCR, to produce an improved radar processor using multiple digital signal processors (DSPs) to achieve much greater efficiency. Improved efficiency will also allow scientists to reduce time resolution of the radar to 1 s or less, for detailed process studies.

At the same time, ETL will add dual-polarization detection capability to the radars in an attempt to mitigate the second problem – the inability of the current radar to distinguish the returns of insects from the returns of clouds in the lower atmosphere. In temperate climates insects in the cloud-free boundary layer often have reflectivities similar to or greater than those of stratus clouds or fog. An example can be seen in Fig. 2 from SGP, where returns below 1 km in the first 2 hours appear as low clouds or fog, but actually are from insects. Since insects are highly depolarizing targets, we plan to measure co- and cross-polarized returns on alternate pulses. New software will separate and ratio the two polarization channels to indicate whether the returns are from insects or non-depolarizing spherical cloud droplets.

Both these prototype improvements will be developed and demonstrated by summer, 1999. Upgrading of radars in the field can begin thereafter. For some potential operational applications

it may be desirable to scan the radar beam in a vertical plane, to produce RHI scans over a broader local region. Because of the radar's small size, such scanning capability should be easy to implement.

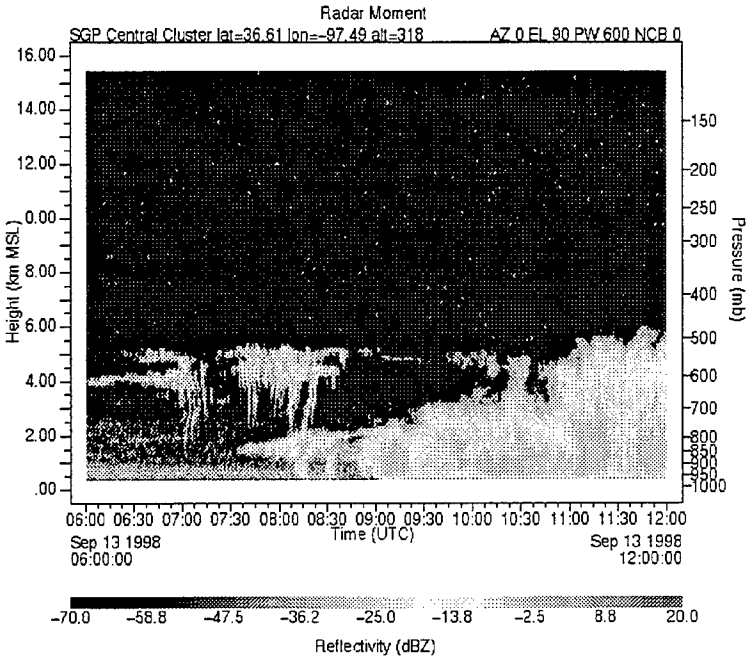


Fig. 2. Reflectivity time-height cross-section from the SGP MMCR near Lamont, Oklahoma. Returns from insects appear below 1 km altitude.

COMMERCIALIZATION

In May, 1997 NOAA's Environmental Research Laboratories entered into a Cooperative Research and Development Agreement(CRADA) with Radian International, LLC., to produce commercial versions of the MMCR. Radian is in the process of building the production prototype, and has received its first order to deliver a commercial unit. It has also received serious inquiries from a number of domestic and international organizations, for both operational and research applications.

SUMMARY

Since the initial report on this unattended Doppler cloud-profiling radar to the DoD community in 1996, considerable experience has been gained on the operational performance of the MMCR system. Its demonstrated performance, planned improvements, and impending commercialization should make it attractive to the military community for air operations, both on land and at sea.

REFERENCES

Kropfli, R.A., B.E. Martner, S.Y. Matrosov, R.F. Reinking, A.S. Frisch, and T. Uttal, "Radar and radiometric measurements of the physical parameters of clouds and precipitation at the NOAA Environmental Technology Laboratory," Proceedings of the 1998 Conference on Battlespace Atmospheric and Cloud Impacts on Military Operations, Hanscom AFB, MA, Dec. 1-3, 1998.

Moran, K.P., B.E. Martner, M.J. Post, R.A. Kropfli, D.C. Welsh, and K.B. Widener, "An unattended cloud-profiling radar for use in climate research," Bull. Amer. Meteorol. Soc., **79**, 443-455, 1998.

Post, M.J. and K.P. Moran, "New cloud-profiling radar for air operations," Proceedings of the 1996 Battlespace Atmospherics Conference, 3-5 Dec. 1996, San Diego, CA., Tech. Doc. 2923, Ed.s J.H. Richter and K.D. Anderson.

THE CLOUDSAT MISSION

Steven J. Walter*[1], Graeme L. Stephens[2], Deborah G.Vane[1],

Jet Propulsion Laboratory, California Institute of Technology[1]
Pasadena, CA 91109
Mail Stop 246-101 (Walter)
Telephone: (818) 354-1626 (Walter), Fax: (818) 354-4341 (Walter),
Email: steven.j.walter@jpl.nasa.gov

Colorado State University, Department of Atmospheric Sciences[2]
Fort Collins, CO 80523
Telephone: (970) 491-8541, Fax: (970) 491-8449
Email: graeme.stephens@reef.atmos.colostate,edu

ABSTRACT

CloudSat is being proposed to measure the vertical structure of clouds. The spacecraft payload consists of a millimeter-wave radar, an optical imager, and a near-IR spectrometer. CloudSat will fly in formation with ICESat, a NASA EOS laser altimetry mission to acquire concurrent lidar-based profiles of clouds and aerosols. This combination of sensors will allow CloudSat to retrieve profiles and characteristics of multi-layer clouds including measurement of cloud bases and tops with 500-meter accuracy. CloudSat in conjunction with ICESat will determine the profiles of cloud ice and liquid content, optical depth, cloud type, and aerosol properties. The mission's primary goal is to furnish data needed to improve how cloud and cloud-climate feedbacks are parameterized in global circulation models (GCMs). The availability of near-real time cloud and aerosol profiles furnishes an important opportunity to demonstrate active sensor technology for future scientific, civilian, and tactical forecast systems. CloudSat has been proposed to the 1998 NASA Earth System Science Pathfinder (ESSP) Announcement of Opportunity (A.O.). Mission selection is slated for December 1998.

MISSION SCIENCE OBJECTIVES

CloudSat is being developed to investigate how clouds affect climate. Climate is the result of numerous chemical, hydrological, and dynamical processes that work in concert to maintain Earth's energy balance. Clouds are key to defining that balance. Clouds can cool the Earth by reflecting incident sunlight back to space. Clouds can also warm the Earth by either absorbing upwelling thermal radiation and then re-radiating it back toward the surface or sublimating into water vapor, a potent greenhouse gas [*Liou*, 1996]. The ability of clouds to heat or cool depends on their height, phase (*e.g.*, ice or liquid), distribution of particle sizes, and water content [*Brown, et. al, 1995*]. The CloudSat mission will provide the first global survey of synoptic and seasonal variations of the altitude of clouds and aerosols, including frequency of occurrence. It will also provide quantitative information on cloud-layer thickness, cloud tops and base altitudes, cloud optical thickness, and cloud water and ice content.

CloudSat will fill a gap in existing and planned observational capabilities. Current space systems only use passive sensors. These measurement techniques can only sense the bulk properties of clouds or probe the top-most cloud layer. They are unable to accurately measure the altitudes of cloud bases; retrieve ice and liquid content, or probe the structure of multi-layer clouds. CloudSat will improve validation of numerical weather models by directly measuring cloud characteristics that currently can only be predicted (i.e. vertical profiles of ice and liquid water, and vertical occurrence/overlap).

The CloudSat science objectives are to:

- Quantitatively evaluate the representation of clouds and cloud processes in global atmospheric circulation models, leading to improvements in both weather forecasting and climate prediction;
- Quantitatively evaluate the relationship between the vertical profiles of cloud liquid water and ice content and the radiative heating by clouds.

The secondary science objectives are to:

- Improve and validate cloud and aerosol information derived from other research and operational meteorological spacecraft; and
- Improve our understanding of the indirect effect of aerosols on clouds by investigating the effect of aerosols on cloud formation and cloud processes.

THE CLOUDSAT MISSION

Mission Overview

The CloudSat payload consists of a 94-GHz Cloud Profiling Radar (CPR) and a near-infrared Profiling A-Band Spectrometer/Visible Imager (PABSI). The CloudSat payload will fly in formation with the EOS ICESat spacecraft, carrying the GLAS lidar. A schematic depicting the mission is shown in Figure 1.

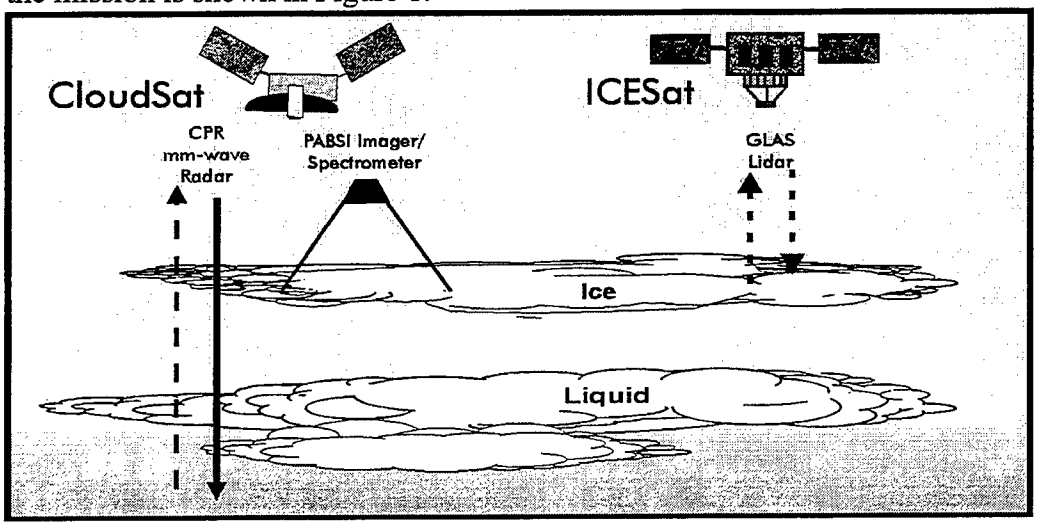


Figure 1. *CloudSat will achieve a breakthrough in atmospheric sensing by flying in formation with ICESat. Together they will retrieve profiles of cloud ice and liquid content, optical depth, cloud type, and aerosol properties with 500-meter vertical accuracy.*

Formation flying enables CloudSat to track the orbit of ICESat. CloudSat will be launched after ICESat and its orbit will be adjusted and monitored to hold the CloudSat spacecraft at a fixed distance from ICESat. The spacecraft will be controlled so that both sets of sensors view the same ground track. In this way, the radar footprint will track the lidar footprint as shown in Figure 2, creating coordinated and essentially simultaneous measurements. The mean separation between the satellites is approximately 450 kilometers which corresponds to a minute delay between lidar and radar measurements. A delay of one minute is a compromise between the desire to minimize the time delay between the radar and lidar measurements and the need to reduce the complexity in the implementation of formation flying.

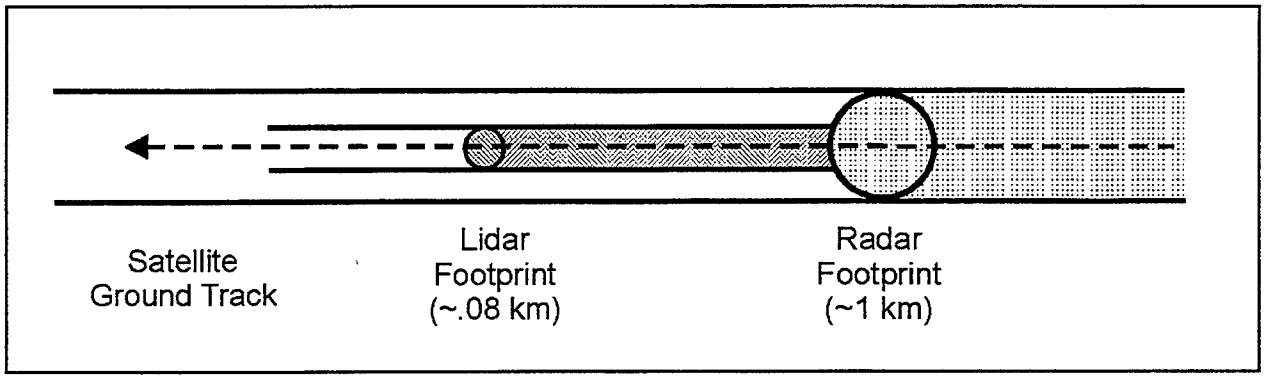


Figure 2. *CloudSat will fly in formation with ICESat. The accuracy of the pointing system be sufficient to co-align the foot prints of the radar, lidar, and spectrometer. This strategy will generate nearly concurrent radar and lidar profiles of clouds and aerosols*

Cloud Profiling Radar (CPR)

The CloudSat Cloud Profiling Radar (CPR) provides calibrated radar reflectivity, (*e.g.*, radar backscatter power), as a function of distance from the spacecraft. CPR will be developed jointly by NASA/JPL and the Canadian Space Agency (CSA). The design has a strong heritage derived from existing ground-based and airborne cloud radars [*Mead et. al*, 1994; *Sadowy et. al*, 1997]. The requirements for CPR are dictated by the science objectives. The sensitivity of CPR must provide a minimum detectable reflectivity factor of -30 dBZ and a 70 dB dynamic range. This will allow CPR to detect almost all radiatively significant clouds. The radar footprint is 0.9 km, and will be averaged over 0.3 seconds to produce an effective footprint of 2 km (along-track) by 0.9 km (cross-track). It will yield 500-m vertical resolution and a calibration accuracy of 1.5 dB. The radar footprint necessitates an antenna diameter of 1.85 meters. The antenna pattern requires that the spacecraft be pointed with an accuracy of 0.5° to minimize direct surface reflections and contamination from sidelobes.

The choice of radar frequency, 94 GHz, is a trade-off between sensitivity, antenna gain, atmospheric transmission, and radar transmitter efficiency. Sensitivity and antenna gain increase with frequency while atmospheric transmission and transmitter efficiency decrease with frequency. Since a space-based platform sets strong constraints on antenna size, a frequency of 94 GHz provides an optimum compromise between the competing factors. An international frequency allocation at 94 GHz has recently been set aside for spaceborne radar use. The choice

of frequency means that a small percentage of the time when very thick clouds or heavy precipitation is present, CPR will not be able to penetrate to the cloud base. The mission objective dictates this choice.

A pulse-coding mode has been proposed to boost sensitivity. This technique requires that the radar transmit a long frequency-modulated chirp which is then received and correlated with a replica of the transmitted signal. The longer pulse provides greater power; hence, greater sensitivity. The correlation process reduces the uncertainty in the height of the reflecting layer induced by the longer pulse. However, it increases height resolution at the expense of generating range sidelobes from the surface and highly reflective clouds. The range sidelobes associated with the earth surface will obscure clouds near the ground. Therefore, CPR will have two operational modes. In the normal mode the -30 dBZ sensitivity is achieved using a 3.33 μs pulse and 4300 Hz repetition rate. The pulse compression mode will gain -36 dBZ sensitivity with a 33.3 μs pulse triggered at an 800 Hz repetition rate.

Profiling Oxygen A-Band Spectrometer and Visible Imager (PABSI)

The Profiling A-Band Spectrometer/Visible Imager (PABSI) instrument both measures the atmospheric radiance of the O_2 A-band rotational spectrum between 761.61 nm and 772.20 nm and records narrow-band images at 747.5 and 761.5 nm. The high-resolution spectrometer determines optical depth and altitude of thin clouds and aerosols by making high spectral resolution (0.5 cm^{-1}) measurements at the oxygen A-band. The oxygen A-band is characterized by a "thicket" of closely spaced spectral lines. Therefore, a small change in wavelength will vary the rate at which light is attenuated as it traverses the atmosphere. With measurements made at a wide range of attenuation lengths, it is possible to determine optical depth, photon path length, characteristics of scattering particles, and cloud and aerosol layer altitude [*Stephens and Heidinger*, 1998]. The imager allows researchers to identify mesoscale weather systems corresponding to the cloud and aerosol profiles. The imager will be able to associate profiles with cloud systems such as tropical storms, cumulus columns, or uniform stratus decks. PABSI has a signal-to-noise of 1000:1 that will enable measurement of cloud and aerosols with an optical depth of 0.02 to 3% accuracy. Both the imager and spectrometer measure reflected sunlight and thus can only operate during daylight.

The imager and the spectrometer are integrated into the same instrument and share most of the same optics. The PABSI detectors are 1024 by 1024 element CCDs with 11 micron square pixels. These devices can be operated without active cooling and are photon-noise limited in this application. Although the imager and spectrometer have different field-of-views (FOVs) and resolution requirements, both systems can use the same CCD detectors. The required spatial and spectral resolution is obtained by summing the pixels. The imager readout electronics uses a 12-bit A/D converter, while the spectrometer's uses a 14-bit A/D converter. This allows the spectrometer to better resolve the radiances observed in the cores of strong O_2 lines where attenuation is high. The imager and spectrometer employ microcontroller-managed FPGA-based digital signal processors that can be reprogrammed on-orbit providing operation flexibility. The processors will be able to

compensate for small changes in instrument alignment that could occur during testing, integration, or on-orbit.

The instrument gathers data synchronously. It operates in a push broom mode utilizing a rectangular instantaneous field-of-view (FOV). A cloud or aerosol feature is first imaged by the 747.5 nm imaging channel with a 15 km swath and an instantaneous field-of-view (IFOV) of 0.5 km. PABSI then makes a measurement with the A-Band spectrometer using a single 0.9-km square footprint (matched to the CPR). Finally, the 761.5 nm imager which also has a 15 km swath and 0.5 km IFOV records an image. This cycle is then repeated.

GLAS Lidar

The primary mission for the ICESat Geoscience Laser Altimeter System (GLAS) is to monitor the amount of ice in the polar ice sheets and investigate how the ice sheets affect changes in global sea level. The secondary missions for GLAS is to measure clouds and aerosols, map surface topography, and measure characteristics of the Earth surface especially vegetation, snow-cover, and sea-ice. To achieve the secondary atmospheric objective, GLAS will measure the vertical structure of radiatively significant clouds and aerosols up to the signal attenuation limit at approximately 2 optical depths [*Rogers*, 1976]. The lidar will measure range-resolved profiles of lidar backscatter with a vertical resolution of 70 m. At this resolution, lidar sensitivity for a 100 m instantaneous field of view is expected to be 10^{-5} m.sr^{-1} corresponding to a cloud or aerosol optical depth of ~0.05. GLAS sensitivity to very thin clouds and aerosols combined with its enhanced vertical resolution complements the CloudSat measurements.

The GLAS lidar uses a solid state, diode pumped Nd:YAG (neodymium-yttrium-garnet) laser that transmits 4 nanosecond pulses of infrared light (120 mJ @ 1.064 nm) and green light (60 mJ @ 532 nm) using a repetition rate of 40 Hz. GLAS has an 80-cm diameter telescope that yields a 70 meter footprint that is sampled at 170-meter intervals. The GLAS footprint can be located to within a few meters using a GPS and star tracker-guided positioning and attitude control systems. The required design lifetime for ICESat is 3 years with a 5-year lifetime goal.

Spacecraft

The CloudSat mission was designed with a two-year lifetime to enable more than one seasonal cycle to be observed. The desired orbit is the ICESat orbit which is a nearly sun-synchronous, 600 km altitude orbit that is inclined at 94°. This orbit will provide hundreds and in some cases thousands of observations that are coincident with the EOS platforms, the Defense Meteorological Satellites, the NOAA Geostationary Weather Satellites (GOES), and international satellites. These concurrent observations will allow validation of the passive meteorological sensor retrieval algorithms with the CloudSat/ICESat active sensor measurements. This will create a unique data base with which to improve the passive sensor retrievals that are dependent on assumptions about cloud height and cloud properties.

CloudSat is designed around the Ball Aerospace RS2000 spacecraft bus that is being used for both QuikScat and ICESat. Communications is accomplished via an S-band transceiver using a nearly, omni-directional patch antenna. The maximum mass of the commercial spacecraft will not exceed 700 kg and the spacecraft subsystems and payload will require a maximum power level of 1170 W.

CloudSat is a proposed NASA mission; however it draws on support and expertise from DoD, DOE, NOAA, universities, federal laboratories, industry, foreign agencies and institutes. Notably, the U. S. Air Force Space Test Program will provide ground operations and manage communications. The Cooperative Institute for Research in the Atmosphere (CIRA) at the Colorado State University (CSU) will handle data processing and archiving the data. The Jet Propulsion Lab will be responsible for mission operations and payload development. Ball Aerospace is providing the spacecraft bus and will be responsible for spacecraft integration and test. Independent calibration of the instrument payload will take advantage of ground-based observational sites such as the DOE Cloud and Radiation Test bed (CART) sites, NASA airborne science campaigns, and university and government research facilities including the University of Utah, Penn State, GKSS in Germany, the NOAA Environmental Technology Lab, Atmospheric Environmental Services (AES) in Canada, and the Communication Research Lab (CRL) in Japan.

CONCLUSIONS

CloudSat is being developed to measure the vertical structure of clouds and aerosols from space. It combines a cloud profiling radar with a profiling A-band spectrometer that is integrated with a visible imager. The ICESat GLAS lidar will complement the CloudSat CPR and PABSI data. CloudSat in conjunction with ICESat will determine the profiles of cloud ice and liquid content, optical depth, cloud type, and aerosol properties. This payload is designed to profile clouds with 500 meter resolution, detect very thin clouds, image the regional cloud field and assist in validating measurements made by the NASA Earth Observing System (EOS) and other meteorological satellites such as the Defense Meteorological Satellites (DMSP). CloudSat is cooperative effort that includes international partners, universities, and U. S. government agencies. CloudSat will furnish an important technology demonstration for future scientific, civilian, and tactical forecast systems. CloudSat has been proposed in response to the 1998 NASA Earth System Science Pathfinder (ESSP) Announcement of Opportunity (A.O.). ESSP mission selections are expected to be announced during December 1998.

REFERENCES

Brown, Illingworth, Heymsfield, McFarquhar, Browning, Gosset, 1995, "The role of spaceborne millimeter-wave radar in the global monitoring of ice cloud," J. Appl. Meteor., 34, 2346-2366.

Liou, 1986, "Influence of cirrus clouds on weather and climatic processes," Mon. Wea. Rev, 114, 1167-1199.

Mead, Pazmany, Sekelsky, and McIntosh, 1994, "Millimeter wave radars for remotely sensing clouds and precipitation," *Proc. IEEE*, 82, 1891-1906.

Rodgers, 1976, "Retreival of atmospheric temperature and composition from remote measurements of thermal radiation," *Rev. Geophys. Space Phys.*, 14, 609-624.

Sadowy, McIntosh, Dinardo, Durden, Edelstein, Li, Tanner, Wilson, Schneider, and Stephens, 1997, "The NASA DC-8 airborne cloud radar: Design and preliminary results," *Proc. IGARSS'97.*

Stephens, G.L. and A. Heidinger, 1998, "Molecular line absorption in a scattering atmosphere: I. Theory." In press; *J. Atmos. Sci.*

ACKNOWLEDGMENTS

This research was partially carried out by the Jet Propulsion Laboratory, California Institute of Technology, under a contract with the National Aeronautics and Space Administration.

OPTICAL PROPERTIES OF CLOUDS DERIVED FROM MEASURED PARTICLE SIZE DISTRIBUTIONS

Karin Weiss-Wrana
Forschungsgesellschaft für Angewandte Naturwissenschaften e.V.
Forschungsinstitut für Optik (FGAN-FfO)
Schloss Kressbach, D-72072 Tuebingen, F. R. Germany
Tel.: 49–7071/709 165, Fax.: 49–7071/709 270, e-mail: wrana@ffo.fgan.de
Doc.: FGAN-FfO 1998/83

SUMMARY

The vertical structure of the atmospheric aerosols size distribution was investigated during cable car ascents along a steep mountain slope in the German Alps. Aerosol size distributions were measured by two particle spectrometer probes operating in diameter ranges of 0.15 - 3 μm and 1 - 95 μm. Aerosol and hydrometeors were sampled under the meteorological conditions of a clear atmosphere, haze, and thick clouds. For each atmospheric layer the phase function $P(\theta)$ and the extinction coefficient σ_{ext} were calculated for the ultraviolet (λ = 0.275 μm, solar blind region), the near IR with Nd:YAG laser radiation (λ = 1.064 μm) and iodine laser radiation (λ = 1.315 μm) and the middle IR with CO_2 laser radiation (λ = 10.59 μm). In the visual and the near IR the aerosol extinction coefficient is not sensitive to variations of the complex refractive index. However for the CO_2 laser radiation the uncertainty in the values of optical constants causes large deviations in calculated aerosol extinction coefficients.

1. OBJECTIVE

The application of electro-optical systems in the atmosphere is often limited by atmospheric effects. An accurate performance assessment of these systems also depends on the accuracy of the atmospheric input parameters. For slant path propagation, the variability of the absorption and scattering properties of the aerosol constituents in the atmosphere, especially the vertical changes in aerosol types, sizes and concentrations are critical.

The FGAN-FfO has participated in the VAST 92 trial (Vertical Atmospheric Structure Trial 1992). The trial was organised by the NATO Research Study Group AC/243 (Panel 04/RSG.08) This site provided facilities for setting up a 2.3 km long and 30° slant optical path. The FGAN-FfO investigated the vertical structure of the atmospheric aerosols by measuring the aerosol size distribution as a function of height. Two particle measuring probes were installed on the cable car, which was operated between the base and the summit of the mountain. One characteristic situation in this orographic environment was a cloud layer between the valley and the summit of the mountain. This cloud layer showed strong temporal and spatial variations. The clouds could not be characterized by well known cloud or fog types. Both the aerosol extinction coefficient and the phase functions of each atmospheric layer were calculated because several effects in the atmosphere are linked with its scattered radiation characteristics and therefore use the phase

function information (e.g. near forward scattering behaviour for multiple scattering and for pulse broadening and the back scattering pattern and for lidar applications).

2. EXPERIMENT

Two particle spectrometer probes with diameter ranges of 0.15 - 3 μm and 1 - 95 μm (Particle Measuring System Inc., USA, PMS Model ASASP-300 and PMS Model CSASP-HV spectrometer probes) were mounted outside the cable car. The cable car valley station is at an altitude of 655 m above sea level (asl) and the mountain station is at 1690 m asl. Fig. 1 shows the mountain terrain. During three ascents, on October 8, 9 and 13, the cable car was running in the so called step-by-step mode; it was stopped at every 100 m altitude change, allowing a measurement period of 5 min at each step. Nine steps were necessary to cover the 1000 m altitude range. A detailed description of the experiments performed during VAST 92 trial can be found in the NATO Technical Report AC/143 [1] and in [2].

During three cable car ascents the conditions were similar, with a cloud or a fog layer between the valley and the summit of the mountain. During each of these cable car ascents atmospheric conditions cover clear atmosphere, haze, thin and thick clouds.

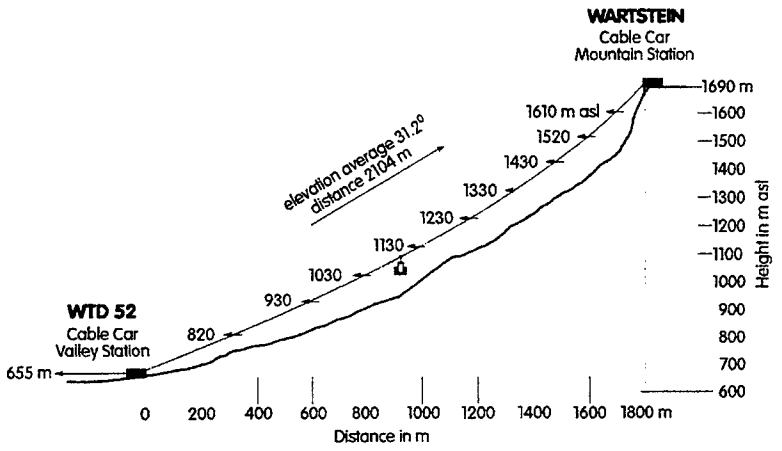


Fig. 1: Profile of the terrain

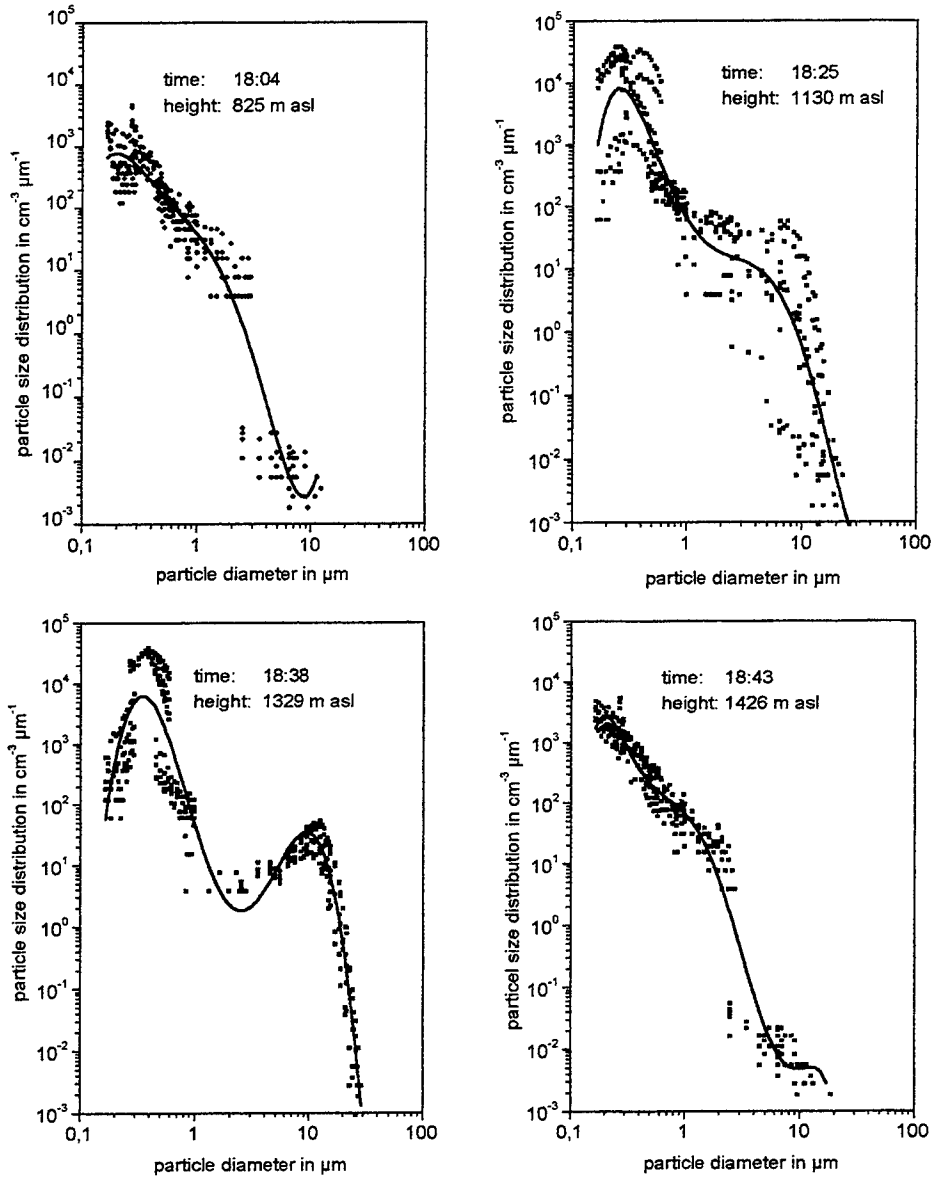
3. PARTICLE NUMBER DENSITY

The sampled data was converted to particle size distributions, expressed in units of cm^{-3} μm^{-1}. For each atmospheric layer, the measured number density, averaged over 5 minutes, was approximated by a polynomial of order 6. Generally, in a double logarithmic presentation the aerosol size distribution of clear atmosphere can be approximated by a straight line over a large size range. For a hazy atmosphere the size distribution shows a lower slope than for a clear atmosphere.

The presented data analysis of the sampled data is limited to the cable car ascent during October 8. The aerosol size distributions measured during October 9 and 13 and their polynomial fit are discussed in detail in [1]. The data analysis for October 13 (e.g. the phase functions and extinction coefficients) can be seen in detail in [2] and [3].

Figs. 2 show typical particle size distributions (dots) and the corresponding polynomial fit

(straight line) measured at four different altitudes in the evening of October 8 when a cloud layer quickly developed between 1100 and 1400 m asl



Figs. 2: Examples of measured particle size distributions (dots) and their polynomial fit from October 8

At a height of 825 m asl there was a clear atmosphere and the size distribution was mono-modal with a predominant particle size below 3 µm diameter.

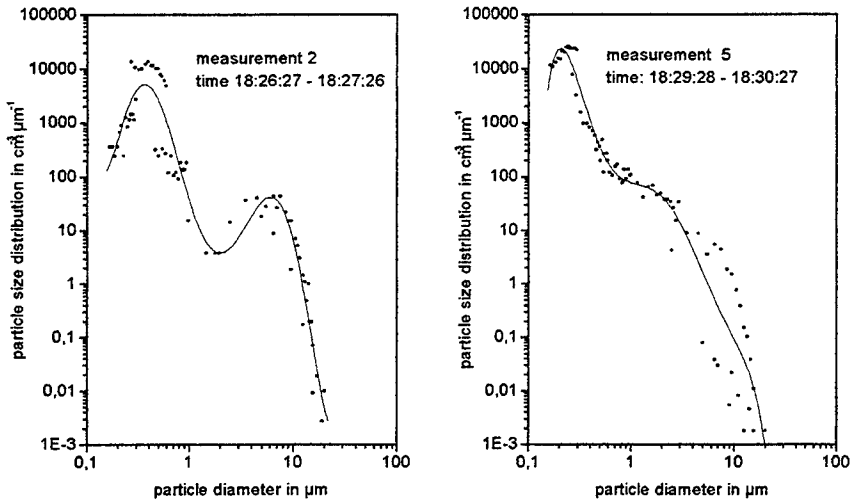
The size distribution measured at 1130 m asl showed a very strong temporal variation of the larger particles during the five minute sampling period. This layer corresponded to the cloud base. In general the atmosphere varies both in time and space in such an environment. The meas-

ured fluctuations corresponded with the lidar results obtained by other field experiment participants [1].

At 1329 m asl the size distribution shows the characteristic pattern of a thick cloud, a second peak with main diameter of the cloud particles of 10 to 20 µm. Inside the cloud layer, the number densities for large particles, typical in clouds, remained relatively stable during the sampling time. However there were spreads in the sampled data of small particles, with diameter < 2 µm, originating from inhomogeneous cloud conditions.

At 1426 m asl and higher the atmosphere again was clear.

Figs. 3 demonstrates strong temporal variations of the size distribution during the sampling time of five minutes as measured at the cloud base at 1130 m asl. For measurement 2, the size distribution indicates a main diameter of the cloud particles of about 7 µm. Just three minutes later, during measurement 5, the particle size distribution had significantly changed.



Figs. 3: Temporal variation of measured particle size distributions (dots) at an altitude of 1130 m asl and their polynomial fit

In thin clouds the main diameter of the sampled hydrometeors was about 8 µm, whereas in thick clouds the main diameter was about 10 – 20 µm [11]. The cloud situations measured during VAST 92 cannot be assigned to the known cloud or fog types described by modified gamma distributions proposed by Deirmendjian [4] and Tampieri et al [5].

4. PHASE FUNCTION AND EXTINCTION COEFFICIENT

The amount of radiation received by an observer looking through the earth's atmosphere is dependent upon the size distribution of the atmospheric particles, their chemical composition and the wavelength λ of the radiation The effect of the chemical composition is described by the complex refractive index $m = n - ik$ of the atmospheric constituents. The extinction coefficient σ_{ext}, which determines the attenuation of the incident radiation, is itself composed of two parts: a scattering coefficient σ_S, which describes the radiation scattered out of the line of sight and the absorption coefficient σ_A, which describes the amount of radiation converted into other forms of energy inside the particle.

The Mie-theory predicts the scattering by and the absorption in an isolated, discrete, homogeneous and isotropic sphere of radius r with a complex refractive index $m = n - ik$ relative to the surrounding medium and illuminated by monochromatic radiation of wavelength λ in the surrounding medium. The theory is given in details in standard texts [6].

The phase function will give the directed distribution of radiation scattered by the aerosol under consideration. The phase function is a function of the radius r, the wavelength λ and the complex index of refraction m.

In dealing with an aerosol model consisting of many particles of identical composition but varying radii, the phase function must be weighted by the size distribution function $f(r)$. The average phase function of a size distribution is found from

$$P(\Theta) = \int_{r\,min}^{r\,max} P(\Theta)\, f(r)\, dr$$

4.1 Aerosol phase function

With the computer code AGAUS of the EOSAEL program library of the US Army Research Laboratory [8], based on the well known Mie-theory, the phase functions were calculated for wavelengths of 0.275 µm, 1.064 µm, 1.315 µm and 10.59 µm. The complex refractive index m of both the aerosols and the hydrometeors depends on the wavelength of the radiation. For aerosols, the complex refractive index is, in addition, sensitive to the relative humidity of the atmosphere. The refractive indices m of different aerosol types as a function of the wavelength and the relative humidity can be found in the literature [8] and [9]. The values of m, used as input parameter for the computer code AGAUS, are listed in Table 1.

Particle Type	Refractive Indices				
RuralAerosol	RH	$\lambda = 0.275$ µm	$\lambda = 1.064$ µm	$\lambda = 1.315$ µm	$\lambda = 10.6$ µm
	50 %	1.53 - 0.01	1.51 - 0.014	1.49- 0.019	1.69 - 0.084
	70 %	-	1.49 - 0.012	1.47 - 0.014	1.63 - 0.082
	80 %	-	1.42 - 0.007	1.40 - 0.008	1.44 - 0.071
	95 %	-	1.37 - 0.003	1.36 - 0.003	1.30 - 0.071
	99 %	-	1.33 - 0.0007	1.33 - 0.0008	1.21 - 0.068
Water		1.35	1.33	$1.32 - 5.10^{-5}$	1.18 - 0.067

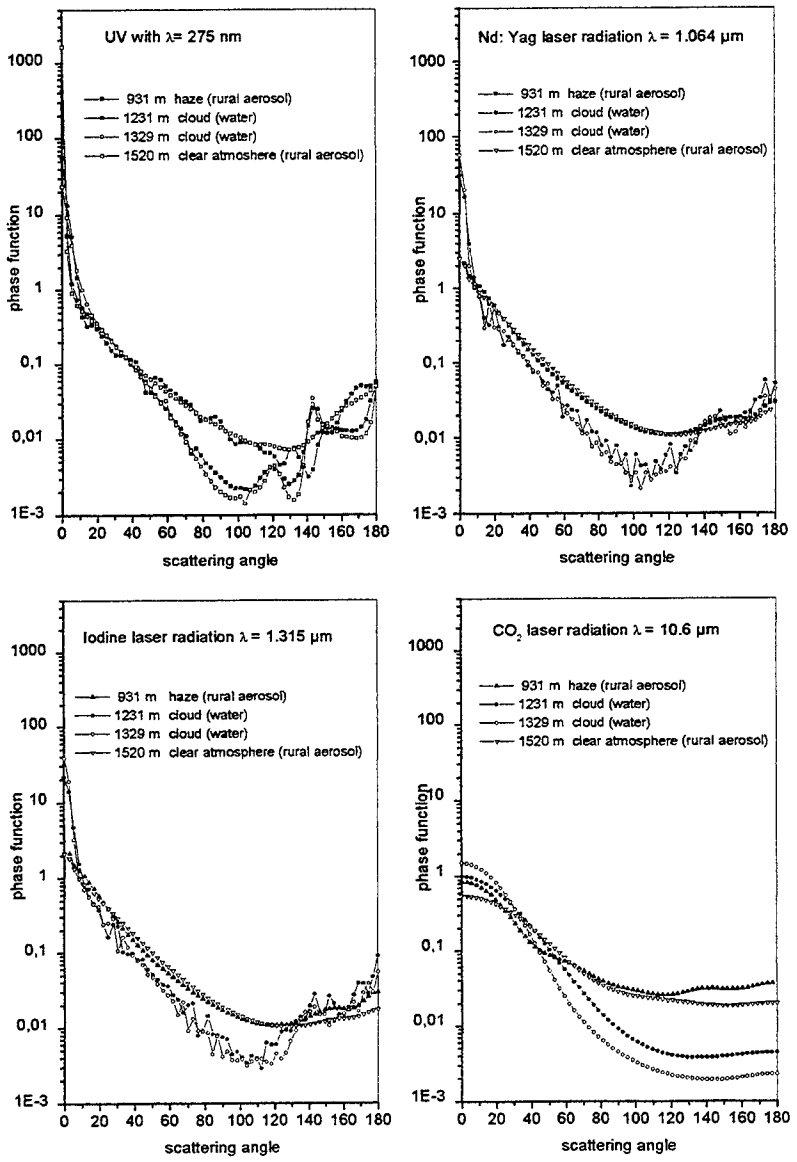
Table 1: Complex refractive indices as a function of relative humidity and wavelength.

Pure water particles are less absorbing than aerosols because of the smaller value of k. With increasing water vapour content in the atmosphere the indices of refraction for the rural aerosol approximate the values for pure water particles. In the UV and near IR range, the values of k are smaller. This results in smaller absorption.

For a hazy and a clear atmosphere we assumed a dry rural aerosol with 50 % RH and for cloud

particles pure water particles. The influence of the index of refraction on the scattering functions are discussed in details in [2].

The phase functions are shown in Figs. 4. The phase functions correspond to thin haze at 931 m, clouds at 1231 m and 1329 m and clear atmosphere at 1520 m. For the UV and the near IR there is no significant difference between the scattering feature corresponding to clear and haze atmosphere and between the two measured cloud size distributions. The scattering functions show a strong and narrow forward scattering due to the corresponding larger Mie-size parameter of the particle distribution, and a significant increase in the backscattering region for both the water droplets and dry rural aerosol.



Figs. 4: Phase functions calculated for the UV (solar blind), Nd:YAG, the iodine laser and the CO_2 laser radiation

Contrary, in the mid-IR the scattering properties differ significantly. Because of the smaller Mie

size parameter the phase function shows a broadened feature for small scattering angles and due to larger value of k, a more or less homogeneous feature in the back scattering region. The phase functions are more sensitive to changes in the size distributions; there is a noticeable difference between clear and hazy atmosphere and between the two different cloud situations. This can also be explained by the smaller Mie size parameter compared to the near IR or the UV. The complex refractive index m strongly influences the pattern of the phase function [2].

4.2 Aerosol extinction coefficient

With the computer code AGAUS the volume extinction coefficients σ_{ext}, the volume scattering coefficients σ_{scat}, the volume back-scattering coefficients σ_{back} in units of km^{-1} and the single scattering albedo were calculated. The albedo A for single scattering is the fraction of energy lost from the incident beam due only to scattering, compared to the sum of the scattered and absorbed ones.

$$A = \sigma_{scat}/\sigma_{ext} = \sigma_{scat}/(\sigma_{scat} + \sigma_{abs})$$

The albedo decreases with increasing volume absorption coefficient. For non absorbing particles, $k = 0$, the albedo is 1.

aerosol type	height m asl	λ = 0.275 µm solar blind		λ = 1.064 µm Nd:YAG laser		λ = 1.315 µm CO_2 laser		λ = 10.6 µm iodine laser	
		σ_{ext} in km^{-1}	albedo $\sigma_{scat}/\sigma_{ext}$	σ_{ext} in km^{-1}	albedo $\sigma_{scat}/\sigma_{ext}$	σ_{ext} in km^{-1}	albedo $\sigma_{scat}/\sigma_{ext}$	σ_{ext} in km^{-1}	albedo $\sigma_{scat}/\sigma_{ext}$
rural	825	0.12	0.82	0.12	0.89	0.11	0.87	0.014	0.56
rural	931	0.16	0.76	0.22	0.90	0.20	0.89	0.017	0.52
rural	1026	0.51	0.86	0.34	0.90	0.34	0.89	0.020	0.46
water	1130	0.57	1.0	0.61-7.7	1.0	0.62-7.7	1.0	0.07-2.2	0.3 - 0.4
water	1231	4.3	1.00	4.5	1.00	4.4	1.00	1.46	0.43
water	1329	42.3	1.00	24.52	1.00	23.0	1.00	12.8	0.51
rural	1426	0.075	0.91	0.074	0.89	0.08	0.87	0.009	0.60
rural	1520	0.032	0.93	0.023	0.91	0.02	0.88	0.002	0.62
rural	1613	0.021	0.83	0.016	0.89	0.013	0.86	0.003	0.68

Table 2: Calculated aerosol extinction coefficients and albedo from particle size distributions measured during the cable car ascent October 8

Table 2 shows the profiles of the calculated corresponding aerosol extinction coefficients σ_{ext}, and the albedo A. σ_{ext} is affected by the assumed complex index of refraction as well as by the Mie-size parameter α of the aerosols (with $\alpha = 2r\pi/\lambda$). Both parameters change with changing

wavelength. Comparing the values of the extinction coefficients, as calculated for the different wavelengths, it is not possible to separate the influence of one of these parameters.

The aerosol extinction coefficients, calculated for the measured aerosol size distributions, cover a broad range of values. In the case of the CO_2 laser radiation, σ_{ext} was found to be between 0.002 km^{-1} (clear atmosphere) and 12.8 km^{-1} (thick fog). In the case of the iodine laser radiation the corresponding values vary between 0.013 km^{-1} up to 23 km^{-1}, for Nd:YAG laser radiation between 0.016 km^{-1} up to 24.5 km^{-1} and for the UV range at wavelength 0.275 μm between 0.021 km^{-1} up to 42 km^{-1}. For most atmospheric conditions, the aerosol extinction coefficients, σ_{ext}, for the CO_2 laser radiation were significantly smaller than for the near IR and the UV.

In the near IR and the UV region, the values of the aerosol extinction coefficients, calculated for cloudy conditions, are not sensitive to the changes in wavelength or index of refraction. However, for the CO_2 laser radiation, σ_{ext} depends strongly on the selected refractive index, and, because the Mie-size parameter α is smaller by a factor of 10, with $\alpha \leq 1$, σ_{ext} is more sensitive to changes in the size distributions.

Our results are in agreement with the results presented by Jennings et al. [10]. The Mie-calculated extinction coefficients of polydispersions of spherical aerosols are almost insensitive to the real part of the refraction index for the UV and the near IR ($\lambda < 3\mu m$). However, changes in extinction by up to an order of magnitude are caused by realistic variations in real or imaginary refractive index for 3 μm $< \lambda <$ 11 μm, with the real index having a greater influence than the imaginary part in affecting extinction.

5. CONCLUSIONS

The vertical profile of the aerosol size distribution was measured along a steep mountain slope in the German Alps. Two particle spectrometer probes with diameter ranges of 0.15 - 3 μm and 1 - 95 μm were operated on a cable car which was stopped at every 100 meters of elevation between the valley and the mountain station, with a total elevation difference of about 1000 m. The aerosol measurements were taken during different atmospheric conditions, clear atmosphere, haze, and clouds. The sampled data showed strong temporal variations originating from inhomogeneous cloud conditions which are typical for such an orographic environment. The cloud conditions measured during VAST 92 cannot be assigned to known cloud or fog types. Phase functions and aerosol extinction coefficients and the single scattering albedo were calculated. The calculated aerosol extinction coefficient σ_{ext} varied between 0.002 km^{-1} and 12.8 km^{-1} for the CO_2 laser radiation. For the UV region the values varied between 0.02 and 42 km^{-1}, for the Nd:YAG laser radiation between 0.016 and 24.5 km^{-1} and between 0.013 and 23 km^{-1} for the iodine laser radiation.

For the UV and the near IR the aerosol extinction coefficient is not sensitive to variations of the complex refractive index. However, for the CO_2 laser radiation, uncertainty in the values of optical constants causes large deviations in the calculated aerosol extinction. To successfully model the vertical structure of the aerosol extinction coefficients in the mid-IR, accurate aerosol size distributions and values of the complex refractive index are required.

REFERENCES

[1] Technical Report NATO AC/243 (Panel 4/RSG.8) TR/18, Slant Path Lidar and Thermal Imaging Measurements, Chapter 3.3.3, 1995.

[2] K. Weiss-Wrana, A. Kohnle, Extinction Coefficients and Phase Functions of Particle Size Distributions Measured inside Cloud Layers, SPIE Vol. 2506, Proceedings on Air Pollution and Visibility Measurements, 552,1995.

[3] K. Stein, K. Weiss-Wrana, A. Kohnle, IR-Imaging of a Point-Target through Inhomogeneous Media along a Slant Path of 2.3 km, SPIE Vol. 2580, Proceedings on Optics in Atmospheric Propagation and Adaptive Systems, 86, 1995.

[4] D. Deirmendijan, Electromagnetic Scattering on Spherical Polydispersions Ed. Elsevier, New York, 75, 1969.

[5] F. Tampieri, C. Tomasi, Size Distribution Models of Fog and Cloud Droplets and their Volume Extinction Coefficients at Visible and Infrared Wavelengths, Pageoph. Vol. 114, 571, 1976.

[6] H. C. Van de Hulst, Light Scattering by Small Particles, Ed. Dover Pub., New York, 1981.

[7] Electro-Optics Systems Atmospheric Effects Library (EOSAEL), Module AGAUS, A. Miller, Mie Code AGAUS 82, US Army Atmospheric Sciences Laboratory Technical Report CR-8301000-3, 1083, 1983).

[8] E. P. Shettle, R.W. Fenn, Models for the Aerosol of the Lower Atmosphere and the Effects of Humidity Variations on their Optical Properties, AFGL-TR-79-0214, 1979. [ADA 085951].

[9] G. W. Paltridge, C.M. Platt, Radiative Processes in Meteorology and Climatology, Ed. Elsevier, New York, 1976.

[10] S. G. Jennings, R.G. Pinnick, H.J. Auvermann, Effects of Particulate Complex Refractive Index and Particle Size Distribution Variations on Atmospheric Extinction and Absorption for Visible through Middle IR Wavelengths, Appl. Opt., Vol.17, 3922, 1978.

HIGH CLOUD STATISTICS MEASURED BY HIRS

Donald P. Wylie* and W. Paul Menzel
Space Science and Engineering Center
University of Wisconsin-Madison
1225 W. Dayton Street
Madison, WI 53706
Phone:608 263 7458
Fax: 608 262 5974

OBJECTIVE

Cirrus clouds have been under counted in past cloud studies because they often are obscured from ground level views and difficult to identify in satellite data. The multi-spectral HIRS (High resolution Infrared Radiation Sounder) flown on the National Oceanic and Atmospheric Administration (NOAA) polar orbiting satellites provides a unique data set for detecting these clouds. The CO2 Slicing algorithm applied to the HIRS data exhibits a higher sensitivity to semi-transparent cirrus clouds than the cloud algorithm used by the International Satellite Cloud Climatology Project (ISCCP, Rossow and Schiffer, 1991). It has better geographical coverage than the SAGE-II sensor (Wang, et al., 1986), which is more sensitive to thin clouds but highly limited geographical coverage. This work is an extension of the four year HIRS data set reported by Wylie et al. (1994). It is ongoing project to measure the frequency of geographical frequencies of cirrus clouds and track their changes in time.

RESEARCH

a. Technique

The technique for extracting cloud height and density information, along with frequency of occurrence (assumed to be synonymous with detection in this paper), from the HIRS data has been described in detail in Wylie et al. (1994) and Wylie and Menzel (1998). This method uses infrared radiation emanating from the earth and atmosphere in partially absorbing CO2 channels from 13 to 15 microns. There is no appreciable solar reflection in these channels. They are spectrally positioned so that each channel detects radiation from different levels in the troposphere, hence the association of the term CO2 Slicing with this technique. The technique is based on a simplification of the radiative transfer equation that assumes the attenuation of upwelling radiation by a cloud occurs at one level in the troposphere. A more realistic depiction requires knowledge of the vertical profile of cloud density; however, since clouds come in a wide variety of vertical distributions, the single layer assumption is the only method for obtaining a unique solution. This approach is consistent with other algorithms proposed for detecting clouds using multi-spectral infrared sounders (Chahine 1974; Smith et al. 1974; McCleese and Wilson 1976; Smith and Platt 1978; Wielicki and Coakley 1981; Susskind et al. 1987; Menzel et al. 1992).

Using the multi-spectral CO2 channel data, the cloud level can be solved directly without knowing the infrared emissivity of the cloud or the fractional cloud cover in the field of view (Wylie et al. 1994). Assuming that the emission and absorption are identical in two spectrally

close CO2 channels, a direct calculation of the cloud level is possible in a radiative transfer formulation. Other techniques use visible channels to estimate the cloud density and emissivity with a radiative scattering model; adjustments are then made to the measured infrared window radiance (at 11 microns) for transmission through the cloud (Minnis et al. 1993a and b). CO2 Slicing does not require visible data and provides an alternate means of detecting upper tropospheric clouds that complements the ISCCP.

In this study, HIRS CO2 channels are used to calculate cloud levels when the cloud radiance signal, defined as the expected clear minus the measured radiance for a field of view (R_{clr}-R_m), is greater than five times the instrument noise level (R_{clr}-$R_m > 5\sigma$); otherwise the infrared window temperature is used to determine an opaque cloud top pressure. This assures that the measured cloud signal is safely outside of the instrument noise and indicates the presence of cloud in the CO2 channels with a high degree of confidence. A field of view (FOV) is determined to be clear if the moisture corrected 11 micron brightness temperature is within 2.5 C of a surface temperature estimate. Over land this is inferred from the Global Data Assimilation System (Kanamitsu 1989; Parrish and Derber 1992; and Parrish et al. 1997) at the National Center for Environmental Prediction (NCEP); over the oceans this is the sea surface temperature analysis from the National Environmental Satellite Data and Information Service (NESDIS). Temperature errors (defined by the root mean square differences between in situ data and the existing analysis values) are between 1 and 3 K. No surface temperature changes nor trends have been found during the course of this eight year cloud analysis; it can be concluded that surface temperature did not cause any trends in UW HIRS cloud study.

HIRS data from NOAA 10, 11, 12, and 14 are sampled to include only data from every third FOV on every third line with a zenith angle less than 10 degrees. With two satellites, about one half of the Earth is sampled each day. Morning orbits (0 to 12 local time) over land are rejected because a good estimate of the morning land surface temperature is unavailable, which makes discerning cloudy from clear FOVs difficult. In multiple cloud layers, the height and emissivity of a single cloud layer best representing the radiative mean of the cloud scene is estimated.

After the cloud level has been determined, the cloud effective emissivity in the 11 micron window is estimated from the ratio of the radiance signal of the measured cloud with the radiance signal of an opaque cloud at the calculated cloud level. The cloud effective emissivity is the product of cloud emissivity, ε, and the fraction of cloud coverage in the FOV, N. Since it is calculated with a radiance measured from a 20 km diameter FOV, when the cloud effective emissivity, $N\varepsilon$, is less than unity, HIRS may be observing broken cloud ($N < 1$, $\varepsilon = 1$), overcast transmissive cloud ($N = 1$, $\varepsilon < 1$), or broken transmissive cloud ($N < 1$, $\varepsilon < 1$). All of these possibilities imply an observation where the HIRS radiometer detects radiation from below a cloud layer as well as radiation from the cloud layer top. All observations where $N\varepsilon < 0.95$ are labeled as transmissive or "cirrus" in this paper; those where $N\varepsilon > 0.95$ are considered to be opaque clouds.

To evaluate which component of $N\varepsilon$, cloud fraction or emissivity, is dominant, Wylie et al. (1994) presented a comparison of $N\varepsilon$ calculated with CO2 Slicing of the 20 km HIRS data to N inferred from 1 km AVHRR (Advanced Very High Resolution Radiometer) data within the HIRS FOV. When $N\varepsilon > 0.50$, all of the HIRS FOVs were entirely cloud covered ($N_{AVHRR} = 1.0$). For thinner clouds, $N\varepsilon < 0.5$, N_{AVHRR} was always greater than $N\varepsilon$. A larger study has been completed using 4 km AVHRR GAC data. N_{AVHRR} was evaluated for all NOAA 12 HIRS FOVs in July 1994 within 20° - 40° latitude over ocean. For $N\varepsilon > 0.5$ (thick clouds), all HIRS FOVs

were found to be completely cloud covered ($N_{AVHRR} = 1.0$), similar to the results in Wylie et al. (1994). For thinner clouds ($N\varepsilon < 0.5$), there was a variety of cloud coverage that had an average N_{AVHRR} of 0.72 within HIRS FOVs. To summarize, this work indicates that $N\varepsilon$ represents ε entirely when $N\varepsilon \geq 0.5$ (optically thicker clouds); otherwise, the contributions of N and ε are approximately equal (optically thinner clouds with $N\varepsilon < 0.5$). Estimates of cloud cover assume total FOV cloud obscuration when $N\varepsilon \geq 0.5$, and 72% cloud obscuration of the FOV when $N\varepsilon < 0.5$.

Cloud optical depths can be estimated from the effective emissivity ($N\varepsilon$) derived from the HIRS data. By assuming that transmission is the complement of emission without scattering, the infrared window optical depth is given by

$$\tau_{IRW} = - \ln [1 - N\varepsilon] . \quad (1)$$

Visible optical depths (τ_{vis}) can be estimated from infrared window optical depths. Theoretical models of radiative scattering, reinforced by lidar and satellite measurements, indicate that the optical depth in the visible is about twice that at 11 microns (Platt 1979; Platt et al. 1987; Minnis et al. 1990; and Wylie et al. 1995). In this work, it is assumed that

$$\tau_{vis} / \tau_{IRW} \cong 2. \quad (2)$$

The threshold for cloud detection appears to require visible optical depths (τ_{vis}) greater than 0.1. More details are given in Wylie and Menzel (1998).

b. Geographical Cloud Distributions

The statistical summary of over 60 million cloud observations from HIRS between June 1989 through February 1997 is shown in Table 1. The statistics are separated by cloud type into clear sky ($\tau_{vis} < 0.1$), thin ($\tau_{vis} < 1.4$), thick ($\tau_{vis} > 1.4$), and opaque ($\tau_{vis} > 6$) clouds and separated by level in the atmosphere above 6 km, between 3 and 6 km, and below 3 km. The frequency of cloud observations in a given level of the atmosphere in Table 1 are the percentages of only observations to that level; this is different from the percentage of all observations (as presented in Wylie et al. 1994). On the average for summer and winter, HIRS finds thin clouds in 22% of all observations, thick clouds in 21%, and opaque clouds in 32%. From section 2, thin clouds cover 72% of the HIRS FOV on average while thick and opaque clouds cover 100%. Thus these HIRS observations imply that clouds cover about 69% of the earth from 65 S to 65 N latitude. This estimate of cloud cover is believed to be valid within 3% (Menzel et al. 1992).

Little variation is found in the boreal summer versus winter cloud statistics; clear skies are found in 27% of all observations in the boreal summer and only in 24% in the boreal winter. High clouds above 6 km are evident in 34% of the observations; six kilometers roughly corresponds to 490 hPa in the tropics and 450 hPa at 50° latitude. Summer to winter, 26 to 32% of the observations at mid-levels between 3 and 6 km found clouds; three kilometers roughly corresponds to 700 hPa in the tropics and 685 hPa at 50° latitude. Observations at low levels below 3 km found clouds 45 to 47% of the time. Cirrus and transmissive clouds (with effective emissivities less than 0.95) were found in 42 to 44% of all observations. All clouds below 3 km are designated as opaque because the CO2 algorithm is not capable of resolving cloud fraction and emissivity low in the troposphere. Many of the mid level transmissive observations are most likely broken clouds.

The major geographical patterns of the eight year summary have not changed appreciably from those reported in the four year summary (Wylie et al. 1994). The Inter-Tropical Convergence Zone (ITCZ) is readily discernible as the region of more frequent clouds and the

mid-latitude storm belts also have frequent cloud cover. The ITCZ is seen to move north with the sun from boreal winter to summer. The subtropical high pressure systems are seen in the regions of less frequent cloud cover. Over the Indonesian region the ITCZ expands in latitudinal coverage from boreal winter to summer. In the central Pacific Ocean, the ITCZ shows both a southern and northern extension during the boreal winter months. In the southern hemisphere, the eastern Pacific Ocean off South America and the eastern Atlantic Ocean off Africa remain relatively free of clouds throughout the year. The southern hemispheric storm belt is evident throughout the year. In the northern hemisphere's mid-latitude storm belts, the frequency of clouds increases during the winter with the strengthening of the Aleutian Low in the north Pacific Ocean and the Icelandic Low in the north Atlantic Ocean. The North American cloud cover shows little seasonal change. Large convective development occurs during the austral summer (boreal winter) in South America and Africa, which is readily apparent in the increased detection of clouds.

Some regions exhibit cloudy conditions for a complete season. In two grid boxes of 2° latitude by 3° longitude in the African ITCZ (8N, 10.5W and 2N, 19.5E), all HIRS observations found cloud during all boreal summers of this study. Eight grid boxes were cloudy for all boreal winters of this study; four were located in the central Amazon (centered at 8S, 58W), two in the African Congo (6S, 26E), and two in the Indonesian area (2S, 113E and 4S, 146E). With each grid box covering approximately 75,000 square kilometers, in the boreal winter there are about 300,000 square kilometers in the Amazon that are always cloud covered. There were no grid boxes where all HIRS observations found cloud in winter and summer seasons.

Comparison with ISCCP data reveals that the UW HIRS multispectral analysis is finding roughly twice as many transmissive clouds than the ISCCP visible and infrared window analysis. Jin et al. (1996) studied collocated ISCCP and HIRS data for four months (July 1989, October 1989, January 1990, and April 1990). HIRS finds cloud in 76% of its observations while ISCCP finds cloud in 63%; the HIRS detection of thin clouds (17% compared to 7% for ISCCP) accounts for most of this difference. Jin et al. (1996) note a lower number of UW HIRS reports of cloud in mountainous areas due to a cold bias in the surface temperatures used in the UW algorithm. In one year (March 1985 - February 1986) of ISCCP data, Hartmann et al. (1992) finds semi-transparent clouds (visible optical depth less than 9.4) 21% of the time; HIRS finds 44% in the eight years of this study (June 1989 - May 1993). These comparisons point to the ISCCP difficulty in detecting thin transmissive clouds; if one were to exclude clouds with $\tau_{vis} <$ 1.4 from the HIRS data (roughly 20% of the observations) and increase the frequency of low opaque clouds in the HIRS data (adding roughly 5%), all adjusted HIRS cloud categories would agree with Jin et al. (1996) and Hartmann et al. (1992) to within a few percent.

Comparison with SAGE II data from the summers of 1989 and 1990 and the winters of 1990 and 1991 (Wylie and Wang, 1997) reveals good correlation (greater than 0.8) in the geographical distribution of clouds above 5 km. This must be considered in the context of the differing observing characteristics of the two systems (SAGE limb scanning over 2.5 by 200 km FOVs versus HIRS nadir 20 km FOVs); in addition SAGE can detect clouds with $\tau_{vis} \geq 0.0002$ while HIRS is sensitive to clouds when $\tau_{vis} \geq 0.1$. There is good comparison of the percentage of observations that find clouds in the winter hemispheres and the tropics (within 5%), but in the summer hemispheres SAGE finds more clouds (up to 15%). On the average, 87% of the SAGE observations found cloud in 1989 and 1990, while 76% of the HIRS observations found cloud;

SAGE is expected to find more clouds given its limb scanning and larger FOV. Overall, the similarities in these two cloud data sets are encouraging.

c. Time trends

Wylie et al. (1994) reported a possible increase in the observation of upper tropospheric clouds. As the HIRS record has grown to eight years and evolved to four satellites, the changes over time in the HIRS data have been re-examined in greater detail. The monthly averages of infrared window brightness temperature and cloud frequency (total and high) have been investigated for each satellite. Oceanic data were distinguished separately from the land data.

To search for trends in cloud cover, monthly averages of the cloud frequencies were calculated for each satellite and plotted as one continuous record. NOAA 12 replaced NOAA 10 in September 1991, and NOAA 14 replaced NOAA 11 in April 1995. Cloud frequency trends over land are credible only for NOAA 10 and 14, as the changes in the NOAA 11 orbit confuse the trends over land for the midday and midnight times. When NOAA 14 replaces NOAA 11 and HIRS observations resume at the nominal slots in the diurnal cycle (2 a.m. and 2 p.m.), there is a noticeable decrease in the frequency of HIRS detection of cloud over land. The trends over ocean reveal that an annual cycle of all clouds over oceans becomes noticeable in 1993 in the southern mid-latitudes; in the tropics and the northern midlatitudes there is little discernible change in cloud cover with the seasons. High clouds show little seasonal fluctuation anywhere. Subtle trends can be seen in the annual increase of cloud cover for all three regions.

Table 2 summarizes the changes in cloud cover during the eight years of this study period inferred from a linear fit to the monthly averages. Over oceans, larger changes are evident in the NOAA 10 and 12 sunrise and sunset observations than in the NOAA 11 and 14 midday and midnight observations. NOAA 10 and 12 find increases in all clouds ranging from 1.7% in the southern mid-latitudes to 6.6% in the tropics. NOAA 11 and 14 find smaller increases from 1.5 to 2.1%. The largest increase in total cloud cover is in the tropics. High clouds (pressure height < 440 hPa) exhibit the largest changes in the northern mid-latitudes where increases of 4.9 and 3.3% are found. The tropics show minimal changes in high cloud. Over land, the NOAA 10 and 12 trends are very small (increases of 2% or less are found). Southern mid-latitude land coverage is small and thus the apparent increase in high clouds is not considered significant. NOAA 11 and 14 trends over land are not included in the table; NOAA 11 trends over land are problematic because of the orbit drift and NOAA 14 trends are difficult as they cover only 1.7 years to date.

SUMMARY and CONCLUSIONS

Clouds with optical depths $\tau_{vis} > 0.1$ cover 69% of the earth between 65 N and 65 S. High clouds are found more often in the tropics than in the northern and southern mid-latitudes, indicating the ITCZ. Large latitudinal movement in cloud cover with the changing seasons is apparent on geographical plots.

Clouds that are semi-transparent in the infrared ($0.1 < \tau_{vis} < 6$) are found in 43% of the HIRS observations. These clouds have a mean effective emissivity between 0.5 and 0.6 (the larger value evident in areas of frequent cloud cover).

Annual trends are small and hard to distinguish from larger seasonal differences. There is evidence of a gradual increase in the occurrence of high clouds in the northern mid-latitudes

(0.5% per year) and all clouds in the tropics (0.8% per year); the southern mid-latitudes show very little change in cloud cover of any type during this study.

The UW HIRS cloud data sets are available for further study at http://www.ssec.wisc.edu/~donw.

REFERENCES

Chahine, M. T., 1974: Remote sounding of cloudy atmospheres. I: The single cloud layer., *J. Atmos. Sci.*, **31**, 233-243.

Frey, R. A. and S. A. Ackerman, 1996: Climate parameters from satellite spectral measurements. Part1: Collocated AVHRR and HIRS/2 observations of spectral greenhouse parameter. *J. Climate*, **9**, 327-344.

Gruber, A., and T. S. Chen, 1988: Diurnal variation of outgoing longwave radiation., *J. Climate and Appl. Meteor.*, **8**, 1-16.

Hartmann, D. L., M. E. Ockert-Bell, and M. L. Michelsen, 1992: The effect of cloud type on the Earth's energy balance: global analysis. *J. Climate*, **5**, 1281-1304.

Jin, Y., W. B. Rossow, and D. P. Wylie, 1996: Comparison of the climatologies of high-level clouds from HIRS and ISCCP., *J. Climate*, **9**, 2850-2879.

Kanamitsu, M., 1989: Description of the NMC global data assimilation and forecasting system, *Wea. and Forecasting*, **4**, 334-342.

Liao, X., W. B. Rossow, and D. Rind, 1995a: Comparison between SAGE II and ISCCP high-level clouds, 1. Global and zonal mean cloud amounts., *J. Geoph. Res.*, **100**, 1121-1135.

_____, 1995b: Comparison between SAGE II and ISCCP high-level clouds, 2. Locating cloud tops., *J. Geoph. Res.*, **100**, 1137-1147.

McCleese, D. J., and L. W. Wilson, 1976: Cloud top height from temperature sounding instruments., *Quart. J. Roy. Meteor. Soc.*, **102**, 781-790.

Menzel, W. P., D. P. Wylie, and K. I. Strabala, 1992: Seasonal and diurnal changes in cirrus clouds as seen in four years of observations with the VAS. *J. Appl. Meteor.*, **31**, 370-385.

Minnis, P., D. F. Young, K. Sassen, J. M. Alvarez, and C. J. Grund, 1990: The 27-28 October 1986 FIRE IFO Cirrus Case Study: Cirrus parameter relationships derived from satellite and lidar data., *Mon. Wea. Rev.*, **118**, 2402-2425.

_____, K. N. Liou, and Y. Takano, 1993a: Inference of cirrus cloud properties using satellite-observed visible and infrared radiances. Part I: Parameterization of radiance fields., *J. Atmos. Sci.*, **50**, 1279-1304.

_____, P. W. Heck, and D. F. Young, 1993b: Inference of cirrus cloud properties using satellite-observed visible and infrared radiances. Part II: Verification of theoretical cirrus radiative properties., *J. Atmos. Sci.*, **50**, 1305-1322.

Parrish, D. F., and J. C. Derber, 1992: The National Meteorological Center's spectral statistical interpolation analysis., *Mon. Wea. Rev.*, **8**, 1747-1763.

_____, _____, J. Purser, W. Wu, and Z. Pu, 1997: The NMC Global Analysis System: Recent improvements and future plans., *J. Meteor. Soc. Japan*, **75**, 359-365.

Platt, C. M. R., 1979: Remote sounding of high clouds: I. Calculation of visible and infrared optical properties from lidar and radiometric measurements., *J. Appl. Meteor.*, **18**, 1130-1143.

_____, and G. L. Stephens, 1980: The interpretation of remotely sensed high cloud emittances., *J. Atmos. Sci.*, **37**, 2314-2321.

_____, J. C. Scott, and A. C. Dilley, 1987: Remote sounding of high clouds. Part VI: Optical properties of midlatitude and tropical cirrus., *J. Atmos. Sci.*, **44**, 729-747.

Rossow, W. B., and R. A. Schiffer, 1991: ISCCP cloud data products., *Bull. A.M.S.*, **72**, 2-20.

_____, and A. A. Lacis, 1990: Global and seasonal cloud variations from satellite radiance measurements. Part II: Cloud properties and radiative effects. *J. Climate*, **3**, 1204-1253.

Smith, W. L., and C. M. R. Platt, 1978: Intercomparison of radiosonde, ground based laser, and satellite deduced cloud heights., *J. Appl. Meteor.*, **17**, 1796-1802.

_____, H. M. Woolf, P. G. Abel, C. M. Hayden, M. Chalfant, and N. Grody, 1974: Nimbus 5 sounder data processing system. Part I: Measurement characteristics and data reduction procedures., NOAA Tech. Memo. NESS 57, 99 pp.

Wang, P. H., P. Minnis, M. P. Mc Cormick, G. S. Kent, and K M. Sheens, 1986: A 6-year climatology of cloud occurrence frequency from Stratospheric Aerosol and Gas Experiment II observations (1985-1990)., J. Geophy. Res., **101**, 29,407-29,429.

Warren, S. G., C. J. Hahn, J. London, R. M. Chervin, and R. L. Jenne, 1986: Global distribution of total cloud cover and cloud type amounts over land., NCAR TN-273+STR, (NTIS number DE87-006903), Available from the National Center for Atmospheric Research, Boulder, CO, 80307.

_____, 1988: Global distribution of total cloud over and cloud type amounts over the ocean. NCAR/TN-317+STR [Available from the National Center for Atmospheric Research, Boulder, CO, 80307]

Wielicki, B. A., and J. A. Coakley, 1981: Cloud retrieval using infrared sounder data: Error analysis., *J. Appl. Meteor.*, **20**, 157-169.

Wylie, D. P. and W. P. Menzel, 1989: Two Years of Cloud Cover Statistics Using VAS. *Jour. Clim.*, **2(4)**, 380-392.

_____, W. P. Menzel, H. M. Woolf, and K. I. Strabala, 1994: Four Years of Global Cirrus Cloud Statistics using HIRS. *Jour. Clim.*, **7**, 1972-1986

_____, P. Piironen, W. Wolf, and E. Eloranta, 1995: Understanding satellite cirrus cloud climatologies with calibrated lidar optical depths., *J. Atmos. Sci.*, **52**, 4327-4343.

_____ and P. Wang, 1997: Comparison of Cloud Frequency Data from HIRS and SAGE II. submitted to *Jour. Clim.* for publication.

_____, 1998: Eight Years of High Cloud Statistics Using HIRS., *J. Climate*, in press.

Table 1. Cloud Types Found in UW HIRS Study between 65 N and 65 S latitude in Summers and Winters during Jun 1989 - Feb 1997

	Summer (Jun, Jul, and Aug)				Winter (Dec, Jan, and Feb)			
	All Clouds	Thin ($N\varepsilon<0.5$) ($\tau_{vis}<1.4$)	Thick ($N\varepsilon\geq0.5$) ($\tau_{vis}>1.4$)	Opaque ($N\varepsilon>0.95$) ($\tau_{vis}>6$)	All Clouds	Thin ($N\varepsilon<0.5$) ($\tau_{vis}<1.4$)	Thick ($N\varepsilon\geq0.5$) ($\tau_{vis}>1.4$)	Opaque ($N\varepsilon>0.95$) ($\tau_{vis}>6$)
> 6 km	34%	15%	14%	5%	34%	15%	15%	4%
3-6 km	26	11	9	6	32	11	11	10
< 3 km	45	0	0	45	47	0	0	47
all levels	73	22	20	31	76	23	21	32

Table 2. The change in the frequency of cloud detection (all clouds and high clouds above 440 hPa) from Jun 1989 to Feb 1997. The change is percentage of observations that found cloud at the end of the study period minus the percentage of cloud observations at the beginning. High clouds observed by NOAA 10-12 increased 4-5% over land and ocean in the northern hemisphere; in the tropics this is closer to 2%. In the southern hemisphere high clouds increased by 3% over water and by 6% over land. NOAA 11 trends over land are problematic because of the orbit drift; NOAA 14 trends are difficult as they cover only 1.7 years to date.

OVER WATER

Latitude belt	All Clouds				High Clouds			
	10/12		11/14		10/12		11/14	
	mean	inc	mean	inc	mean	inc	mean	inc
23°-65° north	75.7	+3.1	74.3	+1.7	31.6	+4.9	33.1	+3.3
Tropics	76.8	+6.6	77.5	+2.1	39.0	+1.6	38.7	-0.4
23°-65° south	77.1	+1.7	76.1	+1.5	28.4	+2.7	29.7	+1.3

OVERLAND

Latitude belt	All Clouds		High Clouds	
	10/12		10/12	
	mean	inc	mean	inc
23°-65° north	75.4	+1.1	30.6	+4.2
Tropics	79.3	-2.1	48.5	+2.0
23°-65° south	73.5	-2.0	29.4	+6.2

Modeling and Simulation (M&S) of Atmospheric and Cloud Effects

Enhancing Wargame Realism Through Atmospheric Effects

Nelson A. Bonito*, *bonito@gpd.plh.af.mil*
Harris L. Gilliam, *gilliam@gpd.plh.af.mil*

Radex Inc.
3 Preston Court
Bedford, MA 01730
(781)275-6767
FAX (781)275-3303

Captain Mark M. Edwards, *medwards@plh.af.mil*

Space Vehicles Directorate, Air Force Research Laboratory
29 Randolph Road
Hanscom AFB, MA 01731
(781)377-4008
FAX (781)377-5640

ABSTRACT: The Atmospheric Effects Server (AES) is a distributed multi-process based system developed at the Air Force Research Laboratory for the purposes of providing realistic atmosphere weather impacts in a distributed interactive simulations. AES contains a multiple model interface to the Electro-Optical Tactical Decision Aids (EOTDA), an example of a legacy model integration, which provides detection and lock-on range predictions for a number of target and sensor types. Information is provided by the AES interface regarding the target background and local weather characteristics for use by the Thermal Contrast Model (TCM2) and Atmospheric Transmission Model (ATM). These models compute the infrared target signature and calculate extinction effect due to the weather as parameters to the Sensor Performance Model (SPM) to determine range predictions for the target. The AES model suite was extended to provide extinction calculations due to clouds (CTDA) based on data produced by the Cloud Scene Simulation Model. Each of these models (TCM2, CTDA, ATM, and SPM) are implemented as individual modules within the AES package, and together they can provide realistic line-of-sight range predictions for IR sensors based on current weather conditions at the target location. The AES offers a solution to the problem as an interface to the physics models that determine the "real" acquisition and lock-on ranges for a target/sensor condition, and forces Computer Generated Forces to alter their behavior in order to deal with current weather conditions.

1.0 Introduction

The current computer industry advancements has offered the opportunity to incorporate many of the earlier modeling and simulation contributions within the distributed simulation environment. The ability to process modeled environment data was usually limit by the available computational resource and the required simulation fidelity. These earlier limitations usually resulted in the application of fewer effects from the environment by defining the simulation outcome based on global area parameters. Real world environment representation and atmospheric effects were not considered and typically not applied within the real time distributed simulation. The Wargaming and Technology Assessment Branch, Surveillance and Control Division, Space Vehicles Directorate, Air Force Research Laboratory (AFRL/VSSW) has been working to advance the state of environmental impacts in a distributed

simulation by applying atmospheric effects to the simulation decision process. Effecting a simulation outcome using atmospheric data is a two step problem, data consistency across all the participating simulations and representation of the environmental effect in the simulation. This paper will address these problems and present the solutions used to incorporate weather effects in a distributed simulation with the development of the Atmospheric Effects Server (AES). The AES was successfully used as the core of the AFRL/VSSW Weather Wargame Series, and demonstrated a method for integration of non-real time legacy model effects into a real time distributed simulation [*Edwards, et al.*, 1997].

2.0 Atmospheric Data Distribution

Distribution of weather data to an interactive wargame simulation can involve numerous stages of data processing before the atmospheric data can be used by an effects server and an individual warfighter simulator. This task can be further complicated, since simulation facilities should attempt to obtain their data using similar method supporting for DoD mission operations, but operation methods are not always similar to the modeling and simulation requirements. The distribution of USAF Weather Agency (AFWA) products currently used to support USAF and US Army operations on a world-wide bases is just one example of the difference in operational and simulation requirements. AFWA produces theater scale weather products on a world-wide bases constantly, while a weather data request for a theater scale simulation may only require a unique time period with very specific atmospheric parameters. A method used to reduce the receipt of constant AFWA products and allow for the further selection of desired time periods is the Defense Modeling and Simulation Office (DMSO) Master Environmental Library (MEL) facility [*Lowe, et al.*, 1997]. MEL offers an access method to the suite of AFWA products including a key product produced using the Pennsylvania State University's Mesoscale Model 5 (MM5) the state of art in numerical weather prediction technology. MM5 model output is rarely used directly and requires "post-processing" diagnostic tools to produce many of the meteorological parameters of interest, but not all of the environmental parameters needed by effects models have been realized. The AFWA standard "post-processing" products have been extended using a MEL interface to AFRLDIAG processing for the remaining data for distribution to the Atmospheric Effects Server (AES) [*Smalley, et al.*, 1998]. Figure 1 represents the weather data and effects distribution paradigm used to support the AFRL/VSSW Weather Wargame Series.

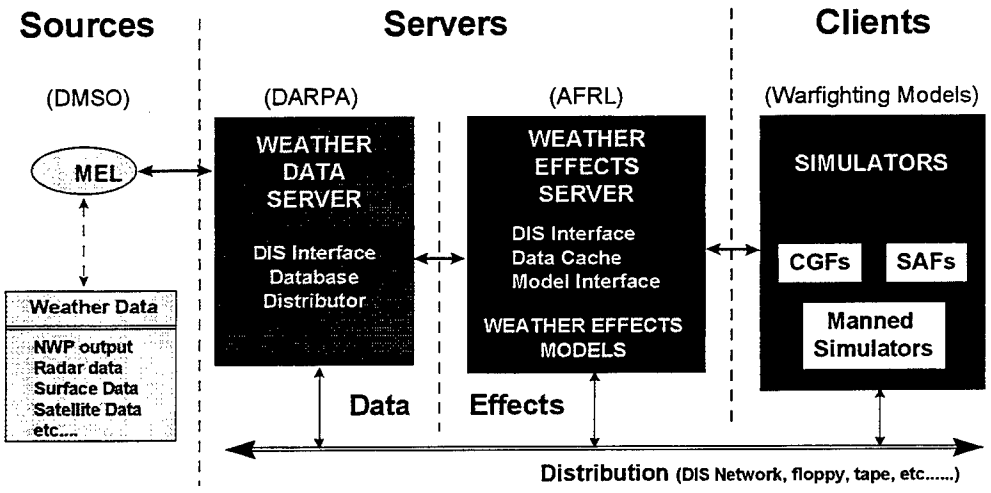


Figure 1 Weather Data and Effects Distribution Paradigm

Defense Advanced Research Projects Agency (DARPA) developed Total Atmospheric Oceanic Services (TAOS) Weather Server is a program designed to ingest weather data parameters and

distribute them, over time, in a distributed simulation. TAOS provides simulations with consistent data to an unlimited number of simulations with minimal impact to the distributed networking facility [*TASC,* 1998]. A limitation still exists between the simple distribution of data and the effect the data has on the simulation outcome, weather data alone does not always alter the warfighter simulator.

During the Synthetic Theater of War 97, TAOS was used as the weather distributor and pre-processed the data for extinction amount and extinction coefficients prior to distribution for use by the dynamic virtual world (DVW) inter-visibility algorithm [*Whitney, et al.,* 1998]. DVW and TAOS represented a major advancement toward introducing effects in the simulation environment, but still required each simulation to perform weather data interpretation and the calculation for inter-visibility. TAOS distributed parameters could still be used directly to perform less involved environment effects, but the more complex effects produced by changing weather data require a separate effects server to maintain uniformity across the simulations. The AES eliminated the redundant simulation processing by offering a "one-stop-shopping" calculation capability which supports numerous simulations with the desired inter-visibility. Another advantage to using the AES is the simplified access to the distributed weather data, and maintaining a consistency across numerous simulations without the requirement for weather data synchronization between distributed simulations.

3.0 Atmospheric Effects Server (AES)

The Atmospheric Effects Server (AES) is a distributed multi-process based system developed at the Air Force Research Laboratory for the purposes of providing realistic weather impacts in a distributed interactive simulations. The AES was conceived as a testbed and was design to be modular, allowing for reconfiguration with different models and to support varying architectures. The goal was not produce the definitive mechanisms for generating environmental effects, but to explore which techniques work best under which situations and the possible alternatives. A previous AFRL program called the Electro-Optical Tactical Decision Aids (EOTDA) was selected as the first legacy model to use in the demonstration of computing atmospheric effects for a simulation. EOTDA provided the three primary components, target signature, transmission loss, and sensor performance, for demonstrating the effect weather data can produce during a simulation. The AES is a stepping stone for major simulation programs now underway (JSIMS, JWARS, JMASS, etc.) to determine the direction that their environmental effects components should pursue.

3.1 EOTDA Server Prototype

The EOTDA Server was the "server" portion of a client/server approach to calculating atmospheric effects on the to 8-12 micron band commonly found in infrared weapon systems. The client was a simple computer generated force (CGF) which requested the information for determining whether or not a potential target was within the specified weapon system's performance envelope. This procedure is performed routinely in mission planning and execution using the appropriate operational data, meteorological information and terminal area forecast (TAF). The primary objective was to perform these operational procedures without intervention and modify the CGF's behavior based on the weather data being supplied. Various test cases were developed and in all cases the a stationary T-72 tank was targeted by an F-16 carrying an AGM-145 IR-guided missile. In each case the sensor detection range and lock-on range were degraded by 20 percent due to the inclusion of atmospheric transmission loss. This was demonstrated by a change in the behavior of the F-16 CGF needing to close the range before launching the Maverick missile at the target (Figure 2).

A further extension of the EOTDA Server was the addition of obscuration due to clouds, as another effect to the CGF's behavior. The use of standard meteorological information can not adequately represent the cloud resolution desired for a realistic engagement area and required the generation of

cloud fields using the AFRL's Cloud Scene Simulation Model (CSSM) coupled with the Fastmap post-processor to derive the 11 micron optical properties. The resulting data set is used by the Cloud Tactical Decision Aid (CTDA) to compute the total optical depth and further added into the total extinction calculation performed by the EOTDA Server module, IRTDA.

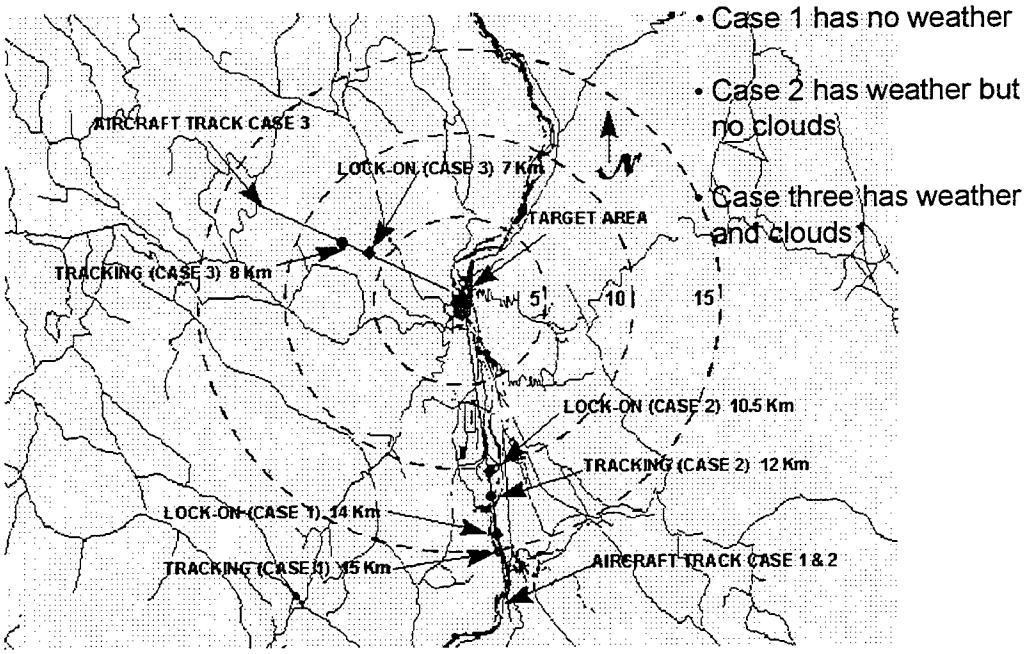


Figure 2 EOTDA Server Bosnia Test Scenario

3.2 AES General Design

AES consists of multiple processes operating independently to acquire sensor, target, and environmental information necessary for the calculation of weather effects on the sensor. A multiple model interface to the EOTDA was developed to further the capability of providing detection and lock-on range predictions for a number of target and sensor types simultaneously. Target background and characteristics along with the local weather parameters are collected from the Distributed Interactive Simulation (DIS) network using the AES DIS interface. The extinction effects are obtained from the model interfaces and passed to the sensor model to determine the realistic line-of-sight ranges. These models have been implemented as individual modules within the AES Model and can access the AES data base and network interface when tasked by a computer generated force (CGF).

The AES is based on a network client/server architecture with multiple processes operating independently in a distributed environment (Figure 3). This method allows the numerous interactions required to support a physics model in an interactive simulation. The simulation information is collected by the DIS Listener process, and filtered for the Protocol Data Units (PDU) required to track entities and the gridded environment. Listener received PDUs are ordered in a rotating buffer allowing a first in first out (FIFO) approach for processing the DIS traffic. Since the Listener only processes DIS traffic and uses shared memory to maintain the PDU data collected it presents a small burden on the computer resource ensuring limited lose of PDU data.

The Cacher, information processor and archive client, performs numerous tasks in conjunction with the Listener process to insure the information for all Entity State PDUs are stored properly. The Cacher uses a dynamic allocation data base storage technique which allows for any site, application, and entity

configuration to be stored and accessed by subsequent application using the entity triplet identification. This method eliminates various data storage problems associated with large exercises performed across numerous sites, and allows an entity to maintain greater information. The basic entity state PDU contents, such as operating condition and position, are stored in the data base and expanded to contain model computed information when available without expanding a relational data base table for all the entries. The Cacher will also process Gridded Data PDUs, distributed by TAOS, to produce a gridded weather field based on the contents and store the information for access by any AES client application.

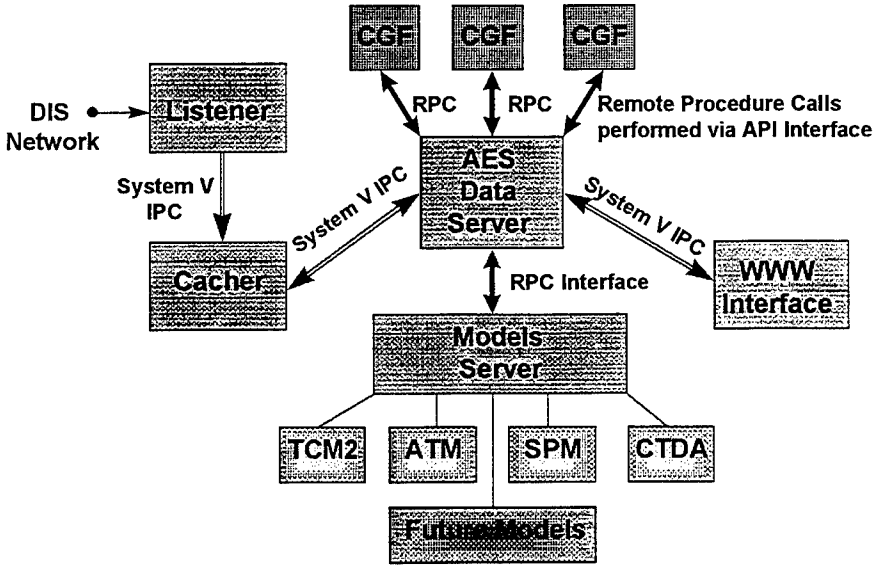


Figure 3 Atmospheric Effects Server Process Flow

The AES Model is written in C and is composed of the physics models that are part of the EOTDA code. The EOTDA models are implemented in FORTRAN and have been separated and embedded in the AES Model as modules which can be replaced in the future. The Model uses these modules to provide range predictions for IR sensors but can just as easily provide predictions for other types of sensors. Additional modules that were not originally part of the EOTDA have been added for cloud extinction calculation and liquid water concentration (LWC) based extinction calculations.

CGFs access the DIS data base information by registration as a client to the AES Data module. This module performs the needed data parameter association required by the physics models, manages numerous CGF request for modeled results, queries the Cacher for the available information needed by the models, and supplies the Cacher the model results for possible use by another request for information. The client/server interface allows CGFs and physics models the capability to interact with sequences of requests and allows the submission of the required batch requests for physics model parameters which can not be obtained in real time.

The Cacher client/server interface with the Data module will determine the need to perform the Model's thermal contrast (TCM2) calculation based on the targets position, orientation and location weather changes. A target motion and orientation are evaluated to determine any inconsistency and the target's data available indicator is modified in the Cacher data base to force a future Model process for updated information. This method eliminates the duplication of a target's thermal contrast calculation for a single CGF entity tracking the target or given numerous CGFs the possible redundant tracking of the same target. The CPU requirement for the TCM2 Model usage was greatly reduced for condition of many stationary targets within a medium scale simulation, and allowed for a larger number of simultaneous CGF engagements.

3.3 AES Distributed Implementation

AES implements various inter-process and networking principles to accomplish the passage of information between the various components. AES DIS Listener client provides the acquired PDU information to the Cacher client using System V IPC communication. The AES package also relies on the Remote Procedure Call (RPC) and External Data Representation (XDR) libraries, developed by Sun Microsystems, which are available on all UNIX platforms, to distribute the processes on the network. This mechanism also allows for a simplified interface to the AES API for the integration within distributed simulations requiring the AES. The Data server process communicates with the Cacher using the IPC mechanism, and communicates with the Model server process using RPC to allow for the distribution of processing load across various systems.

4.0 AES Model Components

The AES Model Server is a modification and extension of the EOTDA package which was also developed at the AFRL. EOTDA is a standalone program that uses three models to provide detection and lock-on range predictions for a number of target and sensor types. It runs in the UNIX environment using a Motif GUI under X Windows and in the DOS environment using a custom designed GUI. The UNIX version was selected as the starting point for the AES Model development, to maintain a single platform for comparison testing [*Dresksler and Goroch,* 1996]. The Thermal Contrast Model (TCM2) is used to compute infrared target signatures and a LOWTRAN based Atmospheric Transmission Model (ATM) is used to calculate an extinction coefficient. This extinction has four components: aerosols, molecular, battlefield contaminants and precipitation. Finally a Sensor Performance Model (SPM) provides range predictions based on the attenuated target signature and the sensor characteristics. These three models have been separated from the original EOTDA program and packaged as modules in the AES. This separation was done primarily for three reasons: first to embed them in a client/server environment, second to provide the output of each model as a product for clients of the AES, third to maximize performance because the AES needs to provide replies to clients with sub-second delays to support multiple engagements. The three EOTDA models coupled with the Cloud Tactical Decision Aid (CTDA) model and the Line Of Sight (LOS) model currently comprise the core of the AES Model Server. The CTDA module, developed by AFRL, uses the output of MM5 and Cloud Scene Simulation Model (CSSM) processing to calculate the extinction due to clouds. The LOS module uses MM5 liquid water concentration data to compute line-of-sight intervisibility.

The EOTDA models use typical weather parameters, temperature, dewpoint, precipitation, wind speed, wind direction, cloud cover and liquid water concentration, to provide realistic weather effects due to atmospheric extinction.. The CTDA model uses data produced by the CSSM to compute an extinction coefficient along the path between a sensor and target. CSSM uses the same MM5 data which is provided for the EOTDA models to produce a three dimensional cloud field. Fastmap processing is used to convert the field into a 3D extinction coefficient field for use by the CTDA model in computing extinction due to clouds for an IR sensor. The CTDA extinction is combined with the EOTDA extinction and passed to the sensor performance model to provide range predictions that take into account both aerosol and cloud impact. Weather Wargame exercises demonstrated the cloud effect on the Maverick missile's sensor by preventing a target acquisition until dropping below the cloud deck.

The EOTDA models provide support for air-to-ground engagements for 8-12 micron sensors, but supplies limited support for air-to-air engagements of 3-5 micron sensors. Work has begun on a

MODTRAN model which can be adapted for use in the AES [*Bernstein, et al.,* 1998], but it has not yet been integrated. As a proof of concept a simpler model was developed, Line Of Sight (LOS), which uses the MM5 3D liquid water concentration field as input. The LOS model processes the liquid water concentration along the path between the sensor and target to derive a "see-no-see" condition based on a specified water content threshold. The resulting indicator is returned to the requesting CGF and used to modify its behavior accordingly. During the Weather Wargame exercises the LOS model supported engagements between the High-Altitude Intercept Simulator (HAIS) and Theater Ballistic Missiles (TBM). The HAIS, a constructive airborne laser (ABL) demonstration, is represented using a command and control aircraft with a 3-5 micron infrared sensor and an ABL. During each of the exercises multiple TBMs were launched from different locations in the theater, which the HAIS needed to track and laser for a minimum of five seconds. Without the AES, a CGF of this type would have selected a cloud height and not engaged the target until the TBM cleared said altitude. The AES demonstrated situations where the HAIS could not track a TBM until it broke through thick low clouds. In another region of the theater with limited cloud cover, TBMs were tracked and destroyed seconds after launch.

5.0 AES Model Optimization

Using UNIX profiling utilities, it was determined that roughly 20% of the execution time was spent in the TCM2 model code. The delay incurred while doing a TCM2 run is typically between one and two seconds. This delay can not be tolerated in distributed simulation exercises with large numbers of participants, because RPC client processes are effectively blocked until the AES responds or the request times out (after approximately ten seconds). Furthermore, RPC doesn't support multiple concurrent connections, causing any client that attempts a communication with the AES to block until the request can be processed by the RPC mechanism. The consequence of these two limitations of RPC is that the first client of the AES incurs a one or two second delay in execution, but clients who make requests while the first is being processed will incur increasingly longer delays. The single request nature of RPC and the long execution time of TCM2 generates a large bottleneck in AES performance. Fortunately the TCM2 model does not need to be run for every CGF request, because the target/background contrast remains the same unless the target has a significant change in location or the weather changes between TCM2 calculations. To take advantage of this situation the results of TCM2 are cached for each target and eliminates the need to perform TCM2 processing on subsequent requests of the same target. The reuse of the cached TCM2 results and passage to the ATM model alone represents a significant increase in performance.

The AES method for processing a CGF request was modified to account for the single request limitation of RPC. When a client makes a request, and thermal contrast needs to be computed, the Model program runs TCM2 as a detached process and the AES replies to the client indicating that: 1) no range could be computed at this time and 2) the client should retry the request at a the next refresh cycle. If the client makes another request for the same target before the TCM2 process completes it will receive the same "try again" reply. Meanwhile, the TCM2 process continues to compute the target/background contrast and when complete caches the result for future requests. When the client eventually retries the request the AES provides a valid answer. This allows the AES to quickly respond to all requests, so as not to cause the client to block, while eventually providing the desired ranges. It also allows TCM2 to be run for multiple targets simultaneously.

The original EOTDA used a number of temporary files both for bookkeeping and passing data between the three models. In addition, the AES Model process originally received input via the RPC mechanism and produced files for the EOTDA code to read into FORTRAN common

blocks during the execution of the models. Profiling revealed that 17.5% of the total execution time was spent reading and writing the temporary and input files. An obvious optimization was to eliminate the use of temporary files and replace them with memory equivalents that could be copied for the RPC structures and FORTRAN common blocks.

The ATM code used in EOTDA computes extinction coefficients based on the weather conditions and aerosols at the target location. This includes surface characteristics and an approximation of the atmosphere below and above the cloud deck. The extinction coefficients are then fed into the SPM code which combines them with target/background contrast, target azimuth, sensor azimuth and sensor height to compute range predictions. During a typical exercise target location and weather conditions change slowly with respect to requests for range predictions. This means that extinction coefficients computed by the ATM code also change slowly. For this reason, extinction for sensor/target pairs is cached and when there has been no appreciable change in target azimuth, sensor azimuth and sensor height the cached extinction can be reused and fed directly to the SPM code.
999
The optimizations we implemented in the AES are a combination of on-demand execution of the models and extensive reuse of computed data, a simple distributed processing scheme providing parallel execution of time intensive code and replacing costly file I/O with in memory data transfers. The on-demand model execution and data caching has the effect of reducing range prediction to just the running of the SPM code for the majority of CGF requests. The Weather Wargame series demonstrated the effectiveness of this approach. We achieved sub-second response times in an exercise involving hundreds of entities. The AES was capable of handling multiple CGF requests per second exercising the TCM2 and extinction caching advantage.

6.0 AES CGF Application Program Interface

The API interacts with the server process, AES Data, to supply the CGF client with the acquisition range and lock on range for the target's current location and configuration. The AES Data interface server performs the processing for a client/server interaction with a CGF using RPC communication allowing the AES to support various CGF applications across a distributed environment. The API interface was applied within a Theater Battle Arena simulation environment generator known as the Theater Simulation Architecture run-time kernel (RTK). The necessary instructions were inserted to control the behavior of a CGF when intervisibility with a target was required. The HAIS simulation process was another CGF which applied the AES API to determine the atmospheric effects. The airborne sensor's intervisibility with a TBM has been implemented using an Atmospheric Transmission and Sensor Performance module within the AES Model Server process. The CGF has a missile detection process and will task another aircraft CGF to search for the transporter erector launcher (TEL) using the AES API for the target acquisition information.

The AES client/server architecture can be monitored using a web interface to allow the simulation operator full knowledge of the data processing status during the exercise. The client interface uses the Data and Cacher API to access needed information regarding the AES operating status. Various client utility routines have been developed to assist in viewing the contents of the Cacher internal data base. The ability to monitor the current gridded weather parameters and the entities being managed has made the network browser interface a valuable capability for tracking the status of the AES. The client utilities incorporate Common Gateway Interfaces (CGIs) requests to allow a quick simple Graphical User Interface (GUI) for the end user. The ease of integrating an AES API routines has allowed for greater web interface development as a tool in the validation process. These tools vary from textual CGF entity information to color coded graphic representations of the theater region.

7.0 Conclusion and Results

Currently Computer Generated Forces (CGF) in DIS simulations operate under the assumption of perfect weather conditions with limited mechanisms for providing the weather impact on a sensor performance. Targets are acquired and locked-on at the maximum theoretical range for a given sensor, which does not provide a realistic scenario for the warfighter modeling and simulation environment. The AES offers a solution to this problem by performing the physics model interface that determines the "real" acquisition and lock-on ranges for a target/sensor condition. The AES has been used to support a series of Weather Wargame exercises that demonstrated the feasibility of incorporating realistic effects codes in a distributed simulation. The exercises have demonstrated how variations in atmospheric aerosols can produce a 20% reduction in the lock-on range for an IR equipped missile without accounting for the line-of-sight extinction due to clouds. Clouds are non-uniform and add a further dynamic component for the computation of intervisibility. This aspect was demonstrated during the air-to-ground engagement in regions of low sparse cloud cover requiring a CGF to launch the missile at a much closer range. The AES also demonstrates the advantage of a modular design with the Model server's capability to support many physics models simultaneously. Future releases will include modules for LASER, TV and RADAR sensors and systems. The current suite of major simulation programs will need to address these issues as well, and if the development of the AES is supported to address air-to-air and space-to-ground effects, their task will be much easier.

REFERENCES:

Bernstein, L.S., et al., *A Rapid 3-5 Micron TDA Simulation Based on MODTRAN4*, Spectral Sciences Inc., Burlington, MA 01803.

Dresksler, S.B. and Goroch, A.K., *UNIX/X-Windows/Motif Electo-Optical Meteorological Decision Aid User Interface Design Document*, Naval Research Laboratory, Working Paper, 1996.

Edwards, M.M., et al., Architecture for Computing Atmospheric Effects Within a Distributed Environment, *Workshop Papers-1997 Spring Simulation Interoperability Workshop*, Vol. 1.

Lowe, S., et al., (1997), Product Generation within the Master Environmental Library (MEL), *Workshop Papers-1997 Spring Simulation Interoperability Workshop,* Vol. 2.

Smalley, D.J. and Mozer, J.B., AFRLDIAG: Tailored Meteorological Products for M&S, *BACIMO 1998*

TASC (The Analytic Sciences Company), TAOS: Dynamic METOC Environmental Simulation Services, *Final Technical Report, US Army Topographic Engineering Center,* 30 Jan 1998.

Whitney, D. et al., Impacts of the Environment on Warfighter Training: STOW 97 Experiences with TAOS, *Proceeding of the 3rd Simulation Interoperability Workshop*, Orlando FL, 1998.

Algorithms for Real-Time Tailoring of Environmental Data for Modeling and Simulation (M&S)

Peter S. Dailey, Todd A. Hutchinson, Steve O. Ouzts*
TASC, Inc.
55 Walkers Brook Drive
Reading, MA 01867-3297
Phone: (781)942-2000, Fax: (781)942-7100
Email: psdailey@tasc.com, soouzts@tasc.com

1. INTRODUCTION

One important objective of the Joint Simulation System (JSIMS) is to integrate physical environmental effects (atmosphere-ocean-space-terrain) across heterogeneous simulations to provide new levels of realism, consistency, and interoperability. In the construction of pre-distributed environmental scenarios, flexibility is critical to satisfy broad training objectives of various interests within the Modeling and Simulation arena. Specifically, on-demand tailoring of environmental data is required to make detailed adjustments to the scenario and to steer the training experience at run-time to meet specific goals. The objective of the JSIMS Environmental Tailoring Services (JETS) project is to develop techniques and guidance for this on-demand tailoring. JETS is sponsored by the Defense Advanced Research Projects Agency (DARPA) Advanced Simulation Technology Thrust (ASTT) program.

There is a significant difference between use and control of the synthetic natural environment (SNE) that has been acceptable in the past as compared to SNE control that is envisioned for JSIMS. In the past, scenario changes were primarily visual and had little impact on simulations. Presently, SNE control includes the ability to affect run-time changes to a scenario. Simulations and their operators need data and products that are consistent and derived from a common SNE if they are to engage in "fair play" and train in a realistic manner. It is the goal of JETS to develop algorithms that will take such run-time changes to the SNE and consistently reflect those changes in other SNE variables and times.

2. ALGORITHM DEVELOPMENT

New SNE technology provided by DARPA's Synthetic Theater of War (STOW) program and the Total Atmosphere Ocean System (TAOS) allows for high-fidelity, dynamic, physically consistent environmental data to be delivered to simulations for the first time [1]. The required ability to tailor *a priori* or edit in real-time the SNE presents a set of technical challenges.

Today there exist various techniques to "dial" the environment, but they are manual procedures requiring the user to deal with consistency and fidelity issues introduced by the edit. The user is ultimately responsible for assuring that edits will not lead to physically unrealistic scenarios and inappropriate training.

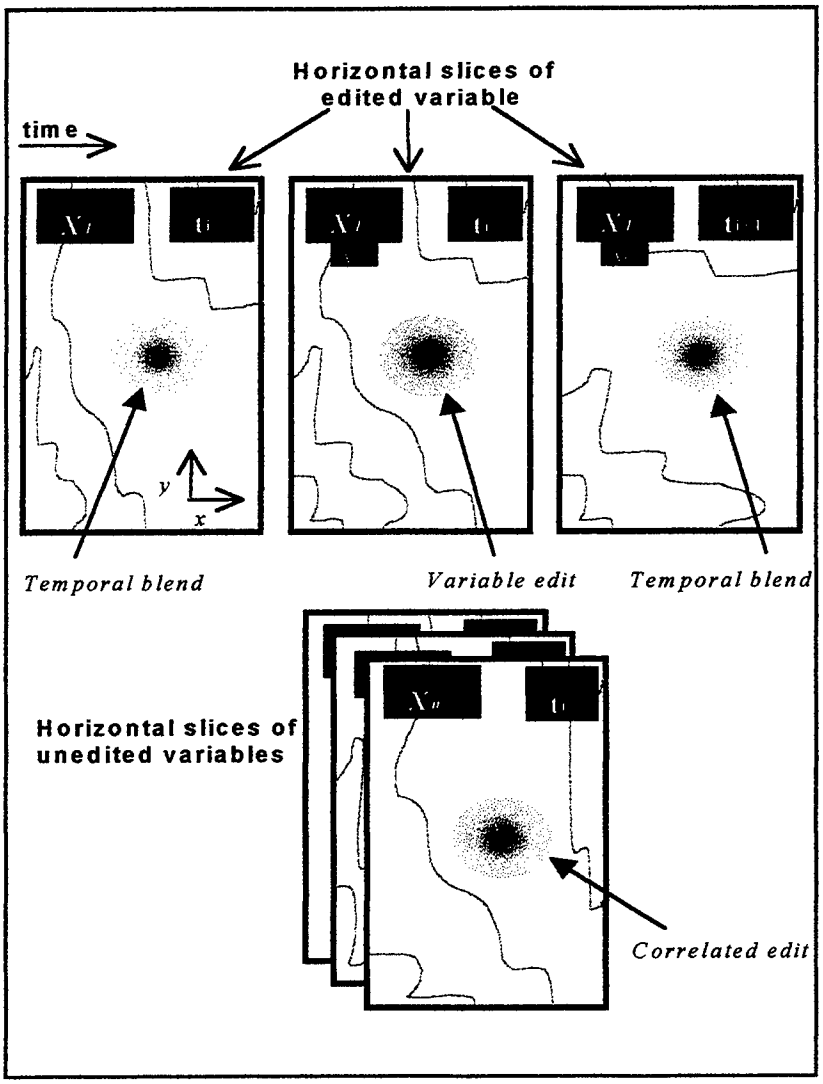


Figure 1. Variable and correlated edits and spatial and temporal blends.

2.1 Research Challenges

The key research challenges facing the JETS project are to:

- Maintain appropriate physical realism of tailored data across scenario(s) at multiple resolutions
- Retain realistic correlations between physically linked environmental parameters
- Achieve run-time efficiency and transparency
- Minimize SNE data and model construction costs while maximizing training benefits and flexibility

These challenges and our technical approach for studying them is detailed in a previous paper [2]. In developing tailoring algorithms for JETS, we will adopt an incremental approach starting with simple efficient procedures and move to more sophisticated ones.

Though tailoring algorithms developed by JETS can be applied pre-exercise or during run-time, it is the run-time application that constrains how computationally complex the approach may be. Namely, solution of the full set of nonlinear differential equations for the atmosphere (or ocean) is not feasible during a distributed exercise. For a real-time editing algorithm to be effective, it should:

1. Assure that edits made to one variable are appropriately reflected in other correlated variables in a realistic manner and that the edit is smoothed with the surrounding region

2. Avoid abrupt temporal changes to the SNE resulting from the introduction of an edit and modification of other variables at the same time

2.2 Definitions

In order to establish a common understanding of the algorithm development process, some terms need to be defined. Figure 1 shows a schematic of three snapshots of some state variable X_1 at times $t-1$, t, and $t+1$ where time t is the time at which SNE tailoring takes place. Below the snapshots of X_1 are snapshots of other correlated variables X_2, X_3, ... X_n at the edit time t.

A *variable edit* is a user-specified change to the environmental scenario over some region, whether it be *a priori* (pre-exercise) or during run-time. Typically, the edit is applied to one variable at a set of grid points within a rectangular subdomain. Variable edits may be implemented using a tool such as the Gridded Weather Editor available in TAOS. *JETS tailoring algorithms will not manipulate the edit itself.* JETS algorithms will however modify the following:

- other (unedited) variables within the region defined by the edit (edit region) at the same time – these are called *correlated edits*

- all variables within the edit region at prior and subsequent times – these are called *temporal blends*

3. A SIMPLE TAILORING ALGORITHM

Based on this procedure, we are currently developing a set of simple tailoring algorithms and are evaluating their performance from both a fidelity and efficiency perspective. Here, we introduce the approach and performance of one such algorithm, called Pressure-derived Field Manipulation (PFM).

3.1 Test Database for Algorithm Evaluation

To evaluate PFM and other algorithms, we have built a test SNE using the PSU/NCAR MM5 (Pennsylvania State University/National Center for Atmospheric Research Mesoscale Modeling

System Version 5) numerical model. An MM5 scenario is generated for a 24 hour period with state data saved every hour. Some model grid details are shown in Table 1. Further details pertaining to the MM5 model can be found in [3].

Lat/Lon Bounds	N-S: 35.8 to 44.2 N. lat E-W: 45.5 to 55.5 E. lon
Vertical levels	23 σ-levels
Grid spacing	50 km
Lowest vertical level	50 m AGL
Grid Projection	Lambert Conformal

Table 1. MM5 Grid Details.

The model is initialized using 1° x 1° NOGAPS (Navy Operational Global Atmospheric Prediction System) analysis fields from May, 1998 and run over a portion of the Middle East. Figure 2 shows the geographical coverage of the model domain.

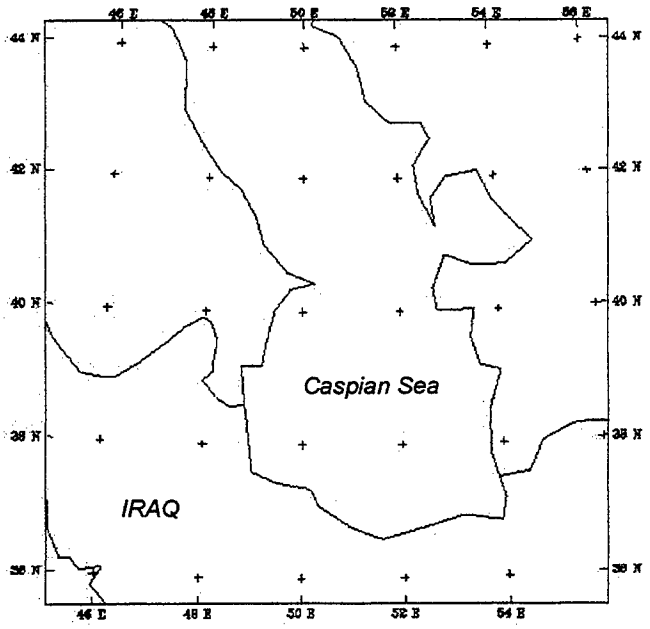


Fig. 2 MM5 model domain

The PFM algorithm is tested using an edit to the temperature field at t = 12 hours placed at 40.0 N latitude and 50.5 E longitude. We define the edit at that location with a magnitude of 5 degrees Celsius and a radius of influence r of 200 km. A weighting function specifies how the edit decays outward from the edit location ramping to zero at r.

Figure 3 shows the base state and edited temperature fields at the lowest model level at time t = 12 hours. Note that near the center of the figure, temperature contours reflect the placement of the variable edit.

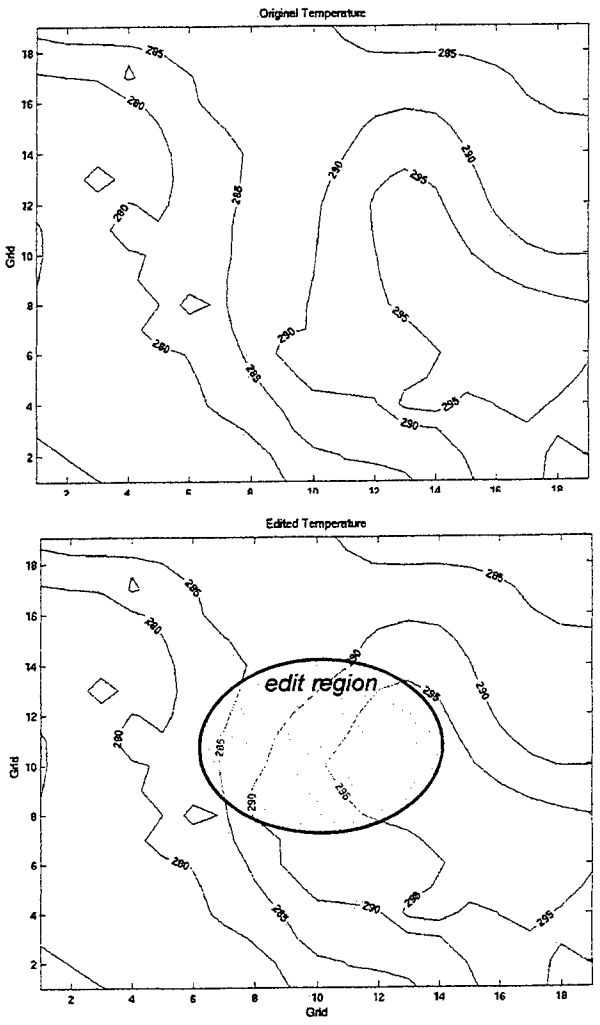


Fig. 3 The (a) unedited and (b) edited temperature fields at the lowest model grid level (50 m).

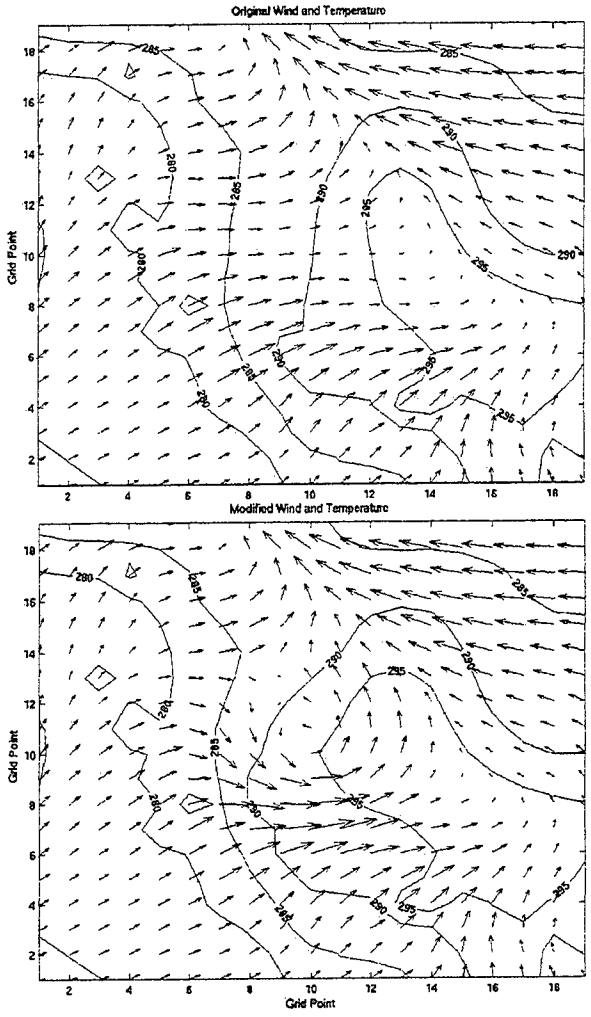


Fig. 4 The (a) unedited and (b) edited wind fields. Overlaid on each plot is the corresponding temperature field.

The goal is to first correlate the edited temperature field with an edit to other base state variables, then temporally blend all of the edited fields with the rest of the SNE. This involves the use of a correlation algorithm (in this case PFM) as well as temporal blending.

3.2 Pressure Field Manipulation (PFM) Algorithm

The first step is to use the edited temperature field to edit correlated fields at the same history time. Our approach is modeled after a method used by the U.K. Meteorological Office to manipulate operational forecasts fields [4]. The technique works as follows. A change to the mean sea level pressure field results in a change to the pressure (or geopotential height) and temperature fields above the edited pressure surface. These modifications are made using two

equations, the Ideal Gas Law and the Hydrostatic Equation[1]. From the modified temperature and pressure fields, we can calculate a new wind field using the Geostrophic Approximation[2]. Special adjustments to the near-surface wind field must be made to account for the effects of terrain and surface friction.

The method was originally developed to take changes to the underlying pressure field and adjust correlated fields such as temperature, winds, and cloud ceiling. Therefore, it is necessary for the technique to be extended for added flexibility. The procedure has been modified as follows. Depending on the variable being edited, a direct or indirect change to the pressure field is deduced. A change to the pressure field may require an iterative calculation that converges on an appropriate pressure field modification. The new pressure field is then used to modify the other fields.

Figure 4 shows the original and edited surface wind fields. Note the original wind field reflects westerly flow in the region of the edit. The *edited* wind field is calculated as follows. The geostrophic wind as it would exist at the surface (prior to the edit) is determined. This is subtracted from the original background winds to determine the "ageostrophic" component of the surface wind. Once edits to the surface pressure field are made, a geostrophic wind is calculated from the pressure field and then adjusted using the original ageostrophic wind. We believe this approach is a reasonable one for purposes of M&S tailoring.

Note in Figure 4, as the result of the temperature edit, there is a counterclockwise circulation in the wind field centered at the edit location. This results from the increase in temperature and corresponding decrease in pressure. This is a dynamically correct result based on meteorological principals of wind and pressure balance.

3.3 Temporal Blending

After application of the correlation process, the next step in consistent tailoring involves temporal blending of the edit with the surrounding SNE. The goal is to eliminate unnatural sharp gradients which occur between the time of the edit and adjoining times.

To perform the temporal blending, we have implemented a modified form of the Barnes' algorithm. The Barnes' approach [5] is typically used to assimilate observations such as radar and satellite data into a mesoscale or synoptic scale analysis and requires no background field for initialization. The iteration is defined as follows:

$$f_A^0(r_i) = \sum_{k=1}^{K_i} W_0(r_{ik}) f_o(r_k) \qquad [1]$$

$$f_A^{j+1}(r_i) + \sum_{k=1}^{K_i} W_{j+1}(r_{ik})[f_o(r_k) - f_A^j(r_k)] \qquad [2]$$

$$W_j(r_{ik}) = \frac{w_j(r_{ik})}{\sum_{k=1}^{K_i} w_j(r_{ik})} \qquad [3]$$

[1] The Ideal Gas Law relates the pressure, temperature, and density while the Hydrostatic Equation relates the vertical rate of pressure change to atmospheric density.

[2] The Geostrophic Approximation relates the wind field to the horizontal pressure distribution.

where $\mathbf{r}_i$ is the location of the ith analysis point, and $\mathbf{r}_k$, $1 < k < K_i$ are the observation station locations within its region of influence. The term f_A is the jth iteration of the analyzed value of f, and $f_o(\mathbf{r}_k)$ is the observation at location $\mathbf{r}_k$. $W_j(\mathbf{r}_{ik})$ is the specified weight function as a function of the absolute distance between observation and analysis gridpoint during the jth iteration and $f_A(\mathbf{r}_k)$ is obtained by forward interpolation of the analyzed value $f_A(\mathbf{r}_i)$ to the observation location.

The specified weight function is typically given by

$$w_j(r_{ik}) = \exp\left(-\frac{r_{ik}^2}{2L_j^2}\right) \qquad [4]$$

and is a function of the iteration number j. L_j is chosen as follows. Define $\gamma = L^2(j+1)/L^2(j)$ for all j, where $0 \leq \gamma \leq 1$. Then, $L^2(j+1) = \gamma^{j+1} L(0)^2$.

The algorithm is typically used to blend data in space, but we have adopted the approach to blend the SNE data in time. When applied to the test data, the Barnes algorithm improves the temporal blend of variable edits with the adjoining times significantly. Unrealistic gradients resulting from variable and correlated edits are smoothed.

The choice of how many prior and subsequent times over which to apply temporal blending is really quite similar in many respects to defining "region of influence" in correlated editing. The span of blend times can be hard coded into the algorithm, left up to the user, or based on a thresholding of temporal gradients resulting from the correlated edits. We are working on different weighting functions to apply in both the correlated edit algorithm (PFM) and the temporal blending algorithm.

It should be noted that temporal blending is often not critical to the integrity of the SNE database since typically the time spacing between data publications is an hour or more apart. That is, the variability of the atmosphere on the time resolution of the SNE data is already quite high. Thus, the additional variability introduced by edits to the SNE may be transparent to the exercise players. We do however believe that temporal smoothing improves the overall fidelity of the SNE.

4. SUMMARY AND FUTURE WORK

We have discussed a simple technique for consistent alteration of an SNE database. It is stressed that, although we are focused on the atmosphere in this example, the procedure can certainly be extended to other dynamic systems such as the ocean and space.

The technique involves the determination of a pressure perturbation resulting from a user-specified edit. The example of a temperature edit over a 200 km region of influence is used as

an example. Based on the modification of the pressure field, correlated edits are made to relevant state variables to reflect the physical effect of the edit (e.g., winds).

The final step involves the temporal blending of the SNE data at adjoining times. A modified version of the Barnes' algorithm is applied to eliminate sharp and unrealistic temporal changes in the edited field as well as correlated modifications to other fields. Again, the goal is to smooth the temporal transition into and out of the edit.

Future work will include the incorporation of more complex derived variables. These modifications to the technique may involve significant tradeoffs in efficiency. JETS' ultimate goal is to provide a flexible toolset of techniques of varying fidelity and complexity so that the user may choose what is appropriate given his or her tailoring needs.

6. REFERENCES

[1] Whitney, D. A., et al.: "TAOS: Providing and Managing Realistic Natural Environments for Virtual Worlds", Proceedings of the Fall Simulation Interoperability Workshop, September 1997.

[2] Driscoll, M. L., P. S. Dailey, and S. O. Ouzts, "Tailoring the Synthetic Natural Environment", Proceedings of Spring Simulation Interoperability Workshop, March, 1998.

[3] Grell, G. A., J. Dudhia, and D. R. Stauffer, 1995: *A description of the fifth generation Penn State/NCAR mesoscale model (MM5).* NCAR Tech. Note TN-398+STR, 122 pp.

[4] Carroll, E. B., "The formulation and testing of schemes to allow three-dimensionally consistent manual alteration of NWP fields", Forecasting Systems Technical Note No. 3, UK Meteorological Office, March, 1996.

[5] Daley, R., *Atmospheric Data Analysis*, Cambridge Univ. Press, 1991, 457 pp.

Acknowledgements

This work is sponsored by the Defense Advanced Research Projects Administration.

Author Biographies

Peter S. Dailey is an atmospheric scientist and the technical lead for atmospheric data integration on the TAOS project. Dr. Dailey received a B.A. and B.A.S. from the University of Pennsylvania, and a M.S. and Ph. D. from the University of California at Los Angeles.

Todd A. Hutchinson is an atmospheric scientist with an M. S. in Meteorology from the University of Oklahoma. Todd has worked on various Modeling and Simulation efforts.

Steve O. Ouzts, a retired US Air Force Colonel, has over 25 years experience in meteorology, space operations, modeling and simulation, and remote sensing. He has a B.S. from Auburn University, a M.S. in Atmospheric Dynamics from the Naval Postgraduate School, and an M.B.A. from the University of Nebraska.

Using a Numerical Weather Prediction Model (NWP) to Create Synthetic Environments for Military Training and Analysis and Cloud Animations

Peter S. Dailey, Todd A. Hutchinson, Robert A. Reynolds, Dana Sherer, Eric A. Kelley, James R. Staudinger
TASC, Inc.
55 Walkers Brook Drive
Reading, MA 01867
Phone: (781)942-2000, Fax: (781)942-2571
Email: tahutchinson@tasc.com

1. INTRODUCTION

Simulation systems play a key role in the ability of the military to prepare personnel for combat. These systems also provide useful information about the performance of weapons, both stockpiled and under development. A critical objective of the next generation of simulation systems is the integration of natural environmental (atmosphere-ocean-space) data to provide high levels of realism and consistency.

The TAOS (Total Atmosphere Ocean Services) system, developed at TASC, is a major application of the Defense Advanced Research Projects Agency's (DARPA) initiative in Advanced Distributed Simulation. TAOS can be termed an *environmental data server*. That is, TAOS software distributes both atmospheric and oceanographic data to virtual and constructive simulations from geographically distributed locations in a common synthetic battlespace. The volumetric data grids used in military simulation are often termed the Synthetic Natural Environment (SNE).

TAOS is designed to provide a consistent, detailed and dynamic description of the atmosphere-ocean-littoral environment using 4-D grids (3-D spatial and time) to provide a common representation of the natural environment. Until now, TAOS has largely relied on gridded forecast products such as those provided by the Defense Modeling and Simulation Office (DMSO) Master Environmental Library (MEL). With the recent availability of mesoscale models able to run efficiently and dependably in a workstation environment, the generation of "custom" gridded fields has become feasible. The long-standing record of success and acceptance for MM5 makes it a logical choice for enhancement of the TAOS system.

2. ENHANCED MM5 FUNCTIONALITY

Most users of TAOS are not meteorologists. Rather, they are members of the Department of Defense's Modeling and Simulation (M&S) community. Note *M&S* has a very specific and perhaps unfamiliar meaning here. Numerical weather prediction (NWP) models (such as the Pennsylvania State University/National Center for Atmospheric Research (NCAR) MM5) can be used to create an environmental scenario or database which, when supplied to these simulations by TAOS, act as their synthetic environment.

Often the lack of meteorological expertise on the part of a TAOS/MM5 user creates a unique challenge. Thus, the challenge becomes: "How to integrate MM5 within the TAOS framework so that it accepts basic constraints set by the *layman* user" From a software perspective, one needs to assure that the model is numerically stable and computationally efficient.

It is important to keep in mind that though the TAOS/MM5 user is a novice when it comes to running a numerical model, (s)he has specific requirements and objectives in mind with regard to the model output. For example, the M&S user may want the synthetic battlespace to be centered over Iraq in mid-December with persistent cloudiness and several precipitation events. In order to drive the model to produce such an environment, the model must be setup and initialized appropriately.

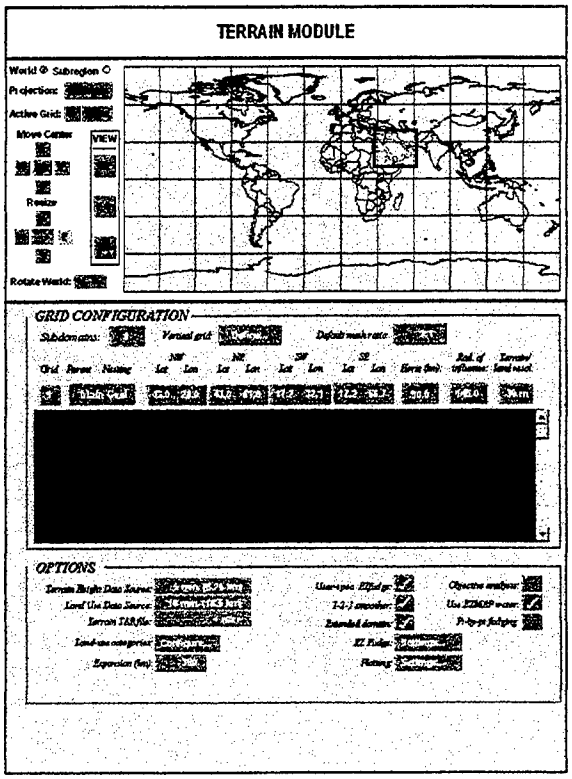


Figure 1. TERRAIN Graphical Interface.

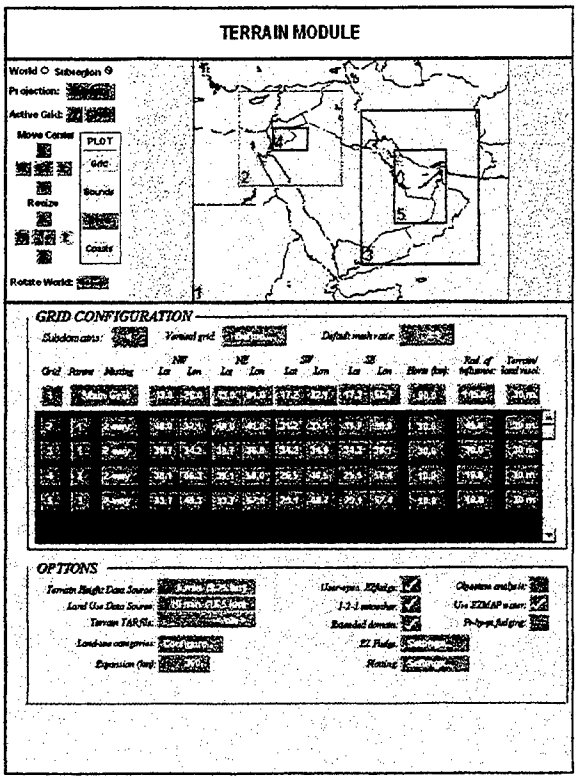


Figure 2. TERRAIN Subregion Interface.

One can envision a configuration of MM5 that allows the model to run repeatedly with minimal run-to-run modification. There are a number of model parameters that can be set *behind the scenes* based on discrete modeling theory and the objectives of the model run. A simple example is the Courant condition which permits an intelligent choice of time step based on the domain spatial resolution.

The three most important considerations for configuring MM5 to run in a semi-automated mode are (1) choice of domain, (2) model initialization, and (3) consistent and appropriate parameterization settings. The following three sections discuss our approach to handling these issues.

3. INTERACTIVE SETUP OF THE MODEL DOMAIN

MM5's TERRAIN module handles the surface elevation and land use categories based on the user's choice of spatial resolution and map projection. To run TERRAIN, the TAOS system must properly specify the TERRAIN parameters at the same time making the domain setup procedure user friendly.

TASC has developed a Graphical User Interface (GUI) which accepts basic user input and creates the TERRAIN deck for MM5 pre-processing (Fig. 1).

At the top of the interface, the user selects the coarse domain by "rubber banding" the desired region with the mouse. A keyboard option allows the user to see the latitude/longtitude position of the cursor for more precise selection. Once a region has been selected, the box can be repositioned or resized using grid positioning tools to the left of the global map. Note that for the military training application described here, MM5 must be setup to run over any portion of the world. Because the cylindrical equidistant world map greatly distorts polar latitudes, there is an option to work from a polar stereographic projection when the user is interested in creating an SNE over high latitudes.

Below the map, the TERRAIN GUI displays the corner coordinates of the coarse grid. It is here that the horizontal resolution and other parameters are defined for each grid. TERRAIN parameters applicable to all grids are included in the Options menu at the bottom of the GUI. Based on the entries in the TERRAIN GUI, a "terrain deck" is produced and used to run the TERRAIN program.

Once the coarse grid has been defined, the user may see a close-up view of the selected domain by choosing the *subregion* option to the left of the world map. The subregion GUI is shown in Figure 2.

The ability to view interactively the selected domain is an attractive feature for the M&S user. There are several map display options included on the Subregion interface including rivers, political boundaries, and grid overlay. The grid overlay option can be particularly useful to the M&S user when the positioning of a strategic location at or near a model grid point is necessary.

Once in Subregion mode, the user may "rubber band" within the coarse grid to define up to nine nests. The corner coordinates and grid parameters are displayed in a scrollable window located below the map. The user may reposition or resize the coarse grid and any predefined nests. Built-in logic assures that nests are created according to MM5 nesting rules. For example, in Figure 2, when Grid #4 is created, the mouse is not allowed outside of Grid #2 boundaries. A two-way nest automatically "snaps" to its mother grid adhering to the 3:1 nesting ratio.

Similar GUIs have been developed to run all of the pre-processing modules as well as MM5 itself. Many parameters in the GUI system have a default setting which is rarely modified. The MM5 Master GUI control (not shown) allows the user to save interface settings once (s)he has settled on a configuration to be used for multiple runs.

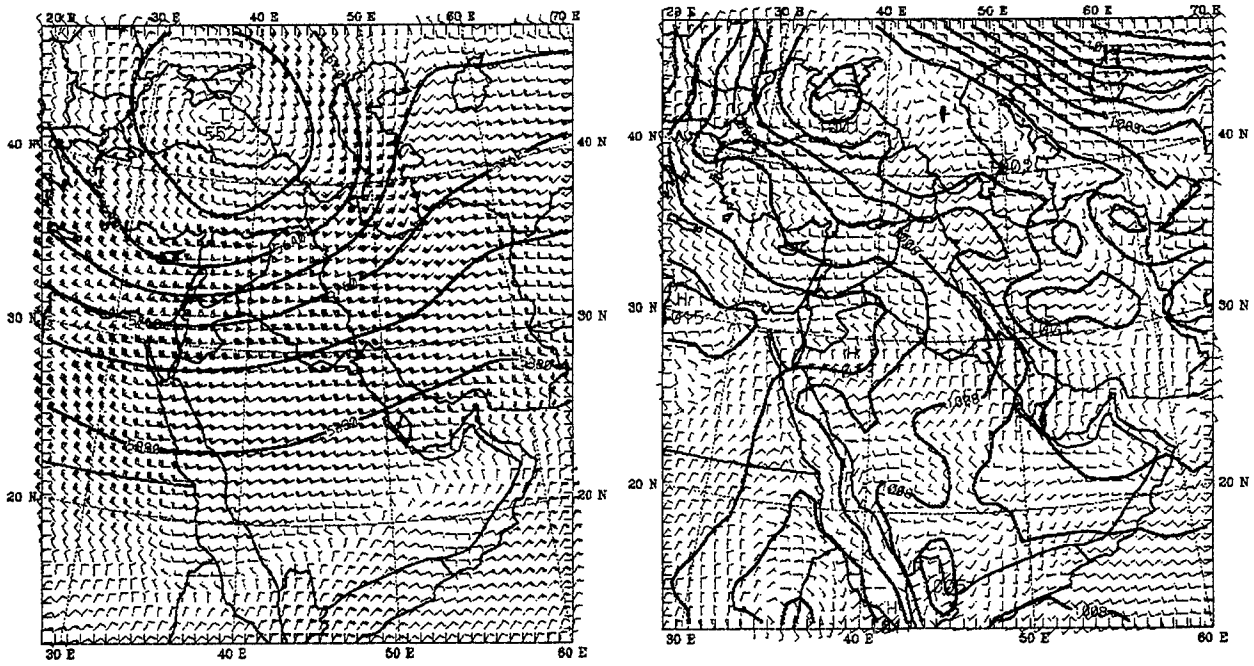


Figure 3. 6 hr MM5 model forecast over the Persian Gulf. Model is initialized using NOGAPS fields from 00 UTC 21 May 1998. Horizontal resolution is 90 km (coarse grid) with 23 standard levels. Panel [a] shows 500 mb heights (60 m contour interval) and wind barbs (2.5 m/s per flag); Panel [b] shows surface pressure (2 mb contour interval) and wind barbs.

4. MODEL INITIALIZATION FOR GLOBAL SIMULATION

Most research and real-time applications of MM5 have been run over the North American continent. The military training community, however, is interested in exercises positioned over many regions of the world. As seen in Figs. 1 and 2, the TERRAIN GUI allows the user global specification of the model domain. The next logical step is to initialize the model for the selected portion of the world.

Though the M&S community is not concerned with running MM5 in real-time, users would like to initialize the model with fairly contemporaneous data suited to a desired scenario (e.g., high-pressure, moist, summer). In order to run the model anywhere in the world, initial fields must be obtained from a global model. These requirements have created the necessity for a new version of the DATAGRID initialization module which is primarily meant to read NCAR's archive of the National Center for Environmental Prediction (NCEP) re-analysis fields.

TASC has formulated a new version of DATAGRID which can be "plugged" in to replace of the old version. The module creates initialization fields based on a user-selectable data source in GRIB (GRIdded Binary) format. Though the module is currently being used to obtain data from the NOGAPS (Navy Operational Global Atmospheric Prediction System) model, it can also be used to import data from models more familiar to the operational community (e.g., AVN, ETA).

TASC has run and tested MM5 initialized with NOGAPS data for four regions of strategic interest to the M&S community: (1) Southwestern Asia, (2) Southwestern United States, (3) Korea, and (4) Europe. The results of one MM5 run over Europe is shown in Figure 3.

The model is run over Saudi Arabia and the Persian Gulf with a coarse grid and two nests. The coarse grid resolution is 90 km with the finest nest resolution set to 10 km. Review of the model output has confirmed that the SNE created by MM5 contains interesting mesoscale structure and greatly enhances the coarse NOGAPS forecast.

5. LOGICAL LINKS FOR MM5 PARAMETERIZATION

In order to integrate the model, the user must appropriately set MM5 module parameters. For many of the MM5 parameterizations, there are a variety of options available to the user. In most cases, model sensitivity to these settings is highly dependent on the environmental scenario being modeled in addition to secondary factors such as orography and synoptic conditions.

A goal of TAOS/MM5 is to avoid forcing the user to modify parameters unnecessarily. At the same time, we must alert the user to those parameters which are an important part of scenario objectives. The "built-in" intelligence which lies behind the GUI system is an important aspect of this tradeoff. Namely, there are a variety of parameters that can be set to a default while others cannot. Of the parameters requiring input, some can be determined by the software based on grid, timing, and resolution settings while others will require direct user input.

Take as an example the choice of map projection chosen for an MM5 run. The TERRAIN module depends on user selection of an appropriate map projection for the chosen domain. The TERRAIN GUI is set up to automatically select a map projection based on the location of the center latitude/longitude pair for the coarse grid. If the grid is centered in the tropics, a Mercator projection is chosen. For middle and polar latitudes, the projection defaults to Lambert Conformal and Polar Stereographic respectively. These *logical links* are a part of the GUI software.

Choice of projection is an example of a "flexible" parameter for which the user may override the GUI selection. There are several reasons a user might want to change the default. For instance, though the center latitude/longtitude may be located in the tropics, a fine resolution nest located in the mid-latitudes may be a strategic part of the synthetic environment thus prompting the user to choose the Lambert Conformal projection appropriate for the fine grid region.

6. SUMMARY

The MM5 modeling system has been used to create synthetic environments for military training and analysis. In order to accommodate the requirements of the M&S community, several of the pre-processing modules were enhanced. A TERRAIN GUI allows the user to interactively specify the model domain including nested grids. The GUI permits resizing and repositioning of

all grids prior to running TERRAIN. It also prevents the user from breaking MM5's grid nesting rules.

A new version of the DATAGRID module was written to allow for ingestion of GRIB data from a variety of operational sources including NOGAPS, the Navy's operational forecast model. The model has been run and tested on several globally strategic areas of interest and has been shown to enhance coarse NOGAPS fields.

The GUI system features logical links so that required user input is limited to necessary parameters. These links allow for relatively simple model setup for the novice user while allowing an expert user to have precise control over model setup and parameterizations.

MODELLING OF THE PERFORMANCE OF LASER RANGE FINDERS UNDER THE INFLUENCE OF OBSCURANTS

A. Dimmeler*, D. Clement
Forschungsgesellschaft für Angewandte Naturwissenschaften e.V.
Forschungsinstitut für Optik (FGAN-FfO)
Schloss Kressbach, D-72072 Tuebingen, F. R. Germany
Tel.: #49-7071/709 145, Fax.: #49-7071/709 270, e-mail: alwin@ffo.fgan.de
Doc.: FGAN-FfO 1998/78

SUMMARY

At the FGAN-FfO, a model is being formulated to predict the performance of LRF while accounting for effects such as multiple scattering, turbulence and target speckle effects.

Time resolved return signals of two laser range finders at 1.54 μm and 10.59 μm are compared with numerical predictions. Using the computed scattering functions, quantitative agreement with respect to temporal behaviour and absolute magnitude of LRF pulses back-scattered by the smoke clouds is obtained in most cases.

Good agreement is found when predicted statistics of LRF ranging results are compared with measured data of US SMOKE WEEK XV. This includes cases where in the experiment the LRFs indicated multiple returns, the first echo being caused by the smoke screen, the second by the hard target behind the screen.

1. OBJECTIVE

There are well established models for predicting the performance of EO devices. Their options for modelling atmospheric effects, however, are often simplistic. On the other hand, there are models which describe the atmosphere in a detailed manner but do not predict EO system performance. There is no model established which predicts the performance of a LRF while adequately accounting for effects such as multiple scattering in smokes, fire induced turbulence, and speckle. To meet these goals, an LRF module is being formulated as part of the more general model COSMOS (Combined Optical/IR Sensor Modelling in the Presence of Obscurants and Smokes).

This paper addresses the modelling of LRF systems operating through smoke clouds. In Chapter 2, analysis results are presented and compared to experiment. Chapter 3 contains the basics of the COSMOS LRF model and the comparison of model predictions with experimental data. Model validation is based on data measured during US SMOKE WEEK XV (SW XV) [Kleindienst, 1995]. Participation in SW XV was possible through the former NATO AC/243 (Panel 4/RSG.15).

2. CALCULATIONS USING NBMSCAT AND COMPARISON WITH MEASUREMENTS

Propagation of laser radiation through smokes is well described in the narrow-beam multiple-scattering module NBMSCAT [Bissonnette, 1995]. For a specific receiver geometry this model calculates the transmitted and backscattered irradiance profiles, the on-axis transmitted power and the lidar returns. This relates to the signal obtained with the LRF from the smoke cloud.

The wavelengths considered correspond to the two LRFs used in SMOKE WEEEK XV. These were a Raman-shifted Nd:YAG operating at 1.54 μm and a CO_2 LRF operating at 10.59 μm.

A smoke specific input for the calculations are the phase function data which were computed for two experimental smokes (brass, fog oil/graphite) of the SW XV trials [Dimmeler, 1998].

Calculation for brass smoke

Fig. 1 (left) shows the return signals for an absorption coefficient of 200 km^{-1}. This value was chosen to yield a single pass transmission of app. 1% with a cloud thickness of 25 m. A single pass transmission of app. 1% is compatible with the measured transmission data.

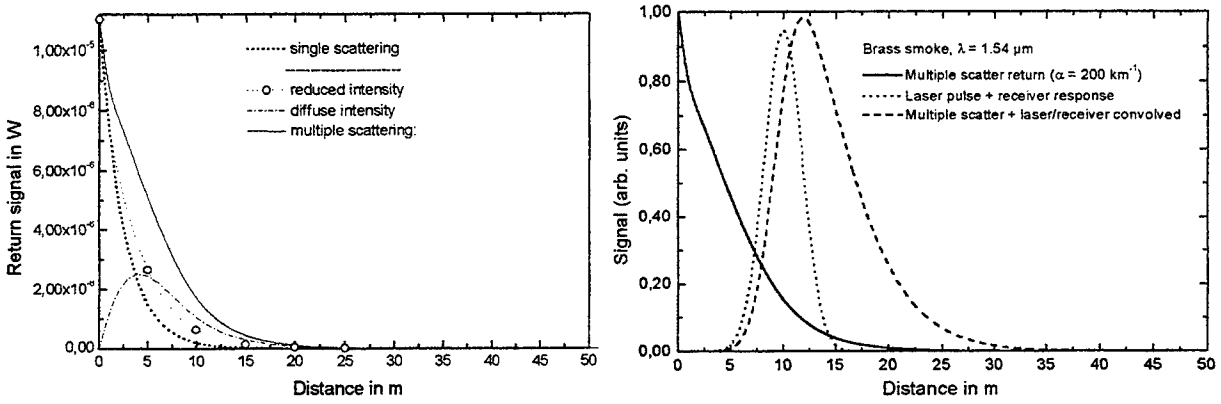


Fig. 1: Computed power backscattered from brass smoke as received by the 1.54 μm LRF for an extinction coefficient of $\alpha = 200\ km^{-1}$ (left). Multiple scattering signal ($\alpha = 200\ km^{-1}$), equivalent laser pulse and receiver electronics response function, and convolution of both (HW is app. 8.5 m).

The scatter signal and the system response due to laser width and receiver bandwidth is given in Fig. 1 (right) in normalised form. The laser HW is app. 0.9 m and the computed pulse width equals apparently about 8.5 m. This value corresponds to the measured value of 5.5 m. The calculated received backscattered power is 11 μW (measured: 10 – 20 μW).

For the CO_2 LRF the same extinction coefficient as for the Nd-Raman LRF was used since the transmission showed the same behaviour at both wavelengths. The result of app. 10 m for the HW is the expected measured value of 11 m. For the CO_2 LRF, however, there is a difference between the calculated (5 μW) and observed (app. 2 μW) power. This is due to uncertainty in emitted CO_2 LRF power giving rise to a large uncertainty in the calculated power received.

Calculation with fog oil/graphite

The results of the calculations showed again the expected values for the HWs of both LRFs. Again, there was a considerable difference between the calculated and observed power for the CO_2 LRF, unlike the Nd-Raman results. As before, this is attributed to uncertainty in emitted CO_2 LRF laser power.

3. LASER RANGE FINDER MODELLING AND COMPARISON WITH SW XV MEASUREMENTS

The class of LRFs discussed uses pulsed laser sources and incoherent detection. For modelling LRF performance it is required to compute the pulse power reaching the detector. This is done

by the *laser radar equation*. Here the effects of e. g. turbulence and aerosol extinction enter.

The detection process is described by the Noise Equivalent Power (NEP) of the system. The Threshold-to-Noise-Ratio (TNR) is set to a certain multiple of NEP to prevent false alarms by noise. To obtain a particular detection probability it is required to maintain a certain Signal-to-Noise-Ratio (SNR) which is a function of threshold (false alarms) and detection probability.

Time Programmed Gain (TPG) or Time Programmed Threshold (TPT) and receiver aperture averaging are not included here.

3.1 Laser radar equation

The signal received by a detector is described by the *laser radar equation:*

$$P_r = P_t \rho \frac{D^2}{4R^2} \tau_o \tau_A \tag{1}$$

P_r: power received by detector,
P_t: effectively transmitted power,
ρ: reflectivity of target (reflected angle = incident angle),
D: diameter of entrance optics,
R: range (distance),
τ_o: transmission of optics (includes reflections and absorption in the receiver as well as losses due to field stops (laser divergence larger than receiver field of view)),
τ_A: atmospheric transmission (double pass).

Eq. 1 implies that the target is larger than the beam diameter. This leads to an R^{-2}-dependence of the return signal. It becomes the equation for determination of range if the undetermined P_r is replaced by the minimum power P_{min} which is required to achieve ranging with pre-set conditions, in practice with a certain probability of detection p_d and a certain false alarm probability.

3.2 False alarm and detection probability in Gaussian noise

The discussion follows [RCA Corp., 1974, 109ff], repeating some of the computational steps. The noise current of the detector or the noise voltage after amplification is described with sufficient accuracy by Gaussian statistics.

False alarm probability and false alarm rate

The relation commonly used for the false alarm rate (FAR) is found in [RCA Corp., 1974],

$$\mathrm{FAR} = \frac{\mathrm{BW}}{\sqrt{3}} \exp\left(-\frac{I_t^2}{2 I_n^2}\right) = \frac{\mathrm{BW}}{\sqrt{3}} \exp\left(-\frac{\mathrm{TNR}^2}{2}\right) \tag{2}$$

I_t: threshold current,
I_n: average noise current,
BW: system bandwidth (BW = $1/(2\tau)$, τ: laser pulse length),
TNR: Threshold-to-Noise-Ratio.

An empirical relation between optimum bandwidth and pulse width (HW τ_H) was found experimentally by developers at the company Eltro

$$BW \cong 1/(3\ \tau_H). \tag{3}$$

This formula is used in the subsequent computations and in the computer code.

The required quantity of LRFs is the false alarm probability p_{FI} during ranging. One approach is to multiply the FAR with the time gate associated with the maximum range of the LRF τ_m

$$p_{FI} = \text{FAR} \cdot \tau_{m.} = \text{FAR} \cdot 2\, R_{max} / c \tag{4}$$

R_{max}: maximum measuring range of the LRF,
c: speed of light.

Eq. 4 is strictly valid if p_{FI} is the value associated with the absence of a real target or when multiple pulses are counted. In a real situation with first pulse logic one would encounter a smaller false alarm probability, because τ_m is cut short with the real return.

Detection probability

The detection probability is [RCA Corp., 1974, 111],

$$p_d \cong \frac{1}{2}\left\{1+erf\left(\frac{I_s - I_t}{\sqrt{2}\, I_n}\right)\right\} = \frac{1}{2}\left\{1+erf\left(\frac{\text{SNR}-\text{TNR}}{\sqrt{2}}\right)\right\} \tag{5}$$

SNR: Signal-to-Noise-Ratio,
TNR: Threshold-to-Noise-Ratio.

The difference SNR – TNR is called the Signal-to-Noise-Excess SNE of a LRF.

Pulse Peak Intensity Jitter of the Emitter

Laser pulses do vary. For the assumption of a Gaussian distribution of the pulse peak intensity jitter with a standard deviation (STD) σ_j the detection probability is [Accetta, 1993]

$$p_d = \frac{1}{2}\left\{1 + erf\left(\frac{\text{SNR}-\text{TNR}}{\sqrt{2}\,(1 + \sigma_j^2 \cdot (\text{SNR})^2)^{0.5}}\right)\right\}. \tag{6}$$

The corresponding definition of the Signal-to-Noise-Ratio SNR′ is

$$\text{SNR}' - \text{TNR} = (\text{SNR} - \text{TNR}) / (1 + \sigma_j^2 \cdot \text{SNR}^2)^{0.5}. \tag{7}$$

3.3 Turbulence effects

With regard to laser propagation, atmospheric turbulence may cause severe fluctuations of the pulse peak intensity. In case of weak turbulence the variance of the log-amplitude (logarithm of the amplitude) of a spherical wave is approximately [Accetta, 1993]

$$\sigma_\chi^2 = 1.058\, \lambda^{-7/6} L^{11/6} C_n^2 \tag{8}$$

λ: wavelength,
L: path length,
C_n^2: refractive-index structure constant (C_n^2 may assume values up to $10^{-13} m^{-2/3}$),
σ_χ^2: log-amplitude variance.

For the log-amplitude variance σ_χ^2 and the variance of the normalised intensity ($\langle I \rangle = 1$) σ_I^2 one has the relation

$$\sigma_\chi^2 = \exp(4\ \sigma_I^2) - 1. \tag{9}$$

Applying this to the experiments with the Nd-Raman LRF and assuming a moderate turbulence of $C_n^2 = 10^{-14}\ \mathrm{m}^{-2/3}$ one finds a standard deviation of the normalized intensity of $\sigma_I = 0.46$.

Scintillation reduction due to averaging by a diffuse scatterer

Laser pulses were recorded prior to the deployment of the smokes. The standard deviation is certainly less than 5% (including the laser pulse intensity jitter) and not the predicted 46%. This unexpected result is explained by scintillation averaging due to diffuse scattering from target.

At a distance L the appearance of the laser beam is determined by the Fresnel length $(\lambda L)^{1/2}$. The correlation length of intensity *and* phase equals approximately the Fresnel length. If the beam diameter $D = 2\delta L$ (δ being the divergence half angle) is larger than the Fresnel length, the beam is broken up in patches (or speckles) with an average length of $(\lambda L)^{1/2}$.

After *diffuse* reflection the patches act as sources independent in intensity and phase. Adding these patches should give the reduction of scintillation. A calculation finds for the scintillation reduction factor [Yura, 1985]

$$A = \frac{\sigma_I^2}{\sigma_L^2} = \frac{1}{1 + \left(1.74\,\delta\sqrt{L/\lambda}\right)^{7/3}} \tag{10}$$

σ_I^2: average intensity variance,
σ_L^2: variance seen by a point detector at L.

For cases of interest the denominator is >>1. Then the scintillation factor is approximately

$$A \approx 0.275\,\frac{\lambda}{\delta^2 L} \tag{11}$$

The geometry of a non-coaxial LRF allows to assume *uncorrelated paths* for the direct and the return path. In this situation the total variance is computed as

$$\sigma_\chi^2\ (\text{two way}) = 2 \cdot \sigma_\chi^2\ (\text{one way}). \tag{12}$$

Including (12) and the scintillation reduction factor in Eq. 8 one has

$$\sigma_{\chi,A}^2 = 2\ \ 1.058\ \ 0.275\ \delta^{-2}\ \lambda^{-1/6}\ L^{5/6}\ C_n^2. \tag{13}$$

It is seen that for a given δ the intensity fluctuation is virtually independent of the laser wavelength - the wavelength dependent change in intensity fluctuation is essentially compensated by the scintillation averaging.

For the experiments and a moderate turbulence ($1 \cdot 10^{-14}\ \mathrm{m}^{-2/3}$) one has $\sigma_{\chi,A}^2 = 4.26\ 10^{-4}$ and $\sigma_{I,A} = 0.04$. This value for *diffuse* reflection is in better agreement with experiment than the value above – for *glint* reflection one has to use Eq. 8.

According to [Accetta, 1993] one calculates the excess SNR factor which is required to obtain a certain detection probability p_d in the presence of turbulence with log-amplitude variance σ_χ^2

$$\text{XFTURB} = \exp\{\sqrt{2}\,\sigma_\chi\,\text{erf}^{-1}(2\,p_d - 1) + 0.5\cdot\sigma_\chi^2\}. \qquad (14)$$

where erf^{-1} is the inverse of the error function. For the averaged variance $\sigma_{\chi,A}^2 = 4.26\ 10^{-4}$ for *diffuse* reflection (see above) and a p_d of 99% one obtains XFTURB = 1.05.

Under the same conditions Eq. 8 yields for *glint* reflection XFTURB = 2.26.

3.4 Range determination of laser range finders

To determine the range of an LRF one uses Eq. 1, replacing the (undetermined) received power P_r by the *minimum power* $P_{min} = P_{r,min}$ adequate for the desired detection attributes

$$P_{min} = P_t\,\rho\,\frac{D^2}{4R^2}\,\tau_o\exp\{-2\,(\beta\cdot R+\alpha\cdot CL)\}$$
$$P_{min} = \text{NEP}\cdot\text{SNR}\cdot\text{XFTURB} = \text{NEP}\cdot(\text{TNR}+\text{SNE})\cdot\text{XFTURB} \qquad (15)$$

NEP: Noise Equivalent Power of the receiver for the actual bandwidth,
SNR: Signal-to-Noise Ratio,
TNR: Threshold-to-Noise Ratio associated with a particular false alarm probability,
SNE: Signal-to-Noise-Excess associated with a particular detection probability,
XFTURB: Excess factor required for detection with turbulence,
β: volume extinction coefficient of the undisturbed atmosphere,
α: volume extinction coefficient of the smoke cloud,
CL: concentration-length product of the smoke cloud.

3.5 Computations with SW XV data and comparison with measurements

Two principal subroutines were coded. These routines were used for the subsequent analysis:

LRFRANGE (R): computes the range R of the LRF for a given set of parameters,

LRFQUANT(R, P_r, $p_{d,act}$): computes received power P_r and detection probability $p_{d,act}$ for a given range R and a given set of parameters.

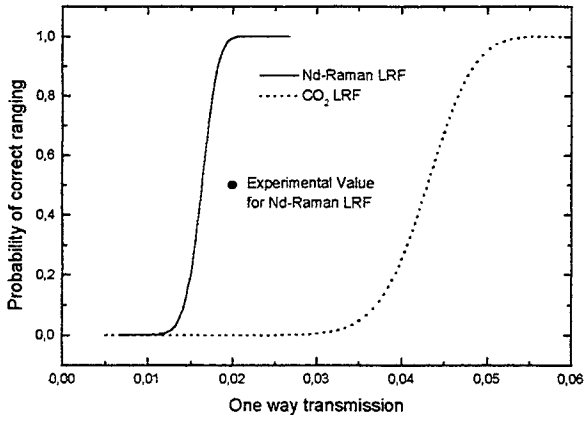


Fig. 2: Probability of detection for the Nd-Raman and the CO_2 LRFs as function of the one-way transmission of the brass smoke during SW XV.

With the given set of parameters the detection probability as a function of the smoke transmission was determined (Fig. 2). The performance of the Nd-Raman LRF is about 2.5 times better

than that of the CO_2 LRF. For real situations, however, actual reflectivities compared to those of the laser target are typically 3 times lower at 1.54 µm but 20 times or more lower at 10.59 µm.

Brass smoke

Fig. 3 shows the time history for transmission measurements as well as actual and computed correct ranging events for the brass smoke trial. For the threshold of the Nd-Raman LRF a transmission value of 2.5% was chosen which is 25% higher than the value suggested by Fig. 2. This takes into account transmission losses due to natural aerosol which were not measured.

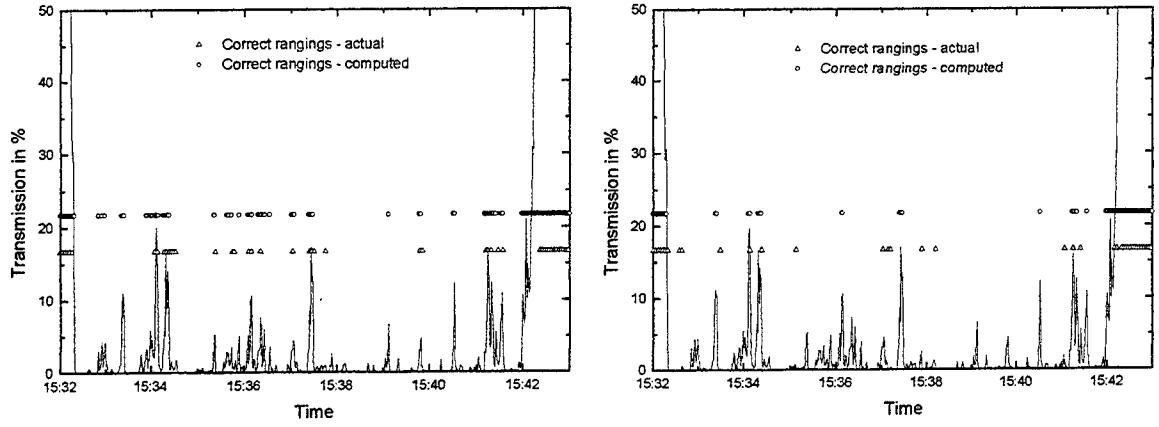


Fig. 3: Measured brass smoke transmission (solid line), overlaid by measured (triangles) and computed (circles) events of the LRF correct ranging. 1.54 µm transmission and Nd-Raman LRF ranging, left, 8-14 µm transmission and CO_2 LRF ranging, right.

When looking at Fig. 3 one sees a partial individual correspondence of computed vs. actual correct rangings. In about 50% of all cases, an individual correspondence is recognisable. Actual and computed ranging are linked just loosely in time, because the LOSs of the LRFs and the transmissometer were some meters apart.

Fog oil/graphite smoke

For the fog oil/graphite smoke events of LRF failures are compared in Fig. 4 (left).

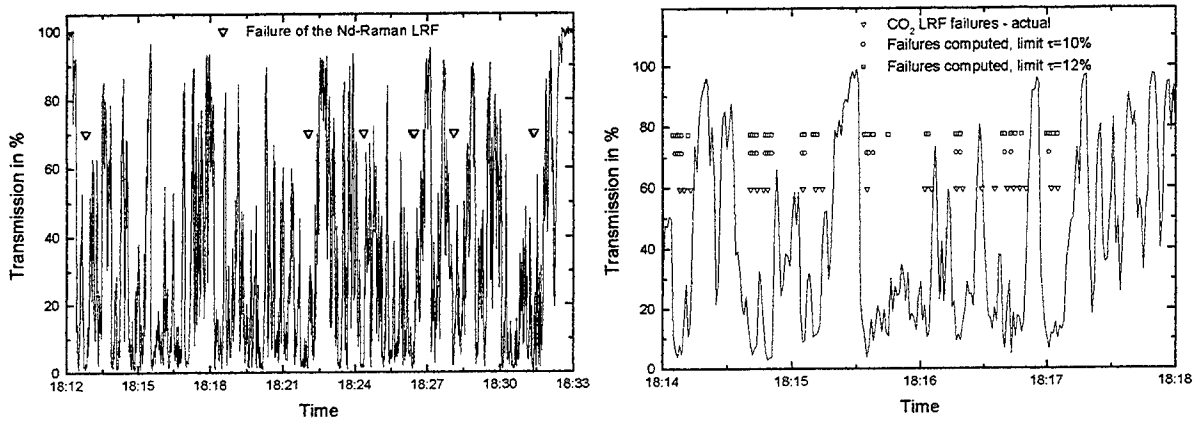


Fig. 4: Measured fog oil/graphite smoke transmission (solid line), overlaid by measured (triangles) and computed (circles) failures of the LRF. 1.54 µm transmission and Nd-Raman LRF, left, 8-14 µm transmission and CO_2 LRF, right. For transmission limits see text.

The ranges were computed at the 1 s-intervals of the transmission measurements whilst the actual LRF ranging occurred every 3-4 s. The transmission values corresponding to failures are close to 2% like in Fig. 3. For the failures of the CO_2 LRF (Fig. 4 (right)) limits of transmission values of 10% and 12% were assumed. From Fig. 4 one concludes that an actual value of 10-12% is linked with the failures. Fig. 2 predicts rather a value of 4-5%. The discrepancy is likely attributable to the degradation of the CO_2 laser which was diagnosed at the measurements.

4. CONCLUSION

A description and analysis of the performance of laser range finders was carried out which predicts the impact of smokes and battlefield effects on the performance of LRF. In particular, multiscattering and turbulence effects are modelled in a realistic way. Scintillation averaging due to diffuse reflection is included. Quantitative agreement between computation and experiment was obtained.

Measurements of two laser range finders during SMOKE WEEK XV were analysed. The lasers were a Raman-shifted Nd:YAG LRF (1.54 µm) and a CO_2 LRF (10.59 µm). Quantitative agreement of temporal behaviour and absolute magnitude of backscattered pulses could be obtained using scattering functions computed from size distributions of brass and fog oil/graphite smokes. Multiple scattering calculations were done using NBMSCAT.

References

Kleindienst, S., Dimmeler, A., Clement, D., "Obscuration effects of smoke clouds", in "Targets and Backgrounds: Characterization and Representation II", Watkins, W. R., Clement, D., Ed., Proc. SPIE 2469, p. 440 - 451, 1995.

Bissonnette, L.R., "Computer code NBMSCAT - narrow beam multiple scattering module", Defence Research Establishment Valcartier (DREV), Canada, 1995.

Dimmeler, A., Büchtemann, W., Clement, D., "Effects of Obscurants on the Performance of Laser Range Finders", Report FGAN-FfO 1998/6.

"RCA Electro-Optics Handbook", Technical Series EOH-11, RCA Corporation, 1974.

Accetta, J., Shumaker, D., Ed., "The Infrared and Electro-Optical Systems Handbook", Vol. 2: "Atmospheric Propagation of Radiation", Vol. 6: "Active Electro-Optical Systems", Environmental Research Institute of Michigan, Ann Arbor, 1993.

Yura, H.T., Büchtemann, W., "Scintillation reduction factor for laser range finder performance calculations", Report FGAN-FfO 1985/51.

HLA Compliant Total Atmospheric Simulations in Real Tactical Scenarios

Patti Gillespie
Alan Wetmore
David Ligon
US Army Research Laboratory
2800 Powder Mill Road
Adelphi, MD 20783

Michael Seablom
TASC
131 National Business Parkway
Annapolis Junction, MD 20701

Abstract

The Weather and Atmospheric Visualization Effects for Simulation (WAVES) suite of models predicts illumination and radiance information for a three-dimensionally variable atmosphere as a function of cloud type and amount, including partly cloudy skies at visual and infrared wavelengths. It also predicts electro-optical (EO) propagation effects for horizontal and slant paths through the natural atmosphere. WAVES output illumination and propagation effects are critical to accurate target acquisition and scene generation for tactical volumes (12x12x12 km). Thus WAVES has broad applications for integrating connections to models providing other environmental effects for the US Army's: wargames and simulations, information and planning, test and evaluation, training, and engineering and development. WAVES computations include direct solar/lunar radiation, multiply scattered solar/lunar radiation, optical turbulence, and forward scattering due to atmospheric aerosols. An HLA compliant API between the engineering models, BLIRB, MODTRAN, CSSM, and ATMOS and the environmental server, TAOS (Total Atmospheric and Oceans Server) is being constructed at the Army Research Laboratory. WAVES, MODTRAN, and CSSM are all slated to be used for the JSIMS simulation. An overview of this work will be discussed, and samples of atmospheric visualizations and image modification will be shown.

INTRODUCTION

The Weather and Atmospheric Visualization Effects for Simulation (WAVES) suite of models predicts illumination and radiance information for a three-dimensionally variable atmosphere as a function of cloud type and amount, including partly cloudy skies at visual and infrared wavelengths. It also predicts electro-optical (EO) propagation effects for horizontal and slant paths through the natural atmosphere. WAVES computed illumination and propagation effects are critical to accurate target acquisition and scene generation. Thus WAVES will have broad applications for integrating connections to models providing other environmental effects for the US Army's: wargames and

simulations, information and planning, test and evaluation, training, and engineering and development.

WAVES computations include direct solar/lunar radiation, multiply scattered solar/lunar radiation, optical turbulence, and forward scattering due to atmospheric aerosols. WAVES was conceived and developed in conjunction with the Cloud Scene Simulation Model (CSSM) (Cianciolo, 1996) and MODTRAN (Acharya, 1993,Berk 1989 & 1995, Chetwynd 1996) to build a complete modeling and simulation of visualization and imaging of the atmospheric environment.

MODELS DESCRIPTION

The main models in the WAVES simulation suite comprise BLIRB, a 3-D spectral radiative transfer code (Zardecki and Davis 1991, Wetmore and Zardecki 1993, Zardecki 1992, 1993a, and 1993b), VIEW, output database access code for line of sight path radiance/transmittance evaluations (Zardecki 1992, 1993a, and 1993b), PixelMod, for image spectral estimation and atmospheric effects modifications of images (Tofsted 1993, 1994), and ATMOS, a turbulence model for evaluating the vertical profile of the refractive index structure parameter (Rachele & Tunick 1994). A number of visualization tools are being developed for the WAVES suite. This software, referred to as the ToolKit, is being designed to allow for the visualization of input, intermediate, and output data from the WAVES suite. Both VIEW and PixelMod will eventually be part of a WAVES Toolkit rather than the atmospheric propagation calculations. We are developing a module to compute smoke plumes, 3DSMOKE (Ayres et al., 1998, Hoock & Giever 1994), within the WAVES framework. The physical models in WAVES have been compared to experimental data (Gillespie et al. 1995, Mozer et al. 1997, Wetmore et al. 1997).

To perform the range-dependent calculations, WAVES uses line of sight radiative transfer calculations that generate the data for image modification. These line of sight calculations require a description of the radiation fluxes and extinction throughout the local environment. Radiation fluxes, turbulence parameters, and extinctions are calculated by the first phase of the WAVES models. The real-time image modification is done by PixelMod, which in turn uses databases created by the BLIRB model. The non-real time image modification is done by the PixelMod program using line-of-sight data created by the VIEW program created by three-dimensional databases generated by the BLIRB program. Specific descriptions of the models and what they calculate are found in the references.(Gillespie et al. 1998, Tofsted et al. 1997, Rachele & Tunick 1994, Tunick et al. 1994, Zardecki, 1993b, Tofsted 1993&1994)

Figure 1 is a logical connection diagram between the different modules currently in the WAVES suite of atmospheric effects models. The PixelMod code uses the output from the VIEW model. Other models, such as the 3DSMOKE model based on COMBIC-STATBIC will become part of this suite in the near future. A new version of COMBIC (Combined Obscurants Model for Battlefield Induced Contaminants, which is the smoke model from EOSAEL), integrating fractal texturing (STATBIC, Statistical Texturing for Battlefield Induced Contaminants), is being developed for WAVES. Vis5D, a product widely available from the University of Wisconsin, is one of the principal products used to visualize the atmospheric properties in WAVES.

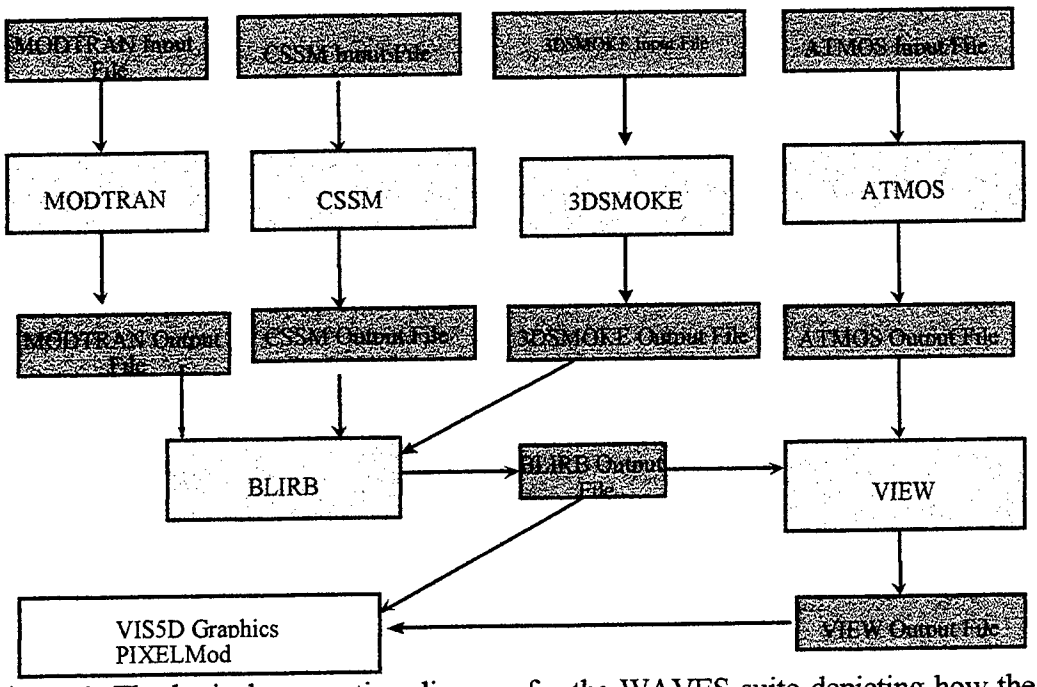


Figure 1. The logical connection diagram for the WAVES suite depicting how the models interact and produce output. (Seablom 1998)

The legacy WAVES has independent models, multiple input files, translating and parsing of output files, it is run by hand, and won't meet the DoD HLA mandate. To meet this mandate, this suite of models is also interfaced to an HLA compliant atmospheric server, TAOS (Total Atmospheric and Oceans Server) through an API (applications programming interface). HLA compliance is achieved for this entire suite of models by using the interface (API) to TAOS and by the API following the basic rules for HLA compliance. WAVES-TAOS integration will provide both proof-of-principle and a reference implementation for integrating with other Object-Oriented Simulation Systems. TAOS will provide universal data ingest. The APIs will allow simple keyword based controller to be written. Figure 2 depicts by diagram how the interaction between TAOS and WAVES will take place. This is the subject of another paper at this conference.

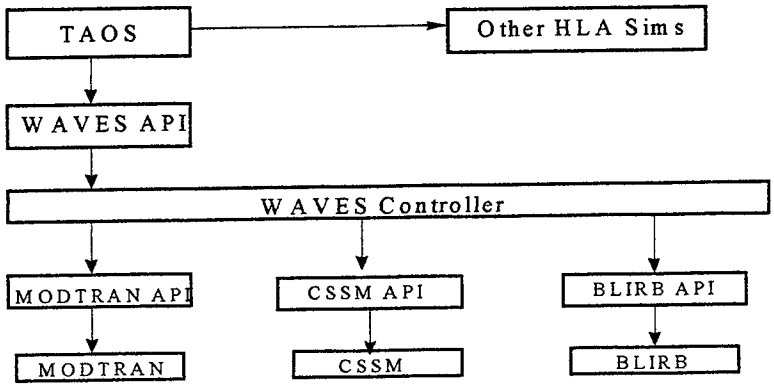


Figure 2. WAVES-TAOS integration

Given this software tool, can we modify images to accurately incorporate the effects of various aerosols on contrast transmission? Can we remove the effects of aerosols to improve the quality of images? Our objective in this paper is to investigate these questions.

IMAGE MODIFICATION AND DATA VISUALIZATION

Data input, computed, or output in various parts of WAVES can be visualized using the WAVES ToolKit, currently under development. An example of illumination values (computed in BLIRB) being visualized is shown here in Figure 3. This figure depicts the intensity of illumination at the surface with some cumulus clouds in the volume of interest. The red indicates more intense illumination and the blue indicates cloud shadows or less intense illumination. The change in illumination is a result of the intervening atmosphere and the clouds. The ToolKit allows one to look at illumination at slices through the atmosphere, the various streams of radiation, slices of the clouds, and any of the quantities handled by WAVES.0

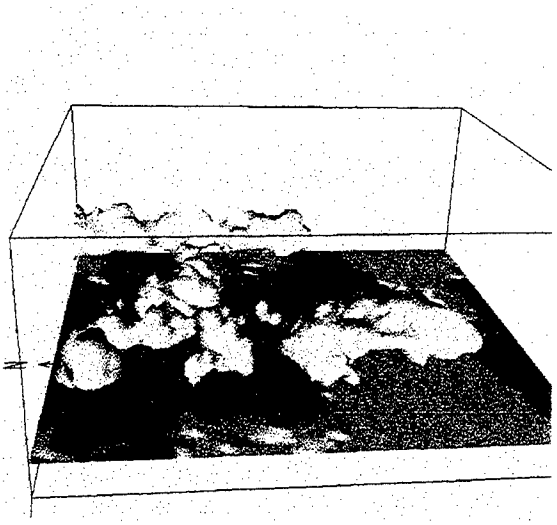


Figure 3. Illumination visualization of a volume of atmosphere.

WAVES is used to modify images, to include scenarios that have a horizontal path length, slant path scenarios, and vertical viewing scenarios. An example of a vertical viewing scenario is shown here. We have used images downloaded from the LandSat commercial satellite Web Page. The views are of a building in Vienna, Austria. Figure 4a is the untreated, clear image. The visibility for the image in Figure 4a is very high. For our purposes we have considered that the only aerosol contributing to image degradation is a background continental aerosol. We have taken that image and imposed a summer haze aerosol for Figure 4b, and imposed a thin stratus cloud in Figure 4c. Notice that the red cars in the parking lot retain their red color better than the blue objects in the scenes with the aerosols or thin cloud. This is what one would expect from scattering by aerosols. The detail in these images is better preserved through viewing an image on a computer screen than a printed page or viewgraph.



Figure 4a. Clear Landsat image of Vienna, Austria.



Figure 4b. Summer Urban haze aerosol inserted over the Vienna, Austria image.

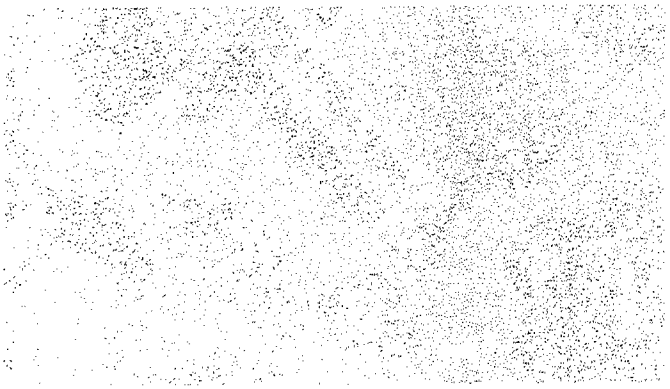


Figure 4c. Thin stratus cloud inserted over the Vienna, Austria image.

The next series of images are video images taken at a slant path near the earth's surface at an US East Coast location. The two images of the same scene, but different days (May 14, 1997 and June 5, 1997), were chosen. These two images were looking north along the coast and three

markers of known distance are clearly visible in the scene. Although these two images were of the same scene, they are not identically the same. The surf conditions in the two images are different and the visibility is clearly different in these two scenes.

Figure 5 is the image looking north along the coast on May 14. Figure 6 is the image looking north along the coast on June 5. In Figure 5, notice the three white disks on the land side (left side) of the image. There is some bright sunlight steaming across the area because it is just after dawn. The visibility for this case is 36 km and the white targets are easily visible. These images were taken by a camera in a tower that is a known distance from the targets. In Figure 6 the white targets are not as easily seen and the surf is more pronounced. The streaming sunlight is not obvious across the landscape as it is in Figure 5. Both Figures 5 and 6 were taken at approximately 7 am, and in Figure 6 the sun is higher in the sky at 7 am than it is in Figure 5.



Figure 5. May 14, 1998, looking north along the coast.

The images we obtain from the video cameras were uncalibrated gray scale images. The actual gain for each image was probably somewhat different since the video cameras adjust the gain to the ambient light conditions to maximize the brightness and contrast of the image. We adjusted the brightness or gain of each image so that they were approximately the same. Although this is not a precise adjustment, it is as close as can be obtained with uncalibrated imagery.



Figure 6. June 5, 1998 looking north along the coast.

For this project we tried to degrade the higher visibility image using the physics models in WAVES and meteorological data collected on the days that the images were made, and compare the degraded version to the lower visibility image. Specifically, the image taken on May 14 was for a visibility of 36 km, and the one from June 6 was for a visibility of 18 km. Through the use of the WAVES model and the meteorological data we reduced the visibility of the 36 km day to 18 km. The WAVES model uses a standard emphemeris model, SLAC, (http://aa.usno.navy.mil/AA/software/), to calculate the solar and lunar position, therefore, the angle of the sun through the atmosphere will be accounted for accurately.

We obtained a grid map of the coastal location, and calibrated the pixel distances in the images to the distances on the maps. This resulted in a range map for the image. We used the meteorological data for the lower visibility day and ran a high resolution model run through the WAVES components, BLIRB, VIEW, and ATMOS. Since the images that we obtained were 8-bit images black and white images, we had to convert the black and white gray scale images to RGB images. The 8-bit images were converted to the 24-bit format needed for the PixelMod calculations. PixelMod used the eye response for the sensor characteristic. Figure 7 is the resulting modified May image.



Figure 7. The modified May image.

Some differences in the original May and June images should be noted. The first is the fact that the sun is at a different location in the sky, that is, the sun is higher above the horizon for the June image than it is for the May image. This cause a bright area and shadow on the beach for the May image that is not in the June image. Above the sea surface in the distance is a low lying aerosol bank in the May image that is not in the June image. Thus the lower sky looks darker in the May image than in the June image and the modified image will also have this effect. There is somewhat more surf in the June image than the May image. This will make the water in the June image seem brighter, even when the contrast is degraded. All of these effects are noted in Figure 7.

The main feature to focus on in all three images are the white disks along the foliage edge to the sand. In the May image (Figure 5) they are bright, in the June image (Figure 6) where contrast is degraded, they are much darker. In the modified May image (Figure 7) to match the contrast conditions in June the white disks are much darker than in May. In the modified May image they have about the same contrast to the background as the June image. The detail visible in the foliage is about the same in the modified May image as in the June image. This indicates that our experiment with modifying the images using weather information to generate a "new" contrast transmittance is successful.

Modifying images to include additional effects implies that it can be used as a planning tool for various contingencies, as an evaluation tool for testing and evaluation, as an engineering tool for development, and most importantly that we may be able to remove these atmospheric effects from degraded images. We do not have an example of removing atmospheric effects as yet.

Future directions include consideration of polarization effects, using WAVES as a tool to study aerosol effects, and expanding the wavelength range. Longer-range projects include integration of the effects of wind, transport and diffusion, atmospheric forecast data, and a turbulence model that can provide realistic scintillation effects for simulation.

SUMMARY

The US Army has an interest in integrating atmospheric visualization into simulation platforms. Many of the simulations sponsored by the Army use an earlier product of the US Army Research Laboratory, EOSAEL, and the US Air Force Research Laboratory, LOWTRAN, to model the atmosphere. The WAVES suite, used with MODTRAN and CSSM, are designed as ideal software products to replace EOSAEL and LOWTRAN with more physically accurate calculations and integrated calculations. The WAVES-CSSM-MODTRAN tools also has potential application in simulating the spectral radiance of new sensors and spec

REFERENCES

Acharya, P.K., D.C. Robertson, and A. Berk, 1993, Upgraded Line of Sight Geometry Package and Band Model Parameters for MODTRAN, Phillips Laboratory Technical Report, PL-TR-93-2127, Geophysics Directorate, Hanscom AFB, MA. [ADA 280952].

Ayres, Scarlett, Stephen DeSutter, Donald W. Hoock, and Robert Sutherland, 1998, Combined Obscuration Model for Battlefield Induced Contaminants (COMBIC92) Users Guide and Technical Documentation, ARL-TR-273-xx, in press.

Berk, A., L.S. Bernstein, and D.C. Robertson, 1989, MODTRAN: A Moderate Resolution Model for LOWTRAN 7, Air Force Geophysics Laboratory Technical Report, GL-TR-89-0122, Hanscom AFB, MA. [ADA 214337].

Berk, A., 1995, Upgrades to MODTRAN Layer Cloud/Rain Models, Report Number SSI-SR-56, Spectral Sciences, Inc., Burlington, MA.

Cianciolo, M.E., M.E. Raffensberger, E.O. Schmidt, J.R. Stearns, 1996, Atmospheric Scene Modeling and Visualization, Phillips Laboratory, Hanscom AFB, MA, PL-TR-96-2079. [ADA 312179].

Chetwynd, J.H., 1996, "Addition of a Correlated-K Capability to MODTRAN," Proceedings of the 19th Annual Conference on Atmospheric Transmission Models, Phillips Laboratory/Geophysics Directorate, Hanscom AFB, MA, PL-TR-97-2069. [ADA 328230].

Gillespie, Patti, Alan Wetmore, and David Ligon, 1998, WAVES Overview, ARL-TR-1721-1, US Army Research Laboratory, Adelphi, MD, 20783, September 1998. [ADA 354236].

Hoock, D.W. and J.C. Giever, 1994, "Modeling Effects of Terrain and Illumination on Visibility and the Visualization of Haze and Aerosols", SPIE Conference on Atmospheric Propagation, Orlando, FL.

Mozer, Joel, Guy Seeley, Alan Wetmore, Patti Gillespie, David Ligon, and Samuel Crow, "Radiometric Validation of CSSM," 1997, Proceedings of the 1997 CIDOS (Cloud Impacts on DoD Operations and Systems), September 1997, Naval War College, Newport, RI., PL-TR-97-2112. [ADA 330020]..

Rachele, Henry and Arnold Tunick, 1994, Energy Balance Model for Imagery and Electromagnetic Propagation, Journal of Applied Meteorology, Vol. 33, No. 8, pp. 964-976.

Seablom, Michael, 1998, "WAVES milestones and evaluation plan," white paper, BAA contract DAAL01-97-C-0152, The Analytic Sciences Corporation, "Object Oriented Programming Environment" and "Visualization Tool Development" for WAVES, Dr. Patti Gillespie, Contracting Officers Technical Representative.

Seablom, Michael, Patti Gillespie, Alan Wetmore, 1998, WAVES Software Users Guide, ARL-TR-1721-7, in review, US Army Research Laboratory, Adelphi, MD, 20783, October 1998.

Tofsted, D.H., 1993, "Effects of Nonuniform Aerosol Forward Scattering on Imagery," Proceedings of the 1993 Battlespace Atmospherics Conference, Las Cruces, NM. [ADA 3322799].

Tofsted, David, 1994, "Spectral Estimation and Processing of Imagery Data," Characterization and Propagation of Sources and Backgrounds, SPIE, Bellingham, WA, vol. 2223, pp. 511-520, Orlando, FL.

Tofsted, D.H., B.T. Davis, A.E. Wetmore, J. Fitzgerrel, R. C. Shirkey, and R.A. Sutherland, 1997, EOSAEL92 Aerosol Phase Function Data Base PFNDAT, ARL-TR-273-9, Battlefield Environment Directorate, US Army Research Laboratory. [ADA 328710].

Tunick, Arnold, Henry Rachele, Frank V. Hansen, Terry A. Howell, Jean L. Steiner, Arland D. Schneider, and Steve R. Evett, 1994, REBAL '92 - A Cooperative Radiation and Energy Balance Field Study for Imagery and Electromagnetic Propagation, Bulletin of the American Meteorological Society, No. 75, No. 3, pp. 421-430.

Wetmore, A. E., and Zardecki, A., 1993, "The Boundary Layer Illumination and Radiative Balance Model (BLIRB)," Proceedings of the Cloud Impacts on DOD Operations and Systems 1993 Conference, PL-TR-94-2188, pp. 201-206, Ft. Belvoir, VA. [ADA 286658].

Wetmore, Alan, Patti Gillespie, David Ligon, Samuel Crow, Michael Seablom, Guy Seeley, and Joel Mozer, 1997, "Experimental Evaluation of the Integrated WAVES-CSSM Model" Proceedings of the 1997 Battlespace Atmospherics Conference, San Diego, CA. [ADA344056].

Wetmore, Alan, Patti Gillespie, and David Ligon, 1998, "Weather Effects and Modeling for Simulation and Analysis" in the Proceedings of the Sensors and Electronics Technology Panel on EO Propagation, Signature, and System Performance Under Adverse Meteorological Conditions Considering Out of Area Operations, March 1998, The Italian Air Force Academy, Naples, Italy.

Zardecki, Andrew and Roger Davis, 1991, Boundary Layer Illumination Radiation Balance Model: BLIRB, STC Technical Report 6211, Final Report under DAAD07-89-C-0035, Las Cruces, NM.

Zardecki, Andrew, 1992, Testing and Evaluation of the Boundary Layer Illumination Radiation Balance Model: BLIRB, STC Technical Report 6222, Final Report for DAAD07-89-C-0035, Las Cruces, NM.

Zardecki, Andrew, 1993a, Validation of the Discrete-Ordinates Method, Interim Report for DAAL03-91-C-0034.

Zardecki, Andrew, 1993b, Three-Dimensional Extension of Boundary Layer Illumination Radiation Balance Model for Imaging Applications, Final Report for Contract No. DAAL03-91-C-0034, TCN Number: 92-480, Delivery Order No. 0541.

RESULTS OF THE REPRESENTATIONAL RESOURCES INTEGRATION EXPERIMENTS

Gary McWilliams
DoD M&S Executive Agent for Air & Space Natural Environment
Air Force Combat Climatology Center
Asheville, NC 28801
Voice: (828) 271-4323
Fax: (828) 271-4324
E-mail: mcwillig@afccc.af.mil

1. INTRODUCTION

Representational Resources Integration Experiments (RRIE) is a Defense Modeling and Simulation Office (DMSO) project that consists of a series of experiments being conducted during the summer and fall of 1998. These experiments are evaluating various (M&S) resources in the context of their combined ability to represent a (1) dynamically consistent synthetic natural environment (SNE) and (2) a SNE that can be properly coupled to the performance of combat systems and the behavior of computer generated forces. Representational resources being evaluated include environmental models, algorithms, and data sets; Semi-Automated Forces (SAF) software; and the procedures and techniques that provide a framework for the proper implementation of these resources.

The experiments involve participation in the Global 98 War Game and computer simulations of two combat systems under acquisition development - the Grizzly Breaching Vehicle and the Advanced Amphibious Assault Vehicle (AAAV). An Integrated Product Team (IPT) comprised of participants from 15 different DoD organizations are conducting the experiments. The three DoD M&S Executive Agents (MSEAs) for the Natural Environment (Air and Space, Oceans, and Terrain) and the DMSO project offices for systems and human behavior representation are coordinating the project. The MSEA for Air and Space Natural Environment (ASNE) is serving as the project lead.

2. APPROACH

The RRIE project is following the experimental method in both form and substance. Hypotheses and controls have been established and an Experimental Plan (DMSO, 1998) has been prepared. A total of five experiments are being performed and the data for conducting these experiments are being collected during the Global 98 War Game Exercise and computer simulations involving the Grizzly and AAAV. A final report will document the results.

The M&S experiments look to identify the cost-effective procedures for the following activities:
(1) coupling the SNE to systems performance

(2) establishing and maintaining physical data consistency within the same environmental domain (e.g. atmosphere)
(3) establishing and maintaining physical data consistency between different environmental domains (atmosphere and oceans)
(4) determining the level of resolution of environmental data needed in a simulation
(5) maintaining consistency between a high-fidelity simulator and a lower-fidelity simulation using the same environmental inputs.

Each of these five modeling activities has an associated experiment and hypothesis. For example, the experimental hypothesis that relates to coupling the SNE to systems performance reads "Coupling the natural environment to systems behavior enables the Project Manager/War Gamer to more accurately and cost-effectively assess system performance."

Controls have been defined for each of the experiments. In the experiments using data from the Global 98 War Game, the control data consist of the data that would have been provided in the absence of the new M&S capabilities that were used to support this exercise. In the experiments involving the simulations of the Grizzly and AAAV, the control data consist of the data associated with benign environmental conditions. Benign conditions for the Grizzly translate to dry soil conditions, and benign conditions for the AAAV translate to sea state 1 conditions (wave height less than 1.5 feet).

When conducting these experiments, every effort is made to use the latest technical resources available to the DoD M&S community. Among these resources are the Master Environmental Library (MEL) (Allard, et al., 1998), the Weather Scenario Generator (WSG)(Lowe, et al., 1998), the Advanced Climatological Model and Environmental Simulation (ACMES) model (Zack, et al., 1998), and the Cloud Scene Simulation Model (CSSM) (Cianciolo, et al., 1996).

The IPT responsible for conducting the experiments is structured into smaller sub working groups who then perform specific experiments. The full IPT meets on an approximately monthly basis to exchange information and discuss the latest progress. Representatives from the three primary DoD laboratories doing atmospheric research – the Air Force Research Laboratory (AFRL), the Army Research Laboratory (ARL), and the Naval Research Laboratory (NRL) are part of the RRIE IPT.

3. DEMONSTRATIONS

The three demonstrations in which RRIE is participating in actuality become the laboratories for the IPT experimenters. Each of the three demonstrations provides the RRIE project with a different environmental focus. The Global 98 exercise highlights the use of atmospheric data. Grizzly simulations emphasize the use of terrain and soil data. Ocean data take the forefront in the AAAV simulations. MEL resource sites will archive the environmental data that are gathered during these demonstrations and provide a means to conveniently access the data.

3.1 Global 98 War Game

The Global War Game is conducted annually by the Naval War College (NWC) in Newport, RI. The Global 98 War Game was conducted 13-31 July and its theme was command and control using network-centric warfare. Global 98 has two military scenarios, one in Northeast Asia and the other in Southwest Asia. The RRIE IPT worked closely with the Navy Training Meteorology and Oceanography Detachment (NTMOD) Newport in preparing the Meteorology and Oceanography (METOC) data products needed for Global 98. NMTOD has the responsibility for providing the environmental data needed to support all the war games conducted at NWC. Most of the METOC products generated were concerned with Electro-Optics (EO), biological and chemical dispersion, amphibious landings, and undersea acoustics.

NWC and NMTOD welcomed RRIE participation because it gave them access to an understanding about new M&S resources such as the WSG and CSSM. These resources give NMTOD the capability to generate a greater variety of METOC products in a more timely fashion. In the past, METOC data has seen limited use in war games due to the lengthy delays encountered in accessing and processing the data.

The NWC had much to gain from participating in Global 98. Although the Global War Game is not a computer simulation, the steps followed in generating the METOC products used here closely emulate those that will be needed to support computer simulations such as the Joint Simulation System (JSIMS) and the Joint Warfighting System (JWARS). Our involvement in Global 98 also gave us the opportunity to evaluate many new M&S resources available for creating an integrated SNE and to inform and educate the war gaming community about the availability and use of these resources.

3.2 Grizzly Breaching Vehicle

The U.S. Army Tank-automotive and Armaments Command (TACOM) is developing the Grizzly as a combat mobility system capable of conducting in-stride breaches of linear obstacles. Grizzly incorporates countermine and counterobstacle capabilities in a single vehicle. Some of Grizzly's most important features are a full-length mine clearing blade, a power driven arm, and a drive-by-wire capability.

The RRIE is collaborating with the Grizzly PM and the Warfighting Analysis and Integration Center (WAIC) to develop a robust Grizzly simulation capability. The simulation is using Joint SAF 2.0 software to represent the Grizzly behavior. The simulation will demonstrate how Grizzly's mobility during mine plowing operations is affected by soil moisture conditions. Simulations will be run for both dry and wet conditions. Other Grizzly simulations will examine how atmospheric conditions affect the dispersion of its self-screening smokes. The environmental setting for the Grizzly demonstration is the region referred to as the Ground Maneuver Box, an area that encompasses the National Training Range and the Twenty-nine Palms Marine Corps Test Range. This region was selected because it is where Grizzly will conduct its operational testing and because a high-resolution terrain database is available for that

region. The simulations will be conducted in mid-November 1998 at both WAIC and the Topographic Engineering Center.

Both the RRIE project and the Grizzly PM will significantly benefit from this demonstration. The Grizzly PM is gaining a simulation capability that can be used to (1) improve experimental design and (2) conduct combined simulated-live field tests and evaluation assessments. The RRIE project is gaining a better understanding of how to (1) couple an integrated SNE to performance behavior of land-based systems (2) create physically consistent atmosphere-terrain representations and (3) determine the resolution of atmospheric data needed to represent smoke dispersion at the system level.

3.3 Advanced Amphibious Assault Vehicle

The U.S. Marine Corps is developing the AAAV to transport dismounted forces from over the horizon, through the littoral region, and to their final objective ashore. The AAAV has the mobility of an M1A1 main battle tank, a water-speed over three times that of the Amphibious Assault Vehicle (AAV), a 7.62 mm machine gun, a 30 mm cannon, and a fire control system derived from M1A1 tank. It is being designed to operate in a much wider range of sea state and weather conditions than is now possible with the AAV. General Dynamics Amphibious Systems (GDAS), the AAAV prime contractor, has formed a team of engineers to apply current M&S technology to the design, optimization, and validation of vehicle features and functionality.

The RRIE project will be assisting the GDAS M&S team by conducting simulations of the AAAV operating during different sea state conditions. The engineering objective of these simulations is to examine how sea state conditions affect the crew's out-the-window visibility. Sea state conditions ranging from levels 1 to 3 (maximum wave height being approximately 5 feet) will be simulated. The Camp Pendleton coastal region is serving as the setting for these simulations. This region was selected because high-resolution bathymetric data are available and because it is the area where the AAAV operational testing and evaluation will occur. These computer simulations will be conducted in mid-November 1998 at the AAAV Technology Center in Woodbridge, VA.

The AAAV simulations have much to offer both the AAAV PM and the RRIE project. Beyond having the results of the visibility assessment, the AAAV PM and GDAS are (1) enhancing their environmental M&S infrastructure by acquiring the new environmental M&S capabilities developed by DMSO over the past several years, and (2) acquiring a good understanding of how to apply these capabilities to address their needs. The RRIE project gains through (1) an improved understanding of how to couple the integrated SNE to system performance behavior of amphibious systems and (2) identification of procedures that provide physically consistent data representations of oceanic and atmospheric conditions.

4. RESULTS

RRIE results are coming in many forms. Reference procedures are being identified for use in constructing a simulation that needs an integrated SNE. Reference data sets are being made

available for use in representing an integrated SNE. Measures of Effectiveness (MOE) and Measures of Performance (MOP) are being formulated to determine the level of physical consistency among the different environmental domains represented in a simulation and to accurately assess the impact of environmental conditions on system performance. Also significant modifications are being made to the SAF software representing the entities being simulated. These modifications allow the entities to more realistically respond to the stresses of the natural environment. Many of these results will be made available over the Internet by using M&S resources such as MEL.

At the time this paper is being prepared, the experimental data are limited to the results from the Global 98 War Game exercise. Analyses of these data are continuing. Data and information have been captured during all phases of METOC responsibility in war gaming. These phases include identifying simulation/exercise environmental requirements, defining specific environmental scenarios, producing the environmental data corresponding to the scenarios, post-processing the environmental data, determining the environmental effects on systems and operations, and displaying the environmental effects information. New M&S capabilities were used to automate all of these phases with the exception of the first and last phases.

Much has been gained from this experience. A detailed set of procedures for creating an integrated (atmosphere-ocean) SNE was defined. An extensive environmental database for creating an integrated SNE for SW Asia and NE Asia are now available.

It was determined that tools need to be developed for automating the means to readily assess the environmental requirements of a war game exercise. Otherwise this process is very costly in terms of manpower and time. The current tendency is to create voluminous environmental data sets to ensure that all possible needs are covered. However this over-kill approach only shifts the problem downstream by forcing the data users to sort through huge data sets.

The need to use standard data formats was evident throughout the exercise. Much effort was devoted to reformatting data for post-processing and for use in environmental effect models.

One very interesting discovery was made in relation to intra-domain data consistency. When the resolution of the numerical weather prediction model (NWP) input data changed from low to high resolution, the character of the cloud field generated by CSSM changed significantly. This observation is being explored further. The initial explanation is that the NWP moisture physics algorithms are only used for high-resolution runs.

5. CONCLUSIONS

In just five months, the RRIE project has made much progress. An IPT was formed with participants from over 15 different government and private organizations. The IPT prepared an Experimental Plan describing five experiments that collect data from three major demonstrations, one being a campaign level war game, the other two being computer simulations

related to system acquisition. The War Game has been successfully conducted and the resulting data are being analyzed. Preparations for the other two demonstrations are near completion. A final report will be prepared by the end of the calendar year. This report will describe the RRIE results. It will also recommend new technology development and integration efforts needed to ensure that the DoD M&S community has ready access to tools for cost-effectively simulating an Integrated SNE that can be coupled to the performance of systems and the behavior of humans and organizations.

6. REFERENCES

Allard, R.A., R.A. Siquig, B. Donaldson, and E. Kihn (1998). "The Master Environmental Library: A Source for Environmental Data for Modeling &Simulation." *Proceedings of the1998 Fall Simulation Interoperability Workshop.* Orlando, FL, 14 -18 Sep.

Cianciolo M. E., Raffensberger M. E., Schmidt E. O., Stearns J. R. (1996). *Atmospheric Scene Simulation Modeling and Visualization, Final Report.* PL-TR-96-2079, Air Force Research Laboratory, Hanscom AFB, MA. [ADA 312179]

Cornish, C. and Xin Li (1998). "HyroSim: Hydrologic Modeling in the Synthetic Natural Environment." *Proceedings of the 1998 Spring Simulation Interoperability Workshop.* Orlando, FL, 9 – 13 Sep.

Lowe, S., E. Kihn, R. Englebretson, R. Siquig (1998). "Weather Scenario Generator: Design and Project Status." *Proceedings of the 1998 Spring Simulation Interoperability Workshop.* Orlando, FL, 9 – 13 Sep.

Zack, J., G. Van Knowe, P. Price, M. Bousquet, S. Young, C. Graves. 1998. *Development of Methods to Generate High Resolution Climatological Databases to Support DoD M&S Programs, AFRL-VS_HA-TR-98-0047,* Air Force Research Laboratory, Hanscom AFB, MA. [ADA 353343].

SCANNING FAST FIELD PROGRAM (SCAFFIP)

John M. Noble
U.S. Army Research Laboratory
ATTN: AMSRL-IS-EE
2800 Powder Mill Rd
Adelphi, MD 20783
Phone: (301) 394-5663
Fax: (301) 394-1155
Jnoble@arl.mil

ABSTRACT

The Scanning Fast Field Program (SCAFFIP) is an atmospheric acoustic propagation model which incorporates many of the effects on the environment on the sound field such as geometrical spreading, refraction, diffraction, molecular absorption, and complex ground impedance. SCAFFIP provides the user with either the attenuation levels with range and frequency for a given geometry, azimuth, and meteorological profile. The meteorological profile and the geometry provide the model the ability to calculate the sound speed profile. The geometry profile is required due to the angular dependence of the sound speed on the wind direction relative to the direction of propagation. This model works over a flat-earth and a non-turbulent atmosphere. Even with these restrictions, the model performs very good for many scenarios. The model contains a friendly user interface which requires a minimum amount of information to run the model yet there are flags which can be set to obtain more detailed information.

INTRODUCTION

The Scanning Fast Field Program (SCAFFIP) is a modification to the Fast Field Program (FFP). The FFP is a one-way solution to the acoustic wave equation originally developed for underwater acoustics and adapted to propagation in the atmosphere by Raspet et al. (1985) and Lee et al. (1986). The FFP calculates the attenuation of sound with range over flat terrain for a single frequency and a single azimuth. The FFP was modified by Noble (1991) to scan through multiple azimuths for a given frequency. Since acoustics sources contain multiple frequencies, SCAFFIP was modified to scan through frequency instead of azimuth. Another innovation in the development of SCAFFIP is the development of a meteorological profile builder and a sound speed profile parser. This paper will discuss the components of the atmosphere, which affect sound propagation and how this version of SCAFFIP evaluates the available information to optimize input to the FFP.

PROPAGATION MODEL

The propagation of sound from a point source at the origin is given by the classical wave equation

$$\nabla^2 p - \frac{1}{c^2}\frac{\partial^2 p}{\partial t^2} = -4\pi\delta(x,y,z), \tag{1}$$

where δ represents a delta function source of unit strength. For simple harmonic motion, transforming into cylindrical coordinates, and assuming azimuthal symmetry, the wave equation becomes

$$\frac{\partial^2 p}{\partial r^2} + \frac{1}{r}\frac{\partial p}{\partial r} + \rho\frac{\partial}{\partial z}\left(\frac{1}{\rho}\frac{\partial p}{\partial z}\right) + k^2 p = -\frac{2}{r}\delta(r), \tag{2}$$

where ρ is the density of the propagation medium. The FFP reduces the dimensionality by applying a zero-order Hankel transform. This reduces the wave equation to a form similar to the equation for a transmission line. By drawing an analogy between the two, the problem can be solved by standard techniques for solving a transmission line. In this analogy, the layers in the atmosphere become elements in the transmission line. By solving the transmission line problem and performing an inverse transform on the results, the FFP calculates the attenuation of sound with range for a give azimuth and frequency.

INCORPORATING ATMOSPHERIC EFFECTS

Before an explanation of how SCAFFIP analyzes the atmospheric profile, the dynamics of the atmosphere which affect sound propagation needs to be addressed. The meteorological variables that affect the speed of sound in air are pressure, temperature, vector wind speed, and humidity. To observe the effect of each meteorological variable, considering each independently, one can examine the equation for the speed of sound. The value of c is defined as

$$c(T) = \sqrt{\gamma RT / M}, \tag{3}$$

where γ is the ratio of specific heats, R is the universal gas constant that is equal to 8314.16 J/(kg K), and M is the molecular weight. The dependence of the speed of sound on pressure and humidity is found in the ratio of specific heats and molecular weight of moist air. However, these dependencies are not very strong and can be ignored when confining the problem to the lower portion of the atmosphere.

The consideration of the wind speed to the speed of sound is a vector relation. The effective speed of sound is calculated using

$$c_{eff} = c(T) + u \cdot \cos(\theta_w - \pi - \theta_R), \tag{4}$$

where c(T) is the speed of sound in the absence of wind at temperature T, u is the magnitude of the horizontal wind speed, θ_R is the beating of the receiver from the target, and θ_w is the direction from which the wind blows. Since the sound speed is a function primarily of temperature and vector wind speed, the sound speed will vary with height since these meteorological quantities vary with height. This will cause the acoustic wave to be refracted as it propagates through the atmosphere. The degree of refraction undergone by the acoustic wave is related to the sound speed gradient present. If the sound speed increases with height, this causes downward refraction of the acoustic wave, Noble (1992). In an upward refraction atmosphere, the formation of a refractive shadow zone can occur. A refractive shadow zone is a region where no refracted or reflected wave can reach.

USER INTERFACE

The current version of SCAFFIP is version 2.0. The program is written to operate on a personal computer running under Windows 95 or Windows NT (code has not been tested for Windows 98). Figure 1 shows the user interface as it appears on the computer. SCAFFIP will calculate the attenuation of sound with range and frequency for a give atmospheric profile over flat terrain and a non-turbulent atmosphere. The user can examine the attenuation of sound with range for different frequencies or attenuation of sound with frequency for different ranges. The attenuation table is stored in an ASCII file. The table can then be loaded into a sensor performance model such as the Battlefield Acoustic Sensor Integration System (BASIS) developed by Applied Research Laboratory at Pennsylvania State University.

Since a user of SCAFFIP may not have a meteorological profile available to perform a calculation, the newest version contains a meteorological profile builder. The profile builder allows the user to input some general information about the atmospheric conditions to run the model against, see figure 2. The profile builder uses this information to develop a meteorological profile for the propagation model to use. The profile builder contains a surface energy balance model developed by Rachele and Tunick (1994) which calculates the parameters for a similarity model, Rachele et al. (1995). The similarity model constructs profiles for the temperature and wind for the FFP to use. Due to the limitations of similarity theory, the meteorological profiles calculated will only be valid for short range propagation calculations (R < 5 km). For longer ranges, it is recommended to use measured profiles or profiles from a boundary layer meteorological forecast model.

The propagation model, FFP, used in SCAFFIP uses constant sound speed layers. In previous versions of the propagation model, a novice running the model could induce error into the computation by having the atmospheric layer thickness large. If the layer thickness is large, this can lead to a large change in the sound speed from one layer to the next. This error can be seen in figure 3. The model matches the data very good until about 16 km. The deviation between the model and the data is the result of large layer thickness. By reducing the layer thickness, the model matched the data up to 20 km. SCAFFIP examines the sound speed profile

calculated from the meteorological profile and determines at which heights more layers are required. Next, a linear interpolation is performed to increase the number of layers to provide a valid solution to the scenario. Figure 4 shows an example of how the number of layers can vary with azimuth and frequency. The line at 43 layers is the number of layers in the meteorological profile. The variation with azimuth is due to the vector effect of the wind on the sound speed as mention previously.

Also, previous versions used the entire meteorological profile whether or not it was required to calculate a valid solution. Although this did not induce errors, the run time was slower since the run time depends on the number of layers in the profile. The propagation of sound depends on the sound speed profile along the azimuth of propagation. If the sound speed decreases with height, the sound will be refracted upward resulting in poor propagation conditions. If the sound speed increases with height, the sound will be refracted downward towards the ground resulting in very good propagation conditions. If the type of propagation is upward refracting, there is no need for the meteorological profile to be very high. Like wise if the type of propagation is downward refracting, the meteorological profile need to be high enough to encompass the sound speed duct. SCAFFIP examines the sound speed profile and determines the best height for the meteorological profile. Figure 5 shows an example of how the meteorological profile height can vary with azimuth. The profile height is not effected by frequency. The dashed line is the original height of the meteorological profile.

SUMMARY

Battlefield acoustics is a very important means of detecting numerous types of tactical targets. Acoustics is valuable since it provides a method to detect and identify targets passively and non-line-of-sight. Computational models like SCAFFIP provide valuable information on how the atmosphere will effect the sound propagation from target to sensor. The user interface for SCAFFIP provides a degree of expertise for the user allowing for reliable and accurate predictions with minor user knowledge. The use of such acoustic propagation models for determining the deployment of passive acoustic sensors in the battlefield will provide improved detection capabilities for detecting tactical targets.

REFERENCES

Lee, S. W., N. Bong, W. F. Richards, and R. Raspet, 1986: Impedance formulation of the fast field program for acoustic wave propagation in the atmosphere. J. Acoust. Soc. Am., **79**: 628-634.

Noble, John M. 1991: Acoustic propagation in the atmosphere using the scanning fast field program. Proceedings of the 1991 Battlefield Atmospherics Conference, 66-72.

Noble, John M. 1992: The importance of ducting in atmospheric acoustics. Proceedings of the 1992 Battlefield Atmospherics Conference, 267-273.

Rachele, Henry R. and Arnold Tunick, 1994: Energy balance model for imagery and electromagnetic propagation. J. Appl. Meteor., **33**: 964-976.

Rachele, Henry R., Arnold Tunick, and Frank V. Hansen, 1994: Energy balance model for imagery and electromagnetic propagation. J. Appl. Meteor., **34**: 1000-1005.

Raspet, R.,S. W. Lee, E. Kuester, D. C. Chang, W. F. Richards, R. Gilbert, and N. Bong, 1985: Fast-field program for a layered medium bounded by complex impedance surfaces. J. Acoust. Soc. Am., 77: 345-352.

FIGURES

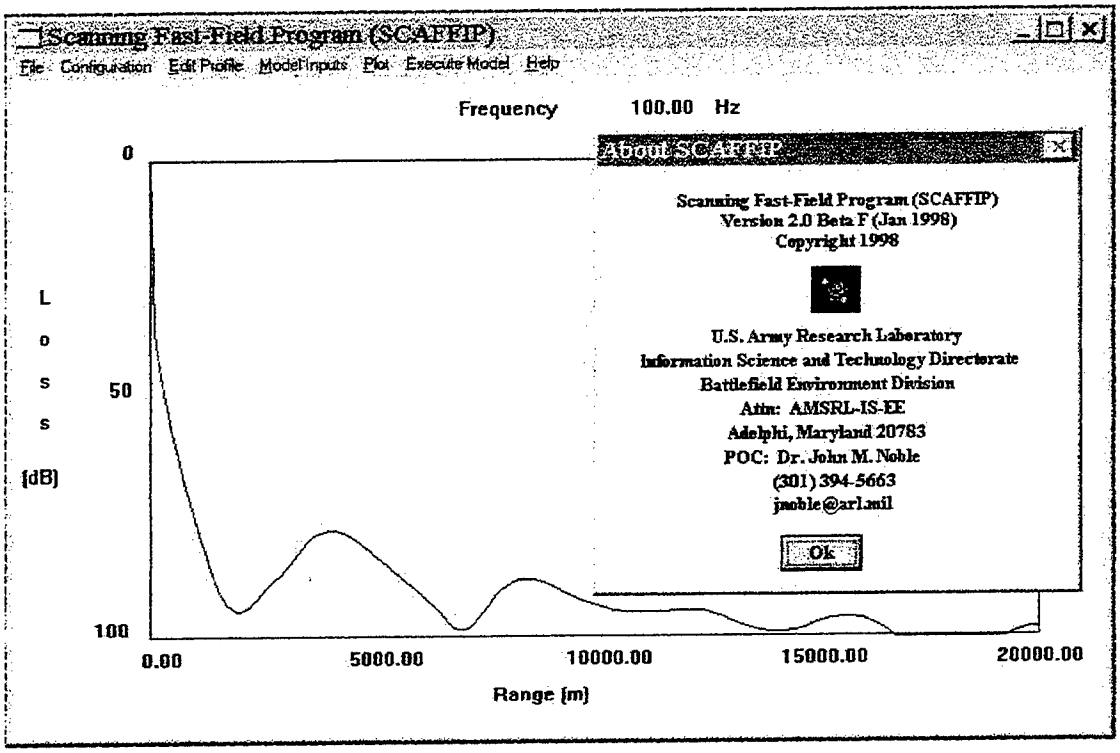


Figure 1. Main window for Scanning Fast Field Program.

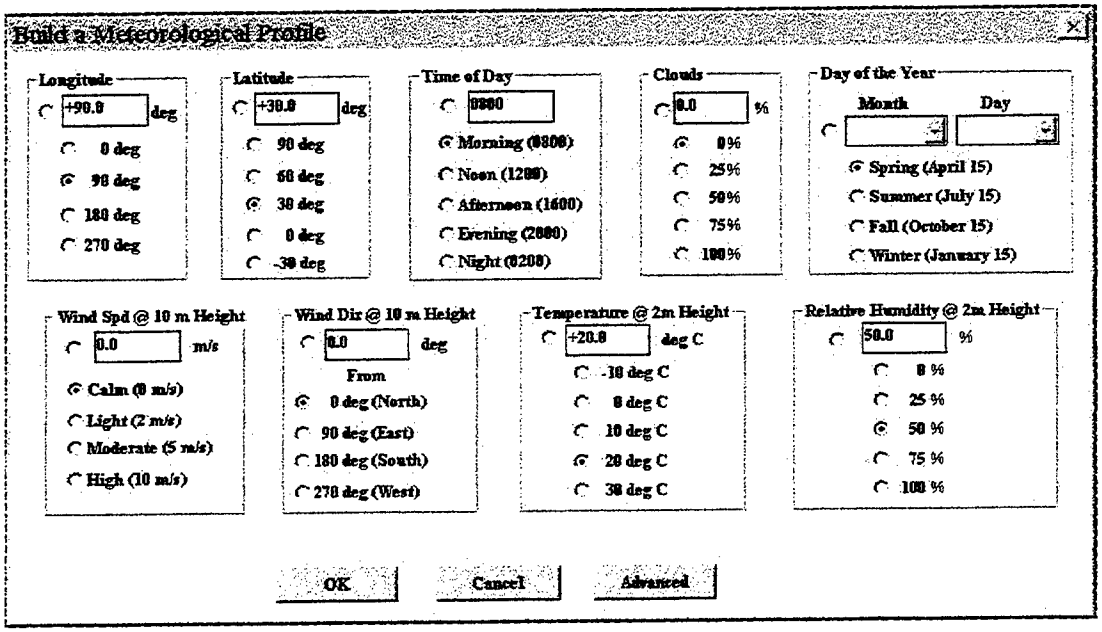


Figure 2. Meteorological profile builder window showing input requirements.

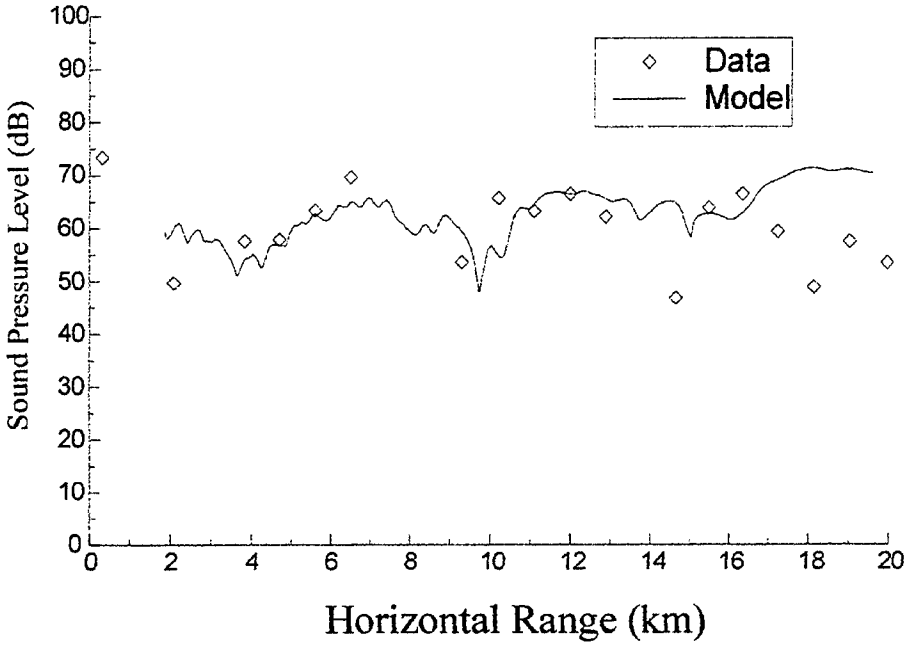


Figure 3. Shows comparison between field data and model prediction from SCAFFIP. The deviation at 16 km is due to improper layer spacing.

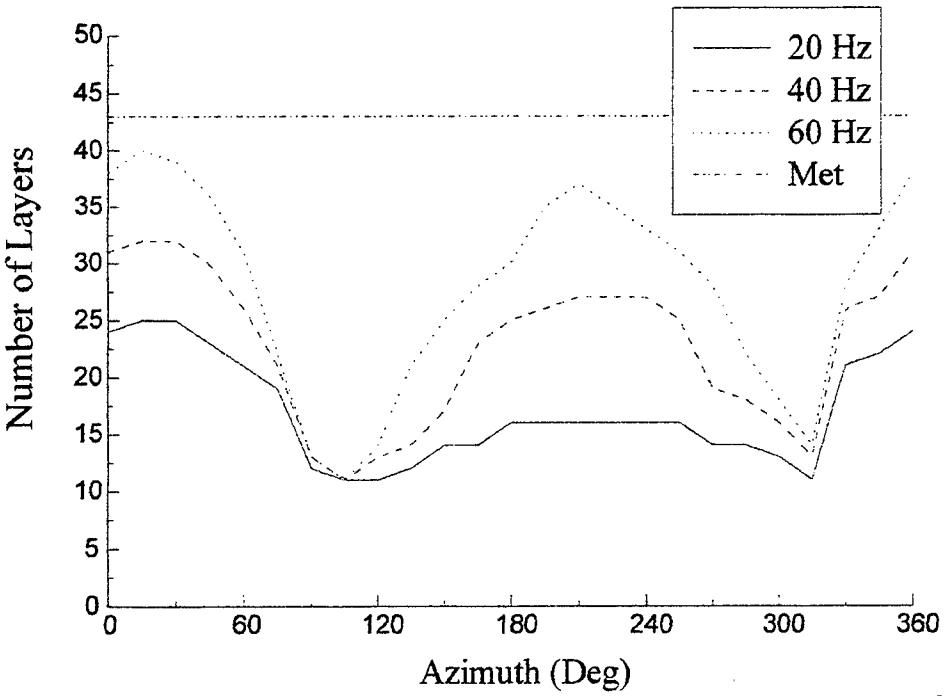


Figure 4. Plot of the number of layers required for a valid solution with azimuth for 3 different frequencies. The original number of layers is the dot-dashed line at 46 layers.

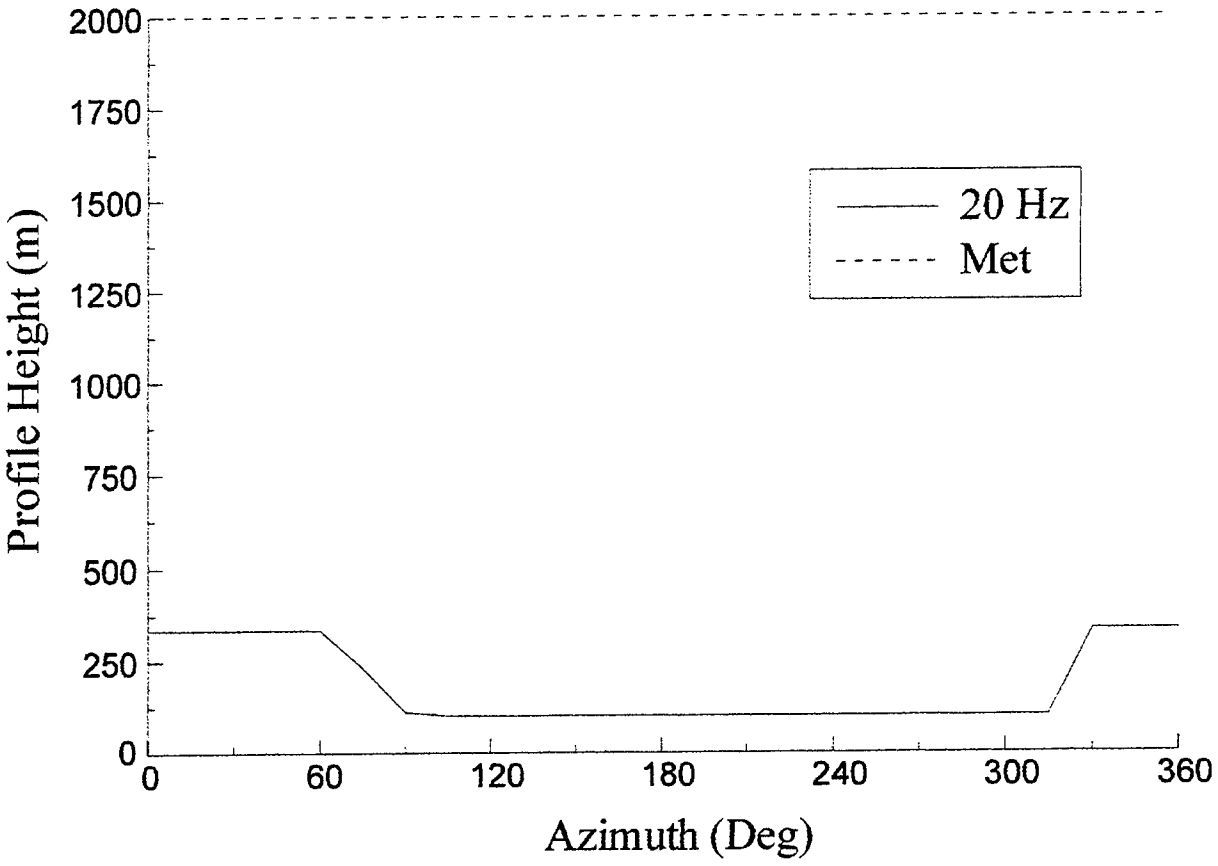


Figure 5. Plot of the profile height used with azimuth. The original profile height is the dashed line at 2000 m.

ASSESSMENT OF SPECTRAL - SPATIAL INFORMATION CONTENT USING CLDSIM / GENESSIS / MOSART AND OPTIMAL FILTERS

Joseph G. Shanks*, Bruce V. Shetler, Steven J. Heising
Photon Research Associates, Inc.
5720 Oberlin Drive
San Diego, California 92121-1723
(619) 455-9741, Fax: (619) 455-0658

William A.M. Blumberg
Air Force Research Laboratory / Space Vehicles Directorate / VSB
Hanscom AFB, MA 01731-5000
(781) 377-2951, Fax: (781) 377-8780

Sponsoring Organization:
Air Force Research Laboratory / Space Vehicles Directorate / VSB
Hanscom AFB, MA 01731-3010

ABSTRACT

Modern optical sensor systems can provide high quality multi/hyper spectral data at high spatial resolution, permitting the application of diverse and sophisticated algorithms for detection and classification of the atmosphere and underlying terrain. Most generally, these algorithms process spectral / spatial / temporal apparent radiance data to achieve their objective. This paper will describe the application of the Vis-LWIR scene simulation tools CLDSIM / GENESSIS / MOSART for estimating the relative information content available to algorithms which use spectral and spatial processing for the detection and classification of man-made objects against natural terrain. The challenges involved in simulating imagery at very-high spatial and spectral resolution will also be addressed.

I. Objective

Deployment of hyperspectral sensors with high spatial resolution (GSD <~ 10 meters) has been proposed for diverse applications in the commercial and government sectors. An important military application is autonomous detection of ground targets in a general battlefield scenario—i.e., possibly camouflaged targets viewed through an atmosphere contaminated by haze, aerosols, or thin clouds.

This paper will address various aspects of system performance associated with detection of ground targets against terrain. (The corresponding results for detection through a haze layer are in progress and will be presented at the BACIMO'98 Conference, see *Shanks, 1997a, Shanks & Lynch, 1994* for a description of previous work.) Specifically, the following issues will be addressed:

1. *Given a noise-free hyperspectral stack, how many Principal Components need be retained to achieve the maximum feasible SNR (Signal-to-Noise Ratio) ?*
2. *What is the change in SNR as spatial processing is added to spectral processing ?*
3. *How do the relative contributions to detection change as the GSD is increased from 1.5 to 3.0 to 6.0 meters ?*

Issue # 1 bears on the processing and down-link load for hyperspectral systems, given their awesome data-collection capabilities. For example, a modest sensor with 256 bands, a 256 x 256 focal-plane and 16 bits of raw data, with a 1 Hz readout produces 34 MB/sec. or 120 GB/hour, not including calibration and "housekeeping" data. Clearly, there is great value in moving much of the processing on-board, reducing preliminary results for down-link. Principal component decomposition is a standard technique in remote-sensing, providing a natural, uncorrelated decomposition of the variance in the spectral stack. Given achievable sensor-noise and the band-band correlations, it is rare to find more than thirty significant principal components. However, this technique must be applied with care when the objective is the detection of *exceptional* features—like sparse targets against a structured background.

Questions # 2, 3 reflect on more fundamental design issues of hyperspectral hardware and data-processing strategy. Clearly, one can trade GSD for spectral resolution (or extent) or on-board processing. Increasing the GSD adversely effects both spectral and spatial response, since a greater fraction of the pixels will then be heterogeneous, increasing spectral mixing, and the definition of distinctive (man-made) elements will be reduced. Neglecting mis-registration, spatial processing will always improve SNR, but perhaps insignificantly.

A number of investigators have explored the trade space of spectral and spatial resolution (see for example Shen, *1997*). However, most of these studies have focused on spatial and / or spectral re-sampling of measured or simulated data followed by the application of standard detection or identification algorithms. Here, we present a method whose aim is to explore the raw information content of simulated hyperspectral data while using, to the maximum extent possible, "perfect" detection techniques as figures of merit. Thus, we employ perfect spatial and spectral matched filters applied to a principal component (PC) transformed hyperspectral stack with theoretical SNR as a figure of merit. The current study explicitly addresses the question of detection. Identification, either spatial - model based ATR approaches, for example – or spectral are related issues which while not addressed here may be amenable to study using a similar approach.

II. Research Accomplished

The sequence of the effort is as follows:

1) Generate hyperspectral stack of terrain imagery, with embedded targets
2) Calculate Principal Components, identify "straw-man" subset for succeeding work

3) Generate SNR image using matched-filter analysis of this subset (spectral only)
4) Apply simple spatial filter to the base set. Generate matched-filter SNR image of combined data (spectral and spatial)
5) Plot weight-vector magnitudes for cases 3, 4.
6) Blur original spectral stack by a factor of two, go to Step 2).
7) Summarize results

The simulated hyperspectral imagery used in this analysis was generated with the latest version of the integrated scene simulation tools GENESSIS, CLDSIM, MOSART and COMPOSITE. In brief, these are UV to LWIR background scene simulation codes in which the physical character of the terrain and clouds is described by data bases describing the topography and material type and mixture for each pixel in the scene. (See references for details: Shanks, *et al.*, 1997a) Additional data bases describe the optical and thermal properties of the materials. These codes are supported by the atmospheric code, MOSART [Cornette, *et al.*, 1997; Westmoreland, *et al.*, 1997] with a 1 wavenumber spectral resolution. COMPOSITE integrates the cloud and terrain contributions for final rendering into the focal-plane.

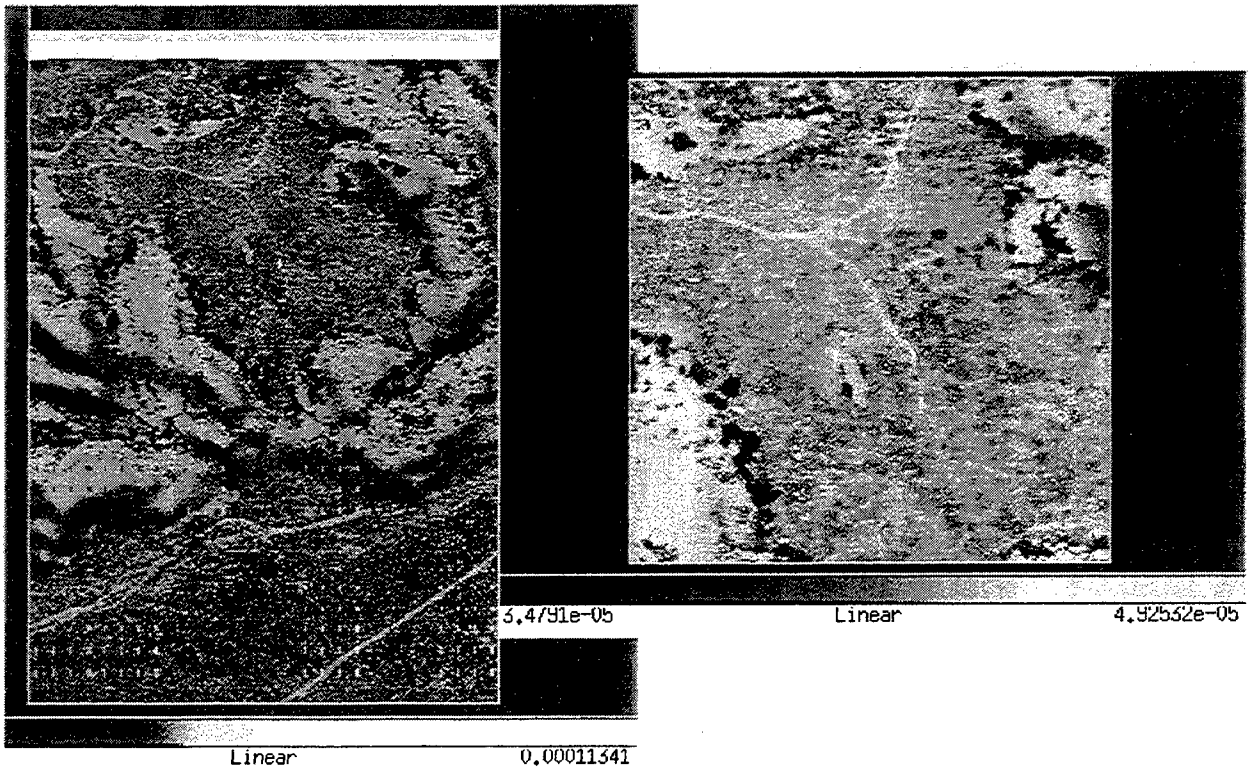


Figure 1a, 1b. Full and 256x256 Sample Scenes @ 0.500 um, (W/um-SR-CM^2)

For the cloud-free scenes discussed here, a version of the *Joshua Tree* terrain data base was used, modified to include dispersed targets inserted at various orientations, as well as a variety of standard panels. The simulated hyperspectral stack is described as follows:

- FOV = 500 x 740 @ 1.5 meter GSD

- Spectral Range: [0.400, 2.500] μm @ 0.005 μm spacing
- Mid-Latitude Summer atmosphere, 11:00 local time

(see Figure-1a) from which a 256 x 256 subset was extracted, as shown in Figure-1b. The target vehicle is clearly visible near the fork in the road at upper-left center. This data base is representative of high desert terrain common to threat regions of the Middle East.

The *principal components* of the spectral stack are defined by diagonalizing the covariance matrix, as shown in equations 1-4, (in which summation on repeated greek indices is implied). This standard technique uses the eigenvectors of the covariance matrix as basis vectors, with the great advantage that the PC's are uncorrelated. Practically speaking, this means that only a few of the PC's capture the bulk of the variance evident in the hyperspectral stack. This is clear from Figure-2, a plot of the first ten eigenvalues, $\lambda^{(a)}$. A mosaic of principal components # 1, 3, 4, 5, 6, 7, 8, 9, 10 is shown in Figure-3 (note that the images were normalized to [0, 255] prior to assembly in the mosaic).

Let $L_\alpha[i,j] \equiv$ radiance of i,j^{th} *pixel in* α^{th} *spectral band*,

$$< L_\alpha > \equiv \frac{\Sigma_{i,j}^{N,N} L_\alpha[i,j]}{N^2}, \quad \delta L_\alpha[i,j] \equiv L_\alpha[i,j] - < L_\alpha > \tag{1}$$

$$Cov_{\alpha,\beta} \equiv \frac{\Sigma_{i,j}^{N,N} \delta L_\alpha[i,j] \delta L_\beta[i,j]}{N(N-1)}, \quad \sigma_\alpha{}^2 \equiv Cov_{\alpha,\alpha} \tag{2}$$

$$Cov_{\alpha,\beta}\xi_\beta^{(a)} = \lambda^{(a)}\xi_\alpha^{(a)} \text{ (rank eigenvalues in descending order : } \lambda^{(1)} \geq \lambda^{(2)} \geq \ldots \lambda^{(N)}) \tag{3}$$

$$PC^{(a)}[i,j] \equiv \xi_\alpha^{(a)} L_\alpha[i,j] \tag{4}$$

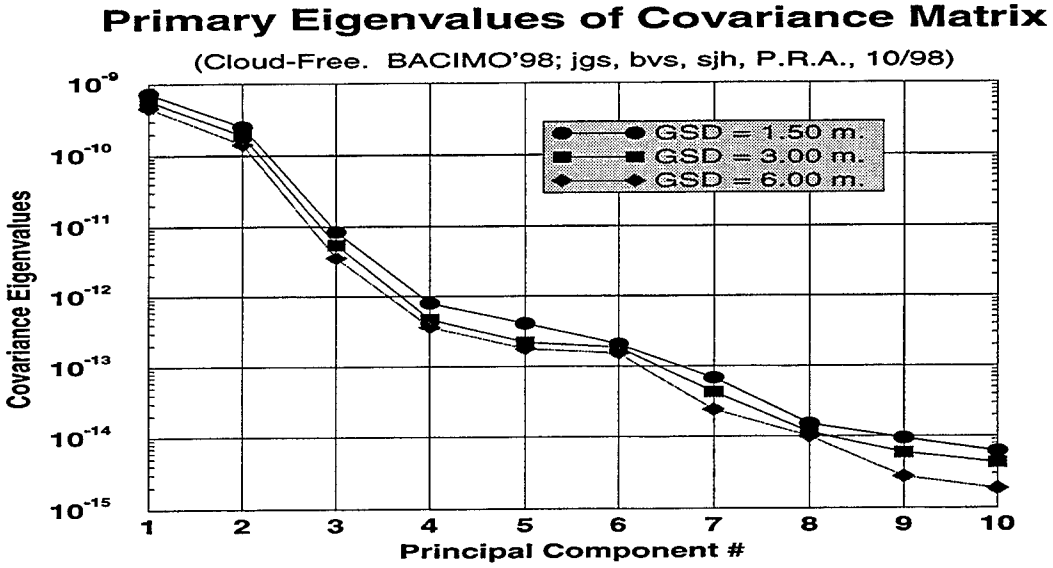


Figure 2. Primary Eigenvalues of Covariance Matrix

Clearly, while the three or four most significant principal components account for ~ 99% of the total variance, the later PC's tend to isolate the target-like features, even those whose spectral content is significantly different from the target of interest. In any case, the subsequent analysis

was limited to the first ten principal components, though higher SNR's would have been obtained with additional terms.

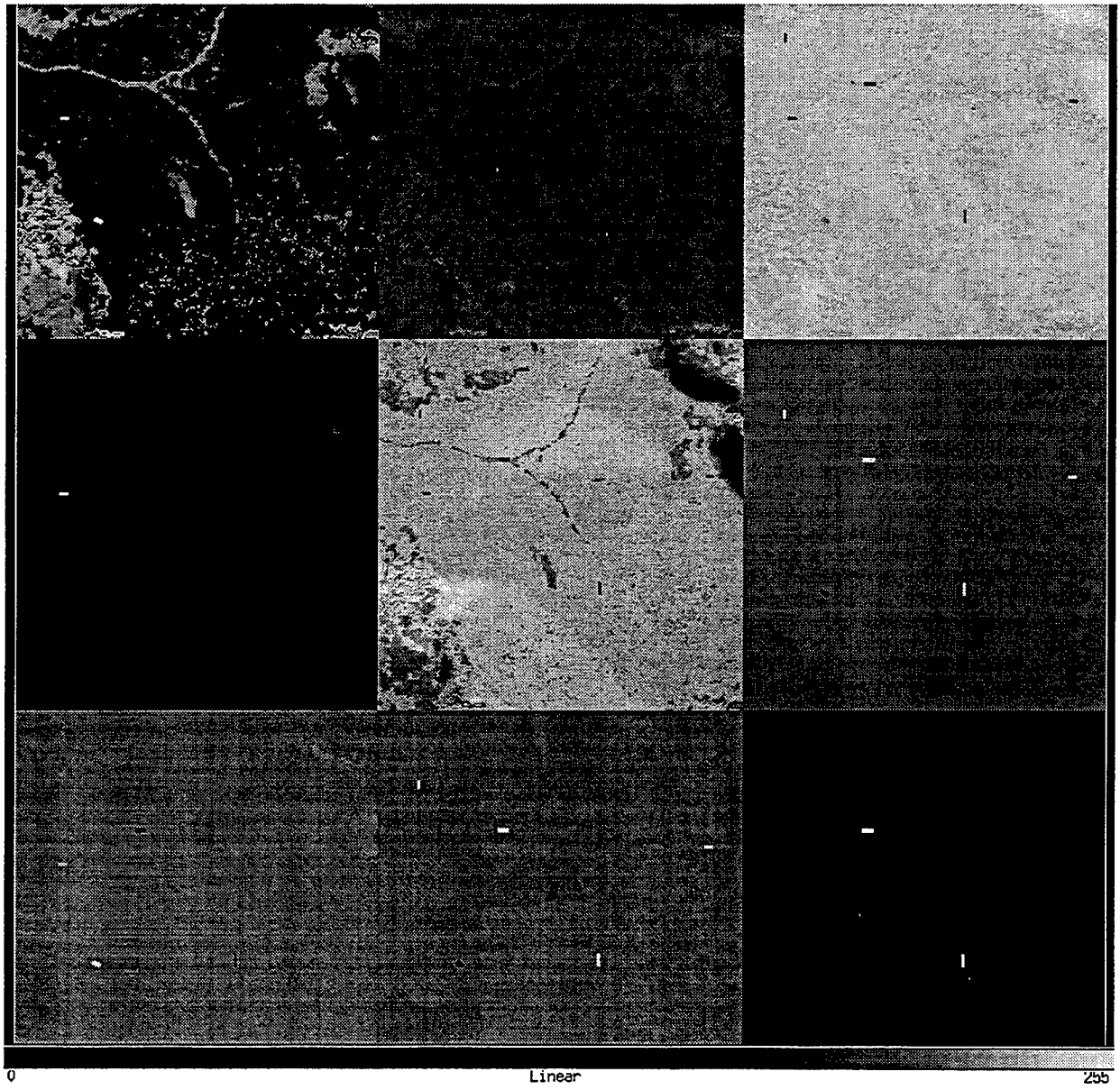


Figure 3. Principal Components # 1, 3, 4; 5, 6, 7; 8, 9, 10, (1.50 meter GSD)

The general objective of the weighted filter is to find the linear combination of input scenes which will maximize the mean signal-to-noise of a particular target against a given background—more precisely, against a background with specified covariance. This technique is used here because it is well-known, reasonably simple and explicitly quantitative. For this purpose, a target vector was developed from the mean value of the 3 x 8 pixel target region, in the space of PC's. For linear processing, the Signal-to-Noise ratio is computed as shown in equation (5) and it is extremized by the weight vector, W_α, defined in equation (6).

$T_\alpha \equiv T$ arg *et vector* (spectral radiance)

$$\text{SNR} = \frac{W_\alpha\ (\text{T}_\alpha - < L_\alpha >)}{\sqrt{W_\alpha Cov_{\alpha,\beta} W_\beta}} \tag{5}$$

$$W_\alpha = Cov_{\alpha,\beta}^{-1}\ (\text{T}_\beta - < L_\beta >) \equiv \text{Optimal Weight vector} \tag{6}$$

Initially, the weights were computed for the spectral (P.C.) components only. Next, a spatial kernel designed to enhance rectangular features the size of a TEL was convolved with the P.C.'s, generating an additional ten planes. The weight vectors were then computed for this combined data set, with the results shown in Figure-4 (shown after Table 1). (Note that the product of the weight and the corresponding $\sqrt{Variance}$ has been plotted, for a uniform comparison and that this product has been scaled by the maximum value in each case. Results at degraded resolution were obtained by block-averaging the original stack and re-computing the PC's.) The message conveyed by Figure-4 is consistent with expectations, given the PC's shown in Figure-3, yet it is somewhat surprising that the greatest contributor to SNR is the *tenth* and last principal component considered, and it is possible that subsequent terms would contribute still more. Further, bands which have poor target/background contrast but are spatially similar to the target are still valuable for detection—see PC # 4. The SNR in the various cases is listed in Table I. The surprising increase in SNR as the IFOV is increased from 1.5 to 3.0 meters simply means that the variance of the background—which includes objects barely resolved at 1.5 m.—decreases more than the signal from the 4.5 m x 12 m. target. This would not occur for a meter-class target.

The actual SNR images at 1.5 meter are shown in Figure-5. At this GSD, the spatial analysis nearly doubles the spectral-only SNR. Note also that the spatial operator was tuned for a horizontal (on the focal-plane) target, nonetheless generating a significant response from the vertically oriented target at lower-right.

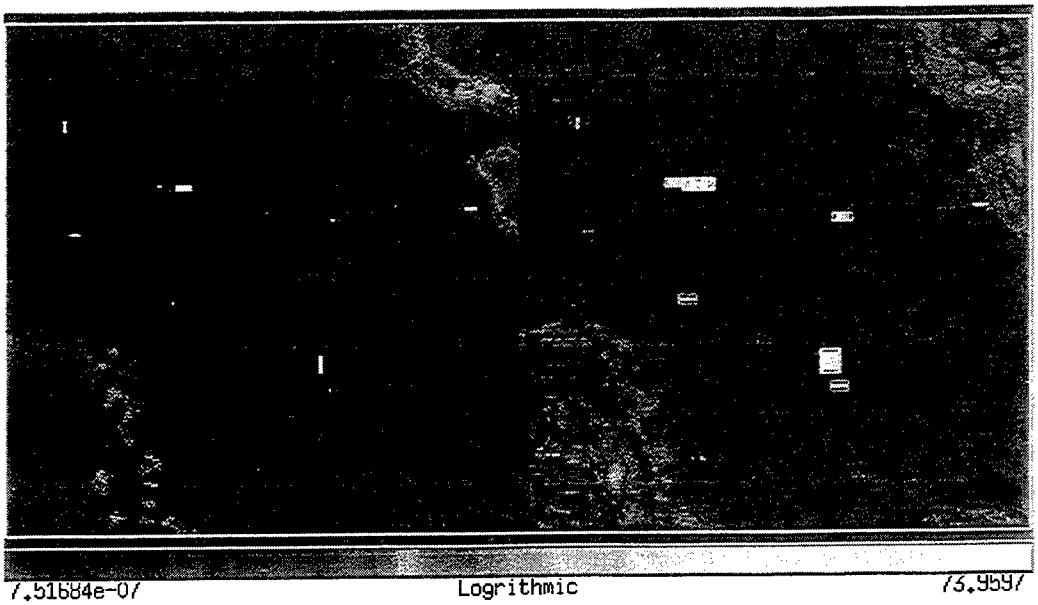
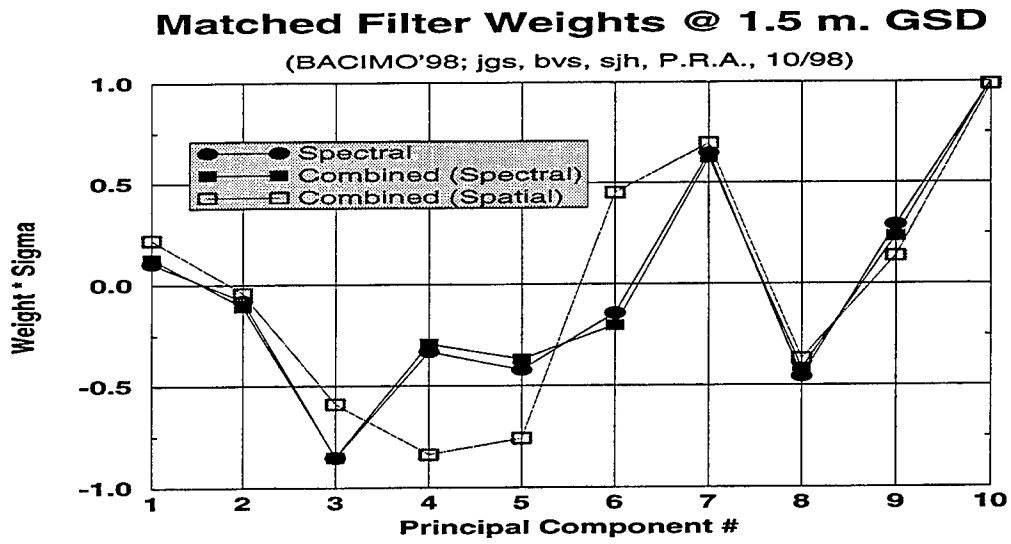
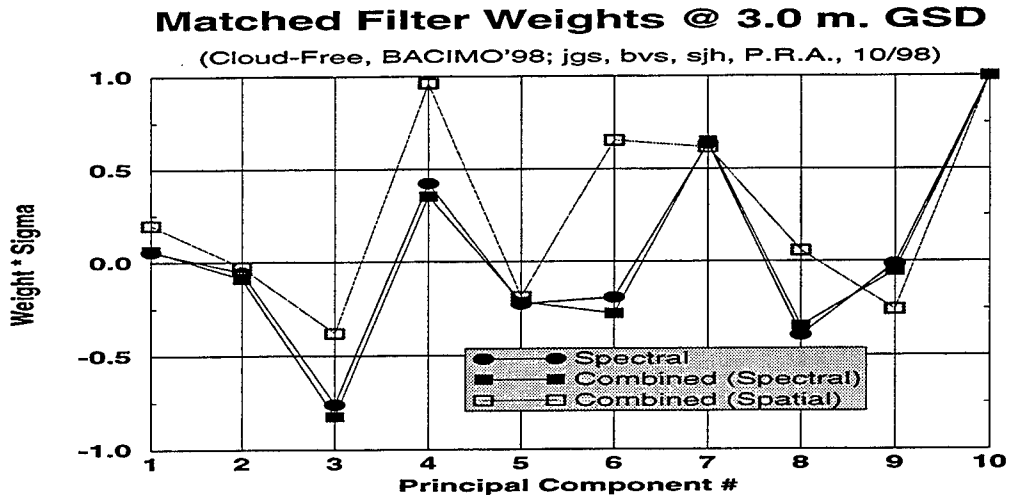


Figure 5. Signal-to-Noise Ratio Images @ 1.5 meter GSD: Spectral, Spectral+Spatial

Table I. Peak Signal-to-Noise Ratio vs GSD and Processing Elements

GSD \ Processing	Spectral	Spectral + Spatial
1.5 meters	38.5	74.0
3.0 meters	49.3	57.9
6.0 meters	43.9	50.7





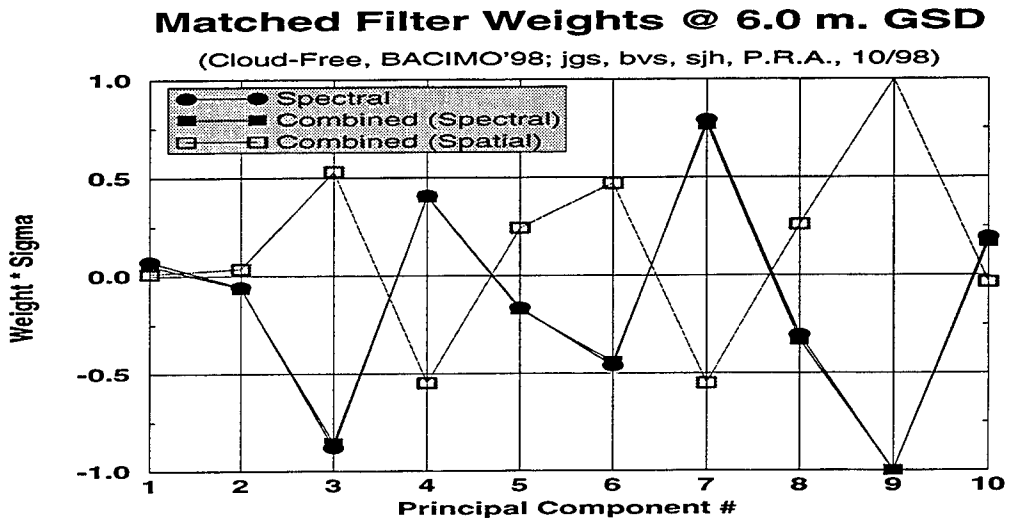


Figure 4a, b, c. Matched-Filter Weights at 1.5, 3.0, 6.0 meter GSD (dimensionless)

III. Conclusions and Recommendations

The methodology presented here provides what we believe is a new approach to answering oft posed questions regarding the relative contributions of spatial and spectral information to target detection and the raw information content of sensor data streams. It would seem that this method could be expanded in a number of ways beyond the simple study presented here. For example, the simple spatial matched filter applied here could be augmented by filters, similarly spatially ideal, but covering a larger parameter space in pose. In addition we will seek to apply the basic methodology to the question of detection, rather than identification, although this will require a more subtle interpretation of matched filter SNR.

IV. Acknowledgements

JGS and SJH gratefully acknowledge the support of the AFRL Space Vehicles Directorate, VSB at Hanscom AFB..

V. References

[Cornette, *et al.*, 1997]
Cornette,W.M., Westmoreland,S.J., Acharya,P.K., Berk,A., Robertson,D.C., Anderson,G.P., Blumberg,W.A.M., Jeong,L.S., *The MOSART Code: 1997* (*20th Annual Review Conference on Atmospheric Transmission Models*, 10-12 June 1997, Phillips Laboratory Geophysics Directorate, Hanscom AFB, MA.), AFRL-VS-HA-TR-98-00057. [ADA 347476].

[Shanks, *et al.*, 1997a]
Shanks,J.G., Mertz,F.C., Westmoreland,S.J., O'Donnell,D.J., Blumberg,W.A.M., Ratkowsky,A.J., Jeffrey,W., Robinson,I.S., Eloranta,E.W., Lisowski,J.L, Najarian,M., *MSTI-III and ARES SW-MW Cloud Data: Comparison with CLDSIM Predictions* (*IRIS Targets, Backgrounds and Discrimination Conf.*, Monterey, Feb. '97)

[Shanks, *et al.*, 1997b]
Shanks,J.G., Mertz,F.C., Filice,J.P., Blumberg,W.A.M., *Simulating Thin-Cloud Effects on Multi-Spectral Target Detection* (*Proc. of CIDOS-97*, Naval War College, Providence, R.I., Oct. 1997), PL-TR-97-2112. [ADA 330020].

[Shanks & Lynch, 1994]
Shanks,J.G., Lynch,D.K., *Remote Sensing Through Cirrus Clouds: Visual and Sub-Visual* (*IGARSS '94 Invited Paper*, Pasadena, August '94)

[Shen, 1997]
Shen, Sylvia S., *Multiband Sensor System Design Tradeoffs and Their Effects on Remote Sensing and Exploitation* *(Proc of SPIE – Imaging Spectrometry III, 28-30 July 1997, San Diego, CA) pp 296 – 303*

[Westmoreland, *et al.*, 1997]
Westmoreland, S.J., F.C. Mertz, and W.M. Cornette. 1997. *Use of HYPEX atmospheric and sensor simulation models for image data evaluation* (*20th Annual Review Conference on Atmospheric Transmission Models*, 10-12 June 1997, Phillips Laboratory Geophysics Directorate, Hanscom AFB, MA.), AFRL-VS-HA-TR-98-00057. [ADA 347476].

AFRLDIAG: TAILORED METEOROLOGICAL PRODUCTS FOR M&S

David J. Smalley*
SenCom Corporation
3 Preston Court
Bedford, MA 01730
e-mail: dave@sleet.plh.af.mil
phone: 781.377.3033
fax: 781.377.8892

Joel B. Mozer
Air Force Research Laboratory
Hanscom AFB, MA 01731
e-mail: mozer@plh.af.mil
phone: 781.377.2945
fax: 781.377.2984

OBJECTIVE

Mesoscale Numerical Weather Prediction (NWP) models are increasingly used to create synthetic atmospheres for modeling and simulation (M&S) applications. These NWP models are typified by voluminous, four-dimensional sets of standard meteorological parameters (e.g. - winds, temperature, and humidity) that hinder direct transition to M&S applications. The primary focus of M&S activities is usually on the study of atmospheric effects and not the processing of large data volumes. In many instances, the M&S application requires a small subset of the NWP data spatially, parametrically, or temporally. AFRLDiag has been developed to address this NWP-M&S transition issue for applications at the Air Force Research Laboratory (AFRL). Its primary benefit is to provide a mechanism for generating value-added, non-prognostic, M&S relevant parameters from the standard NWP data sets.

RESEARCH ACCOMPLISHMENTS

At VSBE, multiple modeling and simulation (M&S) activities are supported with historical simulations. Recent M&S activities along these lines have involved:

- generation of weather diagnostics for simulated military war games for the United States Air Force and Navy,
- scene simulation of aircraft fly-throughs in battle scenarios,
- satellite specification simulation,
- cloud scene simulations and modeling,
- and radiometric validation of cloud models.

All of these efforts require the use of Numerical Weather Prediction (NWP) model

products. Typically, the NCAR/Penn State University Mesoscale Model Version 5 (MM5) or the Coupled Ocean Atmosphere Mesoscale Prediction System (COAMPS) mesoscale models provide the necessary data to fulfill these requirements. Many instances arise, though, where additional data are desirable or a small subset of the NWP data stream is all that is necessary.

AFRLDiag was developed to address the need for value-added products and/or data containment. It includes an embellishment of an earlier program distributed by NCAR, MMDiag, written by F. Chien dated 1995. AFRLDiag consists of the main product generator AFRL_DIAGMM5 and a suite of auxiliary tools that, combined, provide informational and diagnostic/analytical capabilities. The informational tools allow for quick identification of model chronology and domain characteristics of the NWP data. This avails important information to the user to use when tailoring the temporal resolution and duration of the AFRLDiag output product to their M&S input requirements. The diagnostic and analysis set of tools provides the value-added parameters that are often an M&S necessity. These parameters are non-prognostic and geared toward the study of atmospheric effects. For example, the M&S user may require visibility and ceiling computations. These may have specific engineering unit requirements. Also, these parameters may need to be computed for infrared bandwidths instead of those in the visible spectrum. Numerous supportive thermodynamic quantities are also available for computation in AFRL_DIAGMM5. Figure 1 shows the components of AFRLDiag.

Two useful informational tools are AFRL_TIME and HEADERINFO. Both examine the header information that accompanies the data record from the MM5. AFRL_TIME extracts the model time for each record. This is helpful for determining the analysis period of interest from the dataset. It also allows the user to precisely set the timing parameters in the user specification file that the main routine AFRL_DIAGMM5 needs to process the data. HEADERINFO provides an easy way for the user to quickly become acquainted with all that went into the MM5 model run for the queried output dataset.

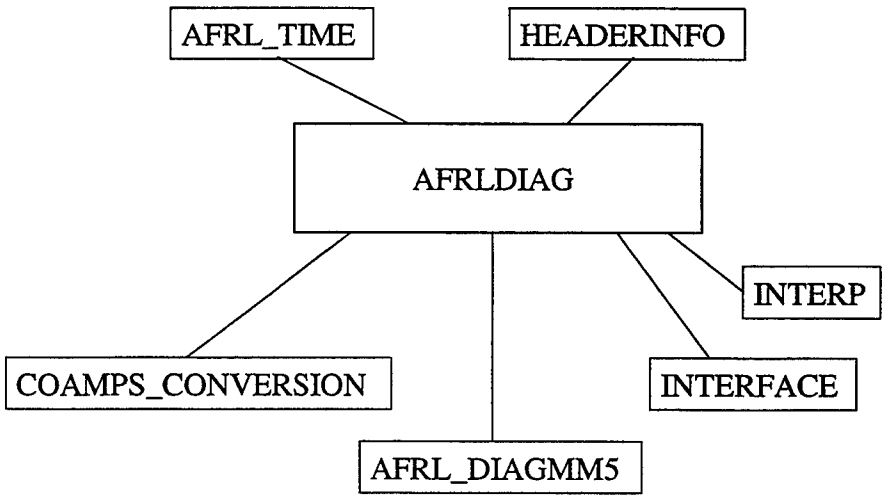


Figure 1. The AFRLDiag components chart.

Typically, the MM5 output data are provided using the sigma vertical coordinate system. This system reflects a ratio of the actual pressure at a point to the surface pressure of that point's model column. Thus, sigma represents a terrain-following coordinate system where one is at the surface and zero is at the top of the model domain. INTERP is used to transform those data to pressure levels determined by the user's needs. INTERFACE is designed to inherit the INTERP output file and generate a set of meteorological data files convenient for use with the AFRL Cloud Scene Simulation Model (CSSM). Those parameters are temperature, dew point depression, wind components, surface barometric pressure, and geopotential height.

AFRL_DIAGMM5 is robust enough to utilize data from different MM5 producers (e.g. – different runs of the MM5). For instance, the U. S. Air Force held Weather War Game II which simulated battle scenarios and utilized MM5 model data from the Air Force Weather Agency (AFWA). The U.S. Navy held a similar simulated War Game effort entitled Global98. The input data for this were from the Navy's COAMPS mesoscale model yielding standard NWP parameters akin to the MM5. However, the COAMPS output data are provided in a significantly different style and structure. A series of COAMPS_CONVERSION shell scripts were developed to transform the COAMPS data into the MM5 format with a minimalist header that satisfied AFRL_DIAGMM5 criteria. This major upgrade to AFRLDiag results in a new methodology for the utilization of COAMPS data in M&S activities.

As mentioned, the core of AFRLDiag is the value-added, non-prognostic product generator AFRL_DIAGMM5. It is modular in design. Thus, it accommodates the incorporation on new subroutines for additional products. The user pre-selects these products in a specification file along with the timing considerations. A user manual is planned to describe this process and available products for selection. Typical basic selections include tailoring standard MM5 data to specific engineering units (such as wind speed in knots, mph, or m s^{-1}). The value-added products include many supportive dynamic and thermodynamic quantities such as vorticity and stability. The primary parameters for M&S, though, are value-added, diagnostic ones such as weather state assessments (which are generated from visibility and ceiling parameters), cloud classification, and transmissivity. Full three-dimensional volumes or two-dimensional surface (or other) planes are available.

AFRL_DIAGMM5 is not the lone post processor of mesoscale model data. The Air Force Weather Agency (AFWA) uses the diagnostics utility MMPOST for similar purposes. The focus of AFRL_DIAGMM5 and MMPOST is slightly different. Thus, they generally have complementary capabilities. There are several factors that distinguish the two from each other and their potential uses that should be highlighted:

- Both AFRL_DIAGMM5 and MMPOST require a priori knowledge of the data variable order to process them properly. They both accept the MM5 output. Additional front-end utilities are available for AFRL_DIAGMM5 to also ingest COAMPS data,
- AFRL_DIAGMM5, through a user specification file, processes selected portions or iterations of the entire input data while MMPOST processes all of the input data,
- Most AFRL_DIAGMM5 output variables are focussed on dynamic or thermodynamic quantities. The majority of the MMPOST variables are synoptic in scope,

- Through a user specification file, AFRL_DIAGMM5 yields only requested, value-added products while MMPOST yields a consistent standard output variable set,
- The output format of AFRL_DIAGMM5 is the same format as MM5 output data while MMPOST yields Viz5D or GRIB format data.

In contrast to the distinctions, both programs also include many of the same standard atmospheric parameters for output. The modular design of AFRL_DIAGMM5 makes it possible to add any MMPOST subroutine to its output suite. An effort is near completion at the time of this writing to integrate the non-redundant AFRL_DIAGMM5 dynamical/thermodynamic subroutines into the MMPOST scheme.

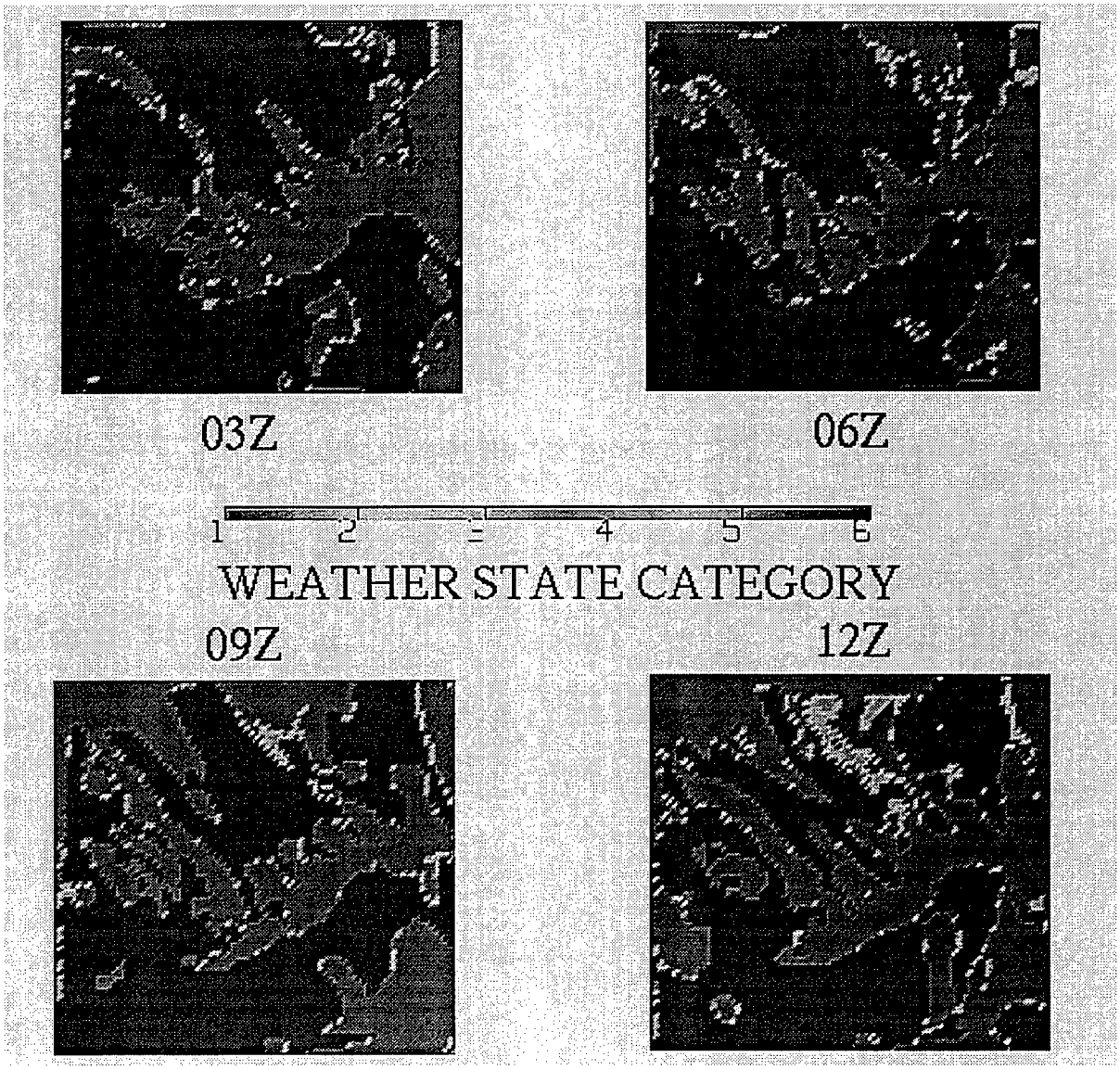


Figure 2. Twelve hour sequence of weather state depictions for a 960105 Global98 simulation of the EPAC theater. See text for discussion.

An example use of the AFRLDiag utility is with the aforementioned U.S. Navy's Global98 simulated war game. This operation required a number of specific value-added, non-prognostic parameters including transmissivity and weather state data. The latter combines visibility and ceiling data (also two value-added products) into a weather state assessment for flight sortie planning. The weather states are categorized from best (category 6) to worst (category 1) conditions and are reported for the battle theater. For Global98, both the Mediterranean and Korean peninsula theaters were simulated.

Figure 2 shows a sequence of weather state depictions for the Global98 EPAC theater. These values were all calculated after the COAMPS_CONVERSION utility was run to construct minimalist-header MM5-style data files for ingest into AFRL_DIAGMM5. The analysis depicts three of the six possible categories. The black region depicts the best (category 6) conditions which represent a combination of visibility greater than five nautical miles (n mi) and cloud base ceilings of at least 12,000 feet (ft). The medium gray region depicts the worst (category 1) conditions where visibility is under three n mi and/or ceilings no more than 500 ft. In some areas, the transition from the best to worst conditions is tempered with mixed conditions (category 3) that correspond to visibility ranging from three to four n mi and ceilings in the range of 1,500 to 3,000 ft. Over time (from 03Z to 12Z), there is a gradual degradation towards lower weather state categories in the upper left region of the theater despite the general maintenance of the overall weather state pattern. The simulation is analyzed by mission planners to schedule sorties in accordance with battle objectives. It is not unusual to have sharp transitions from best to worst categories when using the relatively tight definitions shown here. Those definitions are keyed to sortie loading and planning criteria. This M&S weather state parameter effectively illustrates the potential large impact subtle atmospheric differences can have when applied to a specific objective.

CONCLUSIONS AND RECOMMENDATIONS

AFRLDiag is a useful suite of tools for the tailoring of NWP data for M&S users of MM5 and other mesoscale model outputs. The main feature, AFRL_DIAGMM5, is a flexible value-added meteorological product generator geared to M&S requirements. Its modular design allows for incorporation of future project-specific subroutines. User input enables processing of data subsets on large MM5 files or subsample processing of the time-iterated data it ingests. It is complementary, yet contrasting in style and content, to the AFWA's MMPOST MM5 data post-processor.

It has been used in a number of modeling and simulation applications. For the recent Navy Global98 exercise, it was used to create weather state depictions, support IRTSS fly-through simulations, and provide meteorological data in proper context for use with the CSSM. A future benefit may be to combine some or all of these tools into a GUI display for adept access by the novice user.

An Object-Oriented Paradigm for the WAVES/TAOS Interface

Dr. Alan E. Wetmore*and Dr. Patti Gillespie and Dr. David Ligon
US Army Research Laboratory
2800 Powder Mill Road
Adelphi, MD 20783 USA
awetmore@arl.mil; +1 301 394 2499; FAX +1 301 394 4797

Mike Seablom and Robert Reynolds
TASC, Inc.
Annapolis Junction, MD

Abstract

Ongoing work at the Army Research Laboratory (ARL) is focused upon integrating the Weather and Atmospheric Visualization Effects for Simulation (WAVES) numerical package into both present and planned Defense Modeling and Simulation Organization (DMSO) simulators. Rules governing the implementation of models into such simulators require adherence to object-oriented software development using High-Level Architecture (HLA). Because the WAVES model components consist largely of legacy Fortran code, work is now underway to recast the components of WAVES into instances of abstract data types without performing major rewrites of the scientific "core" of the various codes. Such an effort will result in the "wrapping" of the main Fortran components into software modules accessible from module interfaces. The various interfaces will be controlled by a main application-programmer interface, that may be attached easily to a graphical-user interface or to a user program. Ancillary programs, such as graphical display utilities, will be controlled from the API thus producing a toolkit accessible for a variety of applications. To achieve the HLA requirement, the WAVES API will be linked to the Total Atmosphere-Ocean Services (TAOS) System. The WAVES/TAOS integration provides a cost-effective method of modernizing legacy scientific code.

1 Objective

The Weather and Atmospheric Visualization Effects for Simulation (WAVES) project is an ongoing effort to preare physics based models of three-dimensional radiative transport within inhomogenious atmospheric cloud conditions for use by simulations. In order to allow WAVES to meet the

[0]This paper has been cleard for public release

DoD demands for all simulations to use the High Level Architecture (HLA) infrastructure, a migration from the legacy scientific model approach to the HLA paradigm must be found. One outgrowth of the DMSO and DARPA funding over the last several years has been the Synthetic Theater of War (STOW) project. As part of that project the Total Atmosphere-Ocean System (TAOS) has been used to supply an interface to many environmental model and data sources within the HLA architecture.

By adopting TAOS as our bridge to HLA, we will significantly reduce the cost relative to attempting to force the WAVES models to directly support the HLA architecture.

Adopting a "toolkit" approach to WAVES has allowed us to develop an Object-Oriented API that is used to control the WAVES sub-models and access the data created by those models in a way that allows TAOS in ingest and filter the data into a consistent TAOS representation of the environment that is available to an HLA federation exercise.

2 Research Accomplished

2.1 WAVES Toolkit Design

The first step of the project was to design a toolkit framework that contains the object representations of the WAVES data and model capabilities.

The major component models of WAVES are: MODTRAN[1], Solar Lunar Almanac Core (SLAC), Cloud Scene Simulation Model[2], (CSSM) ATMOS, Boundary Layer Illumination and Radiation Balance[3, 4, 5] (BLIRB).

Each of these models was enclosed in a C++ wrapper that implemented an API for control and execution of the model, as well as access to desired data structures.

Each of the WAVES Toolkit wrappers was designed and implemented with dynamic binding. This design implies that messages to the objects are determined during execution, not at the time of compiling. Dynamic binding is a precondition for development of reusable software architectures that do not depend on specific object types. Within the WAVES Toolkit, all of the major components are instantiated dynamically, and destructors are used with all objects to minimize the risk of memory bleeding.

The WAVES Toolkit is implemented through two abstract data structures: the WAVES Scenario object and the WAVES data objects.

Within the Scenario object are the individual model objects for each of the constituent WAVES numerical models. Above the Scenario Object is the functional class Event Class that contains the API to the WAVES Toolkit. The API can be used by; user programs, to run the models and extract data; a Graphical User Interface (GUI), for interactive use; other applications such as TAOS, as part of a larger simulation.

The objects contained within Scenario fall into two categories: model objects and ancillary objects. The model objects contain the main scientific "core" elements of WAVES: MODTRAN, SLAC, CSSM, ATMOS, and BLIRB. Additional models such as the three-dimensional smoke model COMBIC, may be contained within Scenario in the future without disruption of other model objects. The ancillary objects consist of a collection of data objects and the error object. The error object is a persistent object that allows the user to trace system operations. Many types of notes and errors, both fatal and nonfatal, may be logged easily via the error object. At the end of a

WAVES scenario execution, or at any time during execution, the error log may be dumped and the messages received.

The Scenario class is an abstract, not concrete, class. It defines an organization framework for containment of the model objects and the ancillary objects in a framework that is useful; for future expansion of the system. It does very little work, rather, manipulation of a WAVES Scenario involves implementing a series of commands that execute various models, and move data back and forth as required. The actual commands may change between users or between simulators that invoke WAVES. In previous versions of WAVES, this type of program was known simply as a driver, within the WAVES Toolkit this functionality is known as an event handler. Event handlers ma be tailored for specific applications and each application using WAVES my have a unique event handler. The customization of event handlers is done without modifying the properties of the Scenario class, and all of the event handlers will inherit all of the properties of the Scenario class through inheritance. At the present time we have implemented only one event handler that we call Event.

The methods of the event class perform all of the functions necessary to execute WAVES. Hence, Event is a functional API that may be interfaced to user programs, GUI's, or a simulator.

2.2 WAVES Toolkit Data Objects

Data Objects, provide methods for storing and retrieving model outputs. They allow the user to manage large amounts of information without requiring knowledge of dataset formats, locations of files position of data within files, etc. They also provide a means of communicating information within an event handler. The methods contained within the data objects allow the user to specify symbolic indentifiers for an experiment as well as grid information unique to individual quantities. Employing the methods of the data objects to save and retrieve information allows dataset formats to be altered easily, should that prove necessary. No subsequent changes are need to the user programs or to the event handler. Currently the WAVES Toolkit contains one class named DataObject; there are also descendent classes, which are tailored to a specific model.

2.3 WAVES API

The application programmer interface represents the communication point between WAVES and a user program or a client application such as TAOS. Within the toolkit, the event handlers have the functional responsibility of an API. In the present version of the toolkit, the Event class is provided as a means of issuing high-level commands between the user program and the WAVES components. Event also issues a series of lower-level commands to the models and supporting routines necessary to set up and execute the entire WAVES suite of models.

Event is a descendent class of Scenario, consisting mostly of methods. Event contains few data members other than those inherited from scenario. The constructors for Event call the constructors for Scenario without any embellishment, and the arguments are identical.

There are three methods under construction that will be used in the future for communicating with a GUI: attach_GUI(), EventLoop(), and WaitForEvent(). These will be used to automatically sense the presence of a GUI, and modify program control accordingly.

The most important method within Event is signal(), an overloaded function that is designed to send messages to the model objects. It effectively hides the implementation of the models and the drivers by providing a very specific, guarded interface for the user. It accepts up to two arguments: a keyword and a value, both of that are quality-checked for erroneous input. The messages instruct the scenario to create and destroy model objects, to signal the models to begin execution, or to define local parameters. The Signal() function is the sole method of interacting with the model objects. This type of restricted access is important to our goal of coupling WAVES to large scale simulation infrastructure such as TAOS. The users, or te simulator itself must not be allowed to assign invalid data to for any of the input parameters, nor should they be allowed to execute functions out of sequence. Each of the messages supported by the various models also provides default values for all parameters. This ensures undefined values will be avoided and it provides an "escape hatch" for certain situations in which erroneous input is encountered.

The keywords that are the first argument of the signal() method are enumerated data types defined in the model classes; they are not string arguments and thus quotation marks should not be used. The model keywords are always used used to define parameters local to the model objects.

2.4 WAVES Model Objects

The model objects are wrapped about the "core" science elements of WAVES. They provide communication between the toolkit and the older FORTRAN modules, control access to the model drivers, and serve as a platform for dynamic memory allocation. The software design of the toolkit leaves much of the legacy model code unchanged. Required data structures are passed from the wrappers directly into the model drivers. Within the wrappers, quality checks are performed on the input parameters prior to model execution. Because the wrappers are written in C++, dynamic allocation of large arrays used by the fortran code is possible. In such cases, memory addresses are passed to the model drivers, replacing overdimensioned, static arrays.

The model objects are designed to operate independently, outside of the WAVES toolkit. Each of the objects is a complete instance of a particular model. The Scenario class and the event handler make use of these objects, by way of containment, to formulate a WAVES simulation.

2.4.1 The MODTRAN Model Object

MODTRAN is available[1] from the Air Force Research Laboratory at Hanscom Air Force Base. The version of MODTRAN currently in WAVES is MODTRAN version 3.5. It is not the intent of ARL to redistribute MODTRAN through WAVES, rather, a restricted implementation is being developed in which only the information requiered by WAVES is retrieved. The modifications we have made o the MODTRAN drivers is returned to AFRL for possible implementation in future versions of MODTRAN. The information extracted in WAVES is limited to: the incoming solar irradiance at the top of the WAVES volume, the diffuse radiance at the top of the WAVES volume, and the molecular extinction at a series of altitudes within the WAVES volume. The techniques of information hiing allowed a restricted version of the MODTRAN model to be developed quickly.

Much of the functionality of the MODTRAN interface is designed to replace the original card/based I/O of the original driver. The standard version of MODTRAN requires the user to

[1] http://www.plh.af.mil/VSBM/gpoc/modtran.html

select input by way of an input data set; output is routed to a series of other datasets. Inputs are required to appear in a specific, column-oriented format known as "card image". The WAVES software design targets removal of the I/O system used by MODTRAN, and replacing it with methods for initializing and retrieving private data members. This effort will allow MODTRAN to be coupled easily with the WAVES toolkit and subsequently a simulator. The model output that is required by WAVES is passed back directly to the wrapper. The toolkit interfaces to the FORTRAN subroutine DRIVER. All of the input structures are passed into the model at this point; the required output is also passed back to the wrapper through DRIVER.

Some of the parameters assigned through the MODTRAN model interface have global definitions in the Scenario class. Through the event handler, those definitions will assign similar values locally; no additional action is required. If necessary, the model object keywords may be used to override the global parameters from the event handler.

2.4.2 The CSSM Model Object

The implementation for CSSM is similar to that of MODTRAN, except that here a full implementation is necessary. The interface between the wrapper and the model is the FORTRAN subroutine CLOUD. Nearly all of the parameters required to set up the CSSM grid are passed through this interface. The output array, containing the liquid water quantity is returned.

2.4.3 The BLIRB Model Object

A full implementation of BLIRB is designed for use in the toolkit. The interface point between the wrapper and BLIRB is FORTRAN subroutine EOEXEC. All of the input structures are passed through this point.

The output for BLIRB is currently being saved to a file, conversion routines are available outside of the toolkit to convert this file into a BLIRB data object. In the future, a function to generate a linked list of output quantities will be available an will be called by BLIRB. The purpose of this function is to allow users to write out any quantity necessary, without having to worry about storage space, data formats, or ordering. The linked list will generate an internal file that will be read by the toolkit wrapper; subsequently the toolkit will call a function to generate a BLIRB data object.

2.5 TAOS Integration

The design and implementation of the objects and classes discussed in the previous sections have laid the foundation for a robust interface to the TAOS server architecture. We have made a preliminary design for integrating the Object Oriented WAVES into the TAOS architecture. Our near-term goals are to prepare a version of the interfaces necessary to allow TAOS to ingest the WAVES data objects. Following that we will develop an interface to allow TAOS to pass the initialization data to WAVES.

3 Conclusions and Recommendations

We have implemented an Object-Oriented architecture of wrappers, drivers, and event handlers onto the legacy models that make up WAVES. The models can now be executed with dynamic invocation and dynamic memory allocation. The primary data elements both used within WAVES and also the important output quantities are ready for access through well designed data objects. Our next step is the final integration within the TAOS server architecture and demonstration of access through a larger simulation federation.

References

[1] L.S. Bernstein, A. Berk, D.C. Robertson, P.K. Acharya, G.P. Anderson, and J.H. Chetwynd. Addition of a correlated-k capability to MODTRAN. In *Proceedings of the 1996 Meeting of the IRIS Specialty Group on Targets*, pages 249–258, 1996.

[2] M. E. Cianciola, M. E. Raffensberger, E. O. Schmidt, and J. R. Stearns. Atmospheric scene simulation modeling and visualization. Technical Report PL-TR-96-2079, Air Force Phillips Laboratory, Hanscom Air Force Base, MA, 1996. ADA312179

[3] Patti Gillespie, David Ligon, and Alan Wetmore. WAVES overview. Technical Report ARL-TR-1721-1, U.S. Army Army Research Laboratory, 2800 Powder Mill Road; Adelphi, MD 20783, 1998.

[4] Michael Seablom, Patti Gillespie, David Ligon, and Alan Wetmore. WAVES toolkit. Technical Report ARL-TR-1721-7, U.S. Army Army Research Laboratory, 2800 Powder Mill Road; Adelphi, MD 20783, 1998.

[5] David Ligon, Alan Wetmore, and Patti Gillespie. WAVES model evaluation. Technical Report ARL-TR-1721-7, U.S. Army Army Research Laboratory, 2800 Powder Mill Road; Adelphi, MD 20783, 1998.

Measurements and Modeling of EO Parameters

MODELLING CONCENTRATION DISTRIBUTIONS WITHIN TRANSIENT AEROSOL PLUMES

William S. Andrews and Johnathan R. Costa
Department of Chemistry and Chemical Engineering
Royal Military College of Canada
Kingston, Ontario, Canada K7K 7B4
Phone: (613) 541 6000 ext 6052, Fax: (613) 542 9489
Email: andrews_w@rmc.ca

Gilles Roy
Defence Research Establishment Valcartier
Val-Belair, Quebec, Canada G3J 1X5

A series of field trials has been conducted in order to determine the aerosol concentration distributions within plumes resulting from releases under atmospheric conditions falling within Pasquill stability criteria for categories A, B and A-B. The aerosol examined is kaolin, an inert ceramic having a particle size less than 3 μm and an extinction coefficient of 1.2 ±0.2 m^2/g. Concentration measurements were made using the Defence Research Establishment Valcartier laser cloud mapper, which is based on a scanning LIDAR operating at 1.06 μm.

Predictions of concentration distributions were generated and evaluated using the Gaussian plume algorithm with the appropriate Pasquill dispersion coefficients. These provided poor predictions. Relationships were developed for crosswind dispersion coefficients based on measured data which provided better fits for the Gaussian model. Neural network models were also trained to provide somewhat better predictions than the Gaussian models. Examination of the measured data and the modelling algorithms suggests that atmospheric turbulence dominates downwind advection and diffusion effects close to the point of release.

Introduction

For a number of years, the Defence Research Establishment Valcartier (DREV) has been using a Laser Cloud Mapper (LCM)[1] to support research and development work on obscurant aerosols.[2,3,4]

In the study reported on below, this device has been applied to measuring the spatial and temporal concentration distributions of aerosol plumes. A more detailed description of the apparatus and the conduct of the trials was reported on previously.[5,6,7]

The classical modelling approach for aerosol dispersion in the atmosphere is to apply a Gaussian distribution to either a puff (instantaneous) or a plume (continuous) type of release. As much more work has been conducted on characterizing plumes, the Gaussian plume fitting parameters are felt to be more valid than comparable values used for puff fitting. This paper will concentrate on reporting the adequacy of Gaussian plume models to predict the measured concentration distributions.

Gaussian Plume Model

The two Gaussian models, the plume and the puff, are based on diffusion theory, with the concentration decreasing exponentially from the centreline or centre. The general Gaussian plume equation describing aerosol concentration, C (g/m^3), from a continuous source, is

$$C = \frac{Q}{2\pi\sigma_y\sigma_z u}\left(e^{-\left(y^2/2\sigma_y^2\right)}\right) \times \left[e^{-(z+h)^2/2\sigma_z^2} + e^{-(z-h)^2/2\sigma_z^2}\right], \quad (1)$$

where Q is the source/production rate (g/s), σ_y and σ_z are dispersion coefficients or standard deviations in azimuth and elevation respectively (m), y and z are respective azimuthal and vertical distances from the centreline (m), h is the distance of the plume centreline above ground (m) and u is the wind speed (m/s) taken as being along the x axis.

A Gaussian distribution, by definition, has two fitting parameters, a mean (in this case the centreline concentration provided by the first term on the RHS of Eq.1) and a standard deviation (here contained in the σ_y and σ_z terms, the dispersion coefficients). It is noteworthy that for the aerosol dispersion application, these standard deviations are determined from the appropriate Pasquill stability categories,[8] which in turn are functions of distance from the source (x), cloud cover, i.e., insolation, time of day, etc. The basic assumptions inherent in the Gaussian plume model are constant emission, conservation of mass, (no ground deposition), steady wind and that the results are time averaged. Such parameters as ambient temperature, relative humidity, surface roughness as well as ground deposition, any chemical kinetics or aerosol/atmosphere reactions are not explicitly or even implicitly included in the basic model, although additional terms can be added. Two further limitations are that the Gaussian plume model predicts rather poorly less than 100 m from the source and that the quality of predictions varies inversely with distance from the centreline.[9]

Although some of the limitations mentioned above could be addressed by physically-based or semi-empirical fittings (notwithstanding that the σ_y and σ_z values are themselves semi-empirical in nature), it was decided to use the general Gaussian plume model as the basis of comparison for ANN models.

The instantaneous Gaussian puff model, which intuitively should provide a better prediction of aerosol dispersion from screening grenades than the continuous plume model, was found to perform not nearly as well. This is probably due to the fact that the wider use of the plume model has led to much better characterizations of the standard deviation (σ_y and σ_z) values used for predictions.[10]

Data Collection and Handling

The field trials for the aerosol concentration distribution measurements were held at Canadian Forces Base Valcartier, just adjacent to DREV, on a level plain abutted by a steep, tall hill. The trials were conducted during the periods 26-29 May and 4-12 August 1997, and comprised in all 206 separate releases of kaolin, fog oil, red phosphorus (from L8A1 service screening grenades) and hexachlorethane

(from L5 screening grenades). The releases were effected at or near (within 1 m of) the ground surface.

The aerosol reported on in this paper was kaolin, a fine ground ceramic ($H_2Al_2Si_2O_8.H_2O$) with a particle diameter of less than 3 μm and a measured mass extinction coefficient of 1.2±0.2 m^2/g. The kaolin was released in 50 g lots from a generator, i.e., with both horizontal and vertical momentum. The small size and weight of the particles, however, were felt to minimize the influence of this initial momentum on concentration distributions for cloud areas increasingly removed in time and space from the point of release. The main influences on distributions, then, were felt to be diffusion and advection.

The laser cloud mapper was based on a scanning light detection and ranging (LIDAR) device, using a NdYAG laser operating at 1.06 μm. Resolution of the measured backscatter signals was felt to be 1.5 m in range, with a beam divergence of 4 mrad or about 0.4 m within the aerosol cloud. This would provide potentially 316,800 data points per test. The useful number of data points (actual cloud reflections as opposed to background backscatter), was about 70,000 per test.

The software supporting the LCM employed an inversion algorithm of the LIDAR equation to convert the backscattered signal reflections to volumetric extinction coefficients (σ in m^{-1}).[11] This value is effectively the αC or mass extinction coefficient-concentration product of the aerosol applied to the electromagnetic signal. Its relationship with the mass extinction coefficient (α in $g.cm^{-2}$) can be seen in the Beer-Lambert Law:

$$I / I_0 = e^{-\alpha CL}, \qquad (2)$$

where I/I_0 is the transmittance through the path length L (m). The mass extinction coefficient α (m^2/g) can be considered the removal (scattering and absorption) cross section per unit mass and must be determined empirically. It is a function of aerosol particle size distribution, particle shape, and electromagnetic wavelength.[12] The product αC (m^{-1}) can be considered as the volumetric extinction coefficient, σ, and is the value that is generated by the LCM support software. The volumetric extinction coefficient values can be converted to concentrations by dividing by the mass extinction coefficient value, which for kaolin has been measured as being 1.2±0.2 m^2/g, a value consistent with other sources.[13,14]

In all, a total of 50 kaolin releases were measured during the days of 5, 6, 7 and 12 August 1997. The major difficulty encountered was the measurement of the wind speed and direction. The wind was gusty and constantly changing direction, so measured values were only applicable at the time and location of acquisition, normally just before the kaolin release. Also, the weather station was some 50-100 m from the points of release.

Gaussian Modelling

The process of determining concentration distributions involved initially determining the cloud centroid, which was considered the origin of the Cartesian coordinate system applied to the analysis. The x axis was aligned with the downwind direction at the beginning of the trial, with the y and z axes being orthogonal and in the azimuthal (horizontal) and elevational (vertical) directions, respectively. Specific

volumetric extinction coefficient values corresponding to backscattered signals were then mapped into the new coordinate system. This permitted the search through the LCM-generated files for values in the same sweep (z values) and the same downwind distance (x value).

The kaolin trials were grouped by wind speed, with 24 separate releases being able to be considered as being covered by Pasquill categories A, A-B and B. The wind speeds varied from 0.8 to 3.1 m/s. Further data reduction suggested groupings of appropriate releases as either at low wind speeds (0.8, 1.4 and 1.7 m/s) containing results from 9 releases or at high wind speeds (2.2, 2.8 and 3.1 m/s) involving 15 releases. Cross sections were taken through each of the plumes at downwind distances of 5, 10, 15 and 20 m from the origin and at elevations of 0 and 2.5 m. Cubic spline fits were determined for each of the sections, with data sampled at 10 cm intervals. These values were then averaged to produce average concentration distributions for each of the downwind and elevation intervals mentioned above. An example of an averaged concentration distribution for 5 trials at a wind speed of 2.2 m/s, 5 m downwind taken during the second LIDAR scan (roughly same time after release) can be seen in Fig. 1.

In light of the non-uniform distribution, it was decided to group 13 high wind speed trials together to recalculate an average distribution. Consequently, trials at 2.8 and 3.1 m/s had their measured extinction coefficients linearly rescaled to correspond to 2.2 m/s. The composite average distribution can be seen in Fig. 2.

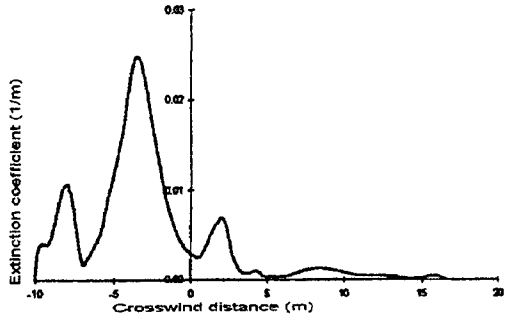


Fig. 1. Average extinction coefficient (concentration) distribution of 5 kaolin releases, 5 m downwind from initial cloud centroid, near ground level at wind speed of 2.2 m/s.

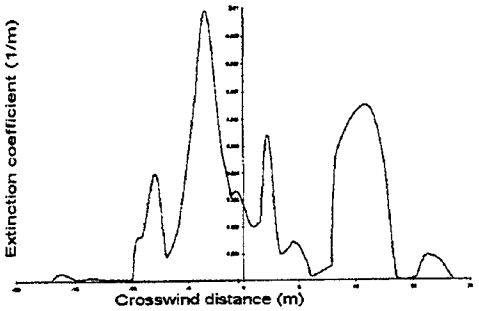


Fig. 2. Average extinction coefficient (concentration) distribution for all high wind speed trials scaled to 2.2 m/s at 5 m downwind from point of release and at near ground level.

Averages were then able to be compared to a corresponding Gaussian plume distribution, which was scaled so that the area under the curve equaled the area under the average distribution. This can be seen in Fig. 3.

It is noteworthy that the unscaled Gaussian (based on conservation of mass) predicted a centreline concentration a factor of 10 higher than the scaled version. This would also suggest axial as well as radial concentration anomolies due to turbulence. In order to remove this effect somewhat, the centroids for each individual cross section were

recalculated and superimposed, to place the mean on the centreline. The effect of this can be seen in Fig. 4.

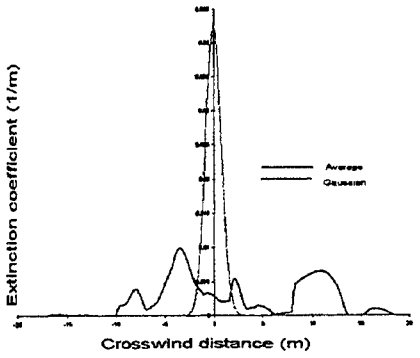


Fig. 3. Comparison between average extinction coefficients scaled to 2.2 m/s and corresponding Gaussian distribution scaled to cover area equal to average distribution. Values are for 5 m downwind near ground level.

In all cases analyzed, the Gaussian has provided poor predictions of the extinction coefficient distribution, overpredicting at the centreline and underpredicting at distances away from it. One would reasonably have expected the opposite trend, as the Gaussian, which is time–averaged over 10 min should be broader than the individual trial distributions which had no averaging imposed. This was probably attributable to the fact that the measured test data were collected at downwind distances and over times outside the conditions used to develop the Pasquill parameters. The dispersion coefficient, σ_y, as shown in Eq. (1), was recalculated to optimize the fit of the Gaussian distribution to the measured averages. Relationships were developed for σ_y for Pasquill categories A (up to 12 m downwind) and B (up to 22 m downwind) as a function of x, the downwind distance, as shown in Table 1.

Table 1. Standard and fitted equations for the dispersion coefficient, σ_y, as a function of downwind distance, x.

Pasquill Category	Standard Equation[10]	Equation fitted to data
A	$0.22x(1+0.0001x)^{-0.5}$	$0.0861x^2$
B	$0.16x(1+0.0001x)^{-0.5}$	$0.0259x^2$

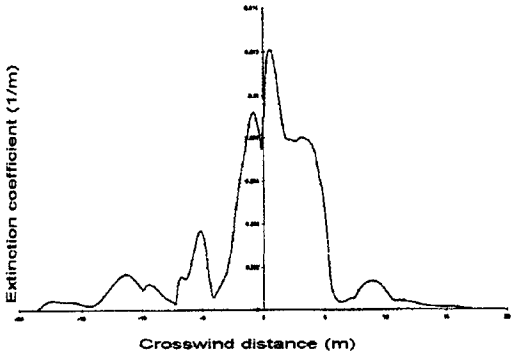


Fig. 4. Average extinction coefficient (concentration) distribution for 15 trials scaled to wind speed of 2.2 m/s with centroids adjusted to centreline.

Artificial Neural Network Modelling

A multilayer feedforward neural architecture based on back propagation learning was used to try to provide a better prediction of the observed results. Input values for the parameters and variables shown below were associated with each measured extinction coefficient value.

Downwind distance x
Crosswind distance y
Elevation z
Wind speed
Temperature
Pasquill category
Humidity
Time of day
Delay time
Atmospheric pressure

Network architecture featured 10 input nodes (above), 5 to 20 hidden nodes in

one layer, and one output node (log σ). As can be seen, the neural network is capable of considering more variables than can the Gaussian model, where several variables or parameters must be combined or blended into the dispersion coefficients.

Networks were developed on a training set balanced over the whole input space and containing 138 994 different data points. A test set, an independent sub set of the data set, contained 1400 data points. Training involved a total of 10^6 inputs, or about 7 times through the training set.

Again, probably due to the chaotic nature of the atmospheric turbulence, and the resulting spread of the measured extinction coefficients, the neural network predictions were also not particularly good. Predictions seemed relatively insensitive to the number of hidden nodes or even hidden layers, suggesting that the optimal solution, modest as it was, was relatively robust.

A comparison of the Gaussian and neural network models was performed for the test set used for neural training, with the average relative errors shown below.

Neural Network Error	9.97
Gaussian Plume Error	37.45

The trained neural network was then used to generate predictions for plume cross sections at varying downwind distances and elevations under two distinct sets of conditions. Figure 5 shows two extinction coefficient distributions (ground level and 2.5 m elevation) for a wind speed of 2.8 m/s, at 21 °C, 45% RH, Pasquill A-B, 30.25 in Hg, a delay time of 40 s at 1200 hrs.

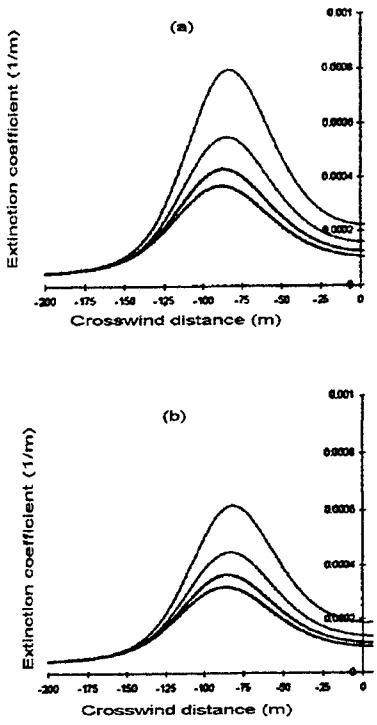


Fig. 5. Neural network predictions at elevations of (a) 0 m and (b) 2.5 m. Curves from bottom to top are x=5, 10, 15, 20 for wind speed of 2.8 m/s.

Fig. 6 contains comparable distributions for a wind speed of 1.4 m/s, at 23 °C, 50% RH, Pasquill A, 30.10 in Hg, a delay time of 10 s at 1030 hrs.

All 4 graphs show "Gaussian-like" distributions which are biased in the negative crosswind direction. As shown earlier, this represents the measured data, although it may also reflect an artefact of the test site, where turbulence caused aerosol movement in that direction during trials.

Also of interest is the fact that the contours of each of the graphs seem reversed. One would have expected the distributions closer to the release point to have higher average centreline values and lower off-axis values. This again may reflect the fact that turbulent effects

probably dominated advection and diffusion.

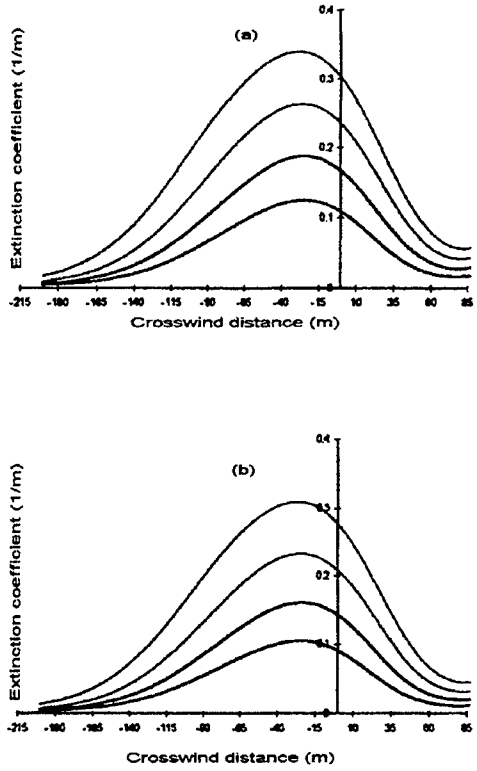


Fig. 6. Neural network predictions at elevations of (a) 0 m and (b) 2.5 m. Curves from bottom to top are x=5, 10, 15, 20 for wind speed of 1.4 m/s.

Conclusion

Based on the examination of concentration distributions of 50 g kaolin samples, a number of conclusions can be drawn. The distributions themselves are not well predicted by the standard Gaussian plume modelling paradigm. This is probably due to the fact that Gaussian models, based on Pasquill dispersion coefficients, were designed to predict concentration distributions within plumes that were beyond 100 m from the point of release and reflected a 10 min time averaging. Consequently, new algorithms were developed for predicting Gaussian crosswind fitting parameters out to 20 m under Pasquill categories A and B.

Neural network models were also investigated. Although these could be trained to provide better predictions than Gaussian models, they still contained significant prediction errors.

In September 1998, 50 more kaolin releases were measured at DREV under conditions slightly different from those reported on above. The examination of these data, along with efforts to provide better models and hence better insights into the observed dispersion phenomena will constitute future work. Coupled with this will be an ongoing effort to assess the ability of COMBIC, ARL's Combined Obscuration Model for Battlefield Induced Contaminants, to predict aerosol dispersion.

Acknowledgement

The data reported on were collected by personnel of the Defence Research Establishment Valcartier. This work was supported, in part, by the Academic Research Program of the Department of National Defence of Canada.

References

1. Evans, A.J., "A Preliminary Assessment of the DREV Laser Cloud Mapper," CDE Porton Down, UK (1982).
2. Evans, B.T.N., Kluchert, R.E. and Levesque, R.J., "Field Evaluation of a Canadian Laser Cloud Mapper and Canadian IR Screening Aerosols," DREV 4271/82, Valcartier, Quebec (1983).

3. Evans, B.T.N., Roy, G. and Ho, J., "The Detection and Mapping of Biological Simulants: Preliminary Biological Results," DREV 4480/89, Valcartier, Quebec (1989).
4. Twardawa, P., Roy, G., Evans, B.T.N. and Vallee, G. "Cold Weather Evaluation of Visual and Infrared Screening Grenades for the Self-Protection of Armoured Fighting Vehicles," DREV R-4632/91, Quebec (1991).
5. Andrews, W.S., Roney, S.D. and Roy, G., "An Examination of Modelling Approaches for Predicting the Dispersion of Aerosols from Obscurant Grenades," Proceedings of the 1996 Battlespace Atmospherics Conference, Naval Command Control and Ocean Surveillance Center, RDT&E Division, San Diego, CA, 3-5 December (1996). [ADA 323038].
6. Andrews, W.S., Roney, S.D. and Roy, G., "Comparison of Modelling Approaches for Predicting Dispersion of Aerosols from Screening Grenades," submitted to *Propellants, Explosives, Pyrotechnics.*
7. Andrews, W.S., Costa, J.R. and Roy, G., "Measuring and Modelling the Influence of Atmospheric Effects on the Concentration Distributions within Transient Aerosol Plumes," Proceedings of the 1997 Battlespace Atmospherics Conference, Naval Command Control and Ocean Surveillance Center, RDT&E Division, San Diego, CA, 2-4 December 1997 (1998).
8. Pasquill, F. and Smith, F.B., *Atmospheric Diffusion, 3rd Ed.*, Ellis Horwood Ltd., Chichester UK (1983).
9. Turner, D.B., *Workbook of Atmospheric Dispersion Estimates, 2nd Ed.*, Lewis, Boca Raton (1994).
10. Hanna, S.R., Briggs, G.A. and Hosker, R.P., "Handbook on Atmospheric Diffusion," DOE/TIC-11223, Springfield VA (1982).
11. Roy, G., Val9e, G. and Marcelin, J., "Lidar-Inversion Technique Based on Total Integrated Backscatter Calibrated Curves," *Applied Optics*,**32**, 33, 20 November (1993).
12. Evans, B.T.N., "An Interactive Program for Estimating Extinction and Scattering Properties of Most Particulate Clouds," MRL-R-1123, Materials Research Laboratory, Ascot Vale, Victoria, Australia (1988).
13. Hoock, D.W. and Sutherland, R.A., "Obscuration Countermeasures," *The Infrared and Electro-Optical Systems Handbook*, ed Pollock, D.H., ERIM and SPIE Press, Washington (1993).
14. Ayres, S.D. and DeSutter, S., *Combined Obscuration Model for Battlefield Induced Contaminants (COMBIC92) Model Documentation*, U.S. Army Research Laboratory, White Sands Missile Range NM (1995).

RETRIEVAL OF ATMOSPHERIC WATER VAPOR FROM HYPERSPECTRAL IMAGING SENSORS

Hsiao-hua K. Burke*, Michael K. Griffin, Dan C. Peduzzi,
Kristine E. Farrar and Carolyn A. Upham

MIT Lincoln Laboratory
244 Wood Street
Lexington, MA 02420-9185

Voice: 781-981-7979, Fax: 781-981-7271. Email: *burke@ll.mit.edu*

Steve Adler-Golden and Mike W. Matthew

Spectral Sciences Inc.
99 South Bedford St #7
Burlington, MA 01803

Sponsored Under Air Force Contract F19628-95-0002

Introduction

With the advent of hyperspectral imaging sensors, it becomes increasingly feasible to detect and identify diverse surface targets, topographical and geological features. However, hyperspectral data is not immune to the effects of the intervening atmosphere. The term "atmospheric compensation" refers to the removal of the unwanted atmospheric components of the measured radiance. For hyperspectral data analysis, the general objective for atmospheric compensation algorithms is to remove solar illumination and atmospheric effects (aerosols and moisture) from the measured spectral data so that an accurate estimate of the surface reflectance can be obtained. The retrieved surface reflectance spectra can then be compared with library spectra of a collection of materials for target identification.

Recent advances in multispectral and hyperspectral sensor capability have led to further development in atmospheric moisture retrieval methodologies. Typical moisture retrieval algorithms operate on IR (or microwave) measurements of the emission spectra of water vapor in the atmosphere. However, various water vapor bands in the near-IR portion of the spectrum have been used to estimate the integrated column water vapor (Gao and Goetz, 1990; Kaufman and Gao, 1992; Gao and Kaufman, 1997). While these bands are used primarily to remove the bulk atmospheric component of water vapor from reflectance measurements, ultimately, these values could be used to augment IR water vapor retrievals. In this paper, the most commonly used hyperspectral water vapor retrieval approach (3-band ratio technique) is reviewed and evaluated for different sensor characteristics. Retrieval estimates using existing hyperspectral data, including those from HYDICE and AVIRIS aircraft measurements will be discussed and compared with "truth" information derived from independent meteorological data.

Hyperspectral Sensors

Through measurements of the solar and near-infrared reflected spectrum, hyperspectral data satisfies a host of scientific research applications including: atmospheric water vapor, cloud properties and aerosols, agriculture and forest properties, mineralogy, soil type, snow and ice hydrology, biomass burning, environmental hazards, calibration of aircraft and satellite sensors, sensor simulation and validation, radiative transfer modeling and atmospheric correction. To meet the requirements for these applications, airborne imaging spectrometers were designed with the intent of achieving substantial improvements over existing systems in the areas of spatial resolution, sensitivity, and accuracy of absolute calibration. Data from two of these sensors are reported on in this paper: the Airborne Visible-InfraRed Imaging Spectrometer (AVIRIS) and the HYperspectral Digital Imagery Collection Experiment (HYDICE).

The AVIRIS instrument contains 224 different detectors, each with a spectral bandwidth of approximately 10 nanometers (nm), allowing it to cover the entire range between 380 nm and 2500 nm. AVIRIS uses a scanning mirror to sweep back and forth in a whisk broom fashion, producing 614 pixels for each scan. Each pixel produced by the instrument covers a 20 meter square area on the ground (with some overlap between pixels), yielding a ground swath width of 10 kilometers for an ER2 flight altitude of 20 km (see Vane, 1987 and Vane, et al., 1984 for more information on AVIRIS).

The HYDICE sensor is a pushbroom imaging spectrometer that uses a bi-prism dispersing element and a two-dimensional focal plane array to enable a single optical path design. The array is a 320 element x 210 detector InSb array which supports operations over the full 400 - 2500 nm spectral range. With an operating altitude range for the CV 580 of 1.5 to 8 km, spatial resolutions from 0.8 to 4 meters can be achieved. Calibration is done in-flight through the full optical system, and is referenced to a NIST ground standard (see Rickard, et al., 1993 for further details).

Hyperspectral Compensation Models

Imaging spectrometers acquire images in an array of contiguous spectral bands such that for each pixel in the image a complete set of reflectance or emittance spectra is measured. The two-dimensional spatial image (elements and lines) combined with a third spectral dimension produces the hyperspectral image "cube." Typical reflectance measurements from hyperspectral sensors contain information not only about the spectral characteristics of the surface but of the intervening atmosphere as well. Since these sensors are primarily used as a tool to derive spectral reflectance information for the surface (including vegetation, targets, geology, etc.), it is advantageous to be able to remove or "compensate" for the effects of the intervening atmosphere. Figure 1 shows an example of the "uncompensated" or "apparent" reflectance spectra (radiance divided by the incident solar flux) for simulated hyperspectral measurements of scenes with a uniform surface reflectance. It is clear that specific atmospheric constituents such as water vapor and aerosol particles can mask the true nature of a probed surface and/or hide targets of opportunity.

Many atmospheric compensation models exist, two of the physics-based models are

discussed here: the Atmospheric REMoval (ATREM) and the Fast Line-of-sight Atmospheric Analysis of Spectral Hypercubes (FLAASH) codes. While each model uses a different method for atmospheric compensation (described below), both use similar 3-band ratio techniques to account for the effects of water vapor on the hyperspectral measurements. This technique will be described in more detail in the following section.

ATREM uses the Malkmus (1967) narrow band spectral model to derive the gaseous transmittance and the 6S (Vermote, et. al., 1996) code to compute the necessary scattering terms using a user selected aerosol model (see Fig. 2). Given a measured radiance spectrum (either from AVIRIS or HYDICE), the apparent reflectance ρ^* is first calculated from the sensor radiance and then the surface reflectance ρ is computed from the following equation,

$$\rho = \frac{(\frac{\rho^*}{T_g} - \rho_a)}{T^{\downarrow}T^{\uparrow} + S(\frac{\rho^*}{T_g} - \rho_a)} \tag{1}$$

where T_g is the gaseous transmittance, ρ_a is the atmospheric reflectance, $T^{\uparrow}, T^{\downarrow}$ are the upward and downward scattering transmittances, and S is the spherical albedo of the atmosphere. The individual gas concentrations are assumed to be uniform across the scene except for water which the algorithm treats separately. In this manner only a single transmittance spectrum is calculated for each uniform gas. Water vapor transmittances, however, are calculated on a pixel-by-pixel basis.

FLAASH (Adler-Golden, et al., 1998) utilizes the full MODTRAN-4 (Berk, et al., 1996) functionality drawing on its complete package of transmittance and scattering methods including a new correlated-k radiative transfer algorithm and full accounting for adjacency

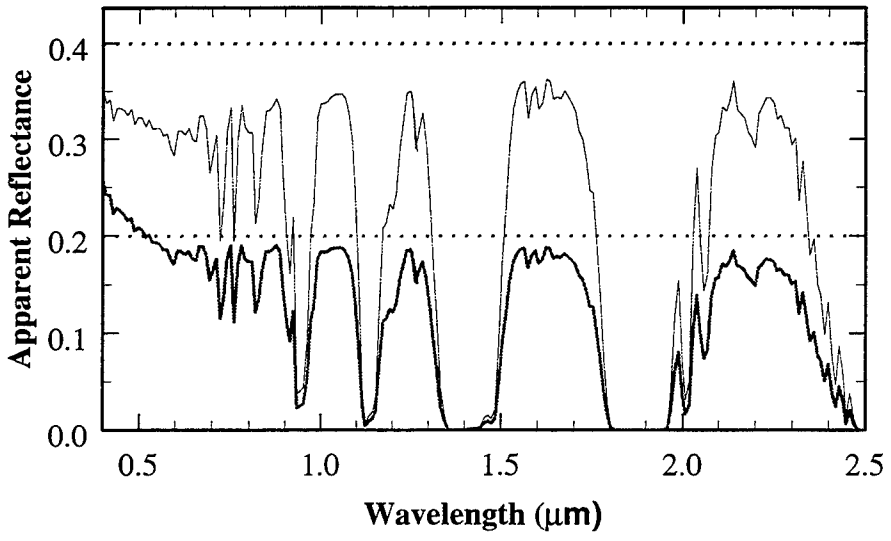


Figure 1. Plots of the apparent reflectance (solid lines) for two values of the surface reflectance (dotted lines), 0.2 and 0.4.

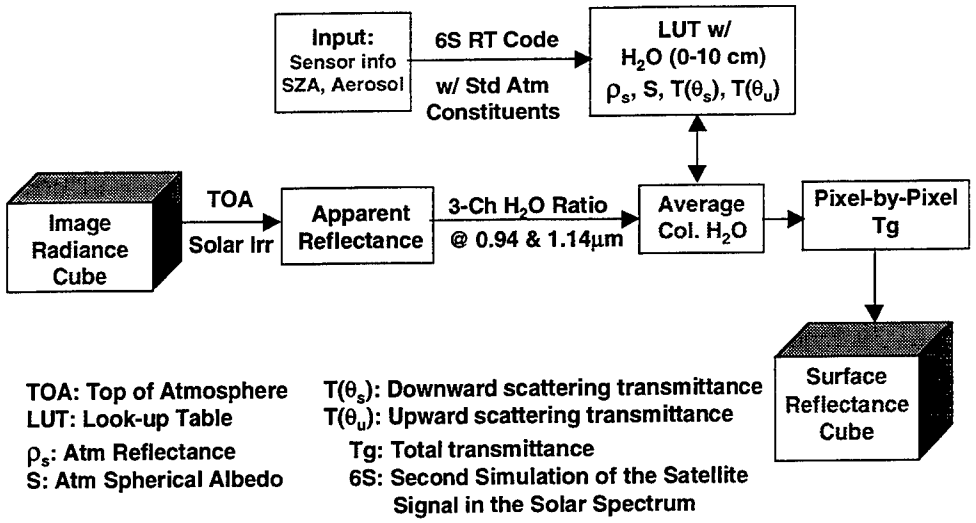


Figure 2. Schematic Flow of the ATREM program.

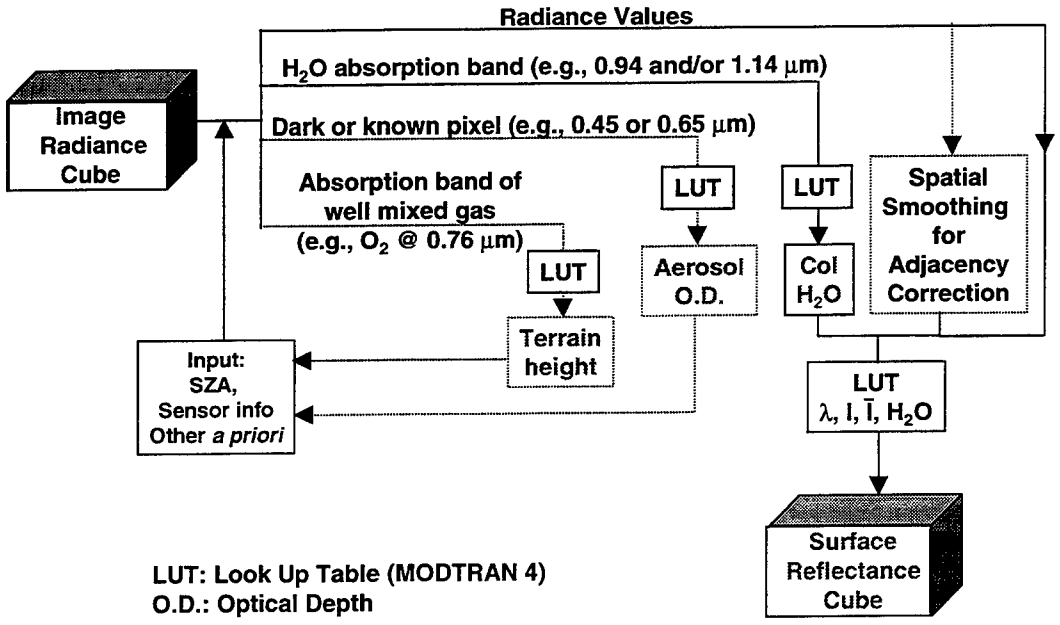


Figure 3. Schematic Flow of the FLAASH code.

effects associated with atmospheric scattering (see Fig. 3). However, the technique used by FLAASH to derive the surface spectral reflectance follows the same steps used in ATREM culminating in the evaluation of Eqn. 1. A key element to deriving an accurate representation of the scene surface reflectance is accurately defining the water vapor transmittance. The next section discusses this aspect of the compensation problem.

Water Vapor Retrievals

Two test cases were selected for evaluating water vapor retrievals from ATREM and FLAASH: an AVIRIS data cube taken over Jasper Ridge, California on 3 April, 1997 and a HYDICE data cube from the Keystone, Pennsylvania collect, on 10 August, 1997 (Fig. 4). The AVIRIS frame is 10 km x 10 km with a pixel resolution of 20 m. The HYDICE frame is on the order of 270 m x 250 m with pixel resolution of 0.76 m. Some "truth" water vapor data were also obtained based on the nearby NOAA-NWS radiosonde observations.

Figure 5 displays the derived images of integrated column water vapor for the AVIRIS Jasper Ridge case based on the FLAASH and ATREM retrievals. As shown, the atmosphere was relatively dry and results from both algorithms were similar and agree well with nearby radiosonde observations. Similar spatial variability was seen on both derived images reflecting some artifact of the interchange between surface characteristics and the atmosphere. However, the standard deviation is of the order of 10% or less, an indication that the degree of the artifact is not significant.

Figure 6 shows similar results for the Keystone case which in contrast with the Jasper Ridge scene displays a moderately moist atmosphere. The derived water vapor images were quite different from ATREM and FLAASH. ATREM retrieved unreasonably high water vapor content while the FLAASH retrieval is close to radiosonde observations and is also climatologically more realistic. Again, less than 10% spatial standard deviation was observed

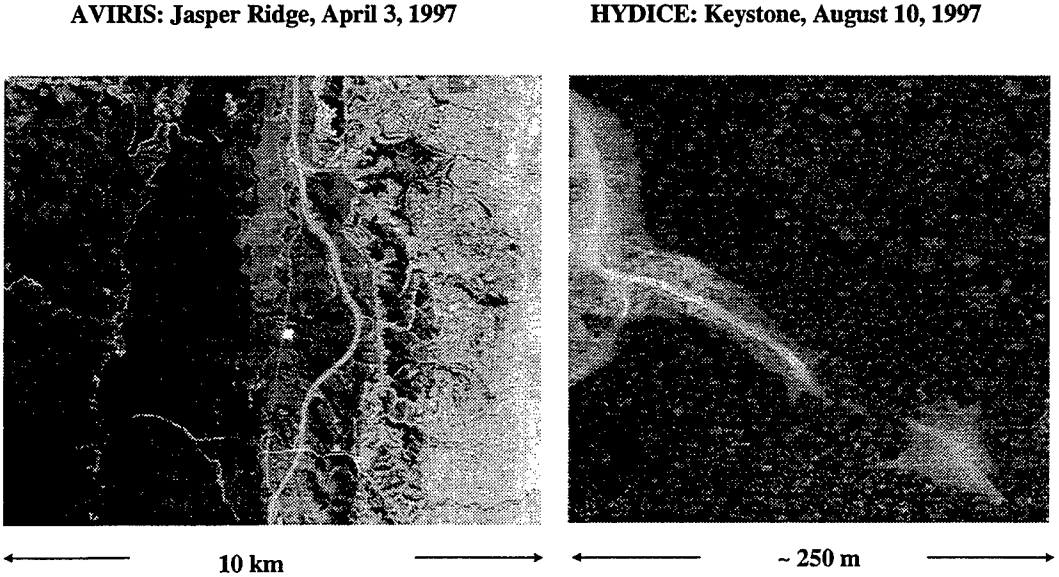


Figure 4. AVIRIS and HYDICE test images.

on this much smaller area for both codes, consistent with our conclusion of the algorithm artifact.

The overestimation of water vapor prompted some more analysis of the ATREM algorithm. Both ATREM and FLAASH utilize a 3-band ratio method to estimate the water vapor transmittance of the intervening atmosphere. The technique selects channels in the 0.94 and 1.14 μm water vapor absorption, computes a mean radiance for both bands, and ratios these water vapor band values with channel radiances in the surrounding window spectral regions. This pseudo-transmittance value is compared with a pre-computed table of ratios vs. computed water vapor transmittance for a range of column water vapor amounts. Transmittance and column water vapor amounts at the closest match to the 3-band ratio are used to define the water vapor characteristics of the pixel. This procedure is repeated for every pixel in the image.

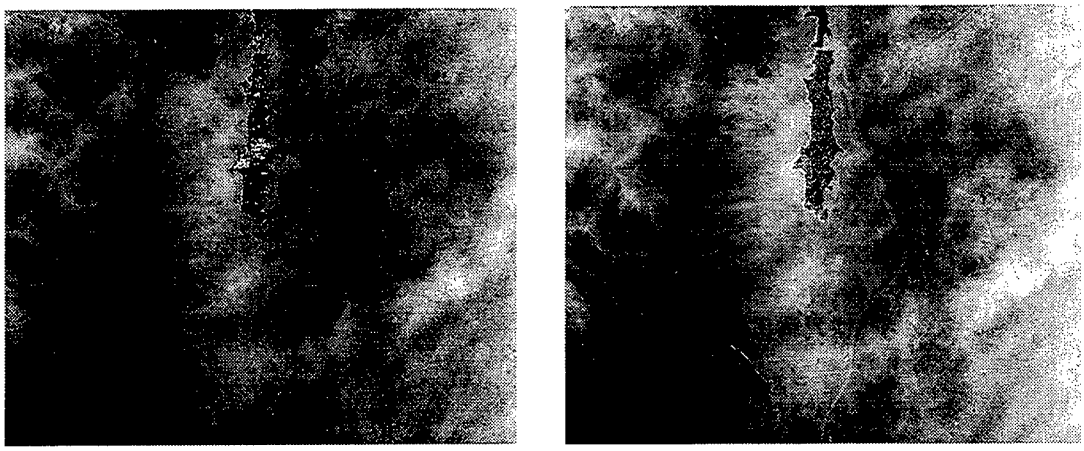
It was found that by using channels offset from the 0.94 μm water vapor band (in the weaker 0.91 μm band) in the ATREM ratio calculation it produced somewhat better values for more moist scenes. ATREM does not include the water vapor continuum calculation in its computation of the water vapor effects which may in part be responsible for the high reported column water vapor values. The continuum contribution is negligible at 0.91 μm so the error due to its omission would be minimal. Also, since the absorption is weaker at 0.91 μm, the dynamic range of water vapor values that can be distinguished may be larger – the side band may be less sensitive to higher amounts of moisture than at the water vapor band centers. Using the 0.91 μm band ratio, the mean water vapor amounts computed by ATREM for the Keystone case reduced from 6.14 to 5.49 cm, a modest reduction in the right direction but still well above the observed value.

To investigate this further, simulated AVIRIS data was generated from MODTRAN calculations for clear-sky, uniform surface reflectance scenes under tropical moisture and aerosol conditions. Curiously, retrievals of the column water vapor amounts from ATREM using the 0.91 μm band were very close (< 0.2 cm) to the input model values for these simulated test cases (see Table 1). Obviously, work still needs to be done in this area to determine why ATREM may produce unrealistic water vapor amounts for hyperspectral data under moist atmospheric conditions.

Table 1. ATREM Retrieved Water Vapor for simulated test cases.

Case #	Surface Albedo	Visibility (km)	Column H_2O (cm)	Derived Column H_2O (cm)	
				0.94, 1.14 μm	0.91 μm
1	0.2	23	0.4	0.4	0.3
2	0.2	10	2.9	4.7	2.7
3	0.2	5	4.1	7.3	4.1
4	0.4	23	0.4	0.4	0.3
5	0.4	10	2.9	5.1	2.8
6	0.4	5	4.1	8.1	4.4

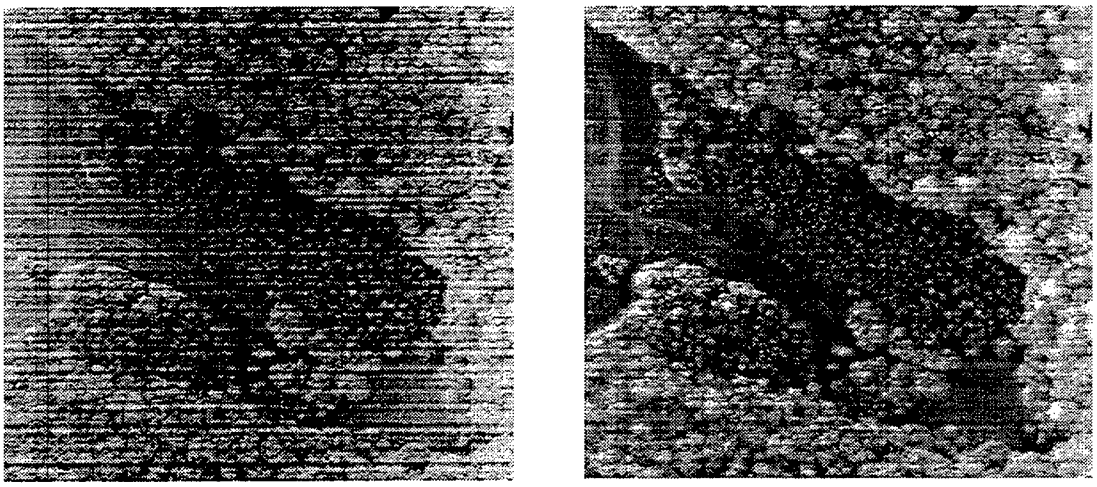
FLAASH Water Vapor **ATREM Water Vapor**



Mean = 0.72 cm, σ = 0.07 cm **Mean: 0.75 cm, σ = 0.05 cm**

Figure 5. ATREM and FLAASH computed water vapor images for the AVIRIS Jasper Ridge Test Scene. Mean and standard deviation column water vapor values are shown for both models; nearby radiosonde values of 0.67 and 1.13 cm were observed.

FLAASH Water Vapor **ATREM Water Vapor**



Mean = 3.40 cm σ = 0.25 cm **Mean = 6.14 cm σ = 0.43 cm**

Figure 6. ATREM and FLAASH computed water vapor images for the HYDICE Keystone Test Scene. Mean and standard deviation column water vapor values are shown for both models; nearby radiosonde values of 2.97 and 3.25 cm were observed.

Summary

Two physics-based water vapor retrieval algorithms for hyperspectral data in the visible and near-IR were reviewed and evaluated with both flight (AVIRIS and HYDICE) data as well as model (MODTRAN) generated scenes. The algorithms in general provide good retrieval results, except ATREM overestimates the water vapor content for atmospheres with moderate to high water vapor. This is in part due to the lack of water continuum treatment in ATREM. Subsequently, a weaker absorption band was utilized where the continuum contribution is minimal which also allows for better near surface moisture characterization. The work will continue to further investigate the sensitivity of various parameters to retrieval accuracy and explore better methodology for atmospheric and surface characterizations from hyperspectral remote sensing data.

References

Adler-Golden, S., A. Berk, L.S. Bernstein, S. Richtsmeier, P.K. Acharya, M.W. Matthew, G.P. Anderson, C. Allred, L. Jeong, and J. Chetwynd, 1998: FLAASH, A MODTRAN4 Atmospheric Correction Package for Hyperspectral Data Retrievals and Simulations. *Proc. of the 7th Ann. JPL Airborne GeoScience Workshop*, Pasadena, CA, 1-6.

Berk, A., L.S. Bernstein, D.C. Robertson, P.K. Acharya, G.P. Anderson, and J.H. Chetwynd, 1996: MODTRAN Cloud and Multiple Scattering Upgrades with Application to AVIRIS. *Proc. of the Sixth Annual JPL Airborne GeoScience Workshop*, JPL Publication 96-4, **1**, Pasadena, CA, 1-7.

Gao, B-C. and A.F.H. Goetz, 1990: Column Atmospheric Water Vapor and Vegetation Liquid Water Retrievals from Airborne Imaging Spectrometer Data. *J. Geo. Res.*, **95**, 3549-3564.

Gao, B-C. and Y.J. Kaufman, 1997: The MODIS Near-IR Water Vapor Algorithm. *Algorithm Technical Background Doc. ID: MOD05 – Total Precipitable Water*, 54 p.

Kaufman, Y.J. and B-C. Gao, 1992: Remote Sensing of Water Vapor in the Near IR from EOS/MODIS. *IEEE Trans.on Geos. & Rem. Sens.*, **30**, 871-884.

Malkmus, W.: Random Lorentz band model with exponential-tailed S line intensity distribution function. *J. Opt. Soc. Am.*, **57**, 323-329.

Rickard, L.J., R. Basedow, E.Zalewski, P.Silverglate, and L.M. Lander, 1993: HYDICE: An airborne system for hyperspectral imaging. *SPIE Proceedings,* **Vol 1937**, 173-179.

Vane, G., 1987: Airborne Visible/Infrared Imaging Spectrometer (AVIRIS). *JPL Publication 87-38,* 97 p.

Vane, G, M. Chrisp, H. Enmark, S. Macenka and J. Solomon, 1984: Airborne Visible/Infrared Imaging Spectrometer: An advanced tool for earth remote sensing. *Proc. 1984 IEEE Int'l Geosc. & Rem. Sens. Symp.*, SP215, 751-757.

Vermote, E., D. Tanre, J.L. Deuze, M. Herman, and J.J. Morcrette, 1996: Second simulation of the Satellite Signal in the Solar Spectrum (6S). *6S User's Guide Version 1*, NASA-GSFC, Greenbelt, MD, 134 p.

Acknowledgements

The authors wish to thank Gail Anderson at AFRL/VSBM for making available versions of MODTRAN 4.0 and FLAASH for our studies prior to their official release.

ESTIMATING NEAR-SURFACE SCINTILLATION (C_n^2) FOR OVERWATER LITTORAL PATHS

Paul Frederickson*[a], Kenneth Davidson[a], Carl Zeisse[b] and Ike Bendall[b]

[a]Department of Meteorology, Naval Postgraduate School, Monterey, CA 93943-5114,
Phone: (831) 656-2563, E-mail: frederic@met.nps.navy.mil

[b]Space and Naval Warfare Systems Center D883, San Diego, CA 92152-7385

1. INTRODUCTION

Electro-optical (EO) imagery through the atmosphere exhibits rapid intensity fluctuations due to atmospheric turbulence, a phenomenon known as scintillation. Scintillation is closely related to the refractive index structure parameter, C_n^2. For example, for a point source and point detector the normalized variance of the intensity of an EO signal, σ_I^2, is related to C_n^2 by the relation:

$$\sigma_I^2 = 0.496\left(\frac{2\pi}{\lambda}\right)^{7/6} L^{11/6} C_n^2, \tag{1}$$

where λ is the wavelength of the signal and L is the path length. In an operational environment it is useful to be able to evaluate and predict the effects of scintillation on EO imagery by estimating C_n^2 from routinely measured air-sea parameters. Bulk models have been developed to estimate near-surface atmospheric turbulence properties from mean meteorological measurements. The relations between these atmospheric turbulence properties and C_n^2 have also been established, thereby allowing C_n^2 to be estimated from mean air-sea measurements. The objective of this study is to determine how accurately C_n^2 can be estimated from routine meteorological measurements using bulk models under various air-sea conditions.

2. MODELING THE REFRACTIVE-INDEX STRUCTURE PARAMETER

The refractive-index structure parameter, C_n^2, can be expressed according to the structure parameters for temperature, C_T^2, and humidity, C_q^2 and the temperature-humidity cross-structure parameter, C_{Tq}, as follows[1]:

$$C_n^2 = A^2 C_T^2 + 2ABC_{Tq} + B^2 C_q^2, \tag{2}$$

where the coefficients A and B are known functions of the wavelength (λ) and the mean atmospheric temperature (T), humidity (q) and pressure (P). Monin-Obukhov similarity (MOS) theory is employed to relate the structure parameters C_T^2, C_q^2 and C_{Tq} to the mean properties of

the atmospheric surface layer. The refractive index structure parameter can then be estimated by an iterative process from the equations:

$$C_n^2 = \frac{f_T(\xi)k^2\left[A^2\Delta T^2 + 2AB\Delta T\Delta q + B^2\Delta q^2\right]}{z^{2/3}\left[\ln(z/z_{oT}) - \psi_T(\xi)\right]^2}, \tag{3}$$

$$\xi = \frac{zg(\Delta T + 0.61T\Delta q)\left[\ln(z/z_{ou}) - \psi_u(\xi)\right]^2}{T\Delta u^2\left[\ln(z/z_{oT}) - \psi_T(\xi)\right]}, \tag{4}$$

where z is the height above the surface, k is the von Karman constant (= 0.4), g is the gravitational acceleration, Δ indicates a mean air-sea difference, z_{oT} is the thermal roughness length, and f_T and ψ_T are stability dependent functions. The reader is referred to previous papers for further details on the bulk C_n^2 model employed in this study[1,2].

The dependence of bulk C_n^2 estimates on the air – sea temperature difference (ΔT) is shown for different wind speed values in Fig. 1, and for different relative humidity values in Fig. 2. A striking feature of these plots is that the C_n^2 values asymptote toward zero at certain values of ΔT. From Eq. 3 we can see that the bulk C_n^2 estimates will be equal to zero when one of two conditions are met: 1) $\Delta T = \Delta q = 0$, or 2) $\Delta T = -\Delta qB/A$, $\Delta T \neq \Delta q \neq 0$. The first condition occurs when the air and sea temperatures are equal and the relative humidity is 100%, as seen in Fig. 2. The second condition is also illustrated in Fig. 2 by the C_n^2 asymptotes moving toward larger ΔT values as relative humidity decreases, since this causes $-\Delta q$ to increase. As $\Delta T \rightarrow -\Delta qB/A$, the bulk model predicts that the refractive index gradient with height approaches zero ($\partial n/\partial z \rightarrow 0$), therefore turbulent eddies cannot produce any fluctuations in the refractive index, resulting in C_n^2 values which rapidly approach zero. We hereafter refer to the asymptote value $-\Delta qB/A$ as the 'critical' air-sea temperature difference, ΔT_c.

From Figs. 1 and 2 we can see that, except for $0 < \Delta T < \Delta T_c$, the bulk C_n^2 estimates increase as $|\Delta T|$ increases, since $C_n^2 \propto (\Delta T)^2$. Variations in wind speed affect the bulk C_n^2 estimates by changing the magnitude of ξ, and thus $f_T(\xi)$. From Fig. 1 we can see that when $\Delta T < \Delta T_c$, an increase in wind speed results in an increase in C_n^2, and when $\Delta T > \Delta T_c$, an increase in wind speed results in a decrease in C_n^2. The effects of humidity variations on the bulk C_n^2 estimates are greatest with small values of $|\Delta T|$, as seen in Fig. 2. For $\Delta T < \Delta T_c$, an increase in relative humidity results in a decrease in C_n^2, and for $\Delta T > \Delta T_c$, an increase in relative humidity results in an increase in C_n^2.

3. THE EXPERIMENT

The EOPACE experiment of May-June 1998 took place in San Diego Bay (see Fig. 3). Infrared (IR) scintillation measurements were obtained by SPAWAR System Center, San Diego (SSC-SD) along a 7 km path over San Diego Bay. The IR source (transmitter) was located at the Naval Amphibious Base at a height of 6.2 m above mean sea level (MSL) and the IR receiver was located at the Naval Submarine Base on Pt. Loma at 4.9 m above MSL. Scintillation C_n^2

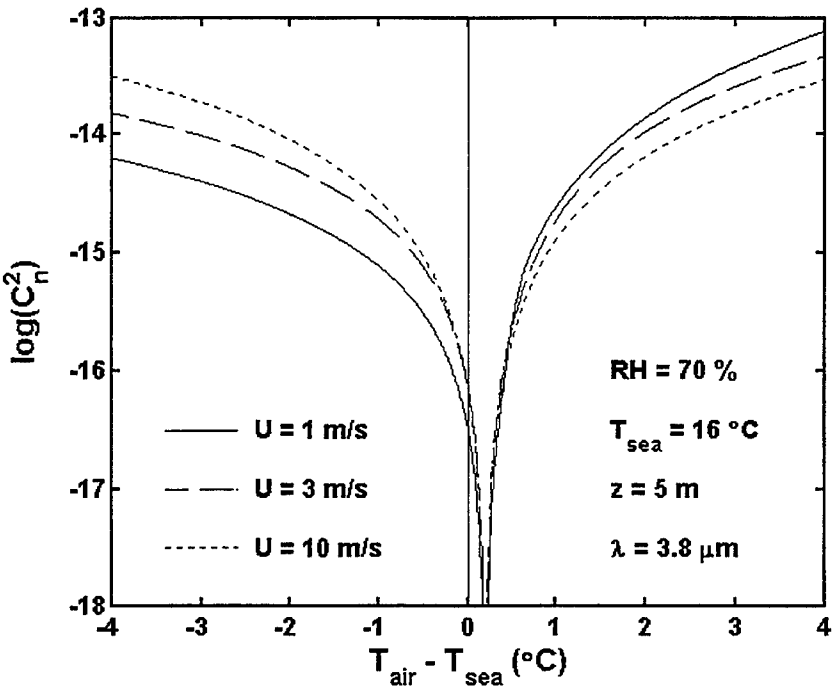


Figure 1. Bulk log(C_n^2) estimates versus air – sea temperature difference, plotted for different values of wind speed: 1 m/s indicated by solid line; 3 m/s indicated by dashed line; 10 m/s indicated by dotted line. C_n^2 computed for relative humidity = 70%, sea temperature = 16 °C, height above the surface = 5 m and wavelength = 3.8 μm.

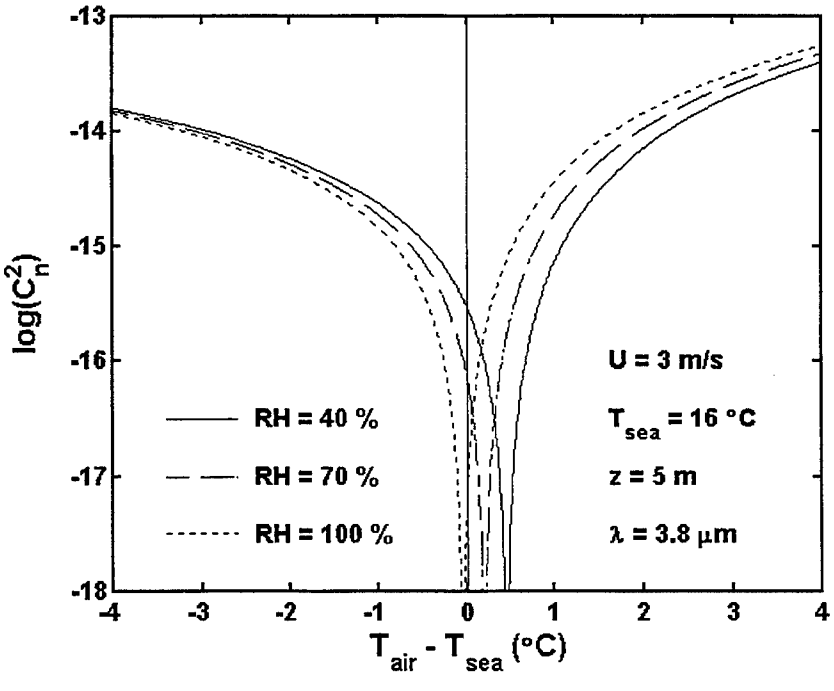


Figure 2. Bulk log(C_n^2) estimates versus air – sea temperature difference, plotted for different values of relative humidity: 40% indicated by solid line; 70% indicated by dashed line; 100% indicated by dotted line. C_n^2 computed for wind speed = 3 m/s, sea temperature = 16 °C, height above the surface = 5 m and wavelength = 3.8 μm.

measurements in the mid-wave IR band (3.5 to 4.1 μm) were obtained every 30 minutes between 21 May and 14 June 1998, using instruments and procedures similar to those described by Zeisse et al.[3].

Meteorological data were obtained concurrently with the scintillation measurements from the Naval Postgraduate School's (NPS) research buoy, located at the mid-point of the optical transmission path. Wind speed and direction, air temperature, relative humidity, atmospheric pressure and sea surface temperature were measured. Bulk estimates of C_n^2 were computed from 10 minute averaged buoy data. High frequency (21 Hz) temperature measurements were obtained on the NPS buoy from a sonic anemometer. Sonic temperature structure parameters were obtained from the temperature spectral densities, $S_{Ts}(f)$, using the relation

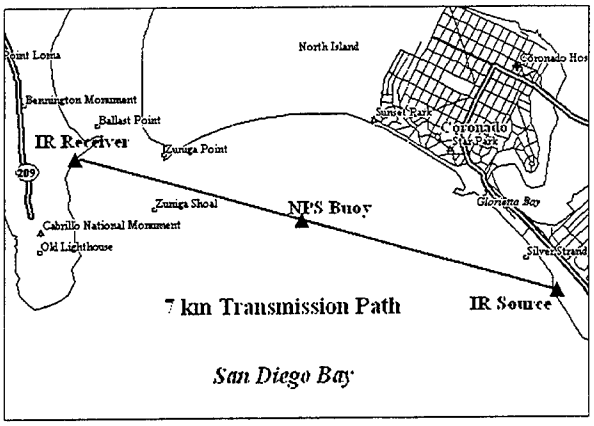


Figure 3. The EOPACE experimental configuration of May-June 1998, showing locations of the IR receiver and transmitter and NPS buoy.

$$C_{T_s}^2 = 4\left(\frac{2\pi}{U}\right)^{2/3} S_{T_s}(f) f^{5/3}, \tag{5}$$

where U is the mean wind speed and f is the frequency. Direct turbulent estimates of C_n^2 were then obtained from the relation $C_n^2 = A^2 C_{T_s}^2$, which assumes that humidity fluctuation effects on C_n^2 are negligible.

4. SCINTILLATION VERSUS BUOY C_n^2 COMPARISON

A time series plot of buoy and optical scintillation data for 24 – 27 May 1998 is presented in Fig. 4. Unfortunately the sonic anemometer on the buoy was not functioning properly during this time, and no turbulent C_n^2 measurements are available. Conditions were unstable through almost the entire period, with the air – sea temperature difference (ΔT) varying between 0 and – 3.3 °C. The good agreement between the bulk C_n^2 estimates and the scintillation-measured data is in general remarkable. During the two periods following the C_n^2 peaks at 0500 PDT, 24 May and 0600 PDT, 25 May the scintillation data become larger than the bulk estimates for 6-8 hour intervals. Fog and drizzle were observed during these periods, which may account for the disagreement between the bulk and scintillation data.

During the last half of 27 May the bulk C_n^2 estimates drop rapidly as ΔT approaches the critical value ΔT_c. No similar rapid drop is observed in the scintillation C_n^2 measurements, although they do slowly decrease after a peak value occurs at 1000 PDT, 27 May. In fact, throughout the experiment the scintillation C_n^2 measurements were never observed to exhibit rapid decreases

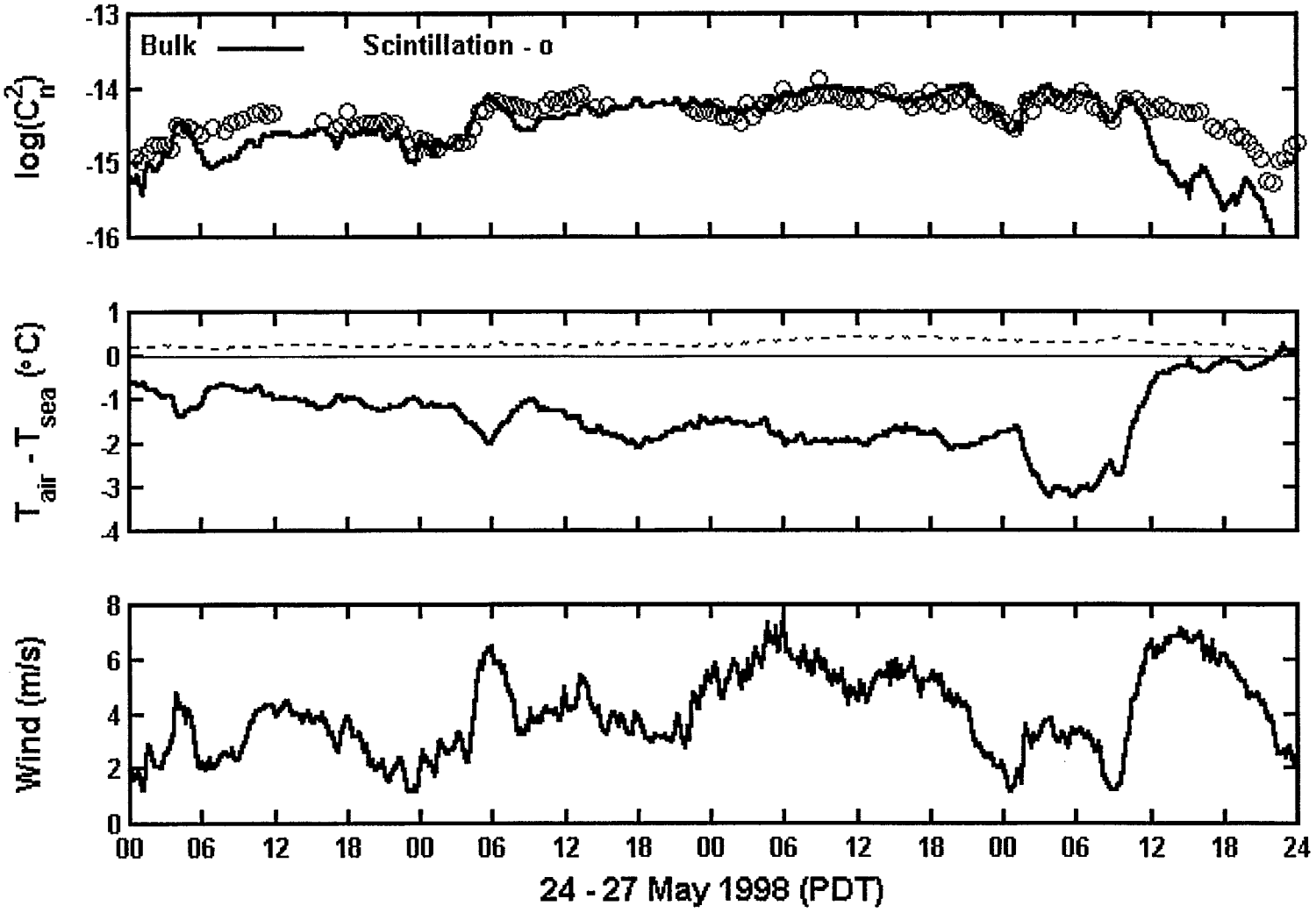


Figure 4. Time series plot for 24 – 27 May 1998 (Pacific Daylight Time). Top panel: bulk log(C_n^2) estimates indicated by solid line and scintillation log(C_n^2) measurements indicated by o's. Center panel: air – sea temperature difference in °C indicated by solid line; critical air – sea temperature difference (ΔT_c) in °C indicated by dashed line. Bottom panel: wind speed in m/s indicated by solid line.

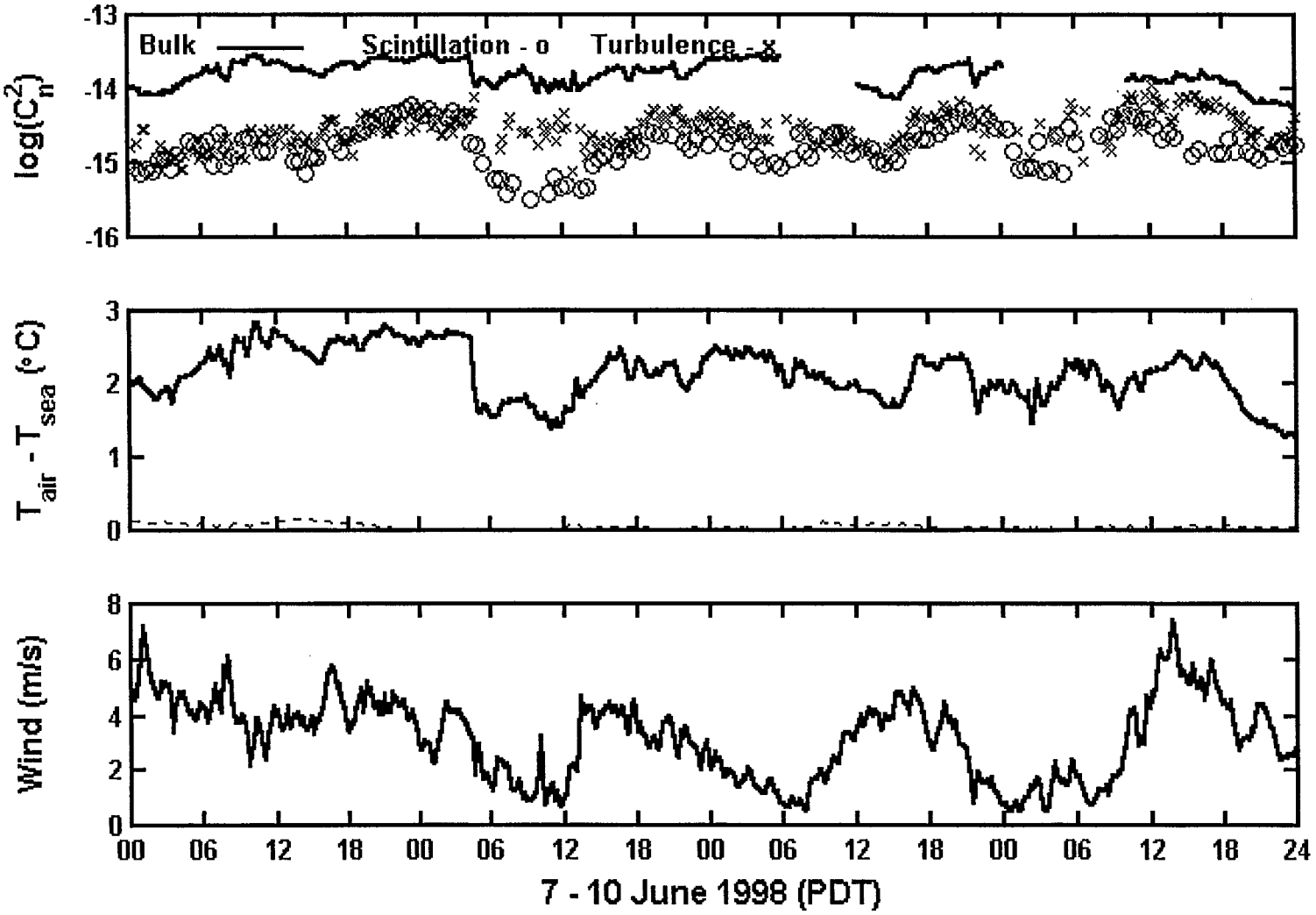


Figure 5. Time series plot for 7 – 10 June 1998 (Pacific Daylight Time). Top panel: bulk log(C_n^2) estimates indicated by solid line, scintillation log(C_n^2) measurements indicated by o's, turbulent log(C_n^2) measurements indicated by x's. Center panel: air – sea temperature difference in °C indicated by solid line, critical air – sea temperature difference in °C indicated by dashed line. Bottom panel: wind speed in m/s indicated by solid line.

toward zero, such as observed in the bulk C_n^2 values when ΔT approaches ΔT_c. Indeed, the lowest scintillation C_n^2 value observed during the entire experiment was just below 10^{-16}.

A time series plot of data for 7 – 10 June 1998 is presented in Fig. 5. Conditions were stable during this entire period, with positive ΔT values between 1.3 and 2.8 °C. During this entire four-day period the bulk C_n^2 values are higher than the scintillation data and very little correlation is exhibited between the two populations. The buoy turbulent C_n^2 measurements, on the other hand, generally agree reasonably well with the scintillation data. These results demonstrate that the bulk model performs poorly in stable conditions

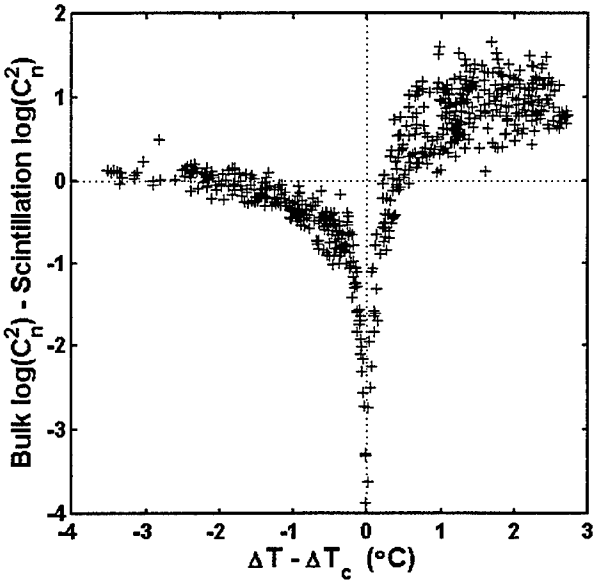


Figure 6. Plot of bulk $\log(C_n^2)$ – scintillation $\log(C_n^2)$ versus $\Delta T - \Delta T_c$.

A plot of bulk $\log(C_n^2)$ – scintillation $\log(C_n^2)$ versus $\Delta T - \Delta T_c$ for the entire experiment is presented in Fig. 6. The agreement between the bulk and scintillation data is quite good for unstable conditions when $\Delta T - \Delta T_c < -1.5$ °C, exhibiting both a small mean bias and low scatter. In stable conditions ($\Delta T - \Delta T_c > 1$ °C) the agreement between the bulk and scintillation data is poor, the bulk estimates being on average about one order of magnitude higher than the scintillation data, and a high degree of scatter is evident between the bulk and scintillation values. As $\Delta T - \Delta T_c \rightarrow 0$, the bulk C_n^2 estimates become gradually smaller than the scintillation measurements, until roughly $\Delta T - \Delta T_c < 0.2$ °C, when the bulk estimates decrease very rapidly and become several orders of magnitude smaller than the scintillation data.

5. CONCLUSIONS

The bulk-scintillation C_n^2 comparisons demonstrate that in unstable conditions C_n^2 can be estimated quite accurately with bulk methods, while in stable conditions the bulk model performed poorly, disagreeing with both the buoy turbulent C_n^2 measurements and the optical scintillation C_n^2 data. It is believed that these results are most likely due to the effects of ocean waves on the near-surface atmosphere. The atmospheric region adjacent to the ocean surface where waves can significantly modify atmospheric properties is known as the wave boundary layer (WBL). At its mid-point the optical path in this experiment passes only 3-6 m above the ocean surface, depending upon the tide and wave conditions, which is almost certainly within the WBL. Theoretical studies and observations have shown that vertical turbulent mixing within the WBL can be enhanced by ocean waves[4]. It is postulated that wave effects on atmospheric mixing would be much greater in stable conditions than in unstable conditions. In unstable conditions the atmospheric stratification promotes vertical motions, therefore the

wave-induced mixing would be small compared to the buoyancy and wind shear-generated atmospheric mixing already present. In stable conditions, on the other hand, the atmospheric stratification suppresses vertical motions, therefore the forced wave-induced mixing in the lower atmosphere could be significant when compared to the low levels of atmospheric mixing expected in stable conditions. This enhanced wave-induced mixing in stable conditions would decrease the vertical refractive-index gradient from the predicted Monin-Obukhov forms, which would in turn lead to lower values of C_n^2 than predicted by the bulk model. This would also explain the large bulk-scintillation scatter observed in stable conditions, since the wave characteristics that effect C_n^2 are not taken into account in the bulk model.

Wave effects may also explain the fact that scintillation C_n^2 values were never observed to decrease rapidly toward zero as $\Delta T \rightarrow -\Delta qB/A$, as predicted by the bulk model. Another possible explanation is that, although path-averaged scintillation measurements are weighted toward the center of the optical path, regions of high scintillation occurring at other points along the path contribute enough scintillation to mask the low C_n^2 values at the mid-point of the path. With a 7 km path length and the non-uniform topographic/hydrographic characteristics of San Diego Bay it is likely that atmospheric conditions along the path could be quite inhomogeneous.

6. ACKNOWLEDGEMENTS

This work was funded by the U. S. Office of Naval Research, program managers Dr. Scott Sandgathe and Dr. Ronald Ferek. The authors thank Mr. Keith Jones and Mr. Doug McKinney (McKinney Technology) for their efforts in deploying the NPS buoy and Mr. Bill Moision and Dr. Brett Nener for their assistance in acquiring the transmission data. A special thanks is due to Dr. Douglas Jensen for his able organizational skills during EOPACE.

7. REFERENCES

1. Andreas, E. L., "Estimating C_n^2 Over Snow and Ice From Meteorological Data", *J. Opt. Soc. Am.*, 5A, 481-495, 1988.

2. Frederickson, P. A., K. L. Davidson, C. R. Zeisse and I. Bendall, "A Comparison of Near-Surface Bulk and Scintillation C_n^2 Measurements during EOPACE," *Proceedings, SPIE Conference on Propagation and Imaging through the Atmosphere II*, Vol. 3433, San Diego, CA, 22-23 July 1998.

3. Zeisse, C., S. Gathman, A. Barrios, B. Moision, K. Davidson, and P. Frederickson, "Low Altitude Infrared Transmission", *Proceedings, Battlespace Atmospherics Conference*, San Diego, CA, 2-4 December 1997. **ADA344056**

4. Hare, J. E., T. Hara, J. B. Edson and J. M. Wilczak, "A Similarity Analysis of the Structure of Airflow over Surface Waves," *J. Phys. Oceanogr.*, 27, 1018-1037, 1997.

A Mobile Laboratory for Measurement of Nighttime Light Spectra

Timothy Hiett

Air Force Research Laboratory
AFRL/VSBE
29 Randolph Road
Hanscom AFB, MA 01731

hiett@plh.af.mil

OBJECTIVE

The Weather Impact Decision Aid (WIDA) Laboratory of the Air Force Research Laboratory (AFRL) has developed a mobile night vision laboratory for measurement of nighttime light spectra. This system performs measurements for validation of the Night vision goggles Operations Weather Software (NOWS) that predicts nighttime illumination levels as well as nighttime target/background contrast. The mobile laboratory carries three low-light sensitive spectroradiometer systems that are tailored for measurement of target radiance, lunar radiance, and whole sky irradiance. Meteorological instruments, as well as night vision cameras, were integrated into the mobile laboratory to provide for a highly detailed dataset. Validation experiments have been fielded for the past year at Otis Air National Guard Base (ANGB) on Massachusetts's Cape Cod. This paper will present an overview of the mobile laboratory and its measurement capabilities.

RESEARCH ACCOMPLISHED

The NOWS validation effort is concurrent with the model development so the measurements are directed at improvement of specific components of the NOWS software. The laboratory is equipped to measure the intermediate radiometric quantities that are derived by the NOWS illumination, transmission, target contrast, and urban illumination models. These measurements include whole sky irradiance, target radiance, and lunar radiance. The inputs to the NOWS models also include target/background characteristics and atmospheric conditions as measured by our on-board weather instrumentation.

To satisfy all the radiometric requirements for model validation, three all-weather spectroradiometer systems based on EG&G Inc. components have been developed. Each system is comprised of a specific light receptor that feeds into a holographic grating monochromator that scans between 350 and 1010 nm. A high sensitivity photomultiplier detector is coupled to the exit of the monochromator. This photomultiplier is required for amplification of weak nighttime light levels. The receptor for the whole-sky irradiance measurement is an 8"-diameter integrating sphere protected by a hemispheric glass dome. The target and lunar radiometers use telescopes as receptors. The telescopes have four field-of-view adjustments between 6 minutes and 3 degrees. All three systems use the EG&G NM-3DH for a monochromator. For the lunar radiometer an EG&G DC-49 photomultiplier detector is used. Its best sensitivity is approximately 5E-15 $W/cm^2*nm*sr$ sensitivity at 500 nm. The whole-sky and target radiometers use an EG&G DC-51C which is about an order of magnitude more sensitive than the DC-49.

Each radiometer system is controlled by an EG&G GS4100 controller. The GS4100 units are each attached via RS232 to our main data acquisition computer. Figure 1 provides a layout of our lunar spectroradiometer system.

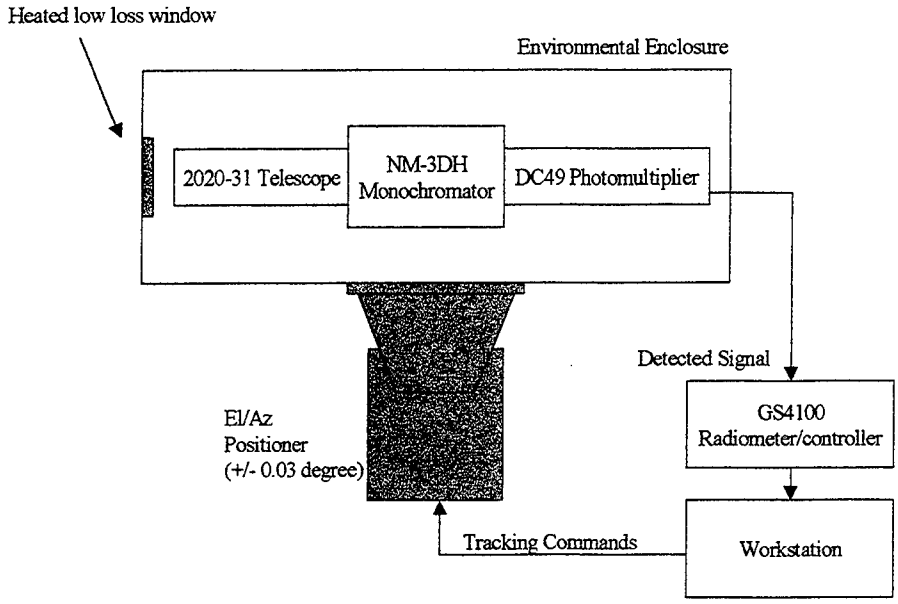


Figure 1. The Lunar Radiometer System Layout

Each radiometer system is custom mounted for its particular measurement. The whole-sky radiometer system is mounted atop a 35' mast that lifts it above all surrounding instrumentation for an unobstructed view of the sky. Lunar and target radiometers are mounted on computer controlled azimuth-over-elevation precision positioning systems, which allow for precise tracking of the lunar disk and field targets.

The radiometer systems are primarily laboratory-grade instruments, therefore, a substantial effort was undertaken to make them field capable. The components used need moderate climate control and support equipment. All radiometers have custom environmental enclosures with heated low-loss apertures for their viewing ports. The mobile laboratory carries a large chilled water distribution system that cools all three photomultiplier systems. Calibrations that normally would take place in a dark laboratory are instead made in the field with weather-tight and light-tight fixtures.

The mobile laboratory carries numerous meteorological sensors for measurement of atmospheric inputs to the NOWS models. A Viasala Milos 500 weather system monitors wind speed/direction, air temperature/humidity, and other standard quantities. An HSS Inc. tactical present weather sensor measures rain amount/rate, precipitation type, and visibility. An Optec Inc. Long Path Visibility (LPV) sensor is sometimes included, which measures atmospheric extinction at 550, 750, 800 and 900 nm.

Experiments also utilize instrumentation and measurements that are not specific to the mobile laboratory. The Otis ANGB weather test facility provides ceilometer and backup weather information. The nearby airfield provides standard hourly observations. The near future will include a 35 GHz cloud profiling radar developed by Quadrant Engineering Incorporated. This new system, called the Air Force Cloud Profiling Radar (AFCPR), will provide us highly detailed cloud structure information. The AFCPR may be integrated onto an elevation-over-azimuth positioning system for three-dimensional scanning of the cloud fields over the test site.

Operational Night Vision Goggle (NVG) systems have been integrated onto the laboratory for meteorological and target measurements. One ITT 4949D monocular has been attached to a video camera that scans the night sky for cloud situation archiving. Another 4949D monocular records the target area throughout the night. Other NVGs are utilized for intermittent observations.

Each system on the mobile laboratory is highly automated. Nearly all instruments are controlled and their data archived by a central UNIX workstation. A laboratory system diagram is shown in Figure 2. Automation has been crucial to this effort since the radiometer systems require extended stabilization periods and must be monitored at all times.

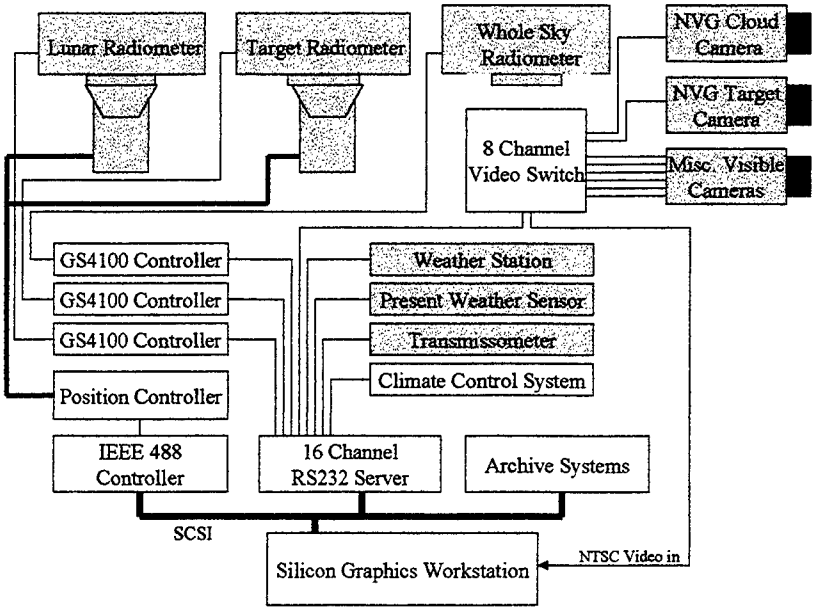


Figure 2 Mobile Laboratory System Diagram.

The mobile laboratory was designed to operate with minimal field support. An on-board 7 kW generator powers the trailer with a fuel capacity sufficient for two days operation. Figure 3 shows the mobile laboratory set up at a recent experiment.

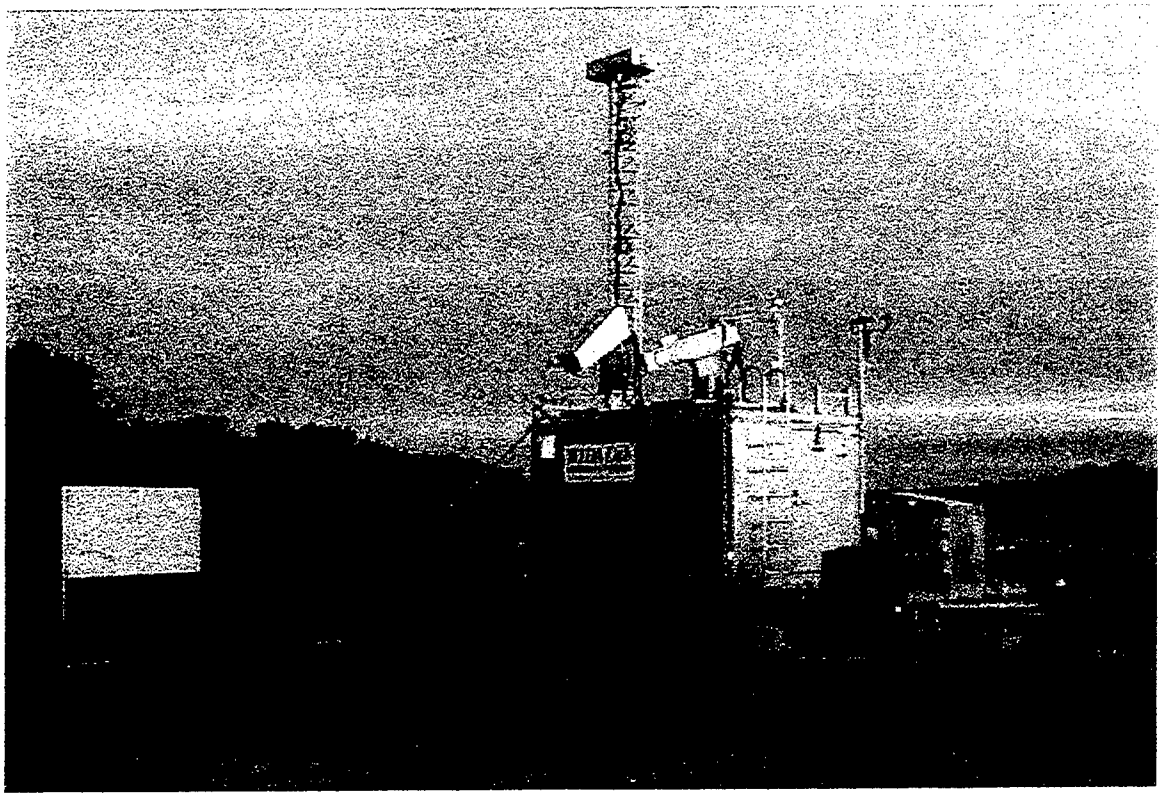


Figure 3 The mobile laboratory setup at Otis ANGB in Massachusetts.

The mobile laboratory is frequently deployed to Otis ANGB for two-week duration experiments. Otis was chosen for its relatively low-light firing range that offers a variety of terrain types. The AFRL/VSBE weather test facility is located nearby for support. A typical two-week experiment commences with deployment from Hanscom AFB. Setup of equipment takes about half of a day. Observations are made nearly every other night with rest days in between. Each nightly observation period results in a Compact Disc (CD) archived data set. These data sets contain all instrument data files, MPEG movies of the various video sources, detailed site maps, and setup documentation. To date 25 datasets have been completed.

An interesting example of the radiometer capabilities is shown in Figure 4. This plot is derived from spectral irradiance measurements taken by our whole sky spectroradiometer system. These measurements were taken during a transition between clear sky to overcast. In this particular example, the moon was near full and above the horizon, thus, contributing to the whole sky irradiance. The first measurement shows the spectral irradiance from the relatively clear sky and unobstructed moon. The second measurement, taken over an hour later, shows the irradiance from a 50% obstructed sky

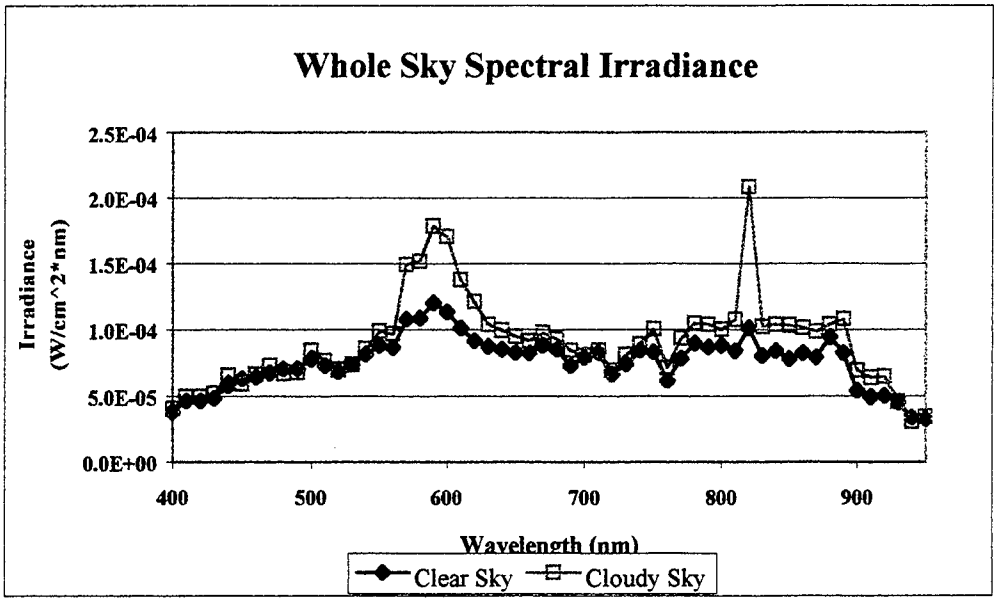


Figure 4 Comparision of clear sky spectral irradiance to that of a cloudy sky.

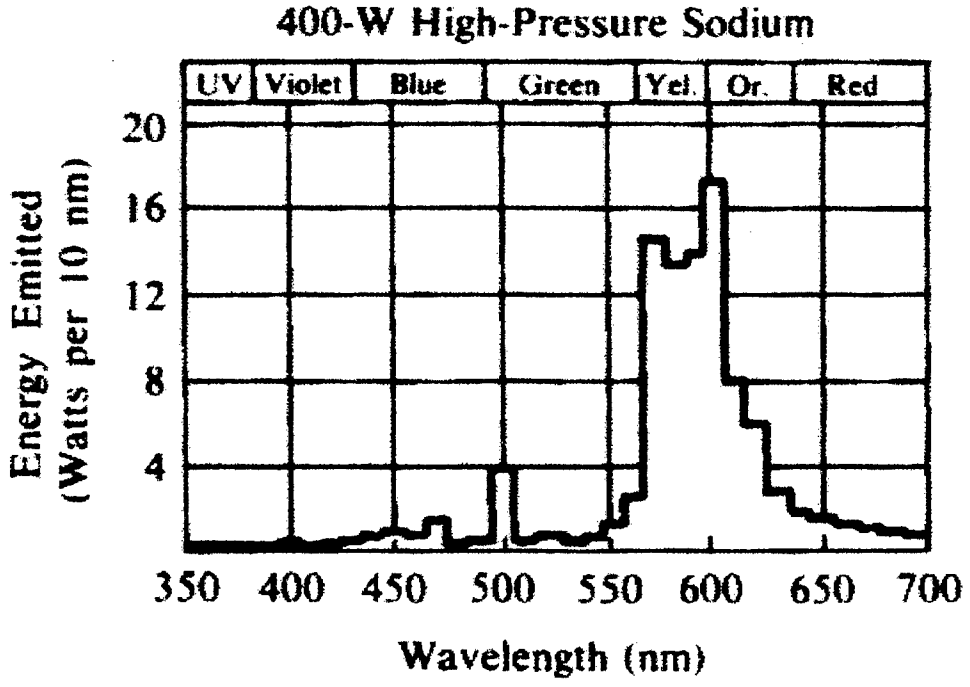


Figure 5 Spectrum of a High-Pressure Sodium Lamp [1].

sky and totally obstructed moon. Interestingly, the obstruction of the moon and sky resulted in an increase in night sky irradiance. The spectral distribution of this irradiance increase suggests that artificial light may be its source. The distribution of the increase is similar in content to both high and low-pressure sodium lamp spectra. Figure 5 illustrates the visible spectrum of a high-pressure sodium lamp. The spectral irradiance increase seen in Figure 4 clearly resembles the sodium lamp emission over the wavelength range of 350 nm to 700 nm. It appears that as the cloud deck moved over a town to the northwest it reflected urban illumination onto the test site. A yellow and orange glow from that town was evident when the clouds moved over the test site.

The significance of the urban illumination contribution to night sky irradiance is becoming of great interest to the WIDA Laboratory. The increasing presence of light pollution has been studied and somewhat modeled over the past two decades [2] [3] [4] with emphasis to its impact on astronomical observations. These studies have understandably focused on clear sky and aerosol influenced conditions. We believe further study of cloud layer impact on light pollution levels is needed to extend the usefulness of the NOWS program. With the 35 GHz AFCPR system soon available to complement the mobile laboratory, this area of study can be pursued in more depth.

CONCLUSIONS AND RECOMMENDATIONS

The Air Force Research Laboratory has developed a uniquely capable mobile night vision laboratory to support validation of its NOWS product. This mobile laboratory measures the spectral content of nighttime light between 350 and 1010 nm in wavelength. The laboratory has proved suitable for measurement of both natural and artificial illumination. Supporting meteorological sensors have been integrated onto the mobile laboratory structure for a detailed investigation of the influence of weather on nighttime light levels. A 35 GHz radar system will soon be added to program capabilities. The radar will enable detailed characterization of the cloud fields over our test site. These new measurements should prove helpful in determining the contributions of clouds to urban illumination.

ACKNOWLEDGEMENTS

Tony Absi of AFRL has donated equipment and guidance since the beginning of this project. Melanie Gouviea, Glen Higgins and Roy Deal of The Analytical Sciences Corporation (TASC) have provided assistance in development of experiment plans and analysis of data. Capt. Dana Madsen, MSgt. Jim Anderson, Ralph Hoar and Steve Luker have contributed immensely to the laboratory construction and field tests.

REFERENCES

[1] Murdoch, J.B., *Illumination Engineering – From Edison's Lamp to the Laser*, Macmillan Publishing Company, New York, NY, 1985.

[2] Garstang, R.H., *Model for artificial night-sky illumination*, Publication of the Astronomical Society of the Pacific, Vol. 98, pp. 364-375, March 1986.

[3] Joseph, J.H., Kaufman, Y.J., and Y.Mekler, *Urban light pollution: the effect of atmospheric aerosols on astronomical observations at night*, Applied Optics, Vol. 30, No. 21, pp. 3047-3058, July 1991.

[4] Pike, R., *A simple computer model for the growth of light pollution*, Journal of the Royal Astronomical Society of Canada, Vol. 70, No. 3, pp. 116-126, June 1976.

[5] Kostkowski, H.J., *Reliable Spectroradiometry*, Spectroradiometry Consulting, La Plata, Maryland, 1997.

[6] Madsen D., Heckman S., Hiett T., Tattelman P., Seeley G., Ayer S., Luker S., Hoar R., Anderson J., *Weather Impact Decision Aids – IR and NVG Model Validation*, Proceedings of the Battlespace Atmospherics Conference, San Diego, CA, 1997. [ADA 323038].

MULTI-SENSOR AEROSOL DETECTION: COMBINING AEROSOL INFORMATION FROM THE GOES-8 AND 9 IMAGERS AND NOAA/AVHRR

Kenneth Knapp, Kenneth Eis* and Thomas H. Vonder Haar

Cooperative Institute for Research in the Atmosphere
Colorado State University
Fort Collins, CO 80523 – 1375
Phone: (970) 491 – 8398 Fax: (970) 491 – 8241
E-mail: knapp@cira.colostate.edu

Department of Defense/Center for Geosciences Phase III

OBJECTIVE

Today's smart weapons rely to a large extent on infrared and visible sensors seeing their targets. Even in an age of GPS-guided systems, terminal guidance, using IR and visible target detection will be needed. Atmospheric aerosols – including smoke, dust, and pollutants – contribute to the degradation of the performance of these weapons; for instance aerosol scattering can limit the lock-on range of most smart weapons today. No high-resolution global data base exists to assist the DOD in analysis of weapons vulnerabilities to aerosol scattering effects with the exception of the NOAA single channel analysis (which is crude and available only over the ocean). This paper describes an aerosol retrieval method that merges data from the AVHRR and the Imagers aboard GOES-8 and 9 that would allow retrievals of aerosol information over some land surfaces. Previous studies investigating satellite retrieval of aerosol optical depth (τ) have primarily used one instrument, thereby limiting the retrieval to the design of a specific instrument. Because the phase function varies enough with view angle, aerosol properties can be determined from AVHRR and the GOES system.

RESEARCH ACCOMPLISHED

Method Description

The amount of radiance scattered from the solar beam toward the satellite instrument field of view is determined by the aerosol phase function, which is a function of the aerosol shape, size distribution and composition, wavelength of radiation and scattering angle. The following sensitivity study will show that this phase function varies enough with view angle to determine aerosol properties from AVHRR and the GOES system.

In preparation for retrieving aerosols from multiple instruments, simulations were performed to investigate the method's sensitivity and feasibility. The Second Simulation of the Satellite Signal in the Solar Spectrum (6S) radiative transfer model [Vermote, 1997] was used to simulate satellite detected reflectances (ρ_{sat}) due to varying aerosol optical depth and mode radius for each satellite sensor: AVHRR channel 1 and the GOES-8 and GOES-9 visible sensors. Aerosol scattering was simulated using a continental aerosol model [Lenoble, 1984] with a single-mode, log-normal distribution ($\sigma = 1.6$). The mode radius (r_m) of the aerosol was varied between 0.01 μm and 0.794 μm ($\Delta \log_{10} r_m = 0.1$) while the τ was varied from 0.02 to 0.8 ($\Delta\tau = 0.02$) [Amato, 1996; Soufflet, 1997]. A Lambertian surface reflectance with spectral characteristics of green vegetation (from the 6S model) was used to simulate retrievals over the land. A realistic sun-earth-satellite geometry was used, that is when NOAA-14 would under-fly

the GOES systems simultaneously observing a location in the southwest U.S. The satellite-detected radiances, ρ_{sat}, values were calculated using spectral response functions from the NOAA-14/AVHRR, GOES/East and GOES/West instruments. The results of the simulations can be displayed as contour plots of ρ_{sat} as a function of τ and r_m. For example, Figure 1 shows the reflectance contours for the GOES-9 Imager channel 1 sensor, demonstrating the response of the sensor to changes in aerosol optical depth and mode radius.

Before proceeding, instrument noise should be discussed. As an example, let $\tau = 0.4$ and $r_m = 0.1\mu m$, then $\rho_{sat} = 0.196$ for the GOES-9 Imager channel 1. However, the precision of this reflectance measurement is limited by the instrument noise. The instrument noise (in reflectance units) for GOES-8, GOES-9, NOAA-14/AVHRR channels 1 and 2 are 0.0086, 0.010, 0.0017 and 0.0017, respectively [Menzel, 1994; Kidwell, 1997]. For the range of signal simulated, instrument noise represents a Gaussian probability distribution with a mean defined by the measured reflectance and standard deviation defined by the instrument noise. Using Gaussian statistics, noise can also be described as the confidence in a certain measurement being within some interval of the actual value. The intervals contoured in Figure 2 are the 50% (thick line) and 99% (thin line) confidence intervals (CI) centered about ρ_{sat} corresponding to $\tau = 0.4$ and $r_m = 0.1$ μm. Therefore from the above example, the actual measured satellite reflectance is within some interval centered on 0.196 (Figure 2b). The product of the probability distributions of the four sensors can be used to calculate a new probability distribution, which allows the performance evaluation of the method. Also, note that the AVHRR channel 2 will not be used in the method because of reasons discussed below, but was included in this example for continuity.

The probabilities for each condition (defined by the plus sign in figure 3) are determined from the product of the probabilities of AVHRR ch. 1, GOES-8 ch. 1 and GOES-9 ch. 1. The 99% CI for the combined probability distributions are contoured in light gray in Figure 3 for discrete combinations of τ (0.1, 0.4, and 0.7) and r_m (0.02, 0.1, and 0.5 μm). The plus signs in figure 3 are the solutions and the size of the shaded areas define the error due to the sensor noise. Of course other error sources (to be discussed below) will increase the size of the shaded contour, but this analysis allows an estimate of the best possible retrieval in the event that accurate a priori data is available. The average error in the retrievals due to sensor noise alone is 0.03 and 0.08 in τ and r_m, respectively; however, retrievals have less error at larger optical depths.

These calculations show that aside from other error sources, combining GOES and AVHRR for the retrieval of aerosol information is possible. However, other retrieval error sources will decrease the accuracy of the method. The problem then becomes: How will the method certainty change taking into account other error sources?

Error Sources

The process of retrieving information convoluted within another dataset is very sensitive to errors in that dataset. In this case, we are retrieving aerosol information which is convoluted in atmospheric observed reflectances from different satellite view angles. Signals in the measured reflectances not associated with aerosol interactions must be accounted for in an error study, these include: calibration problems, gaseous absorption, surface reflectance, and assumed aerosol optical properties (e.g. those properties that are not retrieved). It is also important to understand how these error sources relate to other published aerosol retrieval methods.

Determination of Surface Reflectance

Aerosols allow surface-reflected radiation to transmit through the layer and affect the angular signature of the detected reflectance. This is the source of largest error for any type of aerosol retrieval over land. There are two primary methods in estimating surface reflectance, ρ_{sfc}: the mosaic and the near-IR methods. The mosaic method would make use of images from numerous satellite overpasses to create a composite background, using the darkest pixel for each Earth location. In theory, the pixels in the mosaic would have the lowest aerosol burden, and thus would be a suitable estimate of surface reflectance. Assuming only a background aerosol with a low optical depth is present. the mosaic might even be "corrected" using 6S. The advantage of this method is that it works for all surface reflectances and provides a realistic estimate of surface reflectance. However, angular changes in satellite view angles would significantly lengthen the time needed to get a cloud- and aerosol-free mosaic from polar orbiting data. The resulting mosaic would likely be affected by rain events or seasonal changes in reflectance, thus increasing the uncertainty of the mosaic estimate of ρ_{sfc}.

The alternate method makes use of the relation of the surface reflectance at near-IR wavelengths (2-4μm) to that in the visible (0.4-0.7μm) over dense-dark vegetation (DDV). It has been shown that the surface reflectance at 2.21μm (a wavelength mainly unaffected by aerosol scattering) is correlated to the reflectance at visible wavelengths [Kaufman, 1997]. Therefore, this method can calculate the surface reflectance from the same image that it uses to retrieve aerosol properties, so there is less error from bidirectional reflectance properties. However, the method is limited to DDV surfaces only and the relationship still has large relative errors in the estimation of visible surface reflectance.

It seems that either method will have some significant error. The mosaic can not account for surface reflectance changes on short time scales and the DDV technique has an estimated error near 0.01 (or 5-10% at best). To estimate the magnitude of error incurred by some error in surface reflectance, simulated retrievals were performed. The optical depth was retrieved as simulated by a single channel instrument for a range of surface reflectances and optical depths. For each retrieval, two additional retrievals using different surface reflectances. The alternate surface reflectances were varied by 1 and –1% (a conservative estimate) to allow the calculation of the percent error in an optical depth retrieval caused by a 1% error in surface reflectance. The results for this are shown in figure 4. Aerosol optical depth retrievals were simulated using the 6S model and a mono-modal log-normal distribution with $r_m = 0.005$ and $\sigma = 2.99$, for conservative (refractive index, m, of 1.43 + 0.0i, which has no aerosol absorption) and non-conservative scattering (m = 1.43 + 0.001i, which has some aerosol absorption) at 0.55 and 0.85μm. The surface error is amplified where the τ retrieval error is greater than 1%, and conversely reduced where τ error is less than 1%. Then it can be seen from figure 4 that error amplification is inversely proportional to optical depth and proportional to surface reflectance. Thus, error reduction can occur when τ is large and ρ_{sfc} is near zero. However, it can be seen from Figure 4 that as the observing wavelength or aerosol absorption increases, the error amplification also increases. Therefore, the retrieval of aerosol optical properties is only worthwhile when $\rho_{sfc} < 0.2$ or so. This has large implications on the method described here as well as most other aerosol retrieval methods. Vegetated surfaces have dark surface reflectances in the visible spectrum ($\rho_{sfc} \sim 0.03$-0.15 for $\lambda = 0.4$-$0.7\mu m$) and bright reflectances in the near-IR ($\rho_{sfc} \sim 0.3$-0.5 for $\lambda = 0.7$-$1.5\mu m$), therefore AVHRR ch. 2 ($\lambda = 0.725$-$1.0\mu m$) was not used in this method. However, the second channel would add information to a retrieval system over ocean because $\rho_{sfc} \sim 0.0$-0.05 in the visible to near-IR for ocean surfaces with light winds.

Sensor Calibration

Retrieval of aerosol parameters requires accurate calibration of the instrument measurements. Both the GOES-Imager and AVHRR instruments were calibrated prior to launch, but neither have onboard calibration lamps. So until recently, accurate calibration of the data was unavailable because of the degradation of instrument optics during the satellite's lifetime. NOAA has instituted vicarious calibration schemes for the short wave sensors (channels 1 and 2) which provide monthly updates for the calibration coefficients to within 0.0015 (in reflectance units) [Rao, 1996]. And recently there has been an organized effort to calibrate the imagers aboard the GOES series of satellites. The method of calibration is described by Weinreb [1997] and degradation rates of the sensor optics are presented by Bremer [1998] as 7.6 and 4.9% per year for GOES-8 and 9, respectively. These new degradation estimates were used to compare satellite-detected reflectances from GOES-8 and GOES-9 at local noon for the 105th West meridian (for this longitude line, the Sun-Earth-satellite geometries are symmetric about the solar position). Over a 100-km stretch of dark ocean, the bias between the satellite images was reduced from 14 to 6.4 W $m^{-2}\mu m^{-1}ster^{-1}$, or about 0.012 in reflectance units. This value is nearly within the sensor noise of GOES-8 and 9, yet we feel a more accurate pixel registration should improve this bias.

Aerosol optical properties

Three aerosol properties are very important when considering retrieval from satellite data: the single scatter albedo (ω_o), aerosol size distribution, and the non-sphericity of the aerosol particles.

The single scatter albedo (the ratio of aerosol scattering to aerosol extinction) can not be easily retrieved from satellite imagery, therefore a climatological value is used in most aerosol retrievals, including this method. This can create large errors in a retrieval over areas where the climatological aerosol has a large variance in ω_o.

The aerosol size distribution affects the phase function characteristics of the aerosol. References too numerous to list here use a variety of aerosol size distribution models for satellite aerosol. This method will use a mono-modal log-normal distribution to retrieve aerosol optical depth and mode radius in following with Tanré [1996].

In most aerosol retrievals, aerosol scattering is simulated using Mie scattering theory which assumes spherical scattering. In general, this is a valid assumption because most retrieval methods utilize one scattering angle at different wavelengths. However, non-spherical particles can have vastly different phase functions compared to a similar size distribution of spheres. Therefore, it will be important to check the sensitivity of this retrieval method to the presence of non-spherical aerosol particles using methods similar to that of Mishchenko [1997]. This will be significant for dust and soot aerosols, which tend to be non-spherical and insignificant for the more spherical sulfate and hygroscopic aerosols.

Gaseous Absorption

It has been suggested that gaseous absorption could impact the satellite measurements because both GOES and AVHRR have spectrally wide shortwave channels which encompass ozone and water vapor absorption bands. Simulations using the 6S model show that the gaseous absorption impacts will be inconsequential. Climatological estimates of the absorber amount will be sufficient to account for gaseous absorption and perturbations from climatology in water vapor or ozone would not cause a detectable change in reflectance for the GOES or AVHRR shortwave channels.

CONCLUSIONS AND RECOMMENDATIONS

The proposed method uses measured reflectances from the GOES-system and NOAA/AVHRR to retrieve aerosol optical depth and mode radius. Sensitivity studies show that satellite inter-calibration and possible aerosol non-sphericity are error sources that are specific to this retrieval method. Although, multi-view sensors such as the Multi-angle Imaging Spectro-Radiometer will have similar problems with aerosol non-sphericity. Also other large error sources – including surface reflectance, single scatter albedo and aerosol size distribution uncertainties – are common to all aerosol retrieval methods that utilize reflected solar radiation.

Future work includes the need for determining the sensitivity of this method to non-spherical aerosols. This could likely be performed using non-spherical aerosol scattering calculations, like the T-matrix codes written by Mike Mishchenko [e.g. Mishchenko, 1997]. Also, the satellite inter-calibration needs to be studied to determine how large an affect the poor GOES calibration and small signal-to-noise ratios will have on the method. At the same time, the method should be tested by performing retrievals over land and ocean in areas where surface measurements of aerosol optical depth are available. Upon completion and validation of the aerosol retrieval method, the algorithms could be transferred to the military where it could contribute to Tactical Decision Aids.

REFERENCES

Amato, U., D. Di Bello, F. Esposito, C. Serio, G. Pavese and F. Romano, Intercomparing the Twomey method with a multi-modal log-normal approach to retrieve aerosol size distribution, J. Geophys. Res., 101, 19267-19275, 1996.

Bremer, J. C., J. G. Baucom, H. Vu, M. P. Weinreb, and N. Pinkine, Estimation of long-term throughput degradation of GOES 8 & 9 visible channels by statistical of star measurements, proceedings of SPIE, Vol. 3439, Earth Observing Systems III, 20 July 1998.

Kaufman, Y. J., A. Wald, L. A. Remer, B.-C. Gao, R.-R. Li and L. Flynn, The MODIS 2.1-μm channel – correlation with visible reflectance for use in remote sensing of aerosol, IEEE Trans. Geosci. Rem. Sens., 35, 1286-1298, 1997.

Kidwell, K. B (Ed.), NOAA Polar Orbiter Data User's Guide, U.S. Dept. of Commerce, NOAA/NESDIS,1997.

Lenoble, J. and C. Brogniez, A comparative review of radiation aerosol models, Beitr. Phys. Atmos., 57(1), 1-20, 1984.

Menzel, W. P. and J. F. W. Purdom, Introducing GOES-I: The first of a new generation of geostationary operational environmental satellites, Bull. Am. Met. Soc., 75, 757-781 1994.

Mishchenko, M. I., L. D. Travis, R. A. Kahn and R. A. West, Modeling phase functions for dustlike tropospheric aerosols using a shape mixture of randomly oriented polydisperse spheroids, J. Geophys. Res., 102, 16381-16847, 1997.

Rao, C.R.N. and J. Chen, Post-launch calibration of the visible and near-infrared channels of the Advanced Very High Resolution Radiometer on the NOAA-14 spacecraft, International Journal of Remote Sensing, 17, 2743-2747, 1996.

Soufflet, V., D. Tanré, A. Royer, and N. T. O'Neill, Remote sensing of aerosols over boreal forest and lake water from AVHRR data, Rem. Sens. Env., 60, 22-34, 1997.

Tanré, D., M. Herman and Y. J. Kaufman, Information on the aerosol size distribution contained in solar reflected spectral radiances, J. Geophys. Res., 101, 19043-19060, 1996.

Vermote, E. F., D. Tanré, J. L. Deuze, M. Herman, and J. J. Morcrette, Second simulation of the satellite signal in the solar spectrum, 6S: an overview, IEEE Trans. Geo. and Rem. Sensing, 35, 675-686, 1997.

Weinreb, M., M. Jamieson, N. Fulton, Y. Chen, J. X. Johnson, J. Bremer, C. Smith, and J. Baucom, Operational calibration of Geostationary Operational Environmental Satellite-8 and –9 imagers and sounders, Applied Optics, 36, 6895-6904, 1997.

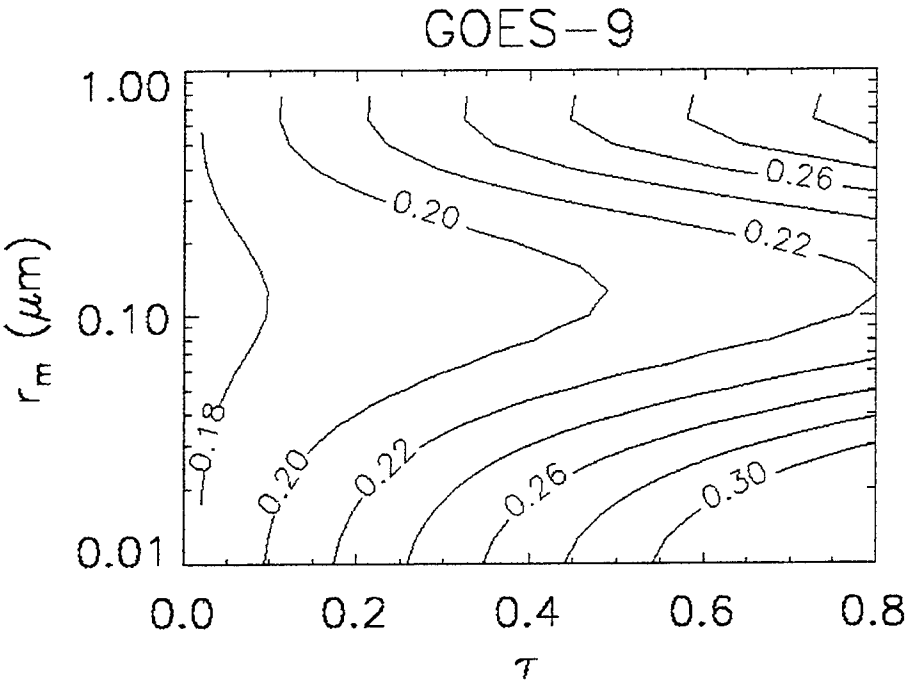


Figure 1 – Contour of ρ_{sat} (in reflectance) for the GOES-9 Imager channel 1 as function of τ and r_m (μm) simulated using 6S.

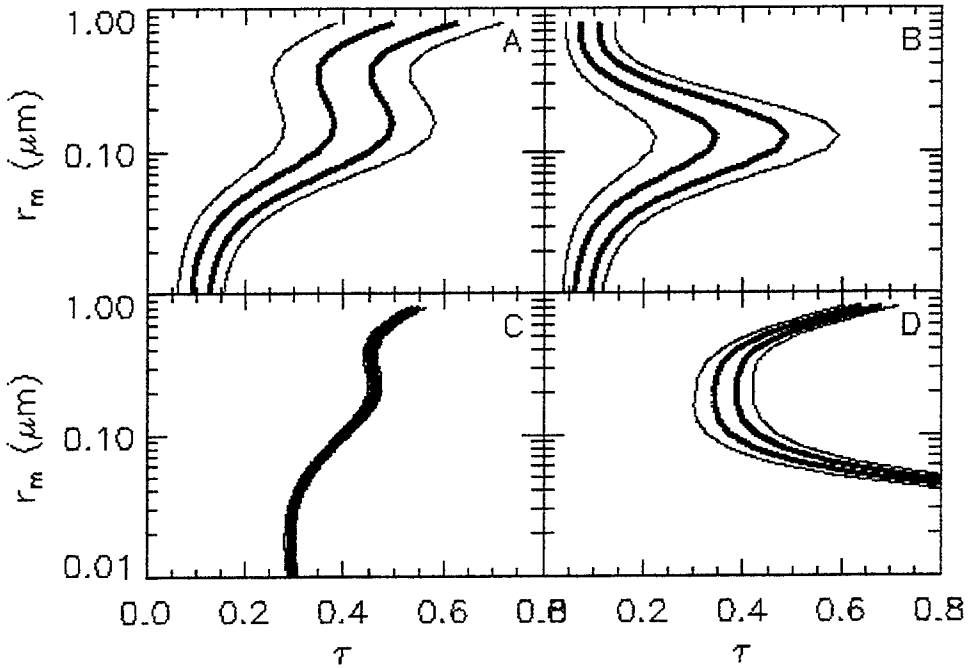


Figure 2 – Contours of the 50% (thick line) and 99% (thin line) confidence intervals for the case when $\tau = 0.40$ and $r = 0.10$ μm, for: a) GOES-8/Imager channel 1, b) GOES-9/Imager channel 1, c) NOAA-14/ AVHRR channel 1 and d) NOAA-14/ AVHRR channel 2.

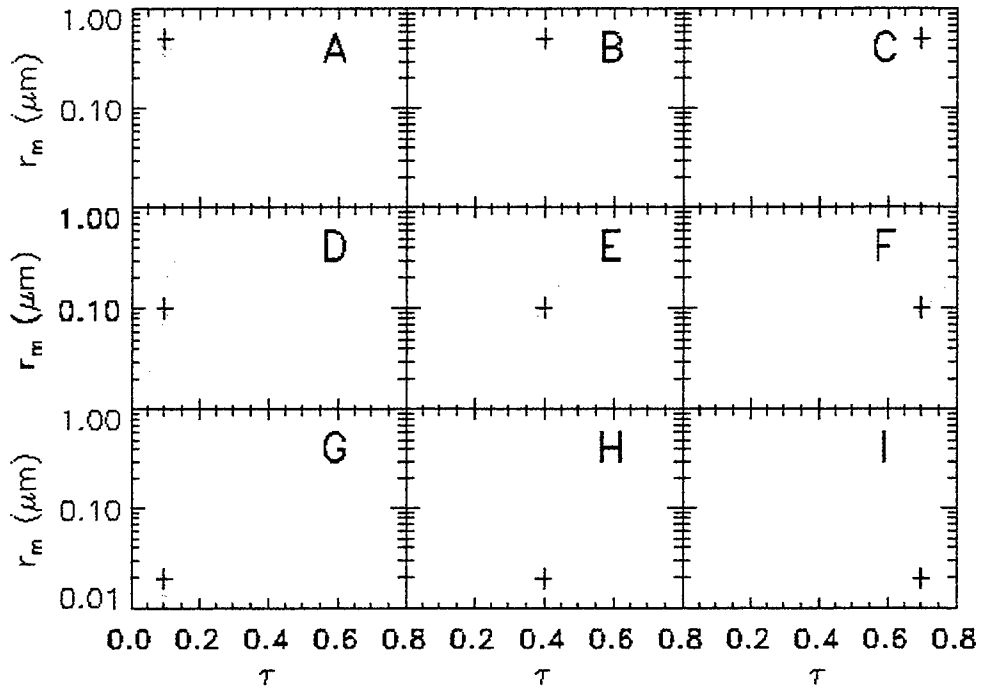


Figure 3 – The light gray area is the 99% confidence interval for conditions defined by the plus (+) signs where the τ, r_m couplings are a) 0.1, 0.5 μm, b) 0.4, 0.5 μm, c) 0.7, 0.5 μm, d) 0.1, 0.1 μm, e) 0.4, 0.1 μm, f) 0.7, 0.1 μm, g) 0.1, 0.02 μm, h) 0.4, 0.02 μm, and i) 0.7, 0.02μm.

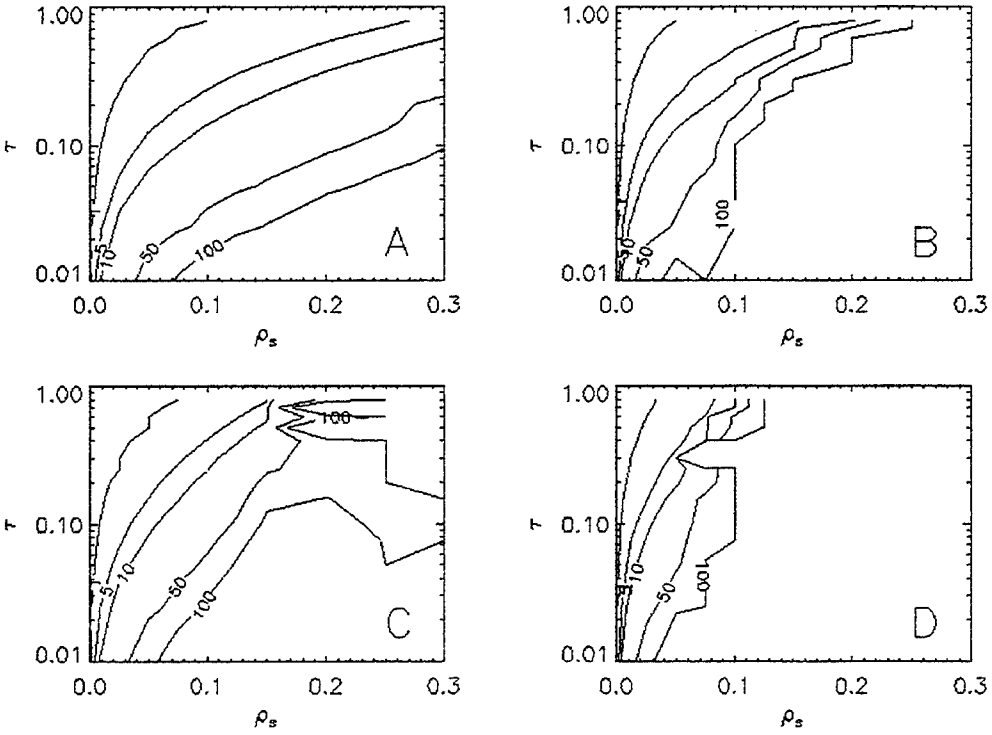


Figure 4 – τ retrieval sensitivity to a 1% error in surface reflectance for different wavelengths and ω_o: a) λ=0.55μm, ω_o = 1.00, b) λ=0.85μm, ω_o = 1.00, c) λ=0.55μm, ω_o = 0.99 and d) λ=0.85μm, ω_o = 0.99.

HYPER- AND MULTI-SPECTRAL AEROSOL DETECTION AND COMPENSATION

J.W. Snow, H.K. Burke*, M.K. Griffin, and C.A. Upham
MIT Lincoln Laboratory, 244 Wood St., Lexington, MA 02420
781-981-7979, fax 7271, burke@ll.mit.edu

AF Contract # F19628-95-C-0002

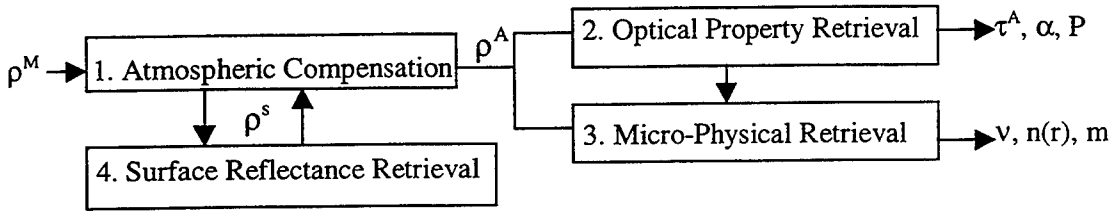
OBJECTIVE

The quantification of atmospheric aerosol properties from environmental satellites is of interest because the global average aerosol optical thickness is substantial, close to 0.13, and the natural variability of aerosols accounts for 90 % of the variation in visible transmission of the cloud-free atmosphere (Fraser, 1975). Basically, variability occurs in the physical (bulk) and micro-physical (particle) aerosol properties. Basic bulk properties are amount and composition; particle properties are shape and size, in particular, the particle size distribution n(r) (cm^{-3} μm^{-1}). The aerosol optical properties result from radiative interactions with the bulk and particle characteristics. Prime optical properties are optical thickness τ^A, single-scattering albedo ω, and single-scattering phase function P. The variability of these is no less than that of the micro-physical properties. The property most frequently retrieved from satellite measurements is τ^A, which is the optical surrogate for amount. The spectral change in τ^A is the second-most common satellite aerosol product, containing some information on n(r).

The spectral transmittances for the three primary atmosphere attenuations – water vapor absorption, aerosols scattering, and both scattering and absorption by all other gases – are depicted in Figure 1. Also shown is the combined total transmittance for the cloud-free mid-latitude summer atmospheric condition. In this paper the single-channel and multispectral techniques presently in use for determining τ^A are summarized and the possibility of specifying n(r) from hyperspectral satellite data is explored.

RETRIEVAL PROCEDURE

Retrieval of aerosol properties from remotely sensed satellite data comprise four basic procedural steps. These are depicted and described below. At least atmospheric compensation and optical property retrieval are always carried out.



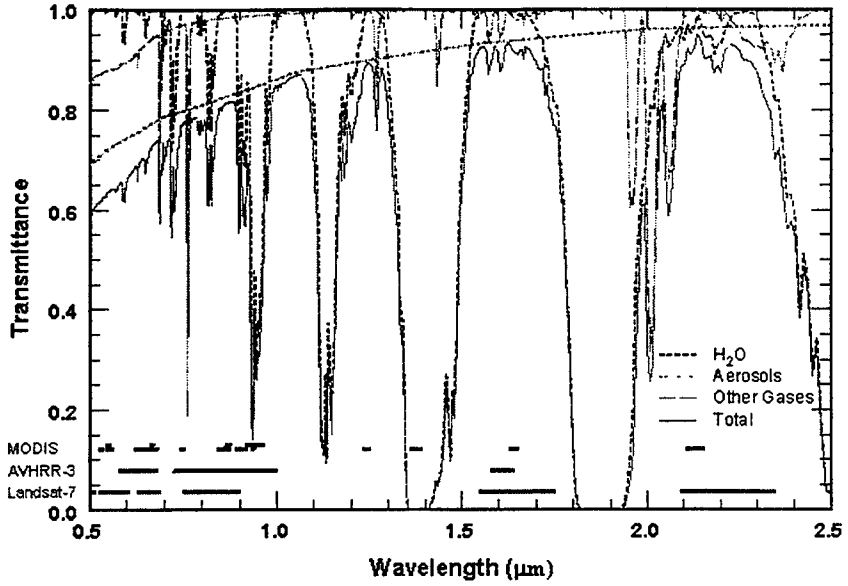


Figure 1. Spectral transmittance of major atmospheric components for total vertical path through mid-latitude summer atmosphere, using MODTRAN. Band-widths of environmental satellite sensors are indicated by line segments.

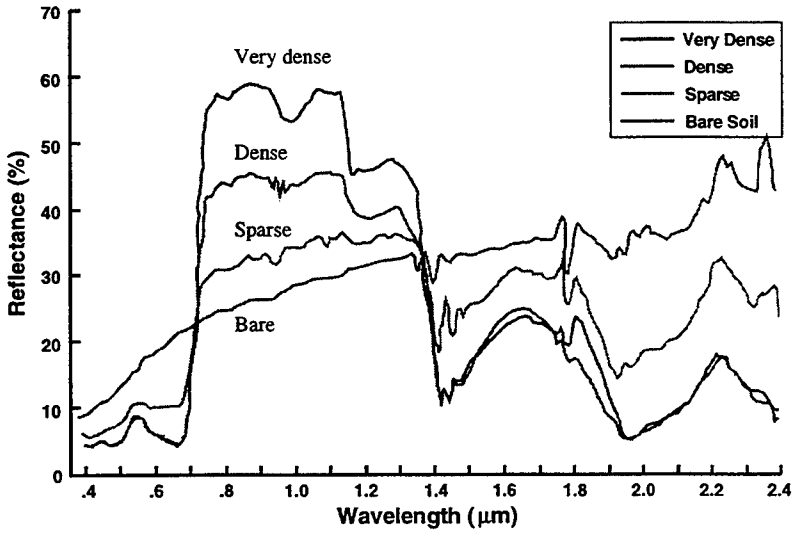


Figure 2. Spectral surface reflectance variation with vegetation cover. measurements made at 3 to 4 m directly above mature alfalfa having biomass and canopy cover indicated, with solar zenith angle of 55°

Step 1: *Compensation for atmospheric and surface effects – the determination of aerosol contribution to the total radiance.*

The satellite-measured radiance is the combination of photons from two basic sources: path radiance backscattered by atmospheric constituents alone, and radiance that has interacted in some way with the surface before emerging from the top-of-atmosphere (toa). Commonly, all radiance components are normalized to reflectance units using the appropriate toa normal-incidence spectral solar irradiance, converted to flux ($\div \pi$). The resulting expression for the measured toa earth-atmosphere reflectance (Chandrasekhar, 1950, sect 72, using eq 201) is

$$\rho^M = t_{abs} [\rho^A + \rho^R + t_{sct} \rho^S / (1 - \sigma \rho^S)] \quad (1)$$

where the reflectance components, the ρ's, are identified by superscripts as: measured, aerosol scattered, Rayleigh scattered, and surface reflected. The atmospheric transmittance factors are the two-way absorption t_{abs}, and the two-way total-path scattering transmittance t_{sct}. The spherical sky albedo is σ. For non-reflective surfaces, specific., for $\rho^S \leq 0.02$, the denominator of the final term approaches unity and Eq (1) is then a linear combination of reflectances. Under such conditions the path radiance is the primary source of aerosol information. When and where $\rho^S > 0.02$, the compensation procedure is more complex and the aerosol retrieval usually depends on proper analysis of the surface-interacting radiance. Given the measured reflectance ρ^M, Eq (1) is solved for ρ^A using assigned surface reflectance ρ^S, and model-computed t_{abs}, t_{sct}, and ρ^R. Over land, the uncertainty in ρ^S is usually the predominate source of error in ρ^A; thus, as discussed in Step 4, both should be simultaneously retrieved.

Step 2: *Finding aerosol optical property values, given* ρ^A.

The single-scattering approximation for τ^A (Hansen and Travis, 1974, using eq 3.40) is

$$\tau^A = \rho^A (4 \mu \mu_o / \omega P) \quad (2)$$

where view and illumination angle cosines are the μ's and the aerosol single-scattering albedo and phase function are ω and P, respectively. The extinction optical thickness τ^A_{ext}, the sum of the scattering and absorption parts, is the property estimated by Eq (2). Also, Eq (2), like Eq (1), is spectral. But neither ω nor P varies as rapidly with wavelength as τ^A does. The most familiar form for the variation of τ^A with wavelength λ is that derived by Angstrom (1929), $\tau_\lambda{}^A \sim \lambda^{-\alpha}$. The Angstrom exponent α, typical range $-0.5 < \alpha < 2.0$, has been used to indicate aerosol type. Eq (2) is an optical expression for τ^A. This type of reflectance analysis is the only practical approach to assessing aerosol amounts on a global basis. The fundamental physical reason for the spectral variation in ρ^A and τ^A is the dependence of the extinction and scattering coefficients on n(r).

Step 3: Specification of aerosol micro-physical properties, in particular, n(r).

Conventionally, pre-defined aerosol models are employed to quantify the scattering parameters in Eq (2), and to specify at least the form of n(r). The most often employed form is the Junge power-law, $n(r) \sim r^{-\nu}$. The Junge exponent ν has, typically, the range $1.5 < \nu < 4.0$ and relates to the Angstrom exponent as $\alpha = \nu - 2$. The advantage of an assigned model is the pre-computation and tabulation of ρ^A-values to facilitate the τ^A retrievals. The shortcoming is the inadequate regard for the localized and transient character of natural aerosols, especially those of anthropogenic origin.

Only a single measure of aerosol scattering is usually available, namely, ρ^A. And it quantifies the integrated atmospheric column value of the aerosol scattering, specifically, $\rho^A \sim \int_z \beta_{sct}\, dz$, where β_{sct} (m^{-1}) is the vertical-profile value of the aerosol scattering coefficient. The spectral variation of β_{sct} contains information on column-average values of n(r). Spherical particles scatter radiation (van de Hulst, 1957, chap. 9) according to

$$\beta_{sct} = \int_r Q_{sct}(\xi,m)\, \pi r^2\, n(r)\, dr \qquad (3)$$

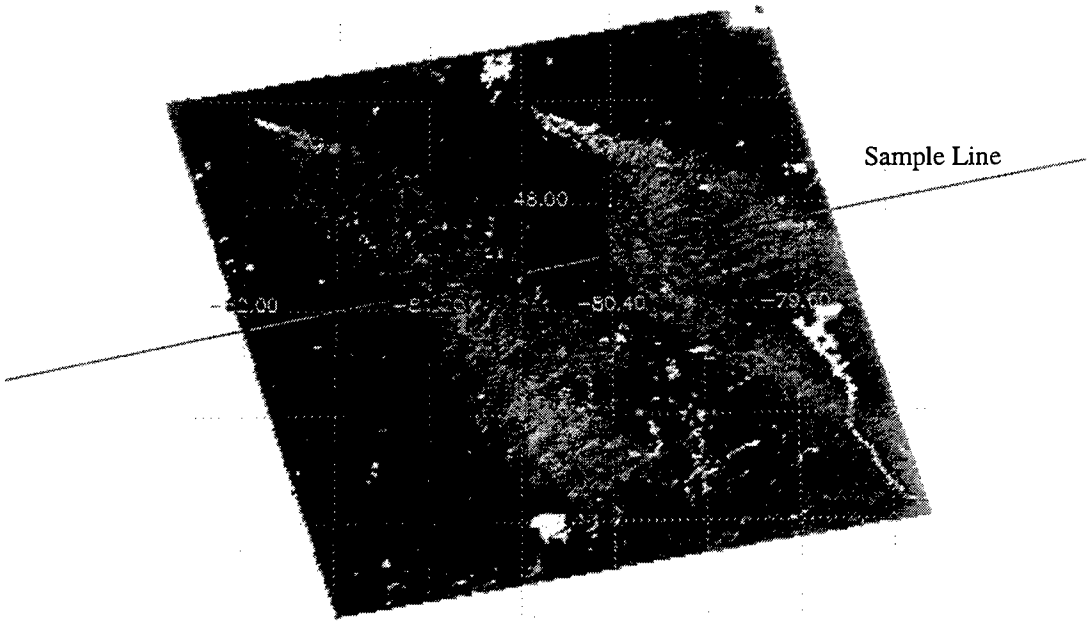
where the scattering efficiency factor Q_{sct} varies with the Mie size parameter $\xi = 2\pi r / \lambda$, and with the index of refraction m. Given m and λ, the values of Q_{sct} for each particle size are pre-computed from Mie-theory. The integration of Eq (3), to provide the scattering coefficient for a population of aerosol particles, usually assumes a fixed form for the size distribution n(r), especially Junge or lognormal. Also, n(r) is not that of a specific volume, as its units ($cm^{-3}\ \mu m^{-1}$) might imply, but rather is representative of the column-mean aerosol population. Hyperspectral data allows form-free retrieval of n(r).

Step 4: Quantification of the surface reflectivity.

The factor limiting the accuracy of retrievals over land is imprecise information on ρ^S. Aerosol property retrieval over land always involves multiple measurements because of the surface component, the third term, in Eq (1). Because the surface reflectance component usually dominates over land, and since it occurs in Eq (1) in a non-linear fashion, then ρ^S must be known with substantially greater accuracy than that permitted for the final aerosol property itself. Pre-assignment of a spectral value of ρ^S is the common expedient, but accuracy is compromised. Figure 2, depicting the spectral variation in vegetative surface reflectivity, indicates the complexity of the problem. As advocated by Kaufman et al (1997), ρ^A and ρ^S should be simultaneously retrieved. Even if precise ρ^S-values are not known, the spectral variation of ρ^S may be reasonably well specified. An example, from Fig 2, is the empirical relationship for the two AVHRR channels (Ch 1 - red, Ch 2 - nir)

$$\rho^S_2 = 0.128\, (\rho^S_1)^{-0.335}, \qquad \rho^S_1 = 2.16 \times 10^{-3}\, (\rho^S_2)^{-2.985} \qquad (4)$$

Since retrievals over land involve more than one measurement, some spectral surface reflectance scheme is usually needed. The accuracy of relationships like Eq (4) is poor, but may still be useful if the surface type is known. Specifically, any retrieval technique using ratios of measured radiances can benefit from expressions like Eq (4).



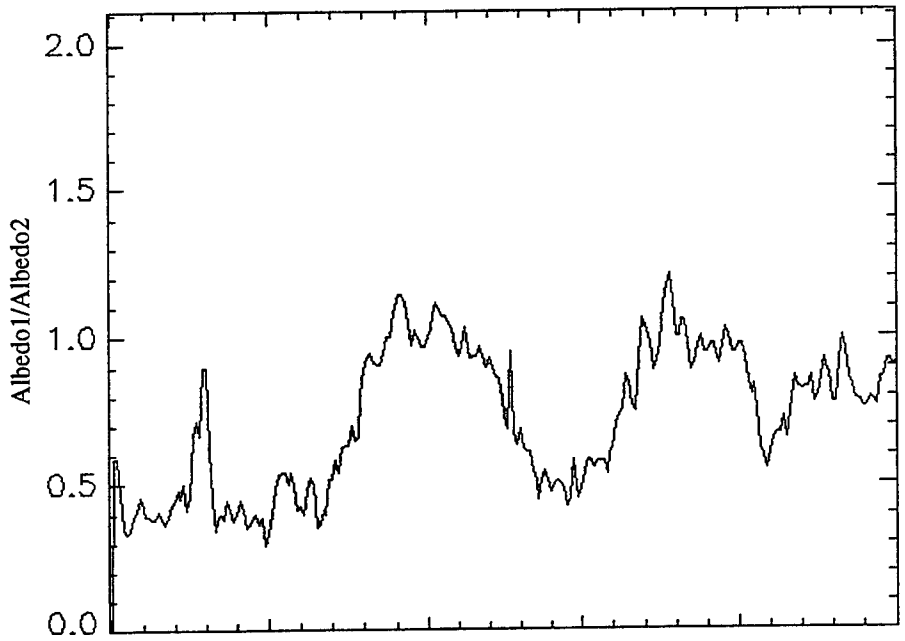


Figure 3. Ratio of NOAA-12 AVHRR Ch 1/Ch 2 reflectance data for cloud-free conditions over southern Ontario, Canada during local forest fires on 10 June 1997. The albedo ratio value of ambient conditions is ~0.5. In intense plumes, the value increases to ~1.

STATE-OF-TECHNOLOGY

The current status of satellite-based aerosol retrieval is briefly reviewed and the two operational models for τ^A are summarized. Retrieval models are classified according to the satellite sensor used. The two operational models apply to the NOAA AVHRR and the LandSat thematic mapper (TM). The third model, under development, uses the EOS moderate resolution imaging spectro-radiometer (MODIS). The process is similar for all: assign surface reflectance, select the most appropriate standard atmosphere, adopt a realistic aerosol model, and pre-compute look-up-tables of ρ^A or τ^A values for increments of illumination, view, and relative azimuth angles. Over oceans or dark vegetation the retrieval process is simpler because the path radiance contains the aerosol information. For bright surfaces (ρ^S(red) > 0.02), the surface-interacting radiance usually dominates and it must be incorporated into the look-up-tables.

The one aerosol property routinely available is $\tau^A_{0.63}$ over ice-free ocean areas, which is retrieved from AVHRR Ch 1 data. Over land case-study analyses of τ^A are available from LandSat data. Any MODIS products are from simulated or aircraft-measured data.

Over land the considerable increase in surface reflectance from the red to the near-infrared bands (e.g., Ch 1 to Ch 2 of the AVHRR) can be used to detect and, in a semi-rigorous manner, to assess the amount of aerosol present. The simple ratio of measured reflectances is sufficient, $\rho^M_1 / \rho^M_2 \equiv \psi_{12}$ is used. From Eq (1) it can be expected that $\psi_{12} < 1$ for small values of ρ^A, since $\rho^S_2 > \rho^S_1$. Also, as ρ^A increases, ψ_{12} is expected to increase due to the relatively larger increase in ρ^M_1. Figure 3 shows values of ψ_{12} for one AVHRR scan-line of NOAA-12, taken during cloud-free conditions over southern Ontario, Canada, on 10 June 1997. Two separate forest fire plumes are seen; one located east and more extensive, the other west and more confined. In both cases ψ_{12} increases from the ambient value 0.5 to the central plume value of 1.0. The interpretation in terms of τ^A, is obtained from Eqs (1) and (2).

ERROR BUDGET ANALYSIS

Error analysis of a linear form of Eq (1), along with Eq (2), provides information on the susceptibility of any τ^A retrieval model to the correctness of treatment for various atmospheric and surface conditions. Table 1 contains the results when applied to the presently operational retrieval models – AVHRR for oceans, LandSat for land. In the left column are the expected errors from either completely neglecting the identified error source or from using generic model rather than the local values of surface, water vapor, or aerosol conditions. Assuming an actual (true) aerosol optical thickness of 0.20, $\Delta\tau^A$ is given in absolute terms and in percent. The right column provides an accuracy assessment – the systematic error remaining after routine procedures for environmental compensation are applied; these can be either positive or negative, but more likely in the same sense as the omission error.

The largest environmental radiative effects are those of Rayleigh scattering and ozone absorption, but both are very completely corrected for, as the systematic errors show. Interestingly, these operate in opposite senses and for wavelengths in the range $0.6 < \lambda <$

0.8 μm, if both corrections are omitted, the result is a near-constant overestimation of τ^A by 15 %. Clearly, the largest error source for τ^A-retrieval over oceans is uncertainty in aerosol absorption (1 - ω); over land it is incorrect spectral surface reflectance. Totals are computed assuming all relevant sources are independent. NPOESS threshold criteria for systematic error, over ocean and land, are given as reference standards.

Table 1. Error Budget Analysis for Retrieval of Aerosol Optical Thickness.

Error Source	Omission Error		Systematic Error	
	Absolute*	Relative# (%)	Absolute*	Relative# (%)
Measurement[a]	---	---	0.01	5
Rayleigh Scatter[@,b]	+ 0.08	+ 40	< 0.001	< ½
Ozone Absorption[@,b]	– 0.05	– 25	0.001	½
Aerosol Absorption[c]	– 0.05	– 25	0.04	20
Aerosol Phase Function[d]	– 0.04	– 20	0.03	15
H_2O Absorption[e]	0.01	5	0.02	10
Ocean Reflectance[f]	+ 0.02	+ 10	0.01	5
Land Reflectance[g]	± 0.02	± 10	0.08	40
Totals for:				
1-Channel Ocean Model	+ 0.01	+ 5	0.05	25
3-Channel Land Model	---	---	0.10	50
NPOESS Threshold Requirements:				
Ocean	---	---	0.03	15
Land	---	---	0.20	100

* Actual value = retrieved value – absolute error. Positive absolute error means retrieved value is an overestimate of actual (true) value. # Assume actual (true) value of $\tau^A_{true} = 0.20$. @ Elementary correction routinely made. [a] Using AVHRR calibration uncertainty of 5 % per channel. [b] AVHRR Ch 1 half-response width, 0.58-0.68 μm. [c] For assumed value $\omega = 0.95$, vs. 1.00, $\Delta\omega = \pm 0.03$. [d] For scattering angle = 150°, P = 0.10, vs. 0.40, $\Delta P = \pm 0.15$. [e] Ocean in Omission. Land in Systematic. [f] Assigned reflectance $\rho^S = 0.015$, vs. 0.002, $\Delta\rho^S = \pm 0.002$. [g] Assigned reflectance ρ^S = 'dense vegetation', vs. 0.15, $\Delta\rho^S = \pm 0.04$.

HYPERSPECTRAL APPLICATION

An application of hyperspectral (very high spectral resolution) data analysis to aerosol property assessment is the retrieval of aerosol particle size distributions. Although the exact details of n(r) are not needed to evaluate an integrated property like τ^A, more detail than is afforded by a simple Junge form of distribution is needed to quantify P or $\beta_{sct}(z)$, and to infer the aerosol fate, especially in conditions where relative humidity affects n(r).

A procedure is considered for the retrieval of the microphysical property of aerosols – the particle size distribution n(r) – by the inversion of a number of coincident reflectance measurements. The underlying strategy is based on the fact that whereas the magnitude

of reflectance correlates with τ^A, the wavelength variation in reflectance, as specified by Eq (3), contains information on the n(r), specifically, $\Delta\tau^A \sim n(r)$. The pre-specification of an aerosol model imposes a distribution form on the aerosol whether appropriate or not. However, departures from simple mathematical forms in the optically active range ($0.1 < r < 2$ μm) are common, particularly for urban, industrial, and biomass-burning aerosols. The direct effect is on the retrieved value of τ^A, in accordance with Eq (3). Since the angular scattering (phase) function P varies with n(r), τ^A is secondarily affected by the particle size distribution through Eq (2). More accurate retrieval of n(r) is now possible.

As developed in Heintzenberg et al (1981), the spectral finite-difference form of Eq (3) is inverted (as in Twomey, 1977, eq 2.6) to provide a form-free (histogram-type) aerosol size distribution which is robust against up to 5 % measurement error. The results are encouraging and the applicability of the technique can be tested using available hyperspectral remote sensing imagery.

REFERENCES

Angstrom, A., 1929: On the Atmospheric Transmission of Sun Radiation and on Dust in the Air. Geogr. Ann., 11, 156-166.

Chandraesekhar, S., 1950: Radiative Transfer. Clarendon – Oxford University Press, (Dover Publications, 1960), 393 pp.

Fraser, R.S., 1975: Degree of Independence among Atmospheric Optical Thicknesses in Spectral Bands Between 0.36 – 2.4 μm. J. Appl. Meteor., 14, 1187-1196.

Hansen, J.E., and L.D. Travis, 1974: Light Scattering in Planetary Atmospheres. Space Sci. Rev., 16, 527-610.

Heintzenberg J., H Muller, H. Quenzel, and E. Thomalla, 1981: Information Content of Optical Data with Respect to Aerosol Properties: Numerical Studies with a Randomized Minimization-Search-Technique Inversion Algorithm. Applied Optics, 20, 1308-1315.

Kaufman, Y.J., D. Tanre, H.R. Gordon, T. Nakajima, J. Lenoble, R. Frouin, H. Grassl, B.M. Herman, M.D. King, and P.M. Teillet, 1997: Passive Remote Sensing of Tropospheric Aerosol and Atmospheric Correction for the Aerosol Effect. J. Geophys. Res., 102, 16,815-16,830.

Twomey, S., 1977: Introduction to the Mathematics of Inversion in Remote Sensing and Indirect Measurements. Elsevier Scientific Publishing Company, (Dover Publications, 1996), 243 pp.

Van de Hulst, H.C., 1957: Light Scattering by Small Particles. John Wiley & Sons, NY, (Dover Publications,1981),470pp

Satellite Estimates of Optical Depth during EOPACE

Carlyle H. Wash, Mary S. Jordan and Philip A. Durkee
Department of Meteorology
Naval Postgraduate School
589 Dyer Rd., Room 254
Monterey, CA 93943-5114, USA
Phone: 831-656-2516 Fax: 831-656-3061
wash@nps.navy.mil

Pepijn Veefkind and Gerrit de Leeuw
TNO Physics and Electronics Laboratory
The Hague, The Netherlands

Michael H. Smith and Martin K. Hill
Centre for Marine and Atmospheric Sciences
University of Sunderland, United Kingdom

OBJECTIVE

Knowledge of the coastal Marine Atmospheric Boundary Layer (MABL) for the entire battlespace is critical for modern Navy operations. To support modern weapon and sensor systems, quantitative assessment of a number of MABL properties are needed. They include: optical depth, boundary layer depth, sea surface temperature, and surface layer temperature and moisture. These needs are even more critical in the coastal zone with the sparse surface observations away from the coast and the high temporal and spatial variability of littoral circulation systems. Satellite remote sensing is the only data source that can measure MABL properties in the coastal zone with the needed high spatial resolution. However, many of the uses of satellite data are qualitative. Quantitative satellite remote sensing methods need to be tested to provide these needed littoral data.

The EO Propagation Assessment in Coastal Environments (EOPACE) program is focused on the characterization of aerosol and boundary layer properties in the coastal zone and the determination if air mass parameters in various coastal locations can be derived, to a practical degree, from satellite imagery. In support of this project, several Intense Observing Periods (IOPs) have been conducted. The combination of satellite data with several in situ surface and aircraft data sets offers an excellent opportunity to monitor significant optical depth and aerosol changes and in the coastal zone. In addition, quantitative comparisons can be made. The objective of this paper is to evaluate satellite-derived aerosol optical depths estimates using aircraft and ship-based aerosol measurements, a ship-based lidar and rawinsonde profiles of the MABL. Results from the April 1996 and March 1997 experiments will be presented in this paper.

RESEARCH ACCOMPLISHED

Radiative transfer theory provides the basis for methods used to characterize aerosol properties from satellite remote measurements. In a cloud-free, marine environment, the

shortwave, solar radiation measured by a satellite radiometer is primarily the result of scattering by both molecular constituents of the atmosphere (Rayleigh scattering) and larger suspended aerosol (Mie scattering). Corrections to solar irradiance of less than 5% for ozone absorption are applied and aerosols are assumed to be non-absorbing. In the absence of sun glint, reflectance from the ocean surface is also small and contributions to the satellite-measured radiance due to surface foam and subsurface reflection are accounted by empirical measurements.

For atmospheres with small optical depths such as the clear, marine atmosphere, contributions by multiple scattering can be neglected. After accounting for Rayleigh scatter, the satellite-measured radiance can be related to optical depth, as illustrated in Equation 1.

$$L_a = \frac{\omega_o F_o}{4\mu} p(\psi_s)\delta_a \qquad (1)$$

where L_a is the measured radiance at the satellite due to aerosol scattering at a given wavelength, ω_o is the single scattering albedo, F_o is the incoming solar radiance at the top of the atmosphere, P is the scattering phase function, ψ_s is the scattering angle, δ_a is aerosol optical depth, and μ is the cosine of the satellite zenith angle (Durkee et al, 1991).

Durkee, et al., (1991) and Rouault and Durkee (1992) proposed a method of parameterizing the scattering phase function, P, based on the ratio of the aerosol radiance measured in channel 1 (visible) and channel 2 (near-IR) of the NOAA AVHRR satellite sensor. Because scattering efficiency of an aerosol distribution is wavelength dependent, scattering for specific aerosol population peaks when the radius of the aerosol is nearly equal to the radiation wavelength. Subsequently, radiance counts measured by the AVHRR visible and near-IR channels will change with aerosol size distribution changes such that the ratio of channel radiances will be larger for smaller size particle distributions and smaller for larger size particle distributions. Durkee, et al., (1991) called the ratio of the channel aerosol radiances the particle size parameter, S12. Since S12 varies pixel by pixel over the entire image, the scattering phase functions can be parameterized pixel-by-pixel allowing variations in aerosol distributions to be properly factored into the optical depth retrieval. In addition, the S12 permits characterization of the aerosol size properties for the clear air in the image.

EOPACE IOPs

This paper is an overview of the EOPACE IOPs directed at monitoring air mass and optical properties using satellite and ship data. In addition, two plume events will be presented. Of the nine EOPACE IOPs, IOP-3 (2-12 April 1996) and IOP-5 (12-20 March 1997) were focused on mapping aerosol and air mass optical properties in the coastal zone. During these IOPs the R/V Point Sur traversed the coastal zone with a vertically pointing 1.06 micrometer lidar (provided by TNO), frequent rawinsonde temperature and moisture measurements (provided by NPS) and surface layer aerosol measurements (provided by Sunderland). Polar orbiting NOAA and GOES-9 satellite data is available for both periods at NPS and ERS-2 ATSR satellite data are available from TNO for three of the IOP-5 experiment days.

Tables 1, 2 and 3 summarize the current status of the satellite air mass categorization studies. Table 1 overviews the results from both IOP-3 and IOP-5. There were 20 possible measurement days however 7 were not acceptable due to clouds. Of the 9 days studied so far, a range of coastal wind regimes is found. Two days are characterized as "marine" with onshore flow throughout the low troposphere. Three days are described as "offshore" with easterly winds dominating. The remaining four days are "mixed", with onshore flow in the boundary layer but offshore flow aloft. There are four days that have not been investigated yet due to sun glint in the NOAA images. These days may be studied using GOES-9 imagery.

Table 1. Air Mass Characterization Summary, IOPs 3 & 5

Clear Days, Successful Studies	9
# Marine Days	2
# Offshore Days	3
# Mixed Days	4
Cloudy Days, Unacceptable Cases	7
Future Cases with GOES-9	4

Tables 2 and 3 present more detailed information on IOP-3 and IOP-5. Listed are the date, dominant cloud or aerosol conditions, the type of coastal flow and a typical S12 index derived from the satellite day near the ship on that day. Note that marine coastal flow days have the lower S12 indices, as expected from the flow off the ocean with larger sea-salt aerosol dominating the aerosol conditions, while the offshore days have larger S12 values indicating the importance of continental aerosol in the scattering signal. One of the most interesting aspects of the experiment was the development of offshore aerosol plumes during the experiment. Aerosol plumes were found on three days, 4-5 April 1996 (IOP-3), and 18 March 1997 (IOP-5). Wash, et al., (1997) describes IOP-3 in great detail. We will briefly cover IOP-3 in this paper, and will present our IOP-5 results for the first time.

Table 2. Satellite Results for IOP-3, 3-12 April 1996

Date	Notes	Coastal Flow	S12 Index
3	NW flow	Marine	1.75
4	Plume develops	Offshore	2.78
5	Ship transits plume	offshore	2.40
6	Ship transits plume	offshore	2.70
7	Cloudy	Mixed	
8	Lower optical depth	Mixed	2.13
9	Ship near San Diego		
10	Sun glint, use GOES-9		
11	Sun glint, use GOES-9		
12	Thin cirrus		

Table 3. Satellite Results for IOP-5, 11-20 March 1997

Date	Notes	Coastal Flow	S12 Index
11	Cloudy		
12	Strong NW surface flow NOAA-14, GOES-9 and ERS-2	Mixed	2.0
13	Clear near San Diego		
14	Thin cirrus		
15	Cirrus and stratus		
16	Thin cirrus		
17	Using GOES-9 (sun glint in NOAA-14)	Marine	
18	Small plume off Los Angeles GOES-9 and ERS-2	Mixed	
19	NOAA-14 and GOES-9	Mixed	
20	Cloudy		

The NOAA satellite data from 2216 UTC 4 April during IOP-3 is presented in Figure 1. High values of optical depth are estimated over the entire Southern California coastal area. Values range from 0.17 to 0.38. There is a distinct plume of aerosols leaving the coast between Los Angeles and San Diego. The S12 ratio from this pass indicates a much higher ratio than 24 hours earlier. Values range from 2.9 to 3.1 indicating small aerosol sizes, typical of continental sources, are dominating the region.

On 5 April, the R/V Point Sur moved southeastward toward the plume observed by the NOAA satellite on 4 April. Subsidence associated with the offshore flow was quite intense this day and the MABL depths were very shallow, less than 100 m. Aircraft profiles and ship-based lidar (not shown) continue to show aerosols in the lowest 1000 km. The aircraft data does not show a distinct layer of elevated extinction, but small values of aerosol extinction are present throughout the lowest 1 km. Satellite data for 2205 UTC 5 April (not shown) indicated lower values of optical depth (0.15 to 0.25) but the remnant of the plume is still detectable.

The ship steamed though the plume location between 15 and 24 UTC 5 April. Stronger lidar backscatter values at that time are consistent with the satellite data. The S12 ratio continues to be high indicating smaller, continental aerosols over the coastal zone. In addition, Doppler wind profilers in the region also show the strengthening of this Santa Ana regime. The profiler at Ontario airport showed NE winds between 25 and 40 knots in the lowest 500 m during the afternoon of the 5 April while the coastal profiler at LAX airport showed N wind of 20 knots below 700 m.

A second plume occurred during IOP-5 on 18 March 1997. The plume is evident in measurements from the TNO lidar (Fig. 2), the ATSR-2 radiometer onboard the ERS-2 spacecraft (Fig. 3), and the GOES-9 satellite (not shown). The ship-based TNO lidar (Fig. 2) recorded a distinct maximum of backscatter from this plume during 1600 to 2200 UTC on the

This page intentionally left blank.

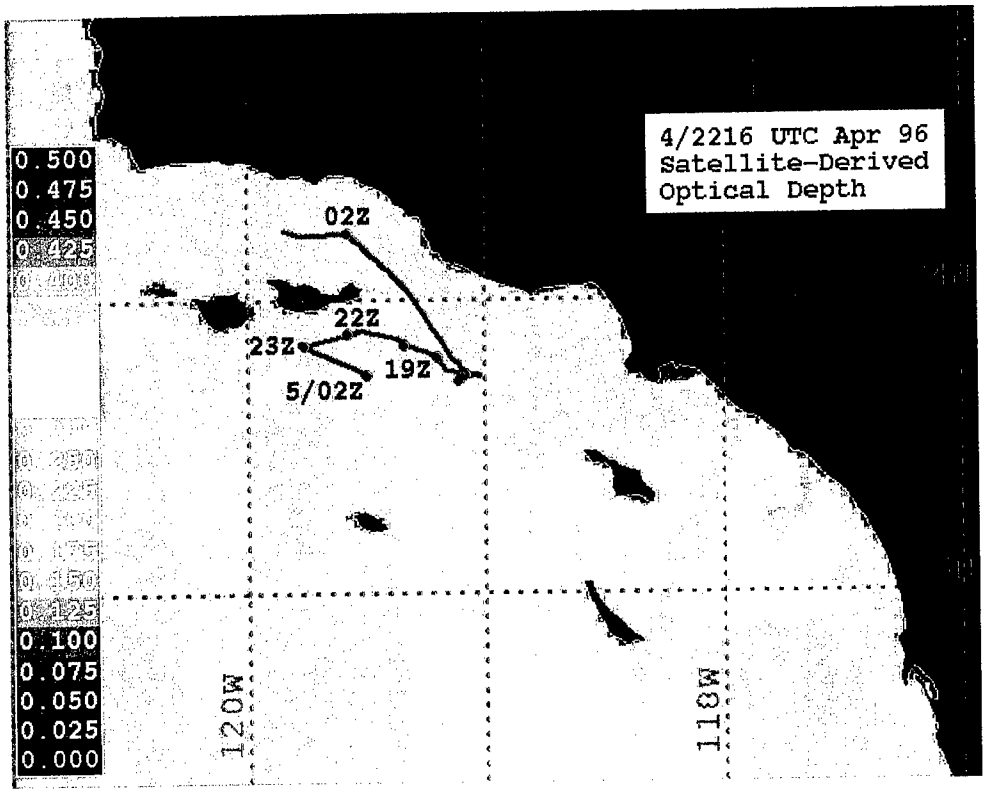


Fig. 1. Optical depth estimates from NOAA AVHRR data for 2216 UTC 4 April 1996. The R/V Point Sur ship track is indicated by the blue line. Rawinsonde launch locations are denoted by the red dots.

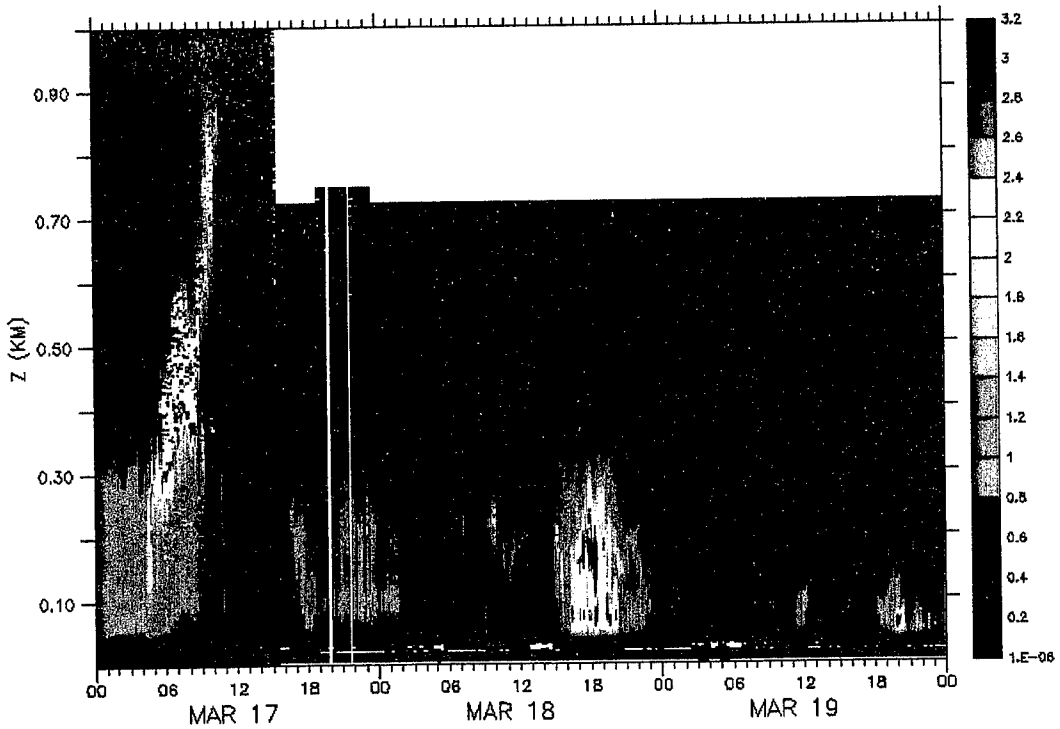


Fig. 2. Backscatter from the TNO mini-lidar aboard the R/V Point Sur for 00 UTC 17 March – 00 UTC 20 March 1997. The emitter is a 60 mJoule Nd/YAG laser and returns are averaged over 10 minutes.

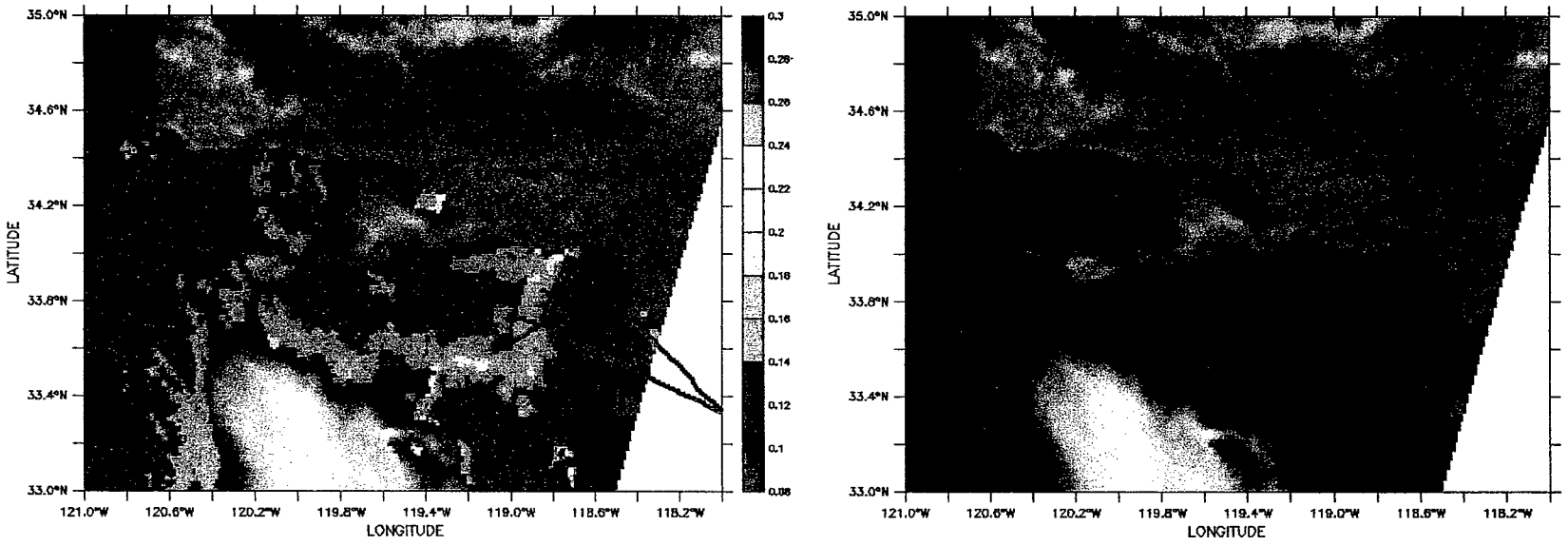


Fig. 3. Aerosol optical depth for 0.659 micrometer (left) and 0.865 micrometer near-visual imagery (right) from the ATSR-2 sensor for 1857 UTC 18 March 1997. The images cover the Southern California bight region. Note the high value of aersosols extending from the coast north of Los Angeles southward. The track of the R/V Point Sur is represented by the red line.

18 March. In situ aerosol size distributions measured on the ship (not shown) indicated a distinct maximum of small aerosols with radius 0.1 to 0.2 microns. Some evidence of the plume is present in GOES-9 imagery as well.

This plume was best observed from space by the ATSR-2 (Fig. 3) sensor. The ATSR-2 has seven spectral bands with four of these bands potentially useful for aerosol retrieval. The effective wavelengths of these bands are 0.555, 0.659, 0.865, and 1.60 micrometers. The spatial resolution of the ATSR-2 is 1 km. ATSR-2 has the dual view capability as well. Figure 3 presents 0.659 micrometer aerosol optical depth and 0.865 micrometer near-visual imagery for the Southern California bight region for 1857 UTC 18 March 1997. Note the high value of aerosols extending from the coast north of Los Angeles southward. The track of the R/V Point Sur is superimposed on the image. The ability of satellite data to detect and monitor plumes of offshore aerosols is valuable to support a various aspects of naval operations.

CONCLUSIONS

During these IOPs, satellite retrievals of aerosol optical depth and the ship and aircraft measurements were in good qualitative agreement. The NOAA satellite S12 ratio successfully depicted regions of maritime aerosol during the beginning and later parts of the IOP-3 and the period of continental aerosol associated with the strong offshore flow of the Santa Ana event. In addition, ATSR-2 sensor onboard the ERS-2 spacecraft captured a second plume during IOP-5.

The new generation of geostationary satellite, GOES-9, was operating over the West Coast during these IOPs. The higher radiometric resolution from GOES-9 sensors provides the opportunity to retrieve aerosol depth with higher temporal resolution. GOES-9 data from this period will be used to add to more temporal resolution to the satellite analyses of these interesting periods of rapid aerosol changes. In particular, GOES data may be able to monitor the development of these aerosol plumes on 4 April 1996 and 18 March 1997.

ACKNOWLEDGMENTS

The NPS work is supported by SPAWAR Systems Center, San Diego through Office of Naval Research funding. The Netherlands Ministry of Defense, assignment A95KM729, and the US Office of Naval Research, Grant N00014-96-1-0581, supports the participation of TNO-FEL in EOPACE. Aerosol retrieval work at TNO-FEL is supported by SRON EO/008. The authors would be to thank Kenneth Davidson, NPS, and Kathleen Littfin, SPAWAR Systems Center, San Diego, CA, for sharing data and their expertise. EOPACE coordination and direction is provided by Dr. D. R. Jensen for the SPAWAR Systems Center, San Diego, CA.

REFERENCES

Durkee, P. A., F. Pfeil, E. Frost, and R. Shema, 1991. Global analysis of aerosol particle characteristics. *Atmos. Env.*, **25A**, 2457-2471.

Rouault, M. and P. A. Durkee, 1992. Characterization of aerosols from satellite remote sensing. In Nucleation and Atmospheric Aerosols, 357-360, N. Fukuta and P. E. Wagoner (Eds), A. Deepak Publishing.

Wash, C. H., M. S. Jordan, P. A. Durkee, P. Veefkind, and G. de Leeuw, 1997. "EOPACE Satellite and In Situ Optical Depth Studies," Proceedings of the Battlespace Atmospherics Conference, San Diego, CA, 2-4 December 1997. ADA344056

Measurement of Solar Ultraviolet Radiation at Different Geographic Locations

Karin Weiss-Wrana
Forschungsgesellschaft für Angewandte Naturwissenschaften e.V.
Forschungsinstitut für Optik (FGAN-FfO)
Schloss Kressbach

The calculation of range performance of ultraviolet (UV) systems requires information about the strength of the atmospheric radiation in different climatic regions. For this reason the strength of the solar ultra-violet radiation was measured at different geographic locations with different climatic conditions: in the Negev desert in Israel and in Tübingen, Germany, Central Europe .

Two sensors were used to measure the uv background in two adjacent spectral ranges. The 290 nm band lies just below the upper wavelengths limit of the solar blind region, whereas the 310 nm band falls just beyond this limit. In the uv region the atmospheric molecular extinction coefficient, which is mainly affected by the constituents oxygen and ozon, increases strongly with decreasing wavelength. For this reason the radiation measured in the 290 nm band is lower than the radiation measured in the 310 nm band. The ratio of the radiation in the 310 nm band to the 290 nm band was computed on a daily basis. Throughout all days the diurnal variation of the this ratio shows a characteristic double-peaked feature. Shortly after sunrise and before sunset the ratio shows its maxima. This is caused by the longer propagation path through the atmosphere. Under this condition the difference between the transmitted radiation in the two bands is more significant.

Examples of the diurnal variations of the measured solar uv radiation and the corresponding ratio, for different seasons and locations, will be presented and discussed.

PAPER NOT AVAILABLE FROM AUTHOR FOR PUBLICATION IN THESE PRE-PRINTED PROCEEDINGS

This page intentionally left blank.

Decision Aids

TARGET ACQUISITION WEATHER SOFTWARE (TAWS)

Richard B. Bensinger, Melanie J. Gouveia, Glenn J. Higgins, Jeffrey S. Morrison,*
Ryan B. Turkington, and Craig V. Gilbert

TASC
55 Walkers Brook Drive
Reading, MA 01867-3297
Phone: (781) 942-2000, Fax: (781) 942-2571
E-Mail: rbbensinger@tasc.com

Sponsored by the Air Force Research Laboratory, Hanscom AFB, MA

The Target Acquisition Weather Software (TAWS) is being developed to replace the current Electro-Optical Tactical Decision Aid (EOTDA) software used today by tactical weather teams supporting Air Force, Army, Navy, and Marine combat operations. TAWS will incorporate a modular system design that will allow "plug and play" upgrades, a user-friendly graphical user interface (GUI), and will operate in a PC environment with Windows 95/NT operating systems. Later versions of TAWS will use a web-browser interface. The TAWS GUI will bring together several high-resolution databases including meteorology, geography, targets, and weapons systems/sensors. TAWS will include automated access to weather and geographic databases. The GUI will allow user-selected information from the databases to operate against several high fidelity physical models operating in the infrared (IR), television/night vision goggle (NVG), and laser wavelengths. For target-oriented analysis, TAWS will predict detection or lock-on range and/or detection probability for a series of targets. For each target, calculations may be performed for a series of potential times, approach azimuths, sensors, and sensor elevations. TAWS will provide the user with output products that can be tailored to their needs, superior target scene visualizations, and support for multiple targets, weapons systems, and missions. TAWS is the next step in precision strike tactical decision aids, providing improvements to system usability, system applicability and functionality, and physical models.

Introduction

The Target Acquisition Weather Software (TAWS) will integrate recent modeling and hardware/software technology improvements to update the Electro-Optical Tactical Decision Aid (EOTDA) software to a user-friendly, Windows environment. TAWS will include automated access to weather and geographic information, as well as target and sensor databases to provide maximum usability. TAWS will include flexible output products that can be tailored to users' needs, superior target scene visualizations, support for multiple targets, weapons systems, and missions, and will attain improved EO model accuracy. The graphical user interface (GUI) will interface with several physical models, initially including 3-5 μm and 8-12 μm infrared (IR), television/Night Vision Goggle (NVG), and 1.06 μm Laser. Other models may be included later as user requirements continue to evolve.

Concept

In the initial concept for TAWS, the process required to carry out a TAWS run may include the following steps:

- The user selects a region of interest from a map
- Geography data is accessed for the region
- The user adds targets to the region, selecting from a database of existing targets or creating customized targets
- The user identifies potential sensors, selecting from a database of existing sensors or creating customized sensors
- The user selects target-oriented analysis or mission (sortie)-oriented analysis
- If the user selects mission-oriented analysis, the user adds targets and waypoints to a series of missions
- The user defines tactics for a series of targets or missions (such as a series of potential times, approach azimuths, sensors, and sensor elevations)
- Meteorology data is accessed for the target or mission locations
- The appropriate physical models are run for the series of targets or series of missions
- The user selects output products to display
- Tailored output products are displayed, over the map background when possible
- The user selects visualization options for a specific target
- The target scene visualization is displayed

Any particular TAWS run may require a subset of these steps.

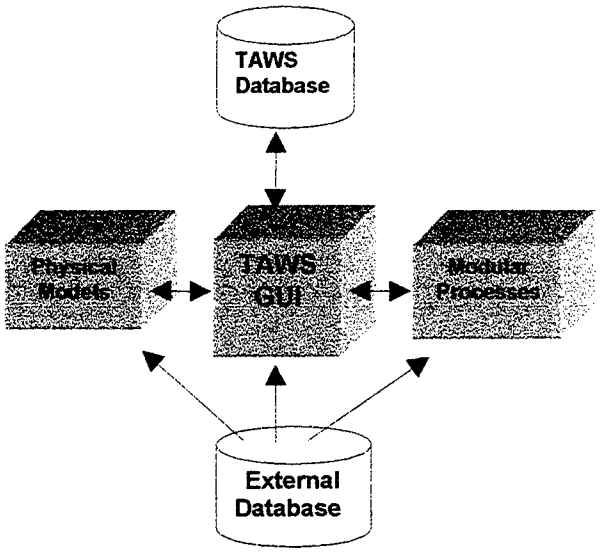
For target-oriented analysis, TAWS will predict detection or lock-on range and/or detection probability for a series of targets. For each target, calculations may be performed for a series of potential times, approach azimuths, sensors, and sensor elevations. For mission-oriented analysis, TAWS will predict detection or lock-on range and/or detection probability for a series of missions. For each mission, calculations may be performed for a series of waypoints and targets along the mission route for a series of potential times, approach azimuths, sensors, and sensor elevations.

TAWS System Architecture

TAWS will feature a new, modular architecture. A candidate TAWS system architecture is shown in Figure 1. This is conceptual only, and details are being worked out with Air Force, Navy, and Army users/customers. TAWS is being developed within an object-oriented framework. In this architecture, the GUI interfaces with the user by accepting input and displaying results. The GUI calls upon the services of other much "smarter" objects to access and populate databases, run models, etc. Processes are separate and therefore easier to expand, update, and replace. Development of the actual architecture is planned to be flexible and incremental, with five major software releases planned over an approximately three year period. Improvements in TAWS are anticipated, and will largely be dictated by customer feedback from earlier TAWS versions. The first (Beta)

release of TAWS is currently planned for Feb 1999.

Figure 1 TAWS Architecture



Graphical User Interface (GUI)

The GUI will interface to many components: progress charts to guide the user through the tasks, a graphical map background with zoom and roam capability, several input forms for data entry, output tables/graphs/maps, interfaces for constructing customized sensors and customized targets, and new and improved target scene visualization. TAWS modules will access multiple databases, including meteorology, geography, targets, sensors, and climatology. TAWS will have all of the functionality of the EOTDA Version 3.1, plus new features including a map-based, goal-oriented design, and the ability to handle multiple targets, multiple locations, and multiple missions.

TAWS will run under Windows NT, Windows 95, and is planned to be easily upgradable to later releases of the PC-Windows environment.

Goal-Directed Interface

To maximize usability, TAWS will present a series of progress charts to the user. At any time during a TAWS run, the user will be able to see which steps of a TAWS analysis have already been performed, which step is currently expected, and which steps are still to be performed. All of the major operations will be available from these dialogs and also from pull-down menus.

Geographic Regions

The TAWS GUI is based on the concept of geographic regions of interest. Using a point and click interface, the TAWS user will be able to pick out a geographic region of interest from a world map. The selected region will be drawn as a detailed map, and will serve as the background for many of the operations of the GUI. The existing EOTDA only allows for a single location, and no map background is available to give context to the scenario. TAWS will allow users to simultaneously manage a set of target locations within a region of interest. The user will be able to switch quickly from location to location without losing any information.

Targets

Once the user has selected a region of interest, the TAWS GUI will allow the user to place multiple targets in the region, and to quickly switch between them. Once a target has been placed on the map, the user will enter target information onto an input form. Like all

TAWS input forms, sliders and other tools will be used wherever possible to minimize the amount of work the user has to do. TAWS will save the information to a database. TAWS will include a selection of predefined targets, as well as a facility for the user to create customized targets. In later versions, it should be possible, through the use of a centralized TAWS World Wide Web site, for new targets to be shared with multiple users, thus building a more extensive target database.

Sensors

TAWS will allow the user to select multiple sensors. TAWS will include a selection of predefined sensors, as well as a facility for the user to create customized sensors. The list of sensor types can grow over time as additional physical models are added to TAWS. The software will save the sensor information to a database. In later versions, it should be possible, through the use of a centralized TAWS World Wide Web site, for new sensors to be shared with multiple users, thus building a more extensive sensor database.

Missions

The TAWS GUI will allow the user to choose, using a point and click interface, a subset of the region's targets to analyze. The user will be able to pick a single target to analyze, or a group of targets that are organized into a mission. Once a target has been selected, the user will enter tactical information, such as the planned time-over-target, the sensor or sensors used to detect the target, and the sensor elevation into an input form. The TAWS GUI will draw the mission graphically by drawing route lines between the target icons, representing the flight path. TAWS will support multiple missions, so users will be able to quickly analyze alternatives for a possible mission, and compare results between alternatives.

Weather Data Ingest

To enhance usability, the TAWS GUI will make use of several strategies to reduce the data entry burden on the TAWS user. In later versions, defaults for most weather data can be derived from an integral climatology database. Since the TAWS GUI allows and encourages working on several targets at once, it will be possible to copy weather information from one target to the next. When the user has networked accesses, the TAWS GUI will be able to make use of a variety of automated weather sources via TCP/IP linkages to retrieve the gridded fine-scale weather information required. Lastly, user-friendly input forms will allow the user to manually input or edit weather information. These data entry forms will make maximum use of graphical, easy-to-understand interfaces. Sources of fine-scale gridded data are still being worked, but will can include the Air Force Weather Information Network (AFWIN), the Navy's Tactical Environmental Data System (TEDS), and the Army's Gridded Meteorological Database (GMDB).

Analyzing the Target

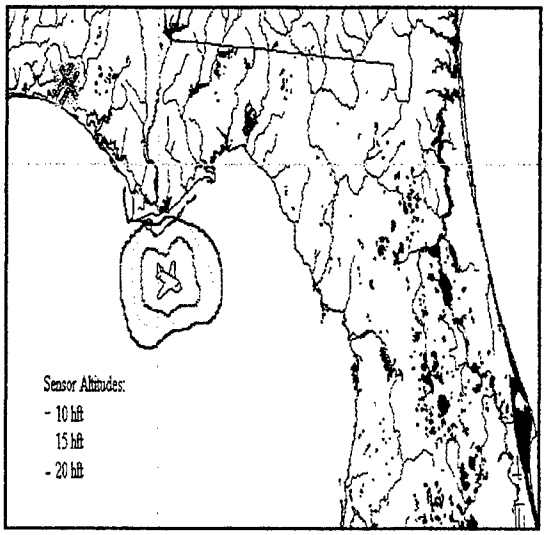
Once the region has been defined, the targets have been added to the region, the tactics have been input, and the weather data ingested, the underlying physical models can be executed. TAWS will encourage working with multiple targets at once, so the user will use the

graphical point-and-click interface to select one or more targets to analyze. The TAWS GUI will manage all communication with the physical models, using standardized data files wherever possible. After running a model, the user will be able to generate and examine the output products and/or generate a target scene visualization.

TAWS Output Products

TAWS will provide flexible output products that can be tailored to users' specific needs. The primary goal is to design output products that are easy to understand. Various types of output products will be available, including tables, graphs, and maps. Users will be able to select the type of output product, and choose the content and scale of tables and graphs. The tailored tables and graphs can be combined with, and displayed with a map background whenever possible. Figure 2 shows a sample map-based output product.

Figure 2 Sample TAWS Output



Physical Models

The physical models included with the EOTDA were the 8-12 μm IR model, the Visible/Near IR (TV/NVG) model, and the 1.06 μm Laser model. Incremental improvements will be made to the physical models as part of the TAWS program. A 3-5 μm IR model recently added to the EOTDA Version 3.1 will be included. Improved IR models, based on upgrades made under the IRTSS program, will be developed. Additional improvements will be made as users require and science allows.

Mid- and Long-Wave Infrared

The TAWS-Beta version will contain the EOTDA-based 3-5 μm and 8-12 μm IR models. These models contain several components: an illumination model, a target model, a transmittance model, and a sensor performance model. The illumination model computes solar and lunar positions using equations based on linear extrapolation of orbital parameters from a reference date of 1 Jan 1977. Recent work on the NVG Operations Weather Software (NOWS) program has determined that the lunar positions predicted by that model are not accurate. Work has been done as part of the NOWS effort to update the illumination model. NOWS uses the U.S. Naval Observatory's Solar-Lunar Almanac Code (SLAC), touted as the state-of-the-art ephemeris model. This work will be carried over to the TAWS program. The Thermal Contrast Model #2 (TCM2) is used to compute target and background temperatures, as well as the thermal contrast between the target and background. The transmittance model estimates the atmospheric attenuation between the target and the

sensor using extinction coefficients derived from LOWTRAN 7. The sensor performance model uses the apparent contrast and the target size to estimate the maximum detection or lock-on range for the target. Several upgrades to the IR model are being implemented as part of ACT/EOS and IRTSS (Tattelman, 1996). The TCM2 physical modeling is being improved based on assessments that AFRL is performing. Radiance models developed as part of the Smart Weapons Operability Enhancement Program (SWOE) are being evaluated for backgrounds. MODTRAN is being used to compute atmospheric transmission. The sensor performance model is also being upgraded.

Visible/Near IR

The TAWS-Beta version will contain a NOWS-based TV/NVG model. Several improvement have been made as part of the NOWS program to models that were originally part of EOTDA. The following list shows the NOWS improvements that are directly applicable to the TAWS TV/NVG modeling effort:

- Detection range for user specified probability level
- Detection probability for a user specified range
- Consolidation of radiative transfer calculations
- Elimination of the representative wavelength approximation
- Incorporation of wavelength-dependent cloud properties
- Modification of term in the NVG sensor performance model

The TAWS TV/NVG model contains several components: an illumination model, and atmospheric transmission model, a target contrast model, and a sensor performance model. As discussed above, the illumination model was updated as part of the NOWS effort. TAWS will use SLAC for all ephemeris calculations. The Fast Atmospheric Scattering Model (FASCAT) is used to compute optical depths, radiance terms, and atmospheric transmissions. The target contrast model takes the various components of radiance at the earth's surface and computes the inherent target and background radiance and the apparent contrast. The sensor performance model uses the apparent contrast and the target size to estimate the maximum detection or lock-on range for the target. As part of the TAWS effort, an enhanced TV/NVG model will be developed based on assessment results from the NOWS validation experiments. Incorporation of model improvements will be ongoing.

Laser

The TAWS-Beta version will contain the EOTDA-based 1.06 μm Laser model. Improvements will be made to the Laser model as necessary. The Laser model contains several components: a simplified target model, a transmittance model, and a sensor performance model. The simplified Laser target/background model uses only the reflectivity of the target and background at 1.06 μm. LOWTRAN-based extinction coefficients for aerosols and rain are used to predict the degradation of laser energy as it propagates through the atmosphere. The sensor performance model computes the minimum detectable signal required at the receiver for successful ranging or lock-on, and iterates to determine ranging or lock on

range. The range is a function of the laser pulse energy, the atmospheric transmission between the designator and the target or background, the atmospheric transmission between the target/background and the receiver, the reflectivity of the target/background, and the minimum detectable signal.

Improved Geographic Data

In the current EOTDA, there is no source of geographic data. There are no geographic background maps and no support for determining target and background information. TAWS will use the National Imagery and Mapping Agency's (NIMA) Vector Map Level 0 (Vmap0) as the primary source of geographic information. VMap provides multiple map layers such as political boundaries, elevation contours, populated places (cities and towns), and transportation. TAWS evolution will follow NIMA's lead.

Global Land Cover Databases

In the existing EOTDA, the user must enter target background information, such as representative background type from which albedo is derived, and background ID. The user is given no assistance in filling out the information. For the equivalent background information, NOWS assists the user by using a global terrain/land cover database. The NOWS land cover database is only 1 degree by 1 degree resolution, but it can be used to supply defaults for the user to override if necessary. The current NOWS terrain database is a product of the remote sensing community that is derived from Advanced Very High Resolution Radiometer (AVHRR) Normalized Difference Vegetation Index (NVDI) satellite data. TAWS will use this approach, with an eye to improving the global terrain database as new databases become available.

Customized Sensors

The TAWS-Beta version will include a customized sensors option to accommodate the user-defined sensors from the EOTDA. The user will be able to add his own sensors to TAWS by entering parameters for each sensor into an input form. Once saved to the sensor database, the sensor would be available for use at anytime. The supported sensors will include 3-5 μm and 8-12 μm IR systems from the EOTDA, NVGs, TV detection/lock-on systems, 1,06 μm Laser receivers, 1.06 μm Laser designators, and 1.06 μm Laser rangers.

Customized Targets

The TAWS-Beta version will include a customized targets option to accommodate the generic targets from the EOTDA. The user will be able to add his own targets to TAWS by entering parameters for each target into an input form. Once saved to the target database, the target would be available for use at any time. The supported targets will initially include a building, a bridge, a bunker, a power plant, a POL tank, a dam, a runway, an IR off-menu target, and a TV/Laser composed target. Later versions of TAWS will include a new target builder being developed for AFRL, and a generic ship model for the Navy.

Visualization

The TAWS-Beta version will include a basic target scene visualization capability, similar to the visualization output product in the EOTDA. TAWS Version 1, however, will include a much-improved Infrared Target Scene Simulation (IRTSS)-based target scene visualization. The enhanced visualization will include terrain shadowing, realistic backgrounds, and three dimensional positioning of the sensor. The IRTSS-based visualization capability can be expanded to support TV/NVG systems. Figure 3 shows a sample IRTSS visualization.

Figure 3 Sample IRTSS Visualization



TAWS Delivery Schedule

To achieve incremental software development and rapid response to changing user requirements, five major software releases are planned over the next three years. The current projected release date for each version is indicated in Figure 4.

Figure 4 TAWS Tentative Releases

TAWS Release	Planned Release Date
TAWS Beta	February 1999
TAWS Version 1.0	August 1999
TAWS Version 2.0	March 2000
TAWS Version 3.0	November 2000
TAWS Version 4.0	August 2001

Summary

TAWS represents a significant step forward in assisting the combat customer with the application of fine-scale meteorology to precision guided munitions. Updated software, easy-to-use graphical interfaces, and a wide suite of output product options will enhance the ability of the METOC officer to become a true force multiplier.

References

Tattelman, P.: Progress Update on Decision Aids for Electro-Optical Weapons Systems. USAF Phillips Laboratory, PL/GPAA, Hanscom AFB, MA, 1996.

Acknowledgements

This effort is sponsored by the Air Force Research Laboratory, Hanscom AFB. MA, under Contract Number F19628-97-C-0087.

WEATHER AUTOMATED MISSION PLANNING SOFTWARE (WAMPS) DEMONSTRATION PROTOTYPE

Richard B. Bensinger*, Ronald F. Fournier, Glenn J. Higgins, Melanie J. Gouveia, Jeffrey S. Morrison, and Ronald F. Wachtmann

TASC
55 Walkers Brook Drive
Reading, MA 01867-3297
Phone: (781) 942-2000, Fax: (781) 942-2571
E-Mail: rbbensinger@tasc.com

Sponsored by the Air Force Research Laboratory, Hanscom AFB, MA

The Weather Automated Mission Planning Software (WAMPS) demonstration prototype will impress upon the mission planning community and warfighting policy-makers how weather, and specifically Weather Impact Decision Aids (WIDAs), can benefit the mission planning process. Historically, the integration of focused weather information into the mission planning process has been difficult and haphazard at best. In the modern air battle campaign, hundreds or thousands of sorties must be planned and flown over a very short period of time. Automation is increasingly required to plan, execute, and re-plan missions quickly. This prototype demonstrates how the operational community can integrate weather and WIDAs into their existing and planned automated mission planning architectures, and use Electro-Optical weapon systems more effectively against enemy targets. The prototype illustrates how weather and WIDAs will help in generating the Air Tasking Order (ATO), monitoring missions, and dynamically re-planning missions that are in the execution phase. In addition to demonstrating the integration of WIDAs into the automated mission planning process, this prototype will illustrate, in a quantitative sense, the value-added of this critical information. Operators will be able to see and understand the impact of focused weather information on the success and failure of individual missions. The WAMPS prototype software will be interactive, run in a web browser, and be hosted on a web server that can be accessed from the Internet.

Concept

Automated mission planning systems enable planners to plan hundreds or even thousands of air sorties per day against thousands of targets. The efficient use of air power resources demands that the planning process results in maximum effectiveness through optimum selection of targets and weapons under given operating conditions. This process demands rapid decision making with a very high volume of information. This can only be achieved with a highly automated information management system. Weather impact decision aids (WIDAs) are being developed to aid the mission planning process. Effective use of these WIDAs can add value to all phases of the mission planning process. WIDAs support force level planning in the 48-72 hour time frame by enabling the optimum positioning of forces and stockpiling of different weapon types based on 2-5 day weather trends. Mission planning at 24-48 hours prior to mission execution is enhanced if the

performance of various weapons against specific targets can be determined as a function of time. This information feeds directly into the selection of candidate targets, selection of the optimum weapon, selection of the best tactics, and determination of the optimum time for mission execution. During mission execution, WIDAs can provide a prediction of weapon lock-on and detection ranges.

WIDA Requirements

WIDAs are becoming increasingly sophisticated as better science forms a foundation for the models, and as technology enables more detailed and sophisticated simulation of tactical flight operations. Scene visualization has only very recently become feasible with the advent of more powerful computers, improved simulation capabilities, and improved databases such as terrain, vegetation, and infrastructure facilities such as cities. The evolving WIDAs will continue to increase the potential for value added to the mission planning process as they increase their utility in the application of these new resources.

The needs of mission planners and pilots for WIDA products have been evaluated by Phillips Lab from a variety of sources, and the findings are summarized briefly as follows:

- Force level planning is best supported with stoplight (red/yellow/green) types of predictions.
- Mission planners who prepare the Air Tasking Order (ATO) want an estimate of the probability that a weapon will operate successfully against a specific target at a safe standoff range.
- Pilots want detection and lock on ranges and mission fly-throughs to aid planning of the execution phase.
- The WIDA products provided to the mission planners must be vertically consistent through all levels of command and horizontally consistent in time.
- Products for a weapons system must be available for multiple targets in a single query.
- The WIDA must be integrated into the C4I system with automated input of target, mission, and weather data. It must provide automated and meaningful display of WIDA output in simple formats.

WAMPS Demonstration

The concept of the WAMPS program is not to deliver operational software to the mission planning community, but to show through a series of interactive prototypes how WIDAs might be integrated into the automated mission planning processes. The prototypes will be iterative in design, allowing users such as pilots and mission planners to make inputs that will drive future developments and product enhancements. The early prototype focuses on the variety of WIDA output products which can support mission planning. Successive iterations will develop the interface and demonstrate capability and impact.

The Mission Planning Process

Mission planning is accomplished at the Joint Force level during theater deployments. The overall process takes place under direction of the Joint Task Force (JTF) commander. The process begins before the force deployment. The planning process at this stage requires a determination of the objectives of the deployment, the

overall strategy, the nature and size of the forces required, and the types of weaponry to be employed. The result is the mobilization and positioning of assets according to the strategic plan.

The Air Operations Center (AOC) is the highest echelon of the command and control elements for air operations. The AOC develops the Air Tasking Order (ATO) in close coordination with the plans of the other service components under the direction of the JTF Commander. The AOC prepares the Air Battle Plan (ABP) and issues the ATO, which contain the detailed force level execution directives that are carried out by the lower echelons of command in the air component.

The ATO is based on a huge mass of information which includes intelligence information, aircraft and weapon resource information, enemy threat information, and target data, along with basic data such as geographical, terrain, and infrastructure data. Automation has made it possible to issue an ATO which makes effective use of this mass of information.

At a high level, the planning process can be categorized into five types: pre-deployment, force-level planning, pre-mission planning, execution planning, and post-mission planning. Ideally, the flow of information would be downward only, such that the products produced at one phase of planning would be used without revision and without feedback. In fact, the mission planning products are constantly subject to revision due to the dynamic and unpredictable evolution of the battle. After deployment, mission planning during theater operations takes place continuously and simultaneously at all echelons of command. In Desert Storm, mission planners were unable to keep up with the rapid evolution of events in the air war. The lessons learned demonstrated the need for automated mission planning systems that would enable rapid response to changing battle conditions.

TBMCS and the DII/COE

A variety of mission planning systems are in varying stages of development as a result of the Desert Storm lessons learned. Unfortunately, these various systems are not suitable for supporting joint operations because they are not interoperable, and they cannot share data resources. The Air Force has initiated development of the Theater Battle Management Core Systems (TBMCS). The TBMCS will integrate the capabilities of the stovepipe systems into an open systems environment in which all of the planning functions can share data resources and communicate with one another. The TBMCS is key to facilitating the complex interplay among the various levels of mission planning. It is only with this great data processing power that the thousands of aircraft sortie/weapon/target combinations can be evaluated, sorted, and structured into a cohesive mission plan.

In order to ensure interoperability, the Deputy Undersecretary of Defense established the Defense Information Infrastructure/Common Operating Environment (DII/COE). The DII/COE is a set of open system standards that is forming the foundation for the recently established Global Command and control System (GCCS). These standards include key features such as cross-platform portability of code, layered architectures, object-oriented software, and segmented and reusable code.

The counterpart to the GCCS at the operating unit level is the Global Combat Support System (GCSS). The combined capabilities of the GCCS and GCSS will produce the Common Operating Picture (COP). The COP is a cohesive representation of all the ingredients of the JTF war effort. Data representation follows

established formats on consistent backgrounds to support appropriate overlays, including overlays of meteorological and oceanographic (METOC) products. All new systems under development must migrate towards compliance with the DII/COE in order to qualify for continued development. Those systems that do not comply will become legacy systems and will eventually be phased out.

The TBMCS will play in the DII/COE as the Air Force's mission planning system. It sets the framework for weather support to all combat operations in the future. As a result, weather support software of the three service components will also migrate to the DII/COE. WAMPS will be developed with the goal of facilitating potential integration into future automated mission planning systems that will be compliant with the DII/COE standards.

Weather Impacts on Mission Execution

Weather impacts the effective execution of tactical missions in a variety of ways. The normal effects of adverse weather during takeoff, landing, and enroute are well known. However, for tactical missions involving today's precision strike munitions, the impact of weather can perhaps be the greatest limiter in mission effectiveness. Examples of three major weapons types are illustrated below:

- Television guided weapons require that the apparent contrast (at the weapon sensor) between a target and its background exceed a certain threshold for successful operation (lock-on). These weapons require a cloud-free line of sight. Furthermore, the inherent contrast is attenuated below the threshold when aerosols such as haze or fog exist along the line of sight. These are usually related to the surface visibility. Another weather parameter that affects performance directly is the depth of the haze layer.

- Reconnaissance, navigation, and targeting systems, such as the Forward Looking Infrared (FLIR) sensors operating at 8-12 μm, are seriously degraded by a number of weather factors. Apparent target/background contrast is extremely sensitive to current and antecedent weather conditions. A cloud free line of sight is required. Furthermore, high values of absolute humidity in the sight path, even in clear air, will seriously degrade the range at which the target can be detected. Aerosols can also degrade the performance of the infrared systems.

- Laser guided systems also require a cloud-free line of sight, and they are also affected by the attenuation of the aerosols in the designator to target path and weapons receiver to target path. Successful operation of these systems requires that the weapon lock on at a threshold range. Avoidance of enemy air defenses by the designator aircraft may require a minimum standoff range during target designation. If aerosol attenuation of the laser beam is excessive, the weapon may be ineffective.

WAMPS will use the Electro-Optical Tactical Decision Aid (EOTDA) physical models and improvements planned in the Target Acquisition Weather Software (TAWS) program (Bensinger, et.al., 1998) to show the effects of WIDAs on these sophisticated systems.

Architecture Concept

Although WAMPS exists only as a demonstration prototype, if actual software were implemented, it would not be a stand alone METOC system, but rather an integrated application existing as part of the TBMCS DII/COE environment. It would exist as part and parcel of that architecture. Within TBMCS functional areas, weather, like intelligence, is a core function.

In the fully developed WAMPS prototype, WIDAs will have direct access to sample mission databases. This interface will enable systematic and automated processing of the large number of sortie, weapon, and target scenarios. WIDAs will obtain their METOC information from fine-scale gridded databases generated by service weather operational centers. The results of the WIDAs will be stored in a relational database that will enable aircrews, mission planners, and JTF command elements to recall data by mission, sortie, target, weapon, and time. Appropriate displays will be presented for review by operations personnel at their user terminals. Tabular mission data can be augmented with performance predictions by weapons type. Probability of detection from WIDAs can be folded in with other mission-limiting factors such as enemy defenses to adjust tactics, and provide an overall kill probability.

Again, in the currently planned WAMPS program, the prototypes can only emulate the fully integrated state. The purpose will be to (1) demonstrate the capability to effectively operate in the TBMCS environment, and (2) minimize the amount of recoding and redesign required for a fully operational WAMPS.

Potential WAMPS Output Products

The examples of weather impacts on mission execution described above provide a context for discussing typical output products for WAMPS.

Typical displays for force-level mission planning could be a red/yellow/green "stoplight" chart that highlights the performance of a variety of weapons systems over time, allowing proper planning for the longer range decisions. Sensible weather for airfields and routes could be displayed graphically on a map background if adverse effects were forecast.

For the pre-mission ATO, decisions must be made about target selection and weapons upload. At this phase, the mission planners desire some detail of the mission profile. They require a measure of the predicted relative performance of the available weapons versus time against specific targets. Products at this level would readily show the planner those target/weapon combinations that have a low (or high) probability of a successful lock-on.

For the mission execution planning, the pilot desires a fly-through with scene visualization and a specific prediction of detection/lock-on range. Typically, this prediction is based on a three-to-six hour forecast. The weapon type is probably predetermined at this point. The pilot may be provided a display of target alternatives with predicted values of detection/lock-on ranges in tabular format. If the weapon guidance system operates in the visible or IR spectrum, the detection/lock-on range may vary with azimuthal position of the weapon relative to the sun. This azimuthal dependence of performance could be presented in a graphical format for each target.

Demonstration of Value Added

An additional portion of the WAMPS prototypes will be the demonstration of value added of weather information to the warfighter. The demonstration of value

added by a support function to combat missions is difficult in the best of circumstances, even when the parameters are exactly predictable and the effect on operations can be quantified with certainty. The result of a given mission if the support had not been provided is often uncertain; in many cases, the same result may have been derived without the support.

Farrell (1996) showed a hypothetical scenario where 5947 sorties were flown on a given day. The distribution of successful and unsuccessful missions were tabulated according to the use of weather information by combat operations (CO). Farrell's table of weather impacts on mission effectiveness is reproduced here in Figure 1 to show how use of weather information would improve mission success in the scenario.

Figure 1 Weather Impact Matrix (from Farrell (1996))

	Successful Missions	Unsuccessful Missions
CO acted on weather impact predictions	297	2
CO ignored weather impact predictions	34	420
No weather impact predicted	4987	57
No weather data available	90	60

Similar Air Force studies have shown that including "tailored weather information" (i.e. WIDA-type products) at both planning and operational levels can result in improved mission effectiveness. TASC and AFRL will continue this effort through the WAMPS program by developing a set of scenarios that can accompany WAMPS prototypes. For example, these demonstrations may utilize realistic target and mission planning data, together with real/simulated weather data. Scenarios will demonstrate WIDA support to the mission planning process. It is anticipated that the development of the value-added demonstration will evolve over the course of the WAMPS development. A limited capability will be available for the second WAMPS prototype.

WAMPS Prototypes and Schedule

The objective of the initial demonstration is to present a screen-by-screen emulation of what would be available in a fully developed WAMPS prototype. A scripted sequence of displays demonstrates the steps required for WAMPS to interact with the mission planning systems. This demonstration capability is not interactive, but uses a fixed set of "canned" data to walk through the mission planning and execution process.

The second WAMPS prototype will build on feedback from the first system. It will bring in interactive functionality over a limited, scripted set of information that will allow the user to mimic the functionality of generating the ATO. WAMPS will display changes in mission alert status in response to user-selected mission effectiveness thresholds, and allow users to replan mission parameters (e.g., sensor, time, azimuth, altitude). Actual TAWS runs will build the WIDA parameters required.

The third WAMPS prototype will also iteratively build on feedback received from users. It is planned to add the capability to mimic mission monitoring and replanning functions for a wider variety of mission scenarios.

The fourth WAMPS prototype is planned to pull together all the comments and suggested improvements, and provide a demonstration that shows the full integration of weather information into the full spectrum of mission planning processes.

The initial WAMPS was delivered in 4CY98. Subsequent releases will occur on an approximately annual basis.

Summary

The WAMPS prototypes will graphically illustrate the value of integrating fine-scale weather information into the mission planning and execution processes. It is designed to show how this information can become part of the TBMCS architecture, rather than a stovepiped system off to the side that is difficult for mission planners to access.

References

Bensinger, R.B., Gouveia, M.J., Higgins G.J., Morrison, J.S., Turkington R.B., Gilbert, C.V., Target Acquisition Weather Software, BACIMO Conference Proceedings, 1998

Farrell, R.J., METOC Support Within Command and Control Systems: Context-Sensitive METOC Decision Support Tools, Battlespace Atmospheric Conference 96, NraD, San Diego, CA, 1996

Acknowledgement

This effort is sponsored by the Air Force Research Laboratory, Hanscom AFB. MA, under Contract Number F19628-97-C-0087.

REAL-TIME CLOUD DEPICTION INTEGRATION INTO THE ARMY'S BATTLEFIELD MANEUVER CONTROL SYSTEM

Ronald F. Fournier*, Richard B. Bensinger

TASC
55 Walkers Brook Drive
Reading, MA 01867-3297

Sponsored by: The Space and Missile Defense Command Battle Lab (SMDCBL)

Abstract

Real-time cloud detection and visualization is being developed to demonstrate the value added from space-based weather satellite imagery products in support of Army mission planning and execution. Mission planners and tactical forces need to know the cloud location to assess the impact that clouds will have on their mission. GOES satellite imagery is first acquired by the Army's Deployable Weather Satellite Workstation (DWSW). Multispectral cloud differencing and thresholding techniques are then applied to the GOES imager data to create a Cloud/Clear mask. The Cloud/Clear mask is subsequently formatted and transferred to the Army's Maneuver Control System (MCS) for visualization by mission planners and warfighters. A proof of concept demonstration is planned where operational exploitation of the Cloud/Clear depiction together with geo-registered battlefield information on MCS will be evaluated as part of the Army Space Exploitation Demonstration Program.

Introduction

In the current modern warfighter era, a large volume of mission planning information is reviewed to plan, execute and re-plan missions so that enemy forces are overwhelmed with the military superiority of friendly forces. Mission planning systems, such as the Army's Maneuver Control System (MCS), have been designed and fielded that assist the complex mission planning and execution process. Although weather often plays a critical role in the success or failure of many missions, even the best of our automated mission planning systems have not fully integrated weather into the planning process. The project presented in this paper represents the sponsor's successful effort to overcome this mission planning deficiency by integrating cloud information into the Army's mission planning process as part of the Army's Space Exploitation Demonstration Program (ASEDP).

An initial weather integration effort has been successfully completed through the generation of a cloud mask overlay onto the Army's MCS situation display. The cloud mask was generated in real-time using GOES multi-spectral imagery obtained through the Army's Deployable Weather Satellite Workstation (DWSW). The cloud mask was forwarded to the Army's Weather Effects Workstation (WEW), which is part of the Integrated Meteorological System (IMETS) and where the MCS compatible cloud mask overlay was prepared. Once the cloud mask overlay was prepared by the WEW, an MCS operator can retrieve the cloud mask overlay from the IMETS database and present it on the MCS situation display.

Approach

Since its inception in 1987, ASEDP has remained at the forefront of integrating space technologies into tangible Army applications. ASEDP has significantly contributed to fulfilling the Army's warfighter requirements using a proof of concept approach. SMDCBL earmarks limited development and integration resources to build an application that fully or partially addresses the warfighter's requirements. This is followed by an end user centered experiment, where experiment participants judge the operational utility of the application(s) in meeting the warfighter's needs. The cloud mask effort detailed in this paper used the same ASEDP approach.

The warfighter requirement that the cloud mask project addressed was to display a representation of cloud/no cloud geographical extent onto the MCS situation map. In addition to the warfighter requirement, initial generation of the MCS cloud mask overlay was subject to the following constraints:

1. Use only Geostationary Operational Environmental Satellite (GOES) imager data covering the region of interest.
2. Cloud mask generation was to occur operationally in near real-time as imagery from GOES was available.
3. Use existing SMDCBL computer information resources available at the Hardware/Software Integration Center (HSIC) located in Colorado Springs, CO.

The first cloud mask overlay constraint necessitated the use of cloud detection algorithm that relies solely on the GOES imager data. Modified versions of the CLAVR-1 cloud detection tests (*i.e.*, Reflectance Gross Cloud Test (daytime only), Thermal Gross Cloud Test, Channel 4 Minus 5 Test, Channel 2 Minus 4 Test, Shortwave Minus Longwave Brightness Temperature Difference and Cirrus Test) as defined by Stowe *et. al.* (1998), were selected for the initial implementation of the cloud mask overlay. The CLAVR-1 cloud tests are based upon the spectral characteristics of the Advanced Very High Resolution Radiometer (AVHRR). Modification to the CLAVR-1 cloud tests was necessary because the spectral characteristics of the GOES Imager differ from AVHRR. The major difference between the CLAVR-1 cloud tests and those implemented for this project primarily involved the thresholds used for cloud detection. Table 1 lists the central wavelength (λ_c) and bandwidth ($\Delta\lambda$) of the GOES Imager and AVHRR instruments.

Table 1: GOES 8 Imager spectral characteristics differ from AVHRR, necessitating modification of the CLAVR-1 cloud tests.

Instrument/ Channel		λ_c (μm)	$\Delta\lambda$ (μm)
1	AVHRR	0.63	0.1
	GOES	0.65	0.2
2	AVHRR	0.83	0.38
	GOES	3.9	0.2
3	AVHRR	3.7	0.38
	GOES	6.8	0.50
4	AVHRR	10.8	1.0
	GOES	10.7	1.0
5	AVHRR	12.0	1.0
	GOES	12.0	1.0

Note that AVHRR has two shortwave channels (Channels 1 and 2), while the GOES 8 Imager has a single visible channel (Channel 1). Although AVHRR and GOES 8 Imager channels 4 and 5 are not identical, they are similar for the purpose of cloud/no cloud mask generation. The full Instantaneous Field of View (IFOV) of the GOES Imager channels 1, 2, 4 and 5 (corresponding to AVHRR channels 1, 3, 4 and 5) were used for the initial implementation of the CLAVR-1 cloud tests. GOES Imager channel 3 was used only during nighttime hours to prevent solar contamination, while channel 1 was used during daytime hours.

Since changing weather conditions may significantly impact the success of a mission, the second cloud mask overlay implementation constraint requires that a cloud mask must be generated in a timely fashion upon receipt of the GOES 8 imagery over the region of interest. The wall clock time required to generate the cloud mask overlay is primarily a function of the imagery volume (*i.e.*, number channels over the region of interest), the computational complexity of the cloud tests (*e.g.*, albedo corrected to Sun overhead for GOES channel 1 imagery, minimization of reflected solar radiance of GOES channel 2 during daylight hours), and available computational resources (*i.e.*, computer processor efficiency and input/output bandwidth). Although a temporal performance criteria was not specified by the warfighter cloud mask requirement, a cloud mask overlay throughput goal of under five minutes was established based on the region of interest size for the experiment. The performance goal is measured from when the last scan line for the region of interest was received by the GOES ground station to when the cloud mask overlay was ready for use by the MCS user.

The third cloud mask overlay constraint is related to effective use of the Army's investment in weather systems available at the HSIC at project initiation. Figure 1 illustrates the systems available for generating the cloud mask overlay. The DWSW, IMETS and MCS were the systems used in the generation and display of the cloud mask overlay.

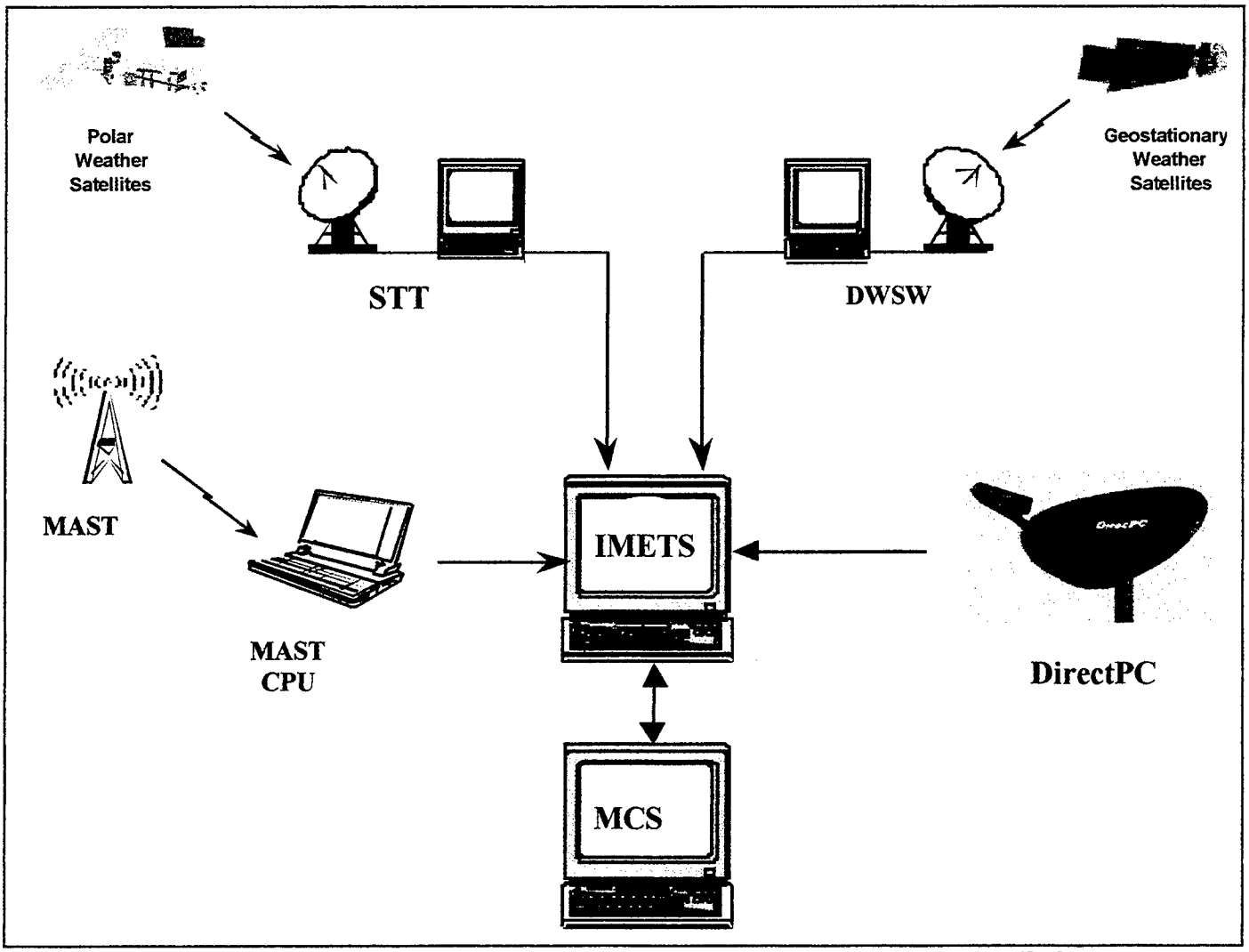


Figure 1: Meteorological related systems present at the Hardware/Software Integration Center, Colorado Springs, CO. at project initiation and used in the cloud mask project included the Deployable Weather Satellite Workstation (DWSW), Integrated Meteorological System (IMETS), and the Army's Maneuver Control System (MCS).

The GOES imagery is first acquired by the DWSW. As GOES channels 1, 2, 4 and 5 are ingested, the DWSW remaps all the channel data to the MCS Mercator situation display projection. As picture elements (pixel) are subjected to the modified CLAVR-1 cloud tests, channel 1 (i.e., visible) is converted to an albedo with Sun overhead. The modified CLAVR-1 cloud tests were also implemented on the DWSW. Results from the Reflectance Gross Cloud Test, Thermal Gross Cloud Test, Channel 4 Minus 5 Test, Channel 2 Minus 4 Test and Shortwave Minus Longwave Brightness Temperature Difference test are all maintained by the software. A cloud mask decision tree implemented on the DWSW then examines the results of the modified CLAVR-1 cloud tests and makes a cloud/no cloud decision at the pixel level. The raster based cloud mask and associated metadata (e.g., valid date/time, geographical extents, projection, etc.) are then forwarded to the WEW by the DWSW. The WEW

retrieves the raster cloud mask, generates the vector based MCS cloud overlay and inserts the overlay into the IMETS database. The MCS user may then overlay the cloud mask onto the situation display.

Modified versions of the CLAVR-1 Reflectance Gross Cloud Test (daytime only), Thermal Gross Cloud Test, Channel 4 Minus 5 Test, Channel 2 Minus 4 Test and Shortwave Minus Longwave Brightness Temperature Difference Test were used to detect the presence of cloud at the pixel level. Figure 2 illustrates the cloud mask processing flow performed on the DWSW and IMETS. The Reflectance Gross Cloud Test was conducted on the 0.65μm visible imagery when the solar zenith angle at the center of the region of interest was less than or equal to 80°. Since solar irradiance contaminates the channel 2 radiances, the Channel 2 Minus 4 Test and Shortwave Minus Longwave Brightness Temperature Difference Test were performed only when the solar zenith angle was greater than or equal to 100°. The remaining infrared tests (*i.e.*, Thermal Gross Cloud Test, Channel 4 Minus 5 Test) were conducted for each image acquired by the DWSW. Individual cloud test results were saved to DWSW mass storage for subsequent visualization and qualitative inspection.

As Fig. 2 illustrates, the cloud decision tree is the next step in the cloud mask generation process. The initial cloud decision tree implementation simply examines the results from the modified CLAVR-1 cloud tests and marks a pixel as cloud if one of the cloud tests indicate the presence of cloud. Otherwise, the pixel is mark as clear. The resulting cloud mask in its raster form is then saved to DWSW mass storage. The raster cloud mask and associated metadata information are also saved to IMETS mass storage. IMETS then retrieves the raster cloud mask from its mass storage and analyzes the mask into an MCS vector overlay format. IMETS then places the MCS cloud mask overlay into its database, where the MCS operator can then retrieve the mask and overlay the cloud mask onto the MCS situation display.

Results

Figures 3, 4, 5 and 6 show the GOES imagery over the region of interest for channels 1, 2, 4 and 5, respectively. Geopolitical boundaries along with point locations are overlay onto the GOES imagery for reference. Note that the 0.65μm visible imagery (Fig. 3) has a smaller instantaneous field of view than the remaining GOES channels (*i.e.*, channels 2, 4 and 5).

The cloud mask software processed the visible imagery (Fig. 3) when the solar zenith angle was less than or equal to 80°. Prior to thresholding (*i.e.*, performed by the modified CLAVR-1 Refelective Gross Cloud Test) the visible picture elements (pixels), the imagery was normalized to Sun overhead and then converted to albedo. To limit the level of processing on the DWSW the 3.9μm (Fig. 4) was only used during nighttime hours when the solar zenith angle was greater than or equal to 100°. The 3.9μm pixel radiance values were converted to temperature prior to the cloud/no cloud processing by the Two Minus Four Test (modified CLAVR-1 cloud detection test). In addition, the 3.9μm channel was also used in conjunction with the 10.7μm channel under the same solar zenith conditions in the Shortwave Minus

Longwave Brightness Temperature Difference Test (another modified CLAVR-1 cloud detection test). The 10.7 (Fig. 5) and 12.0μm (Fig. 6) channels were used for all daytime and nighttime hours in the modified CLAVR-1 Four Minus Five Test. Finally, the 3.9 and 10.7μm channels were used in the modified CLAVR-1 Cirrus Test during the nighttime hours only (*i.e.*, solar zenith angle greater than 100°).

Results from all the modified CLAVR-1 cloud tests were compared and a final cloud/no cloud decision was made. During daylight hours the Reflective Gross Cloud Test dominated the cloud/no cloud decision. During the nighttime hours, the Four Minus Five Test results dominated the cloud/no cloud decision, followed by the Shortwave Minus Longwave Brightness Temperature Difference Test and then the Cirrus Test. The resulting cloud mask generated for the imagery depicted in Figs. 3, 4, 5 and 6 is shown in Fig. 7..

Using existing IMETS software capability, the cloud mask depicted in Fig. 7 was subsequently forwarded to IMETS for the generation of the MCS cloud mask overlay. The MCS cloud mask overlay was then entered into the IMETS database. The MCS user is subsequently able to retrieve the cloud mask overlay for display onto the situation map. *Note: Technical difficulties prevented the inclusion of the actual MCS cloud mask situation map display in time for delivery of this paper.*

The cloud mask is generated within 5 wall clock seconds, measured from the time GOES imagery over the region of interest is collected by the DWSW to the transfer of the cloud mask file to IMETS for subsequent MCS overlay generation. At most five minutes may elapse before IMETS generates the cloud mask overlay. This delay was necessary to conserve IMETS processing capacity such that IMETS could be used in addressing additional warfighter requirements.

References:

Stowe, L.L., Davis, P.A., McClain, E.P., Scientific Basis and Initial Evaluation of the CLAVR-1 Global Clear/Cloud Classification Algorithm for the Advanced Very High Resolution Radiometer, May 1, 1998.

Rao,P.K., S.J. Holmes, R.K. Anderson, J.S. Winston, P.E. Lehr, Weather Satellites: Systems, Data, and Environmental Applications, American Meteorological Society, Boston, 1990. ISBN 0-933876-66-1

U.S. ARMY SPACE AND MISSILE DEFENSE BATTLE LAB, System Test Report (STR) for The Integration Of Weather Products Into The Maneuver Control System (MCS), 28 August 1998

Acknowledgement

The authors gratefully acknowledge the sponsor of this effort, the US Army's Space and Missile Defense Battle Lab, and the associated efforts of Army Research Laboratory scientists and programmers.

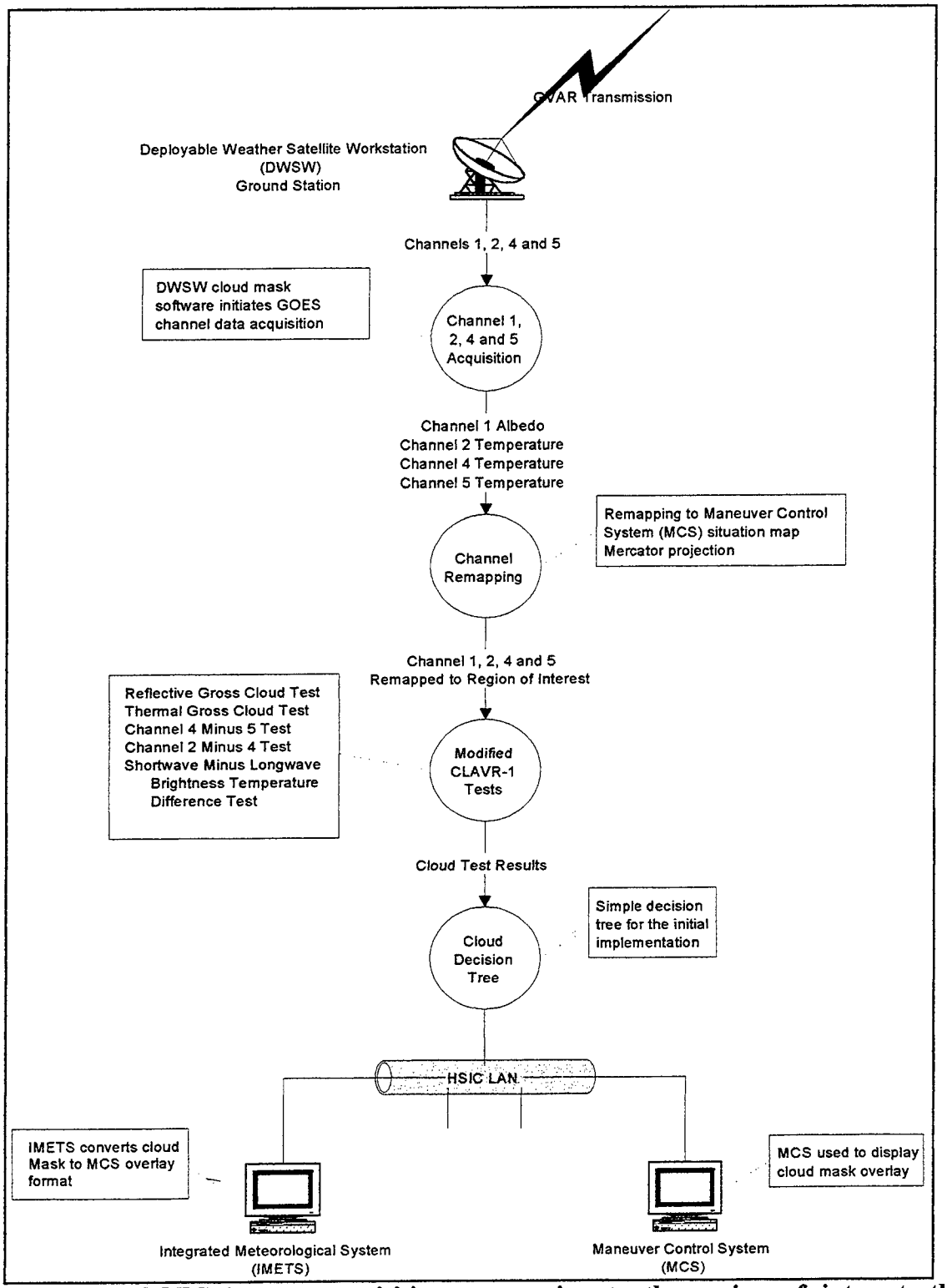


Figure 2: GOES imager acquisition, remapping to the region of interest, the generation of the cloud mask and transmittal to the Integrated Meteorological System (IMETS) is performed on the Deployable Weather Satellite Workstation (DWSW).

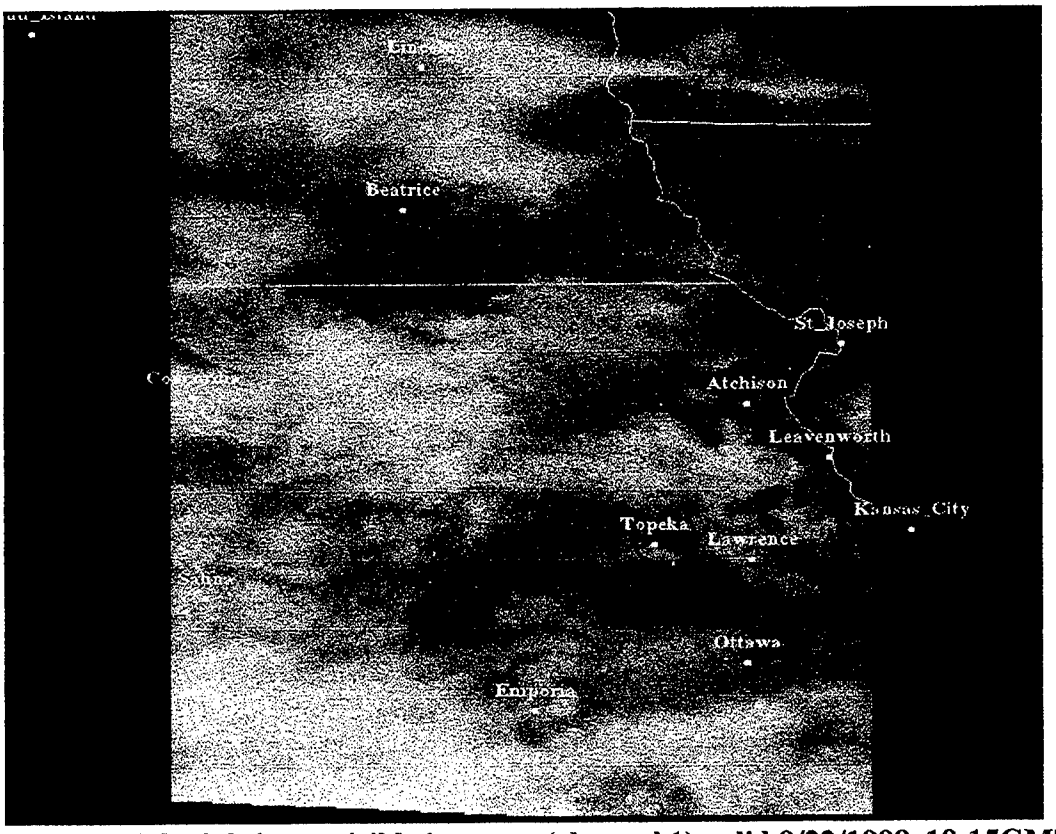


Figure 3: GOES 0.65μm visible imagery (channel 1) valid 9/22/1998, 18:15GMT remapped to the region of interest.



Figure 4: GOES 3.9μm imagery (channel 2) valid 9/22/1998, 18:15GMT remapped to the region of interest.

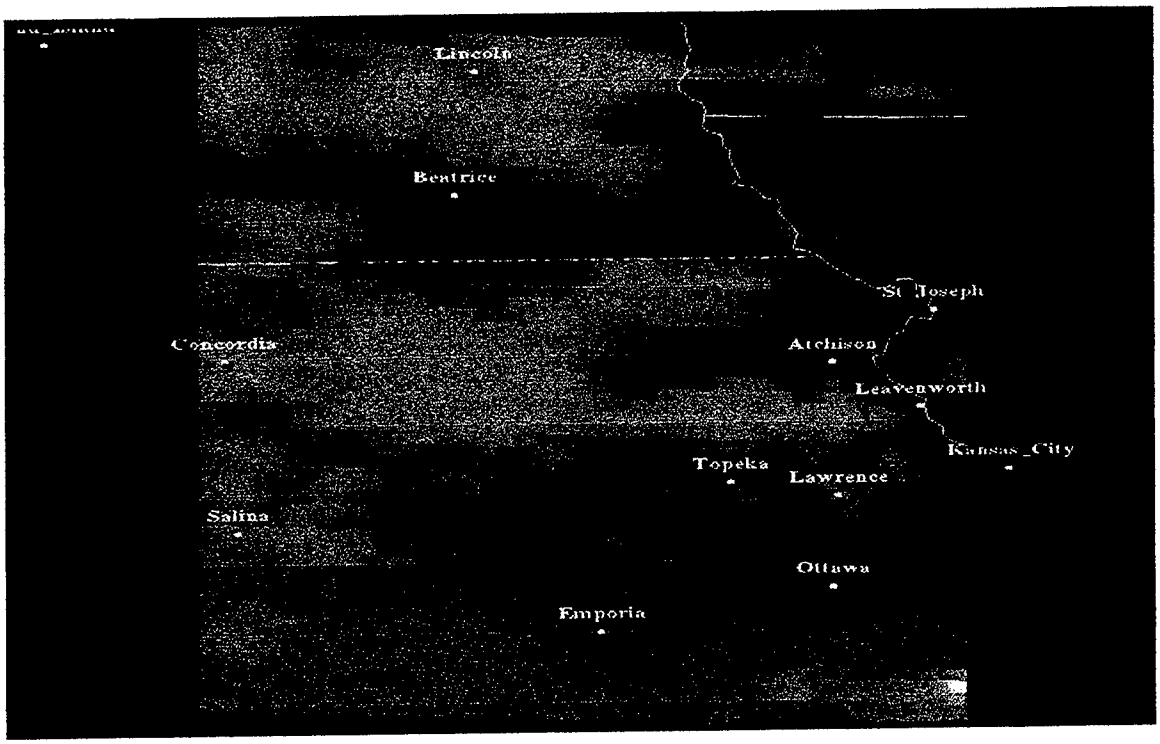


Figure 5: GOES 10.7μm imagery (channel 4) valid 9/22/1998, 18:15GMT remapped to the region of interest.

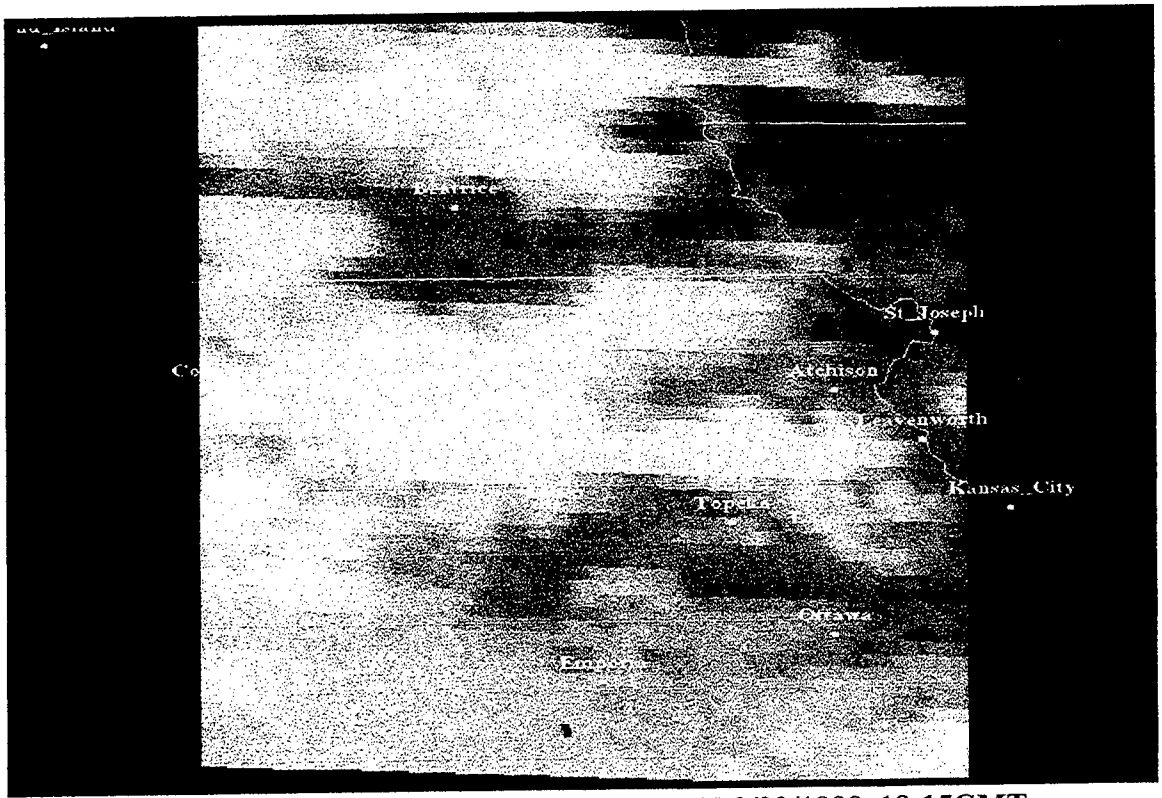


Figure 6: GOES 12.0μm imagery (channel 5) valid 9/22/1998, 18:15GMT remapped to the region of interest.

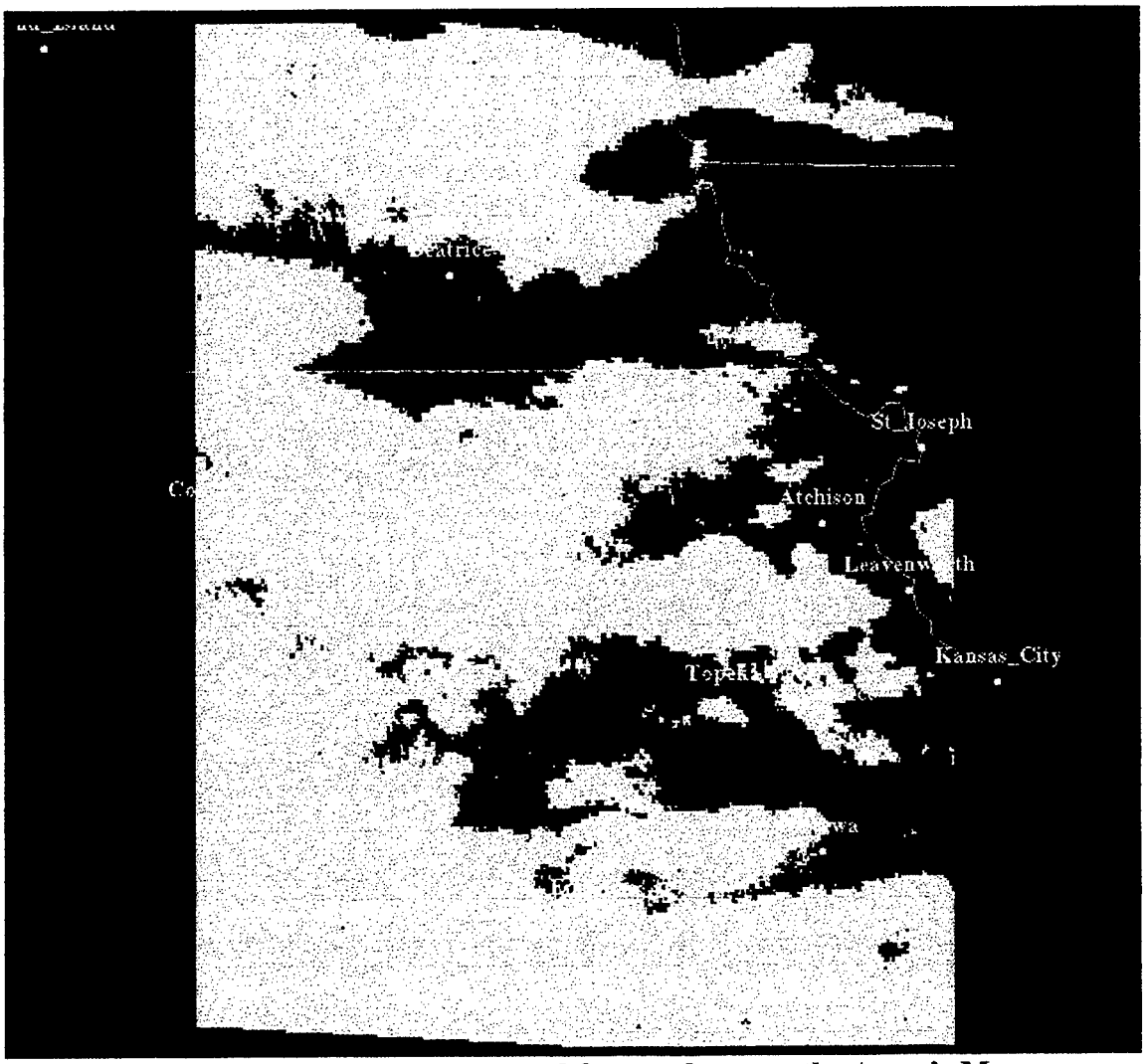


Figure 7: Resulting cloud mask generated for overlay onto the Army's Maneuver Control System (MCS) situation map display valid 9/22/1998, 18:15GMT.

NIGHT VISION GOGGLES OPERATIONS WEATHER SOFTWARE (NOWS)

Melanie J. Gouveia,* Glenn J. Higgins, Jeffrey S. Morrison, Richard B. Bensinger, Craig V. Gilbert, and Ryan B. Turkington

TASC
55 Walkers Brook Drive
Reading, MA 01867-3297
Phone: (781) 942-2000, Fax: (781) 942-2571
E-Mail: mjgouveia@tasc.com

Sponsored by the Air Force Research Laboratory, Hanscom AFB, MA

The Night Vision Goggles (NVGs) Operations Weather Software (NOWS) is being developed to support tactical operators using NVGs in a variety of mission scenarios. Mission planners, pilots, and other tactical forces need to know if it is possible to conduct their missions under low light level conditions using NVGs. These extremely dangerous missions can include target acquisition, helicopter refueling, identification of pickup/drop zones, and search and rescue. NOWS supports mission planning and execution by providing NVG performance predictions for forecasted local weather conditions. Performance predictions include target detection range or detection probability, vulnerability to ground hazards, and loss of visible horizon. NOWS also provides solar and lunar ephemeris information for a series of times or dates at a user-specified location. NOWS is being developed incrementally to include state-of-the-art physical models, a modern graphical user interface, and automated access to meteorological and geographic databases. The capability exists to manually enter data for quick-look projections, or in the event communications paths to data sources are not available. The NOWS project includes an assessment of the accuracy of the physical models using field measurements.

Objective

Air Force / Department of Defense (DoD) meteorologists have a need to support forces performing covert operations using Night Vision Goggles (NVGs). The types of missions that require support include target acquisition/detection, helicopter refueling, identification of pickup/drop zones, and search and rescue. A single mission may include several of these tasks. Mission planners and pilots need to know if it is possible to conduct their missions under low light level conditions using NVGs. NVG performance predictions are required for specified missions and forecasted local weather conditions. These performance predictions can be used by mission planners to make "go/no-go" decisions, to modify mission execution tactics, or to evaluate the general suitability of environmental conditions for NVGs. The performance predictions can be used by pilots to prepare for the expected conditions during a mission or training exercise.

The purpose of this program is to incrementally develop and deliver a practical and user-friendly NVG Operations Weather Software (NOWS) package for use by DoD weather support personnel. State-of-the-art physical models, a modern Graphical User Interface (GUI), and geographic and meteorological databases are being utilized to provide accurate results, maximize usability, and minimize the amount of input data that must be entered manually by the user (Gouveia, et al., 1997). Additional activities involve an assessment of the accuracy of the NOWS physical models using field data.

This paper provides an overview of the NOWS software and presents preliminary results from the NOWS model assessment activity.

NOWS Software Development

NOWS runs on an IBM-compatible personal computer under Microsoft Windows. The currently released version of NOWS requires a 486DX or better processor and runs under Windows Version 3.1 and Windows 95. The next version of NOWS will run under Windows 95 and Windows NT.

Incremental NOWS development has focussed on several areas: system design, GUI development, data sources, physical models, and output products. Each of these areas is described below. Table 1 shows the delivery schedule for the first four versions of NOWS. NOWS Version 5 is planned for February 1999.

Table 1. Incremental NOWS Versions

Version	Release Date
NOWS Version 1.0	31 May 1995
NOWS Version 1.1	31 July 1995
NOWS Version 2.0	30 Nov 1995
NOWS Version 2.0.1	16 Feb 1996
NOWS Version 2.0.2	26 Apr 1996
NOWS Version 3.0	4 Dec 1996
NOWS Version 4.0	24 Nov 1997

NOWS System Design

NOWS is designed to be goal-oriented. Three goals, or analysis types, are currently implemented:

- Illumination analysis involves the computation of solar and lunar ephemeris information for a specified location.
- En route analysis involves the prediction of performance metrics along the flight path of a particular mission.
- Key location analysis involves detailed NVG performance predictions for a particular location along a mission's route.

NOWS is designed to process input from several types of data sources, pass parameters to the appropriate physical models, and generate goal-dependent output products. A schematic of the NOWS process is shown in Figure 1.

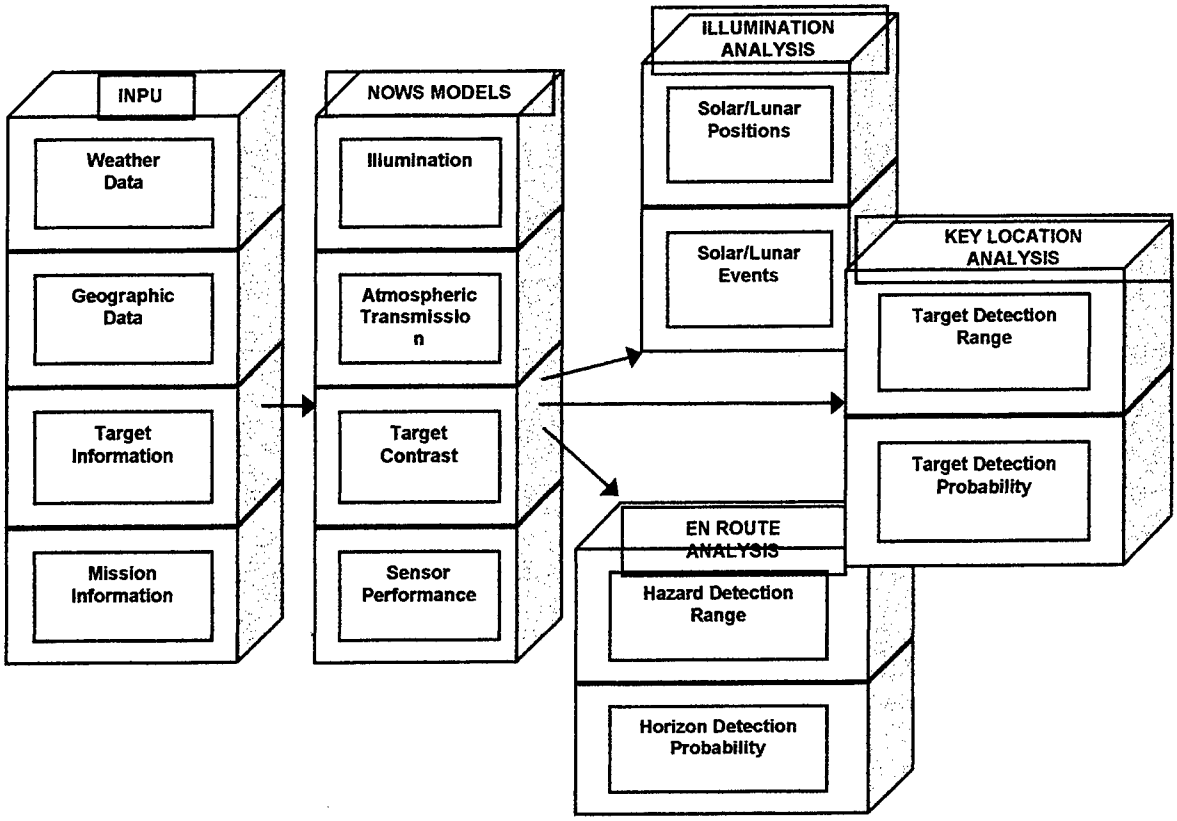


Figure 1. The NOWS Process.

Graphical User Interface (GUI)

The NOWS GUI is map-based. Users point and click to select a region of interest from a world map, then select desired map features. The selected region is then shown as a detailed map. Key locations are added to the region, then locations are linked to form missions. An analysis may be run on one or more specific key locations or on one or more mission legs between locations.

The steps required to perform a NOWS analysis are shown in a series of progress charts. The user proceeds towards the desired goal by clicking on buttons in sequence. NOWS keeps track of which steps have been completed, which steps may be performed next, and which steps are not active yet. Figure 2 shows a sample NOWS map and progress chart.

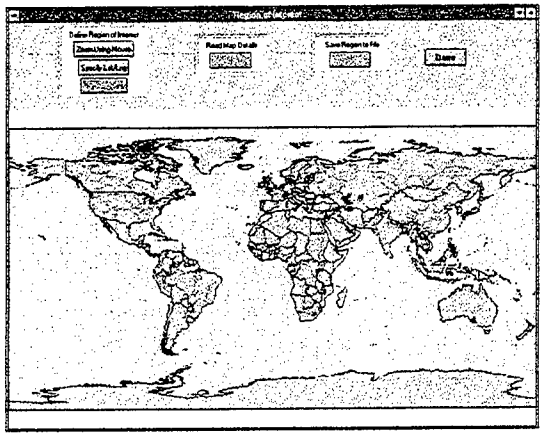


Figure 2. The NOWS GUI.

User inputs are required at several points during the process. Target information, mission information, and weather information must be entered. NOWS Version 4 uses standard GUI features such as menu bars, sliders, drop-down list boxes, and check boxes to simplify the data entry process. NOWS Version 5 will also use tab dialogs and radio buttons where appropriate.

Data Sources

NOWS uses several internal and external databases. NOWS accesses geographic and meteorological data from external sources. An internal database is used to store information about user-specified regions and missions. A selection of predefined targets and NVG sensors is also stored internally. NOWS Version 5 will allow a user to create a customized NVG sensor and add it to the database.

The geographic information required by NOWS includes mapping information, terrain categories, and terrain elevations. NOWS Version 4 uses the Digital Chart of the World (DCW) map information from the National Imagery and Mapping Agency (NIMA). NOWS Version 5 will use NIMA's newer Vector Map Level 0 (VMap0) for map information. VMap0 provides multiple map features such as political boundaries, elevation contours, hydrography, industry, physiography, population, transportation, utilities, and vegetation.

NOWS uses the DeFries and Townshend Land Cover Classification Map (1994a), a global land cover database, to obtain default information about target background and general target area albedo. This database is a product of the remote sensing community, derived from Advanced Very High Resolution Radiometer (AVHRR) Normalized Difference Vegetation Index (NDVI) satellite data. The NOWS land cover database has only coarse resolution, 1 degree by 1 degree, but it can be used to supply defaults for the user to override if necessary.

NOWS obtains terrain elevations from NIMA's Digital Terrain Elevation Data (DTED) database. The terrain elevations are used to determine the distance to the horizon. NOWS uses the horizon distance to calculate the probability of detecting the horizon through the NVGs.

NOWS requires a detailed weather forecast for each key location in the region of interest. To reduce the data entry burden on the user, NOWS makes use of meteorological data sources. NOWS Version 4 allows weather to be automatically downloaded from the Navy Oceanographic Data Distribution System (NODDS), a dial-in source. NOWS Version 5 will allow weather to be automatically downloaded from the Air Force Weather Information Network (AFWIN), a web-based source. NOWS contains logic to derive the weather parameters required by the physical models from those available via automated sources. NOWS allows the user to override the weather parameters, or to enter them manually if an outside connection is not available.

NOWS Physical Models

For a NOWS illumination analysis, solar and lunar positions or solar and lunar event times are computed for a particular location and a series of times. The NOWS illumination model is used for these computations. For a NOWS key

location or en route analysis, the detection range or detection probability is calculated for a "target" at a particular location and time under specified weather conditions, using a particular NVG sensor. The "target" can be the horizon, a refueling tanker, a pickup/drop zone, a ground target, a flight hazard, or–for a reverse viewpoint analysis–the mission vehicle itself. NOWS uses several component models to arrive at a prediction of detection range or detection probability: an illumination model, an atmospheric transmission model, a target contrast model, and a sensor performance model.

The NOWS illumination model computes solar and lunar positions and event times using the U.S. Naval Observatory's Solar-Lunar Almanac Code (SLAC). The SLAC (Bangert, 1996a; Bangert, 1996b) computes the horizon coordinates (altitude and azimuth) of the sun and the moon for a specified location and time. The SLAC also computes the fraction of the moon illuminated. NOWS also uses the SLAC to compute the times of sunrise, sunset, moonrise, moonset, and the times of nautical twilight. SLAC is considered the state-of-the-art ephemeris model.

The NOWS atmospheric transmission model computes atmospheric optical properties, direct and diffuse components of radiance in the target scene, and path radiance and transmission between the target and the sensor. The computations are based on Hering's Fast Atmospheric SCATtering (FASCAT) model for atmospheric optical properties in the visible and near-infrared regions of the electromagnetic spectrum. This model was developed in three stages, for clear (Hering, 1981), overcast (Hering, 1983), and partly cloudy (Hering and Johnson, 1984) meteorological conditions.

NOWS uses a rudimentary urban illumination model to help predict the radiance of scene components influenced by distant city lights. The urban illumination model is a parametric model that assumes that an urban area is a point source of illumination and estimates city brightness as a function of distance from the target scene, look angle, and city population. It assumes a mostly clear atmosphere. The simplified model implemented in NOWS is based on an underlying parametric model by Garstang (1986, 1989).

The NOWS target contrast model computes the inherent radiance, at zero range, of up to three objects in the target scene: the target, its shadow, and the background. The inherent radiance is then used to compute apparent radiance at the sensor's range. Apparent radiance is then used to compute the contrast between different pairs of objects in the scene.

The NOWS sensor performance model computes detection range or detection probability for up to two pairs of objects in the target scene: the target against the background, and the target's shadow against the background. One of the objectives of the sensor performance model is to determine at what maximum range the target or shadow signature is sufficiently strong that an observer using NVGs can detect it with a user-specified level of probability. An alternative objective of the sensor performance model is to determine the probability of detection for an object pair at a user-specified range. The sensor performance

model is a modified version of the Army Night Vision and Electronic Sensors Directorate's 1994 version of the Image Intensifier Code (NVESD, 1994).

NOWS Output Products

NOWS provides tabular, graphic, and map-based output products, depending on the type of analysis that is performed. The user is able to choose the contents of tables and graphs. Figures 3 and 4 show sample output products for key location analysis. Figure 5 shows a sample output product for en route analysis.

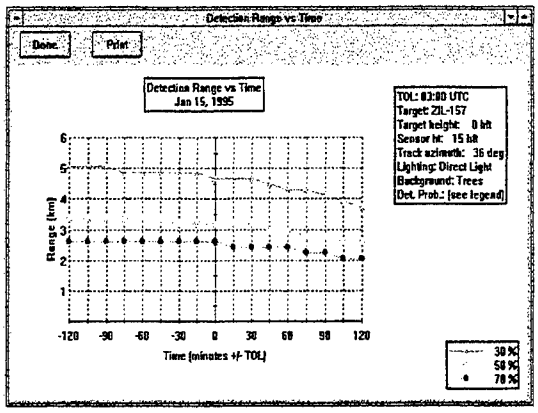


Figure 3. Detection Range as a Function of Time.

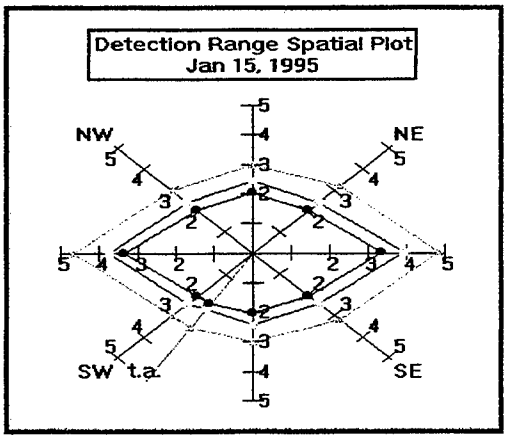


Figure 4. Detection Range as a Function of Approach Azimuth.

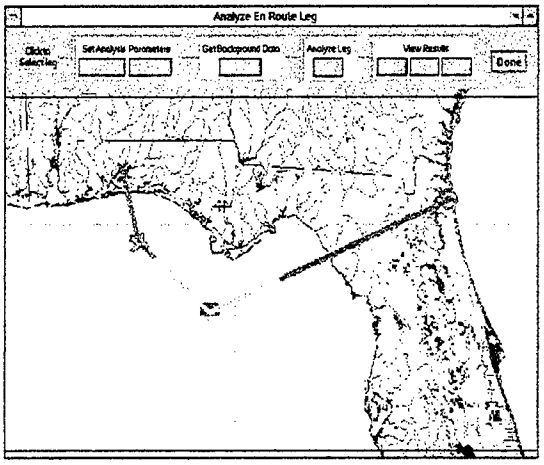


Figure 5. Probability of Detecting the Horizon.

NOWS Model Assessment

The purpose of the NOWS model assessment activity is to evaluate the NOWS models using data collected by AFRL for use as model input and validation of model output. The assessment focuses on the atmospheric transmission and target contrast models, although the illumination and sensor performance models will be examined qualitatively. An assessment plan was written, describing instrumentation to be used, experiments to be conducted, parameters to be measured, and data processing to be done. To date, six experimental episodes have been conducted by AFRL. Preliminary analysis of the first two data sets has led to the following conclusions:

- Total night sky irradiance data are of the same order of magnitude as data presented earlier by Vatsia (1972), but do not show the same spectral structure.
- Total night sky irradiance data show similar spectral structure to data collected earlier by Wright Laboratory (Schemine, 1993), but are an order of magnitude lower.

- Total night sky irradiance data show spectral peaks at 0.45, 0.59, and 0.82 μm that could be due to light pollution. NOWS does not predict these peaks.
- NOWS tends to overestimate total night sky irradiance, particularly under moonlight and twilight conditions.
- NOWS tends to overestimate direct lunar radiance.

Analysis will continue with the next four data sets. The analysis will focus on the direct and diffuse components of the total night sky irradiance, as well as atmospheric transmission.

Conclusions

NOWS is being developed to support tactical operators using NVGs in a variety of mission scenarios. NOWS provides NVG performance predictions for specified missions and forecasted local weather conditions. The performance predictions can be used by mission planners to modify mission execution tactics or by pilots to prepare for the expected conditions during a mission or training exercise. NOWS is being developed to use state-of-the-art physical models, a modern GUI, and geographic and meteorological databases to provide accurate results, maximize usability, and minimize the amount of input data that must be entered manually by the user.

References

Bangert, J.A., 1996a: *A Portable Computer Source-Code Module for Computing Accurate Times of Lunar and Solar Phenomena.* U.S. Naval Observatory, Astronomical Applications Dept. Technical Report.

Bangert, J.A., 1996b: *Solar-Lunar Almanac Code (SLAC) Software User's Guide Verison 1.0.* U.S. Naval Observatory, Astronomical Applications Dept. Technical Report.

DeFries, R.S., and J.R.G. Townshend, 1994a: "NDVI-Derived Land Cover Classification at Global Scales," *International Journal of Remote Sensing*, 15:3567-3586. Special Issue on Global Data Sets.

Garstang, R.H., 1986: "Model for Artificial Night-Sky Illumination," *Publication of the Astronomical Society of the Pacific*, 98:364-375.

Garstang, R.H., 1989: "Night-Sky Brightness at Observatories and Sites," *Publication of the Astronomical Society of the Pacific*, 101:306-329

Gouveia, M.J., W.S. Crawford, R.L. Deal III, G.J. Higgins, and S.H. Olson, 1997: *Night Vision Goggles Operations Weather Software (NOWS) User's Manual.* TR-07611-5. TASC, Reading, MA.

Hering, W.S., 1981: *An Operational Technique for Estimating Visible Spectrum Contrast Transmittance.* AFGL-TR-81-0198. University of California, San Diego, Scripps Institution of Oceanography, Visibility Laboratory, CA. [ADA 111823].

Hering, W.S., 1983: *Analytic Techniques for Estimating Visible Image Transmission Properties of the Atmosphere.* AFGL-TR-83-0236. University of California, San Diego,

Scripps Institution of Oceanography, Visibility Laboratory, CA. [ADA 142524].

Hering, W.S., and R.W. Johnson, 1984: *The FASCAT Model Performance Under Fractional Cloud Conditions and Related Studies.* AFGL-TR-84-0168. University of California, San Diego, Scripps Institution of Oceanography, Visibility Laboratory, CA. [ADA 169894].

Schemine, K.L., 1993: *Direct View Tactical Decision Aid Accuracy Assessment.* WL-TR-93-1138. Avionics Directorate, Wright Laboratory, Air Force Materiel Command, Wright-Patterson AFB, OH.

U.S. Army NVESD, 1994: *Image Intensifier Performance Model, Version 1.4 User's Guide.* U.S. Army Night Vision and Electronic Sensors Directorate, Visionics & Image Signal Processing Division, Ft. Belvoir, VA.

Vatsia, M.L., 1972: Atmospheric Optical Environment.

Acknowledgements

This effort is sponsored by the Air Force Research Laboratory, Hanscom AFB. MA, under Contract Number F19628-94-C-0201.

METEORLOGICAL DECISION AID DEVELOPMENT AND VALIDATION FOR NAVAL AVIATION

Lieutenant Commander Mike Neith*, USN, and Sam Brand
Naval Research Laboratory
Marine Meteorology Division
7 Grace Hopper Road, Stop 2
Monterey, CA 93943-5502
Phone: (831) 656-4887
Fax: (831) 656-6006
e-mail: neith@nrlmry.navy.mil

1. INTRODUCTION

Support of Naval aviation, with a primary emphasis on flight safety and efficiency, has always been a priority of the environmental community within the Navy (Brand and Dreksler, 1995). The Naval Research Laboratory (NRL) Marine Meteorology Division has been involved in the development of several meteorological decision aids (MDAs) to enhance this support. Aviation impact variables (AIVs), such as cloud ceiling, visibility, flight conditions (IFR – Instrument Flight Rules, MVFR – Marginal Visual Flight Rules, VFR – Visual Flight Rules), and aircraft icing have been the focus of the decision aid development efforts thus far.

These decision aids are designed to provide both environmental forecasters and aviators with state-of-the-art graphical displays of AIVs. The primary users of these decision aids will be the Naval Meteorology and Oceanography (METOC) Facilities and Detachments providing aviation weather forecast support ashore and the METOC component onboard major combatant ships that provide this support afloat. The Joint METOC Viewer (JMV), a viewer application developed by the Space and Naval Warfare Systems Command (SPAWAR) along with the Fleet Numerical Meteorology and Oceanography Center (FNMOC), has been the target application for transition of the decision aids (Ravid et al., 1997). JMV has been designed to provide users with a "quick-look" of the environment to evaluate its impact on mission planning and execution.

In addition to the meteorological decision aid development, NRL is also involved in evaluating the accuracy of AIVs derived from the Navy Operational Global Atmospheric Prediction System (NOGAPS) (Hogan et al., 1991). Several algorithms, used in conjunction with NOGAPS model output, have been evaluated for their skill in forecasting derived AIVs such as aircraft icing and clear-air turbulence. Also, sensible weather parameters, such as cloud amount, ceiling, top, type, and fog, derived from model output, have also been evaluated.

2. METEOROLOGICAL DECISION AID (MDA) DEVELOPMENT

Decision aid development at NRL has been divided into two general categories based on the data source. The first category includes displays derived exclusively from aviation text bulletins and the second category includes those derived from numerical weather prediction systems.

The first MDA developed was a simple visual display of METAR surface observations. For a specific geographic area, users are presented with a map background overlaid with symbols indicating the location of current observations. Running a mouse over a particular

symbol reveals the station ID and mouse clicking on the symbol opens a window that displays a formatted and raw version of the original report. Several enhancements have already been made to this display that allow users to select individual or combinations of reported parameters, set thresholds on those parameters, and choose the colors in which to display those parameters. For example, a very useful combination is constructed by setting all stations reporting IFR conditions, that is, ceilings below 1000 feet and/or visibility less than 3 miles, to display in red. Similarly, those stations reporting VFR or MVFR conditions are set to green and yellow, respectively. This MDA is a vast improvement over text-based displays in that it provides both forecasters and aviators with the ability to instantly evaluate current flight conditions over a large geographic area.

The second MDA developed was a visual display of Convective SIGMETS (Significant Meteorological Information). Like the METAR product, this MDA is produced by decoding warning information contained in the text bulletin and overlaying the corresponding warning polygon on a map background. This product is effective in giving forecasters and pilots a "quick-look" at reported hazardous flying conditions in the area of interest. Planned enhancements to this MDA will include other types of aviation warnings such as non-convective SIGMETs, Airman's Meteorological Information (AIRMETs) warnings, Weather Watches (WWs) and Pilot reports (PIREPS).

The third MDA developed was a visual display of Terminal Aerodrome Forecasts (TAFs). Typically, TAFs are co-located with METAR reports. Therefore, when both reports are available for a specific station, a unique symbol is used to indicate station position. When a station with both reports is mouse-clicked a window opens to display both the current METAR report and the current TAF. A significant enhancement underway for this MDA is the ability to modify the display based on a particular forecast parameter or combinations of forecast parameters at a user specified time in the future. For example, for a collection of TAFs valid from 00-24Z, a user could at 03Z, set the MDA to display flight conditions, IFR, MVFR, VFR for all reporting stations at 12Z. We believe this product will be extremely useful for aviators during flight planning by providing them with an easily understood tool to determine forecast conditions at multiple terminals simultaneously.

As mentioned previously, also being developed are a second category of MDAs derived from state of the atmosphere variables produced by numerical models. An aircraft icing decision aid based on the Shultz-Politovich (Schultz and Politovich, 1992) icing algorithm developed at the National Center for Atmospheric Research (NCAR) is currently under development. This MDA will use 6-hour forecasts of temperature and relative humidity from the NOGAPS model and will provide forecasters and aviators with short-range forecasts of icing potential at several levels in the atmosphere.

A second model-derived MDA, based on the Coupled Ocean Atmospheric Mesoscale Prediction System (COAMPS) (Hodur, 1993) is also under development. This product will use 3-hour COAMPS forecasts of cloud droplets to construct a cloud-top temperature field. This cloud-top temperature field is then colored in gray-shades to match temperatures from infrared satellite images. This product is expected to be very useful to forecasters and aviators in determining areas expected to be influenced by clouds.

3. VERIFICATION STUDIES

Three verification studies to determine the accuracy of AIVs derived from numerical prediction systems have been completed at NRL Monterey. Vogel and Sampson, 1996

evaluated turbulence indices using model output from NOGAPS. Vogel, 1997 documented a verification study of aircraft icing potential using four aircraft icing algorithms computed from NOGAPS model data. More recently, a study to evaluate NOGAPS skill in the short-range (0-24 hours) forecasting of cloud amount, ceiling, top, type, and fog has also just been completed (Vogel 1998). The forecasts were verified against METAR surface observations and pilot reports. Results show NOGAPS forecasts of significant cloud cover, indicated by a broken or overcast layer, and no cloud cover were fairly reliable. NOGAPS forecasts of cloud ceiling were less reliable, with only 1 in 5 forecast ceilings within 500 feet of observed ceilings. Cloud ceiling forecasts were generally below what was observed. Cloud tops were consistently forecast to be higher than observed, with 2 of 3 model cloud tops forecast within 4000 feet of observed cloud tops. NOGAPS predictions of cloud type, both stable and convective were good in the lowest atmospheric layer and forecast capability for cumulo nimbus/towering cumulus were better than for cumulus. NOGAPS fog algorithm showed only modest skill in forecasting fog with better skill in the Gulf of Mexico, Great Lakes and Atlantic than the Pacific coast.

4. SUMMARY

NRL Monterey has completed several verification studies involving aviation impact variables including clear-air turbulence, aircraft icing, and cloud amount/ceiling/top/type and fog. All studies thus far have involved the use of NOGAPS model output. In doing so, baseline criteria have effectively been established for the skill of NOGAPS in the short-range forecasting of these AIVs. As improvements in numerical modeling and AIV algorithm development are realized, the effectiveness on the improvement of AIV forecasting can be readily analyzed by comparisons to this baseline. In addition, comparative evaluations could be made with higher resolution mesoscale models such as COAMPS.

In addition to the verification studies, several MDAs have been developed or are under development. Initial development has concentrated on converting text-based aviation-related messages into graphical displays. These displays are effective in presenting large amounts of data in a single image and also provide users with tools to modify the display to suit their particular needs. Aircraft icing potential and cloud decision aids derived from model output are also being developed to provide users with short-range forecasts of these important AIVs. These MDAs will provide Naval forecasters and aviators with effective tools to evaluate the atmosphere's impact on mission planning and execution.

ACKNOWLEDGMENTS: The support of the sponsor, the Space and Naval Warfare Systems Command (PMW-185), and the Program Office, the Oceanographer of the Navy, are gratefully appreciated. This project is supported under PE0603207N.

5. RFERENCES

Brand, S., and S. B. Dreksler, 1995: Environmental Support of Naval Aviation, Naval Research Laboratory Memorandum Report NRL/MR/7543-94-7218.

Hodur, R. M., 1993: Development and Testing of the Coupled Ocean/Atmosphere Mesoscale Prediction System (COAMPS), Naval Research Laboratory Memorandum Report NRL/MR/7533-93-7213.

Hogan, T., T. E. Rosmond, and R. Gelaro, 1991: The NOGAPS Forecast Model: A Technical Description, Naval Research Laboratory NOARL Report 13.

Ravid, E. V., D. Huff and T. Rasmussen, 1997: NODDS - The Next Generation: Joint METOC Viewer, Proceedings of the Thirteenth International Conference on Interactive Information and Processing Systems (IIPS) for Meteorology, Oceanography and Hydrology, Long Beach, CA, Am. Meteor. Society, 203-206.

Schultz, P., and M.K. Politovich, 1992: Toward the Improvement of Aircraft Icing Forecasts for the Continental United States. Wea. Forecasting, 7, 492-500.

Vogel, G. N., and C. R. Sampson, 1996: Clear Air Turbulence Indices Derived from U. S. Navy Numerical Model Data: A Verification Study, Naval Research Laboratory Memorandum Report NRL/MR/7543-96-7223.

Vogel, G. N. 1997: Aircraft Icing Algorithms Applied to U.S. Navy Numerical Model Data: A Verification Study, Naval Research Laboratory Memorandum Report NRL/MR/7543-97-7228.

Vogel, G. N., 1998: Verification of NOGAPS Cloud Forecasts, Naval Research Laboratory Memorandum Report NRL/MR/7543-98-7238.

Infrared Target Scene Simulation Software

Guy Seeley* Radex Inc. and Steve Luker Sencom Inc.
29 Randolph Road, Hanscom AFB, MA 01731
seeley@hurricane.plh.af.mil,sluker@compost.plh.af.mil
AFRL/VSBE

OBJECTIVE:

The Infrared Target Scene Simulation System [IRTSS] is used to produce infrared scene predictions for use by military aircrews and weapons system operators. The system uses categorized multi-spectral satellite imagery to describe the distribution of material types on the earth surface. Surface temperatures are calculated using recent weather history by modeling solar energy input, convective heat loss etc. Atmospheric transmission calculations are performed via MODTRAN and interpolated for scene rendering. A sensor model captures the effect of a specific sensor on the incident radiation. The result is a synthetic scene that predicts what is likely to appear on a weapons system display scope, given current or forecast weather conditions. This paper will summarize recent developments and field experience with the system.

RESEARCH ACCOMPLISHED:

IRTSS employs Internet based technologies for delivery of Weather Impact Decision Aid technology to the warfighter. Internet technology is attractive from several points of view. Platform independence, simplicity of upgrades, a well known user interface paradigm and centralized storage of large amounts of imagery data, are all valuable features of Internet deployment. Figure 1 schematically illustrates the Internet client/server paradigm.

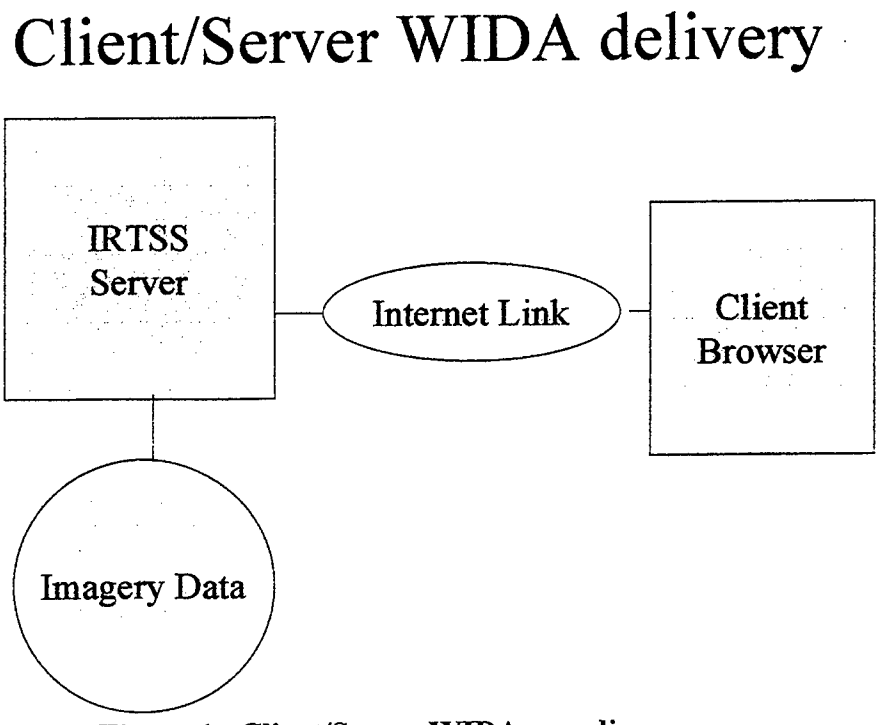


Figure 1 Client/Server WIDA paradigm

This approach has many compelling advantages. The overhead imagery that the system uses represents a large data management challenge. Keeping the imagery stored on a central server reduces the field "footprint" of the system substantially. This architecture keeps the data located close to the rendering system. Only rendered two dimensional images are communicated across the network link. In order to run the system a user needs only a web browser and network connection. The current interface has been largely implemented using CGI /forms. The user selects the geographic area of interest, target location, mission time, approach-heading etc. An example screen is shown in Figure 2. The resulting rendered images appear in the web browser which can be downloaded for use in presentation applications or printed directly to hardcopy.

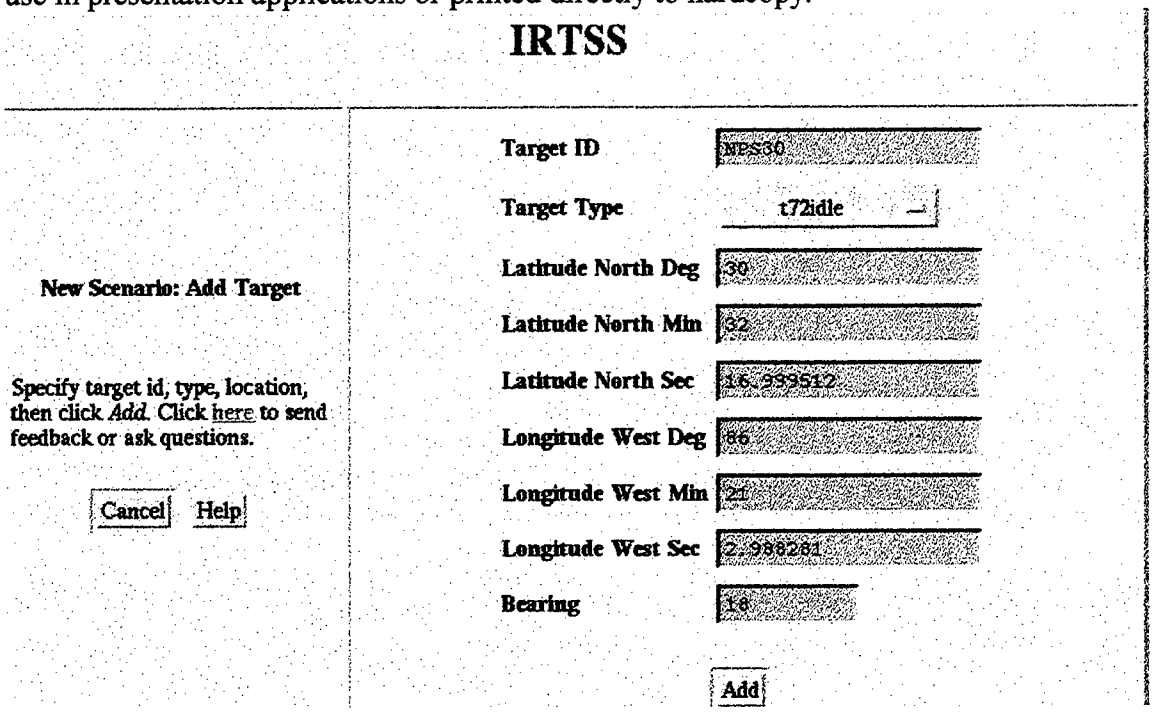


Figure 2 Example IRTSS CGI form

A Java based interface for obtaining automated weather data was recently implemented by Capt. Dana Madsen at AFRL. Java allows more extensive client-side processing of user interface functions. The weather query and editing mechanism is implemented as a Java "applet" that runs inside a client web browser. This applet queries a server at Air Force Weather Agency [AFWA] for an initial set of weather conditions which are transmitted as World Meteorological Organization format observations and Terminal Aerodrome Forecasts [TAF] that are commonly used by operational meteorologists. A meteorologist with local expertise and knowledge to optimize the input weather data can modify the downloaded weather information.

Both visible and 8-12 micron band imagery is available from the system. Figure 3 shows a visible band rendering of a target area. This image is derived from panchromatic satellite data, a three dimensional target geometry has been placed in the center of the scene. The intent of the imagery product is to provide the significant features of a target area in the visible and the IR bands.



Figure 3 A visible band rendering, target at center

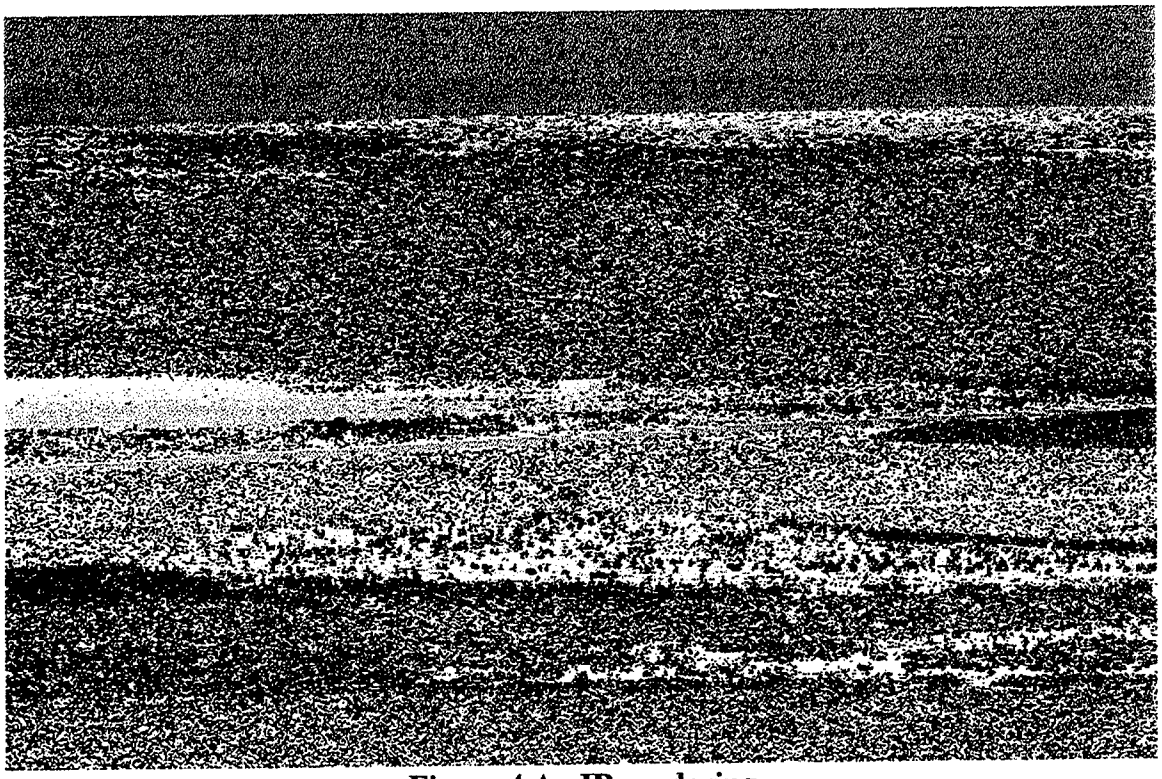


Figure 4 An IR rendering

Numerous 8-12 micron LANTIRN missions have been supported at Fallon NAS. Staff meteorologists at Fallon access the system over the World Wide Web. Feedback from aircrews has been generally very positive.[Wos98] The Fallon crews say that the combination of rendered imagery with traditional EOTDA lock-on ranges is significantly more valuable than EOTDA or imagery support alone. They have reported reasonably good agreement between the IRTSS scenes and traditional EOTDA output. Fallon personnel have pointed out that the IRTSS user interface, while having several good features is not easily utilized by unsupervised E-4 grade personnel. Upgrade and simplification of the user interface is ongoing at AFRL.

Our group at AFRL has reviewed several post-mission videotapes for validation purposes. This review has shown good agreement with most geographic features and target locations. There is however some need for improvement in the modeling of desert materials. One particular case involved a considerable amount of water collecting in a dry lakebed. This type of rapid change of surface material is in general extremely difficult to track and incorporate into the generated imagery. Recent surface imagery that reflects the current configuration of roads and buildings near a target area is an important ingredient in generating synthetic scenes that are truly useful to weapons system operators.

In the recent Air Force Expeditionary Force Experiment IRTSS was deployed in the Expeditionary Operations Center [EOC] to support the live-fly portion of EFX98. Aircrews were presented with IRTSS imagery during the weather portion of their pre-flight brief. Operation of the system was made more difficult by the presence of firewalls between the client browser and the server system. Reconfiguration of the software and the firewall enabled operations to continue. The bandwidth available in the EOC was inadequate for efficient operation. This bandwidth problem affected many other systems trying to use the same network and was not unique to IRTSS. Bandwidth requirements need to be reduced wherever possible to allow system use in real-world communications environments. Aircrew members felt that the imagery product was useful to them in conducting their missions, unfortunately we were not able to gather detailed post-mission validation data for the flights.

IRTSS was recently evaluated in a thesis study conducted by Major Eric V Bryant, [Bryant98] USMC, at the Naval Postgraduate School. The study compared the effects of two mission planning visualization tools, IRTSS and TOPSCENE (a visible-only scene generator), to a baseline mission planning briefing consisting of 2-D imagery and detection/lock-on range predictions from the Electro-Optical Tactical Decision Aid (EOTDA). Three test groups consisting of seven experienced pilots were used in the study. Each group received standard aircrew mission briefs, some with the addition of IRTSS or TOPSCENE imagery. The pilots were then shown Forward-Looking Infrared (FLIR) sensor mission video for seven different targets located on the B-17 Range at NAS Fallon. Bryant concluded that the IRTSS and TOPSCENE training format had significantly faster aircrew reaction times over the basic aircrew training format that included only photos and maps of the respective targets.

Figure 5 [constructed from Bryant's data] shows a reduction in target recognition time by pilots who had a briefing that included IRTSS information.

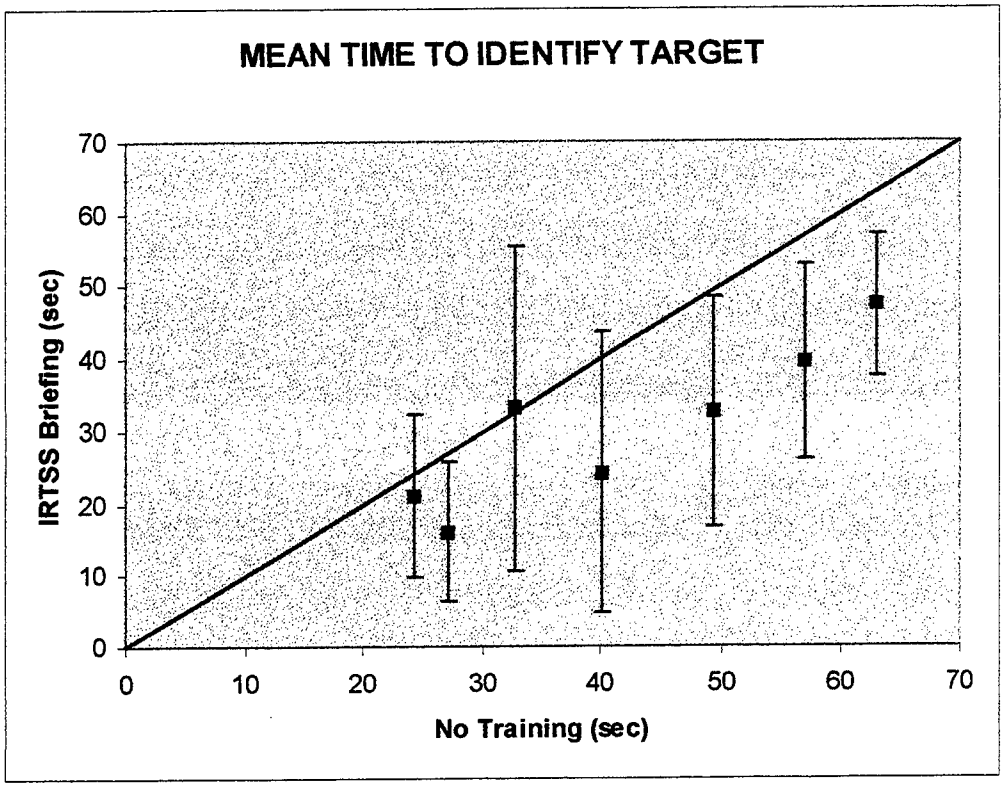


Figure 5 Bryant's target identification data

Although the IRTSS reaction times were a little faster than the TOPSCENE format, there was no statistically significant difference between the two briefing formats. There is, however, a definite and consistent pattern of faster IRTSS reaction times for five of the seven targets, and Bryant offered a logical explanation as to why the first two targets don't follow this pattern. For Target1 the IRTSS image simply was not a very good representation of the FLIR image. For Target2 both the TOPSCENE visible image and the IRTSS infrared image were missing a dirt road in the lakebed that confused subjects whereas the FLIR image showed the road. This only reinforces the importance of accurate imagery support to drive both visible and infrared scene prediction systems. IRTSS relies on an accurate description of the land surface. The Fallon geographic dataset was generated from black and white high-resolution aerial photos. It is difficult to obtain the accuracy needed from single band visible imagery. Undoubtedly there were numerous misclassifications of land use. We believe that a better description of the surface features at NAS Fallon would have allowed IRTSS to significantly reduce aircrew reaction times over TOPSCENE.

CONCLUSIONS:

IRTSS represents a state-of-the-art infrared scene prediction capability that has been deployed over the Internet in a variety of situations. There is some evidence that shows that it aids aircrew in target recognition tasks.

Some disadvantages to Internet deployment have surfaced. Perhaps the most obvious problem is the complete dependence of the system on reliable Internet communications. At times the system is completely useless when communications is disrupted. Another problem that has been observed in field exercises is ungraceful degradation of the system when bandwidth becomes extremely low, various network timeouts can be engaged making the system difficult/impossible to use. These problems affect many new C4I systems and are not unique to weather systems. At the present time it appears likely that a stand-alone capability needs to be in place that can utilize weather and target data from nearly any source.

RECOMMENDATIONS:

Many aspects of IRTSS need continuing development to insure a clearly effective and accurate decision aid. Continuing validation of the IRTSS system is needed to assure accurate performance in diverse environments. Extension to other IR wavebands is needed to meet the requirements of emerging weapons systems. The user interface needs refinement to meet the needs of operational weather officers. Future work will include standardizing geographic data input and producing weapons system efficiency parameters from next-generation algorithms that fully utilize nearly all available information about the battlespace. A significant new capability added to the system is the ability to render clouds in the 8-12 micron and visible wavebands. The development of this capability is detailed in a paper by Ayer presented at this BACIMO conference.

BIBLIOGRAPHY:

Wos98: Wos, Lt. Commander Ken, Weather Impact Decision Aids Conference, Langley AFB VA 1998

Bryant98: "A Process Simulation to Assess Promising Technologies Relevant to F/A-18 Aircrew Target Recognition", Masters Thesis, Naval Postgraduate School, Monterey CA, 1998

WEATHER IMPACTS FOR AGGREGATED SIMULATIONS

Richard C. Shirkey* and Donald W. Hoock
Army Research Laboratory
Battlefield Environment Division
Attn: AMSRL-IS-EW
White Sands Missile Range, NM 88002-5501
Phone: 505-678-5470 (DSN 258)
Fax: 505-678-4449
rshirkey@arl.mil

ABSTRACT

The natural environment is an important factor in determining the outcome of real battles. However playing weather effects in high level simulations is currently in its infancy. These types of simulations deal with aggregated units that can not afford to include physics-based calculations that are computationally burdensome for individual platforms and systems. Thus, a completely new approach is needed to include weather at an appropriate level of fidelity that maintains "faster than real time" simulation capability. We present here such an approach using the rule-based Integrated Weather Effects Decision Aid model (IWEDA) tied with physics-based detection algorithms such as the Night Vision and Electronic Sensors Directorate's Range Performance Model for Target Acquisition Systems, ACQUIRE. We then show how, for given sensors, target and background types, probabilities of acquisition under various weather conditions can be tied directly to rule-based results resulting in weather penalties that are not computationally burdensome to wargames.

1.0 Introduction

Weather and the dynamic natural environment are important factors in determining the course and outcome of real battles. They affect virtually all battlespace functional areas from logistics and maneuver to C4I and combat engagements. Environmental data such as terrain elevations, soil moisture, accumulated snow cover, and gridded meteorological parameters are examples of the basic parameters that characterize the environment. To be useful in war games and in constructive and virtual combat simulations, however, these data must be transformed into features, effects and impacts. Included in this area are weather features (clouds, fronts and thunderstorms, etc.), weather effects such as illumination, thermal emission, scattering and propagation losses that drive target contrast changes, and weather impacts that broadly describe the general environmental limitations on performance. Thus weather, atmospheric transport and diffusion processes, and the attenuating effects of the environment on the propagation of electromagnetic energy all impact target acquisition and high technology weapons performance.

However "playing" weather in simulations is currently in its infancy. Meteorological data and weather scenarios are becoming available through efforts such as the Defense Modeling and Simulation Office's Weather Scenario Generator (WSG) [Lowe, 1998] and the Master

Environmental Library (MEL) [Lowe, 1997]. But converting these meteorological parameters and weather features into quantitative effects and impacts that are not computationally burdening for simulations is a difficult proposition.

Due to the dynamic range of atmospheric processes, weather effects models must represent a spectrum ranging from small-scale, detailed effects, necessary to correctly visualize scenes, to large-scale, general representations of aggregated weather impacts. While progress has been made in this area in recent years, notably in the DARPA Synthetic Theater of War - Synthetic Environments (STOW-SE) [Shirkey, 1996] program, such efforts require dedicated hardware and pre-computed weather effects scenarios. The underlying models in these simulations are inherently computationally intensive. Engineering level line-of-sight propagation models from ARL's Electro-Optical Systems Atmospheric Effects Library (EOSAEL) [Shirkey, 1987] and the Air Force Research Laboratory's MODTRAN [Berk, 1989], while fast, are still burdensome considering the playing area, the potential number of lines-of-sight between entities and the number of pixels needed to generate virtual scenes.

At the other end of the spectrum are the high level simulations that deal with aggregated units. These simulations simply can not afford to include too many detailed calculations for individual platforms and systems. Thus, a new approach is needed to include weather at a realistic level of fidelity and still maintain "faster than real time" simulation capability. Such an approach exists in using rule-based programs, such as ARL's Integrated Weather Effects Decision Aid (IWEDA) model [Sauter, 1996].

2.0 The Integrated Weather Effects Decision Aid (IWEDA)

The Integrated Weather Effects Decision Aid (IWEDA) is a rule-based weather impact model that supports Army weather doctrine. IWEDA allows for simple and fast estimation of weather impacts over large areas (typically 500 x 500 km at 10 km resolution) on units containing a mix of platforms, sensors and weapons. IWEDA currently provides this information through the Army's Integrated Meteorological System (IMETS) which is a fielded tactical weather C4I system. IWEDA displays impact information in the form of red/amber/green (unfavorable/marginal/favorable) common-map overlays derived from 4-D grids of weather impact data. IWEDA includes Army, Air Force, Navy and limited threat systems. Information is provided not only for sensor systems, but also for many other types of weather impacts, such as degraded performance of ground-staked communications antennas under high wind conditions, or diesel vehicles failing to start because of low temperatures. IWEDA is currently coupled to real-time and forecast weather data through the IMETS. However, it can be easily modified to use other sources of meteorological data for its inputs. An example IWEDA display is shown in Figure 1.

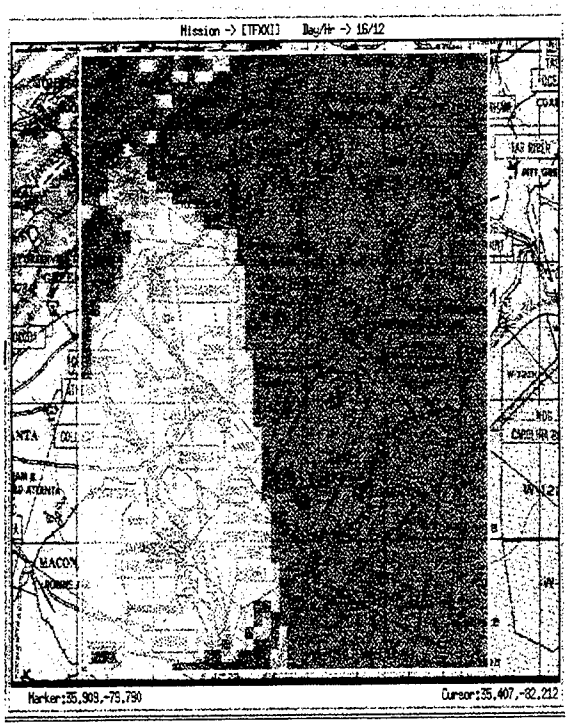


Figure 1. Example IWEDA Weather Impacts Map Overlay

Detailed analysis for the impacted system or sensor can be performed by clicking on any point, shown as a small circle in Figure 1, in the red (or amber) region. The result displays which units and weather conditions produce the red (or amber) condition. As a C4I tool, IWEDA does not dictate a course of action, but only informs the commander that there will be weather impacts or "penalties" on the force (friendly or threat). This color-coded weather impact paradigm can be adapted for use in wargames and simulations simply by linking the red/amber/green matrix to the actual weather simulation values to be imposed on the players.

IWEDA's approach differs from a physics-based modeling approach in that IWEDA is based on a large number (approximately 1000) of weather impact "rules". Each "system" has its list of "sub-systems" and their relevant weather impact rules. Each rule definition includes red-amber-green "critical value thresholds" for one or more of the meteorological parameters that affect the sub-system. These weather impact rules and critical values have been validated through TRADOC organizations, Field Manuals and NGIC for the various systems.

3.0 Approach to Using Rule-Based Impacts in Simulations

In training simulations weather may be used to control the game tempo or to penalize certain classes of players. Thus, for example, an exercise manager might call for a dust storm as the reason to ground all UAV's in a simulation, or ground fog might be imposed to require that the virtual simulators turn on a "fog function" to reduce lock-on ranges. In such simulations IWEDA would provide quantitative guidance for determination of environmental effects and performance impacts relevant under differing meteorological conditions.

The use of IWEDA-like rules and critical value thresholds would also help to identify where the investment in the more detailed physics-based model calculations are most valuable during a simulation. This arises in hybrid simulations that treat many processes at the aggregate unit level. When close enough for engagement, as defined, for example by a target acquisition event, these units then are de-aggregated into individual platforms, weapons and sensors in some doctrinally-defined deployment for playing the detailed line of sight geometries and one-on-one engagements. IWEDA would help define the environmentally driven estimates, such as how close the friendly and threat units need to come before de-aggregation is useful.

The idea of using IWEDA to provide quantitative degradation factors, weather penalties and probabilities also extends to modifying various other parameters in aggregate simulations. These can include Lanchester attrition rates, target acquisition search rates, casualty rates due to heat stress, environmental limitations on mobility and re-supply, and frequency of maintenance down time. One specific example might be to identify game zones where it is snowing and the forecast temperature is low. The impacts for this snow condition could include: severely degraded target acquisition range values and increased search time using visual and IR sensors, larger false alarm rates and signal-to-noise requirements for detection when using MMW sensors, increased thermal contrast values for warm targets moving over cold snow, different reductions in on-road and off-road mobility rates, more rapid rates of personnel fatigue and human error, etc. It is important to understand that IWEDA currently does not produce the actual attrition rate factors, reduction factors in maneuver speed, increase in target contrast, etc. These need to be predetermined and identified with the environmental critical weather value thresholds used in IWEDA as shown below.

In that regard, and for potential use in the IMETS C4I tactical weather intelligence system, ARL is in the process of linking IWEDA's rule-based weather impact software with various physics-based tactical decision aids. These efforts would help to provide the quantitative performance factors and probabilities applicable for keeping aggregated simulations running at faster than real time rates.

4.0 Methodology and Results

A bridge between IWEDA and combat simulations can be made by quantifying the meaning of the IWEDA red/amber/green categories in terms of degradation factors that can be applied as performance penalties or modified conditional probabilities within aggregated simulations. These factors are then imposed on each system or operation being played at weather-impacted grid locations and times.

Although IWEDA can be applied to other scenarios, we consider here only sensor target acquisition and engagement weather impacts for a generic 2nd generation FLIR. Detection algorithms contained in the Night Vision and Electronic Sensors Directorate's Range Performance Model for Target Acquisition Systems, ACQUIRE [ACQUIRE, 1995] are employed. ACQUIRE is an analytical model that predicts target acquisition performance of

This can be quantified even more precisely by considering the probability of target acquisition across many-on-many aggregated units. If there are N targets in an aggregated unit being looked for by M sensors in a different aggregated unit, then the probability that at least one sensor will detect at least one target is [Olsen, 1994]

$$P_{\text{det}} = 1 - (1 - P_{\infty})^{M_{sensors} N_{targets}} \qquad (1)$$

where P_{∞} is the probability that a single sensor will detect a single target. With these multiple sensors and targets, it is easy to see that when $M_{sensors}$ $N_{targets}$ = 14, then a P_{∞} of just 5% is enough to produce a P_{det} of 50%. The implication is that the atmospheric impacts on individual firers are greater than on aggregate units. The individual firer at 5% probability of detection would need to be at least 52% closer under amber conditions and at least 67% closer under red conditions to achieve the same attrition rate as in clear air.

Finally, we can cite the impacts on the DIVLEV aggregate model [AMSAA, 1983]. In that model, the effects of an atmospheric penalty factor were included in the kill rates when smoke was present. For engagements at the same fixed range, the effects of reduced visibility due to smoke were to reduce kill rates to 60% of clear air for tanks using thermal sights and 16% of clear air kill rates for all other direct view weapons.

5.0 Conclusions

IWEDA weather impact decision aids offer a convenient way to play weather in aggregate simulations for those cases where detailed geometric line of sight calculations are not needed. The impact critical value thresholds can be tested against the scenario weather across the play area. Where amber or red conditions prevail, the war game or simulation can impose a relative penalty on the system due to weather. The exact form of that penalty can not be determined from IWEDA alone, however. In some cases (such as target acquisition) it requires that a detailed analysis be performed off line using physics-based models. For other weather impacts, however, it is likely that simple penalty factors will be sufficient, such as general reductions in vehicle speeds, increased rates of casualty due to fatigue, etc.

ACQUIRE has been run with a selected sensor and for given weather conditions. This methodology allows a specific cell within IWEDA's weather matrix to immediately provide: 1) a determination of whether or not a given target can be detected at a queried range and 2) given the target range, what is its probability of acquisition. The results can be viewed directly in the IWEDA displays and can be stored in files for table lookup during simulations.

References

1. Lowe, S., et. al., 1998, "Weather Scenario Generator: System Design and Project Status", Simulation Interoperability Workshop, 98S-SIW-090, http://sisostds.org/, September.

2. Lowe, S., et. al., 1997, "Product Generation within the Master Environmental Library (MEL)", Simulation Interoperability Workshop, 97S-SIW-160, http://sisostds.org/, April.

3. Shirkey, R.C., Turner, J., Schaffer, R., 1996, "Atmospheric Modeling in the Synthetic Theater Of War (STOW 97)", in the Proceedings of the Battlefield Atmospherics Conference, San Diego, CA, NraD Technical Document 2938, December. [ADA 344056].

4. Shirkey, R.C., L.D. Duncan, F.E. Niles, 1987, EOSAEL 87, Volume 1, Executive Summary, U.S. Army Atmospheric Sciences Laboratory Technical Report ASL-TR-0221-1, White Sands Missile Range, NM.

5. Berk, A., Bernstein, L.S., and Robertson, D.C., 1989, "MODTRAN: A Moderate Resolution Model for LOWTRAN 7", GL-TR-89-0122, Air Force Research Laboratory, Hanscom Air Force Base, MA, April. [ADA 214337].

6. Sauter, D., 1996, "The Integrated Weather Effects Decision Aid (IWEDA): Status and Future Plans," in the Proceedings of the Battlefield Atmospherics Conference, San Diego, CA, NraD Technical Document 2938, December. [ADA 323038].

7. "ACQUIRE Range Performance Model for Target Acquisition Systems," 1995, Version 1 User's Guide, U.S. Army CECOM Night Vision and Electronic Sensors Directorate Report, Ft. Belvoir, VA, May.

8. Fiegel, R.P., 1994, "Natural Aerosol Extinction Module, XSCALE", U.S. Army Research Laboratory Technical Report ARL-TR-273-1, Adelphi, MD.

9. Shirkey R., and Hoock D., 1997, "Battlefield Atmosphere Applications for the Master Environmental Library (MEL)", in Proceedings of the International Test and Evaluation Association, December http://155.148.25.235/ITEA/itea97/papers/IntTooCo/IntTooCo.html.

10. Olsen, A.C., 1994, "Casualty Assessment for Expected Value Models," in Military Operations Research Handbook, Vol I, Terrain, Unit Movement, and Environment, W.K Olsen, ed., April.

11. AMSAA Combat Support Division Interim Note No. C-124, 1983, "Computation of Direct-Fire Weapon Kill Rates for DIVLEV," unpublished, June.

STATISTICAL DESCRIPTION OF DETECTION RANGE FOR AN INFRARED MISSILE SENSOR

Espen Stark
Norwegian Defence Research Establishment
Division for Electronics
P O Box 25
N-2007 Kjeller
Norway
Phone: +47 63807282 Fax: +47 63807265
E-mail: Espen.Stark@ffi.no

1. INTRODUCTION

Imaging sensors with sensitivity in the infrared waveband are widely used in military applications. When this type of sensor is used as a missile sensor it is of great importance to know the target detection range in different operational scenarios, i.e. as a function of target contrast and size, missile flight profile, meteorological situation and sensor performance. This paper describes a model for determining the detection range, using an imaging infrared missile sensor for detection of ship targets. The model shows how the detection range can be computed using an equation describing the sensor's signal to noise ratio. The detection range is computed taking into account the sensor performance, the atmospheric transmittance (calculated from meteorological data using Modtran), missile altitude, the earth curvature, target size and contrast against the background. The detection range can thus be computed for each specific meteorological situation.
By regarding the meteorological situation as a stochastic variable, the sensor's detection range may also be regarded as a stochastic variable within a certain time interval. By using meteorological data within a certain time interval at a given position, a statistical description of detection range can be made (i.e. a normal period of 30 years).
Some examples are presented, for a near sea skimming missile, to illustrate how ship size, earth's curvature and climate influences the detection range statistics. The results presented are valid for a sensor operating in the 8-12 μm band. Since the model is based on a spectral description it can be used for any infrared sensor with optical bandwidth within the spectral range ~2-16 μm.
The results presented are based on the performance of an infrared sensor, named "Basis", developed at the Norwegian Defence Research Establishment. "Basis" is an imaging sensor, operating in the 8-12 μm band, originally developed as an IRST for Norwegian Naval ships. Detection range statistics are computed for a cruiser, frigate and a patrol boat to illustrate target size effects. The influence of climatic differences is shown using meteorological data from northern and southern part of Norway.

2. OBJECTIVE

The objective for developing the model described in this paper is to obtain high spectral flexibility in computation of detection range for infrared sensors detecting ship targets and other

objects against the horizon. The model will also be used to evaluate detection range performance for various missile seekers and ship IRST systems.

3. THEORY

The infrared sensor signal-to-noise ratio is given by the following equation:

$$\frac{S(R)}{N} = \frac{A_s \Omega}{\sqrt{A_d \Delta f_n}} \int_0^\infty \left\{ N_{tgt}(\sigma) - N_{bgr}(\sigma) \right\} \tau_a(\sigma, R) \tau_s(\sigma) D_d^*(\sigma)\, d\sigma \qquad (1)$$

where

A_s	-	the sensor's aperture	[cm^2]
Ω	-	solid angle given by the sensor's instantaneous field of view when it's filled with the target, eventually given by the size of the target and the range to the target if it's not filled	[sr]
A_d	-	area of one detector element	[cm^2]
Δf_n	-	noise bandwidth in detector readout electronics between the detector elements and A/D-converter	[Hz]
$N_{tgt}(\sigma)$	-	spectral radiance from the target (σ - wavenumber [cm^{-1}])	[W/cm^{2}sr cm^{-1}]
$N_{bgr}(\sigma)$	-	spectral radiance from the background	[W/cm^{2}sr cm^{-1}]
$\tau_a(\sigma,R)$	-	spectral atmospheric transmittance, function of the range, R, between the sensor and the target	
$\tau_s(\sigma)$	-	sensor spectral transmittance from the dome to the detector window	
$D_d^*(\sigma)$	-	detector spectral detectivity; normally determined by measurements of a complete detector	[cm Hz$^{1/2}$/W]

We will assume that the target (the ship) is detected against a sky background just above the horizon. This is normally the case if the missile altitude is low (sea-skimming missile). At higher altitudes the missile will «see» the sea-surface as the background. In this case a model describing the spectral radiance from the sea-surface then needs to be included. Further we assume that both the background and target radiates as black-bodies, which is a very good approximation for the sky just above the horizon and most targets. The background is a black-body radiating at the atmospheric temperature, T_a, and the target is radiating as a black-body with a temperature that differ from the atmosphere temperature given by $T_{tgt} = T_a + \Delta T$. The difference in radiation between the target and background is then given by:

$$\int_0^\infty \left\{ N_{tgt}(\sigma) - N_{bgr}(\sigma) \right\} d\sigma = \int_0^\infty \left\{ N_{bb}(\sigma, T_a + \Delta T) - N_{bb}(\sigma, T_a) \right\} d\sigma \approx \Delta T \int_0^\infty \left(\frac{\partial N_{bb}(\sigma, T)}{\partial T} \right)_{T_a} d\sigma \qquad (2)$$

Where $N_{bb}(\sigma,T)$ is the black-body spectral radiance (the Planck function). The last approximation in equation (2) is a good approximation for ship targets where the temperature difference, ΔT, normally is small. The model does not contain any information about the specific

ship infrared signature. Ships usually have «hot-spots» that will have a higher temperature than the rest of the ship, e.g. funnel/plume. Such spots can give a longer detection range than the one predicted by the model.
The spectral detectivity of the sensor can be expressed as:

$$D_d^*(\sigma) = r_d(\sigma) D_d^*(\sigma_p) \tag{3}$$

Where $D_d^*(\sigma_p)$ is the maximum value of the detector spectral detectivity, and $r_d(\sigma)$ is the relative spectral responsivity of the detector. For an ideal detector the relative spectral responsivity is defined by:

$$r_d(\sigma) = \begin{cases} \sigma_p / \sigma & \sigma_u \geq \sigma \geq \sigma_l ; \sigma_p \leq \sigma_l \\ 0 & other \end{cases} \tag{4}$$

The signal to noise ratio, with the assumptions above is then given by:

$$\frac{S(R)}{N} = \frac{A_s \Omega}{\sqrt{A_d \Delta f_n}} D_d^*(\sigma_p) \Delta T \int_0^\infty \left(\frac{\partial N_{bb}(\sigma, T)}{\partial T} \right)_{T_a} \tau_a(\sigma, R) \tau_s(\sigma) r_d(\sigma) d\sigma \tag{5}$$

In equation (5) the solid angel Ω is defined by the area of the target giving signal to one detector element divided by the squared range. If the total area of the target is less than the sensors instantaneous field of view, Ω_s, at the range, R, then the solid angel is defined by:

$$\Omega = \frac{A_{tgt}}{R^2} \tag{6}$$

Where A_{tgt} is the area of the target.

In this model the target is defined by two rectangles. These rectangles and the dimensions for the three targets are shown in figure 1.

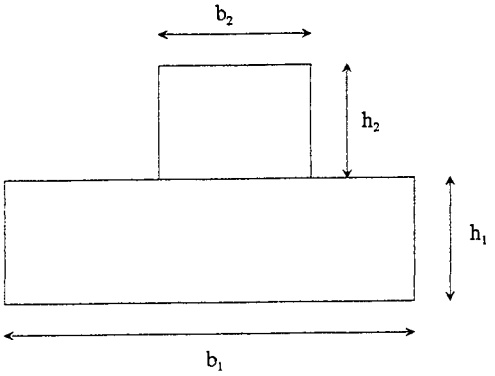


Figure 1. Definition of targets

Ship type	h_1 [m]	h_2 [m]	b_1 [m]	b_2 [m]
Patrol boat (bow)	3.0	2.4	6.2	6.2
Frigate (broadside)	5.5	7.3	135.6	69.6
Cruiser (broadside)	11.8	11.8	172.8	64.7

Due to the curvature of the earth parts of the target will not be visible from the missile sensor when the missile is flying at a given altitude. The distance from the missile to the horizon at a missile altitude, h_{mis}, is given by

$$R_{hor} = \sqrt{h_{mis}\left(h_{mis} + 2R_{earth}\right)} \tag{7}$$

where R_{earth} is the radius of the earth. When the range from the missile to the target is greater than the distance to the horizon the lower parts of the target will be «invisible». Dependent of the missile altitude and the range to the target, parts of the ship will be below the horizon. The height above the ship's waterline shaded by the horizon, h_{inv} is:

$$h_{inv} = \left\{R^2 + \left(h_{mis} + R_{earth}\right)^2 - 2R\sqrt{h_{mis}\left(h_{mis} + 2R_{earth}\right)}\right\}^{1/2} - R_{earth} \tag{8}$$

This reduction in target area is taken into account in this model when the solid angle Ω in equation (5) is determined. However, refractive effects are not taken into account. Refractive effects will affect both the distance to the horizon and the height shaded by the horizon.

To obtain detection the signal to noise ratio must exceed a certain value, c_{th}.

$$\frac{S(R)}{N} \geq c_{th} \tag{9}$$

By combining equation (5) and (8) the result is:

$$\frac{A_s \Omega}{\sqrt{A_d \Delta f_n}} D_d^*(\sigma_p) \Delta T \int_0^\infty \left(\frac{\partial N_{bb}(\sigma, T)}{\partial T}\right)_{T_a} \tau_a(\sigma, R)\, \tau_s(\sigma) r_d(\sigma)\, d\sigma \geq c_{th} \tag{10}$$

In a given meteorological situation the only unknown is the range to the target, R, when the temperature difference, ΔT, is chosen. By solving the equation numerical at equality the longest range where the target is detected is obtained. This range is called the detection range, R_{det}. The equation is solved by using the bisection method to compute the root. This involves computing the atmospheric transmittance using Modtran for the desired spectral range several times for each meteorological situation, which is time consuming. We have therefore used a different approach to reduce the computing time. The transmittance for monochromatic radiation is given as:

$$\tau_a(\sigma, R) = e^{-k(\sigma)R} \tag{11}$$

Where $k(\sigma)$ is the extinction coefficient for a specific wavenumber. If we assume that the relation in equation (11) is valid for each wavenumber when transmittance is calculated at maximum spectral resolution using Modtran, then the extinction coefficient can be found by calculating the transmittance for one reference range e.g. 10 km.

$$k(\sigma) = \frac{-\ln \tau_a(\sigma, 10\,km)}{10\,km} \tag{12}$$

This relation is not quite correct since Modtran is a band model [Berk et al., 1989], with a resolution of $2cm^{-1}$. Tests has shown that the error in computed transmittance using the extinction coefficient calculated at 10 km is less than 5% for ranges up to 40 km. This error is tolerable and it is probably less than the error in the meteorological data. Using this approach a database consisting of extinction coefficients calculated for a spectral range from 2 to 16 μm for a set of meteorological observations along the Norwegian coast is made. Then by using equation (11) in equation (10) and still using the bisection method computing time is reduced dramatically, from about 1 week to a few minutes to solve the equation for one meteorological station for a 30 year period (on a Pentium II machine).

For a number of meteorological situations, N, a detection range will exist for each meteorological situation. A statistical description of the detection range within a given time interval can then be made. If the meteorological situation is regarded as a stochastic variable then the detection range is a stochastic variable. To give a statistical description of the detection range the probability density function (pdf) is chosen, $p(r)$. From this probability density function the distribution function can be found:

$$P(R_{\text{det}} \le R) = \int_0^R p(r)\,dr \tag{13}$$

The mean value, the variance and the median value can also be determined. To generate a statistical description, meteorological data for a given period of time and/or several meteorological stations is needed. The Norwegian Meteorological Institute deliver meteorological data from numerous stations in Norway (908 observing stations). Several meteorological parameters are being observed four times a day, at 1 am, 7 am, 1 pm and 7 pm. Among the observed parameters are; air temperature, pressure, relative humidity, sea temperature (if there is sea nearby), rainfall rate, optical visibility, type of weather, wind speed and so on. All these parameters are being used to generate a user-defined atmosphere with a navy aerosol model for Modtran calculation. In a meteorological context a normal period is 30 years. To make a statistical description of the detection range, a normal a period of 30 years is chosen. This gives 43800 observations for one meteorological station.

4. RESULTS

In this section some results are being presented to illustrate detection range statistics. First statistical description of the detection range against three different ships, a small patrol boat (bow aspect), a frigate (broadside) and a cruiser (broadside), at Sletnes in Finnmark (71.08°N, 28.22°E) is shown. The meteorological data used is from the period 1964-1994. The missile is an imaginary anti-ship missile using "Basis" as an imaging infrared sensor. This is an 8-12 μm sensor, and the specifications for the sensor (as used in the calculations) is shown in table 1.

Optical bandwidth		7.5 - 10.3 μm
Instantaneous field of view	Ω_s	0.18 mrad × 0.18 mrad
The sensor's aperture	A_s	60.4 cm^2
Noise bandwidth	Δf_n	25 kHz
Max. detectivity	$D_d^*(\sigma_p)$	8×10^{10} cm $Hz^{1/2}/W$
Sensor transmittance[1]	$\tau_s(\sigma)$	1
S/N needed for detection	c_{th}	5

Table 1. Specifications for the «Basis» sensor

In the following computations of detection range statistics the missile altitude is 10 meters, and the sensor requires a signal-to-noise ratio of 5 to perform detection. The targets all have a temperature difference, ΔT, of 5K against the background. Figure 2 shows the detection range probability density function, and the distribution function.

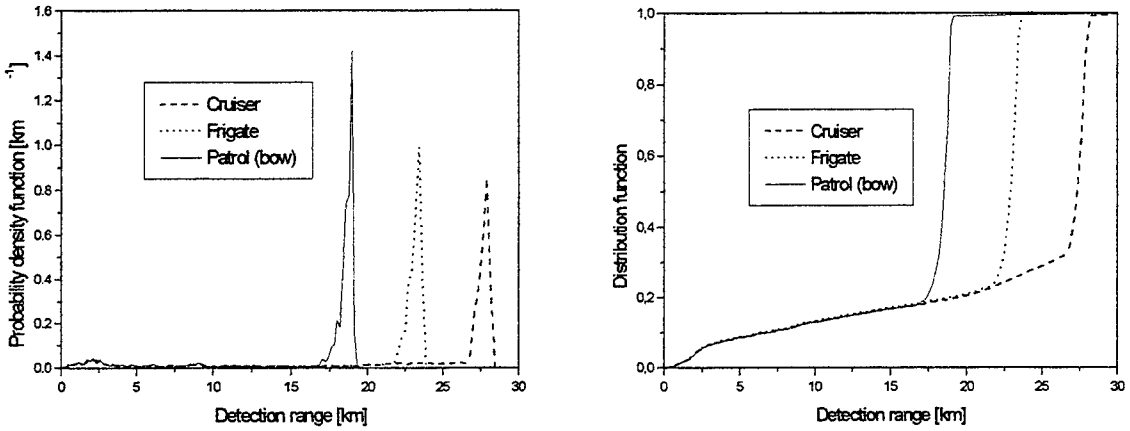


Figure 2. Detection range probability density function and distribution function at Sletnes (71.08°N, 28.22°E); missile altitude 10 m, target temperature difference 5K.

Figure 2 shows that the size of the target, combined with the curvature of the earth and the missile altitude, plays an important role. In this case the atmospheric transmittance is of minor importance. The meteorological station is located in the northern part of Norway, where it is quite cold most of the year and normally high IR transmittance. Snow, rain and fog will obviously give shorter detection ranges. These conditions results in the small peak in the probability density plot between 0 and 5 km. The distribution function shows that the probability is approximately 10% to achive a detection range less than 5 km. To some sense you can say that for 10% of the time the detection range is less than 5 km due to snow, rain or fog. Further the figure shows that detection range is above 22 km approximately 75% of the time for a frigate. With this type of probability density function the median value is a better measure than the mean

[1] The sensor transmittance (from dome to the detector window) is assumed constant within the optical bandwidth and multiplied with the max. detectivity.

value to describe the statistics. From the distribution function it is shown that the median value is respectively 18.4, 22.8 and 27.4 km for the patrol boat, the frigate and the cruiser.

In figure 3 the influence of the climate is clearly illustrated. The missile flight height, sensor data and target ΔT are as specified above, but in this case the target is the cruiser and the statistics is given for two meteorological stations with different climate. One is Sletnes in the northern part of Norway in winter time, where the weather is cold and dry most of the time. The other meteorological station is Ferder (59.03°N, 10.53°E) located in the southern part of Norway, in summer time where it's hot and moist (at least for Norway).

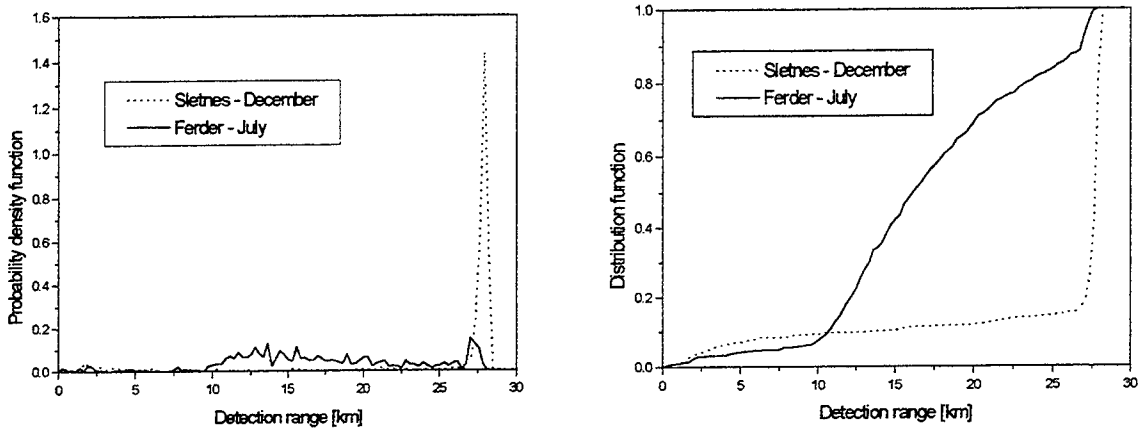


Figure 3. Detection range probability density function and distribution function for detection of a cruiser. Missile altitude is 10 meters, temperature difference is 5 K and the meteorological data is collected at Ferder (59.03 °N, 10.53 °E) in July and Sletnes (71.08 °N, 28.22 °E) in December over 30 years.

In figure 3 the influence of increased absolute humidity and temperature in the atmosphere is clearly shown. The shorter detection ranges at Ferder is mainly due to higher values of absolute humidity, which leads to reduced transmittance in the 8-12 μm-band. In this case the median value is 16.1 km at Ferder in July and 27.7 km at Sletnes in December. The probability density function clearly shows that the variance in detection range is much greater in atmospheric conditions with varying transmittance. At Sletnes in December the probability density function is quite narrow, the variance in detection range is small. This means that in this case the detection range is mainly determined by the size of the target, the missile altitude and the curvature of the earth.

5. CONCLUSIONS AND RECOMMENDATIONS

The model in this paper shows how the sensor signal to noise ratio can be used to compute the detection range. It is also shown how a statistical description of the detection range is made. The model is based on detection of a target (ship) that is detected with the sky just above the horizon as a background. Both the target and the background are assumed to radiate like black bodies. By using Modtran to compute the extinction coefficients for one reference range, and then estimate the transmittance for all other ranges, the computing time are reduced dramatically. This means that the model can extensively be used to evaluate many aspects of the sensor system's performance. It can also be used to evaluate the influence of different target contrasts and sizes.

The model does not take refractive effects into account. Refraction will cause a bending of the radiation from the target. The distance to the horizon and the height shaded by the horizon will be altered. This can be solved by finding the refractivity index profile for each meteorological situation, computed by using e.g. the LWWKD model [Forand, 1997]. The ray bending is then calculated by Snell's law. Work is currently in progress to include this in the model.
The model as described in this paper is valid for sea-skimming missiles. If the model should be adapted to missiles flying at higher altitudes looking down towards a sea background/target, the background model needs to be replaced. The sensor will under these conditions see a sea background where the varying radiation due to the sea surface waves often defines the sensor noise level. Then the radiance from the sea needs to be predicted and this can be done e.g. with SeaRad [Zeisse, 1995].
It is also possible to replace the target model with a specific ship signature. A ship will often have areas that radiates more than the hull, e.g. funnel/plume and engine areas. Such "hot-spots" on the ship can increase the computed detection range.

REFERENCES

Berk, A., Bernstein L. S., and Robertson D. C. 1989. MODTRAN: A Moderate Resolution Model for LOWTRAN 7, Air Force Geophysics Laboratory Technical Report GL-TR-89-0122, Hanscom AFB, MA. [ADA 214337].

Forand J. L. 1997. The L(W)WKD Marine Boundary Layer Model. Defence Research Establishment Valcartier Technical Report DREV-R-9618, Québec, Canada.

Zeisse C. R. 1995. SeaRad, A Sea Radiance Prediction Code. NRAD Techincal Report 1702, San Diego, CA.

This page intentionally left blank.

Meteorological Modeling & Data Assimilation

AN EVALUATION OF THE QUALITY OF LOCAL CLIMATE STATISTICS GENERATED FROM THE OUTPUT OF A 3-D MESOSCALE ATMOSPHERIC MODEL FOR DOD APPLICATIONS IN DATA SPARSE REGIONS

Capt. Matthew K. Doggett*
Tel: (828) 271-4216, Fax: (828) 271-4334
Email: doggettm@afccc.af.mil
Michael Squires, Raymond Kiess
Air Force Combat Climatology Center,
151 Patton Ave, Rm 120
Asheville, NC, 28801-5002

Glenn E. Van Knowe, John W. Zack,
MESO, Inc., Troy, NY

Donald Norquist
AFRL/VSBE
Weather Technology Unit
Offutt Air Force Base, NB

1. OBJECTIVES AND BACKGROUND

The Air Force Combat Climatology Center (AFCCC) is producing high-resolution gridded climatologies by using a method based on a deterministic mesoscale model (Zack et al. 1997). The purpose of the model is to produce high-resolution gridded climatologies over regions with complex terrain or limited observed data. Traditional climatologies generated by summarizing observations made at points are of limited use in mountainous or data sparse regions. This paper examines the initial results of this method and compares the modeled climatologies with the traditional techniques.

AFCCC provides climatological support to Department of Defense agencies. A typical project generates some type of climatological information based on hourly weather data that have been archived from airport weather observations. This is useful information for that site, but in mountainous or littoral regions, the information may not be representative of nearby locations. Another problem is availability of data. AFCCC has data for over 16,000 sites around the world. Many of these sites, however, are located in industrial countries which leaves large regions of the world with few surface weather observations. Even when there is a site that has taken observations, the period of record may be incomplete. Also, the quality of these observations may be subject to the local observing practices and equipment.

There are numerous locations worldwide that have no observing sites. In these areas the local climate is often determined by an interpolation (Inverse Distance Weighting, kriging, etc.) of the nearest point climate information. However, if there are insufficient points or a lack of spatial continuity, the results can be unrealistic since they do not explicitly account for the effects of topography and other mesoscale features.

There are two strategies to help minimize these problems. One can either build a probabilistic or a deterministic model. Probabilistic models have demonstrated an ability to create accurate, high-resolution precipitation and temperature gridded climatologies in complex terrain (Carrega, 1995; Daly et al., 1994). Models of this type use statistical relationships between a particular meteorological element and other information that is available (elevation, aspect, etc.).

If there is sufficient knowledge of the phenomena being estimated, it is possible to use a deterministic model to estimate information where we have no observed data (Isaaks and Srivastava, 1989). Advances in atmospheric numerical modeling systems (ANMS) and computer hardware have now made the deterministic approach possible (Cox, 1998). For AFCCC's purposes, there are

several advantages to using an ANMS coupled with statistical methods. First, ANMS output many other elements in addition to temperature and precipitation such as relative humidity, pressure, wind speed, wind direction, clouds, etc. Second, the information is also output at many levels in the vertical. Additionally, ANMS can be run in parts of the world that have few observational sites. Finally, ANMS explicitly consider the effects of complex terrain and its influence on the mesoscale environment. This ability to have climatologies for many different elements at various levels throughout the atmosphere (surface, 1000 ft., 2000 ft., etc.) for any location in the world is the primary reason AFCCC chose to use a mesoscale model to produce its high-resolution gridded climatologies. The process of producing these climatologies is moving from a prototype stage to a production stage.

2. RESEARCH ACCOMPLISHED

2.1. Methodology Development

MESO Inc. has developed the method called CLImate statistics by a dynamical MODel (CLIMOD) (Zack et al. 1997) based on a deterministic mesoscale model called the Mesoscale Atmospheric Simulation System (MASS) (Manobianco et al.,1996). The methodology involves conducting research for several different climate regimes around the world at a model resolution of 10 km and 40 km. The basic methodology involves initialization of the model with large-scale gridded data fields. The model then uses the large-scale gridded data fields and lateral boundary conditions and periodically ingests the available observed data through one of several possible data assimilation techniques (Newtonian relaxation periodic reanalysis, etc.). Next the model dynamically fuses the available observations with its knowledge of the surface characteristics of the earth and the basic principles of physics to generate estimates of local climate statistics at locations for which no observational data is available.

The method was initially applied and evaluated on a 10-year period in the Eastern Great Lakes Region for the months of January and July (Zack et al. 1997). More recently, the method has been extended to produce data for all 12 months of a 10-year period (1973-1982) over a region in Far East Asia and the Middle East. Model output is created hourly as a 3-D grid on 20 sigma-p levels at both 40 km and 10 km resolutions. The data can then be interpolated to any level or point of interest. The data are then summarized to produce a set of grids and descriptive statistics typically used in climate analysis.

The quality of the CLIMOD method is determined by comparing the model derived climatologies with the climatologies at existing observing locations. NCDC's Global Historical Climatology Network (GHCN) (Vose, et al. 1992) provides extensive coverage of temperature and precipitation monthly means for nearly 500 sites around Far East Asia (Figure 1). At each location, the mean temperature and precipitation for the

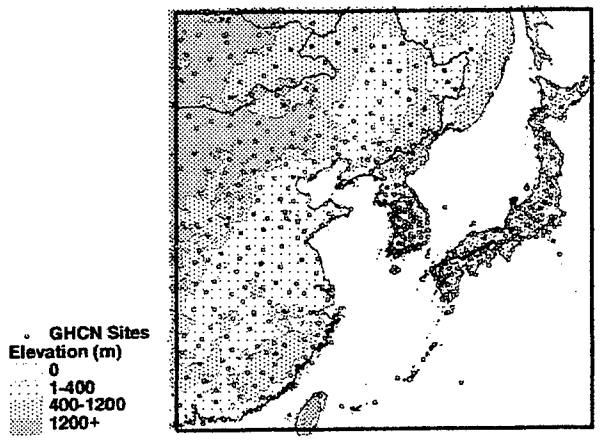


Figure 1. Location of the model domain at 40 Km resolution. Locations of GHCN temperature observing sites are indicated with terrain elevation in meters.

month of January is compared with the model derived mean temperature and precipitation for the same period of record. The modeled values are determined by an inverse distance

weighted interpolation from the nearest model gridpoints to the station location.

2.2. Temperature Results

Typically, when performing a regional climate analysis for our customers, we use the mean temperatures at existing observing sites to construct a contoured analysis for visual interpretation (Figure 2). However, this kind of analysis has several severe limitations.

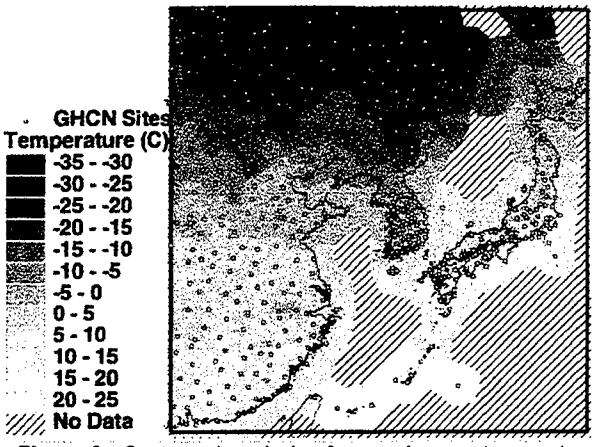


Figure 2. Contoured analysis of mean January temperature from the GHCN. Hatched regions indicate areas beyond 250-km range to the nearest observing site.

First, while observation sites may be fairly dense in some locations, there are large regions over mountainous terrain and especially the oceans where no surface observation sites exist. A second limitation is that a simple interpolation scheme like IDW is not representative between sites where strong mesoscale effects are present (e.g. land/ocean boundaries and mountainous terrain). Another limitation is that climatologies from the GHCN database only include temperature, precipitation, and pressure. While climatologies may be obtained from other sources of surface data, these sources are even more sparsely populated in this region than those in the GHCN.

The use of the CLIMOD method to "fill in the gaps" of the above-mentioned deficiencies is showing some promise. Figure 3 shows the model-derived mean temperature over the entire model domain (40 km resolution). This figure demonstrates that the model is producing a physically consistent climatology that reflects mesoscale climate influences. Most notable are the colder mean temperatures over the mountainous terrain on a mesoscale level.

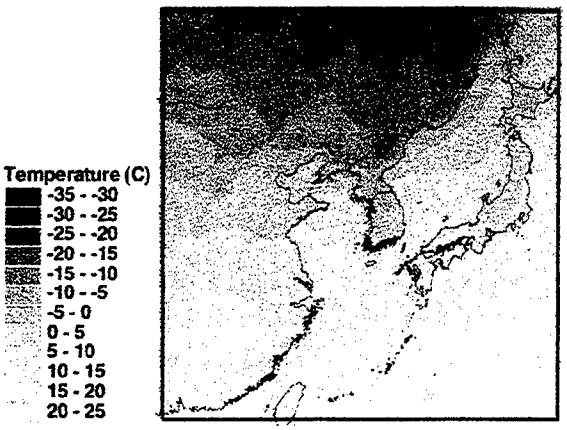


Figure 3. Mean January temperature from the 40km model domain.

Significant differences between the observed and modeled results are shown in Figure 4. Overall, the model tends to have a warm bias of 1.6 °C. This bias, however, is largely a result of the analysis over the oceans. Interpolating over water between land-based observation sites fails to account for the moderating effect the oceans have on air temperature. The model does, however, account for this effect and correctly models warmer temperatures over water. Strictly over the land areas, Figure 4 shows that a majority of the area is within ±1 °C. Another region of significant warm bias is the mountainous terrain in extreme northern China/Russia. Here the model failed to capture the extremely cold mean temperatures seen in this area. There are two possible reasons for this. (1) The vertical resolution of the model near the ground, while higher than in the free atmosphere above the PBL, is still not sufficient to capture shallow inversions which often occur in this region in the winter and contribute significantly to a very low mean temperature. (2) The coarse resolution of the

NMC Reanalysis data used for lateral boundary conditions fails to properly represent these cold shallow inversions. The combination of these two factors results in climatologies that look like the Reanalysis data near the model boundaries.

Many regions where the differences are greatest are located in between the surface observation sites where mesoscale effects such as mountainous terrain or ocean influences are significant. In these areas it is inappropriate to simply interpolate between observations and it is believed the model makes more physical and climatological sense than the observed.

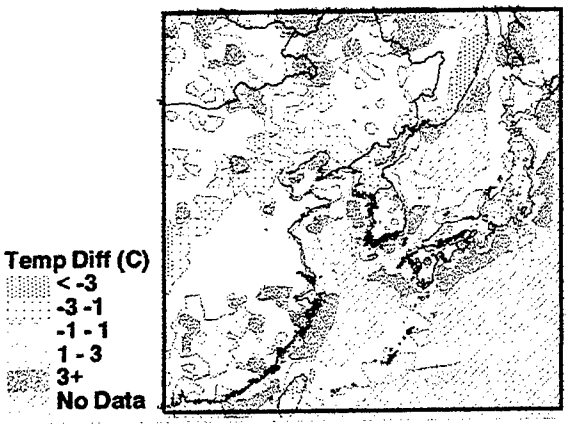


Figure 4. Difference between modeled and observed mean January temperature. Solids indicate regions where the model is warmer than observed.

The CLIMOD performance can be measured by analyzing the differences between the modeled climate and the observed climate at the points where surface observations are recorded. The GHCN provides over 500 observation sites in the region with which to compare the modeled mean temperatures.

An examination of the two distributions reveals several similarities between them (Figure 5). Both modeled and observed show peaks occur near +4, -4, and -18 °C. The model is skewed slightly more toward the warmer temperatures and fails to accurately identify the tail of the distribution at extreme cold temperatures. With the exception of the extreme minimum temperatures, the modeled distribution is remarkably similar to the observed.

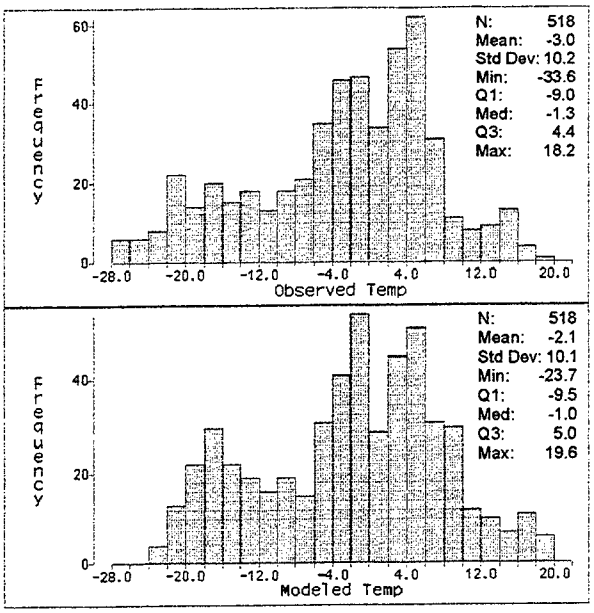


Figure 5. Distributions of observed mean temperature (C) (*top*) and modeled mean temperature (*bottom*) at the GHCN locations.

A scatter plot of modeled vs. observed shows a very strong linear correlation with an R^2 of 0.96 (Figure 6). Only a handful of modeled temperatures depart significantly from observed. A cursory examination of several of these outliers indicates the modeled resolution of 40 km was insufficient to resolve mesoscale features such as terrain and ocean at these locations.

Further examination of the distribution of errors shows that the model has a mean error of +0.8 °C, a mode of +0.3 °C, and is skewed slightly toward a warm bias (Figure 7). Forty-four percent of the locations are modeled within ±1 °C of observed and 75% are within ±2 °C.

These are remarkable results when considering the extremely limited amount of direct observational data that was ingested in the model. Another significant consideration that needs to be made when viewing these results is that this project is only a first attempt at using this method and there is considerable

room for optimizing the methodology and model configuration.

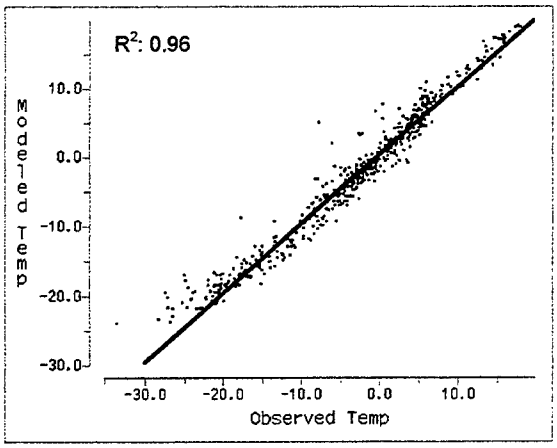


Figure 6. Comparison of modeled vs. observed mean January temperature at GHCN observing locations in Far East Asia.

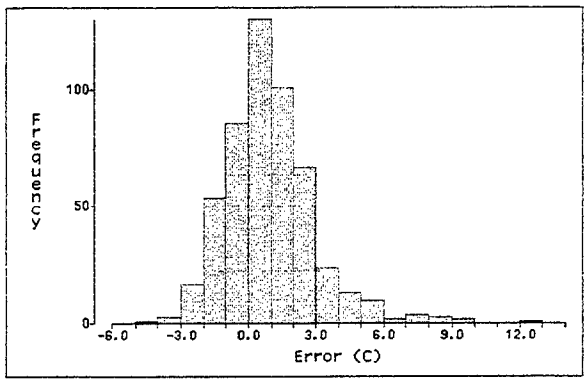


Figure 7. Distribution of the errors in modeled mean January temperature.

2.3. Precipitation Results

The modeled precipitation climatology for the region is shown in Figure **8**. A brief analysis reveals the following characteristics:

1. Precipitation drops off to zero at the model boundaries.*
2. The model correctly identifies mesoscale features such as up-slope precipitation maximums and rainshadow minimums.
3. The rainfall maximum over the ocean southeast of Japan coincides with the observed mean position of the polar frontal zone.
4. The maximum over the northeast region of Taiwan is a result up-slope conditions from the Northeasterly trade winds.
5. The very dry conditions in continental Asia are consistent with observed.

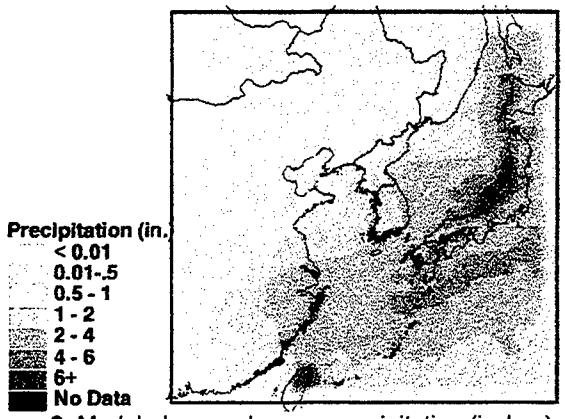


Figure 8. Modeled mean January precipitation (inches).

A comparison of the modeled and observed distributions reveals several similarities (Figure 9). The mean precipitation at all sites is slightly higher from the model than the observed but only by about 10%. The model precipitation amounts are somewhat more spread out but this is largely a reflection of the large difference in the extreme maximums. The differences between the quartiles were all less than 0.10 inches.

In general, the model appears to produce a distribution of precipitation climatology consistent with expected conditions. However, when the modeled precipitation is compared with the observed mean precipitation at the GHCN sites, significant differences are observed.

A scatter plot analysis of modeled vs. observed shows precipitation modeling is much less skillful than temperature modeling. However, it needs to be noted that a 40-km model resolution, which works well for

*Because of this, the observing stations located in this band near the model boundaries have been removed from the following analysis.

temperature, is not adequate to capture fine-scale precipitation patterns that will likely dominate the climatology in complex terrain. Higher model resolution combined with the more complete microphysics will likely have a significant positive impact on precipitation.

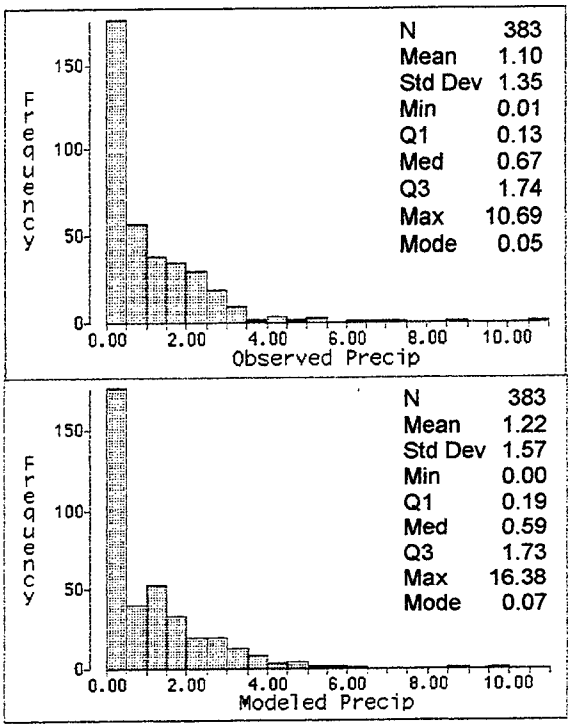


Figure 9. Frequency distributions of observed (*top*) and modeled (*bottom*) mean January precipitation at 383 GHCN sites around Far East Asia.

The traditional linear correlation is compared with the ranked correlation (Figure 10) where the lowest rank corresponds to the driest station. In this analysis, there is a stronger correlation between the driest observed and the driest modeled sites. The locations with the most precipitation are also the same locations where the model is the wettest. The lower traditional R^2 value of 0.53 compared to a much higher rank R^2 of 0.74 indicate that a few deviant pairs are contributing significantly to a low correlation. These locations are identified as A, B, and C in the figure.

Figure 11 shows the error between modeled and observed mean precipitation. As noted earlier, the model appears to be too dry along its boundaries, and since this appears to be a boundary value problem, these sites are not included in this analysis. The regions that appear to contribute significantly to the correlation in Figure 10 are identified as:

A – Taipei, Taiwan

B – Continental Southeast China

C – Four sites in Japan.

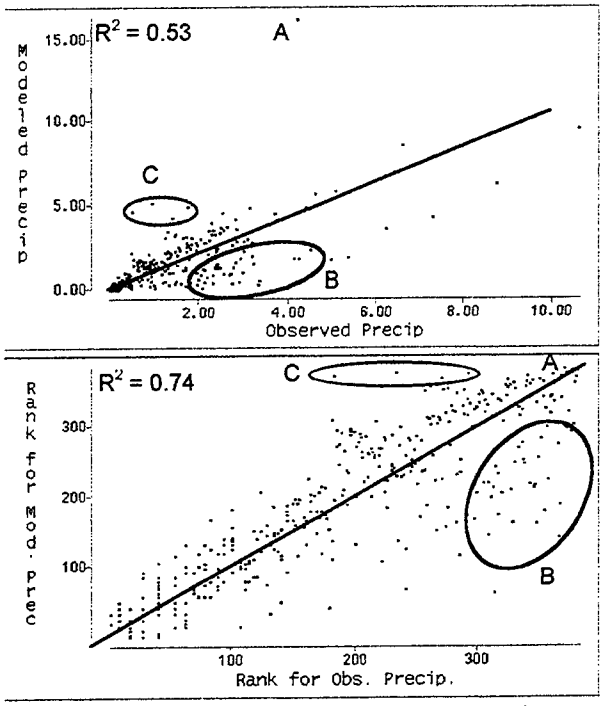


Figure 10. Modeled vs. Observed mean January precipitation at 383 GHCN stations. Bottom is ranked values where the lowest ranks are the driest stations. The solid lines show the expected 1-1 correlation.

Taipei's large discrepancy is a result excessive low-level convergence due to the moisture rich tropical northeasterly trade winds moving into up-slope conditions along the windward side of the island mountains. The island's close proximity to the model boundary is heavily influenced by the coarse Reanalysis data used for lateral boundary conditions. The Reanalysis data is not fine enough to properly resolve Taipei and Taiwan as a whole but the CLIMOD 40 km simulations do. Thus, a conflict is created in the model between the Reanalysis data and the solution from the model in the vicinity of the Island. This conflict creates added

convergence due to the wind differences between the model and the Reanalysis and this leads to extra precipitation. The results for Taipei would likely be significantly better if it were further into the interior of the 40 km grid.

The locations at C present a similar problem. However, all are located within the leeward side of a significant mountain barrier. Although the model does demonstrate the "rainshadow" effects on the leeward side of the mountains, it is apparently not precipitating enough moisture out as systems move across the mountains.

In general, it appears that the model is over-precipitating at many locations where there is mountainous terrain and an ample source of moisture (see Korea and Japan).

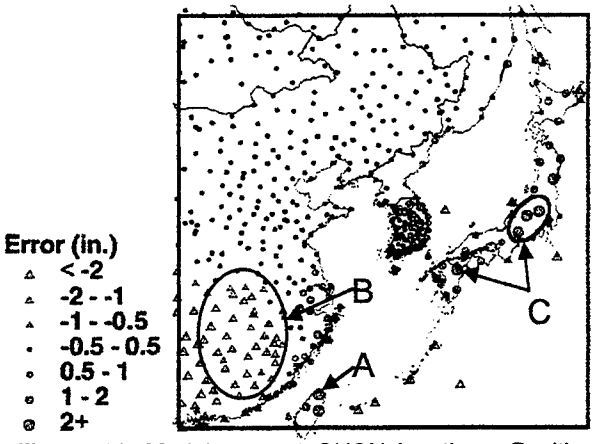


Figure 11. Model error at GHCN locations. Positive values (circles) indicate regions where the model is wetter than observed.

A contrary problem is seen in the locations over continental Southeast China (B) which are much drier than observed. The cause for this appears to be a result of boundary conditions. The model does identify this zone as a region of locally higher precipitation (Figure 8). However, the precipitation amounts quickly diminish to zero inland from the oceans (toward the model boundary).

Ideally a normal distribution of errors strongly peaked near zero is expected (Figure 12). This distribution peaks at 0.04 inches and has a mean of only 0.12 inches. Its skewness is largely influenced by the extreme case at Taipei, Taiwan whose modeled error is in excess of 12 inches (off chart).

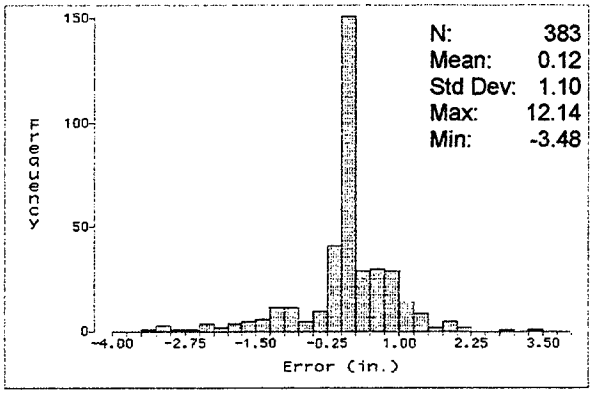


Figure 12. Distribution of errors between modeled and observed mean precipitation at GHCN locations.

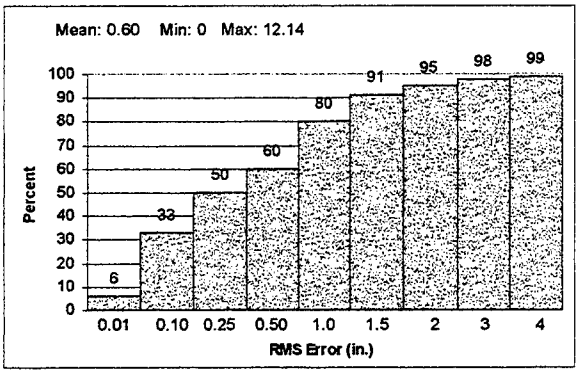


Figure 13. Cumulative frequency distribution of RMS Errors between modeled and observed mean precipitation.

Figure 13 shows the cumulative frequency distribution of root mean square errors (RMSE) between modeled and observed mean precipitation. While the mean error seems rather excessive at 0.60 inches, 50% of the errors were less than 0.25 inches and 80% of the errors were less than 1 inch.

3. CONCLUSIONS

The use of a mesoscale atmospheric model to calculate climate descriptive statistics is producing successful results. The model is very skilled at producing a temperature

climatology with a correlation of 0.96 and a mean error of only 0.8 °C. Although less skillful, precipitation modeling still produced encouraging results. The model demonstrates the ability to identify mesoscale precipitation patterns influenced by the oceans and terrain. With a mean error of 0.12 inches, over 80% of observing sites had an error of 1 inch or less.

The CLIMOD modeling method can be extended to also provide descriptive climatological summaries for dozens of additional DOD impact parameters (e.g. clouds, visibility, IR tranmissivty, winds, thunderstorms, turbulence, icing, soil moisture, frozen ground, etc.). Additional research will be required to determine the model's skill for each of these variables. This project has been a significant first step in developing a methodology that will provide useful climate and historical weather information for the many data sparse regions around the globe. Support for additional development will turn this methodology into a robust production capability.

4. ACKNOWLEDGEMENTS

The authors wish to thank Capt John Thompson for preparing the GHCN data for analysis. Pam Price, and Mary Bousquet of MESO Inc. were invaluable in providing the data needed to perform this analysis.

5. REFERENCES

Carrega, P, 1995: A method for the Reconstruction of Mountain Air Temperatures with Automatic Cartographic Applications. *Theor. and Appl. Clima.*, **52**, 69-84.

Cox, R., B. Bauer, T. Smith, 1998: A Mesoscale Model Intercomparison. *Bull. Amer. Meteor. Soc.*, **79**, 265-283.

Daly, C., R. Neilson, D. Phillips, 1994: A Statistical-Topographical Model for Mapping Climatological Precipitation over Mountainous Terrain. *J. Appl. Meteor.*, **33**, 140-158.

Isaaks, E., R. Srivastava, 1989: *Applied Geostatistics*. Oxford University Press, 561 pp.

Manobianco, J., J. Zack, G. Taylor, 1996: Workstation-based Real-time Mesoscale Modeling Designed for Weather Support to Operations at the Kennedy Space Center and the Cape Canaveral Air Station. *Bull. Amer. Meteor. Soc.*, **77**, 653-672.

Vose, R. S., Richard L. Schmoyer, Peter M. Steurer, Thomas C. Peterson, Richard Heim, Thomas R. Karl, and J. Eischeid, 1992: The Global Historical Climatology Network: long-term monthly temperature, precipitation, sea level pressure, and station pressure data. ORNL/CDIAC-53, NDP-041. Carbon Dioxide Information Analysis Center, Oak Ridge National Laboratory, Oak Ridge, Tennessee.

Zack, J. W., K.. T. Waight III, M. D. Bousquet, C. E. Graves, S. Yalda and G. E. Van Knowe, 1996: An evaluation of local climate statistics generated from the output of a 3-d mesoscale atmospheric model.. Preprints, 11th Conference on Numerical Weather Prediction, Norfolk, VX, Amer. Meteor. Soc., 379-381.

MESOSCALE MODELING OF MARINE REFRACTIVE CONDITIONS DURING THE COAST96 FIELD EXPERIMENT

Tracy Haack* & Stephen D. Burk
Naval Research Laboratory
Marine Meteorology Division
7 Grace Hopper Ave.
Monterey, CA 93943-5502
Phone: (831) 656-4727; Fax: (831) 656-4769
Email: haack@nrlmry.navy.mil

Clive E. Dorman & David P. Rogers
Scripps Institution of Oceanography
La Jolla, CA

Abstract

Marine planetary boundary layer (MBL) characteristics can vary dramatically along coastlines where the marine layer height is confined below that of the coastal topography. Variations in coastal orientation can result in reduced MBL heights and accelerated MBL flow in supercritical regimes south of topographic bends while blocked flow to the north of these topographic features often becomes subcritical, favoring elevated MBL depths and reduced MBL flow. Consequently over the open ocean and in littoral region, the height of electromagnetic trapping layers, which tend to occur at the base of the MBL inversion, can be influenced by changes in the coastline and correlated to changes in flow criticality. In this study we examine the sensitivity of the refractivity field to variations in flow criticality resulting from interaction of MBL flow with coastal orography. Microwave trapping layers and electromagnetic ducting properties of coastal flow regimes are investigated with the use of mesoscale model forecasts that coincide with the collection of observational data during the COAST96 field experiment.

1. Scientific Objective

Abrupt variations in the marine layer along the U.S. West Coast have been studied in conjunction with the orientation of coastal topography by several authors using observational data (Winant *et al.*1988, Rogers *et al.* 1998), hydrodynamics (Winant *et al.* 1988) and shallow water models (Samelson 1992). Figure 1, taken from Winant *et al.*, schematically depicts spatial changes in the MBL observed during the CODE experiment that show the interaction of MBL flow with the Northern California coastline. Variations in the structure of the MBL can also affect the height and strength of refractive trapping layers in some cases causing elevated ducts to become surface based ducts.

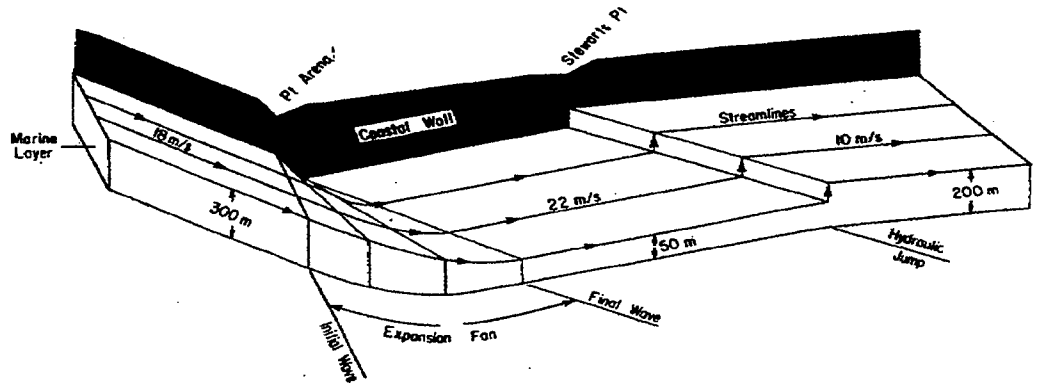


Figure 1: Schematic representation of the MBL structure as it encountered variations in the Northern California coastal topography as measured during the CODE experiment (from Winant *et al.* 1988).

Since flow criticality is an important factor in determining how the MBL responds to the topography, we correlate refractive structure of the MBL to changes in the Froude number $Fr=V/c$, a nondimensional criticality parameter. Here V is the average MBL flow speed, and $c=(g'h)^{1/2}$ is the phase speed of gravity waves travelling along the inversion. The phase speed depends upon the height of the inversion h, and the reduced gravity $g'=g\Delta\theta/\theta$, where $\Delta\theta$ is the potential temperature change across the inversion. Summertime conditions off the U.S. West Coast often produce marine layer flow that is supercritical for which $Fr>1$. Typical summertime synoptic conditions, represented by the warm season climatology composite of Mass and Bond (1996), show a strong cross shore pressure gradient generated by subtropical high pressure over the Eastern Pacific and a thermal low over California's Central Valley. The baroclinic coastal zone produces high speed, northerly low-level winds channeled along the coastal barrier and capped by a strong subsidence inversion confining the MBL below the terrain height. Thus it tends to be bounded both laterally (on one side) and vertically so that shallow water theory applied to channeled flow offers a good first approximation to the MBL dynamics. However, here we are not constrained by shallow water theory and can investigate the supercritical MBL coastal regime with the complexity of a fully stratified, nonhydrostatic mesoscale modeling system. The Navy's Coupled Ocean/Atmosphere Mesoscale Prediction System (COAMPS) (Hodur 1997) contains a full suite of physical parameterization schemes and the flexibility to run both real data assimilation forecasts as well as idealized simulations. We utilize only the atmospheric portion of COAMPS for the present research. The nonhydrostatic, fully compressible equations are formulated after those of Klemp and Wilhelmson (1978).

In supercritical regimes of shallow water flow, the Froude number is greater than unity and perturbations are swept downstream. Thus, a supercritical MBL encountering a convex turn in the coastline exhibits expansion fan behavior associated with isolated localized speed maxima south of the topographic bend. Flow divergence around the bend lowers the marine layer and creates localized pressure gradient accelerations in these locations. In contrast, subcritical regimes have Froude numbers less than unity in which case perturbations can travel freely both upstream and downstream from their point of origin. These transitions in flow criticality are referred to as transcritical flow regimes. While the definition of Froude

number applies to shallow water equations for which a well-defined inversion exists, these quantities are not as readily determined in a real data forecast of fully stratified flow. Thus Froude number values near critical are sufficient for defining transcritical flow. An example of transcritical flow is shown in Figure 2 from the 12 June COAST96 COAMPS case study of flow around Cape Mendocino. Here we have used the 10-m wind field to compute the Froude numbers since the model tended to slightly over predict the MBL flow in this case. Estimates from the COAST96 observational data (Rogers *et al.*, 1998, their Figure 12) implies that although the flow was less supercritical than that modeled, a consistent pattern and transition in flow criticality occurred around the coastal bend.

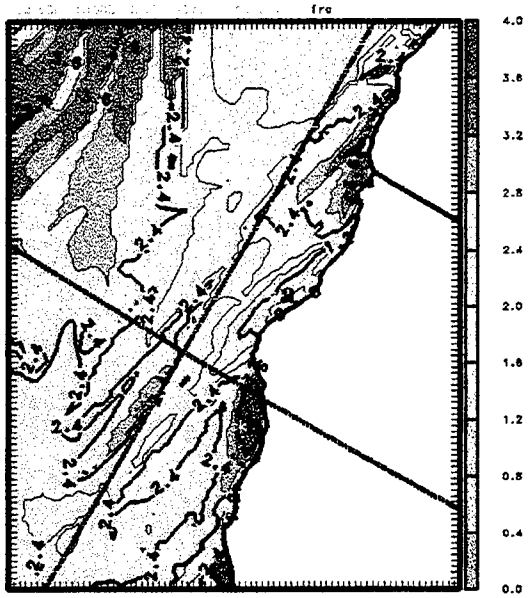


Figure 2: 21Z model computed Froude numbers. The asterisks denote locations of vertical profiles and cross-section endpoints (a) and (b) used in Figures 7 and 8.

Froude number contours delineate bands of subcritical flow on the upwind side of the cape where the flow is blocked by the topography while flow rounding the cape becomes highly supercritical as it lowers and accelerates. This transcritical coastal feature may be more pronounced during the afternoon hours when diurnal heating forces onshore flow. Using the COAMPS model as a research tool with a highly simplified idealized setup, the affect on the MBL of upwind flow criticality to variations in coastal topography was studied in detail by Burk *et al.* (1998). In that study a 2km high piecewise linear terrain field with a single convex bend specified the land/sea boundary and homogeneous background wind and temperature fields were chosen to represent the summertime marine layer. They found that the transcritical regime produces the largest MBL response with the most substantial lowering of MBL heights and greatest flow accelerations. Thus, we focus on the transcritical regime around Cape Mendocino to ascertain how the refractivity is altered both in the littoral region and well away from the coast.

2. Research Accomplished

To investigate the relationship between refractivity and flow criticality along California coastal topography, we initialized a 12 hour, triply nested (45, 15, 5 km grid spacing) COAMPS model forecast at 0Z 11 June 1996 using global fields from the Navy's NOGAPS model and ADP observations. Surface characteristics were specified from the Fleet Numerical Meteorology & Oceanography Center operational database with 1-km resolution terrain data. Ocean temperatures were analyzed at model grid resolution and held fixed for the length of the forecast. Mesoscale detail was allowed to develop over the next 24 hours before beginning the 12-hr forecast of primary interest at 12Z 12 June 1996. During this period, atmospheric data was collected along the flight tracks shown in Figure 3 by the NCAR C130 research aircraft for the COAST96 field study. Rogers *et al.* (1998) gives an overview of the study objectives; the observational data collected and highlights several meteorological features of interest. Although propagation measurements were not taken as part of the COAST96 experiment, we use the aircraft data for the purpose of model validation and then use the high-resolution refractivity forecasts from the inner 5-km grid to assess the trapping and EM-ducting characteristics within the coastal regime.

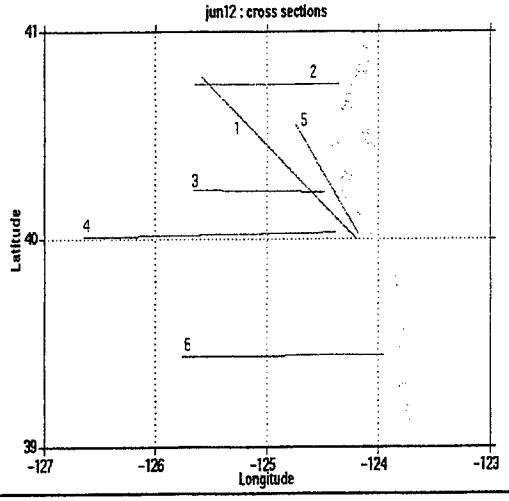


Figure 3: Flight tracks for which aircraft measurements were taken on 12 June 1996 for the COAST96 field program (obtained from the Scripps Institute of Oceanography SIO web site http://penarth.ucst.edu).

Figures 4 and 5 show vertical sections of aircraft data from leg 4 and COAMPS forecast fields respectively from the lowest 1.5-km of the atmosphere. Shaded contours of potential temperature, relative humidity and wind speed are plotted at roughly the same location and time for comparison of observations to model. In the observations, the well mixed MBL slopes abruptly from ~500 m to ~200 m over a ~50 km distance near the coast. This feature coincides with the location of a low-level jet having core speeds over 24 m/s. A thinned and accelerated MBL is characteristic of supercritical expansion fan behavior often seen in the lee of coastal bends. The model fields similarly depict the MBL slope and the jet acceleration near the coast, as well as correctly predict the MBL depth, temperature and inversion strength in this region. Well off shore wind speeds are over predicted by a few meters per second while MBL depth and inversion strength are

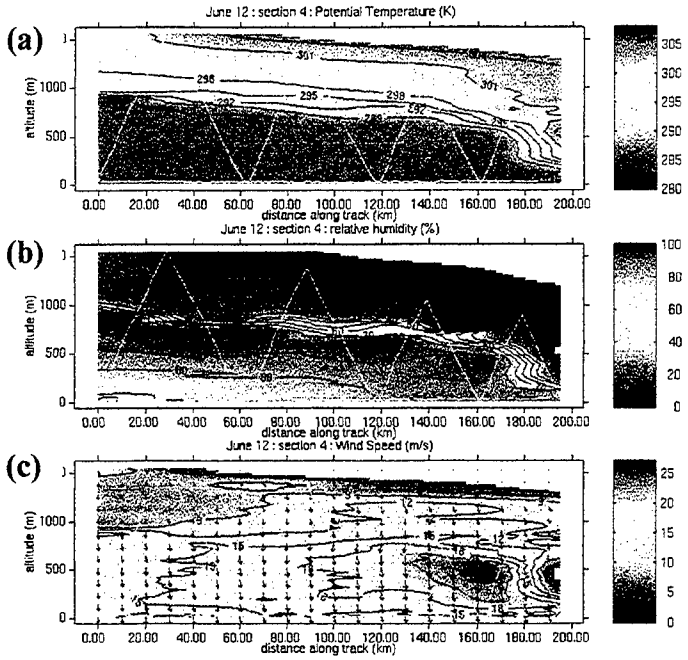


Figure 4: Contour composite from C130 Flight data taken along leg 4 of (a) potential temperature (K), (b) relative humidity (%), and (c) wind speed (m/s) (obtained from web site: http://penarth.ucsd.edu).

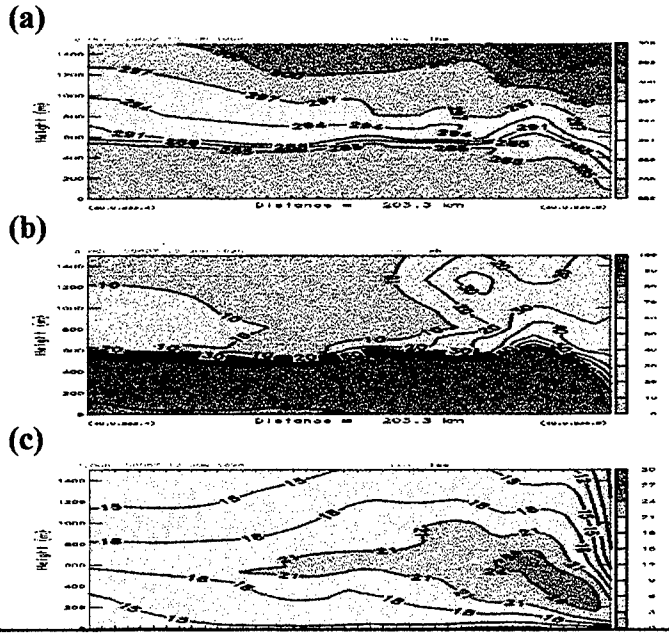


Figure 5: Cross-section of 20Z COAMPS forecast fields along leg 4 of (a) potential temperature (K), (b) relative humidity (%), and (c) wind speed (m/s).

somewhat under predicted by the model. Although the model deficiencies off shore are currently under investigation, we are encouraged by the agreement in the littoral zone and now turn our attention to the model forecast variations in flow criticality along the coastal topography and the corresponding changes in the refractivity field.

Sharp gradients in temperature and moisture can create layers of abruptly varying refractivity that tend to duct microwave propagation. These layers are determined by negative gradients in modified refractivity M:

$$M = \frac{77.6}{T}\left(P + 4810\frac{e}{T}\right) + \frac{z}{R_e} \times 10^6$$

where P is the pressure in millibars, e vapor pressure in millibars, T temperature in Kelvin, z height above sea level and R_e mean radius of the earth (Battan 1973). As shown schematically in Figure 6, a layer in which $\partial M/\partial z$ is negative produces EM trapping. EM propagation ducts occur in the layer between the height of the local minimum M_{min}, (trapping layer top) and the height where $M < M_{min}$ (duct base).

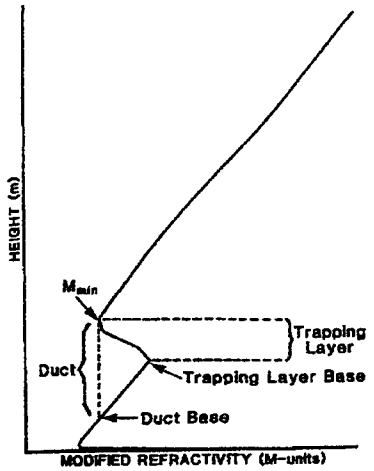


Figure 6: Idealized profile of modified refractivity typical of a well-mixed marine boundary layer (from Burk and Thompson 1996).

Profiles of M computed from the 12 June model fields are shown in Figure 7 for locations corresponding to the asterisks in Figure 2. Profile (a) is a point upwind of Cape Mendocino in the subcritical flow regime and shows an elevated duct between 250 m and 450 m. Profile (b), downwind of the cape in the expansion fan region of enhanced supercritical flow, indicates surface base ducting in the lowest 225 m of the atmosphere.

The profile locations (a) and (b) determine the endpoints of a cross-sectional plot, Figure 8, of forecast potential temperature and wind speed at 21Z. This figure shows a substantial blocking/accelerating pattern in the MBL flow and elevating/thinning pattern in the MBL depths associated with orographic influences. The lowering of the MBL south of the cape creates a surface based duct during the mid-afternoon heating cycle as

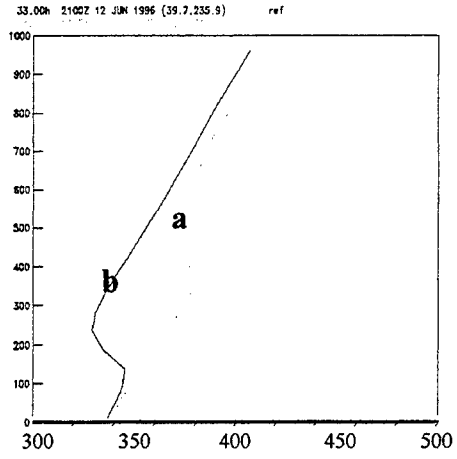


Figure 7: 21Z vertical profiles of modified refractivity (M-units) at the locations shown by the asterisks in Figure 2 (a) upwind and (b) downwind of Cape Mendocino.

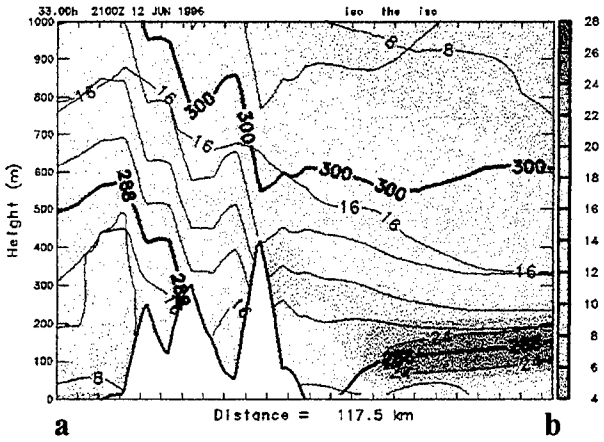


Figure 8: 21Z cross-section of potential temperature (K;contours) and wind speed (m/s;shaded) from location (a) to (b) shown by the asterisks in Figure 2.

diurnally driven subsidence strengthens the gradients across the inversion and further suppresses the marine layer. Examination of Figure 9 indicates that regions of surface based ducting extend over a broad distance. Comparison with the flow criticality contours in Figure 2 show that these regions correlate well with changes in Froude number near 1.0. This result suggests that the supercriticality threshold value (Fr>1.0) may in some situations define regions of surface based ducting. Supercritical expansion fans and transcritical flow contain meso-γ variations in marine layer depth. Because the sharp gradients at the top of the marine layer (particularly in water vapor) are responsible for EM-ducts, these abrupt MBL height changes can result in abrupt variations in the propagation environment near a varying coastline.

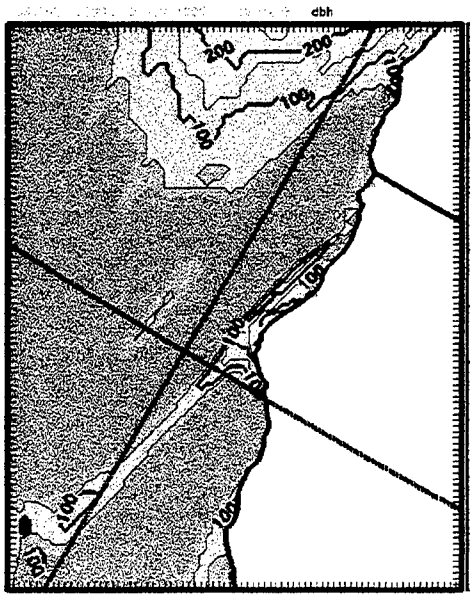


Figure 9: 21Z model computed duct base heights (m). Surface based ducting is represented by the darkest shading.

3. Conclusions

Using high-resolution forecasts from the Navy's nonhydrostatic, compressible mesoscale model, we have investigated the response of marine layer flow to changes in California's coastal topography. Observational data taken during the COAST96 field experiment provided the means for model validation that indicated good agreement in structure and characteristics of the MBL in the coastal region. Analysis of the Froude number indicated abrupt variations in flow criticality around Cape Mendocino that were particularly evident during the afternoon hours. These variations similarly coincided with changes in refractive conditions such that broad regions of supercritical flow correlated well with the location of surface based ducts. These findings suggest that in certain marine environments, for which the MBL is moist and well defined by sharp inversions, the criticality of the background flow can give some insight to the possible ducting characteristics along extended distances over the ocean.

Acknowledgements

This work was supported by the Office of Naval Research, program Element 0602435N.

References

Battan, L.J., 1973: *Radar Observations of the Atmosphere*. University of Chicago Press, 324 pp.

Burk, S.D. and W.T. Thompson, 1996: Mesoscale modeling of summertime refractive conditions in the southern California bight. *J. Applied Meteor.*, **36**, 22-31.

Burk, S.D., T. Haack, and R.M. Samelson, 1998: Mesoscale simulations of supercritical, subcritical, and transcritical flow along coastal topography. *J. Atmos. Sci.*, in press.

Hodur, R.M., 1997: The Naval Research Laboratory's coupled ocean/atmosphere mesoscale prediction system (COAMPS). *Mon. Wea. Rev.*, **125**, 1414-1430.

Klemp, and Wilmhelmson, 1978: The simulation of three-dimensional convective storm dynamics. *J. Atmos. Sci.*, **35**, 1070-1096.

Mass, C.F. and N.A. Bond, 1996: Coastally trapped wind reversals along the United States West Coast during the warm season. Part II: Synoptic evolution. *Mon. Wea. Rev.*, **124**, 446-461.

Rogers, D.P., C.E. Dorman, K.A. Edwards, I.M. Brooks, W.K. Melville, S.D. Burk, W.T. Thompson, T. Holt, L.M. Ström, M. Tjernström, B. Grisogono, J.M. Bane, W.A. Nuss, B.M. Morley, A.J. Schanot, 1998: Highlights of Coastal Waves 1996. *Bull. Amer. Meteor. Soc.*, **7**, 1307-1326.

Samelson, R.M., 1992: Supercritical marine-layer flow along a smoothly varying coastline. *J. Atmos. Sci.*, **49**, 1571-1584.

Winant, C.D., C.E. Dorman, C.A. Friehe, and R.C. Beardsley, 1988: The marine layer off northern California: An example of supercritical channel flow. *J. Atmos. Sci.*, **45**, 3588-3605.

ASSIMILATION OF SURFACE OBSERVATIONS AND CLOUD IMAGE DATA TO ANALYZE CONVECTIVE POTENTIAL

Frank H. Ruggiero*
Air Force Research Laboratory
AFRL/VSBE, Hanscom AFB, MA
(781) 377-2940 FAX: (781) 377-8892
ruggiero@arcdbs.plh.af.mil

George D. Modica and Alan E. Lipton
Atmospheric and Environmental Research, Inc.
Cambridge, MA

1. Objective

The United States Air Force requires forecasts of various environmental parameters (including the depiction of explicit clouds) at a horizontal resolution of 10 km. At this scale, local forcing can be a significant factor. Purdom and Marcus (1982) have pointed out, for example, that most of the morning and early-afternoon summertime convection that occurs in the southeastern United States is predominantly locally driven. One of the primary drivers of locally forced convection is differential surface heating, which causes adjustments to the wind field that result in local areas of convergence. One mechanism for generating differential surface heating is differential cloud shading (Bailey et al. 1981, Segal et al. 1986, 1993).

Our objective was to develop a hybrid four-dimensional data assimilation approach to improve the diagnosis of potential for convective initiation caused by cloud shading-induced differential surface heating. To accomplish this, data from a geostationary satellite imager and hourly-reporting surface stations were employed. The satellite imager data assimilation was carried out in the time-continuous fashion following the method developed by Lipton (1993) while the hourly surface observations were assimilated intermittently as described by Ruggiero et al. (1996).

2. Research Accomplished

a. Assimilation System

The model used for this study was the National Center for Atmospheric Research/Pennsylvania State University (NCAR/PSU) Mesoscale Model 4 (MM4) version 8. The model was run in nested mode with the coarse grid domain of 50 × 55 points at 45-km resolution and a nested grid domain of 67 × 85 points at 15-km resolution. All the results presented here are for the nested grid. The high-resolution boundary layer parameterization uses K-theory with a non-local plume model for unstable regimes (Zhang and Anthes 1982). Cumulus convection is carried out by the modified Kuo scheme (Anthes 1977). The MM4 holds ocean surface temperatures constant using values from the National Centers for Environmental Prediction global analysis. Over land, the MM4 computes surface temperatures using a prognostic surface energy budget equation that includes terms representing the sensible and latent heat fluxes to the atmosphere, sensible heat flux into the

soil, and solar and infrared radiative fluxes (Zhang and Anthes 1982). The MM4 formulation accounts for cloud effects on surface radiation by way of fractional cloud cover parameters n_i that are computed solely on the basis of the relative humidity field. The subscript i refers to the three layers of cloud represented in the model, 1) low, 2) middle, and 3) high. The solar transmittance of a cloudy atmosphere is computed as a simple function of n_i (Benjamin 1983). This is similar to how the current mesoscale models employed by the Air Force and Navy handle clouds in their insolation parameterizations (i.e. Grell et al. 1995; Hodur 1997).

The method employed in this study for retrieving and assimilating cloud radiative effects from satellite imager data is, in many respects, similar to the one reported in Lipton (1993). The method involves retrieving from satellite image data the effective solar transmittances (τ_{eff}) and infrared emittances (ε) over cloudy areas within the domain, and then assimilating that information into the model computations of surface downwelling radiation. The satellite-retrieved values of τ_{eff} and ε at each mesoscale model grid point are temporally interpolated between satellite observation times so that values are available at every time step. In the experiments discussed below, values of τ_{eff} and ε were retrieved for the entire nested grid area. The coarse-grid model area outside of the nested grid area was assumed to be cloud free.

To account for substantial haze that was apparent in the satellite images over most of the analysis, pyranometer data from South Carolina State University was used. It indicated an aerosol transmittance of 0.91. As a first-order means to account for the aerosols, this transmittance value was used as a constraint, such that $\tau_{eff} \leq 0.91$ throughout the domain. Likewise, in control experiments without satellite data assimilation, the computed insolation was constrained by 0.91 $Q_{s(clear)}$.

The satellite imager data used in this study were from the GOES-7 Visible and Infrared Spin Scan Radiometer (VISSR), which had the ability to take image data in one visible band and in several infrared bands. The visible data were taken at a nominal ground resolution of 1 km. Seven image data sets, taken hourly over the period of 0700-1300 EST 23 Aug 1993, were obtained from the archives of the University of Wisconsin Space Science and Engineering Center.

The surface observations were assimilated via intermittent assimilation in which a regular cycle of analysis and model integration was carried out. The objective analysis of the surface data was accomplished by the successive correction scheme of Bratseth (1986) as adapted by Ruggiero et al. (1996). The surface data analysis is univariate and performed on the model's lowest sigma layer. Before the analysis begins, corrections are made to the observations to adjust for height differences between the model's lowest sigma level grid points and the observations. After the analysis is complete, the deviations from the first guess at the model's lowest sigma layer are dynamically blended in the vertical with other model layers following the turbulent mixing-based scheme outlined in Ruggiero et al. (1996). For this work, the correction to the observed temperature to account for height differences was improved. The method was designed to be consistent with the MM4 formulation for the surface heat flux (Blackadar 1979). In the new adjustment method, the surface layer friction temperature (T_*) is assumed to be constant throughout the model's lowest layer.

Table 1. Outline of experiments.

Experiment	Assimilate satellite data	Assimilate shelter-height temperature
CON		
SAT	X	
SAT+TEMP	X	X

b. Experiment Design

The synoptic situation for this case study has been discussed by Lipton and Modica (1998) and will be briefly summarized here. The case is from 23 August 1993 and encompasses the southeast United States. On that morning, stratiform clouds covered a broad region from central Georgia to western North Carolina (Fig. 1a). The rest of the case study domain was essentially cloud free at that time. Most of the stratiform cloud region was free of precipitation although an embedded convective cloud produced a modest amount of rain in southern North Carolina and brief, light showers occurred in western South Carolina and northern Georgia. Otherwise the case was synoptically quiescent. The stratiform clouds dissipated slowly during the morning so that, by early afternoon, they were largely gone (Fig. 1b). During the morning, convective clouds developed in most of the area surrounding the earlier stratiform cloud deck, implying that ground warming and convective destabilization were being locally inhibited by shading in the area covered by stratiform clouds.

The effect of the stratiform clouds on the daytime heating pattern near the surface is apparent in an analysis of the observed change in shelter-height temperatures from 0700 to 1300 EST (Fig. 2). Temperature rises were at a minimum in the area of the stratiform clouds and in the coastal areas. The effect of the cloud-induced shading on the temperature patterns was large and distinct. The local minimum over the North Carolina border was apparently caused by augmentation of the shading effect by evaporative cooling in the rain showers that occurred there.

To satisfy the objectives of the project, four experiments were run. The attributes of the experiments are in Table 1. All of the experiments began at 0700 EST with the MM4 successive corrections objective analysis package (Benjamin and Seaman 1985), and the MM4 non-linear normal-mode adiabatic initialization (Errico and Bates 1988).

c. Results

In order to assess the impact of the assimilation schemes on the low-level temperatures, shelter-height (2-m) temperatures were computed from the model data. The shelter-height temperatures were computed by inverting the model's surface layer parameterization and were

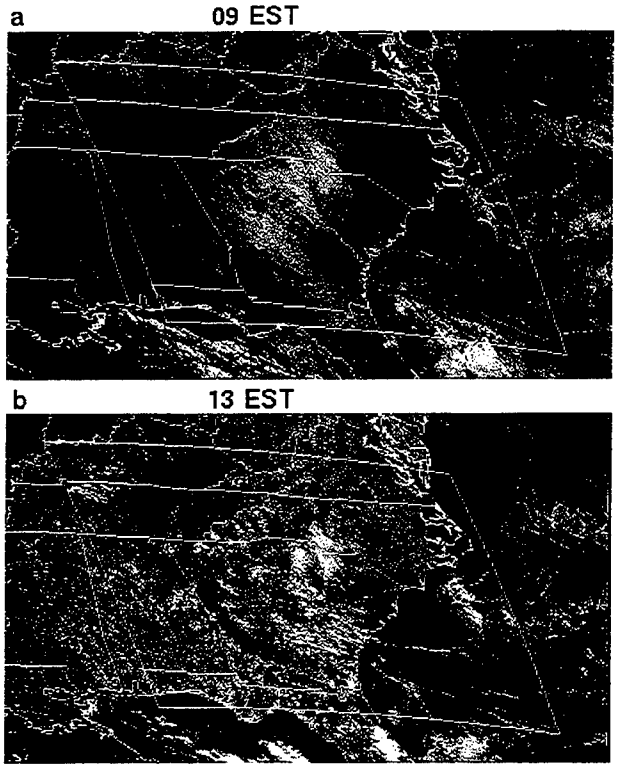


Fig. 1. GOES visible satellite images at a) 0900 and b) 1300 EST, 23 August 1993. The analysis domain is outlined in both frames.

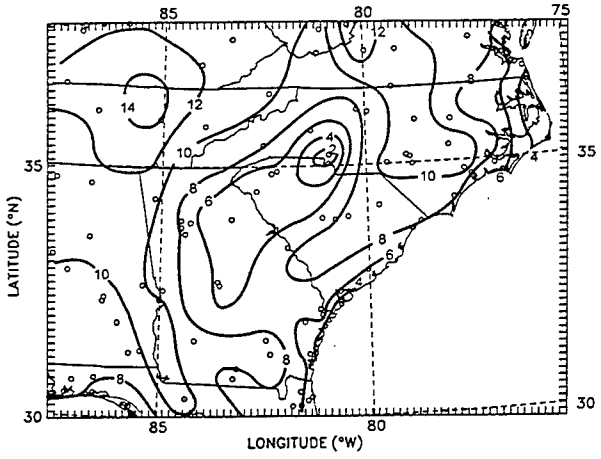


Fig. 2. Change in shelter-height temperature (contoured every 2°C) from 0700 to 1300 EST based on surface observations taken at the stations marked with circles.

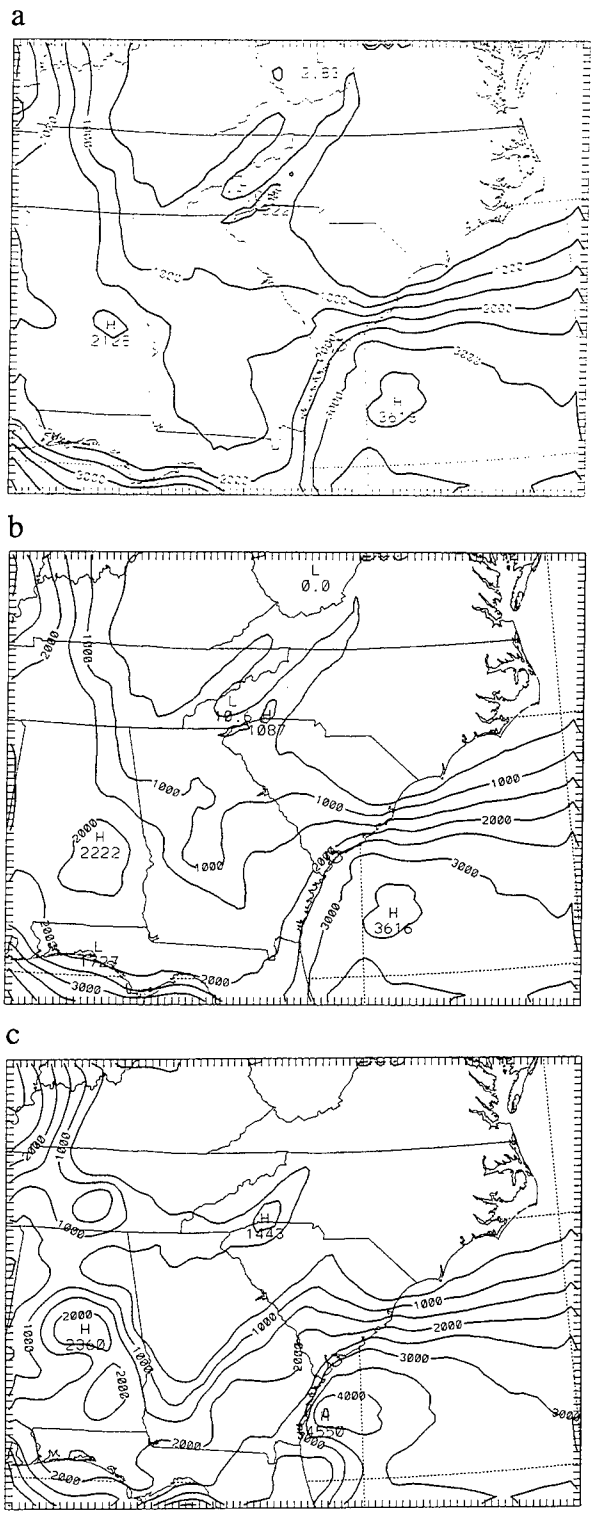


Fig. 3. CAPE values valid at 1000 EST contoured every 500 J kg^{-1} for the a) CON, b) SAT, and c) SAT+TEMP experiments.

Table 2. Errors in shelter-height temperatures (°C).

Experiment	1000 EST		1300 EST	
	Bias	RMS	Bias	RMS
CON	-0.5	1.7	-1.1	1.9
SAT	0.3	1.4	0.4	1.5
SAT+TEMP	-0.1	1.1	0.2	1.2

then compared with the observed shelter-height temperatures at 1000 and 1300 EST (Table 2). It is important to note that for the SAT+TEMP run, the comparisons shown in the table were done before the shelter-height temperatures were assimilated for that particular hour; therefore, the evaluations were done on independent data. The CON run for both times exhibited a cold bias that is indicative of the model's inability to properly identify enough clear area and produce the appropriate amount of solar heating. The SAT and SAT+TEMP runs were all better than the CON run with respect to both the bias and rms error. The best of the three runs was the combined SAT+TEMP assimilation run.

To assess the ability of the experiments to analyze convective potential, the convective available potential energy (CAPE) was computed for the CON, SAT, and SAT+TEMP results valid at 1000 EST (Fig. 3). All four runs showed a region of values > 2000 J kg^{-1} in Alabama which matched up well with the convection seen in the area by 1300 EST (Fig. 2b) and which intensified into the evening (not shown). However, only the runs that assimilated the shelter-height temperature fields showed a minimum of CAPE of < 500 J kg^{-1} associated with the shaded region. While convection may be suppressed even in areas with high values of CAPE, this result is consistent with the lack of convection noted in the shaded region at 1300 EST.

The effect of the satellite imager data and shelter-height temperature assimilation on mesoscale circulations is illustrated in Fig. 4 by cross-sections valid at 1300 EST. Both assimilation runs depicted moisture divergence at low levels in the stratiform cloud area and moisture convergence on the adjoining sides. The CON run showed very little divergence or convergence. The assimilation runs produced a slightly stronger sea-breeze circulation, as evident by the stronger onshore flow, and a stronger updraft over the high ground to the northwest of the cloudy area, in comparison with the CON run. The assimilation runs produced suppressed boundary layer development over the stratiform cloud area. All the assimilation runs had enhanced boundary layer development on each side of the cloudy region.

3. Conclusions and Recommendations

It is obvious from our results that the MM4, on its own, can not be relied on to accurately reproduce the low-level perturbations caused by the cloud shading. This

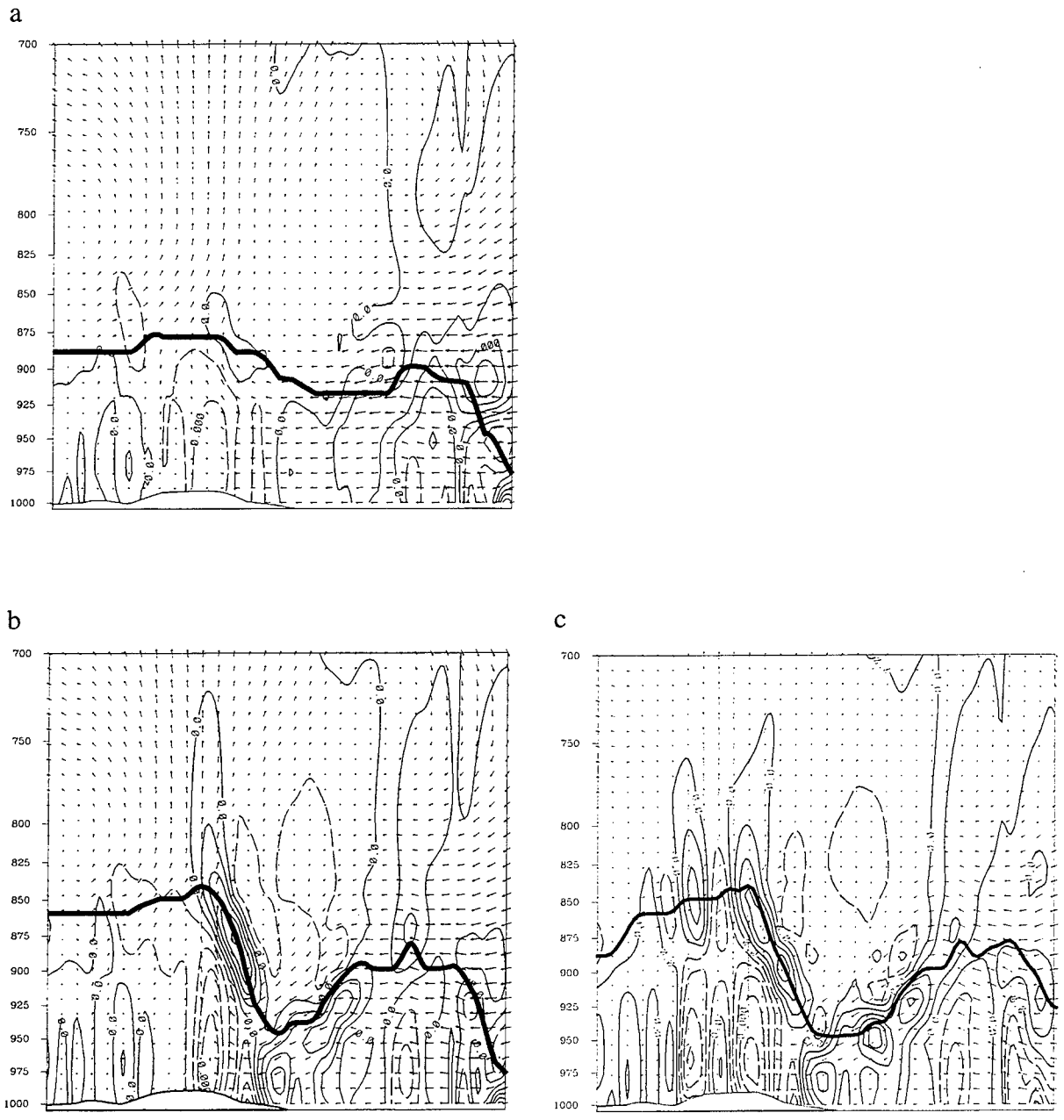


Fig. 4. Cross-sections of wind and moisture divergence at 1300 EST from the a) CON, b) SAT, and c) SAT+TEMP experiments. The cross-sections go from northwest (left) to southeast (right) along the line shown in Fig. 8a. The contour interval is 2×10^{-7} s^{-1}, with the negative contours dashed. The vector scaling is 6 m s^{-1} and 0.6 Pa s^{-1} per vector interval in the horizontal and vertical directions, respectively. The heavy solid line marks the top of the boundary layer.

shortcoming is most pronounced in the absence of strong synoptic forcing such as the case presented here. It is certainly not the purpose of this paper to single out the MM4 for criticism in this regard. Other widely used mesoscale models (e.g. Grell et al. 1995; Hodur 1997) use similar cloud parameterizations for short-wave radiation as the MM4. The main problem with the current model parameterization in the case presented here is that it relies on relative humidity to diagnose clouds, and the relative humidity is not well correlated with the actual cloud cover. The result is that the MM4 inferred excessive cloud cover, so in regions that were actually clear it did not allow sufficient solar radiation to reach the ground, leading to a cool bias of computed shelter-height temperatures and a lack of appropriate mesoscale detail. Without the production of the cloud shading thermal effects, little prior indication of convective activity is given by the MM4 without assimilation.

Assimilating the satellite imager data separately resulted in improved analyses compared to the CON run. In addition, synergistic improvement was evident when assimilating both the satellite imager data and the shelter-height temperature data. There was an improved depiction of the shelter-height temperatures for the combined assimilation of satellite imager data and shelter-height temperatures, as compared to the runs that assimilated the satellite imager data only. The combined assimilation run also produced more realistic moisture divergence fields and indices of potential for convective cloud development, as evaluated by consistency with observed patterns of cloud development.

Given the limitations of mesoscale models in reproducing the local forcing from differential cloud shading, it is recommended that the models be augmented with assimilated data such as shown in this paper. While using both surface observations and satellite imager data produced the best results, data denial would prevent the use of surface observations in some situations. In those cases the results here show that the assimilation of satellite imager data by itself can be beneficial.

Acknowledgements. We thank T. Stoffel of the National Renewable Energy Laboratory for providing the pyranometer data and D. C. Peduzzi and G. B. Gustafson of Atmospheric and Environmental Research, Inc. for writing the cloud-clear discrimination program for satellite imagery. In addition we thank T. Walker for help in preparing figures. Surface weather observation data were provided by the USAF Combat Climatology Center. This research was supported in part by the Air Force Office of Scientific Research under project 2310 and by the Department of Defense High Performance Computing Shared Resource Centers at the Army Corps of Engineers Waterways Experiment Station and at the Naval Oceanographic Office.

REFERENCES

Anthes, R. A., 1977: A cumulus parameterization scheme utilizing a one-dimensional cloud model. *Mon. Wea. Rev.*, **105**, 270-286.

Bailey, M. J., K. M. Carpenter, L. R. Lowther, and C. W. Passant, 1981: A mesoscale forecast for 14 August 1975—the Hampstead storm. *Meteor. Mag.*, **110**, 147-161.

Benjamin, S. G., 1983: Some effects of surface heating and topography on the regional severe storm environment. Ph. D. dissertation, The Pennsylvania State University, 265 pp.

Benjamin, S. G., and N. L. Seaman, 1985: A simple scheme for objective analysis in curved flow. *Mon. Wea. Rev.*, **113**, 1184-1198.

Blackadar, A. K., 1979: High-resolution models of the planetary boundary layer. *Advances in Environmental Science and Engineering,* Vol. 1, No. 1, J. Pfafflin and E. Ziegler, Eds., Gordon and Breach, 50-85.

Bratseth, A. M., 1986: Statistical interpolation by means of successive corrections. *Tellus*, **38A**, 439-447.

Errico, R. M., and G. T. Bates, 1988: Implicit normal-mode initialization of the PSU/NCAR mesoscale model. NCAR Tech. Note, NCAR T/N-312+IA, 112pp. [Available from NCAR Information Services, P. O. Box 3000, Boulder, CO 80307.]

Grell, G. A., J. Duhia, D. R. Stauffer, 1995: A description of the fifth generation Penn State/NCAR Mesoscale Model (MM5). NCAR Tech. Note, NCAR T/N-398+STR, 122pp. [Available from NCAR Information Services, P. O. Box 3000, Boulder, CO 80307.]

Hodur, R. M., 1997: The Naval Research Laboratory's Coupled Ocean/Atmospheric Mesoscale Prediction System (COAMPS). *Mon. Wea. Rev.*, **125**, 1414-1430

Lipton, A. E., 1993: Cloud shading retrieval and assimilation in a satellite-model coupled mesoscale analysis system. *Mon. Wea. Rev.*, **121**, 3062-3081.

Lipton, A. E., and T. H. Vonder Haar, 1990: Mesoscale analysis by numerical modeling coupled with sounding retrieval from satellites. *Mon. Wea. Rev.*, **118**, 1308-1329.

Lipton, A. E., and G. D. Modica, 1998: Assimilation of visible-band satellite data for mesoscale forecasting in cloudy conditions, *Mon. Wea. Rev.*, in press.

Purdom, J. F. W., and K. Marcus, 1982: Thunderstorm trigger mechanisms over the southeast United States. Preprints, *12th Conf. on Severe Local Storms*, San Antonio, Amer. Meteor. Soc., 487-488.

Ruggiero, F. H., K. D. Sashegyi, R. V. Madala, and S. Raman, 1996: The use of surface observations in four-dimensional data assimilation using a mesoscale model. *Mon. Wea. Rev.*, **124**, 1018-1033.

Segal, M., J. F. W. Purdom, J. L. Song, R. A. Pielke, and Y. Mahrer, 1986: Evaluation of cloud shading effects on the generation and modification of mesoscale circulations. *Mon. Wea. Rev.*, **114**, 1201-1212.

Segal, M., W. L. Physick, J. E. Heim, and R. W. Arritt, 1993: The enhancement of cold-front temperature contrast by differential cloud cover. *Mon. Wea. Rev.*, **121**, 867-873.

Zhang, D., and R. A. Anthes, 1982: A high-resolution model of the planetary boundary layer—Sensitivity tests and comparisons with SESAME-79 data. *J. App. Meteor.*, **21**, 1594-1609.

Evaluation of COAMPS Mesoscale Modeling in the Persian Gulf Region

Carlyle H. Wash[1*], Mary S. Jordan[1] and John Cook[2]
[1]Department of Meteorology
Naval Postgraduate School
589 Dyer Rd., Room 254
Monterey, CA 93943-5114
Phone: 408-656-2516 Fax: 408-656-3061
wash@nps.navy.mil
[2]Naval Research Laboratory, Monterey, CA

OBJECTIVE

The US Navy conducted a Ship ASW Readiness and Effectiveness Measuring exercise (SHAREM 110) in the Persian Gulf during 5-17 February 1995. As part of SHAREM, additional mesoscale measurements were made by ships and aircraft. After the exercise, the Naval Research Laboratory, Monterey ran the research version of the Navy Coupled Ocean/Atmosphere Mesoscale Prediction System (COAMPS) for the entire SHAREM period, without incorporating the mesoscale observations into model data assimilation.

The purpose of this research is to study the mesoscale features in the SHAREM data set and to evaluate the COAMPS predictions of these phenomena. The period of 8-11 February 1995 includes three distinct synoptic and mesoscale phenomena, which will be studied in this paper. A mesoscale disturbance is evident in ship soundings and aircraft data on 8 February, in advance of a cold front. The front passed through the Persian Gulf on 9 February, and ship and aircraft data for that day shows subsidence, drying, and establishment of a strong inversion behind the front. A Shamal occurs on 10-11 February. Aircraft and ship data on 11 February provide in situ measurements of the Shamal and the resultant deep mixed layer in the Persian Gulf. This paper includes evaluations of COAMPS at three separate times: 06-12 UTC 8 February, 06 UTC 9 February, and 06 UTC 11 February 1995. In addition, evaluation of COAMPS for a period of strong land-sea breeze circulations during 14-15 February will be reported at the conference.

RESEARCH ACCOMPLISHED

As part of SHAREM 110, participating US Navy ships launched rawinsondes and rocketsondes as frequently as every three hours. In addition, the British Meteorological Research Flight (MRF) C-130 aircraft, coordinated through the United Kingdom Meteorological Office, flew low-level sawtooth vertical profiles to measure temperature, moisture, winds, and pressure in the lower atmosphere. The C-130 research aircraft flew sawtooth vertical profiles between 15-1350 meters and sampled cross-sections in three parallel lines over the participating ships in the Persian Gulf. Each cross-section consists of a west-to-east set of 4-5 sawtooth profiles, followed by the return (east-to-west) leg of sawtooth profiles. Byers (1995) describes the synoptic and mesoscale meteorological events during the entire SHAREM experiment period.

The Navy COAMPS nonhydrostatic, mesoscale model was run for the entire SHAREM 110 period by NRL Monterey for COAMPS validation and testing (Hodur, et al., 1996). The COAMPS data assimilation system was used in all model runs. Data assimilation was performed every 12 hours and 24 hour forecasts were produced. The COAMPS nested grids were defined at 81, 27 and 9 km. Boundary conditions were provided from the NOGAPS global model. Forecasts on the 9 km inner grid are used in this study.

8 February 1995

The DMSP visible image for 0529 UTC on 8 February (Fig. 1) shows the prefrontal cloudiness prior to the aircraft measurements. A rope cloud associated with a cold front approaching the Persian Gulf is present on the edge of the image. The satellite data also shows embedded convection, with upper-level cirrus, in the southwest flow over the Persian Gulf. Figure 1 shows the aircraft sawtooth profile cross-section locations are indicated by the lines on the image. The northernmost cross-section flight occurred at 0652-0747 UTC, the middle cross-section at 0754-0900 UTC, and the third (southern) at 0908-1016 UTC. The location of the USNS Silas Bent (SBN) and the USS Lake Erie (LKE) at 06 UTC are indicated by the dots. The Silas Bent and Lake Erie moved to the northwest throughout the day, roughly parallel to the cross-sections.

Note that there is convection in the western portion of each cross-section, but no convection at the eastern end. The variation in MABL structure over the 180 km cross-sections (not shown) is quite surprising. The western end of the cross section shows weak stability with moisture mixed to 1 km while the eastern end of the cross section has a strong inversion at 500m with very dry air above the inversion. See Jordan, et al., (1997) for a more detailed description of the stability changes along the cross section and its impact on EM propagation conditions. Similar variations are present in the other two cross-sections. The line of convection near the west end of the cross section is consistent with the weak stability conditions in the aircraft cross sections.

Figure 2 presents a cross-section of aircraft measured winds for 0829-0900 UTC. Easterly flow occurs below 600 meters. Wind variations associated with the mesoscale disturbance are evident in the winds above 600 meters. There are southerly winds in the eastern half of the cross-section, but light westerly winds in the western half.

Frequent soundings from two ships in the prefrontal region are available. A time series of ship soundings is discussed in Jordan, et al., (1997). Figures 3 and 4 present a 12 h forecast of winds at 920 mb (vt 8/12 UTC) compared to soundings from the USNS Silas Bent at 06 and 15 UTC. The 920 wind forecast clearly shows the wind shift from southwesterly to northwesterly winds associated with the prefrontal mesoscale circulation. This system is responsible for the weaker stability and outbreak of convection discussed above. At 06 UTC, the Silas Bent is east of the 920 mb wind shift and its sounding indicates an inversion near 600 meters with low level easterly and strong (20 kt) dry southerly winds above the inversion . The aircraft data (Fig. 2) and ship data (Fig. 4) verify the COAMPS forecast of this feature.

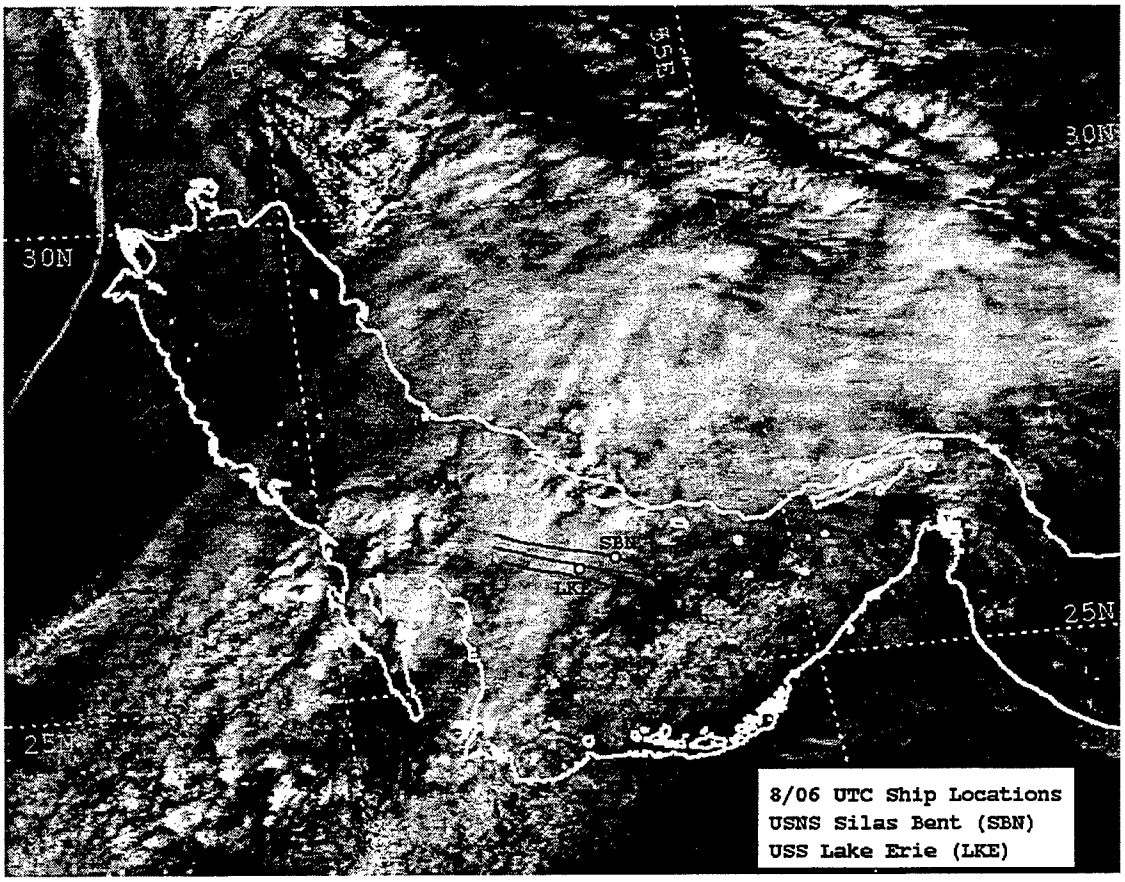


Fig. 1. DMSP (F-12) visible image for 0529 UTC on 8 February 1995. The aircraft cross-section locations are indicated by the lines, and the location of the USNS Silas Bent (SBN) and the USS Lake Erie (LKE) at 06 UTC are indicated by the dots.

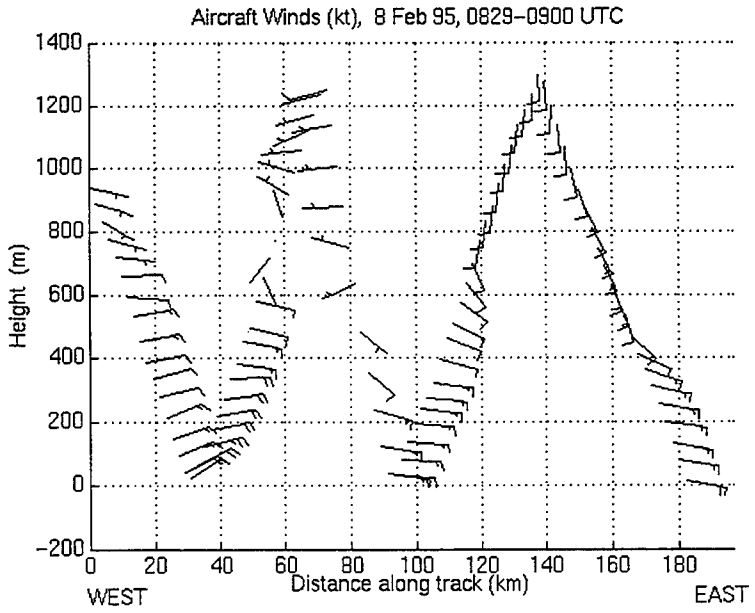


Fig. 2. Cross-section of aircraft measured winds (kt) for 0829-0900 UTC, which is the middle cross-section in Fig. 1.

Jordan, et al., (1997) also showed COAMPS 6 h forecast upward vertical motion along the west edge of the cross section consistent with the convection outbreak.

The effects of the moist, upper level flow from the southwest is evident in the 15 UTC sounding. The entire sounding is quite moist and the winds above 800 meters are steady from the west at 10-20 knots. By 21 UTC (not shown), prefrontal, southerly flow develops below 600 meters. The winds throughout the sounding shift to the west and northwest at 00 UTC on 9 February, which Byers (1995) identifies as the cold front passage and the onset of the Shamal (northwest flow) period.

The 12 h forecast of 920 mb winds (vt 8/12 UTC) by COAMPS (Fig. 3) shows the eastward progress of this system. Ship soundings from the USS Lake Erie at 12 UTC (not shown) and USNS Silas Bent at 15 UTC (Fig. 4) show the perturbation has moved past the ship locations because the winds above the boundary layer have shifted from southerly to westerly. Note also the increase in moisture in both soundings above boundary layer and weakening of the inversion. The COAMPS forecast of these stability, moisture and wind changes continues to be successful, however COAMPS does move the system a little faster than observed. The impact of this feature on EM propagation conditions is discussed in Jordan, et al., 1997. The ability of COAMPS to resolve the structure of this prefrontal mesoscale system is very encouraging.

9 February 1995

During the next 24 hours the cold front moves over the Persian Gulf. DMSP infrared satellite imagery (Fig. 5) at 9/0257 UTC shows the frontal band over the southern part of the Gulf. Note the sharp edge of the rear of the front. The location of the C-130 aircraft cross-section, which started three hours after the time of this image, is denoted by the line on the image.

The aircraft cross-section for 0627-0658 UTC 9 February (Fig. 6) presents a striking view of the thermodynamic and moisture structure at the rear of the front. These data show moisture vertically mixed to the top of the cross-section at the east end but significant drying occurring to the west. A strong subsidence inversion also is present at the base of the dry zone in the potential temperature cross-section. This aircraft cross-section has captured the large changes associated with the rear of the front. Strong subsidence must be present over the western half of the cross-section explaining the drying and formation of a strong inversion above the mixed layer.

Figures 7 and 8 give COAMPS depiction of this cross-section from the 6 h and 18 h forecasts. COAMPS resolves the intense drying (somewhat more intense than observed) over the western portion of the cross-section. Also forecast is the formation of a stable layer under the dry zone over the well-mixed layer in the cold air behind the front. The 18 h forecast of these features is displaced eastward indicating the model is somewhat fast is predicting the motion of the front. But the ability of the model to resolve the vertical motions and resultant vertical temperature and moisture structure at the rear of the front is very impressive.

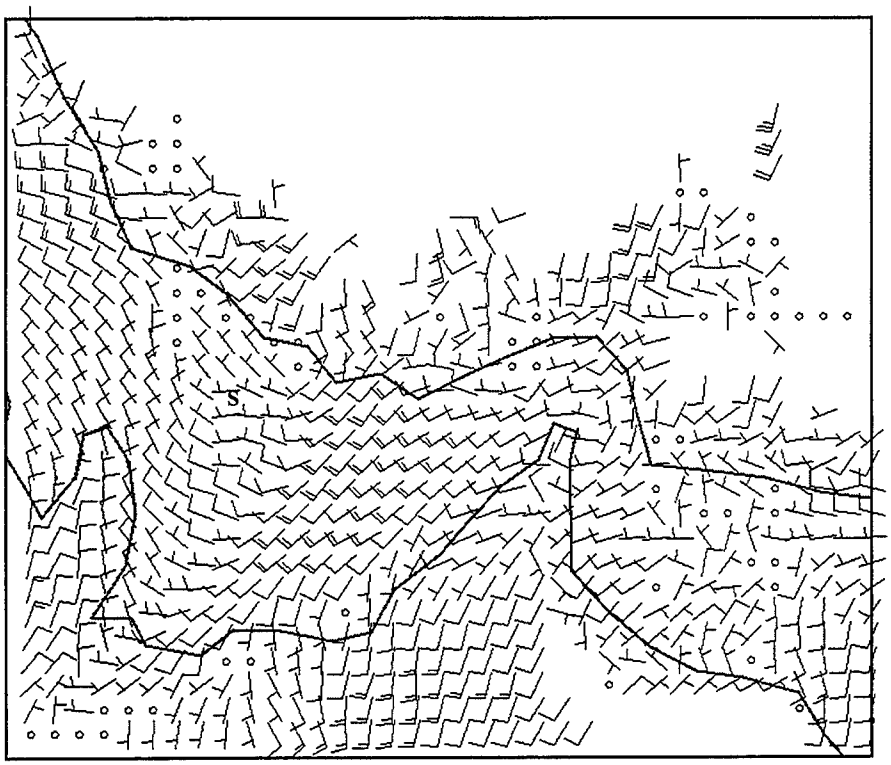


Fig. 3. COAMPS 920 mb winds (knots), 12 hr forecast, valid at 1200 UTC 8 February 1995. The 1500 UTC USNS Silas Bent position is indicated by the letter S. At 0600 UTC, the Silas Bent was located 50 km ESE of the its 1500 UTC location.

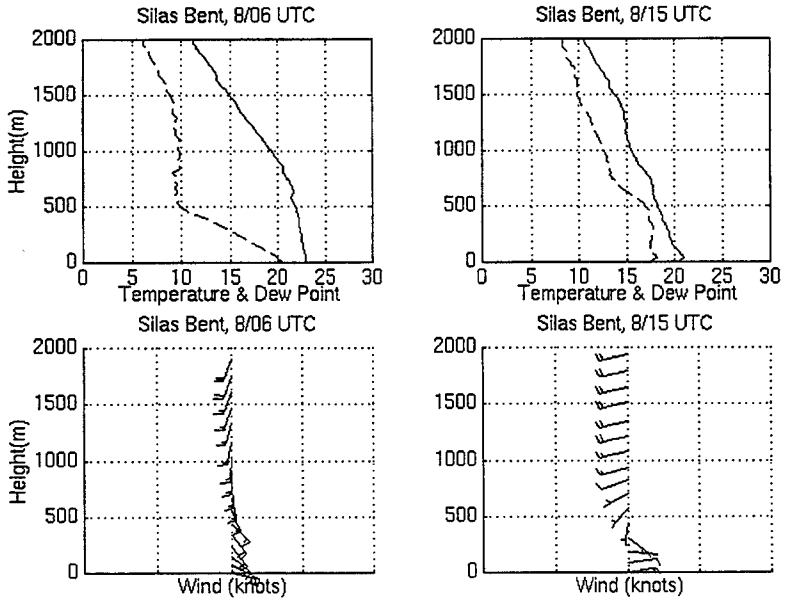


Fig. 4. Rawinsondes for USNS Silas Bent at 0600 UTC and 1500 UTC 8 February, at the locations indicated in Fig. 3. Temperature and dew point (dashed) in Celsius, wind speed in knots. The 920 mb level is at approximately 850 meters.

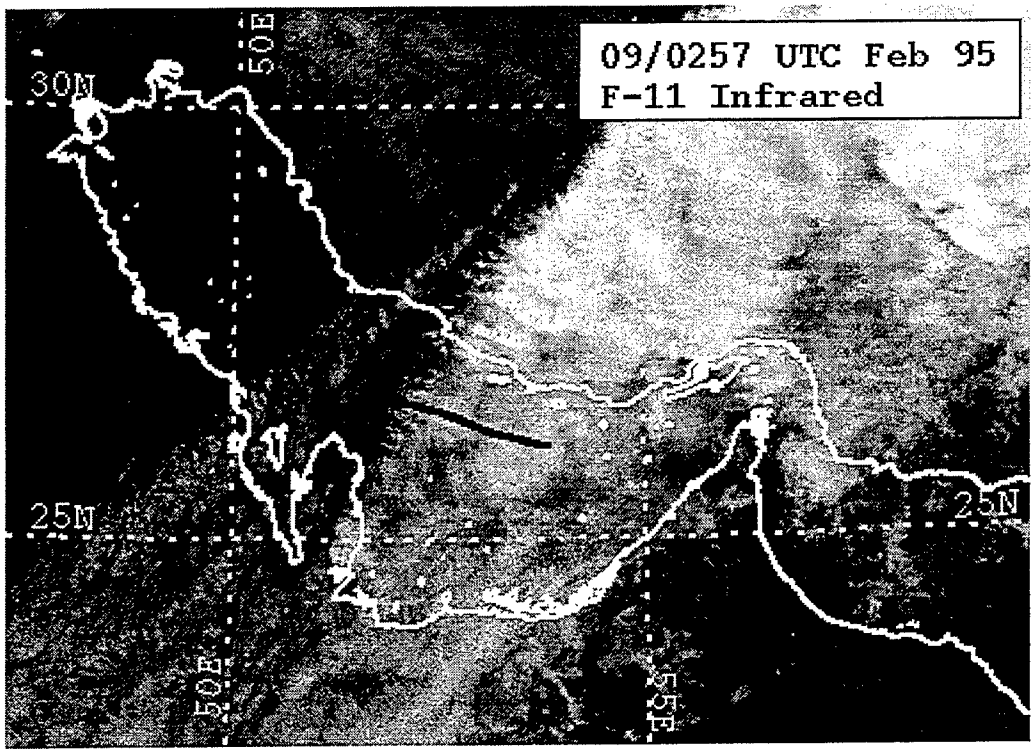


Fig. 5. DMSP (F-11) infrared image for 0257 UTC on 9 February 1995. The aircraft cross-section location is indicated by the line.

11 February 1995

On 11 February, the C-130 measured a deep well-mixed layer to 925 mb that formed during the strong Shamal period following the passage of the front discussed above. The depth of this layer decreases slowly during the day. The 11/0552 UTC sounding from the Silas Bent (Fig. 9, solid line) illustrates this deep mixed layer and the dry air above it. The ability of the COAMPS 6 h and 18 h forecasts to resolve this structure is illustrated by the two COAMPS forecasts soundings overlaid on the ship data (Fig. 9). The 6 h forecast is very successful with the deep mixed layer well forecast. The 18 h forecast give the correct general structure but the depth of the mixed layer is forecast more shallow than observed. Study of forecasts from the 10/00, 10/12 and 11/00 UTC model runs do show a trend by COAMPS to forecast too much subsidence and a too shallow mixed layer towards the end of the forecast period. However, the model displays high skill in resolving the mixed layer and inversion structure, which are important to cloud and EM/EO assessment for DOD operations.

CONCLUSIONS

Boundary layer structures during a prefrontal, postfrontal, and deep mixed layer periods over the Persian Gulf were analyzed using aircraft measurements, ship-based rawinsondes, surface observations, DMSP satellite imagery, and COAMPS mesoscale model predictions. The aircraft data revealed a dramatic changes in the MABL structures within a 180 km distance for the prefrontal and postfrontal cases. COAMPS mesoscale model predictions did resolve

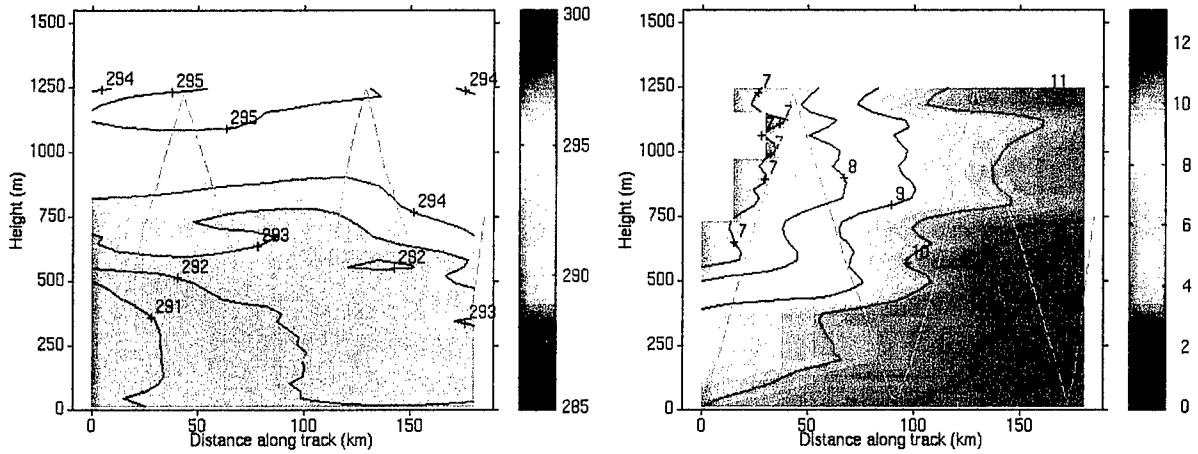


Fig. 6. Aircraft cross-sections of potential temperature (K) and specific humidity (g/kg), respectively, at 0627-0658 UTC 9 Feb 95. The horizontal axis is the distance along the ground track, from west-to-east. The green dotted line indicates the aircraft sawtooth flight path.

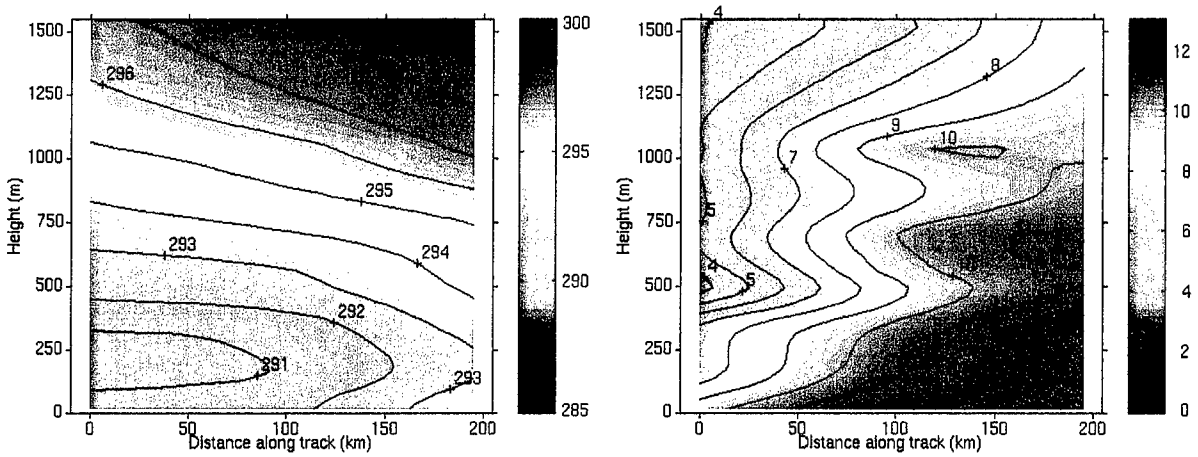


Fig. 7. COAMPS 6 hr forecast of potential temperature (K) and specific humidity (g/kg), respectively, valid at 0600 UTC 9 Feb 95, which is nearly coincident with the cross-section in Fig. X. The horizontal axis is the distance along the ground track, from west-to-east.

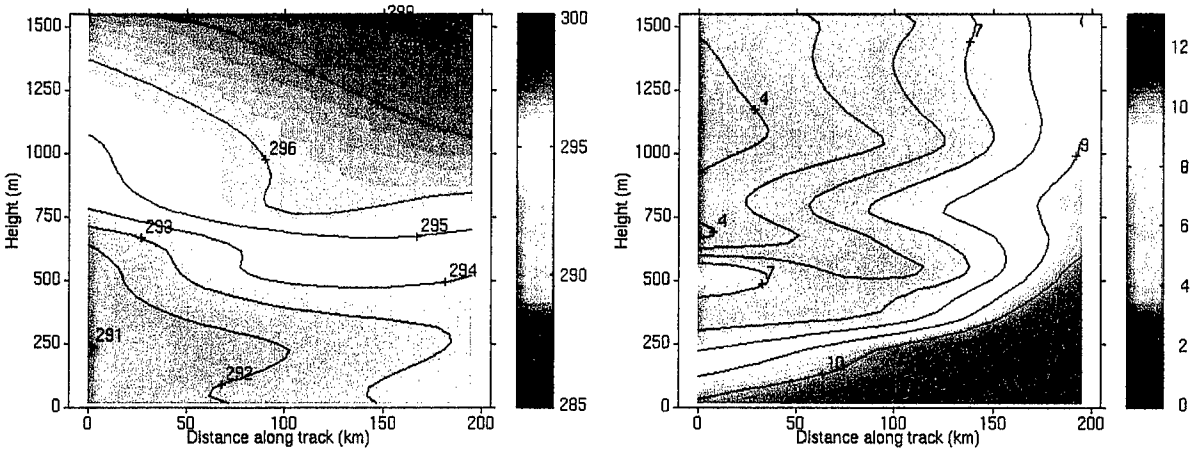


Fig. 8. COAMPS 18 hr forecast of potential temperature (K) and specific humidity (g/kg), respectively, valid at 0600 UTC 9 Feb 95, which is nearly coincident with the cross-section in Fig. 5. The horizontal axis is the distance along the ground track, from west-to-east.

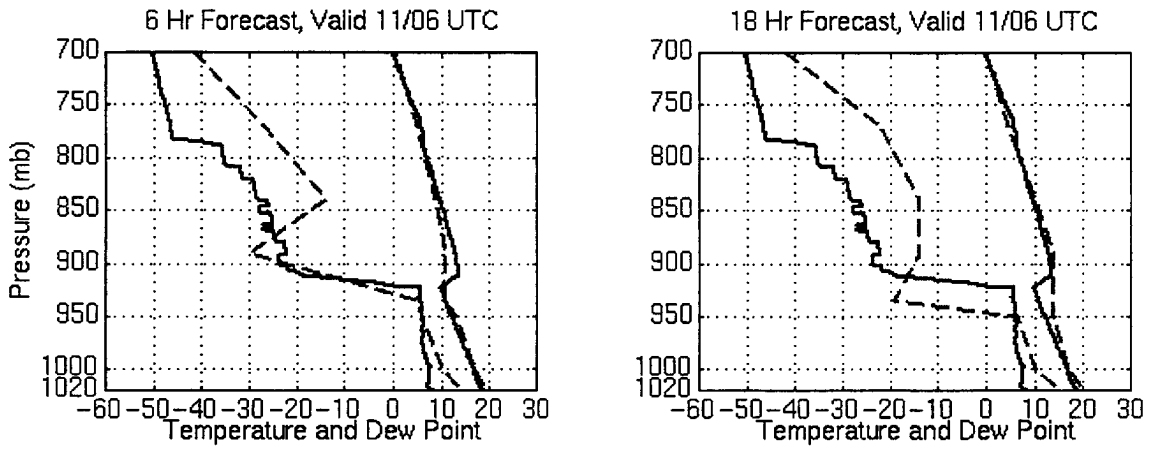


Fig. 9. COAMPS 6 hr and 18 hr forecasts of temperature and dew point, valid at 0600 UTC 11 February 1995, are compared with the 0552 UTC rawinsonde from the USNS Silas Bent. The solid lines represent the Silas Bent (located at 26.1N 53.2E) ; dashed lines represent COAMPS values at 26.0N 53.0E.

important vertical structure of both the prefrontal mesoscale disturbance and rear of the major cold front. This complex structure impacts the assessment of electromagnetic (EM) propagation within this region as well as cloud formation. Successful mesoscale forecasts like these will substantially improve forecasting of clouds, weather, and EM propagation conditions to support DOD operations.

ACKNOWLEDGMENTS

This research is part of the SHAREM 110 Mesoscale Refractive Features study funded by the Office of Naval Research. SPAWAR PMW-185 provided support for the SHAREM 110 exercise. We thank Dr. Teddy Holt, NRL Monterey, for providing the COAMPS model run and Prof. Wendell Nuss and Mr. Bob Creasey, NPS, for assistance with the Visual graphics software to display the COAMPS dataset. We also thank the British Meteorological Flight (MRF) for their cooperation to acquire, process and provide the aircraft data for this study.

REFERENCES

Byers, D.J., 1995: "Synoptic and Mesoscale Influences on Refraction during SHAREM 110," Masters Thesis, Naval Postgraduate School, Monterey, CA, 126 pp..

Hodur, R.M., R.L. Brody, R. Englebretson, T. Holt, S. Lowe, C.H. Wash, and L. Zambresky, 1996: "Validation Test Report for the Coupled Ocean/Atmosphere Mesoscale Prediction System (COAMPS)," FNMOC Report.

Jordan, M. S., C. H. Wash, and B. J. Cook, 1997: "Boundary Layer Variations Affecting Refraction During SHAREM 110," Proceedings of the Electromagnetic/Electro-Optics Prediction Requirements and Products Symposium, Monterey, CA, 3-5 June 1997.

Preceding Page Blank

THE REFRACTIVITY STRUCTURE OF THE LOWER ATMOSPHERE: CONNECTING TURBULENCE AND METEOROLOGY

John C. Wyngaard*[1], Martin Otte[1], Kenneth E. Gilbert[2], Xiao Di[2], and Nelson Seaman[1], [1]Department of Meteorology, [2]Applied Research Laboratory, Penn State University, University Park, PA 16802

814-863-7714, 814-865-3663 (Fax); wyngaard@ems.psu.edu

1. Objective

The traditional treatment of electromagnetic (EM) wave propagation through turbulence has two main elements: the statistical representation of refractive-index turbulence, and the statistical effects of this turbulence on EM waves. The most prominent of the former, the Kolmogorov notions (Tennekes and Lumley, 1972) of the various ranges and scaling parameters of the turbulence spectrum, the structure-function parameter, and local isotropy, are generally accepted today. Likewise, the Monin-Obukhov (M-O) similarity hypothesis (Panofsky and Dutton, 1984) is the standard framework today for interpretation and prediction of turbulence statistics in the near-surface portion of the atmosphere.

As micrometeorologists extended their studies to the boundary layer as a whole, they developed other unifying similarity notions that parallel the M-O hypothesis. There now exists excellent documentation of the statistical structure of refractive-index turbulence in the atmospheric boundary layer and the impact of meteorology on this turbulence, particularly for the inertial and dissipative spectral ranges. These results are generally presented in similarity frameworks. Since the energy-containing range of turbulence is directly impacted by buoyancy and vertical inhomogeneity, its more complicated statistical structure is less well documented. Andreas (1990) has compiled an excellent summary of refractive-index statistics in the atmospheric boundary layer.

Micrometeorologists, like most scientists, tend to write for their colleagues. In so doing they have not generally made it clear that their turbulence statistics refer not to properties of an actual, realizable atmosphere, but to the properties of a large ensemble of realizations of an atmosphere. The Kolmogorov spectrum, the structure-function parameter, local isotropy, and Monin-Obukhov and other similarity relations do not exist in any actual realization. They exist only as statistical properties of a large collection of realizations.

Parabolic-equation (PE) codes now allow the direct calculation of EM propagation in the lower atmosphere. These calculations need instantaneous realizations of the three-dimensionally turbulent refractive-index fields, not their statistics. Our objective here is to discuss how one can use the hard-earned statistical results of micrometeorologists in this new approach to EM propagation.

2. Research Accomplished

Because of the huge range of spatial scales of atmospheric turbulence, a numerical solution of its governing equations to yield the three-dimensional, time-dependent evolution of all its "eddies" is impossible. In fact, it is apt to be impossible in any turbulent flow of real interest. Such numerical solutions are possible only at very low Reynolds numbers, those barely above that of transition to turbulence.

In the computational technique called large-eddy simulation (LES), only the largest eddies in a turbulent flow are calculated from the governing equations; those smaller than the numerical grid are treated very approximately through a "subgrid model."

Many researchers (e.g., Deardorff, 1972; Moeng, 1984; Mason and Thomson, 1987; Schmidt and Schumann, 1989; Sykes and Henn, 1989) have applied LES to atmospheric boundary-layer flows. Today's LES codes are broadly similar to that pioneered by Deardorff, although there are differences in the spatial discretization (some use spectral techniques in the horizontal, some use finite differences) and subgrid models. Today's larger computers easily allow 10^6 spatial grid points, making a $96 \times 96 \times 96$ grid, for example, quite feasible.

The difficulty of assembling suitable data bases on atmospheric turbulence makes definitive testing of atmospheric LES results difficult. Most testing has been against ensemble-mean statistics from the atmosphere and from laboratory models of the atmosphere. In general this testing supports the fidelity of LES.

LES does have limitations, including the poor performance of its subgrid model and its restriction (by computer hardware) to limited domain size. Within the boundary layer the energy-containing range of eddies is typically well resolved by LES, with a negligible portion of the turbulent fluxes carried by the subgrid-scale eddies. Near the lower surface, however, this is not the case, and LES performance in the first few tens of meters can be poor.

Peltier and Wyngaard (1995) demonstrated that today's LES codes can calculate reliably the refractive-index statistics in the atmospheric boundary layer. Their structure-function profiles from LES agreed well with observations in the lower and mid-portions of the convective boundary layer and in the interfacial layer at its top. The requirement that the energy-containing range of spatial scales be resolved, plus the current computational limit of 100–200 grid points per direction, restricts LES in boundary-layer applications to domains no larger than about 10 km in the horizontal, however. In many cases one would like to be able to use domains perhaps an order of magnitude larger. That can be accomplished by coupling LES with mesoscale modeling.

One key to such coupling is that EM refractive index, being determined essentially by temperature and water vapor, is governed by linear differential equations whose solutions are superposable. Thus, we write the three-dimensional, time-dependent water vapor mixing ratio field q, for example, in the atmospheric boundary layer as

$$q(x_i, t) = q^t(x_i, t) + q^b(x_i, t) + q^m(x_i, t). \tag{1}$$

Here q^t and q^b are the "top-down" and "bottom-up" fields, respectively (Wyngaard and Brost, 1984; Moeng and Wyngaard, 1984). q^t is the turbulent field generated by the entrainment process at the boundary-layer top. The air above the boundary layer is usually drier (as measured by mixing ratio) than the air within the boundary layer, and entrainment in the presence of a q change across the top generates a q disturbance below. The turbulent field q^b is generated by a surface flux, either from the surface to the air or vice-versa; either changes the q field above. q^m (m is for mesoscale) is the boundary-layer-scale turbulent q field induced by the horizontal advection of very-large-scale q gradients, which are "chewed up" by the boundary-layer turbulence. We are studying q^m now through large-eddy simulation; we know of no published research on it.

Each of the q^t, q^b, and q^m fields can be written as the sum of a mean part and a fluctuating part. The mean is traditionally the ensemble mean—the limit of the average over different realizations of the flow as the number of realizations approaches infinity. It is not a spatial mean or a time mean. In practice it can be approximated in our application by the mesoscale *resolvable-scale* field—the low-pass spatially filtered field with cutoff in the mesoscale, at a scale of a few km to a few tens of km, say. The fluctuating (also called turbulent) part is the deviation from the mean. By the definition of turbulence it is three dimensional, time dependent, and random—different in each realization.

The mean part of q is important for ducted propagation. In principle it can be calculated adequately through the mesoscale model, although the model may have to be specifically enhanced or even built for this purpose (Otte et al., 1996). For nonducted propagation, where EM *troposcatter* can be important, the critical part is the fluctuating refractive index field. For a mesoscale model this is subgrid scale, meaning that most of its variance is contributed by scales that are smaller than the spatial cutoff scale.

In order to provide the refractive-index input for a PE solver, the mesoscale model, having horizontal grid scale Δ_h and vertical scale Δ_v, needs a subgrid-scale refractive-index field within the atmospheric boundary layer. LES of the boundary layer on a horizontal domain Δ_h provides the refractive-index field on horizontal scales from Δ_h down to the LES resolution δ, which is typically a few tens of meters. If the LES refractive-index fields are calculated for the conditions in the mesoscale grid element $\Delta_h \times \Delta_h \times \Delta_v$, then the linearity of the refractive-index conservation equation allows us to add the LES field to the mesoscale field.

Running LES on demand in this way is wildly impractical, so such "brute-force" superposition is out of the question. The simple similarity expressions of Wyngaard and Brost (1984) suggest an alternative. They wrote for the convective boundary layer

$$q^t = \frac{F_{top}}{w_*} f^t, \quad q^b = \frac{F_{bott}}{w_*} f^b, \tag{2}$$

where the F are the driving fluxes for the q fields, w_* is the turbulent velocity scale for the boundary layer, and the f are dimensionless random functions. There is some interesting physics in the f; for example, in the convective boundary layer the f^t and f^b are strongly correlated (Moeng and Wyngaard, 1984.)

This approach assumes that there is some statistical universality to the functions f, so that the q fields in any particular realization of a given type of boundary layer can be generated by appropriately scaling the f. The idea here is that a small set of a given f (ten, say) can be precalculated through LES and archived; they are then scaled and used within the mesoscale model. The small set of f of provides several different realizations.

To pursue this approach, we will need to know what minimum set of boundary layer states (e.g., very convective, weakly convective, inversion-capped neutral, slightly stable, very stable) is representative. For each such state there will need to be a small set of f fields generated through LES. We will also need a similarity formulation for the refractive-index components in each of these states (e.g., (2) for the convective state) in order to scale these f functions for applications.

A question naturally arises: is this range-dependent detail needed in order to calculate troposcatter reliably? Could the fine structure instead be added through fine-vertical-resolution radiosonde profiles that do not include fine structure in range?

K. E. Gilbert and X. Di have studied this question (Khanna et al., 1998). In simulating EM propagation in the VOCAR experiment (Paulus, 1994) they compared results for the "plywood approximation" (refractive index that varies in the vertical but not in range) and for refractivity with three-dimensional variations calculated through LES. They found that signal levels were typically 15–20 dB higher for the "plywood approximation". They also found that with the "plywood approximation" the horizontal and vertical coherence of the EM field was much greater than one would expect for a realistic turbulent atmosphere.

3. Conclusions and Recommendations

Connecting an LES code to a mesoscale model opens the possibility of physically realistic PE calculations on the mesoscale. We have described an instantaneous refractive-index model system that exploits the statistical similarity of refractive-index fine structure in the atmospheric boundary layer. The core of the system is a mesoscale meteorological model; its subgrid-scale refractive-index fields are produced by scaling archived fields calculated through large-eddy simulation. These scaled, instantaneous, random fields cannot be identical with the actual subgrid-scale fields, which are formally filtered out of the mesoscale equations and are, therefore, irretrievable. They can have the correct statistics, however, and that goal seems within reach. The vast storehouse of data on the statistical structure of refractive-index turbulence, as compiled by Andreas (1990) in his milestone volume, can be used to help reach that goal.

Acknowledgments

This research was sponsored in part by ONR Grant N00014-92-J-1688 and by US Navy Contract N00039-92-C-0100.

References

Andreas, Edgar L., Ed., 1990: *Turbulence in a Refractive Medium.* SPIE Milestone Series, v. MS 25. SPIE, Bellingham, WA., 693 pp.

Deardorff, J. W., 1972: Numerical investigation of neutral and unstable planetary boundary layers. *J. Atmos. Sci.*, **29**, 91–115.

Khanna, S., K. E. Gilbert, X. Di, M. Otte, and J. C. Wyngaard, 1998: Electromagnetic wave propagation through simulated atmospheric refractivity fields. Submitted to *Radio Science.*

Mason, P. J. and D. J. Thomson, 1987: Large-eddy simulation of the neutral-static-stability planetary boundary layer. *Quart. J. Roy. Meteor. Soc.*, **113**, 413–443.

Moeng, C.-H., 1984: A large-eddy-simulation model for the study of planetary boundary layer turbulence. *J. Atmos. Sci.*, **41**, 2052–2062.

Moeng, C.-H. and J. C. Wyngaard, 1984: Statistics of conservative scalars in the convective boundary layer. *J. Atmos. Sci.*, **41**, 3161–3169.

Otte, M., N. Seaman, D. Stauffer, and J. C. Wyngaard, 1996: A mesoscale model for EM ducting in the marine boundary layer. *Proc. 1996 Battlespace Atmospherics Conference.* NRAD Technical Document 2938, 622 pp. **ADA323038**

Panofsky, H. A. and J. A. Dutton, 1984: *Atmospheric Turbulence.* Wiley, New York, 397 pp.

Paulus, R.A., 1994: VOCAR: An experiment in the variability of coastal atmospheric refractivity. *Proceedings of the International Geoscience and Remote Sensing Symposium*, California Institute of Technology, Pasadena CA, August 8-12, 1994, Vol. I, 386–388.

Peltier, L. J. and J. C. Wyngaard, 1995: Structure-function parameters in the convective boundary layer from large-eddy simulation. *J. Atmos. Sci.*, **52**, 3641–3660.

Schmidt, H. and U. Schumann, 1989: Coherent structure of the convective boundary layer deduced from large-eddy simulation. *J. Fluid Mech.*, **200**, 511–562.

Sykes, R. I. and D. S. Henn, 1989: Large-eddy simulation of turbulent sheared convection. *J. Atmos. Sci.*, **46**, 1106–1118.

Tennekes, H. and J. L. Lumley, 1972: *A First Course in Turbulence.* MIT Press, Cambridge, 300 pp.

Wyngaard, J. C. and R. A. Brost, 1984: Top-down and bottom-up diffusion of a scalar in the convective boundary layer. *J. Atmos. Sci.*, **41**, 102–112.

4DVAR MESOSCALE DATA ASSIMILATION OF GOES-8 AND DMSP MOISTURE SOUNDINGS

Xiaolei Zou and Qingnong Xiao
Department of Meteorology, Florida State University, 404 Love Bldg., Tallahassee, FL 32306
Voice: (850) 644-6025; Fax (850) 644-9642; zou@met.fsu.edu

Alan E. Lipton and George D. Modica
Atmospheric and Environmental Research, Inc., 840 Memorial Drive, Cambridge, MA 02139
Voice: (617) 547-6207; Fax (617) 661-6479; gmodica@aer.com

Sponsored by the Air Force Office of Scientific Research

OBJECTIVES: DoD operations and systems are directly and indirectly affected by the weather in the troposphere. Despite the best efforts of system designers and mission planners to make weather "irrelevant," the fact remains that knowledge of the present and future state of the troposphere can lead to both tactical and strategic advantages. At the Air Force Research Laboratory (AFRL), a major goal of weather related research is to yield new techniques that will mitigate the negative effects tropospheric weather has on the Air Force mission. One area of weather under investigation in recent years is tropospheric moisture. The presence (or lack) of moisture has many important and well-known effects on DoD systems. It is also an important ingredient in many kinds of weather systems that can also impact operations. With this in mind, one of the goals of the tropospheric weather research program in recent years has been the development of techniques that will lead to improvements in theater-scale analysis of water in all of its phases. A second goal or objective is to utilize effectively some of the latest space-based measurements of tropospheric moisture. Space-based measurements can provide two important advantages over conventional (land-based) measurements: First, most measurements are passive so that data collection does not compromise security by giving away the location of friendly forces. Second, space-based platforms are able to provide information in data-denied areas that otherwise would not be easily accessible with conventional instrumentation. Another objective of this research is to improve theater-scale prediction of moisture related quantities (rain, snow, etc.) so that the three-dimensional distribution will be known at the desired point in the future. Finally, we hope that tropospheric weather research will improve the community's understanding of meteorological phenomena.

This paper reports on the results of an effort to utilize some of the latest numerical techniques and data sources that are hoped will lead to achievement of these objectives. In this study, we utilized the method typically known as four-dimensional variational (4DVAR) data assimilation. The method will be described in more detail in the next section.

RESEARCH ACCOMPLISHED: The data we chose for this study were taken from the 1995 Atlantic Hurricane Season. This was a particularly active year for tropical storms in the Atlantic; we chose data from the sixth named storm of the season—Felix. Felix began as a tropical wave off the African coast on 6 August and reached hurricane strength at about 00 UTC 11 August while centered about 500 nm east-northeast of the Leeward Islands. The post-analysis "best track" is shown in Fig. 1. By 13 August, Felix was centered 300 to 400 nm south-southeast of

Bermuda. Over the next couple of days (15 and 16 August), Felix continued on a northwestward track that brought the storm center within 65 nm of Bermuda and toward the North Carolina coast. Afterward, Felix stalled, moved northeastward, and performed an anticyclonic loop before finally turning north on the 20th and then northeastward on 21 August. Although the track errors of official Felix forecasts were generally lower than the long-term averages maintained by the National Hurricane Center (now known as the Tropical Prediction Center) there were some large individual errors, including five over 500 nm at 72 hours. Other track model errors were only slightly lower than the official forecast errors. Some large 72-hour intensity forecast errors (35 to 45 knots) occurred. The largest of these did not properly take into account the rapid strengthening on the 11th and 12th, nor the weakening thereafter. Some of these significant changes in the weakening and track errors could have been related to the ingestion of drier air into the circulation. Although Felix never made landfall in the United States, some of the official forecasts and several of the track prediction models indicated this possibility. Watches and warning were issued for the appropriate coastal areas.

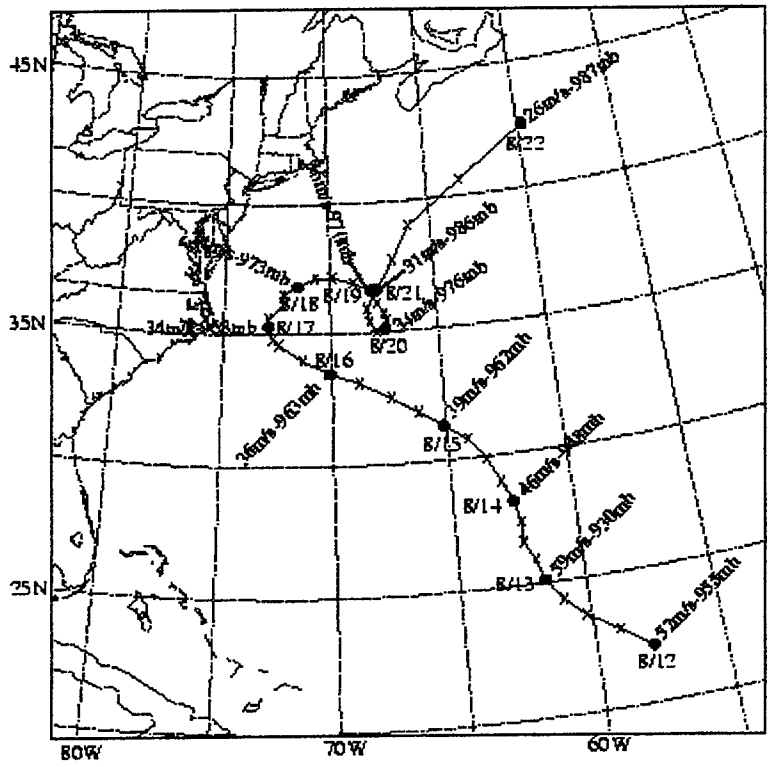


Figure 1. Observed track (best track determined by the National Hurricane Center) of Hurricane Felix during the period from 00 UTC 12 August 1995 until 00 UTC 22 August 1995. The storm's minimum sea-level pressure (mb) and maximum low-level wind (ms^{-1}) at 00 UTC each day are shown. The large dots indicate the position of the storm at 00 UTC and the x's indicate the 0600, 1200 and 1800 UTC storm positions.

The model used to simulate Hurricane Felix is the Penn State/NCAR MM5 model. The grid system and physical options for each of the triply nested meshes in the present study are summarized in Table 1. There are 27 σ layers for all grid meshes with horizontal resolution of 90 km for the coarse mesh A, 30 km for the intermediate mesh B, and 10 km for the fine mesh C_i domain (see Fig. 2). The domains A and B are fixed and the 10 km domain C_i moves along the hurricane track, with C_1, C_2, C_3, and C_4 for the periods of 0-18 h, 18-24 h, 42-55 h and 55-84 h, respectively. The model physics include a cumulus parameterization scheme described by Grell (1993), the mixed phase microphysics scheme (Reisner scheme) and the high-resolution

planetary boundary layer parameterization (Blackadar scheme). The land surface temperature is predicted using surface energy budget equations. For a more detailed description of MM5, refer to Dudhia (1993) and Grell et al. (1993). The model was initialized at 12 UTC 15 August 1995. The initial data are obtained from the National Centers for Environmental Prediction (NCEP) 2° resolution global analysis, horizontally interpolated onto the regional domain for the mesh resolutions and enhanced with rawinsondes and surface observations. Among the surface observations were numerous ship reports received in the vicinity of Felix. These were helpful in defining the extent of tropical storm force winds.

Table 1 Model Design for Felix Experiments

	Domain	Resolution	Dimension	Physics option		
				Explicit	Cumulus	PBL
Forecast	A	90 km	45x51x27	Stable Precipitation	Grell	Blackadar
	B	30 km	76x85x27	Dudhia simple ice	Grell	Blackadar
	C	10 km	121x121x27	Reisner mixed-phase	Kain-Fritsch	Blackadar
Initialization	B	30 km	76x85x27	Stable Precipitation	Grell	Bulk

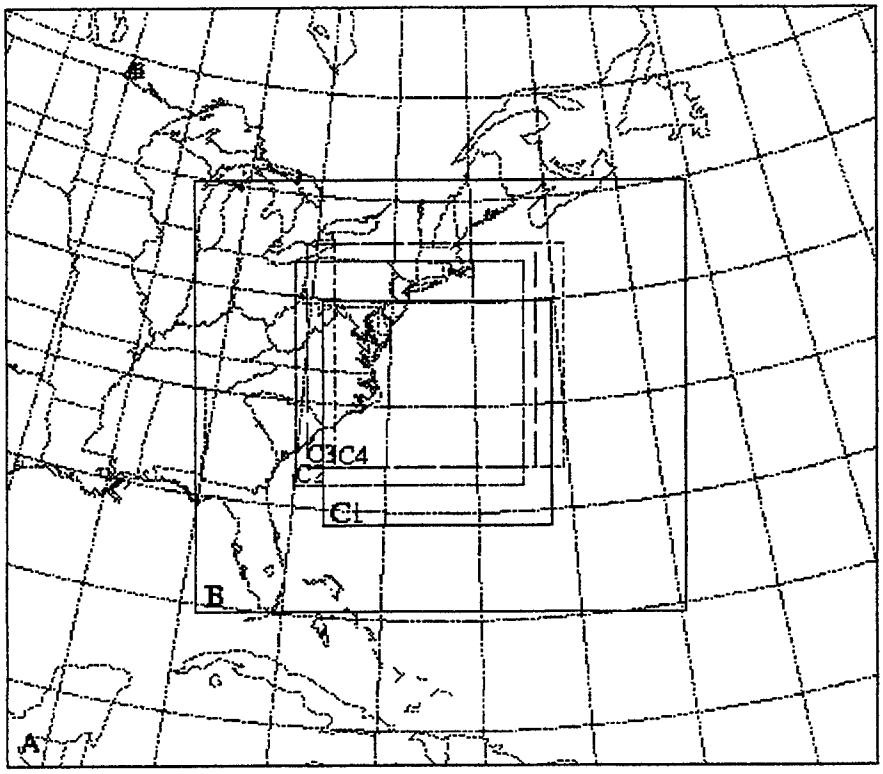


Figure 2. Position of model domains

The importance of having a proper initial vortex at the start of the model prediction is widely recognized and has been recently demonstrated in Liu et al. (1997). In the current study, the initial vortex was specified with the use of an objective vortex initialization scheme (Zou and Xiao 1998). This scheme permitted the surface low to be specified based on the radius of the cyclone and its position and central pressure, which were available from observational reports. These bogus data are used as "observations," which will then be assimilated along with satellite radiances into MM5 to generate a model initial state that incorporates all possible instantaneous information and model dynamical and physical constraints. More specifically, the hurricane initialization procedure is carried out by minimizing a cost function J_{bogus}, which is defined as follows:

$$J_{bogus}(\mathbf{x}_0) = \sum_{t_i} \sum_{i,j \in \Re} (P - P^{bogus})^T W_P (P - P^{bogus}) + \sum_{t_i} \sum_{r_l} ((R - R^{satellite})^T W_r (R - R^{satellite})) + J_b \quad (1)$$

where the summation over t_i is carried out over a half-hour window. $\Re$ is a circular 2-dimensional domain of a 300 km (as a radius) circle centered at the hurricane center, (i, j) represents model horizontal grid points within $\Re$ at the lowest σ level (σ = 0.995), and r_l is the physical location in the 3D space representing all available satellite radiances. W_P and W_r are diagonal weighting matrices and their values are determined empirically. Variables P and R represent sea-level pressure and satellite radiances, respectively. J_b represents a simple background term that measures the distance between the model state and the MM5 analysis based on the large-scale NCEP analysis.

The variational initialization is carried out on domain B (30 km resolution) using the adjoint modeling system of MM5 as described by Zou et al. (1996). The physical parameterizations included in the initialization are a bulk aerodynamic formulation of the planetary boundary layer, a dry convective adjustment, grid-resolvable large-scale precipitation, and the Grell cumulus parameterization (see Table 1).

Infrared and microwave satellite data were collected at AFRL using the AFRL Interactive Meteorological System (AIMS) facility. Data were collected from the imager and sounder aboard GOES-8. The GOES-8 sounder data were cloud-cleared to correct for the complicating effects that hydrometeors have on the interpretation of IR brightness temperatures. Cloudy GOES-8 individual fields of view (IFOVs) were identified using a person-computer interactive cloud-clear discrimination program that operated on images made with data from the visible channel and from the infrared channels at 3.7 and 11.0 micrometers. To create a single sounding field of view (SFOV), sets of IFOVs were averaged horizontally. The purpose of the averaging is to compensate for data noise. In order to select a set of averaging areas for a given field of sounder data that minimized the gaps in coverage caused by clouds, we used the method outlined in Lipton (1998). Data were collected from 3x3 boxes of GOES-8 IFOVs. At least four clear IFOVs were required to make a SFOV and an isolation limit of K=9 was used. Microwave data were collected from the Defense Meteorological Satellite Program (DMSP) Special Sensor Microwave/Temperature-2 (SSM/T-2) instrument aboard the F11 satellite. A different method was used to accomplish the cloud clearing for the SSM/T-2 data than for GOES, since the SSM/T-2 data had much coarser resolution than the GOES data (48 vs. 10 km, nominal) and because hydrometeors affect microwave brightness temperatures differently than they do for

infrared brightness temperatures. In this case, the goal was to eliminate the microwave IFOVs in which large amounts of atmospheric liquid water and/or large ice particles were present; however, we wished to retain those IFOVs that contained only few or small cloud particles (e.g., thin cirrus). In order to accomplish this, we adopted a version of the cloud analysis algorithm named after Support of Environmental Requirements for Cloud Analysis and Archive (SERCAA; Gustafson et al. 1994). The SERCAA algorithm performs a series of cloud detection tests. One of the GOES cloud detection tests in the SERCAA algorithm is a temporal difference test. This test utilizes a temporal differencing technique to identify new cloud development and existing cloud features that have changed from a previous time. The two time levels used for this were chosen to bracket each available time of SSM/T-2 data. The SERCAA algorithm was used to flag GOES-8 image pixels that tested positive for low-level clouds but not cirrus. The SSM/T-2 SFOVs were next collocated with the flagged pixels from the SERCAA test through the use of a merge program. Any SSM/T-2 SFOVs coincident with at least some threshold amount of low-level clouds were discarded. Areas of precipitating cloud were also flagged with the use of a SSM/T-2 based test (Pickle et al. 1996). For this case we did not have confidence in the SERCAA low cloud product used to select the 1030 UTC SSM/T-2 soundings because, without sunlight, it missed many clouds. For this time only, all cloudy SSM/T-2 SFOVs were removed from the sample.

Following the cloud and precipitation clearing steps outlined above, the satellite data were further processed by removing the bias between the satellite radiances and those calculated from collocated radiosonde observations. For this we used a shrinkage estimator (Fleming et al. 1991) which is a modified regression technique. In our application of the shrinkage estimation technique, we used as predictors the satellite channels, and the latitude and satellite zenith angle of the satellite observation.

To assess the impact of the satellite data and surface data on the model forecasts, three separate integrations are performed, each starting from a different set of initial conditions. The first integration (E.ctrl) begins with an initial condition containing the original vortex resolved by the NCEP global analysis. The second and third begin from the initial condition modified by minimizing J_{bogus} in (1), first without the satellite term (E.bg) and then with the satellite term included (E.bg+sat). Minimization of J_{bogus} is carried out on the 30 km mesh (i.e., domain B). The finer mesh domain (C_1) initial conditions are obtained by interpolating the modified initial conditions on domain B to domain C_1). The initial conditions were valid 12 UTC 15 August.

Each of the model predictions is run in a two-way interactive, movable, triply nested grid technique. Coarser meshes provide the finer meshes with time-dependent lateral boundary conditions while the finer mesh solutions feedback to coarser meshes every time step. The outermost lateral boundary conditions (for mesh A) are specified by linearly interpolating the 12 h NCEP analyses.

Minimization of J_{bogus} for the E.bg experiment converged in 30 iterations. During the minimization procedure, the sea-level pressure was forced toward an estimate of the bogused surface low, while the wind, temperature and moisture were free to develop a model-consistent structure. Such an initialization ensures a smooth start of the integration of the prediction model. Since the development of a realistic vortex structure is crucial for successful hurricane prediction, some comments are presented on the vortex generated in this study. The

improvement in the structure of the specified vortex is apparent at initial time t = 0 h (not shown). The distribution of the sea-level pressure, horizontal wind vectors and wind speed at 850 hPa at the initial time before and after minimizing J_{bogus} reveals that the specified vortex after variational initialization is much more compact and considerably more intense than the vortex in the global analysis.

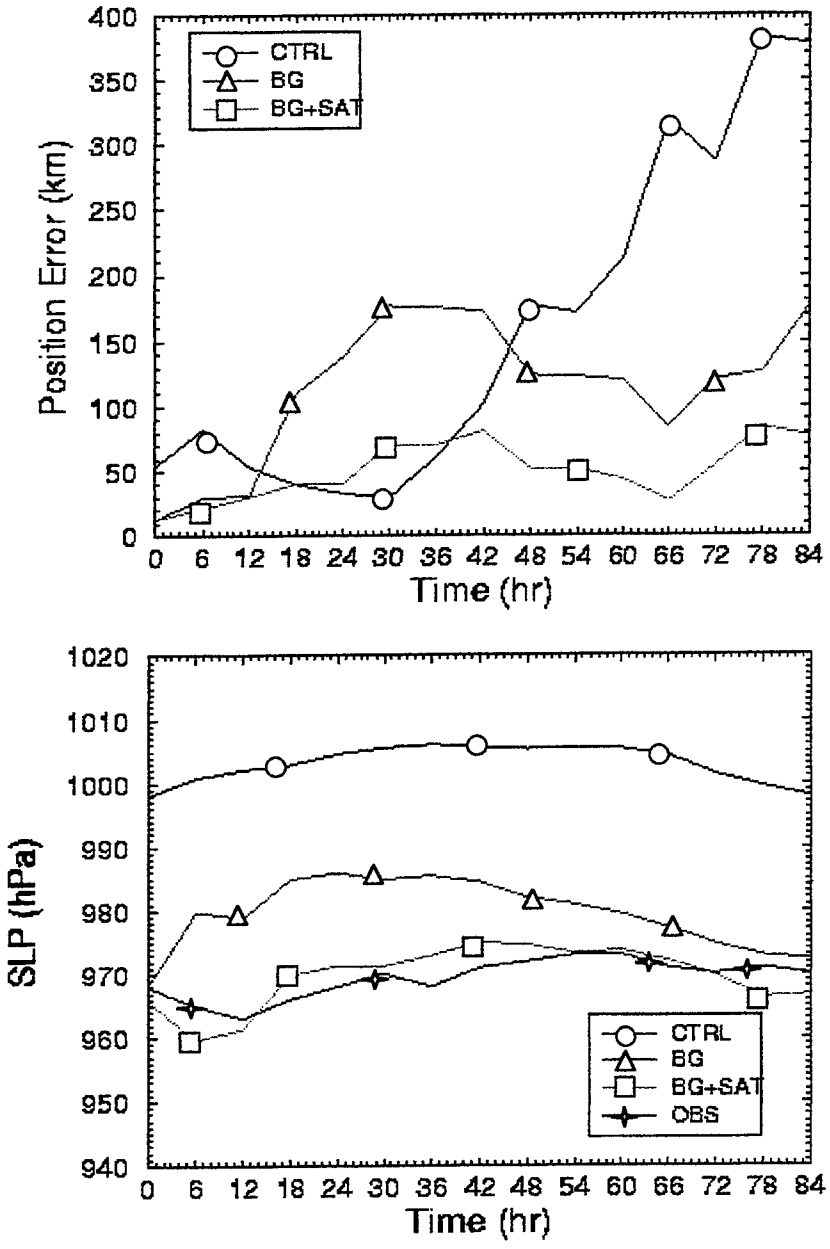


Figure 3. Time plots of a) position error (km) and b) sea-level pressure (hPa) of the simulated hurricane center. CTRL is for the E.ctrl simulation; BG and BG+SAT are for the E.bg and E.bg+sat runs, respectively. See text for details.

Figure 3 shows the effect on (a) track error and (b) sea-level pressure of the different initial conditions. The results presented for E.bg+sat are for the use of surface pressure observations and GOES-8 radiances only; radiances from the DMSP SSM/T-2 instrument will be added soon, both separately and in combination with the GOES radiances. Figure 4a reveals that the E.ctrl run has the smallest position error between 18 and 36 h. The reason for this is not known at this

time. The inclusion in the initial conditions of radiance information (E.bg+sat) results in clear improvement over the E.bg experiment after 12 h of integration. Between 30 and 84 h this improvement lies between 50 and 100 km. Figure 4b shows that the sea-level pressure from the E.bg+sat run is superior (closest to the observed) to the other runs at all times of the forecast.

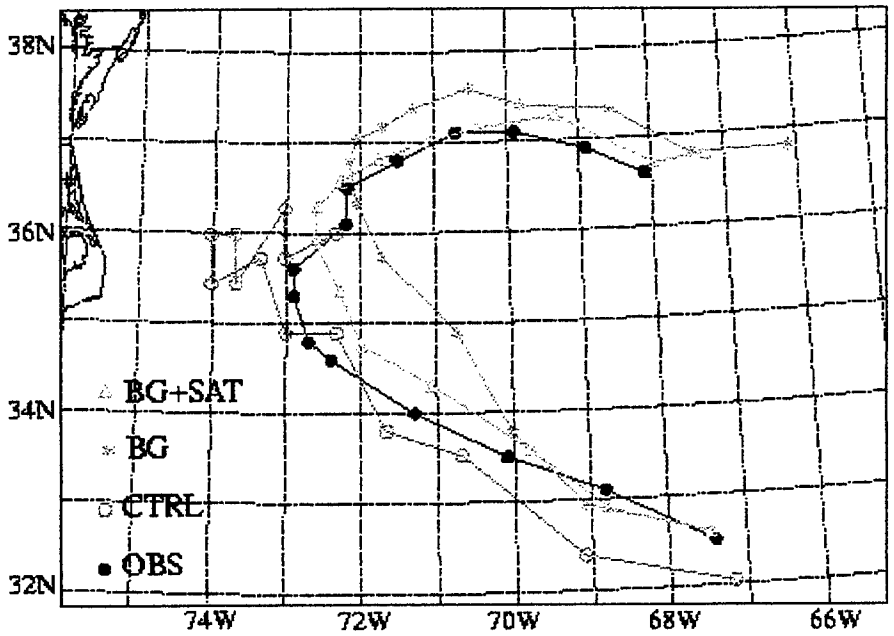


Figure 4. 84-hour Hurricane Felix track starting from 12 UTC 15 August 1995

CONCLUSIONS AND RECOMMENDATIONS: In this report, we have presented results of a study on the impact of observed data on the simulation of a tropical cyclone. Conventional and satellite-based radiance data from the GOES-8 sounder were assimilated using the 4DVAR technique to arrive at an initial condition. Simulations started from three different initial conditions were carried out for an 84 h period. The analysis results show that the bogussed sea-level pressure reports from ships in the vicinity of Hurricane Felix were indeed able to provide the information needed for the MM5 adjoint system to "spin-up" a realistic hurricane vortex (E.bg case). The hurricane prediction model serves as a strong constraint to spin-up other fields not readily observed such as the divergence and vorticity fields. The proposed scheme requires minimum information about the size, location and the central value of the specified low. This vortex had more detailed structure than that in the control analysis and led to better simulations of the tropical system during a subsequent model integration in terms of track error and intensity. When radiance information from the GOES-8 sounder was added to the analysis (E.bg+sat), the result was a marked improvement in both forecast position error and intensity over and above that from the E.bg run (see Fig. 4).

Application of the proposed scheme to another hurricane simulation—Hurricane Fran—also shows similar improvements to the initial conditions (Xiao and Zou, 1998). Tests of this scheme with subjectively assigned parameter values of the size of the surface low have produced similar results, showing a minimum sensitivity to the subjectively determined radius of the surface low. More case studies need to be conducted—especially for cases when the initial vortex is weak. Given the current state of numerical forecast models and large-scale analysis, these results suggest that it may be possible to predict reasonably well the track, intensity and inner-core

structures of hurricanes with a minimum of targeted observations such as a few surface observations and satellite radiances in the near-storm environment. A further interesting prospect is that the next-generation of space-based weather instruments (e.g., the National Polar-Orbiting Operational Environmental Satellite System, or NPOESS) will have enormously greater spatial and spectral resolution with the potential to provide additional benefits to theater-scale analysis and prediction.

REFERENCES

Dudhia, J., 1993: A nonhydrostatic version of the Penn State-NCAR mesoscale model: Validation tests and simulation of an Atlantic cyclone and cold front. *Mon. Wea. Rev.*, **121**, 1493-1513.

Fleming, H.E., N.C. Grody, and E.J. Kratz, 1991: The forward problem and corrections for the SSM/T satellite microwave temperature sounder. IEEE Transactions on Geoscience and Remote Sensing, **29:4**, 571-583.

Grell, G.A., 1993: Prognostic evaluation of assumptions used by cumulus parameterizations. *Mon. Wea. Rev.*, **121**, 764-787.

Grell, G.A., J. Dudhia, and D.R. Stauffer, 1994: A description of the fifth-generation Penn State/NCAR mesoscale model (MM5). *NCAR Technical Note*, NCAR/TN-398+STR, National Center for Atmospheric Research, Boulder, CO, 138 pp.

Gustafson, G.B., R.G. Isaacs, R.P. d'Entremont, J.M. Sparrow, T.M. Hamill, C. Grassotti, D.W. Johnson, C.P. Sarkisian, D.C. Peduzzi, B.T. Pearson, V.D. Jakabhazy, J.S. Belfiore, and A.S. Lisa, 1994: Support of Environmental Requirements for Cloud Analysis and Archive (SERCAA): Algorithm Descriptions. PL-TR-94-2114, Phillips Laboratory, Hanscom AFB, MA, ADA 283240, 100 pp.

Lipton, A.E., 1998: Improved GOES sounder coverage of cloud-broken data fields. J. Appl. Meteor., **37**, 441-446.

Liu, Y., D. –L. Zhang, and M.K. Yau, 1997: A multiscale numerical study of Hurricane Andrew (1992). Part I: Explicit simulation and verification. *Mon. Wea. Rev.*, **125**, 3073-3093.

Pickle, J.D., R.G. Isaacs, V. Jakabhazy, M. Griffin, and V.J. Falcone, 1996: Detection of precipitation using SSM/T2 measurements. Eigth Conference of Satellite Meteorology and Oceanography, Jan 28-Feb 2, AMS, Boston, MA, 238-242.

Zou, X. and Q. Xiao, 1998: Initial structures within a mature hurricane vortex generated by a variational initialization scheme. *J. Atmos. Sci.* manuscript in preparation.

Zou, X., F. Vandenberghe, M. Pondeca, and Y. –H. Kuo, 1997: Introduction to adjoint techniques and the MM5 adjoint modeling system, *NCAR Technical Note,* NCAR/TN-435-STR, National Center for Atmospheric Research, Boulder, CO, 110 pp.

Battlespace Sensing Techniques and Applications

SSBC[1] : AN ACCURATE ATMOSPHERIC SOUNDING SYSTEM

Michel Aïdonidis*
EPSHOM[2], BP426, 29275 Brest Cedex, France
Tph : 33~298 22 09 47 ; Fax : 33~298 22 18 64
aido@shom.fr

Marcel Zéphoris and Franck Lavie
Météo-France/SETIM[3], 7 rue Teisserenc-de-Bort, BP202, 78195 Trappes, France
Tph : 33~130 13 64 33 ; Fax : 33~130 13 63 21
Marcel.Zephoris@meteo.fr
Franck.Lavie@meteo.fr

Abstract

Impact of meteorological parameters on EM propagation can be decisive in the assessment of target detection risk. Observation still remains the basic estimation of atmospheric profiles.

Until now, only balloon soundings have given essential environmental information in the vicinity of a ship. To take advantage of the NATO survey –Rapid Response 98- last February and the presence of the BO D'Entrecasteaux[4], SHOM[5] and Météo-France have tested different sensors useful to describe atmospheric parameters : balloon, SSBC and TOVS (the latter is not described in the follow-up).

Use by all Met. Office of the world, the balloon is the most conventional type of support. During this campaign, its data were used as standard measure.

SSBC sensor, developed by Météo-France, has already been used since a few years by gliding clubs. But, on that occasion, it was the first use in marine environment aboard an Alouette III. Small, accurate and easy to install, this system is prepared before each flight and, then, ready for a 2h15min mission until up to 5000 meters altitude.

Through two examples, where balloon profiles are too smoothed to show ducts nevertheless detected by SSBC sensor, difference of accuracy between these two systems is highlighted.

At the same time, a GPS-localization has been appraised. The aim is to avoid flight constraint during sounding. First results should be presented during BACIMO'98.

---

[1] SSBC : Système de Sondage en Basses Couches/*Low level sounding system*
[2] EPSHOM : Établissement Principal du Service Hydrographique et Océanographique de la Marine, located in Brest
[3] Météo-France/SETIM : (french met. Office) Service des Équipements et des Techniques Instrumentales de la Météorologie
[4] BO D'Entrecasteaux : french oceanographic research vessel with helicopter platform
[5] SHOM : Service Hydrographique et Océanographique de la Marine, Head Office of the EPSHOM, located in Paris

1. Objective

Observation still remains the basic estimation of target detection probability at any moment. Until now, only sounding by balloon gives information close to a ship, at its vertical. At present, atmospheric variability is not well observed. So, it seems to be desirable to assess some sensor contribution recently developed.

BO D'Entrecasteaux presence in the Cadix Gulf (Spain) during NATO survey *Rapid Response 98* has permitted the SHOM, in close collaboration with Météo-France, to collect atmospheric profile data from these sensors :

- a probe suspended from a balloon ;
- a probe, called SSBC, installed on an Alouette III, boarded on BO D'Entrecasteaux ;
- TOVS[6] sensors on NOAA-14 satellite.

The survey objectives, called *LASR98*, are :

- to check data validity obtained from SSBC and satellite ;
- to detect possible horizontal atmospheric shearing ;
- to assess SSBC behavior in marine atmosphere ;
- to verify possibility in using SSBC during nondedicated operational flight ;
- to assess possible interest in AWW[7] domain.

Satellite data are not studied in this presentation.

2. Description of sensors

Different sensors studied measure basic meteorological parameters : dry air temperature, humidity and pressure.

2.1 Sounding by balloon

Installed on several ships of the navy, it's the most conventional mean of measure, used by all Met. Office in the world. Soundings are used to be made twice a day, at 00 and 12UTC.

The whole system is composed with a probe suspended from a balloon filled with helium. Carried along by wind, it climbs until up to several thousand meters, often until up to 25 kilometers and more. Data are sent by the sonde during the ascent. Besides usual reception equipment, there was a « basin » where the balloon was filled before the release. For security reason, due to helicopter presence, this basin has been installed on the port bow.

During *LASR98* survey, sounding by balloon was the standard measure.

[6] TOVS : Tiros-N Operational Vertical Sounding
[7] AWW : Above Water Warfare

2.2 SSBC sensor

Gliding clubs have used this system, developed by Météo-France, boarded on small planes for a few years. The whole system is made up of these parts :

- a probe, overall height/width/length : 20 x 10 x 13 cm, 1.2 kg weight ;
- a measure treatment software ;
- a data visualization software ;
- a probe grading case.

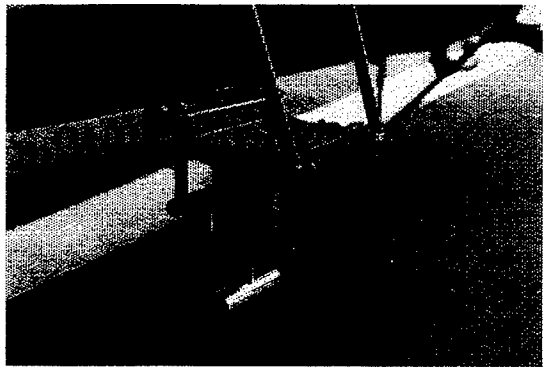
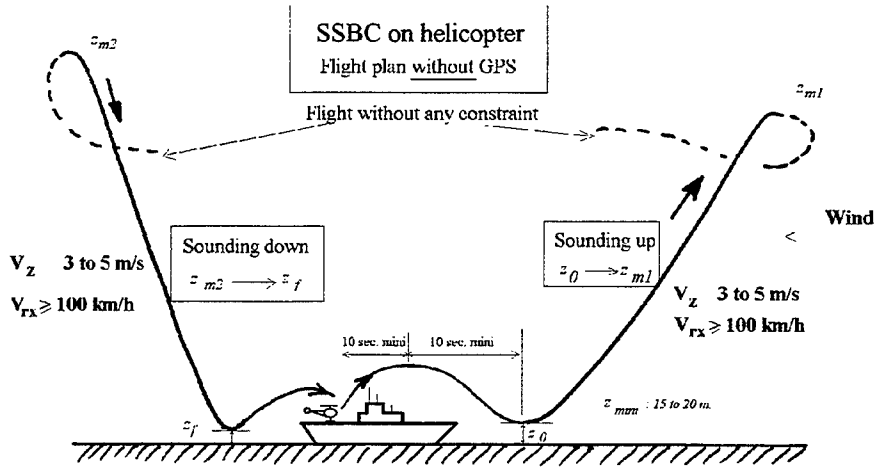


Photo 1 : SSBC on Alouette III step

Small, accurate and easy to use, SSBC has been assessed for the first time in marine atmosphere during this survey. This probe is prepared before each flight in its case. This operation takes about 10 to 15 min. Then, the probe is installed on a special platform just before the flight (cf. photo 1).

In this first version, the probe mustn't be subject to severe flight conditions. So, pilot has to respect a flight plan during ascent and descent rather strict (cf. figure 1). Indeed, during abrupt motion (banking, irregular vertical speed), superpressure or underpressure may occur. Furthermore, in this version, the helicopter has to come back to its point of departure to get data registered during all the flight.



- Steady climb against the wind
- As horizontal to the ground as possible
- Probe working time : 2 h 15 min.

Figure 1 : flight plan without GPS

The second version, in the process of development by Météo-France, consists of a GPS localization, removing motion constraint. So, this survey has allowed a first evaluation of this new system.

During the period of measurement, 13 flights have realized soundings, 2 have got GPS data. GPS results should be available by the end of 1998.

The daily use has shown that the SSBC could be installed on helicopter because the calibration made after the mission has not detected any drift of the probe, neither fault in its running system.

3. Data analysis

The meteorological situation was stable during the whole period : high pressure was installed over Western Europe, leading to east flow, notably speeded up by straight of Gibraltar. Wind was often higher than 40 kt. So, sensors assessment has been only possible in one kind of weather.

3.1 Comparison between balloon and SSBC

On the whole, profiles observed with balloon and SSBC seem to be very similar. February, 24th example shows a nearly perfect likeness between dry air temperature profiles (cf. figure 2) with an inversion located at about 870 hPa. Dew point temperature differences observed remain minor (akin to 1 to 2 °C), except in the lower layers (akin to 2 to 3 °C).

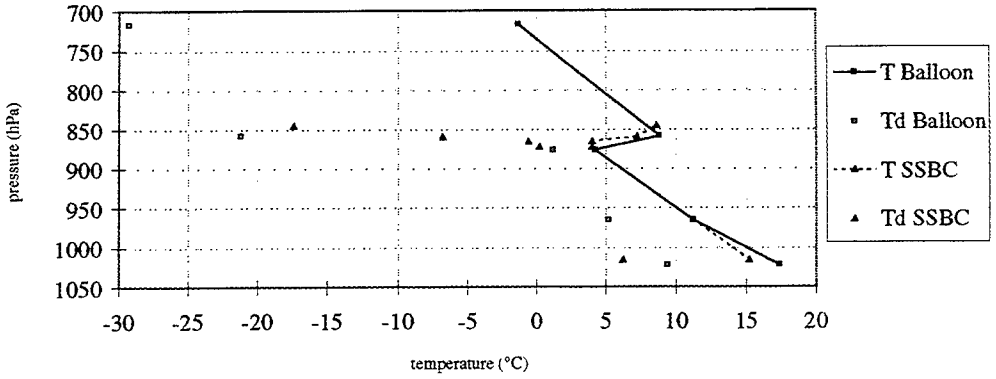


Figure 2 : dry air (T) and dew point (Td) temperature comparison between balloon and SSBC data ; February, 24th 1998.

However, in some cases, balloon data show inaccuracies at subsident inversion level. The increase of temperature and the drop of humidity are less sharp than with SSBC data (cf. figure 3, February, 19th example).

These differences have an important impact on modified refractivity index M, which variations indicate the possible presence of ducts. M expresses on temperature, humidity, pressure and altitude of the measure. If M decreases, there is a duct. Differences between balloon and SSBC data are sufficient to modify M profiles. Thus, an elevated duct is detected with SSBC data and not with balloons one (cf. figure 4).

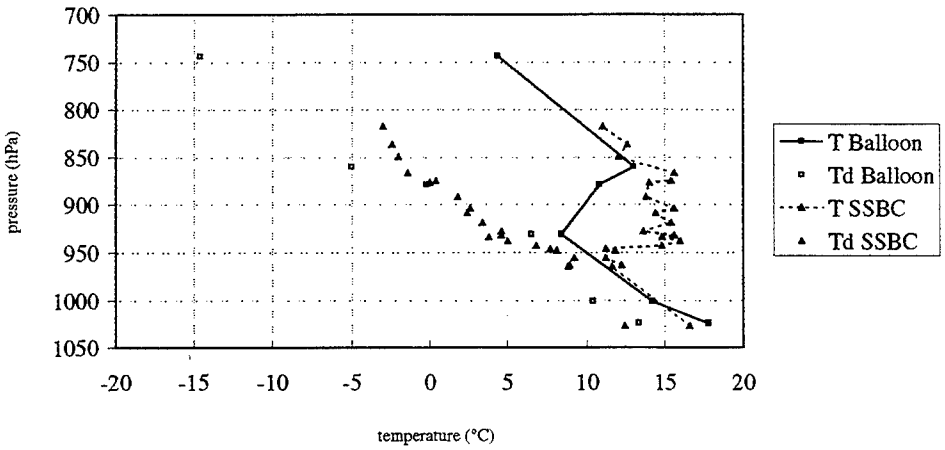


Figure 3 : dry air (T) and dew point (Td) temperature comparison between balloon and SSBC data ; February, 19th 1998.

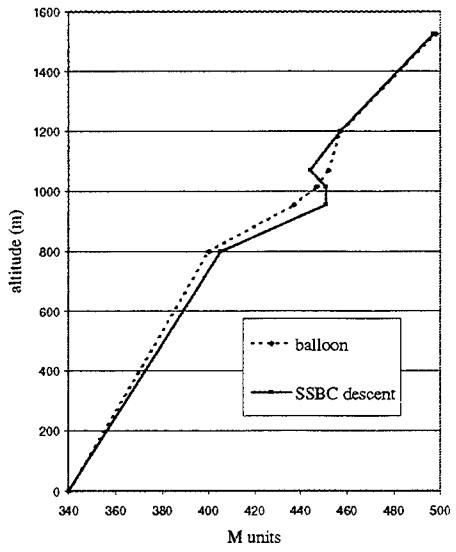


Figure 4 : modified refractivity (M-units) from balloon and SSBC data ; February, 19th 1998.

At last, 1 to 2 °C differences in dry air temperature are systematically observed in very lower layer, balloon temperature is always greater than SSBC one. The principal reason is due to superstructure heating measured by balloon while helicopter probe records data just above the sea (or the ground) at the beginning and the end of the sounding.

3.2 Atmospheric horizontal variability assessment

SSBC can give ascent and descent sounding several kilometers away one from another. For example, it's conceivable to get a sounding above the sea and, another one above the land. So, atmospheric variability can be visualized, mainly at the land/sea interface where heavy discontinuities of meteorological parameters are located in the lower layers. February, 27th example shows this « border effect» with two soundings realized near the Spanish coast (cf. figure 5). Over a few kilometers, we can see two notable differences :

- ascent subsident inversion is located at about 930 hPa, the descent one is at about 910 hPa ;
- humidity layer is seen between 890 and 880 hPa during ascent, invisible during the descent.

Impact of these differences is perceptible on modified refractivity index M (cf. figure 5). An elevated duct is well seen during the ascent at about 900 meters and 200 meters thick ; the same one is located at 1000 meters during the descent, 100 meters thick and less sharp.

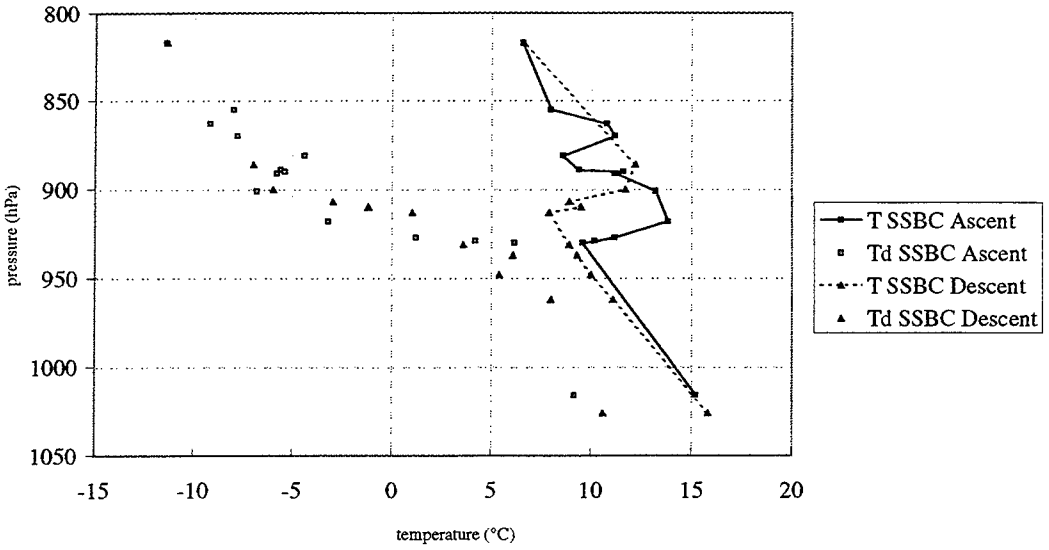


Figure 5 : dry air (T) and dew point (Td) temperature comparison between ascent and descent SSBC data February, 27th 1998.

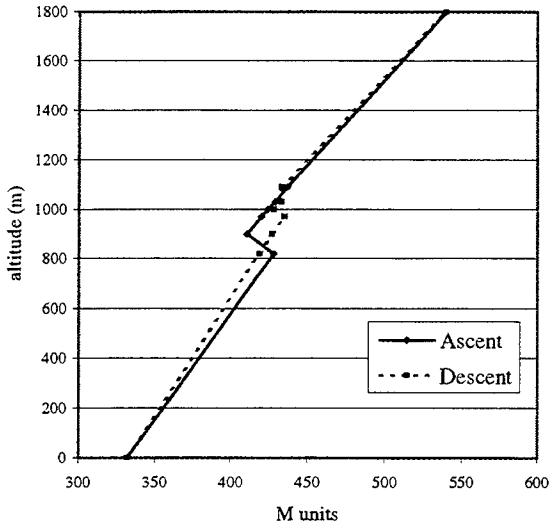


Figure 6 : modified refractivity (M-units) from ascent and descent SSBC data February, 27th 1998.

Inaccuracies of the measure, due to sensor response time, aren't the principal problem. The first one is that higher response time of the radiosonde decreases gradient and raises its altitude too. So, it appears that SSBC probe can soften, indeed remove, these uncertainties.

4. Conclusions and recommendations

If an operational test on a navy ship is desirable, two developments are to be considered :

- first is GPS localization, freeing aircraft from flight constraint, mainly turns ;
- second could be the need of real time data transmission, based on mean flight duration study.

Operational use of the SSBC seems to be justified for many reasons. Accuracy of the measure, in the lower layers in particular, and the cost of the equipment make it a supplementary system with balloon. More, its behavior in marine atmosphere has not revealed any premature damage.

It is confirmed that there is, until now, not only one type of sounding equipment able to give atmospheric data, with accuracy, over a large area. Only a set of various equipment, used together or separately can give pertinent information. It was the case with balloon, it's the case now with the SSBC or equivalent. It should be the same with satellite data –such as TOVS or IASI sensors- but in a more or less long period.

The MMS-Profiler: Present and Future

J. Cogan, E. Measure, E. Vidal, E. Creegan, and G. Vaucher

Information Science and Technology Directorate
Army Research Laboratory
White Sands Missile Range, NM 88002

Abstract - The Meteorological Measurement Set - Profiler (MMS-P) is a major product improvement to the MMS wherein a suite of remote sensing instruments combined with a meteorological satellite receiver eventually will replace the current rawinsonde system. The primary remote measurement instruments are a wind profiling radar and a passive microwave radiometer for temperature profiles. A new Semi-Automated Meteorological Station (SMS) now in the Army inventory provides surface measurements. Atmospheric profiles from the ground-based systems are combined with soundings generated from meteorological satellite data to form merged soundings that can extend from the surface to about 30 km. The current prototype MMS-P also has a GPS rawinsonde capability to provide comparison data, and to provide a substitute for the satellite soundings if needed. The entire system fits in a shelter carried by a High Mobility Multi-purpose Wheeled Vehicle (HMMWV) plus a High Mobility Trailer (HMT) for the radar. A separate vehicle tows a "silent" generator. This paper briefly describes the latest version of the prototype MMS-P, and provides a sample of output from the system. Preliminary comparisons with rawinsonde data suggest the accuracy of the resultant merged profiles. Certain planned upgrades are discussed such as neural network methods to derive temperature and wind soundings from satellite data. Emphasis is placed the current system and planned upgrades.

1. Introduction

The Army Research Laboratory, Information Science and Technology Directorate, with assistance from the National Oceanic and Atmospheric Administration, Environmental Research Laboratories, Environmental Technology Laboratory, developed a mobile system for measurement and analysis of atmospheric profiles in close to real-time (Cogan et al, 1997; Wolfe et al, 1995). The early system described in the aforementioned references was modified by upgrading the wind radar antenna and placing it on a new High Mobility Trailer (HMT), removing the Radio Acoustic Sounding System (RASS), combining the radiometers into a single smaller instrument, and installing the processors and some other equipment into a shelter on a High Mobility Multi-Wheeled Vehicle (HMMWV) towing the wind radar trailer, while increasing capability and user Afriendliness.Δ The radiometer with upgraded software takes over the function of temperature sounding from the ground, thereby eliminating the need for a RASS. A new Semi-Automated Meteorological Station (SMS) now in the Army inventory provides surface measurements. Atmospheric profiles from the ground-based systems are combined with soundings generated from meteorological satellite data to form merged soundings that can extend from the surface to about 30 km. The current version also has a GPS rawinsonde capability to provide comparison data, and to provide a substitute for the satellite soundings if needed. A second vehicle tows a "silent" generator to provide power at field locations. The resultant system, the prototype of the planned Meteorological Measurement Set - Profiler (MMS-P), will

be a major product improvement to the MMS wherein the suite of remote sensing instruments combined with the meteorological satellite receiver eventually will replace the current rawinsonde system. This paper briefly describes the latest version of the prototype MMS-P, and provides a sample of output from the system. Preliminary comparisons with rawinsonde data, and comparison data from field experiments using the earlier "mobile" system, suggest the accuracy of the resultant merged profiles. Certain planned upgrades are discussed such as neural network methods to derive temperature and wind soundings from satellite data. Emphasis is placed on the current system and planned upgrades.

2. System Description

Figure 1 shows the several component Ąsensors∆ of the Profiler after a series of recently completed upgrades presented as the current system in Table 1. The processors fit inside the HMMWV shelter shown in figure 1. The new software package contains the algorithms noted in

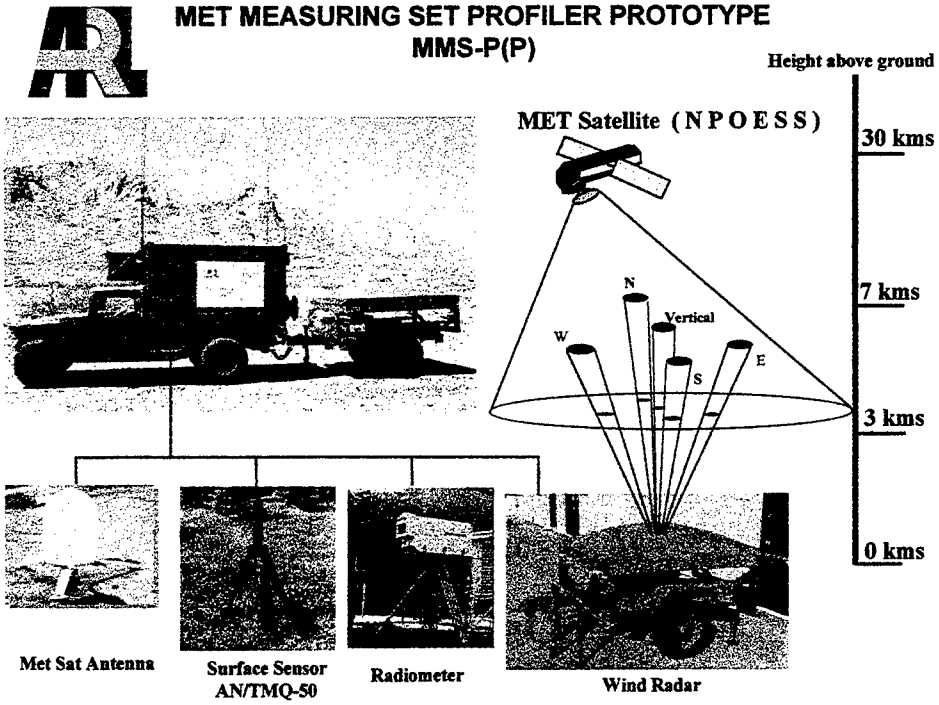


Figure 1. View of the planned configuration showing principal components. Processors located inside shelter.

Cogan et al (1997) and Wolfe et al (1995), plus others for integration of the several sensors and processors into an integrated system. The integration software is largely written in Java and is portable across different processors using different operating systems (e.g., NT and UNIX). Processing of moment information is being replaced by spectral processing for better quality control and more accurate met output. These algorithms will use a version of the LAP-XM (Radian International) or equivalent processing system to collect the raw radar data. Use of the

on-board Battlescale Forecast Model (BFM) will allow analysis and short term prediction over mesoscale areas (Knapp and Haines, 1997). All component sensors are working, and we have begun to collect test data. The entire upgraded system, the prototype Meteorological Measuring Set - Profiler (MMS-P), should be ready for use in field tests before the end of 1998.

Table 1. Profiler sensors, selected software packages, and characteristics. This table presents the current configuration and certain planned upgrades.

System	Current Profiler.
	Potential Upgrades..
Radar wind profiler	924 MHz phased array, signal tapering, 5000 W peak power.
	Electronic beam steering, non-level operation.
MW Radiometer	T: 50-60 GHz (O_2), PW, LW: 23.8, 31.4 GHz, one radiometer "container", tunable (O_2 band).
	Added capability for moisture profiles, also tunable.
Satellite receiver and processor	HRPT from NOAA and direct read-out DMSP. Soundings and imagery.
	PC based system with upgraded capability.
Portable surface station	Portable Surface Meteorological Sensor (AN/TMQ-50).
	No change planned at this time.
GPS receiver	Provides site location. Small relatively rugged antenna.
	No major change at this time.
Radar wind processing software	Wind velocity computed from moment data.
	Upgrade to spectral data processing by end of 1998.
Mesoscale Model	BFM for analysis and short term forecasts over mesoscale areas.
	Upgrades in algorithms and data handling capability.

3. Field Test Results

A series of field tests demonstrated the ability of the original Profiler to produce accurate and timely data. Cogan et al (1997) and Wolfe et al (1995) present a summary of results from

the Los Angeles Free Radical Experiment, and Cogan et al also show results from an experiment at Wallops Island. Tables 2 and 3 summarize the results from Wallops Island.

Table 2. Means and standard deviations of differences (ms^{-1}) of wind speed between Profiler (3 min. averages) and pibal (•a≈), and between pibals (•b≈) 3 min apart. Averages of 100 m layer values shown, for the surface to 1.9 km. Days in July 1995. Number of comparisons (No.) also shown.

		Mean		Standard Deviation	
Day	No.	a	b	a	b
18	8	-0.70	0.00	0.91	0.63
20	9	-0.31	-0.01	0.69	0.84
21	5	-0.36	-0.09	0.92	0.65

Table 3. As in Table 3 except for wind direction (deg). Values in parentheses are for z ≥ 300 m.

		Mean		Standard Deviation	
Day	No.	a	b	a	b
18	8	19.14 (18.92)	-0.31 (1.25)	13.00 (9.72)	9.53 (5.67)
20	9	7.13 (4.46)	-0.66 (-1.08)	8.56 (8.55)	8.13 (8.30)
21	5	11.71 (9.00)	0.64 (0.65)	3.96 (3.86)	4.21 (3.01)

The experiment described in Cox et al (1998) illustrated the usefulness of rapid refresh data from the Profiler. In this experiment wind profiles for the lowest 4 km were sent via a wireless LAN to a separate shelter containing the processors that hosted the models used for near real time analysis and prediction. A diagnostic mesoscale wind model was run every half-hour, with the resultant wind field feeding a Gaussian puff diffusion model. Cox et al reported that using the Profiler in place of 1 to 3 rawinsondes reduced the error in the location of the centroid of the predicted vs. the measured plume from about 50 % to 10 % after about 4 hours. The azimuth error decreased from 26° to 9° at a distance of 32 km, and the distance error dropped from 10 km too long to 4 km too short.

The current prototype was undergoing final assembly as of the time of this paper (September 1998). While complete profiles had not yet been compared with data from other sources (e.g., rawinsonde), some data were available from individual sensors or combinations of

sensors. An early check out of the new radar antenna led to the set of data shown in figure 2. These data were acquired near Erie, CO in April 1998. A series of five consecutive rawinsonde wind speed profiles, each representing a 10-minute average, were taken along with a rawinsonde sounding. The first radar profile occurred just before the rawinsonde launch, with the other four afterwards. Figure 2 shows both the comparison with the rawinsonde and the variation during the 50 minute period of the five radar profiles. Note that the rawinsonde started near the surface.

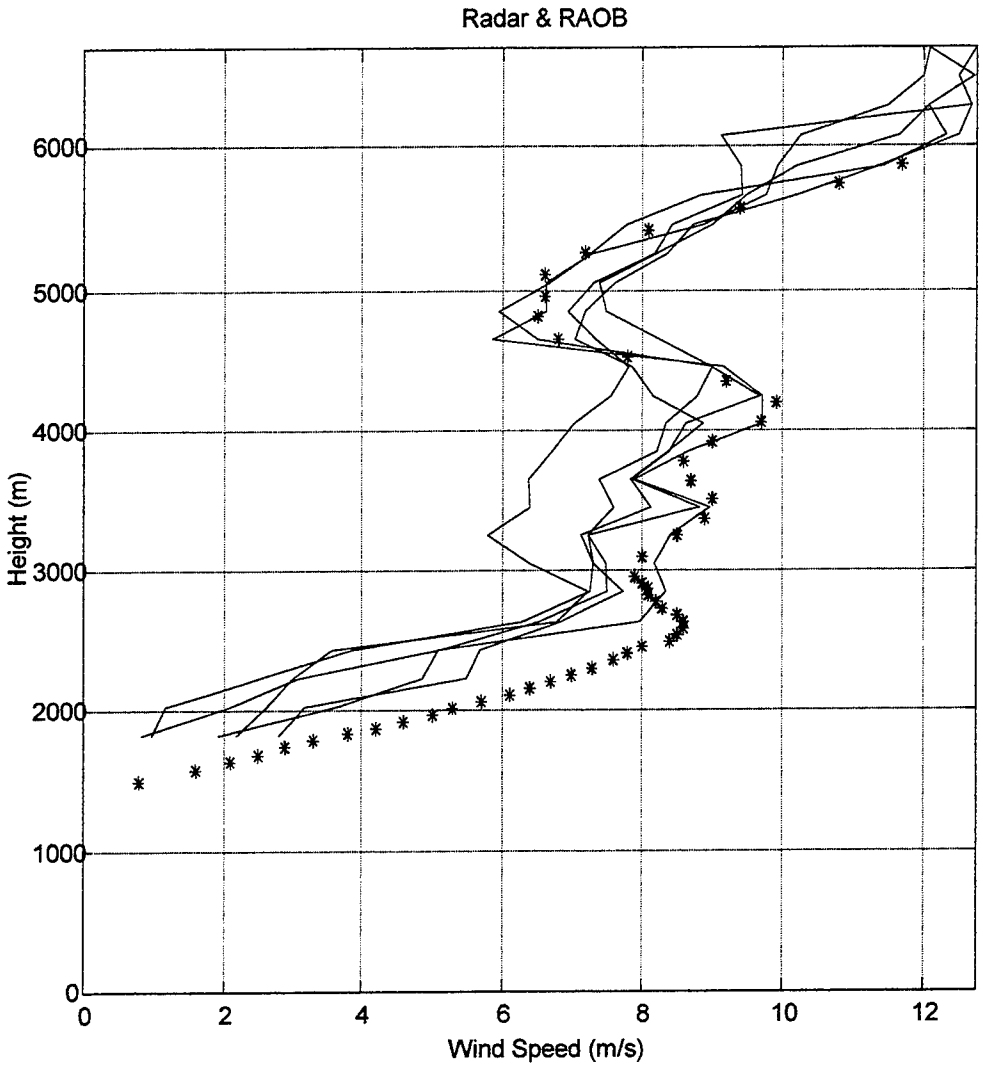


Figure 2. Wind speed (m/s) from five radar wind profiles compared with that from a rawinsonde (asterisks). Heights (m) are above mean sea level (MSL).

4. Upgrades

A series of planned upgrades (table 1) will enhance the capability and ease of use of the

system. The Environmental Technology Laboratory (ETL), NOAA, is developing a new antenna for use on NOAA oceanographic vessels. It will steer the radar beam via electronic switching instead of the current electro-mechanical switches. By allowing very rapid adjustment of beam parameters (< 1 ms) the system can account for movement of the ship without special stabilizing equipment. Effectively, the radar will aim at a selected "point" in the sky. In a similar manner, this type of antenna has applications for systems on land where rapid setup and tear down are required, and may allow for data acquisition on the move. For example, the current antenna must be leveled to a horizontal position, an operation that takes some tens of minutes. While this time represents a major improvement over previous antenna systems (setup time of a few hours), it may be too long in certain situations (on the battlefield or other hazardous locations as near a forest fire). An electronically steered antenna can operate once the system is stopped and cables hooked up (a few minutes). It can provide useful data when on a slope of up to 30°. On surfaces that are not too rough the system could take data "on the fly."

Another upgrade involves the development of a better means to retrieve satellite soundings through the use of neural network methods. Results to date show considerable potential, equal to or better than current retrieval methods in terms of root mean square error (RMSE). Work to date suggests that a neural network method can retrieve temperature profiles to an accuracy at least equal to standard methods, more rapidly, and using fewer computer resources in an "operational" mode. The network may be retrained as more data become available over time. Bustamante and Pearson (1998), Bustamante et al (1998), Gutman et al (1998), Measure et al (1998), Butler et al (1996), and Pearson and Bustamante (1998) present some recent work in neural network temperature retrievals. Cogan et al (1998) looked into the use of neural networks to extract wind velocity profiles. Early results suggest an RMSE for the tropopause of about the same size as that for cloud or moisture tracking techniques (Nieman et al, 1997; Velden et al, 1997). An advantage of the neural network technique is the ability to obtain wind velocities at several standard levels vs. one or two heights or layers by the tracking methods. All the above methods, both neural network or conventional, have errors (retrieved temperature vs. raob value) at one or more levels in individual soundings that greatly exceed the RMSE.

Investigation of the errors for temperature soundings revealed a complex error structure (Pearson and Bustamante, 1998). However, it appears that the neural network temperature retrievals may have an advantage over conventional methods in terms of fewer "outlier" errors.

Other enhancements include additional upgrades to the advanced signal processing for the wind radar being installed in the MMS-P prototype. The result should lead to more reliable wind velocities with fewer gaps in the data and more consistently reaching higher altitudes. The on-board mesoscale model (BFM) itself will have improved physics and better data handling. Additional output parameters include, for example, an estimate of precipitation rate and cloud cover for target areas.

5. Conclusion

The early version of the profiler has demonstrated its ability to obtain useful data for a variety of applications from airfield operations to transport and diffusion experiments. The new

version (MMS-P prototype) should prove even more useful by allowing rapid deployment to locations where fixed site systems are too costly or impractical. The planned upgrades to the sensors and software (some listed in table 1) should lead to even greater accuracy and reliability of the MMS-P prototype, and allow the generation of new types of output. The MMS-P has clear military and civilian applications. Civilian applications include obtaining atmospheric profiles and short term predictions for airfield operations, fighting forest fires, and emergency response to hazardous releases and other man-made and natural disasters. Military uses can extend beyond the field artillery to include applications such as airfield operations and defense against biological and chemical attack.

6. References

Bustamante, D., J. Cogan, and A. Duddenhoeffer, 1998. Neural network retrieval of atmospheric temperature profiles from TOVS data, *Meteor. Appl*, accepted.

Bustamante, D. and R. A. Pearson, 1998. Effects of cloud contamination on neural network retrieved temperature profiles, *Workshop on Artificial Intelligence Res. in the Environmental Sci. (AIRIES'98)*, Victoria, BC, Canada, 21-23 Oct 1998, accepted.

Butler, C., R. Meredith, and A. Stogryn, 1996. Retrieving atmospheric temperature parameters from DMSP SSM/T-1 data with a neural network, *J. Geophys. Res.*, 101(D3), 7075-7083.

Cogan, J., W. Gutman, E. Measure, D. Bustamante, and G. Vaucher, 1998. Neural network methods for wind velocity profiles from satellite data. *First International Conf. On Multisource-Multisensor Information Fusion*, Las Vegas, NV, 6-9 July 1998, 505-508.

Cogan, J., E. Measure, and D. Wolfe, 1997. Atmospheric soundings in near-real time from combined satellite and ground based remotely sensed data. *J. Atmos. Oceanic. Technol.*, **14**, 1127-1138.

Cox, R., J. Cogan, J. Sontowski, C. Dougherty, R. Fry, and T. Smith, 1998. Comparison of atmospheric transport calculations over complex terrain using a mobile profiling system and rawinsondes. *Meteor. Appl.*, submitted.

Gutman, W., D. Bustamante, J. Cogan, E. Measure, and G. Vaucher, 1998. Neural network temperature profile retrieval sensitivity analysis, *First Conf. On Artificial Intelligence*, Phoenix, AZ, 11-16 Jan 1998, 37-40.

Knapp, D., and P. Haines, 1997. Improving field artillery meteorological data for the U. S. Army using a PC-based mesoscale model. *Proc. 1997 Battlespace Atmos. Conf.*, 2-4, Dec 1997, San Diego, CA, 389-393.

Measure, E., J. Cogan, G. Vaucher, W. Gutman, R. Okrasinski, and D. Bustamante, 1998. Neural network retrieval of atmospheric temperature profiles from satellite and surface based radiometry, *First Conf. On Artificial Intelligence*, Phoenix, AZ, 11-16 Jan 1998, 41-44.

Nieman, S., W. Menzel, C. Hayden, D. Gray, S. Wanzong, C. Velden, and J. Daniels, 1997. Fully automated cloud-drift wind in NESDIS operations, *Bull. Amer. Meteor. Soc.*, 1121-1133.

Pearson, R. A. and D. Bustamante, 1998. Improving error structure in temperature profile retrievals from satellite observations, *Workshop on Artificial Intelligence Res. in the Environmental Sci. (AIRIES'98)*, Victoria, BC, Canada, 21-23 Oct 1998, accepted.

Velden, C., C. Hayden, S. Nieman, W. P. Menzel, S. Wanzong, and J. Goerss, 1997. Upper-tropospheric winds derived from geostationary satellite water vapor observations, *Bull. Amer. Meteor. Soc.*, 173-195.

Wolfe, D., and Co-authors, 1995. An overview of the mobile profiler system: Preliminary results from field tests during the Los Angeles free-radical study, *Bull. Amer. Meteor. Soc.*, **76**, 523-534.

Passive Radar Observation of the Battlespace Environment: Weather Echoes from Exploitation of an ASR-9

Capt Robert D. Duncomb Jr. and Mr. Robert J. Farrell Jr.
Air Force Research Laboratory Information Directorate
Acquisition Meteorology Office
Rome, NY 13441-4514

Mr. Paul F. Gilgallon
Air Force Research Laboratory Sensors Directorate
Surveillance Radar Technology Branch
Rome, NY 13441-4514

ABSTRACT

Battlespace sensing in the near-target environment is essential to gaining accurate target forecasts for the warfighter. Unfortunately but understandably, there are few sensor systems that would even attempt to take such measurements because of the hostile threat environment. The Surveillance Radar Technology Branch of AFRL's Rome Research Site has found a solution to this sensing problem. They have developed a passive sensor, called PROBE, that can be hand-carried into the forward deployed regions of the AOR and/or used on-board UAVs like the Predator without threat of detection. Once deployed, it receives electromagnetic emissions from whatever transmitters are available to exploit, both friendly and enemy. This has applicability to many sensing problems including that of sensing the weather.

Weather radars deployed in theater will be too far from the forward regions of the AOR to be of any use for most target area weather predictions. That is why this technology is so attractive. PROBEs on board UAV platforms and deployed with Army and Special Forces units can provide the battlespace weather radar picture directly to the aircrews in flight as well as back to the AOC where it can be distributed to whoever else needs it. The types of data obtainable are only limited by which frequencies are being intercepted but would likely include radar reflectivity and velocity information at the very least. This information can be used for dynamic replanning of sorties already in flight as well as ingest into the next forecast model run for enhanced target forecasts.

INTRODUCTION

At last year's Battlespace Atmospherics Conference, the authors presented a paper [Farrell, 1997] that described the existing deficiencies in weather data collection and offered PROBE as part of the solution (another part being exploitation of existing aircraft surveillance sensors like the TPS-75). The University of Oklahoma [Wurman, 1994] and the National Center for Atmospheric Research both have active bistatic weather radar programs and have proven that the concept works. They used bistatic receivers to gain both three-dimensional full vector winds

with no assumptions necessary and estimated rainfall totals from polarimetric data in a manner much cheaper than purchasing additional transmitters.

But, even with this relatively inexpensive means of obtaining weather data, funding has been slow to materialize even though many have shown interest in the technology. This is due to a whole host of complex reasons, not the least of which is the Air Force Weather Reengineering effort, which has been near the top of people's priority list for some time now. Nevertheless, because of the intense interest of ACC, AFSOC, ESC, and AFW in this sensor, AFRL internal funding was used to accomplish a weather data collection effort on the 1st of April 1998. This paper presents the initial results of that weather data collection effort.

SENSOR DESCRIPTION

Extensive work has been done to make the hardware as small as possible, and this work continues. The antenna (Fig. 1) is designed to operate in the S-Band frequency range. The elements are a flared notch dipole, which is an inherently wideband antenna element.

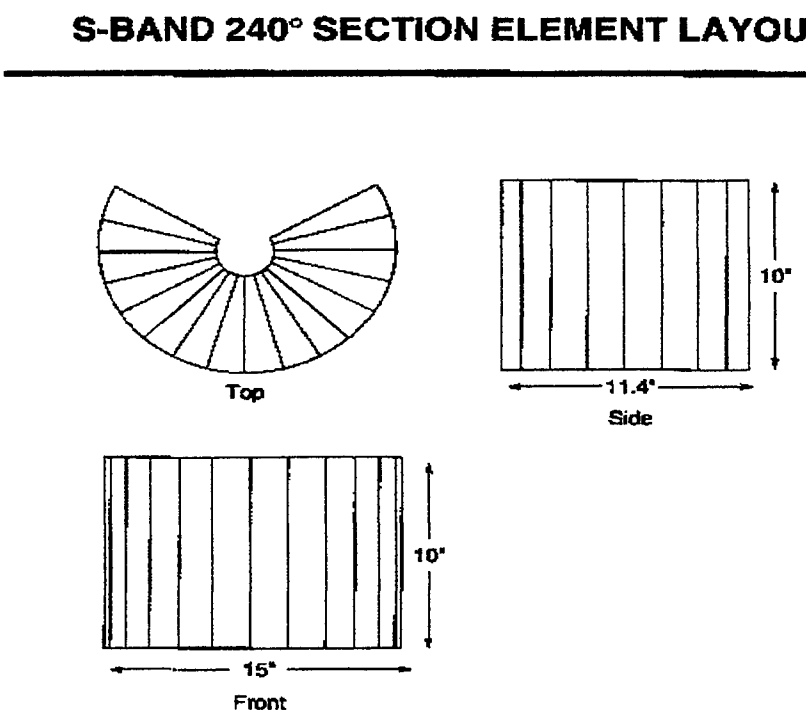


Figure 1

Table 1 provides the dimensions and operating characteristics of the antenna. The antenna can be installed in a variety of configurations.

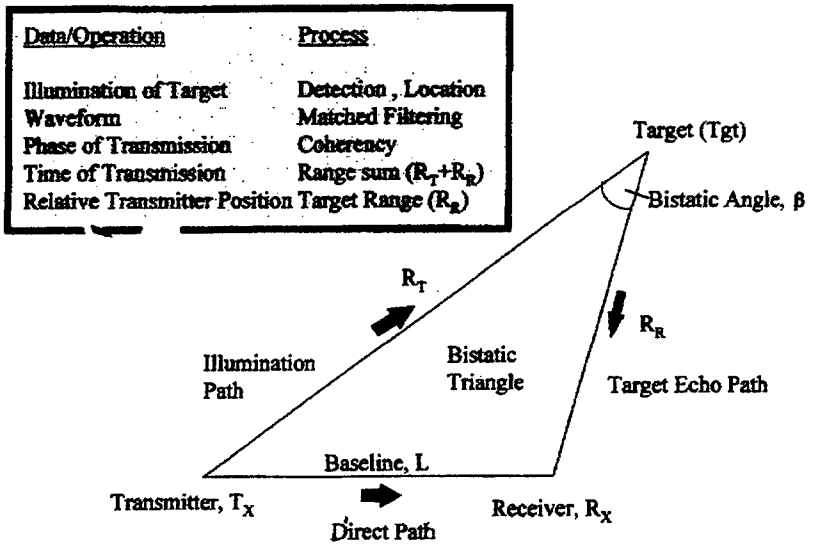
24 Element Array
15" Diameter, 10" High
3:1 Switches
8 Active Elements
15° Steering
16 Element Section
240° Section
±60° Steering

Table 1

The current receiver subassembly is a totally self-contained package that includes power supplies, digital signal processors and receivers. This subassembly weighs approximately 80 pounds and fits in a rack mountable chassis measuring 19 inches across by 24 inches high and 24 inches deep. We anticipate a weight/size reduction of almost half (45 pounds and 12 inches square) in the very near future. The system has been tested in a variety of ground-based, airborne and sea borne configurations.

SIGNAL PROCESSING

The technology used to passively detect and track an atmospheric event is based upon bistatic radar technology developed by the Air Force Research Laboratory. Figure 2 describes the basic parameters and geometry's needed for the operation of a bistatic radar system.



Bistatic Geometry and Typical Bistatic Radar Requirements

Figure 2

The receiver passively surveys the ambient electromagnetic environment and identifies potential host emitters. These emitters can be any emission source that outputs Radio Frequency (RF) energy in a form suitable for exploitation for the purposes of detection, tracking and analysis. For this experiment, we exploited the signal from an S-Band ASR-9 radar located at

Syracuse's Hancock International Airport. The bistatic baseline was approximately 9 nautical miles (ASR-9 to PROBE). Table 2 delineates the characteristics of the ASR-9.

Operating Frequency: 2735, 2830 MHz
Pulse Width: 1 microsecond
Pulse Repetition Interval (PRI): Staggered .8 - 1.2 millisecond [1 millisecond nominal]
Scan Time: 4.6 seconds

Table 2 ASR-9 Characteristics

Once a suitable host emitter has been selected we identify its position. Since we know our own position we are able to solve the bistatic equations responsible for position location. Our process is a coherent process. We sample the direct path emission from the host emitter and utilize it to coherentize our receive process. We sample on a pulse to pulse basis and electronically switch our receive beam to synchronize with the transmitter main beam to provide for complete volumetric coverage of the surveillance region. Since this is a coherent receiver, we are able to extract range, angle and Doppler information from the target.

WEATHER DATA COLLECTION

On April 1st of this year, PROBE was used for the first time to collect weather data. The frequency of the ASR-9 (Table 2) is very close to that of the WSR-88D NEXRAD radar (2900 MHz), which makes this an attractive transmitter to exploit for weather data collection. The availability of the transmitter, though, was only one important component of the data collection effort; we also needed some precipitation to occur.

Precipitation covered virtually the entire experiment region on April 1st, but this analysis will focus on a NNW-SSE oriented line of showers and thunderstorms that affected both the Rome and Syracuse areas. On the Binghamton, NY (76nm S of Syracuse) radar (WSR-88D), a line of thunderstorms formed west of Syracuse at approximately 1949Z (Fig. 3) and eventually passed through the Rome area at around 2030Z (Fig. 4). The intensity is a bit exaggerated in these images since they are composite reflectivity images. The echoes that affected Rome and Syracuse were mostly moderate to heavy rainshowers with some embedded thunderstorm activity. Thunderstorms were both more numerous and more intense along the southern part of the line.

PROBE began collecting data at around 2016Z with the line of storms approximately 35 km ENE of the sensor. A qualitative assessment shows at least satisfactory agreement between PROBE's imagery (Fig. 5) and the NEXRAD imagery near the same time (Fig. 6). The NEXRAD image is the .5 degree elevation scan for reflectivity with echoes less than 24 dBZ filtered out. The filtering was done to more closely match the level of noise filtering done in signal processing the PROBE data. The echoes in Fig. 5 to the immediate S and SE of Syracuse are ground clutter returns from hills. The other dots and lines in Fig. 5 are aircraft tracks identified by PROBE.

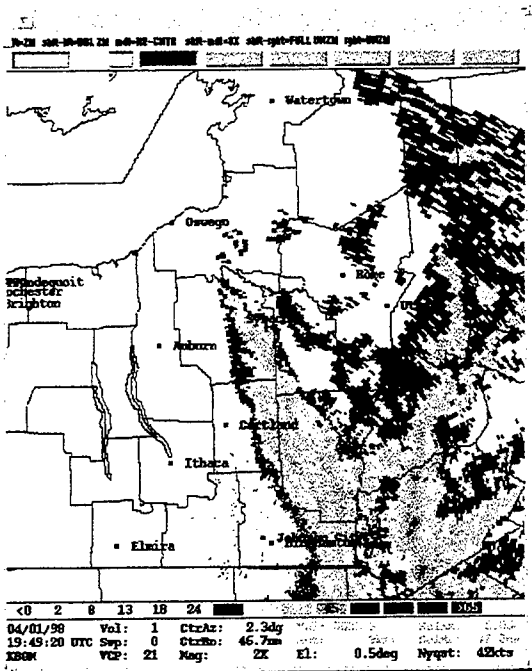


Fig 3. Composite Reflectivity – 01/1949Z

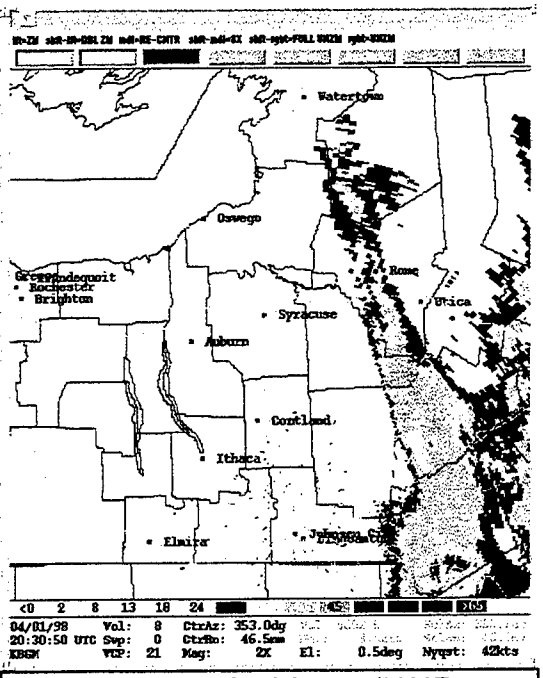


Fig 4. Composite Reflectivity – 01/2030Z

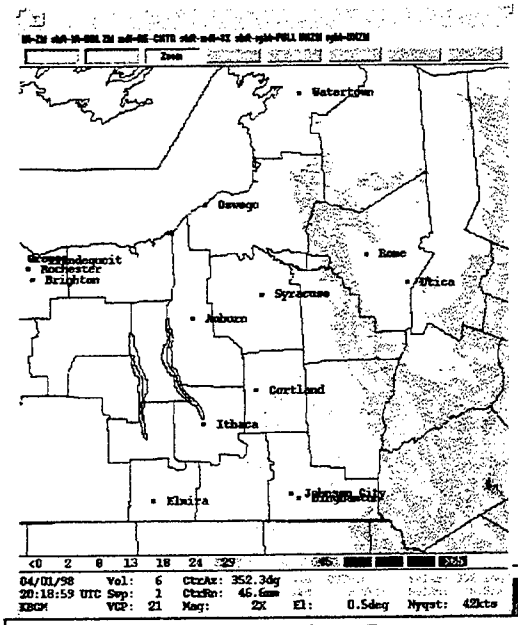


Fig 5. BGM NEXRAD – 01/2018Z

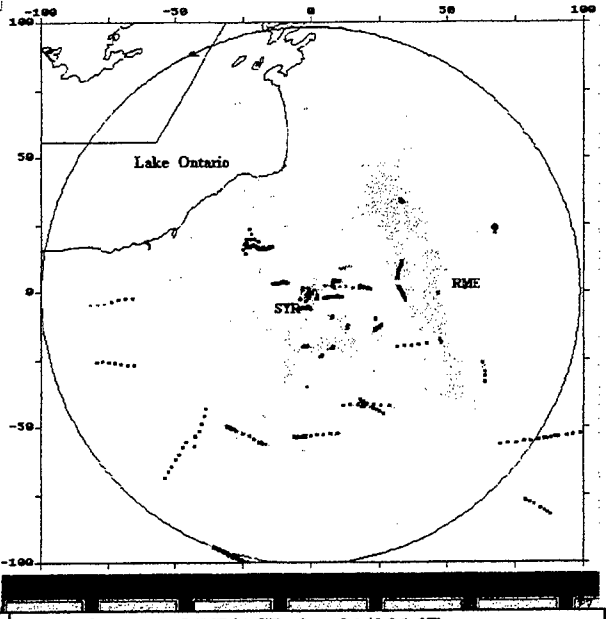


Fig 6. SYR PROBE/ASR-9 – 01/2016Z

Though there is little detail in the PROBE image, it is at least obvious that there is a line of showers and storms between Rome and Syracuse. This is a good start toward identifying when storms may be approaching a deployed location. Many of the differences between the two

images can be accounted for by the differences in viewing angles, distance from the storms, and resolution of the two sensors.

Additional ground measurements have been taken and those results will be presented at a future date. PROBE has also been flown aboard AFRL's UAV-emulating Cessna Research Aircraft to collect aircraft surveillance data, but the times it has flown, to this point, have been during times when there were no showers or thunderstorms occurring. So the first successful airborne weather data collection effort has yet to occur.

CONCLUSION AND RECOMMENDATIONS

These initial results are encouraging and warrant further data collection efforts to further substantiate PROBE's ability to collect weather data from various radar sources at different frequencies both in airborne and ground emplacements. Future collections should collect at varying distances from the transmitting radar to get an estimate of the expected weather-range of the PROBE sensor. Collecting doppler winds should also be attempted to see how well it does. More work will also be done to reduce the size, weight, and power requirements of PROBE to make it "person-portable" for Army and Special Operations ground forces. But, for this work to continue, funding support is needed to go along with the advocacy.

An issue that must be tackled is defining how PROBE should be used to enhance Combat Weather Support. Some of the pressing questions that need to be answered include: 1) Who needs to see this data (OWS, CWTs, combatant decision-makers)?, 2) How is it going to get to them (radio, SATCOM)?, 3) How is this information fused with other sources?, 4) Where should that fusion take place (fusion center, command center, OWS, AFWA)?, 5) Who will have the ground-based PROBEs (Special Ops, ALOs, etc.), and 6) Which airborne platforms will carry PROBEs? We ask for your help in answering these questions so that PROBE will meet as many of AFW's data collection needs as possible.

ACKNOWLEDGMENTS

This work was done by Syracuse Research Corporation under contract to the Air Force Research Laboratory Sensors Directorate, Rome, NY.

WSR-88D Algorithm Testing and Display Software (WATADS) was used to evaluate the NEXRAD data for this date. This software was provided by NSSL.

AF Combat Climatalogy Center, Asheville provided the NEXRAD data tapes.

REFERENCES

1. Farrell, R.J. Jr., Duncomb, R.D. Jr., Gilgallon, P.F., 1997: "Passive Radar Observation of the Battlespace Environment", *BAC 97 Proceedings*, pg. 671. [ADA 344056].

2. Wurman, J., 1994: "Vector Winds from a Single Transmitter Bistatic Dual-Doppler Radar Network", *Bulletin of the American Meteorological Society*, **75**, pp 983-994

A HIGH RESOLUTION FMCW S-BAND RADAR FOR BOUNDARY LAYER PROFILING AND CLOUD APPLICATIONS

Turker Ince*, Andrew L. Pazmany, Steve J. Frasier, Robert E. McIntosh

Microwave Remote Sensing Laboratory
University of Massachusetts at Amherst, MA, 01003, USA

Tel:(413) 545-3495, Fax:(413) 545-4652, e-mail:pazmany@mirsl.ecs.umass.edu

Sponsored by the Army Research Office

INTRODUCTION

Radar study of the Atmospheric Boudary Layer allows the measurement of the C_n^2 structure function parameter and its dynamics at a spatial resolution of a few meters. The remote measurement of the ABL is, however, complicated by the low radar reflectivity of turbulence structures. FMCW radars have proven to be a solution to this difficult problem as four such radars have been built and succesfully applied to study the ABL since 1969 [Richter, 1969] [Strauch et al., 1976] [Ligthart, 1980] [Eaton et al., 1995]. In spite of tantalizing results from these insruments, their high development and operating costs prevented their widespread use in the atmospheric science community. In response to a need for a low cost remote sensing tool to study the ABL, the University of Massachusetts Microwave Remote Sensing Laboratory (MIRSL) is currently developing an S-band FMCW radar using modern, commercially avilable parts. The UMass radar will have similar range resolution and sensitivity as previous ABL profiling FMCW radars.

DESIGN CONSIDERATIONS

The design goal of the FMCW S-band radar is to maximize sensitivity to C_n^2 and to resolve range variations in reflectivity as small as few meters while minimizing the system size and cost. An FMCW radar is ideal for these objectives because it can achieve both excellent sensitivity and fine range resolution at relatively low cost. A continuous wave radar, however, has the disadvantage that it requires two antennas to maintain sufficient transmitter/receiver isolation to prevent saturation of the receiver. The two antennas must be aligned precisely so their center axis are parallel to each other. At close ranges there is only a partial overlap between the two beams, which degrades sensitivity and must be accounted for to calibrate the reflectivity measurements. Transportation and scanning of a dual-antenna radar is also difficult particularly when larger antennas

are needed for narrow beamwidths. Antenna size may be reduced, while maintaining beamwidth, only by increasing the operating frequency. For this application, however, the operating frequency is limited to a few GHz because the radar wavelength must be similar to the spatial dimensions of the index of refraction (n) variations in the atmosphere to maintain sensitivity in clear air. The short-wavelength limit of spatial variation of n is determined by viscous damping and is given by the Kolmogrov microscale. In the boundary layer, wavelengths greater than 10cm (3.0 GHz) can reliably be used to detect fluctuations of n up to 2km. Above that height, lower frequency radars perform more reliably for clear air measurements of atmospheric turbulence. Since the primary purpose of the proposed radar is to study the atmosphere below 2km, the operating frequency of the radar is 2.8-3.0 GHz which allows the use of two moderate size, 8' diameter antennas with 3° beamwidths.

TRANSMIT WAVEFORM TRADEOFF ANALYSIS

For an FMCW radar, the bandwidth of the FM sweep, BW_s, determines the minimum range resolution according to

$$\Delta_r = \frac{c}{2 * BW_s}, \tag{1}$$

while the sweep time, T_s, is the inverse of the measurement bandwidth, B, which is proportional to the equivalent system noise power. A long sweep time is, therefore, desirable, because it is a means to improve sensitivity, as long as the measurement bandwidth is wider than the spectral width of the scatters. Once the sweep time is is similar to the scattered signal decorrelation time, B is "matched" to the received signal, and signal to noise ratio no longer improves with longer sweep times. For a 3 GHz radar that uses narrow beam antennas, the spectral width of the scattered signal typically ranges from 20 to 40 Hz so sweep times beyond 50 ms would rarely be beneficial. The minimum desired range resolution of the proposed radar is 2 m, so a 75 MHz sweep bandwidth is sufficient.

Although the primary data product of this radar is reflectivity, a Doppler operating mode is also available to obtain either the the first three moments (reflectivity, mean velocity and spectral width) or the full Doppler spectrum. The technique to derive Doppler information from FMCW radar measurements involves sweep-to-sweep processing of the complex FFT range bins [Strauch et al., 1976] [Chadwick et al., 1976] similarly to the pulse-to-pulse (FFT or pulse pair) processing of pulsed radar measurements. As for a pulsed radar, the maximum unambiguous velocity, v_{max}, is determined by the pulse spacing. For an FMCW radar it is determined by the sweep time according to

$$v_{max} = \pm\lambda/4T_s. \tag{2}$$

Consequently, a 50 ms sweep time is too long to obtain Doppler information because the corresponding maximum unambiguous velocity is only $\pm.5ms^{-1}$. Using a shorter sweep, however, unambiguous Doppler velocity can be increased at the cost of degraded range resolution.

SAMPLING REQUIREMENTS AND PROCESSING

Range discrimination with an FMCW radar involves the spectral analysis of the down-converted received signal. With a digital data acquisition and processing system this is accomplished by sampling the receiver output and then computing the discrete Fourier transform of sampled data. The required sampling frequency, f_s, is determined by the transmit sweep slope, m ($m = BW_s/T_s$), and the maximum range, r_{max}, according to

$$f_s = 2mr_{max}/c, \tag{3}$$

and for real time processing, the digital signal processor (DSP) has to be able to perform a $f_s * T_s$ point Fast Fourier Transform (FFT) within the duration of the transmit sweep. For a maximum range of 4 km and 75 MHz sweep in 50 ms, the necessary sampling rate is 40 KHz. At this sampling rate, 2048 points can be obtained which is sufficient to resolve range variations on the order of 2m. Since the 40 KHz sampling rate is well within the capability of current digitizer technology, these requirement can be met with a relatively low cost data acquisition system. Figure 1 shows the block diagram of the data acquisition system. The data system consists of a PC computer which provides the user interface to control the radar operation, displays the radar parameters in real-time, and contains the mass storage units, and digitizer and digital signal processor cards manufactured by Spectrum, Inc..

SYSTEM DESCRIPTION

Figure 2 shows the component level block diagram of the FMCW radar. The transmit waveform is generated by a Sciteq digital synthesizer that produces the ultra-linear, low noise, 75 MHz bandwidth sawtooth frequency sweep necessary for fine spatial resolution. This signal is upconverted, and pre-amplified before entering the coupler that initiates the internal calibration loop. The transmit signal is then amplified by a 250 W CW TWT amplifier, manufactured by Applied Systems Engineering, and transmitted by one of two identical 8' parabolic dish antennas by Gabriel Electronics. The received signal, captured by the second antenna, is first amplified then filtered and downconverted to audio frequency. Here the receiver bandwidth is established by an anti-aliasing filter

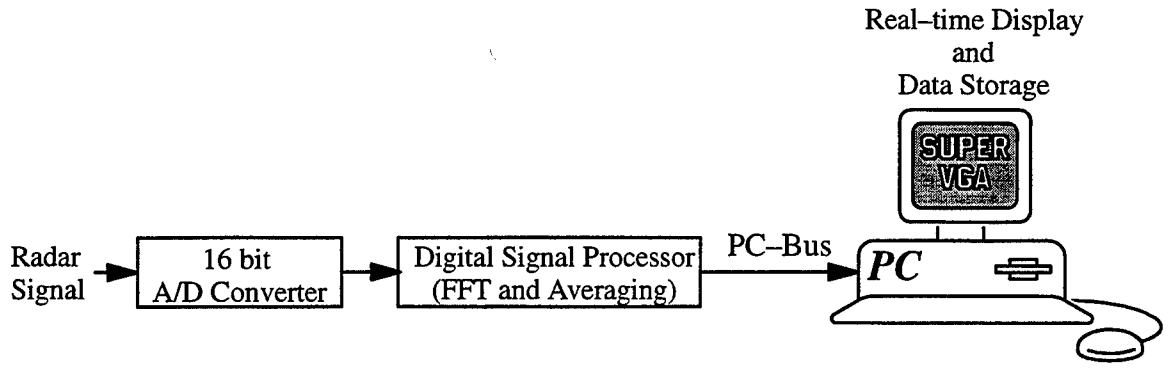


Figure 1: Data acquisition system block diagram.

before the signal is sampled by a Spectrum 16-bit A/D converter in the data acquisition and real time processor system.

In the calibration loop, a fraction of the transmitted signal is delayed by $5\mu s$ using an acoustic delay line, then injected into the receiver to monitor the linearity of the transmitted sawtooth frequency sweep, receiver gain variations and signal processing effects such as range sidelobes caused by FFT processing. Table 1 lists the key specifications and operating parameters of the radar.

SENSITIVITY ANALYSIS

The sensitivity of a weather radar is often expressed by the reflectivity of a volume scatterer that the radar can detect at unity signal-to-noise ratio (SNR). The received power, P_r, of a weather radar is given by [Doviak and Zrnic, 1984]

$$P_r = \frac{P_t C_A G^2 \lambda^2 \theta^2 \Delta_r \eta}{(512 ln2)\pi^2 r^2}, \tag{4}$$

and the equivalent system noise power, P_n, is

$$P_n = kTBF, \tag{5}$$

where
P_t is the transmitted signal power,
C_A is the range weighting function that accounts for the partial overlap of the two antenna beams,
G is the antenna gain,
λ is the radar wavelength,

Table 1: Specifications of the UMass Boundary Layer Profiling FMCW Radar.

Transmitter	
Operating frequency	2.9 GHz ± 37.5 MHz
Transmitter power	250 W continuous
Sweep time	2.5 - 50 ms (selectable)
Sweep bandwidth	75 to 10 MHz (selectable)
Receiver	
Dynamic range	84 dB (14 effective bits out of 16)
Noise figure	2 dB
Bandwidth	50 KHz
Minimum detectable signal	-160 dBm after 5 min. integration
Range resolution	2 or 20 m (selectable)
Maximum number of range gates	4096
Recorded radar parameters	Reflectivity or Reflectivity and Doppler
Unambiguous velocity (in Doppler mode)	± 10 ms^{-1}
Antennas	
Type (diameter)	Parabolic dish (8 ft)
Half-power beamwidth	3°
Gain	34 dB
Spacing	9 ft
Polarization	Single, linear

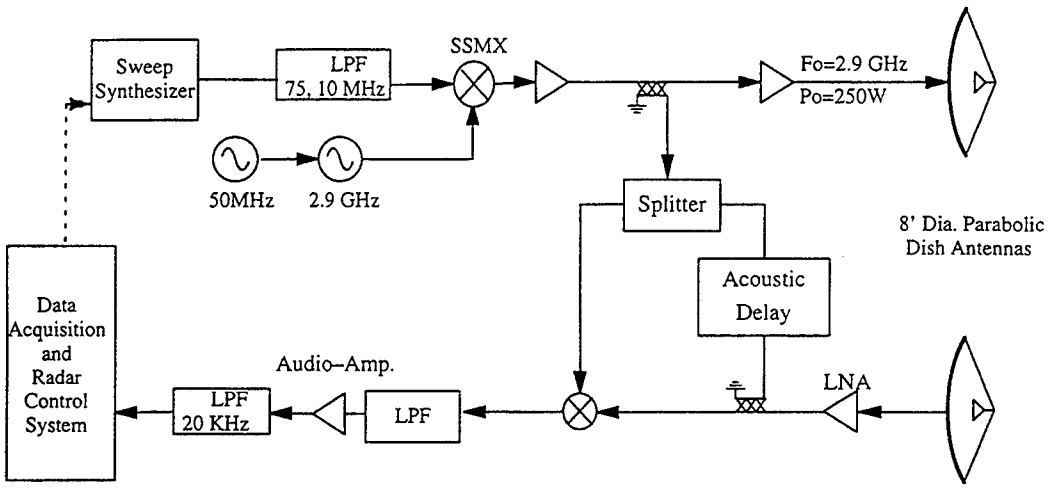


Figure 2: Component level block diagram of the FMCW Radar.

θ is the half-power beamwidth,
Δ_r is radar range resolution,
η is the radar reflectivity of a volume scatterer,
r is radar range,
B is Boltzman's constant,
T is temperature,
and F is the receiver noise figure.

The C_n^2 structure parameter is related to η using [Ottersten, 1969]

$$\eta = .38 C_n^2 \lambda^{-1/3}, \tag{6}$$

to obtain the expression for the minimum detectable structure parameter, $C^2_{n_{(min)}}$, at unity signal-to-noise ratio before averaging:

$$C^2_{n_{(min)}} = \frac{kTBF(512ln2)\pi^2 r^2}{.38 P_t C_A G^2 \lambda^{5/3} \theta^2 \Delta_r \eta}. \tag{7}$$

The antenna correlation term, C_A, is an important parameter in the estimation of sensitivity and in the calibration of measurements particularly at short ranges. C_A accounts for the partial overlap of the two antenna beams and is a function of beam width, antenna spacing, and range. If the antenna beams can be aproximated as symmetrical

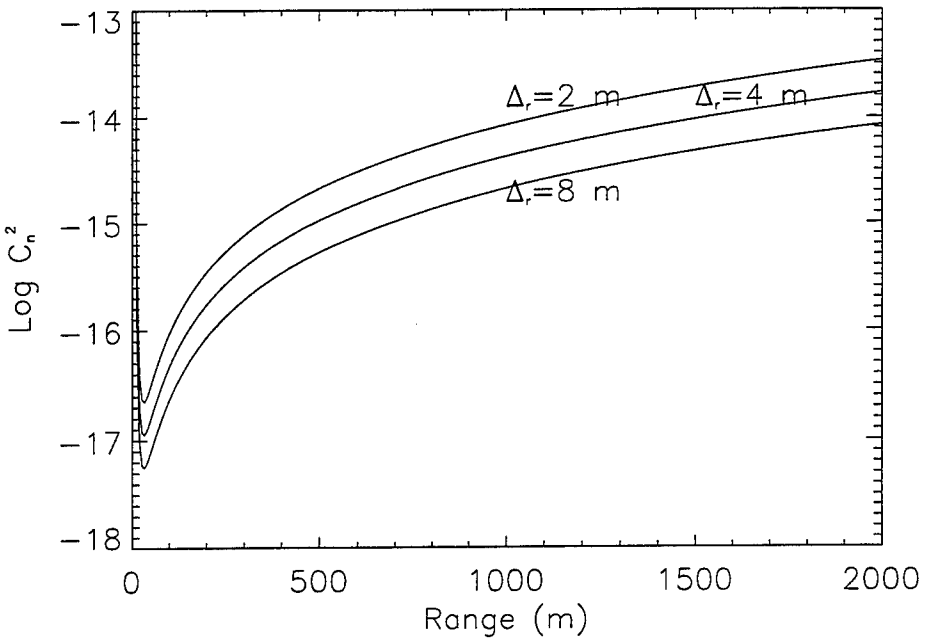


Figure 3: Minimum detectable C_n^2 at unity signal-to-noise ratio.

Gaussian beams aligned with the center axis parrellel with each other, then C_A can be expressed according to

$$C_A = exp(\frac{-2ln2(D/2)^2}{sin^2(\theta/2)r^2}). \tag{8}$$

The resultant overall sensitivity of the radar is shown in Figure 3.

Under typical conditions, radar backscatter from a meteorological radar results from the coherent sum of scatter from a large collection of particles or reflective structures. As long as the resultant signal is not dominated by one or a few scatterers, the scattered power will be exponentially distributed. The meaningfull estimation of the mean scattered power requires a substantial number of independent samples. Time to independence may be approximated by the inverse of the Doppler spectal width, corresponding to 25-50 ms at 3 GHz. Given sufficient sweep time to assure independence, 15 samples are required to estimate the reflectivity so the standard deviation of this estimate is within 1 dB. This accuracy is sufficient to detect the minimum C_n^2 levels shown in Figure 3 at about 85% probability while keeping false alarm rate caused by thermal noise to below 15%. Increasing the integration time to 5-10 minutes would result 100-200 independent samples, which would furter reduce the 85% detectable signal level by 5-6 dB.

References

[Chadwick et al., 1976] Chadwick, R. B., Moran, K. P., Strauch, R. G., Morrison, G. E., and Cambell, W. C. (1976). A new radar for measuring winds. *Bull. Am. Meteorol. Soc.*, 57(9):1120–1125.

[Doviak and Zrnic, 1984] Doviak, R. J. and Zrnic, D. S. (1984). *Doppler Radar and Weather Observations.* Academic Press Inc.

[Eaton et al., 1995] Eaton, F. D., McLaughlin, S. A., and Hines, J. R. (1995). A new frequency-modulated continuous wave radar for studying planetary boundary morphology. *Radio Science*, 30(1):75–88.

[Ligthart, 1980] Ligthart, L. P. (1980). System considerations of the FMCW DELFT atmospheric radar (DARR). In *IEEE International Radar Confererence*, Arlington, Va.

[Ottersten, 1969] Ottersten, H. (1969). Atmospheric structure and radar backscattering in clear air. *Radio Sci.*, 4:1261–1268.

[Richter, 1969] Richter, J. H. (1969). High resolution tropospheric radr sounding. *Radio Science*, 4:1261–1268.

[Strauch et al., 1976] Strauch, R. G., Cambell, W. C., Chadwick, R. B., and Moran, K. P. (1976). Microwave FMCW Doppler radar for boundary layer probing. *Geophys. Res. Lett.*, 3(3):193–196.

ADVANCED REMOTE SENSING CONCEPTS IN SOIL MOISTURE ANALYSIS

Andrew S. Jones, Stephen Barlow*, and Thomas H. Vonder Haar
Cooperative Institute for Research in the Atmosphere (CIRA)
Colorado State University, Fort Collins, CO
Phone: (970) 491-8628, Fax: (970) 491-8241
email: jones@cira.colostate.edu

OBJECTIVE

The remote sensing of soil moisture is a complex problem requiring several distinct perspectives from an observational point-of-view. Passive microwave and infrared satellite data (from DMSP SSM/I, GOES IR, TRMM TMI and VIRS) are used in combination to generate soil moisture products with resolutions as high as 5 km using multisensor data fusion methods. In addition, mesoscale atmospheric models are used in a coupled satellite-model system to quantify the surface soil moisture amounts via the model's surface parameterization. Certain crop type conditions (such as irrigated cropland) are shown to produce interesting surface signatures. These results are corroborated by high-resolution Landsat data. The strengths and weaknesses of the various methods are compared.

This work is relevant to both model simulations and operational arenas. In particular, initializations of atmospheric/hydrological models require better specification of the heterogeneous surface fields for accurate weather/runoff forecasts. The observational surface wetness product should also be useful as a data source for improved trafficability indices in data-denied regions. These data sets offer the potential of high temporal monitoring of surface wetness and vegetation conditions over areas of military interest.

RESEARCH ACCOMPLISHED

Two remote sensing approaches have been applied to a morning case study located in the central Great Plains region on 8 September 1991.

MICROWAVE EMISSIVITY RESULTS

The first method combines DMSP SSM/I and GOES IR data to retrieve microwave surface emissivity (Jones and Vonder Haar 1997). The data are quality controlled with the removal of cloud contaminated data, and an atmospheric correction is applied to remove water vapor attenuation effects in both the microwave and infrared spectral regions. For this case day, the wet/dry contrast due to the surface flooding is apparent in the microwave emissivity results (Figure 1), with low emissivities over the wet surface regions, and high emissivities over the dry regions. The USDA Crop Moisture Index reports during this time indicated that standing water was observed for portions of these areas in eastern Kansas and Oklahoma. The radar summaries (Figure 2) show that the rainfall occurred the previous night with its spatial coverage limited to

the eastern portions of the region. The convection was propagating in a north-northeastward direction. Thus, the microwave emissivity data set appears to be a promising indicator of surface flooding events. However, analysis of a 70 day period over the central U.S. found that vegetation and irrigation effects make quantitative surface wetness estimates difficult. Landsat irrigation classifications also indicate a correlation of the lower emissivity regions with known irrigation regions. However, a more detailed analysis indicates that the vegetation effects are dependent on several other complicating factors, including surface roughness, fractional vegetation, vegetation amount, vegetation type, etc. Therefore, the microwave surface emissivity is a better subjective indicator of surface wetness features, and is applicable to change detection methods, and/or to the monitoring of extreme events.

SATELLITE DATA ASSIMILATION METHOD RESULTS

A satellite data assimilation procedure has also been developed for incorporating GOES infrared heating rates into the CSU-regional atmospheric mesoscale modeling system (RAMS) (Jones et al. 1998a). The data assimilation procedure is a direct inversion of the RAMS surface parameterization and includes a prognostic soil model and simple "big leaf" vegetation parameterization. The method is an extension of the McNider et al. (1994) data assimilation method and includes the effect of the diurnal heating rate on the model vegetation. The bare soil data assimilation component has an iterative solution procedure, while the inverted vegetation parameterization is solved as an analytical function of the original model equations.

The basis of the satellite data assimilation is the satellite-derived heating rate. GOES-7 Visible Infrared Spin-Scan Radiometer (VISSR) data were navigated and aligned for temporal analysis of the satellite surface skin temperature heating rates using a multisensor-multispectral data fusion analysis package (Jones et al. 1995). The results for 8 September 1991 at 1501, 1531, and 1601 UTC are shown in Figure 3. Very low heating rates are observed over the east portion of the sector where significant rainfall events have occurred.

The satellite data assimilation method consists of four major steps (see Figure 4). Initially, a high contrast case study is selected using the microwave surface emissivity as guidance. The second step of the method is to initialize the model vegetation with Normalized-Difference Vegetation Index (NDVI)-based vegetation land classification categories to describe the relevant model vegetation characteristics. The model is then run in a normal prognostic mode (Step 3) until the satellite data assimilation period begins (Step 4) (for this case 1500 UTC), then the land surface parameterization model equation set is replaced with the satellite data assimilation model equation set which directly couples the satellite-derived heating rates to the model surface parameterization variables, thus forcing the surface of the model with the satellite-derived heating rate observations. Since the method is limited to clear-sky conditions, the data assimilation period was only 1 hour for this case, due to cloud conditions that interfered with a consistently clear view of the morning heating. After the satellite data assimilation period, the model carries the assimilated soil moisture conditions into its normal prognostic mode (for this case, the remainder of the model simulation after 1600 UTC).

The satellite data assimilation method was performed for 8 September 1991 over the central U.S. (Jones et al. 1998b). The model configuration was initially 2 grids (40 km and 10 km grid

spacing) with a 3rd grid (5 km grid spacing) added after the satellite data assimilation period (1600 UTC). Two simulations were performed: a run using horizontally homogenous soil moisture (CONTROL), and a run implementing the satellite data assimilation method (SAT). A west to east cross section of the bare-soil soil moisture results are shown in Figure 4. Both results show a relatively rapid dry down of the soil moisture due to the 10 m s^{-1} surface wind speeds (from observational and simulated results). The main feature of Figure 5 is the dry region in the western portion of the domain of the satellite assimilated results (SAT), and a contrasting wet region over the eastern portion of the domain. Thus the method is able to correctly capture the dry/wet contrast of this case study day. However, once assimilated, the model dried up most of the soil moisture by early afternoon, thus the morning's assimilated soil moisture had only a minor impact on this particular day's meteorological features.

CONCLUSIONS AND RECOMMENDATIONS

Results indicate that the two methods are complimentary, with the microwave emissivity method performing well as a subjective indicator, and the satellite data assimilation method performing as a more quantitative method. The strength of the microwave emissivity is its ability to be less influenced by cloud effects, and the potential to expand that work to lower frequencies, which are more sensitive to the surface moisture effects, (e.g., 10 GHz) such as are on the TRMM TMI sensor (Kummerow et al. 1998). This method could also be augmented by other sensor data (e.g., SAR data). The data assimilation method while more quantitative, requires additional verification efforts, and more extensive calibration efforts, by implementing the method on longer term case studies. Efforts are underway to transition this work to more routine product generation for various application needs.

REFERENCES

Jones, A. S., K. E. Eis, and T. H. Vonder Haar, 1995: A method for multisensor-multispectral satellite data fusion. *J. Atmos. and Oceanic Technol.*, **12,** 739–754.

Jones, A. S., and T. H. Vonder Haar, 1997: Retrieval of microwave surface emittance over land using coincident microwave and infrared satellite measurements. *J. Geophys. Res.*, **102,** 13609–13626.

Jones, A. S., I. C. Guch, and T. H. Vonder Haar, 1998a: Data assimilation of satellite diurnal heating rates as proxy surface wetness data into a regional atmospheric mesoscale model, Part I: Methodology. *Monthly Weather Review,* **126,** 634–645.

Jones, A. S., I. C. Guch, and T. H. Vonder Haar, 1998b: Data assimilation of satellite diurnal heating rates as proxy surface wetness data into a regional atmospheric mesoscale model, Part II: A case study. *Monthly Weather Review,* **126,** 646–667.

Kummerow, C., W. Barnes, T. Kozu, J. Shiue, J. Simpson, 1998: The Tropical Rainfall Measuring Mission (TRMM) sensor package. *J. Atmos. Oceanic Technol.*, **15,** 809–817.

McNider, R. T., A. J. Song, D. M. Casey, P. J. Wetzel, W. L. Crosson, and R. M. Rabin, 1994: Toward a drynamical-thermodynamic assimilation of satellite surface temperature in numerical atmospheric models. *Mon Wea. Rev.*, **122,** 2784–2803.

ACKNOWLEDGEMENTS

This work was supported by the DOD Center for Geosciences under ARO grant DAAH04-94-G-0420.

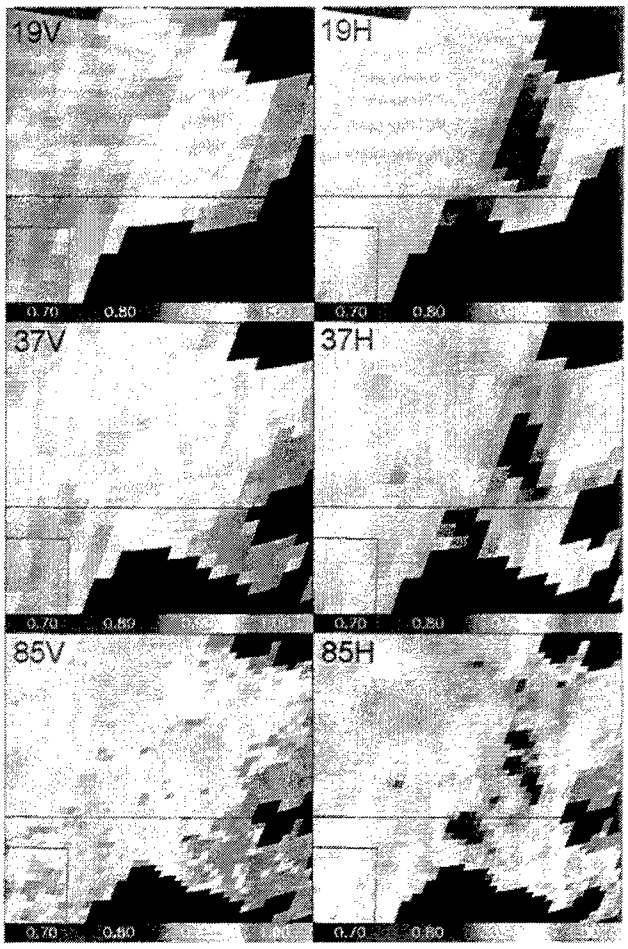


Figure 1. Atmospheric-corrected microwave surface emissivity for 8 September 1991 1529 UTC for the Kansas/Oklahoma region. Results from vertical (V) and horizontal (H) polarizations at the SSM/I frequencies of 19, 37 and 85.5 GHz are shown. Light shades denote high microwave emissivity, while dark shades represent low microwave surface emissivity. The northeast corner and south and southeast portions of the sector were cloudy and are shaded black.

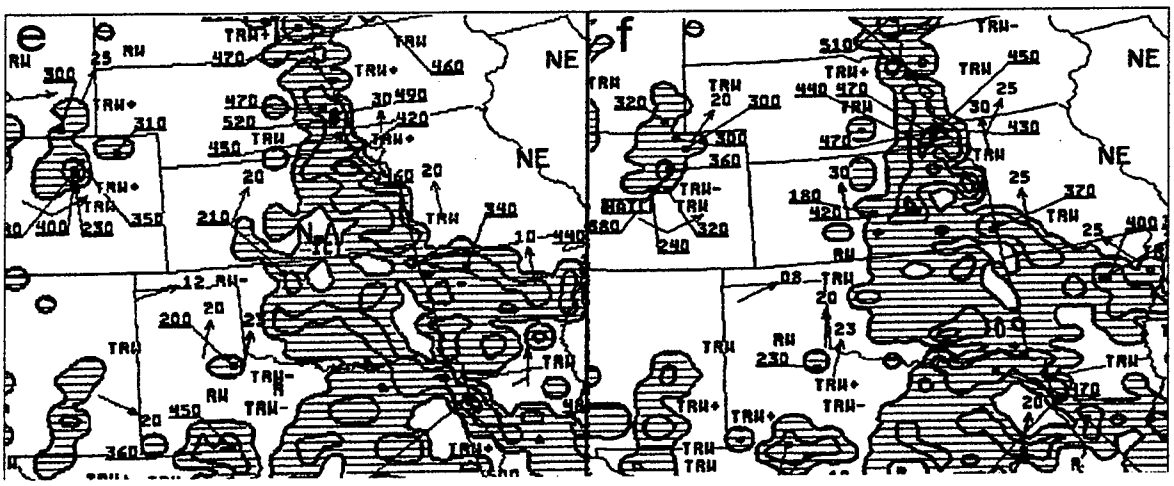


Figure 2. Radar summaries for 7 September 1991 at e) 2135, and f) 2235 UTC.

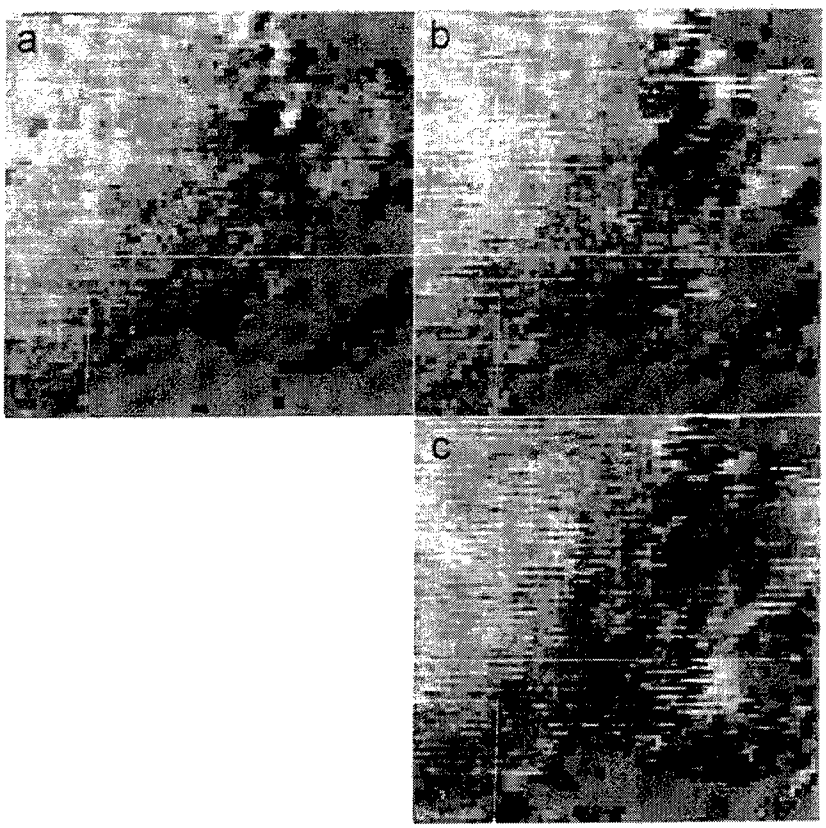


Figure 3. Cloud-free satellite-derived surface skin temperature heating rates for 8 September 1991 a) 1501 UTC, b) 1531 UTC, and c) 1601 UTC, for the Kansas/Oklahoma region. Dark regions represent low heating rates (nearly 0 K/h for the darkest regions), while lighter regions denote high heating rates (approaching 5 K/h for the lightest areas). Cloudy conditions are denoted by the uniform gray shading.

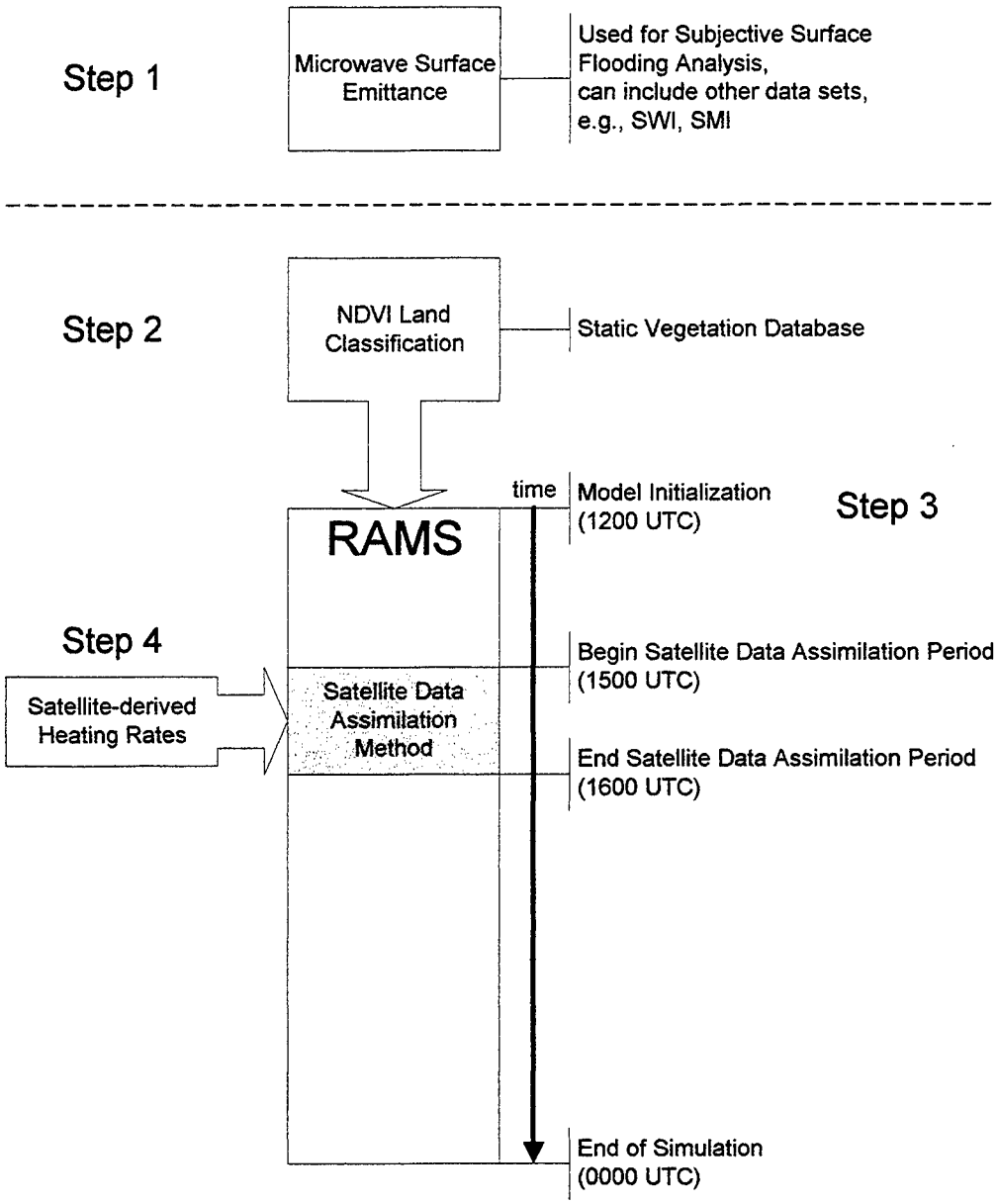


Figure 4. The satellite data assimilation method's processing steps.

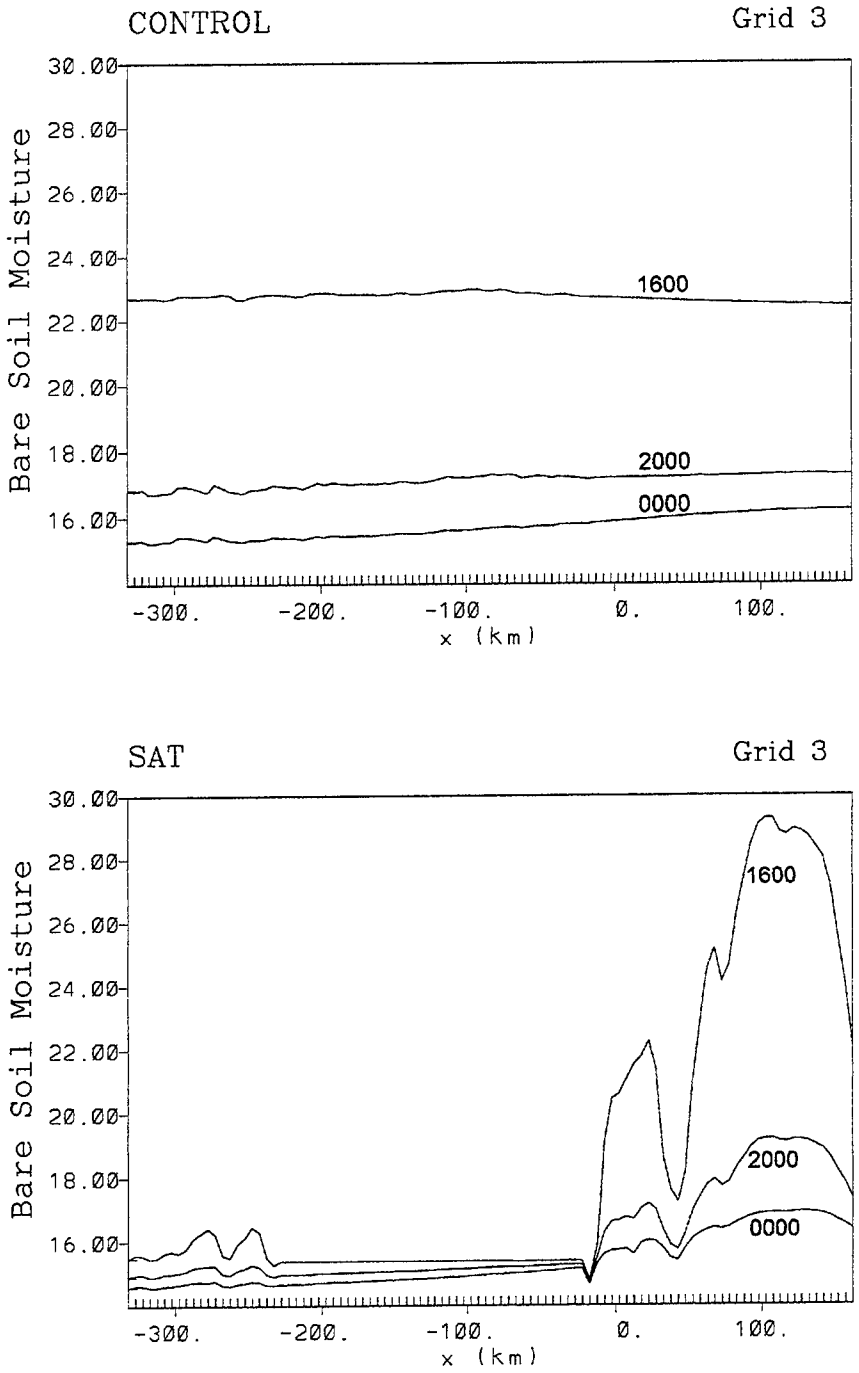


Figure 5. West to east cross section of bare-soil soil moisture (%.) at 1600, 2000, and 0000 UTC for the CONTROL and SAT simulations. The cross section is through the mid-point of grid 3 and corresponds to the previously shown sectors.

First Local Area Products from the NOAA-15 Advanced Microwave Sounding Unit (AMSU)

Stanley Q. Kidder, Andrew S. Jones*, James F. W. Purdom, and Thomas J. Greenwald
Cooperative Institute for Research in the Atmosphere
Colorado State University, Fort Collins CO 80523-1375
kidder@cira.colostate.edu

Objective and Relevance: The weather satellite NOAA-15 was successfully launched May 13, 1998, into a near polar orbit, carrying the first Advanced Microwave Sounding Unit (AMSU) sensors. The microwave sounding capabilities of AMSU allow for near all-weather penetration of various cloud fields, and the vertical profiling of atmospheric temperature and water vapor fields. By minimizing the influence of cirrus clouds (as compared with infrared sensors), the AMSU data are expected to improve the analysis of convection in data-sparse (battlespace) regions, and thus serve as a very useful tool in battlespace data-denied regions. Results of the first products produced by this sensor and disseminated to National Weather Service (NWS) offices via the Internet are presented. This work is the first semi-operational dissemination of near real-time polar microwave data into the NWS field offices. Operational uses of the data are highlighted.

Research Accomplished: AMSU is a next-generation microwave sounder and is similar to a combined DMSP SSM/T-1 and SSM/T-2 instrument, but with higher spatial resolution (Table 1). AMSU is a cross-track scanning, passive microwave sensor with 20 channels (Table 2). It is composed of two sounding instruments, AMSU-A (temperature sounder) and AMSU-B (water vapor sounder). Each sounder also includes several complementary microwave "window" channels from which geophysical parameters similar to those from the DMSP SSM/I instrument can be derived (Figure 1).

Table 1. Microwave Instrument Comparison[a]

Parameter	*SSM/T*	*MSU*	*SSM/I*	*AMSU-A*	*AMSU-B*	*SSM/T-2*
Satellites	DMSP	NOAA	DMSP	NOAA K, L, M	NOAA K, L, M	DMSP
No. of Channels	7	4	7	15	5	5
Frequency Range (GHz)	50.5–59.4	50.3–57.95	19.35–85.5	23.8–89.0	89.0–183.3	91.6–183.3
NEΔT (K)	0.4–0.6	0.3	0.4–1.7	0.25–1.20	0.8	0.5
Beam width	14°	7.5°	0.3°–1.2°	3.3°	1.1°	3.3°–6.0°
Best Ground Resolution (km)	204	110	12.5–50	48	16	48–84
Scan steps	7	11	64–128	30	90	28
Swath width (km)	2053	2347	1394	2179	2179	2053

[a]After Kidder and Vonder Haar (1995)

Table 2. Microwave Frequencies[a] (GHz) and Polarizations[b,c]

Channel	*SSM/T*	*MSU*	*AMSU-A*	*AMSU-B*	*SSM/I*	*SSM/T-2*
1	50.5H	50.30R	23.8R	89.0R	19.35H	183.3±3R
2	53.2H	53.74R	31.4R	150.0R	19.35V	183.3±1R
3	54.35H	54.96R	50.3R	183.3±1R	22.235V	183.3±7R
4	54.9H	57.95R	52.8R	183.3±3R	37.0H	91.7R
5	58.4V		53.6R	183.3±7R	37.0V	150R
6	58.825V		54.4R		85.5H	
7	59.4V		54.9R		85.5V	
8			55.5R			
9			57.2R			
10			57.29±.217R			
11			57.29±.322±.048R			
12			57.29±.322±.022R			
13			57.29±.322±.010R			
14			57.29±.322±.0045R			
15			89.0R			

[a]*Notation*: $x \pm y \pm z$; x is the center frequency. If y appears, the center frequency is not sensed, but two bands, one on either side of the center frequency, are sensed; y is the distance from the center frequency to the center of the two pass bands. If z appears, it is the width of the two pass bands. This pattern is easily implemented with radio frequency receivers, and it effectively doubles the signal (two pass bands instead of one).

[b]V = vertical, H = horizontal, R = rotates with scan angle.

[c]After Kidder and Vonder Haar (1995)

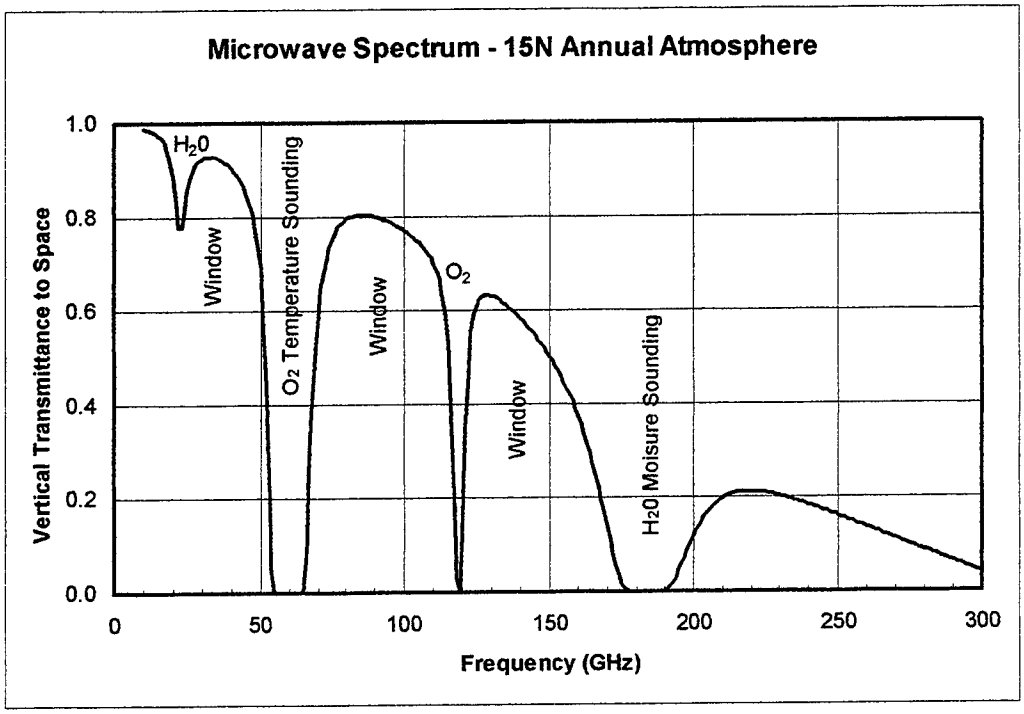


Figure 1. Microwave spectrum.

Data processing. AMSU data are downlinked to one of the two ground stations: one at Wallops Island, VA, and the other at Gillmore Creek, AK. The AMSU data are also transmitted in real time to users within sight of the satellite via the High Resolution Picture Transmission (HRPT) broadcast. Data from either Wallops Island or Gillmore Creek are processed by the National Environmental Satellite, Data, and Information Service (NESDIS) intoLevel 1B brightness temperatures. These data are further processed by NESDIS's Microwave Sensing Group to produce 5 parameters in addition to the 20 brightness temperatures. The products produced are shown in Table 3. Also, NESDIS's Soundings Team retrieve temperature and moisture soundings from the brightness temperatures.

Table 3. AMSU products produced by NESDIS's Microwave Sensing Group

Product	*Range/Units*
Total Precipitable Water (TPW)	0–60 mm
Instantaneous Rain Rate (RR)	0–35 mm/hr
Cloud Liquid Water (CLW)	0–6 mm
Snow Cover (SNO)	0–100%
Sea Ice Cover (ICE)	0–100%

CIRA Products. At CIRA, we acquire the ASMU brightness temperatures and products generated by the Microwave Sensing Group in Hierarchical Data Format (HDF). We convert them to McIDAS format and make them available over the Internet. To access the data, start with our Web site: *http://amsu.cira.colostate.edu.* Here you can find the three ways to access our data:

1. Using the File Transfer Protocol (FTP) download single-orbit files in McIDAS area format of any of the 20 brightness temperatures or 5 derived products. Figure 2 is an example of this type of data. At 89 GHz, ocean appears cold (black), and land appears warm (white). Glaciers, as on Iceland (near the center of the image) and Greenland (on the left edge), appear cold. Clouds and water vapor over the ocean appear milky.

2. Using McIDAS, access Mercator mapped images of the 5 products and 2 brightness temperatures (89 and 150 GHz) on CIRA's McIDAS server. (The Web page tells exactly how to do this.) Figure 3 is an example of such an image. It is a 150 GHz image of Hurricane Georges, and it shows scattering from ice at the top of rain bands. Note that the microwaves penetrate the central dense overcast to reveal the rain structure below. this is is one of AMSU's greatest advantages. Most National Weather Service (NWS) users of the AMSU data access them by this method.

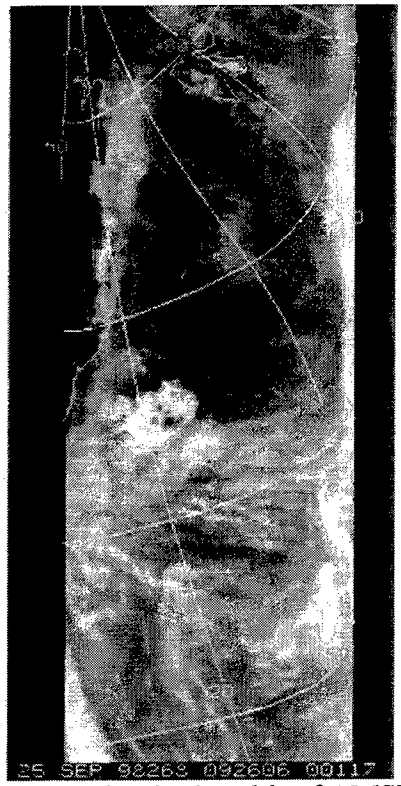


Figure 2. A portion of a single orbit of AMSU-B 89 GHz data.

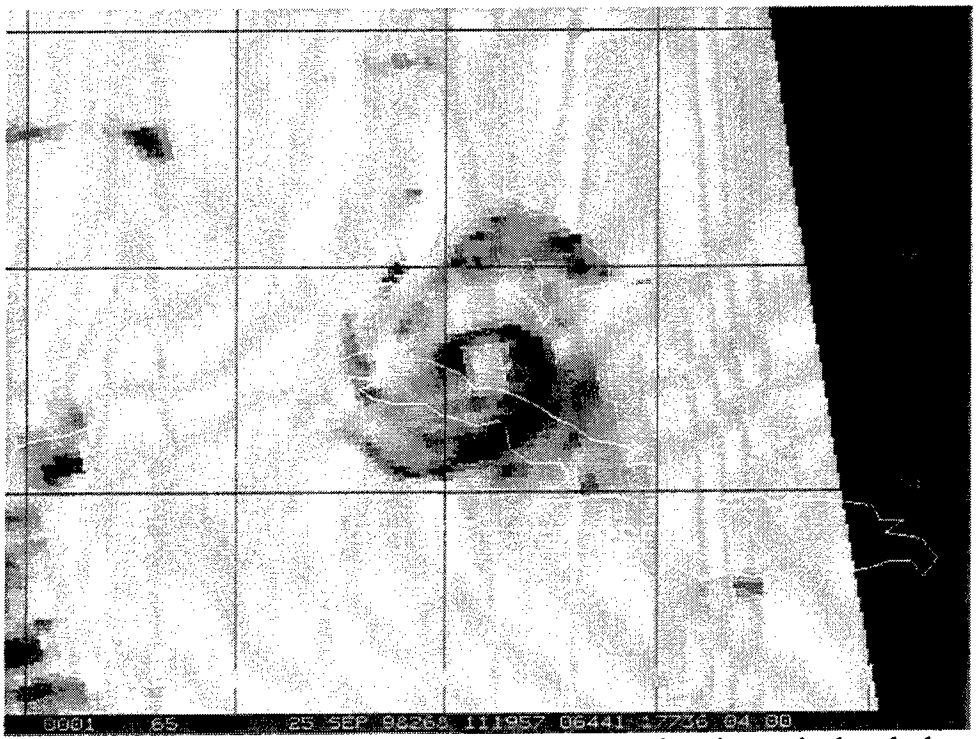


Figure 3. 150 GHz AMSU-B image of Hurricane Georges showing rain bands beneath the central dense overcast.

3. Using a Java-capable Web browser, browse the Mercator-mapped images. Figure 4 shows the window in which the data appear. In this case, TPW is displayed. The image has been annotated. Note that this browser is active. The "hot cursor" shows the data values below the cursor. This last way of viewing the images may be the best for field use because allows interaction with the data, and it is nearly platform independent.

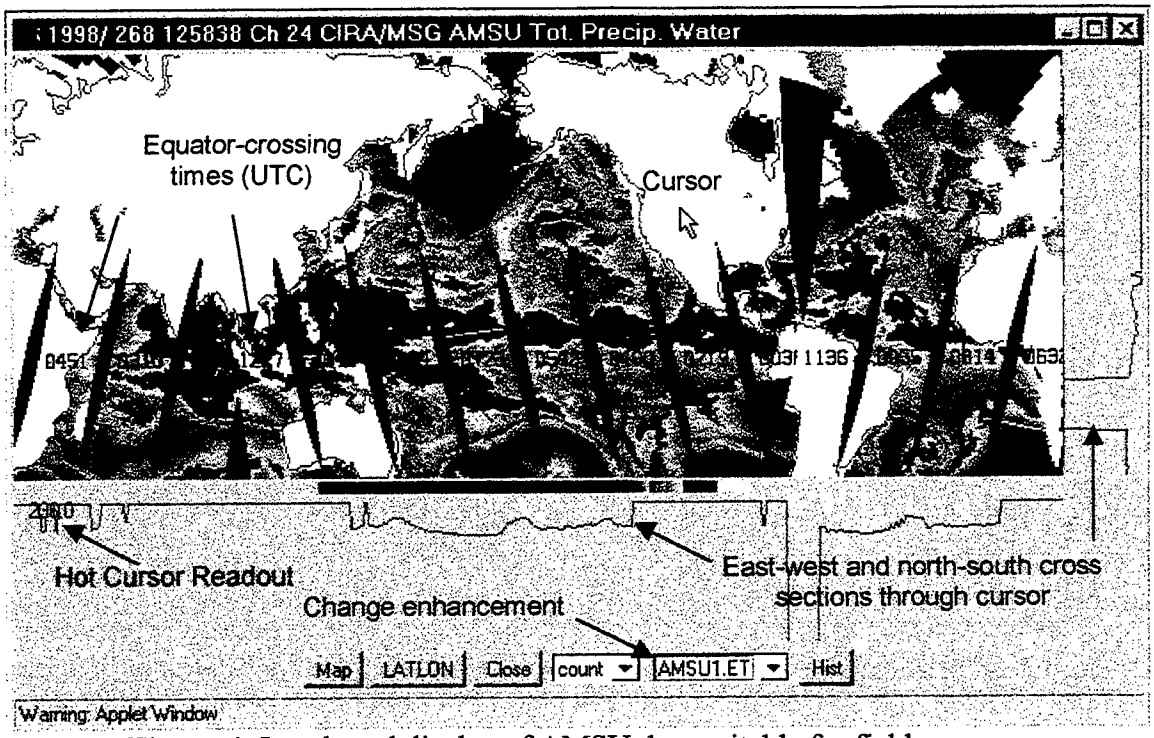


Figure 4. Java-based display of AMSU data suitable for field use.

Conclusions and Recommendations: Near real-time access to microwave observations is a major advance in satellite meteorology. It will improve National Weather Service forecasts, and if the data can be made available to him, it promises aid the military field forecaster as well.

BIBLIOGRAPHY

AMSU Retrievals for Climate Applications, http://orbit-net.nesdis.noaa.gov/ora/st/amsuclimate/amsu.html

CIRA's AMSU Web Page, http://amsu.cira.colostate.edu.

Kidder, S. Q., and T. H. Vonder Haar, 1995: *Satellite Meteorology: An Introduction.* Academic Press, San Diego, 466 pp.

Microwave Surface and Precipitation Products System (MSPPS) Home Page, http://orbit18i.nesdis.noaa.gov/

New GOES Imager System Products Suitable for Use on Field-Deployable Systems

Stanley Q. Kidder, Kenneth E. Eis*, and Thomas H. Vonder Haar
Cooperative Institute for Research in the Atmosphere
Colorado State University, Fort Collins CO 80523-1375
kidder@cira.colostate.edu

Objective and Relevance: Recent research has yielded three satellite-based values of significance to the military. These three are isotropic albedo, 3.9 μm albedo, and surface skin temperature. Isotropic albedo is used to correct for cloud reflection near the terminator. This correction factor allows the forecaster to get a better display of clouds at dawn and dusk when many strike operations occur. The 3.9 μm albedo provides a clear discriminator for fog, stratus, and CI clouds. The surface skin temperature gives the EOTDA weapons planner the IR temperature for the background, so critical to target contrast analysis and in the calculation of the background to target inversion time. Past EOTDA support has relied on knowledge of surface features, moisture, and soil structure to estimate skin temperature. Now it can be directly measured.

Research Accomplished: The algorithms calculate (1) isotropic albedo, (2) 3.9 μm albedo, (3) surface skin temperature, and (4) a blended product consisting of 3.9 μm albedo at night and isotropic albedo during the day. They are presented in the next four sections.

Isotropic albedo. The isotropic albedo product is the familiar GOES visible image corrected for solar zenith angle. It is especially useful near sunrise and sunset for analyzing cloud fields. The isotropic albedo can be extracted as follows.

The raw, 10-bit, GOES Variable (GVAR) count (0-1023) measured by the GOES Imager can be converted to a reflectance, R, by the calibration equations of Weinreb et al. (1998). This reflectance would be the albedo *if the sun were overhead at every point.* It is not, of course, but it is easy to correct for the variation in solar angle. We do two things to the reflectance: (1) multiply by the secant of the solar zenith angle and (2) multiply by the square of the ratio of the earth-sun distance to the mean earth-sun distance. The latter correction is small (within ±3.4%) but easily accomplished because it is a byproduct of the zenith angle calculation. In equation form,

$$\textit{Isotropic albedo} = R(d/d_{\text{mean}})^2 \sec\zeta \qquad (1)$$

where ζ is the solar zenith angle, d is the earth-sun distance, and d_{mean} is the annual-average earth-sun distance. We call the result the *isotropic albedo* because it does not take into account bidirectional effects, i.e., it is what the albedo would be if the scene were an isotropic reflector, one which reflects uniformly in all directions. This is not a new calculation. It has been done for many years by people who study the radiation budget of earth and others (see chapter 10 of Kidder and Vonder Haar 1995 for an explanation and bibliography).

Figure 1 compares the normal visible image display (uncorrected albedo) with the isotropic albedo. The clouds are similar in the southeastern part of the images, but near the terminator, the clouds disappear into the dark background in the top image. The cloud information in the dark area is not totally lost; it can be brought out of the normal image with image enhancement techniques (e.g. "stretching"), but only by over brightening the rest of the image. The isotropic albedo can be viewed as a physically based enhancement, which brings out the clouds (the meteorologically important features in the image) uniformly across the image. A good example of this is seen in the cirrus clouds over Kansas, Oklahoma, and Texas. Note that the bright band

near the terminator is a bidirectional effect, the result of the fact that at low sun elevation angles (high zenith angles) clouds are not isotropic reflectors.

The chief use of the isotropic albedo product is in analyzing clouds, especially near sunrise and sunset. This product could also be useful in constructing cloud climatologies (Reinke et al. 1992; Gould and Fuelberg 1996) because the threshold for distinguishing clouds is much less strongly related to sun angle than in the uncorrected visible image.

3.9 μm albedo. The so-called "fog product" has revolutionized fog and liquid water cloud detection at night. As described by Ellrod (1995), liquid water clouds have a lower emittance (emissivity) at 3.9 μm (GOES channel 2) than at 10.7 μm (channel 4). Whereas the emittance of a "thick" liquid water cloud at 10.7 μm is near 1.0, the emittance at 3.9 μm is near 0.7. The result is that at night, the brightness temperature at 3.9 μm ($T_{3.9}$) is less than that at 10.7 μm ($T_{10.7}$). This difference ($T_{10.7} - T_{3.9}$) has been exploited to produce the "fog product."

Emittance and albedo are related: they sum to one. Therefore, liquid water clouds with a 3.9 μm emittance of about 0.7 have an albedo of about 0.3. Solar radiation at 3.9 μm is not negligible, as it is at 10.7 μm. When the sun comes up, liquid water clouds reflect solar radiation to the satellite, and it appears that the clouds warm. $T_{3.9}$ becomes larger than $T_{10.7}$. In the fog product, liquid water clouds turn black due to the reflected solar radiation. To handle this problem, the "reflectance product" has been developed (Dills et al. 1996).

Because the reflection of solar radiation in the daytime and the lowered brightness temperatures at night over liquid water clouds are caused by the same phenomenon (decreased emittance / increased albedo), it is possible to develop a simple, unified product which is applicable both day and night. The radiance measured by the GOES Imager at 3.9 μm is composed of reflected and emitted parts. The emitted part can be approximated as

$$\textit{Emitted radiation} = \varepsilon_{3.9}\, B_{3.9}(T_{10.7}) = (1 - A_{3.9})\, B_{3.9}(T_{10.7}), \tag{2}$$

where $A_{3.9}$ is the 3.9 μm albedo. The reflected radiation starts with the 3.9 μm solar irradiance of the scene, which can be approximated as

$$\textit{Solar irradiance} = B_{3.9}(T_{\text{sun}})\, \Omega_{\text{sun}} \cos\zeta, \tag{3}$$

where Ω_{sun} is the solid angle of the sun subtended at the earth (6.8×10^{-5} sr), and, based on Thekaekara (1972), T_{sun} = 5888 K at 3.9 μm. The radiance reflected to the satellite from a particular point or location is the product of the bidirectional reflectance and the solar irradiance. Assuming that the point is an isotropic surface, the bidirectional reflectance is simply $\pi^{-1} A_{3.9}$ (see Kidder and Vonder Haar 1995, pp.79-81, for details). Thus, the reflected radiation is simply:

$$\textit{Reflected radiation} = \pi^{-1}\, A_{3.9}\, B_{3.9}(T_{\text{sun}})\, \Omega_{\text{sun}} \cos\zeta. \tag{4}$$

Therefore, the radiance measured by the satellite can be written as the sum of the emitted and reflected radiation:

$$L_{3.9} = \pi^{-1}\, A_{3.9}\, B_{3.9}(T_{\text{sun}})\, \Omega_{\text{sun}} \cos\zeta + (1 - A_{3.9})\, B_{3.9}(T_{10.7}), \tag{5}$$

or, solving for $A_{3.9}$,

$$A_{3.9} = \frac{L_{3.9} - B_{3.9}(T_{10.7})}{\pi^{-1}\, B_{3.9}(T_{\text{sun}})\, \Omega_{\text{sun}} \cos\zeta - B_{3.9}(T_{10.7})}. \tag{6}$$

At night ($\zeta > 90°$) the same equation applies if we simply set $B_{3.9}(T_{\text{sun}}) = 0$.

To construct the 3.9 μm albedo product, GOES Imager data for channels 2 and 4 are processed using eq. (6). Then 3.9 μm albedos from –50% to +50% are displayed as a gray scale from black to white. Negative albedos result from thin cirrus, probably because of inhomogeneities in the partially transparent cirrus, which result in $T_{3.9}$ being larger than $T_{10.7}$.

Figure 2 shows the 3.9 μm albedo product for three times spanning sunrise. Land and ocean have near zero 3.9 μm albedo and thus appear gray. Liquid water clouds appear white, and cirrus appears black at night. With the exception of cirrus, there are no large changes between day and night. Eq. (6) has a problem just after sunrise, when the denominator goes from negative, through zero, to positive. This causes an anomaly in the displayed image.

Lee et al. (1997) have also discussed a day/night 3.9 μm product. The Lee et al. derivation is much more complicated than the 3.9 μm albedo presented in this paper.

The chief use of the 3.9 μm albedo product is in locating liquid water clouds/fog, especially at night.

Surface temperature. The third product to be described in this paper is called the surface temperature product (T_{sfc}). Based on the work of McMillin and Crosby (1984), the split widow channels (channel 4, 10.7 μm; and channel 5,12.0 μm, on the GOES Imager) can be used together to correct one of them for the effects of atmospheric absorption. The formula is

$$T_{sfc} = T_{10.7} + \eta(T_{10.7} - T_{12.0}), \tag{7}$$

where,

$$\eta = \frac{1 - \tau_{10.7}}{\tau_{10.7} - \tau_{12.0}}, \tag{8}$$

and τ is atmospheric transmittance (see Kidder and Vonder Haar 1995, pp. 219–225, for details). MODTRAN (Berk et al. 1989) calculations for the standard mid-latitude atmosphere show that for the GOES Imager $\tau_{10.7}$ is about 0.68 and $\tau_{12.0}$ is about 0.53, which means that η is approximately 2. This derivation is similar to sea surface temperature algorithms (McClain et al. 1985), but it is simpler. Figure 3 shows an example T_{sfc} image with the corresponding isotropic albedo image for comparison. T_{sfc} is mostly of value in humid situations to "clear" the water vapor from the satellite signal to reveal the surface (skin) temperature. T_{sfc} appears quite similar to the usual $T_{10.7}$ image, but with slightly more noise because it is a combination of two channels and therefore has compounded noise.

The chief use of the surface temperature product is to determine changes or boundaries in the low-level temperature. Color enhancement tables can be used to quickly quantify the surface temperatures and help track changes.

Day/night albedo. It is easy to combine the 3.9 μm albedo and the isotropic albedo to produce a day/night albedo product. The combined product displays the 3.9 μm albedo when the sun is down and the isotropic albedo when the sun is up. Figure 4 shows that this product is particularly useful for monitoring low (liquid water) clouds across the terminator.

Although we have presented these four products as GOES products, nearly the same spectral channels are present on the Advanced Very High Resolution Radiometer (AVHRR) instrument on the polar-orbiting NOAA satellites. To convert AVHRR counts to radiances, see the *NOAA Polar Orbiter Data User's Guide* (1997) for the TIROS N and NOAA 6 through 14 satellites, or see the *NOAA KLM User's Guide* (1997) for NOAA 15 and higher. Because the channels are different, slightly different parameters are necessary: at 3.7 μm, $T_{sun} \approx 5827$ K (Thekaekara 1972), and $\eta \approx 3$ (Price 1984).

Conclusions and Recommendations: We have presented four simple products which can be constructed from GOES Imager data (or AVHRR data) to improve weather analysis and forecasting. They are the isotropic albedo product, the 3.9 μm albedo product, the surface temperature product, and the day/night albedo product. Each of these products has been tested using *GOES-8, GOES-9,* and *GOES-10* imagery. We believe that these are the type of products which should be available to forecasters. They are simple, easily produced, reliable, and physically based. These products extend the usefulness of the raw channel data from the GOES satellites. They are suitable for use on field-deployable systems, and they could be reconfigured from remote sites.

REFERENCES

Berk, A., L. S. Bernstein, and D. C. Robertson, 1989: *MODTRAN: A Moderate Resolution Model for LOWTRAN 7*, U.S. Air Force Geophysics Laboratory Tech. Rep. GL-TR-89-0122, Hanscom AFB, Mass. [ADA 214337].

Dills, P. N., D. W. Hillger, and J. F. W. Purdom, 1996: Distinguishing between different meteorological phenomena and land surface properties using the multispectral imaging capabilities of GOES-8. *Eighth Conf. on Satellite Meteorology and Oceanography*, American Meteorological Society, 339–342.

Ellrod, G. P., 1995: Advances in the detection and analysis of fog at night using GOES multispectral infrared imagery. *Wea. Forecasting*, **10**, 606-619.

Gould, K. J., and H. E. Fuelberg, 1996: The use of GOES-8 imagery and RAMSDIS to develop a sea breeze climatology over the Florida panhandle. *8th Conf. On Satellite Meteorology and Oceanography,* American Meteorological Society, Boston, 100–104.

Kidder, S. Q., and T. H. Vonder Haar, 1995: *Satellite Meteorology: An Introduction.* Academic Press, San Diego, 466 pp.

Lee, T. F., F. J. Turk, and K. Richardson, 1997: Stratus and fog products using GOES-8–9 3.9-μm data. *Wea. Forecasting*, **12**, 664–677.

McClain, E. P., W. G. Pichel, and C. C. Walton, 1985: Comparative performance of AVHRR-based multichannel sea surface temperatures. . *Geophys. Res.*, **90**, 11587-11601.

McMillin, L. M., and D. S. Crosby, 1984: Theory and validation of the multiple window sea surface temperature. *J. Geophys. Res.*, **89**, 3655-3661.

NOAA KLM User's Guide, 1997: NOAA/NESDIS, Washington, DC. [Available on line at http://perigee.ncdc.noaa.gov/docs/klm/index.htm.]

*NOAA Polar Orbiter Data User's Guide,*1997: NOAA/NESDIS, Washington, DC. [Available on line at http://perigee.ncdc.noaa.gov/docs/podug/index.htm.

Price, J. C., 1984: Land surface temperature measurements from the split window channels of the NOAA–7 Advanced Very High Resolution Radiometer. *J. Geophys. Res.*, **89**, 7231-7237.

Reinke, D. L., C. L. Combs, S. Q. Kidder, and T. H. Vonder Haar, 1992: Satellite cloud composite climatologies: A new high-resolution tool in atmospheric research and forecasting. *Bull. Amer. Meteor. Soc.*, **73**, 278-285

Thekaekara, M. P., 1972: *Photonics Spectra*, **6**, 32-35. [Data available from ftp://ftp.ngdc.noaa.gov/STP/SOLAR_DATA/ATM_HANDBOOK/]

Weinreb, M. M. Jamieson, N. Fulton, Y. Chen, J. X. Johnson, J. Bremer, C. Smith, and. J. Baucom, 1998: Operational calibration of Geostationary Operational Environmental Satellite-8 and -9 Imagers and Sounders. *Applied Optics*, **36**, 6895-6904.

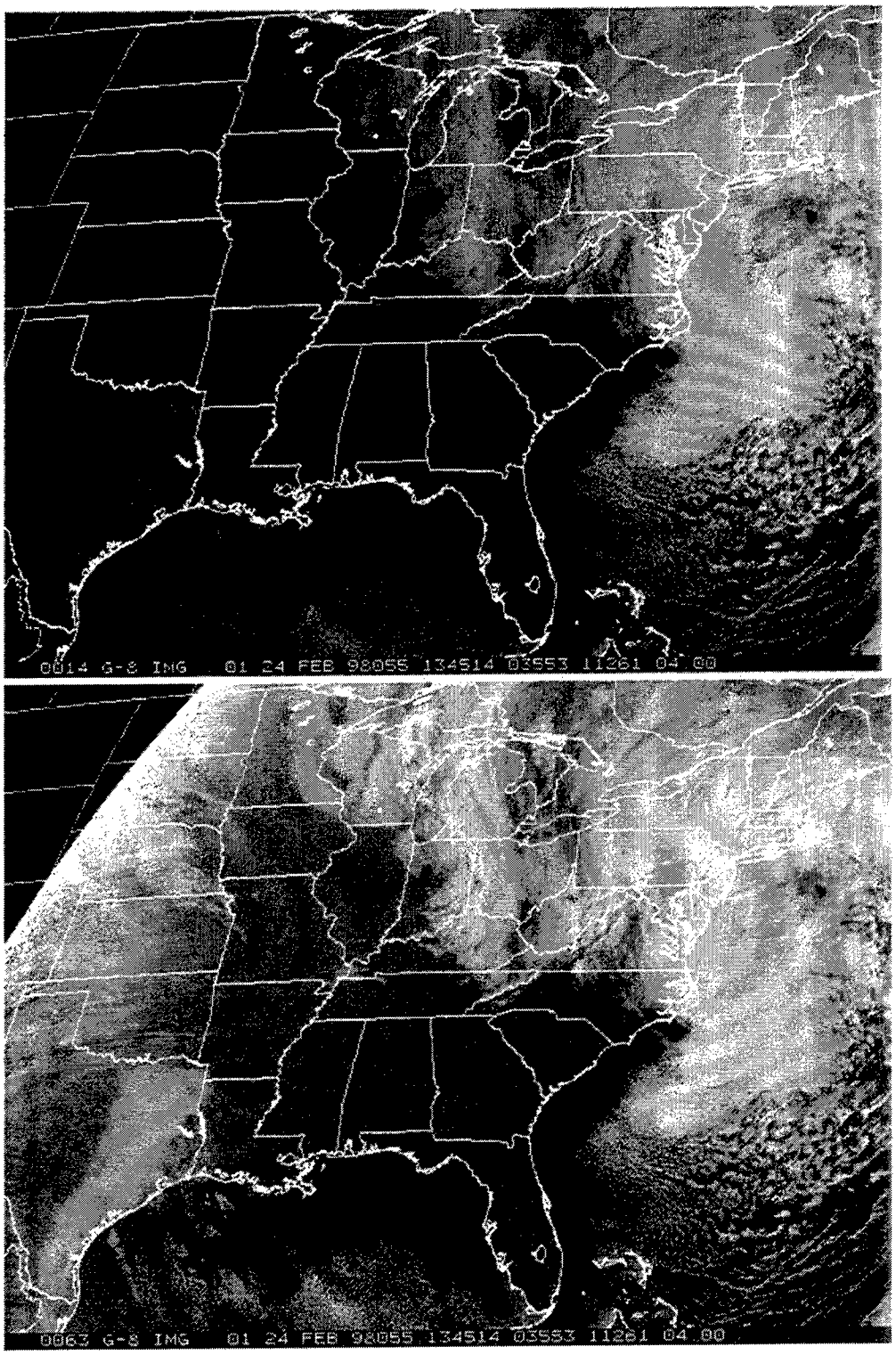


Figure 1. (Top) GOES visible image (channel 1, 0.67 μm). (Bottom) Isotropic albedo.

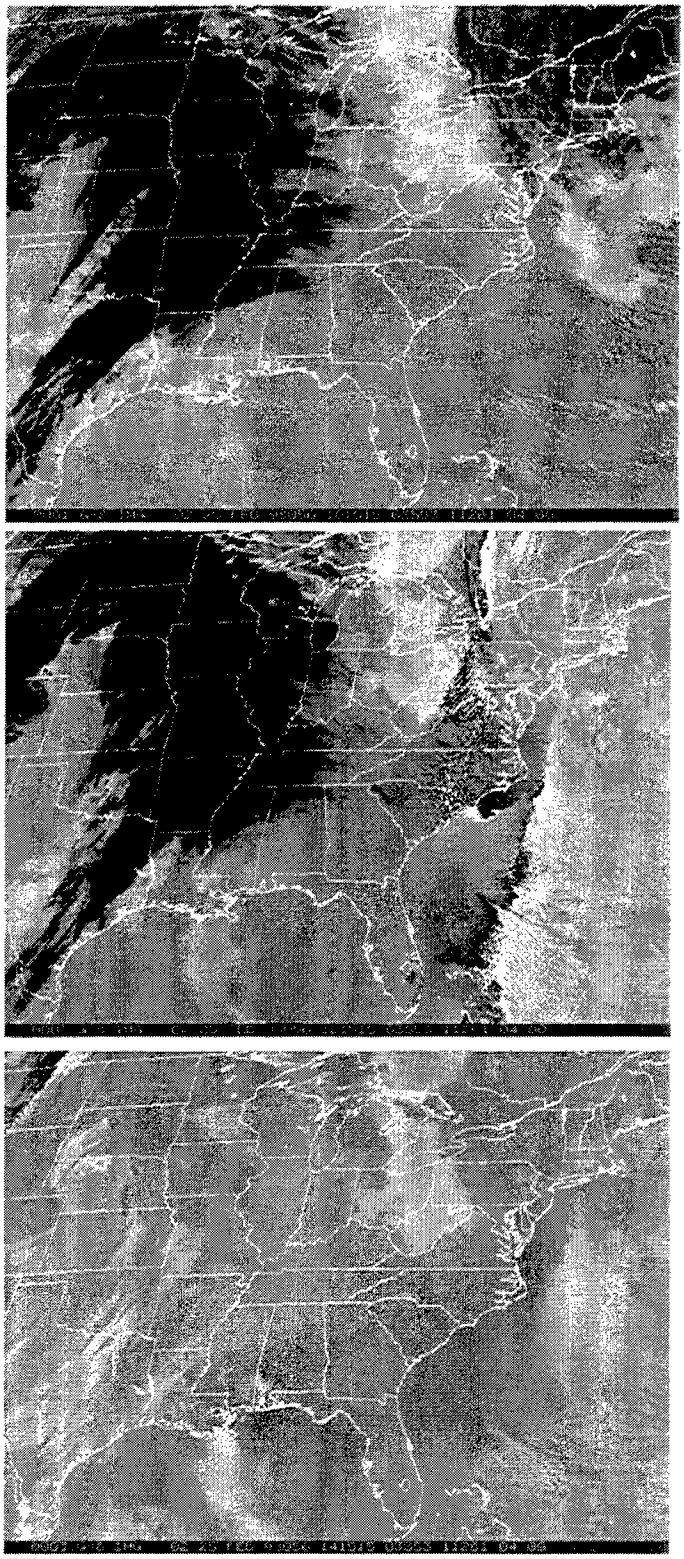


Figure 2. 3.9 μm albedo product for three times spanning sunrise: (top) 1015 UTC, (middle) 1215 UTC, (bottom) 1415 UTC.

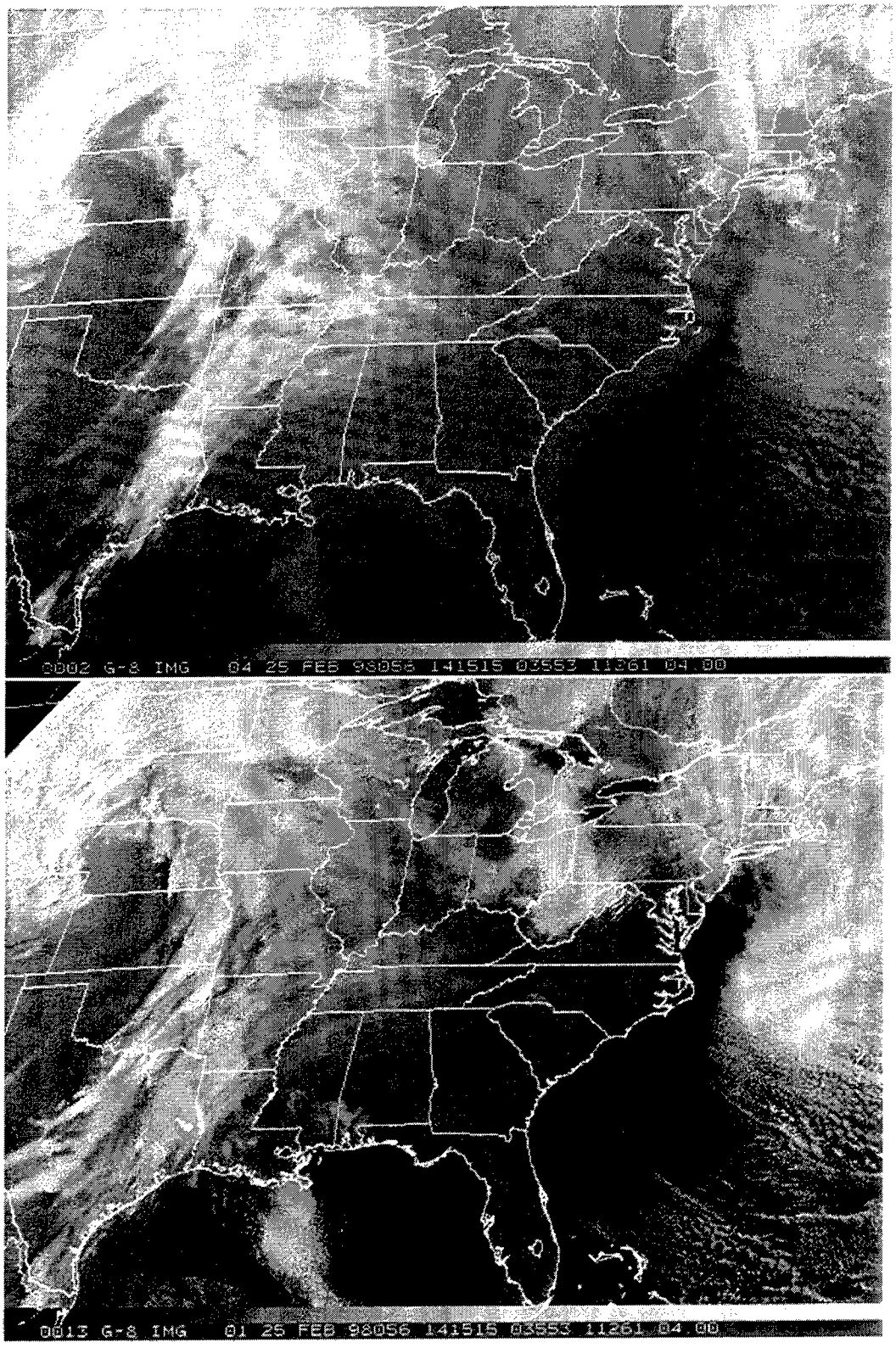


Figure 3. (Top) The surface temperature product. (Bottom) isotropic albedo.

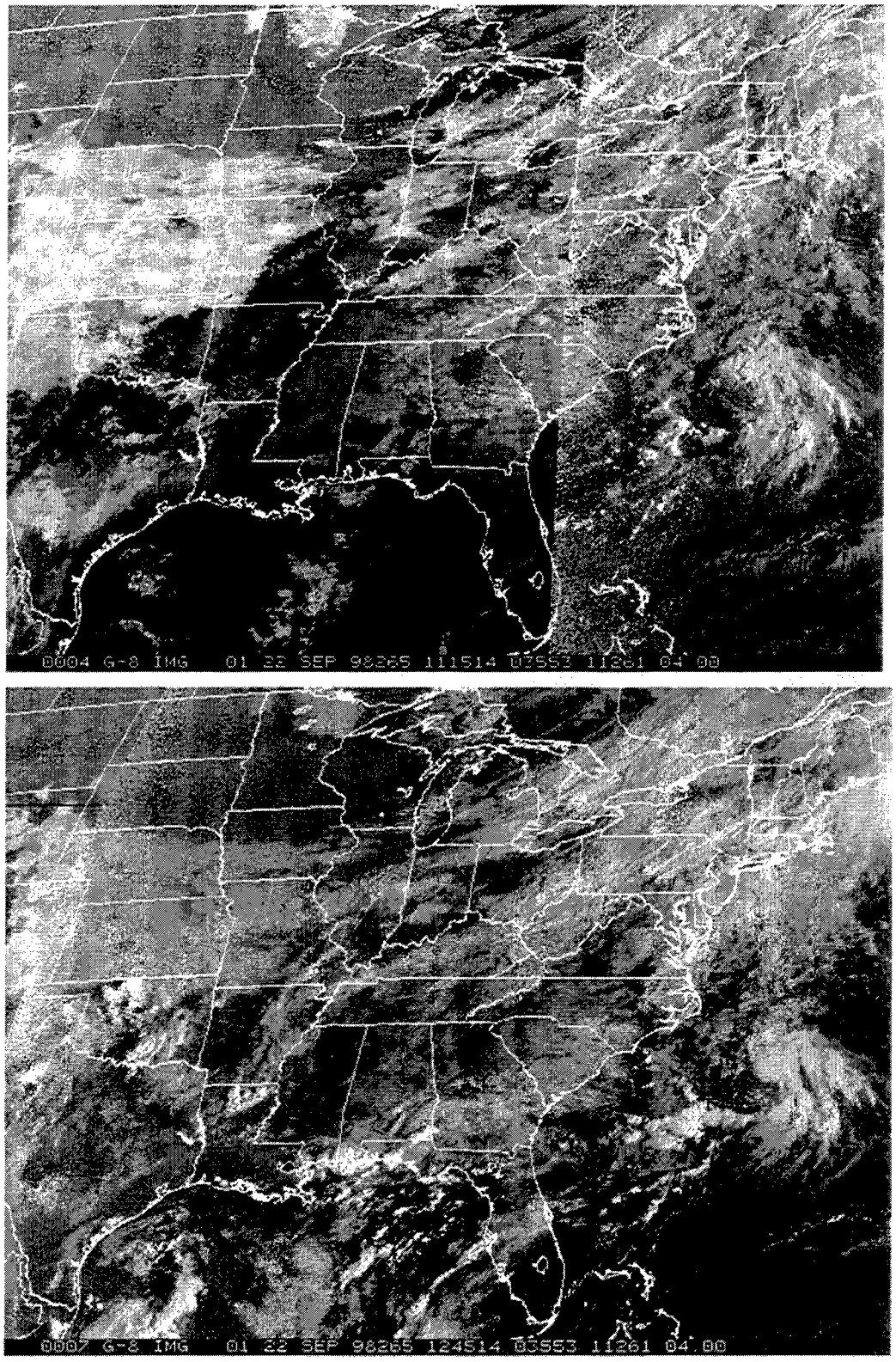


Figure 4. Day/night albedo product at two times: (top) 1115 UTC, (bottom) 1245 UTC.

OPTICAL REMOTE SENSING OF ATMOSPHERIC PROPERTIES

C. Russell Philbrick* and Daniel B. Lysak, Jr.
The Pennsylvania State University
Applied Research Laboratory and
Department of Electrical Engineering
PO Box 30, State College PA 16804
814-865-2975, (fax) 863-8457, crp3@psu.edu

ABSTRACT

Techniques have been demonstrated which show the capabilities of lidar to measure the profiles of many meteorological and optical properties in the troposphere. The Lidar Atmospheric Profile Sounder (LAPS) instrument was prepared by the Applied Research Laboratory of Penn State University for the US Navy as an operational prototype that provides the profiles of water vapor and temperature as real time data products to support requirements for RF-refraction and meteorological data. The capability to measure the optical extinction at three wavelengths has been added to the instrument. The sounder was successfully demonstrated on the *USNS SUMNER* in Fall 1996 and has been used to gather data during several scientific research programs since that time. The data have provided an opportunity to investigate the variations of atmospheric properties with much finer resolution of the temporal variations than has been possible previously. Examples of some interesting variations in the properties of the lower atmosphere, including weather front passage and convective events, are used to show the importance of lidar measurements. The future directions for advancing our technical capabilities are apparent from the advances that have been made with the LAPS instrument. Future instruments will enhance the capabilities demonstrated here by further automation of lidar systems which use these Raman measurement techniques.

INTRODUCTION

The Lidar Atmospheric Profile Sensor (LAPS) instrument was prepared and tested to determine the capability of laser remote sensing to provide profiles of atmospheric properties during semi-automated shipboard operation over a wide range of meteorological conditions. Tests were conducted onboard the *USNS SUMNER* during September and October 1996 near the Florida coast. The instrument measures the water vapor profile based on the vibrational Raman scattering and the temperature profile based on the rotational Raman scattering. These measurements are used to calculate profiles of RF refractivity. Profiles of the Raman signals were stored each minute with a vertical resolution of 75 meters from the surface to a user selected altitude, typically between 5 and 15 km. The measured profiles are integrated, for selected intervals, typically 1, 5 or 30 minutes, to calculate the real time atmospheric profiles with their associated $\pm 1\sigma$ standard deviation for specific humidity, temperature, optical extinction and ozone. Daytime measurements of water vapor, extinction and ozone are made using the "solar blind" ultraviolet signals to obtain useful measurements without the intense daytime background. The LAPS prototype instrument includes several sub-systems to automate and monitor its operation, and it provides real-time display/transfer of the profiles. The instrument includes an X-band radar to detect aircraft as they approach the beam and automatically shuts down the laser to protect a 6 degree cone angle around the beam. The

weather sealed instrument has been designed to include environment control, calibration, and performance self-tests to check many functions. The testing program has proven the qualities of ruggedness, reliability and general performance of the LAPS lidar system.

LAPS Instrument Development

The objective of the LAPS program was to develop a lidar profiler capable of providing real time measurements of atmospheric and meteorological properties, particularly those profiles which directly determine the RF refractivity. The LAPS Program was begun in 1991 with the goal of using laser remote sensing techniques to provide an operational lidar sensor prototype instrument for at sea demonstration within 5 years. Lidar is a radar at optical wavelengths, where the laser transmitter sends a pulsed beam to scatter from the molecules and particles of the atmosphere. The arrival time of the backscattered light pulse provides a precise altitude for the scattering volume, and the intensity at the transmitted wavelength, as well as at several frequency shifted wavelengths (Raman scattering), provides a wealth of information on the atmospheric properties. Using the ratios of Raman shifted scattered radiation removes most of the uncertainties in deriving accurate data and provides a robust measurement of atmospheric properties. The primary sub-systems making up the LAPS lidar system are listed in Table 1.

Table 1. LAPS Lidar instrument sub-systems

Transmitter	Continuum 9030 -- 30 Hz 5X Beam Expander	600 mj @ 532 nm 130 mj @ 266 nm
Receiver	61 cm Diameter Telescope	Fiber optic transfer
Detector	Seven PMT channels Photon Counting	528 and 530 nm – Temperature 660 and 607 nm – Water Vapor 294 and 285 nm – Daytime Water Vapor 276 and 285 nm – Raman/DIAL Ozone
Data System	DSP 100 MHZ	75 meter range bins
Safety Radar	Marine R-70 X-Band	protects 6° cone angle around beam

The LAPS lidar instrument has been developed from lessons learned during the development and testing of five prior lidar research instruments. The LAPS lidar has been specifically designed to be a rugged instrument, to provide automated operation, and to be field serviceable, so that it can be operated by technicians on Navy ships with a reasonable amount of training. More than twenty sub-systems have been designed into the instrument to control and simplify the instrument operation. It is intended that a weather officer could obtain the data on demand or acquire data according to a planned schedule. The LAPS lidar has many advantages over current balloon techniques for atmospheric properties, it is capable of providing the RF refractivity profiles directly into radar propagation models for a continuously updated description of the local RF-propagation conditions, also the electro-optical propagation conditions can also be described. The LAPS instrument hardware was completed in mid-1996 and it was successfully tested onboard the *USNS SUMNER* in September/October 1996. The long term plan for the instrument is to replace most of the current balloon sonde profiling and enable continuous data collection to support radar operations or weather affected missions.

Raman Lidar Measurement Techniques

Raman scattering is one of the processes that occurs when optical radiation is scattered from the atmospheric molecules. Even though the intensity of Raman scattered radiation is much less than that scattered at the transmitted fundamental laser wavelength, it is most useful because the vibrational Raman scattering occurs at distinct wavelength shifts for each species and correspond to specific vibrational energy states of the molecules. The rotational Raman scattering provides a signal where the relative intensity of the shifted wavelengths depends directly upon the atmospheric temperature. The ratio of vibrational Raman back scatter signals from the molecules of the water vapor at 660 nm and 294 nm from the 2^{nd} (532 nm) and 4^{th} (266 nm) harmonics of Nd:YAG laser and molecular nitrogen (607 nm and 285 nm) are at wavelengths widely separated from the exciting laser radiation and can be easily isolated for measurement using modern filter technology and sensitive photon counting detectors. The ratio of rotational Raman signals at 528 nm and 530 nm provides measurements which are sensitive to atmospheric temperature [Nedeljkovic 1993, Philbrick 1994, Haris 1995, and Balsiger 1996b]. Table 2 lists the measured signals acquired by the LAPS lidar. The altitude range of the measurements is extended at night using visible data channels, however the primary range of interest for RF-refractivity is between the surface and 3 km.

Based upon developments by other groups and in our laboratory, we now have the capability for reliably profiling most of the important properties of the atmosphere with lidar [Philbrick 1991, Whiteman 1992, Hauchecorne 1992]. In order to push the lidar measurement capability into the daylight conditions, we have used the "solar blind" region of the spectrum between 260 and 300 nm. Nighttime measurements are made using the 660nm/607nm (H_2O/N_2) signal ratio from the doubled Nd:YAG laser radiation at 532 nm. Daylight measurements are obtained using the 295nm/284nm (H_2O/N_2) ratio from the quadruple Nd:YAG laser radiation at 266 nm. A correction for the tropospheric ozone must be applied, it can be obtained from the ratio of the O_2/N_2 signals 278nm/284nm, thus the troposphere ozone profile is also obtained.

Table 2. The LAPS measurements from Raman scatter signals are summarized.

Property	Measurement	Altitude	Time Resolution
Water Vapor	660/607 Raman 294/285 Raman	Surface to 5 km Surface to 3 km	Night - 1 min. Day/Night - 1 min.
Temperature	528/530 Rotational Raman	Surface to 5 km	Night 30 min.
Optical Extinction 530 nm	530 nm Rotational Raman	Surface to 5 km	Night 10 to 30 min.
Optical Extinction 607 nm	607 N_2 - 1^{st} Stokes	Surface to 5 km	Night - 10 to 30 min.
Optical Extinction 285 nm	285 N_2 - 1^{st} Stokes	Surface to 3 km	Day and Night 30 min.
Ozone	276/285 Raman/DIAL	Surface to between 2 and 3 km	Day and Night 30 min.

The molecular density effect on the refraction can be determined from the temperature profile and a surface pressure measurement. We have been able to demonstrate that the

rotational Raman signal provides a useful temperature profile. The design and construction of the narrow band filters to eliminate the large back scatter signal from the nearby fundamental laser line presents the primary challenge. The ratios of the measured signals at 530nm/528nm from the doubled Nd:YAG at 532 nm have been used to provide a technique to obtain the temperature profile. The Raman techniques, which use ratios of the signals for measurements of water vapor and temperature, have the major advantage of removing essentially all of uncertainties, such as any requirement for knowledge of the absolute sensitivity and non-linear factors caused by aerosol and cloud scattering.

RF-Refractivity Measurements

Over a wide range of radar wavelengths, the refractive effects of the atmosphere can be simply described based upon the profiles of water vapor and temperature, because these describe the distribution of the molecular scatterers. It's larger scattering cross-section and extremely irregular spatial distribution cause water vapor profiles to be most significant for describing refractivity. The RF-refractivity, N, represents the significant figures of the refractive index, n,

$$N = (n - 1) \times 10^6 , \qquad (1)$$

and is based upon the following empirically derived relationship,

$$N = 77.6\, P/T + 3.73 \times 10^5\, e/T^2 , \qquad (2)$$

where the water vapor partial pressure, e (mbar), is related to the specific humidity, r (gm/kg), by the relation,

$$e\ (\text{mbar}) = (r\, P)/(r + 621.97). \qquad (3)$$

The errors associated with the measurement may be considered based upon analysis of the propagation of errors. The errors have the approximate values given by,

$$\Delta N = (\delta N/\delta r)\, \Delta r + (\delta N/\delta T)\, \Delta T + (\delta N/\delta P)\, \Delta P , \qquad (4)$$

$$\delta N/\delta r \sim 6.7 \qquad \delta N/\delta T \sim -1.35 \qquad \delta N/\delta P \sim 0.35$$

$$dN/dz = 6.7\, dr/dz - 1.35\, dT/dz + 0.35\, dP/dz . \qquad (5)$$

The values used in these relationships, which are typical of the lower atmosphere, show that it is the gradients in water vapor that are most important in determining RF ducting conditions. The Raman lidar technique provides the water vapor and temperature profiles which can be used in these equations to directly determine the refractivity profile for input to propagation models [Philbrick 1995, Philbrick 1996b].

RESEARCH ACCOMPLISHED

The LAPS instrument was installed on the *USNS SUMNER* on 30 August at Pascagoula MS. Testing of the LAPS instrument was carried out during the period 1 September - 15 October 1996 in the Gulf of Mexico and along the Atlantic coast. The LAPS instrument has also participated in several scientific research projects, NARSTO-Northeast (Gettysburg PA, August 1996), SCOS (Hesperia CA, August-September 1997), ARM-Northslope (Barrow AK, March 1998), FIRE (Barrow AK, May 1998), NEC-OPS (Philadelphia PA, August 1998).

LAPS Measurements Onboard the *USNS SUMNER*

During the period while the USNS Sumner was at sea, the LAPS lidar was used to gather data in 352 hourly subdirectories. Thus measurements were obtained during an average of 10 hours each day during the sea trials. Measurements were obtained during both day and night time conditions. On several occasions, the LAPS lidar instrument was run continuously for

extended periods, including one period of 24 hours and one of 36 hours. Measurements were made in all weather conditions and the instrument was available 99 % of the time. It was only down during one period of 10 hours for scheduled routine maintenance and alignment. The operations during cloudy periods where generally successful in providing sufficient data below and between clouds and through light clouds to provide useful profiles. During approximately 5 to 10 % of the time period, clouds with high optical thickness limited the operations and profiles are only provided below the cloud base at those times.

The LAPS development has been directed toward the measurement of the refractivity of the atmosphere for determination of electromagnetic ducting conditions. Figure 1 shows an example of time sequences of the LAPS lidar data for water vapor and temperature profiles during a 6 hour period on 11 October 1996 during the shipboard tests. Figure 1 (c) shows the time sequence of the RF-Refractivity profiles obtained from the water vapor and temperature shown in the accompanying plots. The lidar derived time sequence provides continuous updates of the radar refractivity and meteorological profiles for operational use, the sequence plots are useful because they show trends and immediately detect any changes in conditions.

The optical extinction profile from the LAPS instrument is determined from the signal loss in the molecular profiles caused by scattering by clouds and aerosol particles. The gradient observed in the major molecular species profiles can be compared with the neutral density scale height to directly determine the optical extinction. In general, we have found that the optical extinction cannot be determined from the backscatter signal at the fundamental laser wavelengths [Rau 1994]. However, the extinction can be determined from the profiles of primary molecular species at the Raman shifted wavelengths [Philbrick 1996a, Stevens 1996a, O'Brien 1996, Stevens 1996b, Philbrick 1997a]. The optical extinction profiles can be determined from the gradients in each of the measured molecular profiles, at 607 (N_2), 530 (rotational Raman) and 284 (N_2) nm. Figure 2 shows a example of extinction measurements obtained directly from the Raman signals of the LAPS lidar during the *USNS SUMNER* tests. The wavelength dependent optical extinction can be used to describe changes in the particle size distribution as a function of altitude for the important small particles. These measurements can then be interpreted to determine the air mass parameter and atmospheric optical density.

We have also demonstrated that a new bi-static technique can be used to estimate particle density, size and distribution widths (of spherical scatters) by using the unique information contained in the polarization ratio of the scattering phase function versus angle. A bistatic receiver has been developed to provide data on the scattering phase function of the aerosols [Stevens 1996a,b, Philbrick 1998]. This technique can be implemented to utilize the same transmitter beam of the lidar to provide additional information on particle size and density.

LAPS Performance Summary

Examples of the LAPS profiles compared to individual balloon rawinsondes have been shown in several reports [Balsiger 1996a, Philbrick 1996b, Philbrick 1997b]. The important result for this investigation is that many comparisons were made to examine how well the instrument performed on the ship when a single calibration constant is applied and the measurements are compared to the reference of standard rawinsonde balloons. Here the LAPS

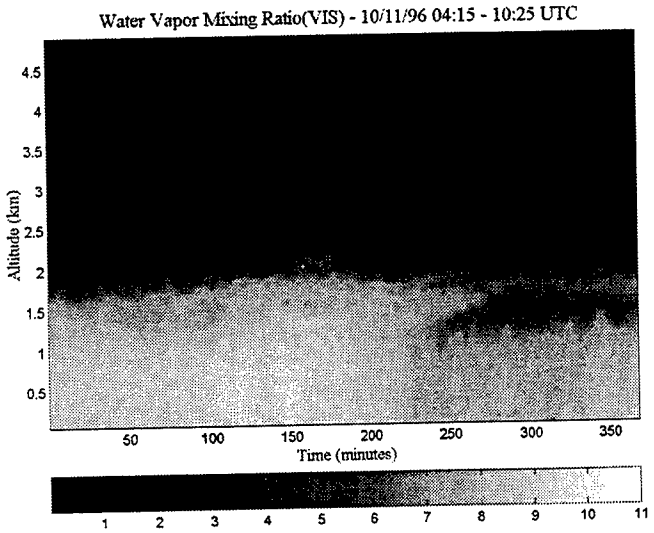


Figure 1 (a). A time sequence shows 6 hours of the water vapor profiles (specific humidity in gm/kg) measured onboard the *USNS Sumner* on 11 October 1996. The top of the boundary layer is clearly shown. Notice the dry layer at 1.5 km after 08:00 UTC and the upper moist layer between 3.5 and 4 km.

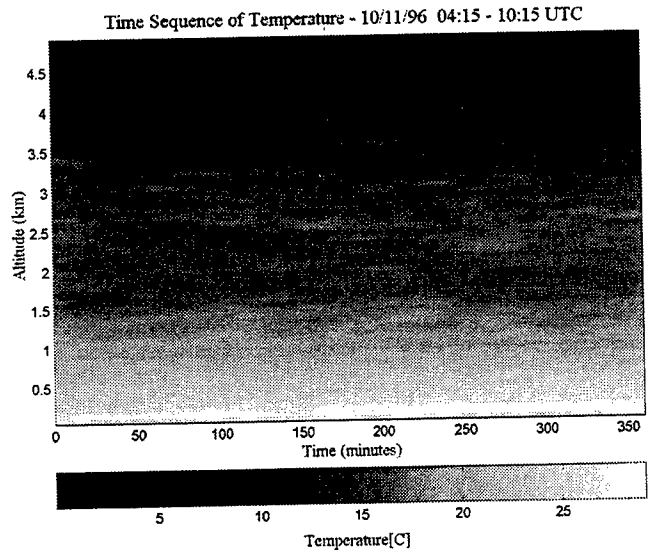


Figure 1 (b). Temperature profiles (C) measured during the same 6 hour period as the water vapor shown above. The temperature profiles show an inversion near 150 meters.

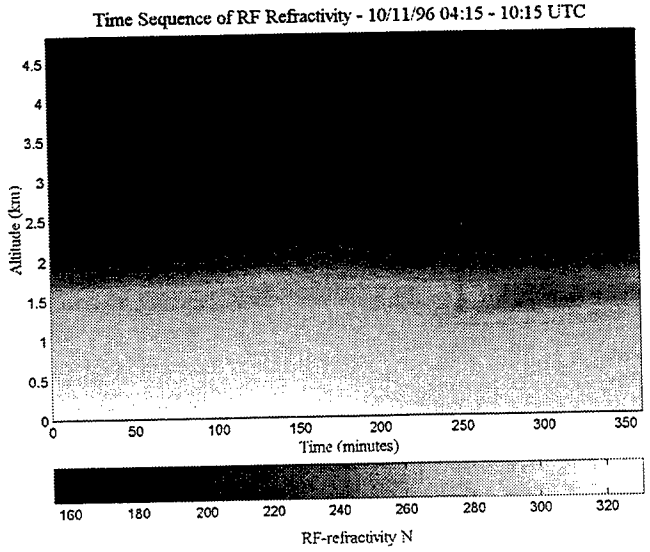


Figure 1 (c). The time sequence of the RF-refractivity profiles calculated directly from the water vapor and temperature profiles measured by the LAPS lidar. The time sequence gives an impression for the changes in refraction. Notice that the dry layer at 1.5 km and the water vapor gradient on the top of the boundary layer cause significant gradients in RF-refraction.

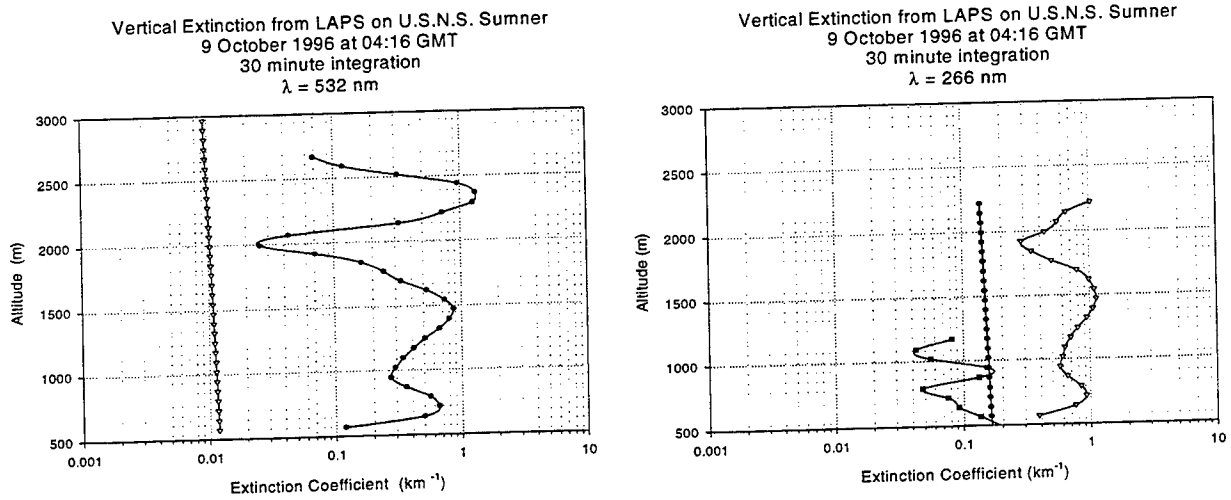


Figure 2. The extinction profiles measured by the LAPS instrument on the *USNS SUMNER* at visible (530 nm) and ultraviolet (285 nm) wavelengths. The profiles show the molecular, aerosol and ozone extinction components.

lidar results have been compared to the results for 97 rawinsonde flights. Several balloon instruments failed to give results, all of those which are available are summarized in Figure 3. The results here are based upon the average value of a ratio of the lidar and balloon data for each flight. The lidar data are taken from the 30 minute integration at the time of the balloon release. Any error in the balloon measurement, difference in the atmosphere between the vertical lidar profile and the balloon location (at times 50 km away by 5 km), or differences due to a changes in the height of a profile sharp gradient have been ignored. The last factor has been found to yield significant differences at times because the balloon data are point measurements during assent while the lidar integrates any effect due to a gradient that moves. The differences observed between the lidar and the sonde result in an average difference of ±4%, which is quite good considering the different measuring conditions. The major differences correspond to a few sondes at times when the visible channels have been effected by exposure to high solar intensity which temporarily shifts the detector gain due to saturation.

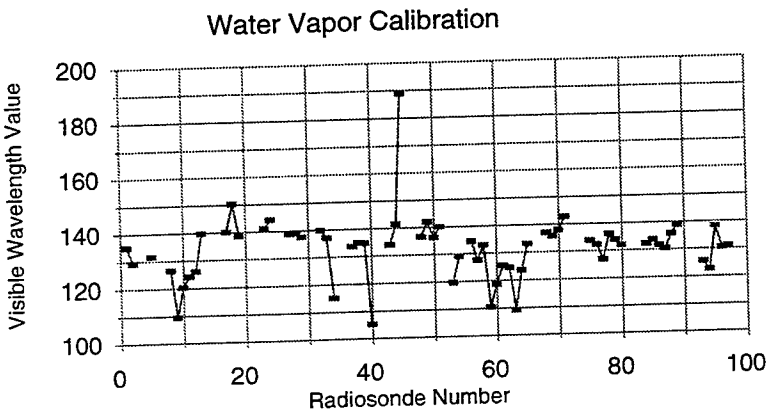


Figure 3. The average ratio of all data points of the lidar and balloons results for water vapor using the visible channels. Each point represents the average for the flight and corresponding lidar profile. A few of the points (for example #45) show the saturation effect from exposure to intense daytime radiation.

CONCLUSIONS AND RECOMMENDATIONS

The LAPS instrument was originally prepared for the Navy as an operational prototype for use on large ships and at shore sites. Many factors make it important to implement this new technology, these include items such as the limited temporal and spatial resolution of sonde measurements, balloon instrument expense and support costs, personnel support requirements, shipboard volume (for storing expendable instruments/helium and preparation of the balloons), pollution from battery acid, radio signal announces ship location, and other factors. The LAPS instrument approach can replace most of the requirements for radiosonde balloons. The lessons learned in the development of the LAPS instrument have provided the basis for an advanced design which will result in a smaller instrument. Planned upgrades should: (1) improve the vertical resolution and dynamic range using new higher speed electronics, (2) improve the detector design to allow automated self calibration, (3) provide capability to measure the wind velocity, and (4) add ability to describe the electro-optical environment.

The frequently large temperature gradients between the surface and the overlying air mass, particularly due to the warmer water surface and cooler overlying air mass lead to development of turbulent convective cells over the water surface. The aerosols generated by the surf, by choppy conditions over the open sea, and the churning propellor during the passage of a ship (IR ship tracks) are entrained in the convective cells. Several investigators in the EOPACE (Electro-Optical Propagation Assessment in the Coastal Environment) project have worked to characterize the physical properties of the aerosols with point measurements of the size, density, and composition [Gathman 1996, Lifkin 1997, Kiser 1996, Kiser 1997]. Understanding of the atmospheric optical properties is critical for use and interpretation of the many operational sensor systems. The lidar investigations are helping to provide the physical understanding of the atmospheric scattering properties which can form a basis for development of tactical decision aids for advanced optical sensor systems.

The LAPS instrument was operated and data obtained on every operation attempted or planned during the period of the sea trial. Investigations of the data show that the instrument was successful in demonstrating the capability to obtain the meteorological data during day and night conditions and in a wide range of weather conditions. The LIDAR system offers the capability to obtain high quality RF ducting prediction data with real time data products and routine update without the use of radiosonde expendables. We expect that the "operational environmental system" of the future will be based upon lidar profiles combined with a mesoscale grid model, which provides the spatial continuity and provides a prediction of short-term and long-term conditions, within constraints imposed by the measured profiles.

ACKNOWLEDGMENTS

The development of the LAPS instrument was supported by the US Navy SPAWAR PMW-185 and ONR and testing was on the *USNS SUMNER* operated by NAVOCEANO. The METOC support for rawinsonde balloons was coordinated by Prof. K. Davidson and LCDR D. Harrison of the Naval Postgraduate School. The LAPS development was possible due to efforts of D.B. Lysak, Jr., T.M. Petach and the engineering staff of the PSU Applied Research Lab. Several graduate students of the PSU Department of Electrical Engineering have contributed much to the LAPS development, particularly P.A.T. Haris, T.D. Stevens and M.D. O'Brien.

REFERENCES

Balsiger, F., and C. R. Philbrick, "Comparison of Lidar Water Vapor Measurements Using Raman Scatter at 266nm and 532 nm," in **Appl. of Lidar to Current Atmos. Topics**, SPIE Vol. 2833, 231-240, 1996a.

Balsiger, F., P. A. T. Haris and C. R. Philbrick, "Lower-tropospheric Temperature Measurements Using a Rotational Raman Lidar," in **Optical Inst. for Weather Forecasting**, SPIE Vol. 2832, 53-60, 1996b.

Gathman, S. G., and Jensen , D. R., "Maptip (Marine aerosol properties and thermal imager performance): Aerosol Characteristics in a Coastal Region", Naval Command, Control and Ocean Surveillance Center, San Diego, CA. RDT and E Div., NTIS ID No.: AD-A300 255, Aug 1995.

Haris, Paul A.T., "Pure Rotational Raman Lidar for Temperature Measurements in the Lower Troposphere," PhD Thesis for Penn State University, Department of Electrical Engineering, August 1995.

Hauchecorne, A., M. L. Chanin, P. Keckhut, and D. Nedeljkovic, "Lidar monitoring of the temperature in the middle and lower atmosphere," Appl. Phys. B55, 29-34, 1992.

Kiser, R. E., "The Generation and Characterization of Surf Zone Aerosols and Their Impact on Naval Electro-Optical Systems", MS Thesis, Naval Postgraduate School, Monterey, CA, December, 1996.

Kiser, R. E., K. L. Davidson ad C. R. Philbrick, "The Generation and Characterization of Surf Zone Aerosols and Their Impact on Naval Electro-Optical Systems," in **Proc. of the Electromagnetic/Electro-Optics Performance Prediction Sym.**, Naval Post Graduate School, Monterey CA, 355-375, June 1997.

Littfin, K. M., and D. R. Jensen, "An Overview of EOPACE (Electrooptical Propagation Assessment in Coastal Environments), Including In Situ and Remote Sensing Techniques", AGARD Conference Proceedings 582, Toulouse, France, pp. 10-1 to 10-8, October 1996.

Nedeljkovic, D., A. Hauchecorne and M. L. Chanin, "Rotational Raman lidar to measure the temperature from the ground to 30 km," IEEE Trans. Geos. Remote Sens. 31, 90-101, 1993.

O'Brien, M.D., T. D. Stevens and C. R. Philbrick, "Optical Extinction from Raman Lidar Measurements," in **Optical Instruments for Weather Forecasting**, SPIE Proceedings Vol. 2832, 45-52, 1996.

Philbrick, C.R. "Lidar Profiles of Atmospheric Structure Properties," in **Earth and Atmospheric Remote Sensing**, SPIE Vol. 1492, 76-84, 1991.

Philbrick, C.R. "Raman Lidar Measurements of Atmospheric Properties," **Atmospheric Propagation and Remote Sensing III**, SPIE Volume 2222, 922-931, 1994.

Philbrick, C.R., and D. W. Blood, "Lidar Measurements of Refractive Propagation Effects," in **Propagation Assessment in Coastal Environments**, NATO-AGARD CP 567, Paper 3, 1995.

Philbrick, C.R., M. D. O'Brien, D, B. Lysak, T. D. Stevens and F. Balsiger, "Remote Sensing by Active and Passive Optical Techniques," **NATO/AGARD Proc Remote Sensing**, AGARD-CP-582, 8.1-8.9, 1996a.

Philbrick C. Russell, and Daniel B. Lysak, Jr., "LIDAR Measurements of Meteorological Properties and Profiles of RF Refractivity," 1996 Battlespace Atmospheric Conference, San Diego CA, December 1996b.

Philbrick, C. Russell, Michael D. O'Brien and Christophe Bas, "Optical Properties of the Lower Atmosphere," 1997 Battlespace Atmospheric Conference, San Diego CA, December 1997a.

Philbrick C. Russell, and Daniel B. Lysak, Jr., "Measurement Capability of the LAPS Lidar," 1997 Battlespace Atmospheric Conference, San Diego CA, December 1997b.

Philbrick, C.R., and D.B. Lysak, Jr., "Atmospheric Optical Extinction Measured by Lidar," in **E-O Propagation, Signature and System Performance Under Adverse Meteorological Conditions**, NATO Sensors & Electronics Technology Panel (SET), Naples, Italy, March 1998.

Rau, Y.-C., "Multi-Wavelength Raman-Rayleigh Lidar for Atmospheric Remote Sensing," PhD Thesis for Penn State University, Department of Electrical Engineering, May 1994.

Stevens, T.D., and C. R. Philbrick, "Particle Size Distributions and Extinction Determined by a Unique Bistatic Lidar Technique," **Proc of IGARSS96 Conf on Remote Sensing for a Sustainable Future** (Int Geophysics and Remote Sensing Sym) at Lincoln NB, May 1996, Vol II pg 1253-1256, 1996a.

Stevens, Timothy D., "Bistatic Lidar Measurements of Lower Tropospheric Aerosols," PhD Thesis for Penn State University, Department of Electrical Engineering, May 1996b.

Whiteman, D.N., S. H. Melfi and R. A. Ferrare, "Raman lidar system for the measurement of water vapor and aerosols in the Earth's atmosphere," Appl. Optics 31, 3068-3082, 1992.

Multiple-frequency Radar Observations of the Atmospheric Boundary Layer

Stephen M. Sekelsky*,Robert E. McIntosh
Microwave Remote Sensing Laboratory
University of Massachusetts at Amherst, Amherst, MA
tel:(413)545-4217, fax:(413)545-4652,e-mail:sekelskyalex.ecs.umass.edu

Warner L. Ecklund
Cooperative Institute for Research in Environmental Sciences (CIRES)
University of Colorado, Boulder, CO

Kenneth S. Gage
National Oceanic and Atmospheric Administration (NOAA)
Aeronomy Laboratory, Boulder, CO

ABSTRACT

Combining radar measurements from microwave and millimeter-wave radars improves discrimination of atmospheric targets in the lower atmosphere. Microwave radars operating at 915 MHz and 2.8 GHz are sensitive to Bragg or 'clear air' scattering caused by variations in the atmospheric index of refraction. These low frequency systems are also sensitive to precipitation, clouds and other non-hydrometeor targets such as birds and insects. Millimeter-wave (MMW) radar systems operating at 33 GHz and 95 GHz are designed to take advantage of the Rayleigh backscatter dependence of small hydrometeors. They are extremely sensitive to clouds, precipitation and insects but not to clear air scattering.

The following sections review Rayleigh and Bragg scattering and present radar measurements at 920 MHz, 2.8 GHz, 33 GHz and 95 GHz collected during the Maritime Continent Thunderstorm Experiment (MCTEX). These data show how millimeter-wave systems enhance the ability of lower frequency systems to identify liquid clouds and drizzle in the boundary layer where reflections from these targets are sometimes overwhelmed by the clear air signal.

BACKGROUND

Several studies have demonstrated the utility of combining measurements at different radar wavelengths to quantify particle size distributions and to classify hydrometeor type. Particle size in ice clouds and precipitation can be measured using 95 GHz and a lower frequency such as 33 GHz or 2.8 GHz, [Sekelsky & McIntosh, 1996;Matrosov, 1993; Sekelsky *et al.*, 1998; Firda *et al.*, 1998]. Multi-wavelength cloud classification has been demonstrated using 33 GHz and 95 GHz [Lohmeier *et al.*, 1997]. Gage has also shown that simultaneous measurements at 920 MHz and 2.85 GHz can differentiate clear air and hydrometeor scattering [Gage *et al.*, 1998].

The frequency dependence of scattering from hydrometeors and from clear air turbulence differ substantially. Scattering from small, Rayleigh-sized particles is proportional to λ^4. Equivalent radar reflectivity is given by:

$$Z_e = \frac{10^{10}\lambda^4}{\pi^5}|K_w|^{-2}\int_0^\infty \xi_b(D,n)D^2N(D)dD, (mm^6m^{-3}). \quad (1)$$

The dimension-less quantity K is given as $K = (n^2-1)/(n^2+2)$, where n is the complex index of refraction and λ[m] is radar wavelength. ξ_b is backscatter efficiency and $N[mm^{-1}m^{-3}]$ is the particle number density as function of particle diameter D[mm]. Note that the dynamic range of the observed reflectivity values is large so reflectivity is often expressed as dBZ_e, where $dBZ_e = 10log(Z_e)$.

Turbulent scattering from the lower atmosphere is dominated by variations in the atmospheric index of refraction. The volume backscatter coefficient for turbulence is given by:

$$\eta = 0.38{C_n}^2\lambda^{-1/3}, (m^2m^{-3}). \quad (2)$$

where ${C_n}^2$ is the turbulence structure parameter. Equivalent radar reflectivity is given as:

$$Z_e = 0.38{C_n}^2 10^{18}\pi^{-5}|K_w|^2\lambda^{11/3}, (mm^6m^{-3}). \quad (3)$$

Table 1 compares ${C_n}^2$ and hydrometer scattering at selected wavelengths. It shows that millimeter-wave radars are very sensitive to clouds but they are not sensitive enough to detect turbulent scattering. Column 2 gives reflectivity for ${C_n}^2 = 10^{-14}$ and column 3 gives the ratio Z/Z_{920MHz}. This shows the relative decrease in equivalent reflectivity for ${C_n}^2$ versus wavelength. Given the sensitivities of current millimeter-wave systems (see Table 2) these calculations show that millimeter-wave systems are incapable of detecting clear air scattering. This assumption is supported by measurements presented in the following section.

Column 4 shows the relative sensitivity of selected wavelengths to distributions of small water droplets. This data is applicable to liquid clouds but not to drizzle or precipitation where non-Rayleigh or Mie scattering may occur. At millimeter-wavelengths differences between measured backscatter and that predicted by the Rayleigh approximation are observed for precipitation and cloud particles [Lhermitte, 1988]. The degree of non-Rayleigh scattering is a measure of effective particle size and is estimated by comparing millimeter-wave reflectivities to those measured at a lower frequency. In general, the smallest measurable particle diameter depends on the shortest radar wavelength used while the largest measurable diameter depends on the longest wavelength used.

RESEARCH ACCOMPLISHED

Microwave and millimeter-wave sensors operating at 920 MHz, 2.8 GHz, 33 GHz and 95 GHz were fielded by the University of Massachusetts and the NOAA Aeronomy Laboratory during the Maritime Continent Thunderstorm Experiment (MCTEX). MCTEX was

Table 1: Comparison of scattering from $C_n{}^2$ and hydrometeors. Note that $|K_w|^2 = 0.93$ for data in the fourth column.

Wavelength/frequency	dBZe ($C_n{}^2 = 10^{-14}$	$10log(Ze/Ze_{920MHz})$ ($C_n{}^2 = 10^{-14}$)	$10log(Ze/Ze_{920MHz})$ (small hydrometeors)
32.6 cm/ 920 MHz	-6.6 dBZe	0 dB	0 dB
10.7 cm/ 2.8 GHz	-24.3 dBZe	-17.7 dB	19.3 dB
0.95 cm/ 33.12 GHz	-63.7 dBZe	-57.1 dB	62.3 dB
0.32 cm/ 94.92 GHz	-80.2 dBZe	-73.8 dB	80.5 dB

Table 2: Radar parameters.

	UMass W-band	UMass Ka-band	NOAA S-band	NOAA UHF
Frequency (GHz)	94.92	33.12	2.835	920 MHz
Transmit Polarization	V or H	V or H	V	V
Receiver Polarization	V and H	V and H	V	V
Peak Power (kW)	1.5	120.	0.38	0.5
Antenna	1 m lens	1 m lens	3 m dish with shroud	microstrip phased-array
Two-way 3dB Antenna Beamwidth (deg)	0.2	0.6	3.2	6.4
Range Resolution (m)	30,75	30,75	105,495	105,495
Minimum Detectable Reflectivity (dBZe) (R=1km, 30 sec averaging)	-59	-63	-40	-18

conducted on the Tiwi Islands north of Darwin Australia during the annual transition from dry to wet seasons late in 1995. Table 2 lists relevant system parameters for these systems. Additional hardware details can be found in [Sekelsky & McIntosh, 1996] and [Ecklund *et al.*, 1998].

Figure 1 shows observations collected on December 6 with the UMass and NOAA radars. All radar systems detect precipitation at **A** and and the deep ice cloud **B**, which is above **A**. The 920 MHz system does not detect the continuous layer **C** between 8 km and 13 km. This is not surprising since the 920 MHz system is least sensitive to hydrometeors. The 920 MHz and 2.8 GHz radars see a strong boundary layer return below 4km (**D**). The 33 GHz and 95 GHz systems see only a few scattered targets in this region. Depolarization data (not shown) confirms that these are insects. Because the clear air signal is so strong it is unclear whether the microwave radars detect the liquid cloud **E** and light drizzle **F** seen by the millimeter-wave systems.

Figure 2a shows boundary layer detail at 33 GHz corresponding to the dashed region in Fig. 1. Figs. 2b and 2c plot horizontal cuts of dBZe at 926m and 3.55 km for all radar wavelengths. The difference between precipitation and clear air scattering at 920 MHz and 2.8 GHz is obvious in both Figs. 2b and 2c. While dBZe values for hydrometeors are nearly identical, dBZe values for clear air scattering differ by nearly 18 dB. This difference is reduced when hydrometeor echoes are weak.

Figure 2b shows that clear air scattering overwhelms the return from the liquid cloud. Neither the 920 MHz radar nor the 2.8 GHz radar detect it. Clear air scattering also dominates the 920 MHz return from the drizzle in Fig. 2b ($R_r \approx 0.05mm/hr$) and the virga identified in Fig. 2c. Both the 920 MHz and 2.8 GHz systems identify the drizzle in Fig. 2c at 3.55 km. At this height the clear air return is reduced and the drizzle return is increased ($R_r \approx 0.1mm/hr$) . Note that only Doppler moment data has been shown. Full spectra data may allow separation of clear air and drizzle returns. However, it is doubltful that full spectra data could differntiate between liquid clouds and clear air scattering.

Mie scattering is also apparent in the precipitation centered near the one hour hash marks in Figs. 2b and 2c. Peak rain rates are 3-4 mm/hr and differences between 95 GHz reflectivity and that from the other frequencies are substantial in the precipitation. While a portion of this difference is due to differential water vapor absorption and hydrometeor extinction. When attenuation is removed these differences can be related to rain rate[Lhermitte, 1987; Sekelsky & McIntosh, 1996; Firda *et al.*, 1998].

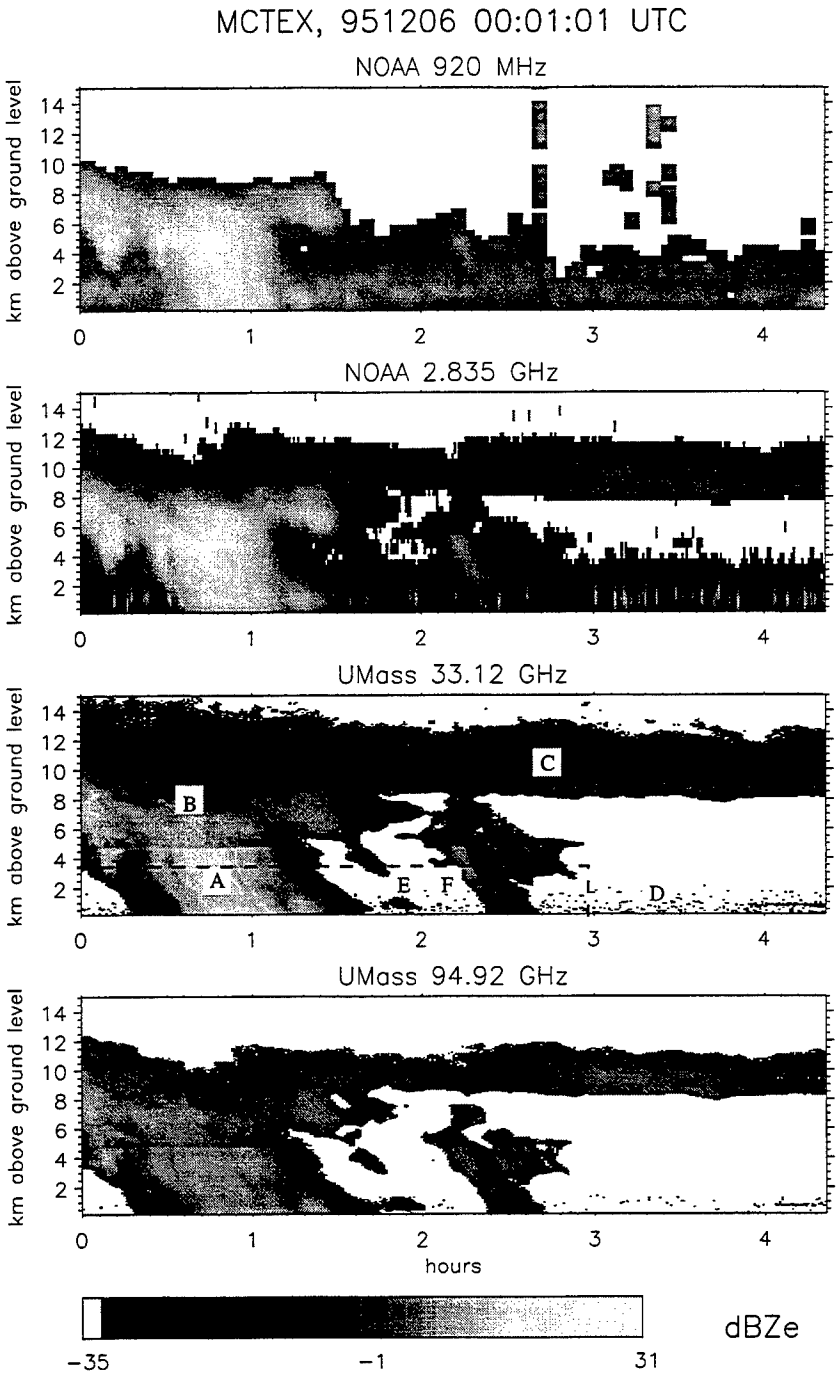


Figure 1: UMass and NOAA radar observations from MCTEX.

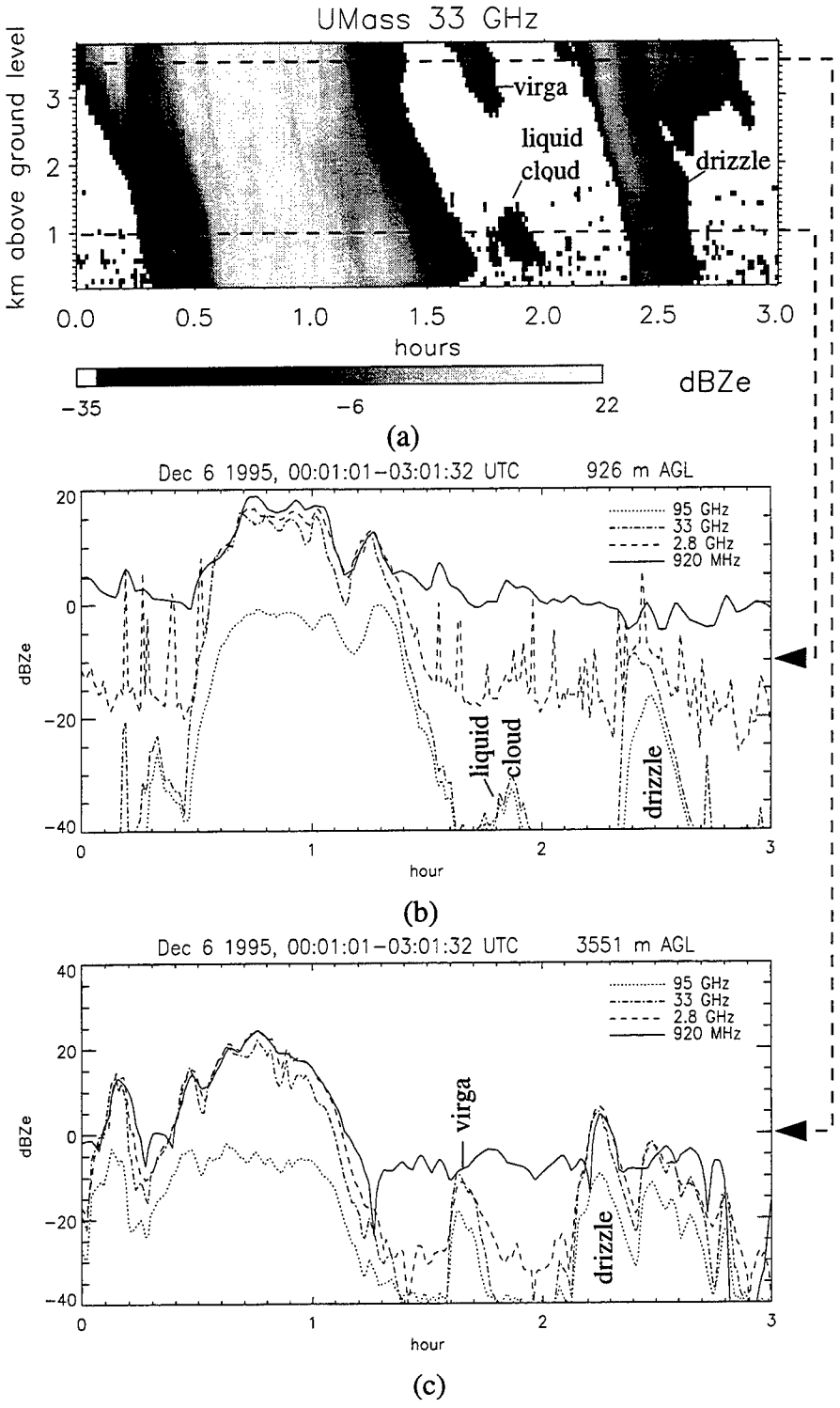


Figure 2: Detail of boundary layer measured at 33 GHz(a) corresponding to dashed box in Figure 1. Horizontal cuts at (a) 926 m and (b) 3.55 km.

REFERENCES

Ecklund, W.L., Williams, C.R., Johnston, P.E., & Gage, K.S. 1998. A 3 GHz Profiler for Precipitating Cloud Studies. *Journal of Atmospheric and Oceanic Technology*, submitted.

Firda, J.M., Sekelsky, S.M., & McIntosh, R.E. 1998. Application of Dual-Frequency Millimeter-wave Doppler Spectra for the Retrieval of Drop Size Distributions and Vertical Air Motions in Rain. *Journal of Atmospheric and Oceanic Technology*, accepted for publication.

Gage, K.S., Williams, C.R, Ecklund, W.L., & Johnston, P.E. 1998. Use of Two Profilers During MCTEX for Unambiguous Identification of Bragg Scattering and Rayleigh Scattering. *Journal of the Atmospheric Sciences.* accepted for publication.

Lhermitte, R. M. 1987 (Sept). *Observations of Stratiform Rain with 94 GHz and S-band Doppler Radar.* Tech. rept. AFGL-TR-0268. Air Force Geophysics Laboratory. ADA192013

Lhermitte, R. M. 1988. Cloud and precipitation remote sensing at 94 GHz. *IEEE Trans. Geosci. Remote Sens.*, **26**, 207–216.

Lohmeier, S. P., Sekelsky, S. M., Firda, J. M., Sadowy, G. A., & McIntosh, R. E. 1997. Classification of particles in stratiform clouds using the 33 and 95 GHz polarimetric cloud profiling radar system. *IEEE Transactions on Geoscience and Remote Sensing*, **35**(2), 256–270.

Matrosov, S. Y. 1993. Possibilities of cirrus particle sizing from dual-frequency radar measurements. *Journal of Geophysical Research*, **98**(11N), 20675–20683.

Sekelsky, S. M., & McIntosh, R. E. 1996. Cloud Observations with a Polarimetric 33 GHz and 95 GHz radar. *Meteorology and Atmospheric Physics*, **58**, 123–140.

Sekelsky, S.M., Ecklund, W.L., Firda, J.M., Gage, K.S., & McIntosh, R.E. 1998. Particle size estimation in ice-phase clouds using radar reflectivity measurements collected at 95 GHZ, 33 GHZ and 2.8 GHZ. *Journal of the Applied Meteorology.* accepted for publication.

BATTLESPACE FORECASTING OF AVIATION ICING HAZARDS

Steven J. Walter*, Philip I. Moynihan
Jet Propulsion Laboratory, California Institute of Technology
Pasadena, CA 91109
Mail Stop 246-101 (Walter)
Telephone: (818) 354-1626 (Walter)
Fax: (818) 354-4341 (Walter)
Email: steven.j.walter@jpl.nasa.gov

ABSTRACT

Aircraft icing endangers aviators, restricts surveillance opportunities, and reduces combat effectiveness. During freezing conditions, clouds and precipitation can contain appreciable amounts of subfreezing liquid water. Aircraft traversing these clouds accumulate ice as supercooled liquid freezes to the wings and airframe. Ice accretion can be very rapid compromising the aerodynamics of the wings and propellers, as well as adding weight and increasing drag.

Advanced warning of weather hazards posed by existing and impending meteorological conditions would allow commanders and aviators to develop mitigation strategies. The resolution and accuracy of forecast of in-flight and ground icing are currently limited by a lack of data on cloud and precipitation phase (liquid or ice), cloud temperature, and cloud droplet or raindrop size. Active systems such as short-wavelength radars, lidars, and passive sensors such as microwave radiometers and in-situ meteorological probes can provide these data. These sensors can be packaged into lightweight, compact, low-power units that could be deployed on the ground or on airborne platforms. When coupled with state-of-the-art retrieval algorithms, these sensors would improve the reliability and timeliness of regional weather forecasts. It is even feasible to develop an integrated field system for forecasting in-flight and ground aviation icing hazards.

INTRODUCTION

In-flight and ground aircraft icing presents a serious hazard for military aviation. Improved forecasting capability would provide important tactical and strategic advantages during mid-latitude winter and year-round polar operations. The ability to accurately forecast icing hazards is an essential component in enhancing safety and mission effectiveness during in-flight and ground icing conditions.

Aviation hazards can be managed with information. Improvements in the capability to characterize clouds and precipitation will lead to improvements in the reliability and effectiveness of icing forecasts and nowcasts [*Stack*, 1996; *Ryerson*, 1996]. The techniques needed to achieve an advanced level of cloud sensing capability have already been developed. In fact, many of the

technologies have been used in icing research for more than a decade. Implementing improvements in cloud and precipitation detection, identification, and characterization are essential for advancing current measurement capabilities beyond the use of data to mitigate adverse weather. In the future, this capability will allow adverse weather to be exploited to obtain a strategic advantage.

ICING METEOROLOGY

Freezing rain and freezing drizzle are usually responsible for creating ground and in-flight icing conditions. A frequent scenario for generating freezing precipitation occurs when rain falls from a warm zone into an underlying subfreezing region. [*AOPA*, 1994] These conditions are common near the edge of a cold front. As liquid precipitation traverses the subfreezing region, it supercools, but does not freeze due to the lack of condensation nuclei. Icing conditions are also common in winter storms where there is a boundary separating frozen precipitation (snow) from liquid precipitation (rain) as illustrated in Figure 1. Non-precipitating clouds also can pose serious icing hazards. Rapid cooling of cloud liquid near the border of a front can also create large reservoirs of supercooled liquid. It is the presence of supercooled liquid that poses a threat to aircraft.

The hazard associated with freezing precipitation and supercooled cloud liquid is a function of the liquid density, drop size distribution, ambient temperature, and aircraft-specific characteristics. The abundance of supercooled liquid water is usually the most important parameter for forecasting icing hazards. Liquid density determines the reservoir of liquid available for accretion. [*AOPA*, 1994]. Drop size also affects the level of hazard. Large droplets (droplets with diameters > 50 μm) are more likely to flow backward along the wing where they can freeze aft of ice protection systems [*Al-Khalil*, 1996].

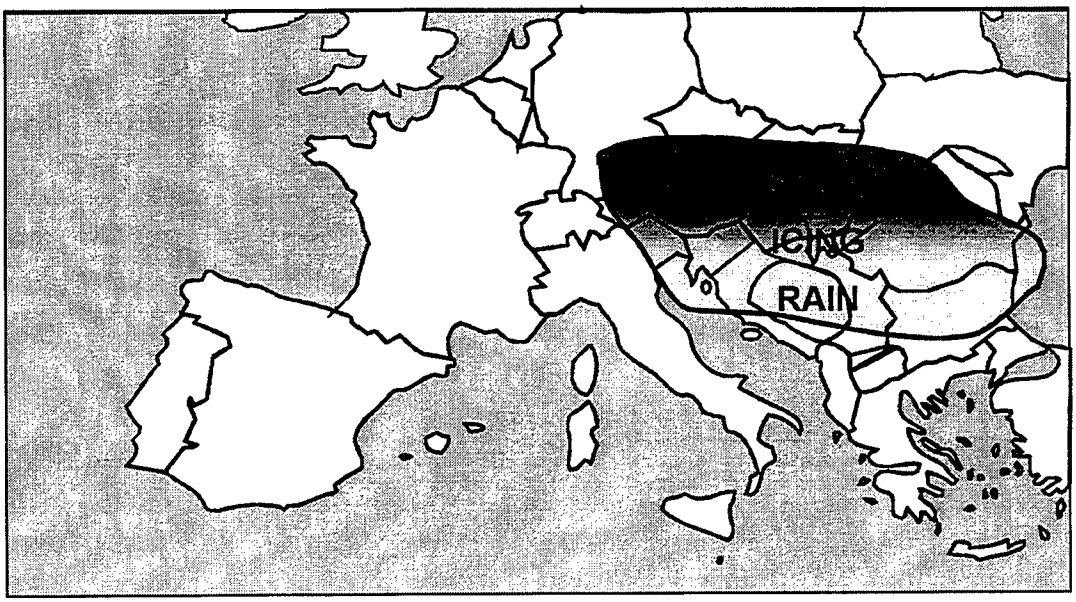


Figure 1. *In-flight and surface icing conditions often occur in a winter storm's transition zone that separates the region of snowfall from the region of rain.*

AVIATION HAZARDS

Ice accretion primarily affects aircraft performance by changing the aerodynamics of the wings and propellers. Icing also increases the weight of the airframe, increases drag, and can disable control surfaces. On occasion, ice being shed from the airframe can impact and damage adjacent aircraft structures. The rate at which ice accumulates depends on meteorological conditions and aircraft-specific characteristics. The exposure duration is an important factor in assessing the severity of the hazard because lengthening the exposure time increases the mass of accreted ice.

Aircraft that tend to fly at lower altitudes where icing conditions occur most frequently and also tend to operate close to their performance margins are most susceptible to icing. These classes of aircraft include helicopters, piston-engine airplanes, turboprops, and remotely piloted vehicles. Smaller aircraft and helicopters are often not certified to fly in icing conditions and are therefore not equipped with deicing systems. This puts them at greater risk when they encounter unforecasted icing conditions. Ryerson [1996] provides a brief review of how icing affects military air operations.

SENSOR TECHNOLOGY

The choice of sensors requires a systems analysis. Issues affecting a sensor's selection include its contribution to the existing meteorological network, technological maturity, suitability for the intended platform, and its affect on other military systems. In-situ sensors directly sample local meteorology, while remote sensors probe meteorological properties at a distance. Microwave remote sensors usually have an advantage over optical sensors because they can penetrate optically thick clouds and precipitation. Remote sensors can be categorized as active sensors that emit signals and then measure their interaction with the environment and passive sensors that measure natural radiation emitted by the environment. Although active systems usually provide the most complete characterization of the meteorological environment, they also tend to require more power, are harder to conceal, are more expensive, and are more likely to interfere with other C^3I systems. The choice of sensors requires optimizing system needs, cost, and logistical requirements

Sensors for improving icing forecasts have already been developed [*Stankov et al.*, 1995; *Han and Westwater*, 1995] and many are commercially available. However, there are two areas where targeted research and development would yield significant benefit. Considerable value could be derived from re-engineering the existing research instrumentation. Scientific sensors developed with a design emphasis that maximized capability, accuracy, and operational flexibility should be redesigned with a focus on developing an application-specific design, increasing reliability, improving automation, and reducing cost. R&D is also needed to develop advanced airborne sensors to detect and forecast icing. Commercial airborne sensors currently detect ice formation with acoustic, optical, and impedance probes. The next generation of sensors will likely measure meteorological parameters and estimate the icing rate prior to ice forming on the aircraft. This approach will give aviators additional time to formulate effective avoidance and mitigation strategies.

There are several methods used to measure cloud temperature. In-situ temperature probes measure cloud temperature directly. In-situ probes require transport on an aircraft or balloon and

telemetry to downlink the signal. Temperature probes are currently carried on some commercial airplanes and routinely measure the temperature profile near major airports. As an alternative, IR radiometers are often used to retrieve cloud base temperature. They measure the infrared brightness of the cloud base and derive cloud base temperature from the measured radiance.

Atmospheric temperature profiles can be measured in the presence of clouds with microwave radiometry, radio-acoustic sounding, and in-situ measurements. A microwave radiometric temperature profiler is a sensitive radio receiver tuned to the 60 GHz emissions of molecular oxygen. The radiance of oxygen emissions depends on temperature. Measurements made at several frequencies and elevation angles will yield the temperature profile. Radio acoustic sounding systems (RASS) are active sensors that transmit a powerful acoustic pulse and track its upward propagation with a VHF radar. Since the acoustic velocity is a sensitive function of temperature, the temperature profile is retrieved from the acoustic pulse propagation velocity. RASS provides higher resolution than microwave temperature profilers, although they are much more expensive, noisy, and require orders of magnitude more power and area to operate. RASS are not easily adaptable to airborne platforms, whereas airborne radiometers are routinely used on NASA aircraft to profile temperature.

Cloud temperature is retrieved from the temperature profile with a simultaneous determination of cloud altitude using a Ka-band radar, lidar, ceilometer, or in-situ sensor. While a lidar is a laser radar, a ceilometer is a simple lidar designed to measure only vertical cloud base altitude. High-power lidars can penetrate multiple cloud layers. However, Ka-band radars are often preferred because they can penetrate much thicker clouds with comparable signal power. In-situ balloon-borne, capacitive and resistive humidity sensors are routinely used to identify cloud height. Detecting cloud height with in-situ humidity sensors has limited utility because it infers cloud occurrence from humidity. This creates a bias because the humidity at which clouds form and sublimate spans a range of humidities and therefore can not be accurately predicted using a humidity threshold [*Gaffen and Elliott*, 1993].

Dual polarization radars, lidars, and microwave radiometers can determine cloud phase (ice or liquid). Polarization sensitive measurements discriminate between ice and liquid hydrometeors by providing sensitivity to the scattering particle height-to-width aspect ratio. As an ice crystal melts, its aspect ratio changes, altering the ratio of reflection cross-sections at each orthogonal polarization. Since radar reflectivity depends on both drop size and total water content, single-frequency radars, alone, are unable to independently determine liquid content. However, research is underway to develop the use of dual-frequency radars to retrieve liquid content [*Reinking et al.*, 1996]. Lidars are limited in range due to hydrometeor-induced attenuation. Liquid-sensing microwave radiometers are sensitive radio receivers tuned to the continuum emissions of liquid water in the 30 GHz and/or 90 GHz atmospheric windows. The radiance of a cloud is proportional to the columnar liquid content. Microwave radiometers can discriminate between ice and water because the dielectric constant of ice is two orders of magnitude smaller than that of liquid and is therefore "transparent" to the radiometer. Thus, clouds or precipitation that emit significant amounts of microwave radiation must contain liquid. Although radiometers do not provide distance information, they have an advantage in some applications because they are passive and much less expensive than radars and lidars. Combining radars and radiometers can be a very powerful strategy because it allows cloud liquid to be profiled [*Stankov et al.*, 1995; *Han and Westwater*, 1995].

In-situ sensors are very effective at determining the phase of precipitation and cloud water. For ground-based applications, rain gauges can differentiate between snow and rain. Supercooled liquid precipitation can be detected with a vibrating wire or rod [*Hill*, 1994]. Supercooled liquid freezes to the wire or rod, thereby changing the vibrating mass. The associated shift in resonant frequency signals the presence of supercooled liquid. Vibrating wires and rods are used in ground-based stations and have been flown on radiosondes.

Characteristics such as drop size and liquid water content can be inferred by combining microwave radiometers with radars. Drop size and liquid water content can also be retrieved using lidars. In-situ instruments are able to resolve the drop-size spectrum and liquid content by measuring the intensity and angular distribution of light scattered by an atmospheric sample [*Lawson and Cormick*, 1995]. Ground-based systems that record light scattering along a short atmospheric path can be used to retrieve information on the drop size distribution and thermodynamic phase by determining the precipitation rate of descent.

Generating a detailed picture of icing-hazards on a regional scale requires a systems approach. Advanced warning of icing hazards requires enhanced surveillance using a variety of measurement techniques from multiple locations. These data need to be rapidly integrated into a regional forecast model. The forecasts, in turn, need to be promptly disseminated to users in a format that highlights possible impacts to air systems, operations, and maneuvers. It is the combination of enhanced surveillance, improved modeling, integrated information systems, and reliable communications that can extend the time available to effectively mitigate the hazard, or avoid it altogether.

CONCLUSIONS

Advanced warning of freezing precipitation and supercooled cloud liquid is needed to improve the safety, reliability, and effectiveness of air operations. This can be achieved by improving the capability of the existing meteorological observational network to characterize clouds and precipitation. Technology exists that can provide a more complete picture of clouds and precipitation such as short-wavelength radars, microwave radiometers, and in-situ meteorological probes. These ground-based and airborne sensors will improve the capability of regional forecast models to provide accurate, timely forecasts of hazards. The resulting improvements in forecasts will provide commanders, aviators, and aviation support functions with additional time to formulate plans to mitigate and possibly exploit impending weather hazards. Additionally, these measurement systems can be engineered to be quite compact and low cost. Integrating autonomous and networked sensors into the meteorological sensor network is an essential strategy for enhancing the accuracy of forecasting aviation icing hazards.

ACKNOWLEDGMENTS

The research described in this paper was partially carried out by the Jet Propulsion Laboratory, California Institute of Technology, under a contract with the National Aeronautics and Space Administration.

REFERENCES

Al-Kahlil, K., "The formation of an ice ridge beyond protected regions," *Proc. FAA Int.Conf. on Aircraft In-Flight Icing, Vol. II* (Tech Rep. **DOT/FAA/AR-96/81,II**), p. 285, (1996).

AOPA, "AOPA's Aviation USA," Ed. M. R. Twombly, Aircraft Owners and Pilot's Association, (1994.)

Gaffen, D. J., W. P. Elliott, "Column Water Vapor Content in Clear and Cloudy Skies," *Jour. Of Climate*, **6**, p. 2278, (1993).

Han, Y. and E. R. Westwater, "Remote Sensing of Tropospheric Water Vapor and Cloud Liquid Water by Integrated Ground-Based Sensors," *Jour. Of Atmos. and Oceanic Tech.*, **12**, p. 1050, (1995).

Hill, G. E., "Analysis of Supercooled Liquid Water Measurements Using Microwave Radiometer and Vibrating Wire Devices," *Jour. Of Atmos. and Oceanic Tech.*, **11**, p. 1242, (1994).

Lawson, R. P., R. H. Cormack, "Theoretical design and preliminary tests of two new particle spectrometers for cloud microphysics research," *Atmos. Res.*, **35**, p. 315, (1995).

Stack. D, "In-flight Icing – The Critical Need for Improved Forecasts and Indexing of the Hazard," *Proc. FAA Int.Conf. on Aircraft In-Flight Icing, Vol. II* (Tech Rep. **DOT/FAA/AR-96/81,II**), p. 297, (1996).

Stankov, B., B. Martner, M. Politovich, "Moisture Profiling of the Cloudy Winter Atmosphere Using Combined Remote Sensors," *Jour. Of Atmos. and Oceanic Tech.*, **12** , p. 488, (1994).

Reinking R. F., S. Y. Matrosov, B. E. Martner, R. A. Kropfli, "Differentiation of Freezing Drizzle from Ice Hydrometeors and Freezing Rain with Dual Polarization Radar," *Proc. FAA Int.Conf. on Aircraft In-Flight Icing, Vol. II* (Tech Rep. **DOT/FAA/AR-96/81,II**), p. 331, (1996).

Ryerson, C., "Remote Detection and Avoidance of In-flight Icing," *Proc. FAA Int.Conf. on Aircraft In-Flight Icing, Vol. II* (Tech Rep. **DOT/FAA/AR-96/81,II**), p. 179, (1996).

This page intentionally left blank.

Co-Sponsors

Air Force Research Laboratory
Hanscom AFB, MA

Space and Naval Warfare Systems Center
San Diego, CA

Army Research Laboratory
Adelphi, MD